frontiers | Research Topics

Advanced oral disease therapy: Approaches, biotechnology, and bioactive materials, volume II

Edited by
Xing Wang, Hai Zhang, Xianqi Li, Jianyun Zhang and Yuan Yin

Published in
Frontiers in Bioengineering and Biotechnology

ISSN 1664-8714
ISBN 978-2-8325-4620-8
DOI 10.3389/978-2-8325-4620-8

About Frontiers

Frontiers is more than just an open access publisher of scholarly articles: it is a pioneering approach to the world of academia, radically improving the way scholarly research is managed. The grand vision of Frontiers is a world where all people have an equal opportunity to seek, share and generate knowledge. Frontiers provides immediate and permanent online open access to all its publications, but this alone is not enough to realize our grand goals.

Frontiers journal series

The Frontiers journal series is a multi-tier and interdisciplinary set of open-access, online journals, promising a paradigm shift from the current review, selection and dissemination processes in academic publishing. All Frontiers journals are driven by researchers for researchers; therefore, they constitute a service to the scholarly community. At the same time, the *Frontiers journal series* operates on a revolutionary invention, the tiered publishing system, initially addressing specific communities of scholars, and gradually climbing up to broader public understanding, thus serving the interests of the lay society, too.

Dedication to quality

Each Frontiers article is a landmark of the highest quality, thanks to genuinely collaborative interactions between authors and review editors, who include some of the world's best academicians. Research must be certified by peers before entering a stream of knowledge that may eventually reach the public - and shape society; therefore, Frontiers only applies the most rigorous and unbiased reviews. Frontiers revolutionizes research publishing by freely delivering the most outstanding research, evaluated with no bias from both the academic and social point of view. By applying the most advanced information technologies, Frontiers is catapulting scholarly publishing into a new generation.

What are Frontiers Research Topics?

Frontiers Research Topics are very popular trademarks of the *Frontiers journals series*: they are collections of at least ten articles, all centered on a particular subject. With their unique mix of varied contributions from Original Research to Review Articles, Frontiers Research Topics unify the most influential researchers, the latest key findings and historical advances in a hot research area.

Find out more on how to host your own Frontiers Research Topic or contribute to one as an author by contacting the Frontiers editorial office: frontiersin.org/about/contact

Advanced oral disease therapy: Approaches, biotechnology, and bioactive materials, volume II

Topic editors

Xing Wang — Shanxi Medical University, China
Hai Zhang — University of Washington, United States
Xianqi Li — Matsumoto Dental University, Japan
Jianyun Zhang — Peking University Hospital of Stomatology, China
Yuan Yin — Fourth Military Medical University, China

Citation

Wang, X., Zhang, H., Li, X., Zhang, J., Yin, Y., eds. (2024). *Advanced oral disease therapy: Approaches, biotechnology, and bioactive materials, volume II*. Lausanne: Frontiers Media SA. doi: 10.3389/978-2-8325-4620-8

Table of contents

frontiers | Frontiers in Bioengineering and Biotechnology

TYPE Editorial
PUBLISHED 06 March 2024
DOI 10.3389/fbioe.2024.1391548

OPEN ACCESS

EDITED AND REVIEWED BY
Hasan Uludag,
University of Alberta, Canada

*CORRESPONDENCE
Xing Wang,
kqwx100@163.com

RECEIVED 26 February 2024
ACCEPTED 28 February 2024
PUBLISHED 06 March 2024

CITATION
Zhang X, Li X, Yin Y, Zhang J, Zhang H and Wang X (2024), Editorial: Advanced oral disease therapy: approaches, biotechnology, and bioactive materials, volume II.
Front. Bioeng. Biotechnol. 12:1391548.
doi: 10.3389/fbioe.2024.1391548

Editorial: Advanced oral disease therapy: approaches, biotechnology, and bioactive materials, volume II

Xiaoxuan Zhang[1], Xianqi Li[2], Yuan Yin[3], Jianyun Zhang[4], Hai Zhang[5] and Xing Wang[1]*

[1]Shanxi Medical University School and Hospital of Stomatology, Taiyuan, China, [2]Department of Oral and Maxillofacial Surgery, Matsumoto Dental University, Shiojiri, Japan, [3]State Key Laboratory of Military Stomatology, Department of Periodontology, Fourth Military Medical University, Xi'an, China, [4]Department of Oral Pathology, Peking University School and Hospital of Stomatology, Beijing, China, [5]Department of Restorative Dentistry, University of Washington, Seattle, WA, United States

KEYWORDS

biotechnology, bioactive materials, antibacterial, orthodontic, bone defects, diagnosis

Editorial on the Research Topic
Advanced oral disease therapy: approaches, biotechnology, and bioactive materials, volume II

Introduction

In recent years, notable advancements have been made in the research and utilization of biomaterials within the field of dentistry. These developments hold great promise in addressing various dental issues such as defects, bone-related concerns, tumors, infections, and other related conditions. Biomaterials possessing drug delivery capabilities have the potential to modulate cell proliferation and suppress bacterial growth. They play a crucial role in the restoration of defects in hard tissue like teeth and bones, as well as in the management of infected wounds. Simultaneously, investigations into disease mechanisms offer the potential for the development of novel therapeutic interventions.

Antibacterial property of dental materials

The presence of bacteria in the oral cavity can lead to dental caries and peri-implantitis. The antibacterial properties of biomaterials are crucial.

Efficiently eliminating dental plaque from implant surfaces has emerged as a critical concern that requires immediate attention in the realm of disease prevention and treatment around implants. With the advancement of materials and pharmacology, extensive research has been undertaken to improve the antibacterial efficacy of implants. This includes the application of antibacterial coatings on implant surfaces, adjusting the surface morphology of implants, and developing new implant materials. The research on surface modification of

implants and enhancing their antibacterial properties is reviewed by Zhai et al., providing theoretical basis for the prevention of diseases around implants in the future. In the samples of periimplantitis lesions, there was a significant increase in M1 macrophages to pro-inflammatory. In order to better understand the pathogenesis of periimplantitis, the review by Li et al. summarizes research related to macrophage polarization in periimplantitis, and proposes potential immunomodulatory treatment options for periimplantitis. Li et al. designed a novel biomimetic nano-morphology coating on the surface of titanium-based implants with antibacterial copper by combining plasma electrolytic oxidation and hydrothermal treatment. The biological interaction between the coating and stem cells promotes cell adhesion, diffusion, and proliferation during the initial attachment process, and this new coating reduces the activity of mixed bacteria (*Fusobacterium* nucleatum and Porphyromonas gingivalis).

In terms of tooth hard tissue infectious diseases, Qu et al. reviewed the anti-caries application of chitosan, and focused on classifying and summarizing the characteristics of chitosan as a caries-prevention material, including its antibacterial effect, biomimetic mineralization, and the delivery ability of caries-prevention drugs and vaccines.

The insufficient corrosion resistance and antibacterial performance of fixed orthodontic devices lead to enamel demineralization. Chen et al. constructed a uniform and dense polydopamine graphene oxide nanocoating on nickel-titanium (NiTi) archwires by self-assembly, reducing Ni dissolution in NiTi alloys and exhibiting antibacterial activity against *streptococcus* mutans.

In the case of a skin infection resulting from the presence of biofilm, Li et al. developed a hydrogel containing the active ingredient berberine hydrochloride liposomes to destroy the biofilm, thus accelerating the healing of infected wounds in mice.

Biomaterial for regeneration of bone defects

Biomaterial must adhere to stringent criteria for the reconstruction of bone defects in the craniomaxillofacial region. It necessitates adequate support and surface porosity to facilitate cell attachment and vascular growth. Additionally, the material should possess bone induction and conduction capabilities to encourage the crawl and growth of adjacent bone tissue. Metal materials have become important bone scaffold materials with advantages of support and plasticity. Zhang et al. used a 3D printing technology to produce porous tantalum scaffolds, and then constructed the nano-morphology of the scaffold surface through alkali heat treatment with NaOH solution and hydrothermal treatment in deionized water. The tantalum scaffold has promoted the proliferation and osteogenic differentiation of BMSCs and accelerated the formation of new bone in the mandibular defect angle of rabbits, achieving rapid bone integration. Compared with Ti_6Al_4V, tantalum has better mechanical properties, osteogenic ability, and microstructure, becoming a potential alternative material for bone repair. Large-area bone defects are often accompanied by loss of surrounding soft tissue. 3D printing-assisted fibula osteoseptocutaneous flap combined with antagonistic thick flaps is used to repair a wide range of composite defects. Xu et al. evaluated the repair capacity and patient satisfaction of this treatment, elaborated on the advantages and challenges of the method, and provided a basis for the selection of clinical surgical treatment.

Research for orthodontic aligners

Orthodontic clear aligners have gained popularity among the general population because of their aesthetic appeal; however, there is a lack of evidence regarding the mechanical performance of transparent braces in the oral cavity. Cintora-López et al. investigated the effects of temperature and load on the deformation of aligners. Mechanoluminescent materials provide the possibility for visualizing stress changes. A bite splint was prepared by mixing phosphors with polydimethylsiloxane, which can establish the relationship between mechanical force and light signal. Zhang et al. evaluated the biological safety of bite splints mixed with $BaSi_2O_2N_2$ phosphors in order to explore the possibility for clinical application.

Diagnosis and treatment of oral tumors and immune diseases

Early detection of various oral diseases, including tumors, is advantageous for predicting outcomes. Currently, an accurate diagnosis depends on tissue biopsy, a highly invasive surgical procedure with limited timeliness. Extracellular vesicles participate in intercellular communication, promote disease progression, and reflect the location and status of lesions. The review by Zhang et al. discusses the involvement of extracellular vesicles in the diagnosis, development, and treatment of oral squamous cell carcinoma (OSCC), providing new insights for the diagnosis and treatment of OSCC. Sjogren's syndrome is an autoimmune disease characterized by the destruction of salivary glands (SG), leading to loss of secretion function and the presence of focal lymphocyte infiltration in the SG. Hasegawa et al. used effective monocytes to inhibit lymphocyte infiltration and alleviate SG damage in Sjögren syndrome.

Conclusion

With the advancement of technology, the utilization of biomaterials in oral diagnosis and treatment is progressively expanding, offering a wider range of functionalities. Various tools and materials, such as scaffolds designed with osteogenic properties, aligners capable of detecting mechanical changes, dental filling materials for treating caries, and substances with antibacterial properties, are utilized to address issues in the intricate oral microenvironment. The ongoing advancement of research into the pathogenesis of oral diseases will enhance the precise and prompt diagnosis and treatment of oral conditions.

Author contributions

XZ: Writing–original draft. XL: Writing–review and editing. YY: Writing–review and editing. JZ: Writing–review and editing. HZ: Writing–review and editing. XW: Writing–original draft, Writing–review and editing.

Funding

The author(s) declare that no financial support was received for the research, authorship, and/or publication of this article.

Conflict of interest

The authors declare that the research was conducted in the absence of any commercial or financial relationships that could be construed as a potential conflict of interest.

Publisher's note

frontiers | Frontiers in Bioengineering and Biotechnology

TYPE Original Research
PUBLISHED 24 April 2023
DOI 10.3389/fbioe.2023.1144624

OPEN ACCESS

EDITED BY
Xianqi Li,
Matsumoto Dental University, Japan

REVIEWED BY
Xiangxiang Hu,
The Ohio State University, United States
Mohammad A. Alfhili,
King Saud University, Saudi Arabia

*CORRESPONDENCE
Yoshinori Sumita,
y-sumita@nagasaki-u.ac.jp

†These authors have contributed equally to this work and share first authorship

RECEIVED 14 January 2023
ACCEPTED 14 April 2023
PUBLISHED 24 April 2023

CITATION
Hasegawa K, Raudales JLM, I T, Yoshida T, Honma R, Iwatake M, Tran SD, Seki M, Asahina I and Sumita Y (2023), Effective-mononuclear cell (E-MNC) therapy alleviates salivary gland damage by suppressing lymphocyte infiltration in Sjögren-like disease.
Front. Bioeng. Biotechnol. 11:1144624.
doi: 10.3389/fbioe.2023.1144624

Effective-mononuclear cell (E-MNC) therapy alleviates salivary gland damage by suppressing lymphocyte infiltration in Sjögren-like disease

Kayo Hasegawa[1†], Jorge Luis Montenegro Raudales[1†], Takashi I[1†], Takako Yoshida[1], Ryo Honma[1,2], Mayumi Iwatake[1], Simon D. Tran[3], Makoto Seki[4], Izumi Asahina[2,5] and Yoshinori Sumita[1*]

[1]Department of Medical Research and Development for Oral Disease, Nagasaki University Graduate School of Biomedical Sciences, Nagasaki, Japan, [2]Unit of Translational Medicine, Department of Regenerative Oral Surgery, Nagasaki University Graduate School of Biomedical Sciences, Nagasaki, Japan, [3]Laboratory of Craniofacial Tissue Engineering and Stem Cells, Faculty of Dental Medicine and Oral Health Sciences, McGill University, Montreal, QC, Canada, [4]CellAxia Inc, Tokyo, Japan, [5]Depatment of Oral and Maxillofacial Surgery, Juntendo University Hospital, Tokyo, Japan

Introduction: Sjögren syndrome (SS) is an autoimmune disease characterized by salivary gland (SG) destruction leading to loss of secretory function. A hallmark of the disease is the presence of focal lymphocyte infiltration in SGs, which is predominantly composed of T cells. Currently, there are no effective therapies for SS. Recently, we demonstrated that a newly developed therapy using effective-mononuclear cells (E-MNCs) improved the function of radiation-injured SGs due to anti-inflammatory and regenerative effects. In this study, we investigated whether E-MNCs could ameliorate disease development in non-obese diabetic (NOD) mice as a model for primary SS.

Methods: E-MNCs were obtained from peripheral blood mononuclear cells (PBMNCs) cultured for 7 days in serum-free medium supplemented with five specific recombinant proteins (5G culture). The anti-inflammatory characteristics of E-MNCs were then analyzed using a co-culture system with CD3/CD28-stimulated PBMNCs. To evaluate the therapeutic efficacy of E-MNCs against SS onset, E-MNCs were transplanted into SGs of NOD mice. Subsequently, saliva secretion, histological, and gene expression analyses of harvested SG were performed to investigate if E-MNCs therapy delays disease development.

Results: First, we characterized that both human and mouse E-MNCs exhibited induction of CD11b/CD206-positive cells (M2 macrophages) and that human E-MNCs could inhibit inflammatory gene expressions in CD3/CD28- stimulated PBMNCs. Further analyses revealed that Msr1-and galectin3-positive macrophages (immunomodulatory M2c phenotype) were specifically induced in E-MNCs of both NOD and MHC class I-matched mice. Transplanted E-MNCs induced M2 macrophages and reduced the expression of T cell-derived chemokine-related and inflammatory genes in SG tissue of NOD mice at SS-onset. Then, E-MNCs suppressed the infiltration of CD4-positive T cells and facilitated the maintenance of saliva secretion for up to 12 weeks after E-MNC administration.

Discussion: Thus, the immunomodulatory actions of E-MNCs could be part of a therapeutic strategy targeting the early stage of primary SS.

KEYWORDS

Sjögren syndrome, xerostomia, cell therapy, peripheral blood mononuclear cell, macrophage

1 Introduction

Primary Sjögren syndrome (pSS) is a systemic autoimmune disease characterized by lymphocytic infiltration of the exocrine glands, primarily the salivary and lacrimal glands, leading to xerostomia and eye dryness (Ramos-Casals et al., 2012; Nocturne and Mariette, 2013). In addition, there are many systemic features of pSS, such as Raynaud's syndrome, fatigue, dry skin, and joint and muscular pain, and these symptoms seriously affect patients' quality of life (Brito-Zerón et al., 2016; Both et al., 2017). Therefore, scientists have sought to develop effective treatments, and during this process, much progress has been made in disclosing the pathogenesis of SS. However, the etiology of SS remains unclear owing to its complexity. Consequently, there are currently no adequate treatments that do not involve suppression of autoimmune responses, and therefore, developing an adequate treatment for SS is urgently needed.

Over the past decade, cell-based therapies have been examined as potential therapeutic approaches for SS (Khalili et al., 2014; Elghanam et al., 2017; Genç et al., 2022). A particularly promising therapeutic option is the use of mesenchymal stem cells (MSCs). MSCs originating from either the bone marrow, umbilical cord, or adipose tissues have shown potential in the treatment of SS due to their anti-inflammatory and immunomodulatory effects (Khalili et al., 2012; Yao et al., 2019; Liu et al., 2021). For example, we have shown that a cell-based therapy using bone marrow cells or bone marrow MSCs (BMMSCs) could prevent SS in a non-obese diabetic (NOD) mouse model (Khalili et al., 2012; Khalili et al., 2014). BMMSCs ($CD45^-/TER119^-$) prevented the loss of saliva flow and reduced lymphocytic infiltrations in salivary glands (SGs). In the developing stages of SS, the production of inflammatory cytokines such as tumor necrosis factor (TNF)-α and transforming growth factor (TGF)-β is usually elevated, but expression of these cytokines was downregulated in NOD mice treated with BMMSCs (Jonsson et al., 2006; Hall et al., 2010). MSCs reportedly secrete anti-inflammatory vesicles and suppress the immune system (Chang et al., 2021). These findings demonstrated that bone marrow cells or BMMSCs reduce lymphocytic infiltration and improve the saliva secretory function in mice with Sjögren-like disease (Khalili et al., 2012; Khalili et al., 2014). However, the clinical use of BMMSCs carries some risks. For example, although these cells possess attractive self-renewal and vigorous proliferation capacities, these properties may also lead to undesirable consequences such as tumor formation or progression (Norozi et al., 2016; Clément et al., 2017). Therefore, we subsequently examined the therapeutic potential of bone marrow cell- or MSC-extract/lysate (soup) on atrophic irradiated SGs or SGs from mice with SS-like disease (Misuno et al., 2014; Abughanam et al., 2019). An extract of the soluble intracellular contents of bone marrow cells or MSCs exhibited immunomodulatory effects in NOD mice by inhibiting the production of pro-inflammatory cytokines such as TNF-α, TGF-β1, and interleukin (IL)-1β and promoting the secretion of IL-10. However, it remains a challenge to expand a sufficient number of highly-functional MSCs in culture to obtain an adequate amount of cell extract/lysate from autologous MSCs. This is because there are large individual differences in cell proliferation and function caused by the patient's age, gender, and/or underlying medical conditions (Agata et al., 2010; 2019; Asahina et al., 2021). In addition, various unavoidable problems such as cytotoxicity against host immune cells or increased tumor recurrence associated with immunosuppressive effects remain with the use of allogenic MSCs (Norozi et al., 2016; Clément et al., 2017). Further investigation is thus required to develop a highly effective cell-based therapy for SS patients.

We recently developed an effective culture method that enhances the anti-inflammatory and vasculogenic phenotypes of peripheral blood mononuclear cells (PBMNCs) (Kuroshima et al., 2019; I et al., 2019). Mouse PBMNCs were expanded for 5 days in primary serum-free culture medium containing five specific recombinant proteins (which we designated as "5G-culture"), and then the resulting effectively conditioned mononuclear cells [effective-mononuclear cells (E-MNCs)] could be obtained. E-MNCs contained an enriched population of CD11b/CD206-positive (M2 macrophage-like) cells and $CCR4^+/CCR6^-$ cells (Th2 cells), and this characteristic change strongly suggested that PBMNCs acquire anti-inflammatory or immunomodulatory properties during 5G-culture. Indeed, experiments to confirm the efficacy of E-MNC transplantation on radiation-damaged SGs showed that it reduced the expression of inflammation-related genes and promoted various tissue-regenerative activities, such as increased expression of stem cell markers, activation of cell proliferation, and vigorous blood vessel formation. Subsequently, through the induction of acinar and ductal cell proliferation and the suppression of fibrosis, E-MNCs ultimately mediated the regeneration of damaged tissues in mice, leading to the recovery of saliva secretory function (I et al., 2019). Thus, E-MNC transplantation is a promising approach for the treatment of radiation-injured SGs, and a first-in-humans study of E-MNC therapy for patients with severe radiogenic xerostomia is currently in progress (Sumita et al., 2020). Moreover, several studies have reported that treatment with M2-macrophages exhibiting anti-inflammatory and immunomodulatory properties can alleviate the symptoms of autoimmune diseases such as glomerulonephritis, multiple sclerosis, and encephalomyelitis (Du et al., 2016; Chu et al., 2021). Therefore, we hypothesized that E-MNCs would be therapeutically efficient against autoimmune diseases such as SS.

The aim of this study was to investigate whether E-MNCs could hinder the development of SS-like disease and preserve the saliva secretory function in NOD mice. This study is a pre-requisite for future clinical trials aimed at developing cell-based therapies for SS.

TABLE 1 Growth factors used in 5G culture.

Antibody/isotype name	Company, catalog no.	Final concentration (ng/mL)
h SCF	Prepotech, # AF-300-07	100
h flt-3 ligand	Prepotech, #AF- 300-19	100
h TPO	Prepotech, #AF-300-18	20
h VEFG	Prepotech, # AF-100-20	50
h IL-6	Prepotech, # AF-200-06	20
m SCF	Prepotech, #250-03	100
m flt-3 ligand	Prepotech, #250-31L	100
m TPO	Prepotech, #315-14	20
m VEFG	Prepotech, #450-32	50
m IL-6	Prepotech, #216-16	20

h: human, m: mouse.

2 Materials and methods

2.1 Animals

CB6F1/Slc mice (Japan SLC Inc., Shizuoka, Japan) and NOD/ShiJcl mice (CLEA Japan Inc., Tokyo, Japan) were used for E-MNC culture. In transplantation experiments, female NOD/ShiJcl mice with Sjögren-like disease were used as recipients (CLEA Japan Inc.), and male CB6F1/Slc mice in which the MHC class I matched that of NOD mice were employed as donors. Starting at 8 weeks of age, body weight and blood glucose levels of NOD mice were monitored once a week (Accu-Check; Roche Diagnostics, Laval, QC, Canada). The mice were diagnosed with diabetes after observing two consecutive daily blood glucose concentration measurements of >200 mg/dL. These diabetic mice were injected with insulin on a daily basis (Humulin N, Lilly, ON, Canada). All mice were kept under clean conventional conditions at the Nagasaki University Animal Center. All experimental procedures were performed in accordance with the guidelines approved by the Nagasaki University Ethics Committee (1605061303, 1812141494, and 1912111584).

2.2 E-MNC culture

Human PBMNCs were cultured using a specific culture method (CellAxia Inc. Tokyo, Japan) that we established and designated as "5G-culture" (I et al., 2019). Briefly, 50 mL of peripheral blood was obtained from healthy volunteers, and PBMNCs were isolated by density gradient centrifugation using Histopaque®-1,077 separating solution (Sigma Aldrich, St. Louis, MO, United States). PBMNCs were seeded into 6-well Primaria tissue culture plates (BD Biosciences, San Jose, CA, United States) at a density of 2×10^6 cells/well in 2 mL of serum-free medium (Stemline II Hematopoietic Stem Cell Expansion Medium; Sigma Aldrich) supplemented with five recombinant proteins [Flt3-ligand, IL-6, stem cell factor (SCF), thrombopoietin (TPO), and vascular endothelial growth factor (VEGF)] and cultured for 6 days. Experiments were carried out in compliance with the Declaration of Helsinki. Sample collection was approved by the Ethics Committee of Nagasaki University Graduate School of Biomedical Sciences (17082131), and written informed consent was obtained from all donors. For mouse E-MNC culture, PBMNCs were isolated from

TABLE 2 Antibodies and isotype controls for flow cytometry.

Antibody/isotype name	Company, catalog no.
PE-Cy7 anti-human CD11b	Biolegend, # 301322
PE-Cy7 mouse IgG1, κ isotype Ctrl	Biolegend, # 400126
APC-Cy7 anti-human CD206	Biolegend, # 321120
APC-Cy7 mouse IgG1, κ Isotype Ctrl	Biolegend, # 400128
APC-Cy7 anti-mouse/human CD11b	Biolegend, # 101225
APC-Cy7 rat IgG2b, κ Isotype Ctrl	Biolegend, # 400623
APC anti-mouse CD206 (MMR)	Biolegend, # 141707
APC rat IgG2a, κ isotype Ctrl	Biolegend, # 400713
PE anti-mouse CD3	Biolegend, # 100205
PE Rat IgG2b, κ Isotype Ctrl	Biolegend, # 400607
APC-Cy7 anti-mouse CD4	Biolegend, # 100413
APC-Cy7 Rat IgG2b, κ Isotype Ctrl	Biolegend, # 400623
PE-Cy7 anti-mouse CCR4 (CD194)	Biolegend, # 131213
PE-Cy7 Armenian hamster IgG, isotype Ctrl	Biolegend, # 400921
APC anti-mouse CCR6 (CD196)	Biolegend, # 129813
APC Armenian hamster IgG, isotype Ctrl	Biolegend, # 400911
APC anti-mouse CCR2 (CD192)	R&D Systems, #FAB5538A
APC Rat IgG2b, κ Isotype Ctrl	Biolegend, # 400611
PE-Cy7 anti-mouse/human Mac-2 (Galectin-3)	Biolegend, # 125417
PE-Cy7 rat IgG2a, κ isotype Ctrl	Biolegend, # 400521
FITC anti-mouse Msr-1 (CD204)	Bio-rad, # MCA1322FT
FITC rat IgG2b, κ isotype Ctrl	BD biosciences, # 553988

heparinized blood samples obtained by cardiac puncture and density gradient centrifugation with Histopaque®-1,083 (Sigma Aldrich). PBMNCs were cultured for 7 days as described above with equivalent mouse recombinant proteins at a seeding density of 5×10^6 cells/well. The concentrations of human and mouse recombinant proteins used in the 5G medium are listed in Table 1.

2.3 Evaluation of the characteristics of E-MNCs

Freshly isolated PBMNCs and E-MNCs (human and mouse) were subjected to flow cytometry to determine the surface antigen positivity of macrophage subpopulations (human monocytes and/or naïve macrophages: $CD11b^+/CD206^-$; human M2 macrophages: $CD11b^+/CD206^+$) (mouse monocytes and/or naïve macrophages: $CD11b^+/CD206^-$; mouse M2 macrophages: $CD11b^+/CD206^+$, $CD11b^+/$macrophage scavenger receptor 1 $(Msr1)^+$ or $CD11b^+/CCR2^-/galectin3^+$) (Shirakawa et al., 2018) and T lymphocyte ($CD3^+/CD4^+$) subsets (mouse Th1 cells: $CXCR3^+$; mouse Th2 cells: $CCR4^+/CCR6^-$). The relevant antibodies are listed in Table 2. Cells were resuspended in 2 mmol/L of EDTA/0.2% BSA/PBS buffer (2×10^5 cells/200 μL). Flow cytometry analysis was performed using an LSRFortessa cell analyzer (BD Biosciences) and FlowJo software (Tomy Digital Biology Co., Ltd., Tokyo, Japan). The percent positivity of macrophage and T lymphocytes subpopulations per each gate among PBMNCs or E-MNCs was evaluated and then calculated in relation to that of the whole cell population.

2.4 Evaluation of anti-inflammatory potential of E-MNCs

To assess the anti-inflammatory potential of E-MNCs, an assay using co-culture conditions with T lymphocyte–stimulated PBMNCs was utilized. The wells of a 24-well plate were coated overnight with 15 ng/mL of CD3 monoclonal antibody (eBioscience, Vienna, Austria) and 5 ng/mL of CD28 monoclonal antibody (eBioscience). Human PBMNCs were isolated from healthy donors (three men aged 28, 34, and 35 years) as described above and seeded in the pre-coated 24-well plates (2.5×10^6 cells/well) in 1 mL of RPMI 1640 medium (Thermo Fisher Scientific Life Sciences, Waltham, MA, United States). After 1 h of incubation at 37°C, a Transwell® 0.4-μm pore polycarbonate membrane insert (Corning Life Sciences, Amsterdam, Netherlands) was placed above the seeded PBMNCs. E-MNCs (5×10^6 cells) were added to the inside compartment of the Transwell® and co-cultured without cell-to-cell contact between E-MNCs and PBMNCs for 1 and 3 h. Finally, PBMNCs were collected, and total RNA was extracted using Trizol reagent (Invitrogen) to assess mRNA expression of the *tnf-α*, *interferon (inf)-γ*, *il-1β*, *il-6*, *il-4*, and *il-10* genes.

2.5 Evaluation of vasculogenic potential of E-MNCs, and gene expression of cells and tissues

To investigate the vasculogenic potential of PBMNCs (pre–5G-culture) obtained from CB6F1/Slc mice and E-MNCs, the cells were seeded in 35-mm Primaria dishes (BD Biosciences) at 1×10^5 cells/dish. Endothelial progenitor cell–colony forming assays (EPC-CFAs) were performed using semi-solid culture medium (MethoCult SFBIT; STEMCELL Technologies, Inc., Vancouver, Canada) with pro-angiogenic growth factors/cytokines (Table 3), as we previously reported (Masuda et al., 2011; I et al., 2019). Briefly, 7 days after initiation of the EPC-CFA, the number of adherent colonies (EPC colony-forming units; EPC-CFUs) per dish was determined under a microscope. The EPC-CFA was adopted to monitor two different types of EPC-CFUs, as primitive EPC-CFUs (PEPC-CFUs) and definitive EPC-CFUs (DEPC-CFUs), which were composed of small cells and large cells, respectively. The PEPC-CFUs and DEPC-CFUs were counted separately. These analyses were repeated six times for PBMNCs and E-MNCs. Simultaneously, to confirm the endothelial characteristics of colonized cells, we used fluorescence microscopy to assess the biochemical binding of isolectin B4–conjugated fluorescein isothiocyanate (ILB4-FITC; Vector Laboratories, Burlingame, CA, United States), which is a marker of endothelial cells, and the uptake of acetylated low-density lipoprotein labeled with 1,1′-dioctadecyl-3,3,3′,3′-tetramethylindocarbocyanine perchlorate (AcLDL-DiI; Biomedical Technologies, Inc., Stoughton, MA, United States), which is metabolized in endothelial cells via a receptor-mediated process.

TABLE 3 Contents of semisolid culture medium used for EPC-CFA.

Contents	Company, catalog no.	Final concentration
VEGF	Peprotech, #450-32	50 ng/mL
basic FGF	Peprotech, #450-33	50 ng/mL
EGF	Peprotech, #315-09	50 ng/mL
IGF-1	Peprotech, #250-19	50 ng/mL
SCF	Peprotech, #250-03	100 ng/mL
IL-3	Peprotech, #213-13	20 ng/mL
Heparin	YOSHINDO, #121-154	2 U/mL
FBS	SAFC Biosciences, #12303	30%

To analyze the gene expression in PBMNCs, E-MNCs, and submandibular glands, total RNA was extracted using Trizol reagent (Invitrogen, Waltham, MA, United States), and first-strand complementary DNA synthesis was performed using SuperScript First-Strand Synthesis (Invitrogen). Complementary DNA was amplified using Takara-Taq (Takara Bio Inc., Shiga, Japan). PCR reactions were performed on an Mx3000P QPCR System (Agilent Technologies). The primers used for the reactions are shown in Table 4. As an internal control standard, glyceraldehyde-3-phosphate dehydrogenase (gapdh) was used in both human and mouse reactions.

2.6 Microarray analysis of PBMNCs and E-MNCs, and transplantation of E-MNCs

For microarray analysis, PBMNCs and E-MNCs obtained from CB6F1 mice were collected, and total RNA was extracted. Each RNA sample was assessed using a microarray (SurePrint G3 Human Gene Expression 8 × 60 K v2.0; Agilent Technologies, Palo Alto, CA,

TABLE 4 Primer sequences used for quantitative PCR analysis.

Gene	Forward primer	Reverse primer
Human		
gapdh	5′-GGAGTCCACTGGCGTCTTCAC-3′	5′-GCTGATGATCTTGAGGCTGTTGTC-3′
tnf-α	5′-AATGGCGTGGAGCTGAGA-3′	5′-TAGACCTGCCCAGACTCGG-3′
inf-γ	5′-CTGTTACTGCCAGGACCCAT-3′	5′-ACACTCTTTTGGATGCTCTGGT-3′
*il-1*β	5′-CACAGACCTTCCAGGAGAAT-3′	5′-TTCAACACGCAGGACAGGTA-3′
il-6	5′-GTACATCCTCGACGGCATC-3′	5′-AGCCACTGGTTCTGTGCCT-3′
il-4	5′-GCCACCATGAGAAGGACACT-3′	5′-ACTCTGGTTGGCTTCCTTCA-3
il-10	5′-TGAAAACAAAGAGCAAGGCCG-3′	5′-TAGAGTCGCCACCCTGATGT-3
Mouse		
gapdh	5′-TGTGTCCGTCGTGGATCTGA-3′	5′-TTGCTGTTGAAGTCGCAGGAG-3′
tnf-α	5′-CCACCACGCTCTTCTGTCTA-3′	5′-AGGGTCTGGGCCATAGAACT-3′
inf-γ	5′-ACAGCAAGGCGAAAAAGGATG-3′	5′-TGGTGGACCACTCGGATGCA-3′
*il-1*β	5′-GCTGAAAGCTCTCCACCTCA-3′	5′-AGGCCACAGGTATTTTGTCG-3′
ccl5	5′-TGCTGCTTTGCCTACCTCTC-3′	5′-TCCTTCGAGTGACAAACACGA-3′
ccl6	5′-CAAGCCGGGCATCATCTTTA-3′	5′-TTCCCAGATCTTGGGCCTTG-3′
ccl8	5′-ACGCTAGCCTTCACTCCAAA-3′	5′-GTGACTGGAGCCTTATCTGG-3′
ccl19	5′-AGACTGCTGCCTGTCTGTGA-3′	5′-GCCTTTGTTCTTGGCAGAAG-3′
cxcl19	5′-CTCGGACTTCACTCCAACACA-3′	5′-ATCACTAGGGTTCCTCGAACT-3′

United States). Differentially expressed genes were selected and divided into functional categories using Database for Annotation, Visualization, and Integrated Discovery (DAVID) (https://david.ncifcrf.gov/). The signal intensity of highly expressed genes was converted into z scores and plotted in a heatmap using GraphPad Prism, version 9.4.1 (GraphPad Software; San Diego, CA, United States).

For transplantation of E-MNCs, eight-week-old female NOD mice were anesthetized with 0.1 mL/10 g body weight of mixed anesthetic agents (domitor, 1 mg/mL; midazolam, 10 mg/2 mL; and butorphanol tartrate, 5 mg/mL) given by intraperitoneal (ip) injection. E-MNCs (1×10^5 cells) obtained from male CB6F1/Slc mice were suspended in 5 μL of IMDM medium (Sigma Aldrich) and injected into the submandibular glands of NOD mice (E-MNC-group; sacrificed at 1, 3, and 7 days, and 4, 8, and 12 weeks post-transplantation, $n \geq 5$ for each time point, total $n \geq 30$). In control mice, an equal volume of IMDM without cells was injected into the SGs (Ctrl-group; n ≥ 5 for each time point, sacrificed at 1, 3, and 7 days, and 4, 8, and 12 weeks post-transplantation, $n \geq 5$ for each time point, total $n \geq 30$). At 4, 8, and 12 weeks post-transplantation, mice were sacrificed after collecting saliva, and the submandibular glands were harvested for histological observations. To track transplanted E-MNCs, the cells were labeled using a PKH26 Red Fluorescent Cell Linker kit (Sigma Aldrich) prior to transplantation. The same mice then received transplantation of E-MNCs in one gland (right side) and only IMDM, as a control, in the other gland (left side) for further gene expression (*ccl6*, *ccl8*, *ccl5*, *ccl19*, *ccl9*, *tnf-α*, *inf-γ*, and *il-1β*) and histological (CD206) analyses. Subsequently, the submandibular glands were harvested at 1, 3, and 7 days after transplantation ($n = 3$ at each time point).

2.7 Salivary flow rate (SFR) after transplantation

To measure the saliva secretory function (SFR) of SGs, mice were kept under general anesthesia via ip injection of 10 μL/g body weight of triple anesthetic combination. Whole saliva was collected after stimulation of secretion with 0.5 mg/kg body weight pilocarpine (Sigma Aldrich) administered subcutaneously, as previously described (Sumita et al., 2010; I et al., 2019). Saliva was obtained from the oral cavity using a micropipette and placed into pre-weighed 1.5-mL microcentrifuge tubes. Saliva was collected for a 10-min period, and the volume was determined gravimetrically. SFR was determined at 4, 8, and 12 weeks post-transplantation ($n = 8$/group at each time point).

2.8 Epidermal growth factor (EGF) concentration

The concentration of EGF, which stimulates the proliferation of epithelial cells, in saliva (n = 3/group in Ctrl- and E-MNC–group) was measured by ELISA (Abcam). This assay employed a quantitative sandwich enzyme immunoassay technique, with the intensity of the color measured being proportional to the amount of EGF. The sample values were compared to an EGF standard curve. EGF concentration was determined at 12 weeks post-transplantation.

2.9 Histological observations of submandibular glands

Harvested submandibular glands were fixed in 4% paraformaldehyde and embedded in paraffin. Sections (5 μm) were stained with hematoxylin and eosin (H&E) and examined microscopically under ×100 magnification, with analysis of five different specimens per mouse ($n = 5$/group at 4, 8, and 12 weeks post-transplantation). The percentage of lymphocyte infiltrate area (focus score area) was analyzed using ImageJ software (National Institutes of Health, Bethesda, MD, United States). Immunohistological staining was performed using rat anti-mouse F4/80 antibody (1:100, Bio-Rad Laboratories, Inc.,

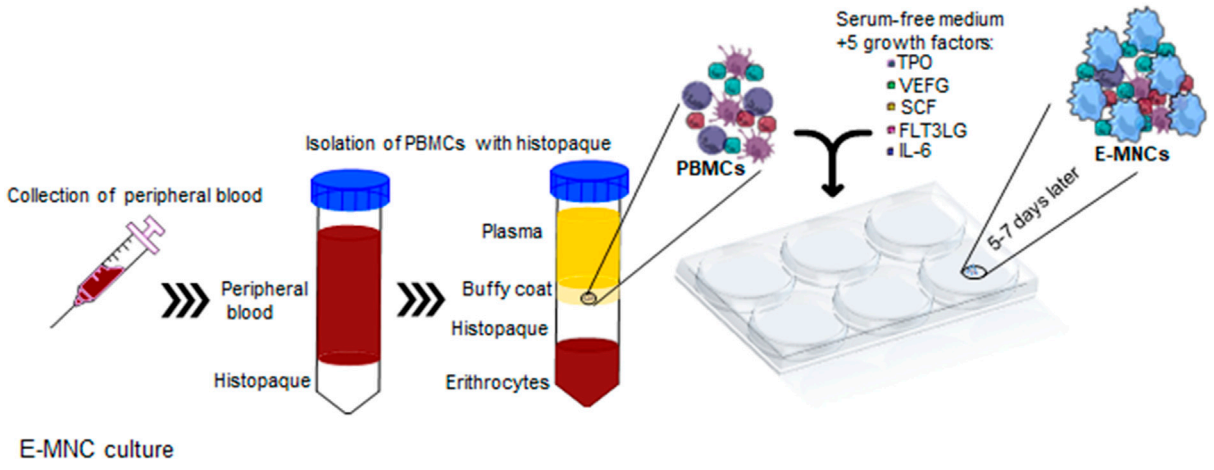

FIGURE 1
Schematic diagram describing 5G-culture. PBMNCs were isolated from buffy coat and cultured for 6–7 days in serum-free medium supplemented with five recombinant proteins, TPO, VEGF, SCF, Flt-3 ligand, and IL-6. After cultivation, effective-mononuclear cells (E-MNCs) were obtained.

Hercules, CA, United States), rabbit anti-mouse CD206 antibody (1:500, Abcam, Cambridge, United Kingdom), and rat anti-mouse CD4 antibody (1:50; R&D Systems, Minneapolis, MN, United States). The slides were then incubated with Alexa Fluor 647–conjugated goat anti-rat antibody (1:200; Invitrogen™, Carlsbad, CA, United States) for F4/80 and Alexa Fluor 488–conjugated donkey anti-rabbit antibody (1:200; Invitrogen™) for CD206 as secondary antibodies and counterstained with mounting medium for fluorescence with DAPI (Vector Laboratories). Specimens stained with F4/80 and CD206 antibodies were examined microscopically under ×40, ×200, and ×400 magnification, with five different specimens per mouse (n = 3/group at 1, 3, and 7 days post-transplantation). Two examiners independently counted CD206-positive cells in a blinded manner. For CD4 staining, a VECTASTAIN ABC kit (Vector laboratories) was used, and specimens were counterstained with hematoxylin. CD4-positive cells were examined using a fluorescence microscope under ×100, ×200, and ×400 magnification. Two examiners independently counted CD4-positive cells in the lymphocytic infiltrate of each specimen/four sections (n = 3/group at 4 and 8 weeks after transplantation) in a blinded manner.

2.10 Statistical analysis

The Student's t-test was used to determine the significance of differences between paired data, and one-way ANOVA with *post hoc* Tukey's multiple comparisons were performed for multiple groups. Experimental values are presented as mean ± SD; $p < 0.05$ was considered statistically significant.

3 Results

3.1 Characteristics of human E-MNCs

At 6 days of 5G-culture (Figure 1), adherent human E-MNCs became larger and changed their morphology to a macrophage-like round shape (Figure 2A). Flow cytometric analysis showed a distinct increase in FSC/SSC (cell size/granularity) gated cells, and the M2 macrophage–enriched fraction ($CD11b^+/CD206^+$) distinctly appeared among E-MNCs (from 0.20% ± 0.12% to 93.47% ± 1.62%) (Figures 2B, C). In contrast, monocytes and/or naïve (Mono-naïve) macrophages ($CD11b^+/CD206^-$) decreased (from 28.2% ± 4.56% to 2.09% ± 0.74%), and the Mono-naïve/M2 macrophage ratio in E-MNCs decreased markedly compared with that in PBMNCs (from 162.55 ± 60.4 to 0.02 ± 0.01) (Figure 2C).

3.2 Characteristics of mouse E-MNCs

Among E-MNCs obtained from CB6F1 mice, adherent cells also became larger and changed their morphology to macrophage-like round or elongated shapes, similar to human E-MNCs (Figure 3A) at 7 days of culture. Flow cytometric analysis clearly revealed that the M2 macrophage-enriched fraction ($CD11b^+/CD206^+$) increased among E-MNCs (from 0.26% ± 0.22% to 5.54% ± 4.04%) (Figure 3B). The ratio of Mono-naïve macrophages ($CD11b^+/CD206^-$) among E-MNCs exhibited minimal variation (from 4.2% ± 1.89% to 5.56% ± 2.32%; no statistical differences between PBMNCs and E-MNCs), and the Mono-naïve/M2 macrophage ratio in E-MNCs decreased compared with that in PBMNCs (from 12.71 ± 3.42 to 1.35 ± 0.70) (Figure 3C). The fraction shifted to a predominance of immunomodulatory M2 macrophages ($Msr1^+/CD11b^+$; from 1.33% ± 1.07% to 2.97% ± 1.47%) (Figure 3D). Focusing particularly on the CD11b-positive cell fraction among PBMNCs and E-MNCs, $galectin3^+$ cells (as immunomodulatory macrophages) clearly increased (from 3.04% ± 0.66% to 57.60% ± 20.8%) after 5G-culture (Figure 3D). Th2 cells ($CD3^+/CD4^+/CXCR3^-/CCR6^-/CCR4^+$) increased (from 0.090% ± 0.036% to 4.20% ± 0.95%; Figure 3E), whereas Th1 cells ($CD3^+/CD4^+/CXCR3^+$) slightly decreased (from 1.90% ± 0.33% to 0.69% ± 0.44%; data not shown). Expression of pro-inflammatory mRNAs (*il-1β*, *inf-γ*, and *tnf-α*) in E-MNCs was significantly downregulated compared

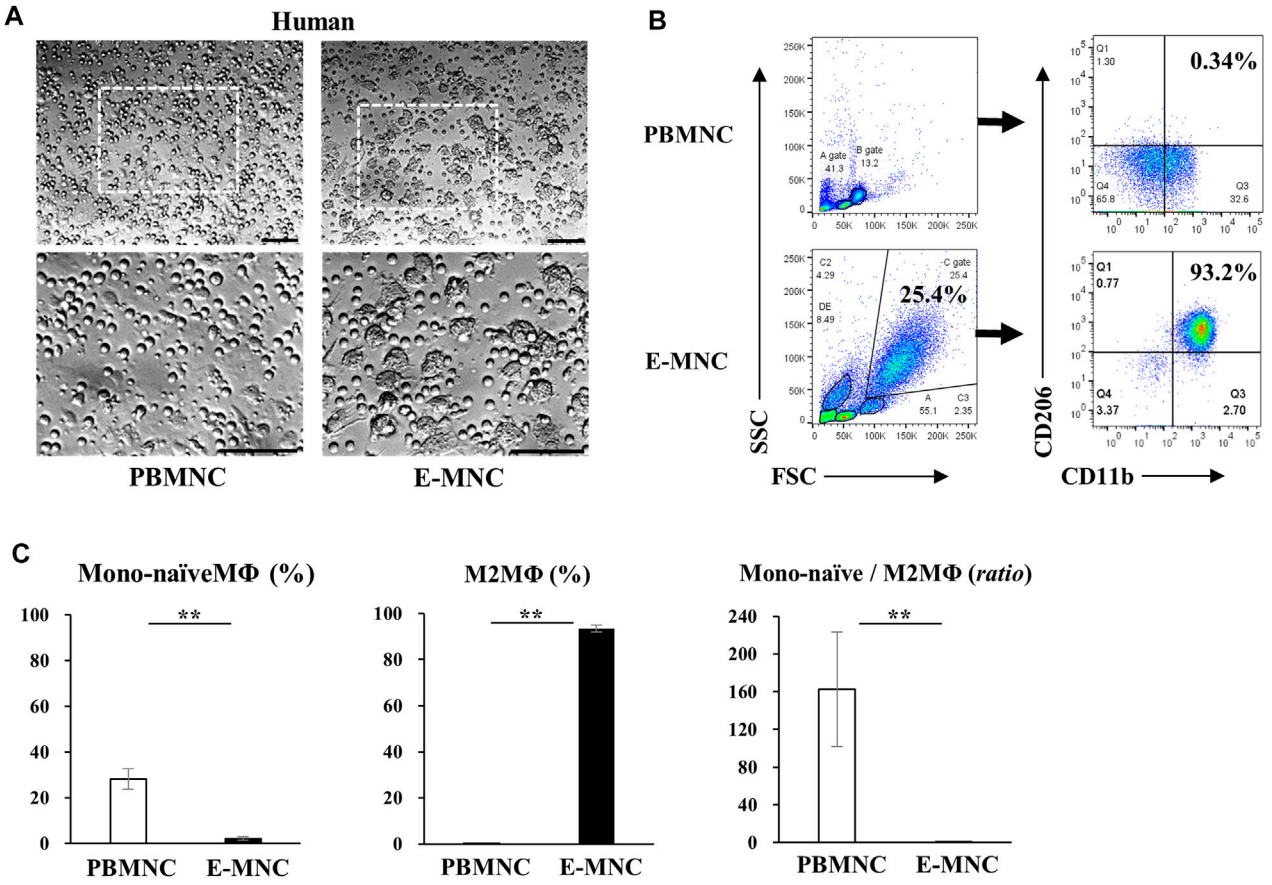

FIGURE 2
Characteristics of human E-MNCs. **(A)** Phase-contrast imaging of human PBMNCs (at day 0) and E-MNCs (at day 6). White boxed areas in the upper images (scale bar, 100 μm) were magnified in the lower images (scale bar, 100 μm). **(B)** Flow cytometric analysis of FSC/SSC gated cells, $CD11b^{+}/CD206^{-}$ [Monocytes and/or naïve (Mono-naïve) macrophages] and $CD11b^{+}/CD206^{+}$ (M2) macrophages, among PBMNCs (at day 0) and E-MNCs (at day 6). **(C)** Percentages of Mono-naïve ($CD11b^{+}/CD206^{-}$) and M2 ($CD11b^{+}/CD206^{+}$) macrophage fractions and their ratios (Mono-naïve/M2) among PBMNCs and E-MNCs (**$p < 0.01$). For statistical analysis, the Student's t-test was performed to determine the significance of differences among PBMNCs and E-MNCs.

with that in PBMNCs (Figure 3F). Further microarray analyses indicated that overall, pro-inflammatory, anti-angiogenesis, and pro-apoptosis genes were downregulated in E-MNCs, whereas the expression of anti-inflammatory, angiogenesis, anti-apoptosis, and apoptosis clearance–related genes was upregulated when compared with PBMNCs (Supplementary Figure S1A). In addition, as previously indicated in human/mouse EPC-CFA, two types of EPC colonies were morphologically detected: PEPC-CFUs and DEPC-CFUs. The total number of CFUs and the ratio of DEPC-CFUs derived from E-MNCs increased markedly compared with PBMNCs (Supplementary Figures S1B, C). These colonies were positive for ILB4-FITC (ILB4; binds to endothelial cells) and took up the AcLDL-DiI fluorescent dye (AcLDL labels endothelial cells) (Supplementary Figure S1D). These results indicated that the E-MNCs had acquired vasculogenic characteristics during 5G-culture. Furthermore, experiments to determine whether E-MNCs can be produced from NOD mice as an animal model of SS, macrophage-like round or elongated shapes were observed in addition to CB6F1 mouse E-MNCs at 7 days of 5G-culture (Supplementary Figure S2A). The M2 macrophage-enriched fraction ($CD11b^{+}/CD206^{+}$) increased among E-MNCs after 5G-culture (from 1.05% to 3.49%) (Supplementary Figure S2B). Additionally, galectin3-positive cells (as immunomodulatory macrophages) clearly increased (from 18.19% to 90.6%) after 5G-culture (Supplementary Figure S2C).

3.3 Anti-inflammatory effect of E-MNCs against inflamed PBMNCs

In preliminary experiments, mRNA expression of pro-inflammatory genes in CD3/CD28-stimulated PBMNCs peaked at around 2 h of incubation (data not shown). Therefore, E-MNCs were added to the culture at 1 h after stimulation of PBMNCs (Figure 4A). At 1 h after addition of E-MNCs, the E-MNCs downregulated the mRNA expression of *tnf-α*, *ifn-γ*, *il-1β*, *il-6*, and *il-4* in stimulated PBMNCs to the same levels as unstimulated PBMNCs, whereas E-MNCs upregulated the expression of anti-inflammatory *il-10* mRNA (Figure 4B). At 3 h, although E-MNCs significantly reduced mRNA expression of *tnf-α*,

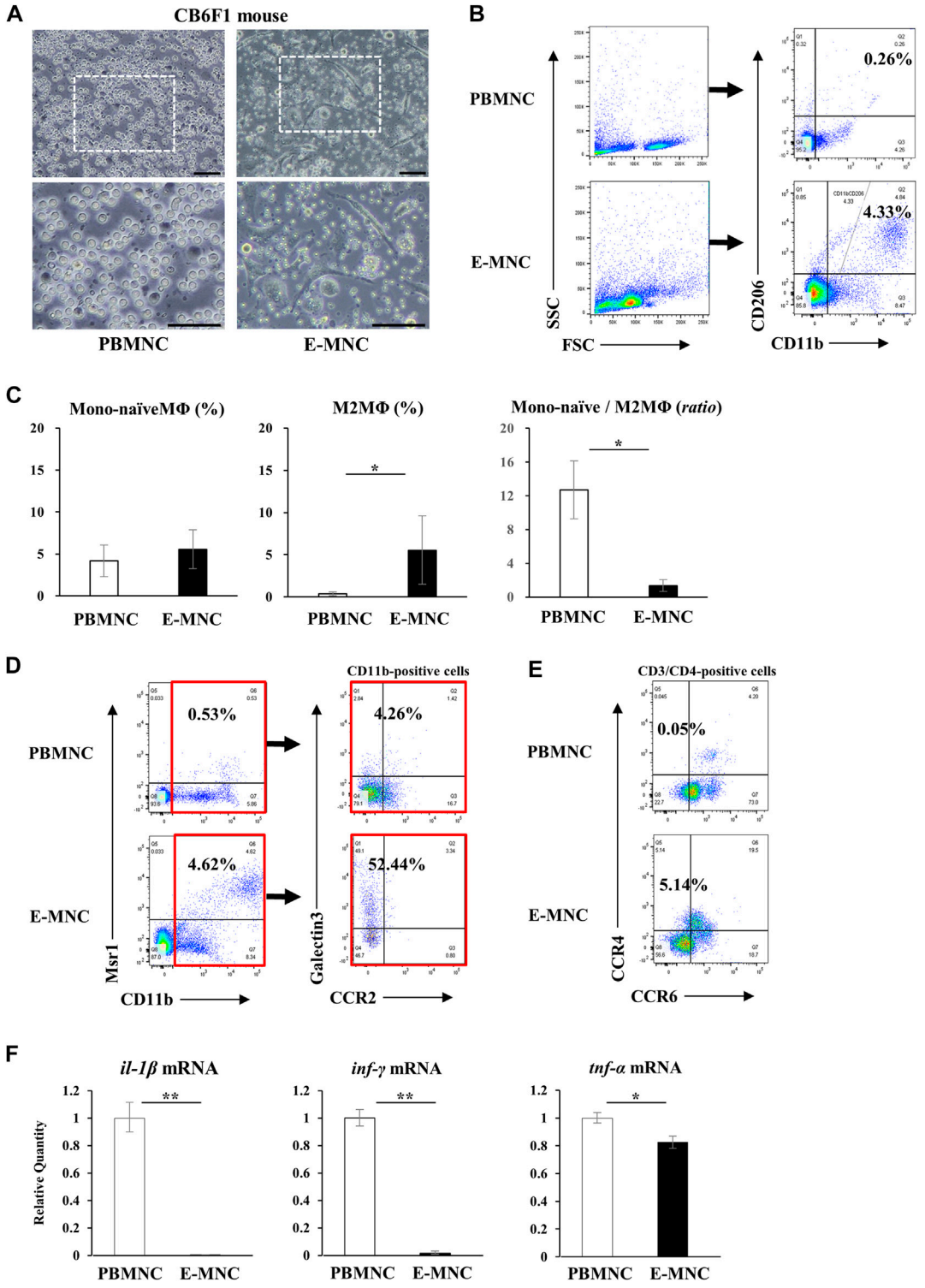

FIGURE 3
Characteristics of mouse E-MNCs. **(A)** Phase-contrast imaging of CB6F1 mouse PBMNCs (at day 0) and E-MNCs (at day 7). White boxed areas in the upper images (scale bar, 100 μm) were magnified in the lower images (scale bar, 100 μm). **(B)** Flow cytometric analysis of FSC/SSC gated cells, $CD11b^+$/$CD206^-$ (Mono-naïve) and $CD11b^+$/$CD206^+$ (M2) macrophages, among PBMNCs (at day 0) and E-MNCs (at day 7). **(C)** Percentages of Mono-naïve ($CD11b^+$/$CD206^-$) and M2 ($CD11b^+$/$CD206^+$) macrophage fractions and their ratios (Mono-naïve/M2) among PBMNCs and E-MNCs (*$p < 0.05$). **(D)** Flow cytometric analysis of $CD11b^+$/$Msr1^+$ (M2c; left panels) macrophages and CCR2/galectin3^+ (right panels) CD11b-positive macrophages among PBMNCs (at day 0) and E-MNCs (at day 7). **(E)** Flow cytometric analysis of $CCR6^-$/$CCR4^+$ Th2 cells in $CD3^+$/$CD4^+$ gated cells of PBMNCs (at day 0) and E-MNCs (at day 7). **(F)** Expression of pro-inflammatory mRNAs (*il-1β*, *ifn-γ*, and *tnf-α*) in PBMNCs (at day 0) and E-MNCs (at day 7) (*$p < 0.05$, **$p < 0.01$). For statistical analysis, the Student's t-test was performed to determine the significance of differences among PBMNCs and E-MNCs.

10.3389/fbioe.2023.1144624

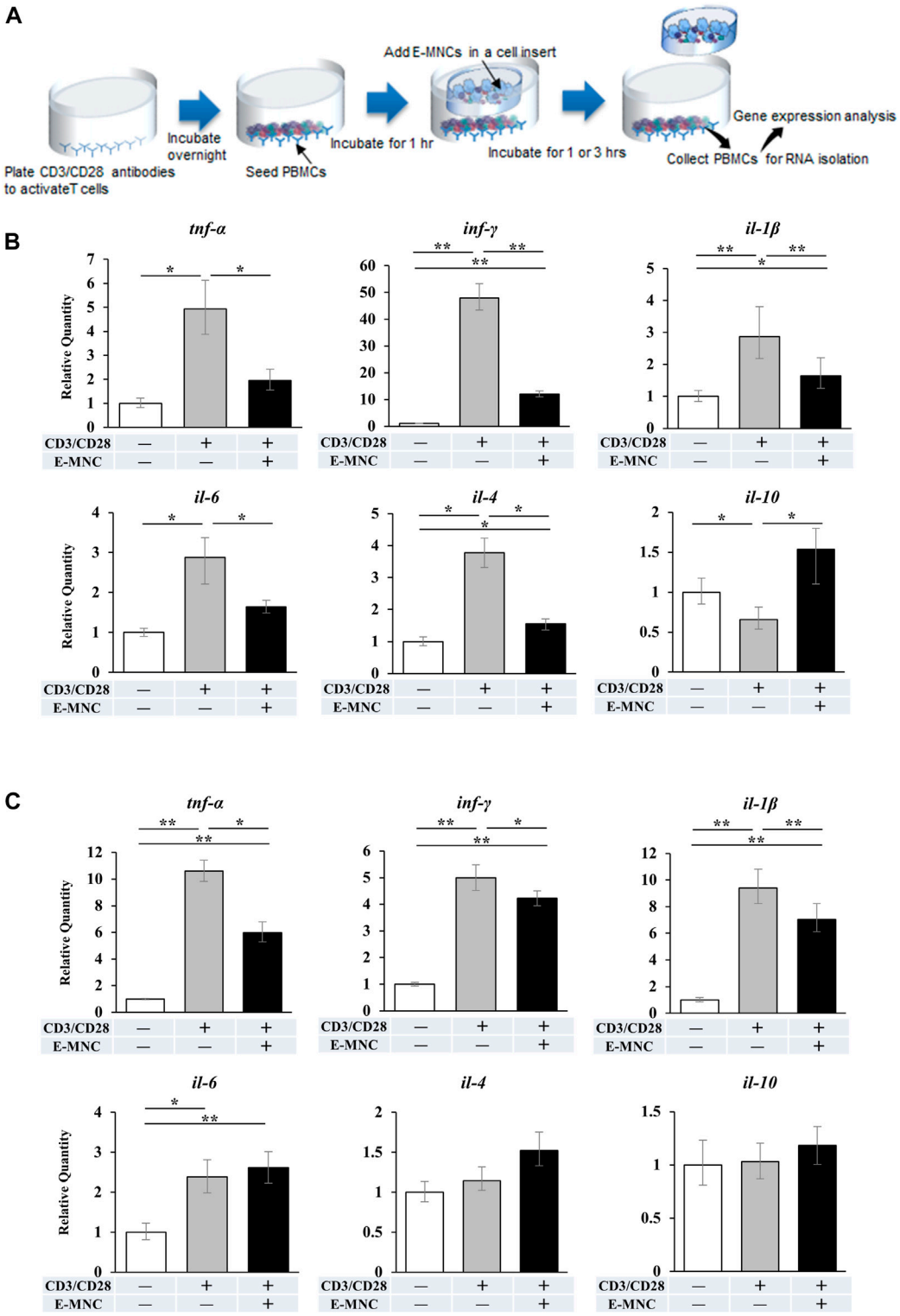

FIGURE 4
mRNA expression in CD3/CD28-stimulated PBMNCs after co-culture with E-MNCs. **(A)** Schematic diagram describing the experimental design for co-culture of E-MNCs and T-cell–activated PBMNCs. Anti-CD3 and -CD28 antibodies were added to the wells of a 24-well plate and incubated overnight. PBMNCs were then seeded in the wells and cultured at 37°C for 1 h. Subsequently, E-MNCs were seeded in the upper chamber and co-cultured with stimulated PBMNCs for 1 or 3 h **(B and C)** mRNA expression of *tnf-α*, *ifn-γ*, *il-1β*, *il-6*, *il-4*, and *il-10* in PBMNCs and CD3/CD28-stimulated PBMNCs with/without E-MNCs for 1 h **(B)** or 3 h **(C)** (*$p < 0.05$, **$p < 0.01$). For statistical analysis, one-way ANOVA with *post hoc* Tukey's multiple comparisons were performed for multiple groups.

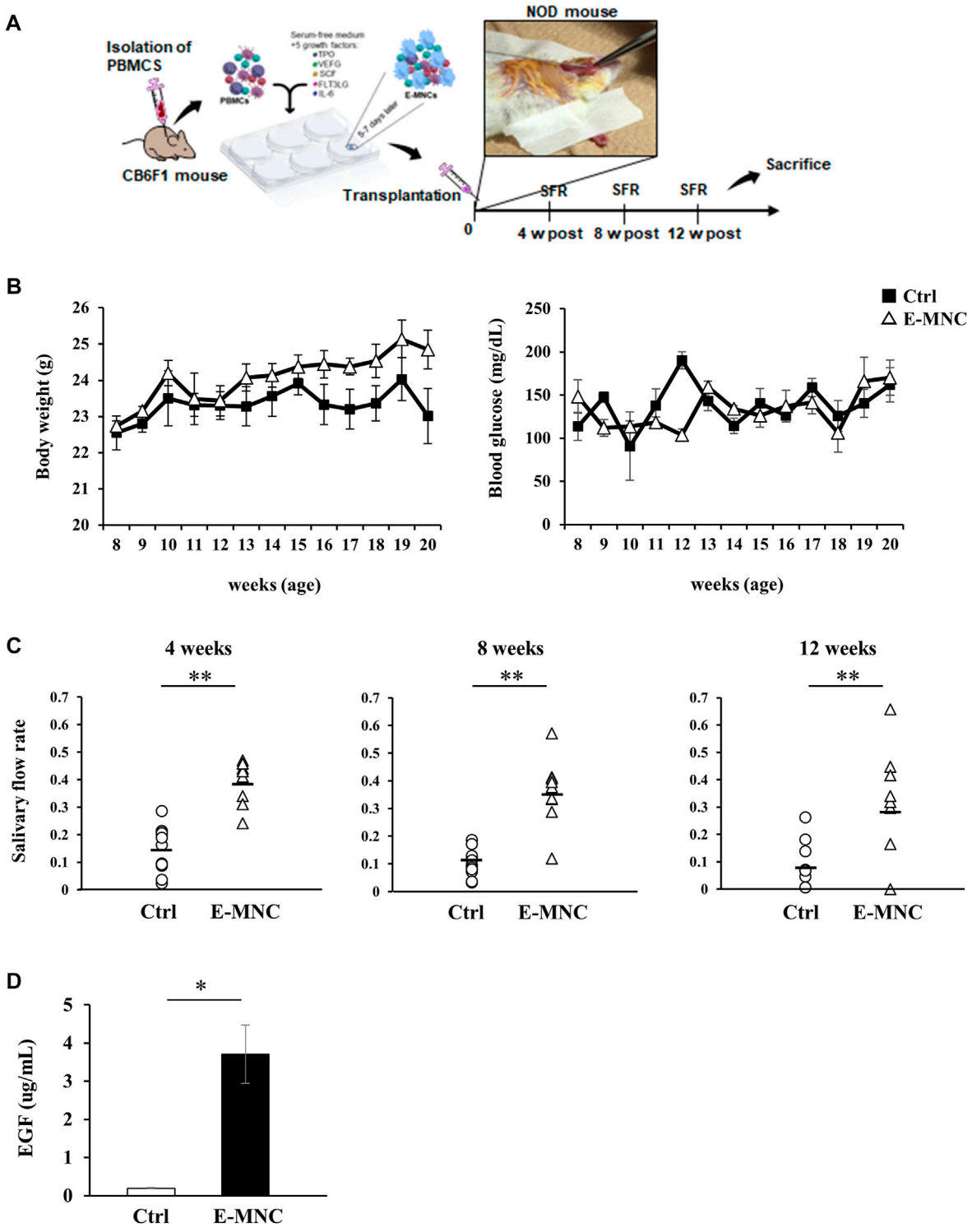

FIGURE 5
Transplantation of E-MNCs into NOD mice at the onset of SS-like disease. **(A)** Schematic diagram describing the experimental design for E-MNC transplantation. E-MNCs were injected into the submandibular glands directly, and then saliva and saliva glands were harvested at 4, 8, and 12 weeks. **(B)** Changes in body weight and blood glucose of non-treated mice (Ctrl) and E-MNC–treated mice (E-MNC). **(C)** Change in saliva production (salivary flow rate; SFR) at 4, 8, and 12 weeks post-transplantation (**$p < 0.01$). **(D)** EGF concentration in saliva of non-treated mice (Ctrl) and E-MNC–treated mice (E-MNC) at 12 weeks post-transplantation (*$p < 0.05$). For statistical analysis, the Student's t-test was performed to determine the significance of differences among Ctrl- and E-MNC-group.

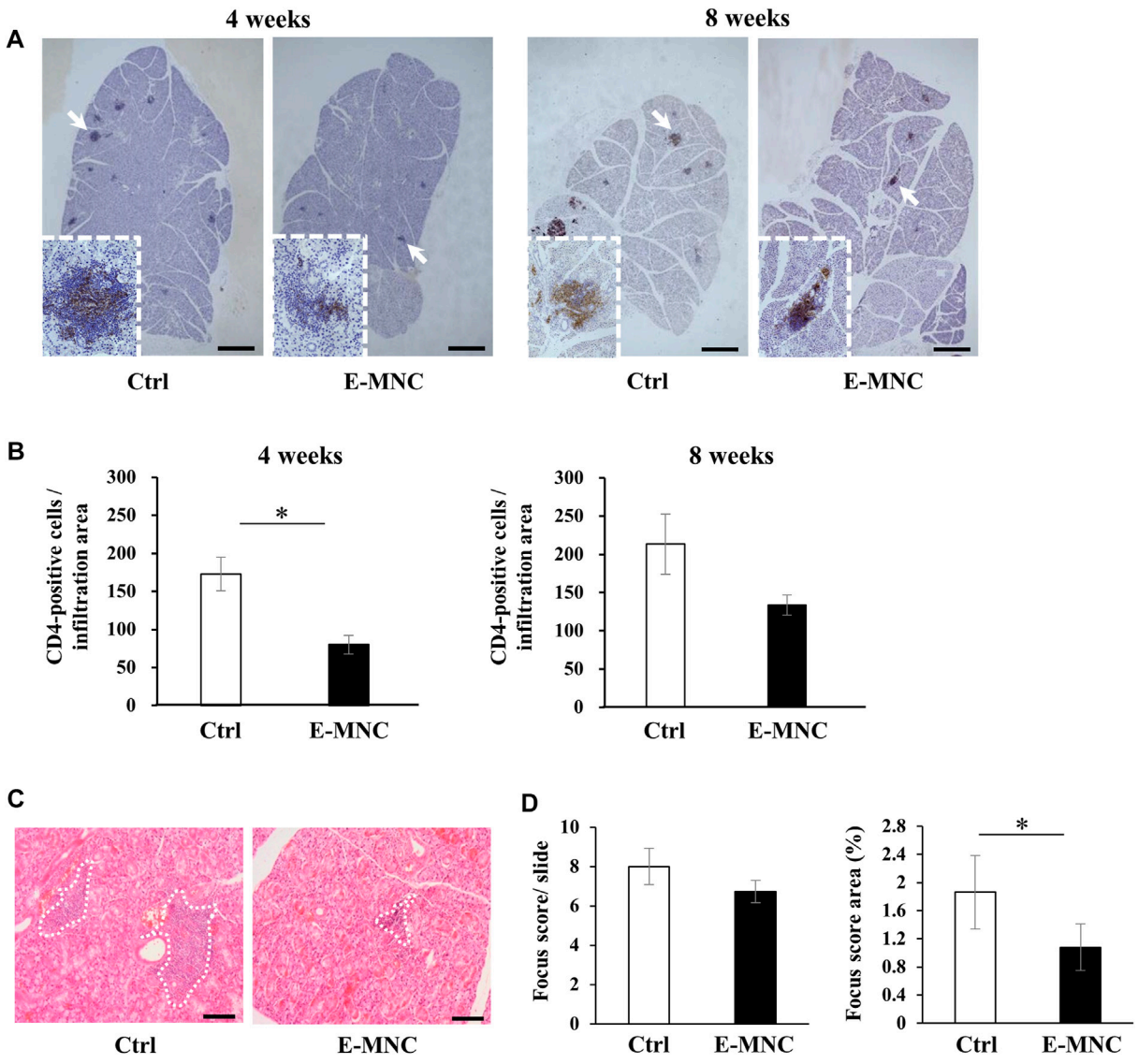

FIGURE 6
Lymphocyte infiltration after E-MNC treatment. **(A)** CD4 staining of submandibular glands in non-treated mice (Ctrl) and E-MNC–treated mice (E-MNC) at 4 and 8 weeks post-transplantation (scale bar, 1,000 μm). Cells positive for CD4 (T-helper cells) appear brown in the foci. **(B)** Number of CD4-positive cells in lymphocyte infiltrated areas at 4 and 8 weeks (*$p < 0.05$). **(C)** H&E staining of submandibular glands in non-treated mice (Ctrl) and E-MNC–treated mice (E-MNC) at 4 and 8 weeks post-transplantation (scale bar, 200 μm). White dotted lines indicate the portion used to determine the focus score. **(D)** Focus score and area in non-treated mice (Ctrl) and E-MNC–treated mice (E-MNC) (*$p < 0.05$). For statistical analysis, the Student's t-test was performed to determine the significance of differences among Ctrl- and E-MNC-group.

inf-γ, and *il-1β*, the anti-inflammatory effect of the E-MNCs decreased over time. Indeed, no significant change was observed in *il-6*, *il-4*, or *il-10* mRNA expression among stimulated PBMNCs co-cultured with/without E-MNCs (Figure 4C).

3.4 Therapeutic effects of E-MNCs on the onset of SS in NOD mice

E-MNCs obtained from PBMNCs of CB6F1 mice via 5G-culture were transplanted into the submandibular glands of 8-week-old NOD mice (Figure 5A). During the monitoring period up to 12 weeks post-transplantation, the body weight gradually increased after E-MNC treatment (Figure 5B). In contrast, the blood glucose level showed no clear difference between E-MNC–treated and non-treated mice (Figure 5B). However, 8- to 11-week-old NOD mice were considered to have developed SS, as lymphocyte infiltration began to be observed in SGs at these ages (data not shown). With regard to functional evaluation, E-MNC treatment clearly increased saliva secretion at 4, 8, and 12 weeks post-transplantation compared with non-transplanted mice (Figure 5C). The EGF concentration in harvested saliva at 12 weeks post-transplantation was markedly elevated in samples from E-MNC–treated mice compared to that in non-transplanted mice (Figure 5D). Areas of lymphocyte infiltration in submandibular glands appeared to decrease following E-MNC

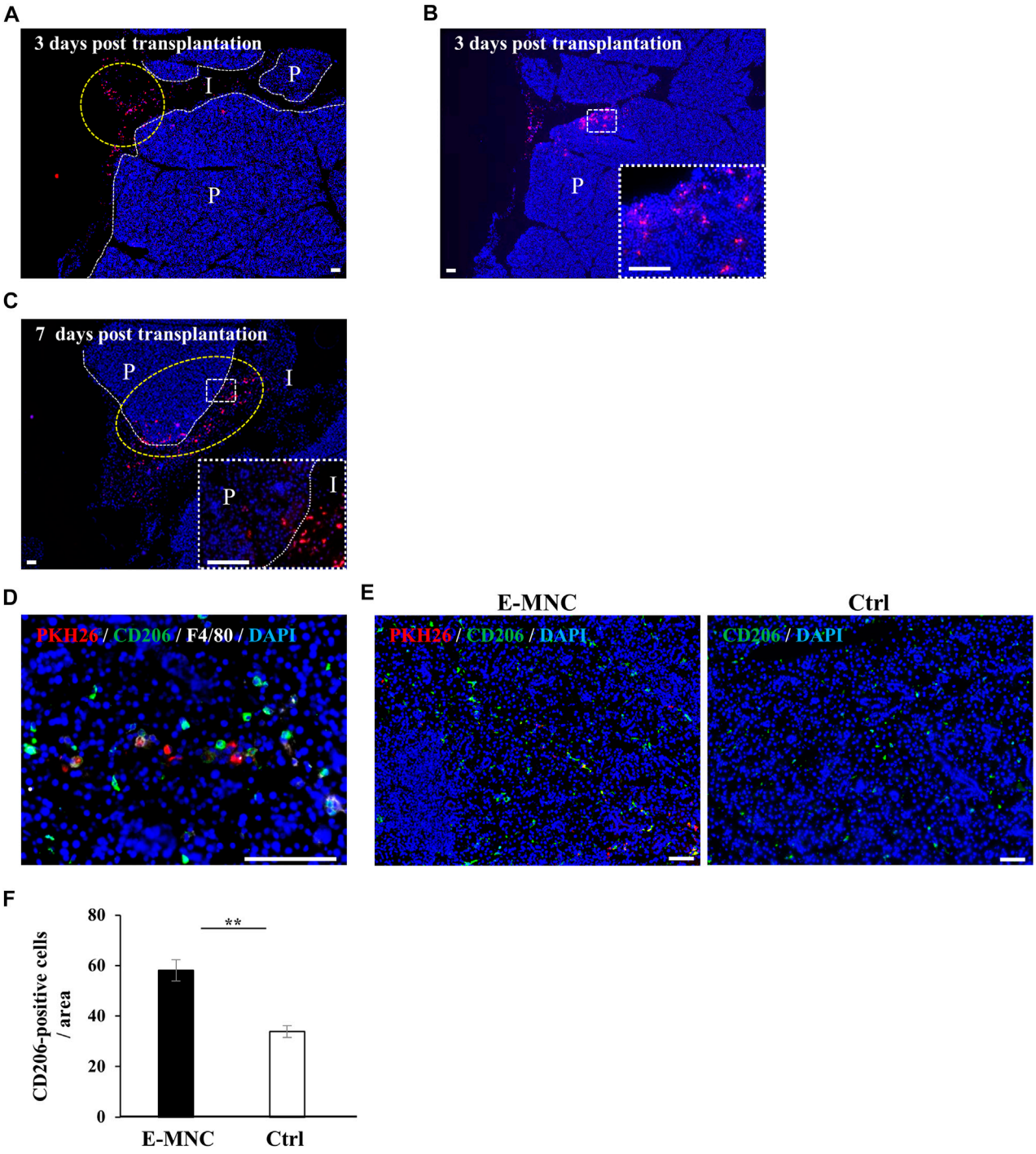

FIGURE 7
Detection of transplanted E-MNCs and M2 macrophages in submandibular glands. **(A)** At 3 days post-transplantation, PKH26-expressing E-MNCs (red) were detected in the interlobular space (I) (yellow dotted circle) and parenchyma (P) of submandibular glands (white dotted lines, boundary between interlobular area and parenchyma; red, PKH26-labeled cells; blue, DAPI; scale bar, 100 μm). **(B)** At 3 days post-transplantation, PKH26-expressing E-MNCs (red) were detected in the parenchyma (P) of submandibular glands. White dotted square area was magnified in the lower right panel (red, PKH26-labeled cells; blue, DAPI; scale bar, 100 μm). **(C)** At 7 days post-transplantation, PKH26-expressing E-MNCs (red) migrated to the deeper interlobular space (I) and penetrated into the parenchyma (P) (yellow dotted circle) in submandibular glands. White dotted square area was magnified in the lower right panel (white dotted lines, boundary between interlobular and parenchyma; red, PKH26-labeled cells; blue, DAPI; scale bar, 100 μm). **(D)** At 1 day post-transplantation, PKH26-expressing E-MNCs and host M2 macrophages expressed F4/80 (white) and CD206 (green) in the parenchyma of the submandibular glands (blue, DAPI; scale bar, 100 μm). **(E)** Detection of transplanted E-MNCs (red) and CD206-positive cells (green) in E-MNC-treated glands (left image) and non-treated glands (right image) (blue, DAPI; scale bar, 50 μm). **(F)** Number of CD206-positive cells/field (×200) in the parenchyma of submandibular gland tissues in E-MNC-treated glands (E-MNC) and non-treated glands (Ctrl) at 7 days post-transplantation (**$p < 0.01$). For statistical analysis, the Student's t-test was used to analyze differences between E-MNC-group and Ctrl-group.

treatment at 4 and 8 weeks post-transplantation (Figure 6A). Indeed, the number of CD4-positive cells in lymphocyte infiltrated areas decreased markedly at 4 weeks in E-MNC–treated specimens compared with non-treated specimens (Figure 6B). However, after 8 weeks, the number of CD4-positive cells increased in both groups, though their numbers were still suppressed by E-MNC treatment (Figure 6B). At 12 weeks post-transplantation, the number of lymphocyte-infiltrated areas (focus score) in glands decreased slightly in E-MNC–treated specimens, whereas the average size of the lymphocyte-infiltrated areas was significantly reduced by E-MNC treatment (Figures 6C, D).

3.5 Behavior of transplanted E-MNCs in submandibular glands

To assess the behavior of transplanted E-MNCs in submandibular glands, PKH26-labeled E-MNCs were analyzed on days 1, 3, and 7 after transplantation. At 3 days, scattered PKH26-labeled cells were primarily observed in the interlobular space (Figure 7A), from which some cells appeared to invade the gland parenchyma (Figures 7A, B). Subsequently, labeled cells migrated to the deeper space between the lobules (Figure 7C), and numerous cells penetrated the gland parenchyma at 7 days post-transplantation (Figure 7C). Observation of E-MNCs in the gland parenchyma at 1 day post-transplantation revealed F4/80/CD206-positive E-MNCs and host cells (as M2 macrophages) (Figure 7D). At 7 days, E-MNC–treated glands exhibited a higher number of cells positive for F4/80/CD206 (as M2 macrophages) than did non-treated glands (Figures 7E, F). In particular, a number of CD206-expressing host cells were seen at the periphery of PKH26-labeled E-MNCs containing CD206-positive cells (Figure 7E).

3.6 Gene expression in submandibular glands in the initial post-transplantation stage

To further assess the therapeutic effects underlying the anti-inflammatory activity of E-MNCs, the expression of inflammatory chemokine genes, especially genes related to lymphocyte infiltration, was examined in the initial post-transplantation stage. At 1 day post-transplantation, *ccl5*, *ccl6*, and *cxcl9* mRNA expression was significantly downregulated in E-MNC–treated glands, but no apparent decline in expression of the *ccl8* and *ccl19* genes was observed (Figure 8A). Subsequently, mRNA expression of these chemokines in E-MNC–treated glands was generally suppressed at 3 days compared with that in non-treated glands (Figure 8B). Consistent with these observations, the expression of pro-inflammatory genes such as *tnf-α*, *inf-γ*, and *il-1β* was markedly downregulated at both 1 and 3 days post-transplantation (Figures 8C, D).

4 Discussion

This study demonstrated that a cell therapy approach based on E-MNCs has a therapeutic efficacy on the onset of pSS-like disease in NOD mice. The major findings of this study were as follows: 1) transplanted E-MNCs obtained from peripheral blood consistently preserved salivary secretion, 2) E-MNCs clearly suppressed the infiltration of CD4-positive lymphocytes into SGs and the progression of SS-like disease, and 3) E-MNCs might affect these phenomena in a paracrine manner and/or in cooperation with induced recipient anti-inflammatory M2 macrophages. These outcomes suggest that this strategy could be a promising option for developing future treatments.

Regarding the first outcome, NOD mice exhibited lower levels of saliva output over time, but the levels were maintained near those of normal mice in E-MNC–treated mice when compared with NOD mice (2.46-fold at 12 weeks; 3.59-fold at 16 weeks; 3.19-fold at 20 weeks of age). This therapeutic effect on SG function was preserved during the 12-week observation period following a single administration of E-MNCs. These phenomena indicate that E-MNCs exert a certain therapeutic efficacy in preventing the progression of SS-like disease or restoring the secretory function of injured glands. In previous studies, we demonstrated that administration of bone marrow MSCs is effective for both preventing lymphocytic infiltration and suppressing hyposalivation in SGs of NOD mice (Khalili et al., 2012; Khalili et al., 2014; Abughanam et al., 2019). Also, other studies have reported similar therapeutic effects of MSCs in treating NOD mice with SS-like disease (Shi et al., 2018; Gong et al., 2020; Cong et al., 2022; Sun et al., 2022). The anti-inflammatory and immunomodulatory properties of MSCs are responsible for the therapeutic effects against SS-like disease. Therefore, MSCs are ideal candidates for cell-based therapies. However, as mentioned above, the availability of autologous MSCs for effective therapy may be limited due to the relatively low number of cells that can be obtained from donor tissues, degeneration of their plasticity during cell expansion and passaging, patient age, and invasiveness. In contrast, E-MNCs exhibit promise for clinical applications because the peripheral blood is a readily accessible source of cells that can be obtained with minimal invasiveness in elderly patients. The most significant advantage is that this functional primary culture system can induce immunomodulatory cells into E-MNCs from a patient's peripheral blood. Furthermore, E-MNCs may contribute to the functional restoration of atrophic glands more directly than MSCs, because exogenous MSCs play a role in tissue regeneration by inducing macrophage polarization toward an anti-inflammatory M2 phenotype (Nemeth et al., 2009; Zhang et al., 2010). The human E-MNCs in this study were approximately 24.5% M2-dominant monocytes/macrophages (0.5% $CD11b^+/CD206^-$ Mono-naïve macrophages; 24% $CD11b^+/CD206^+$ M2 macrophages). We found that this heterogeneous cell fraction exhibited anti-inflammatory effects against activated PBMNCs. The M2 macrophage fraction was also enriched among CB6F1 mouse E-MNCs, although their abundance was approximately 4%. However, genes associated with Th1 cells, such as *tnf-α*, *inf-γ*, and *il-1β*, were significantly downregulated, while the fraction of Th2 cells associated with M2 macrophage polarization increased during 5G-culture. In addition, a notable number of Msr1-or galectin3-expressing immunomodulatory macrophages were observed among E-MNCs. Overall, these data indicate that mouse E-MNCs consistently exhibit anti-

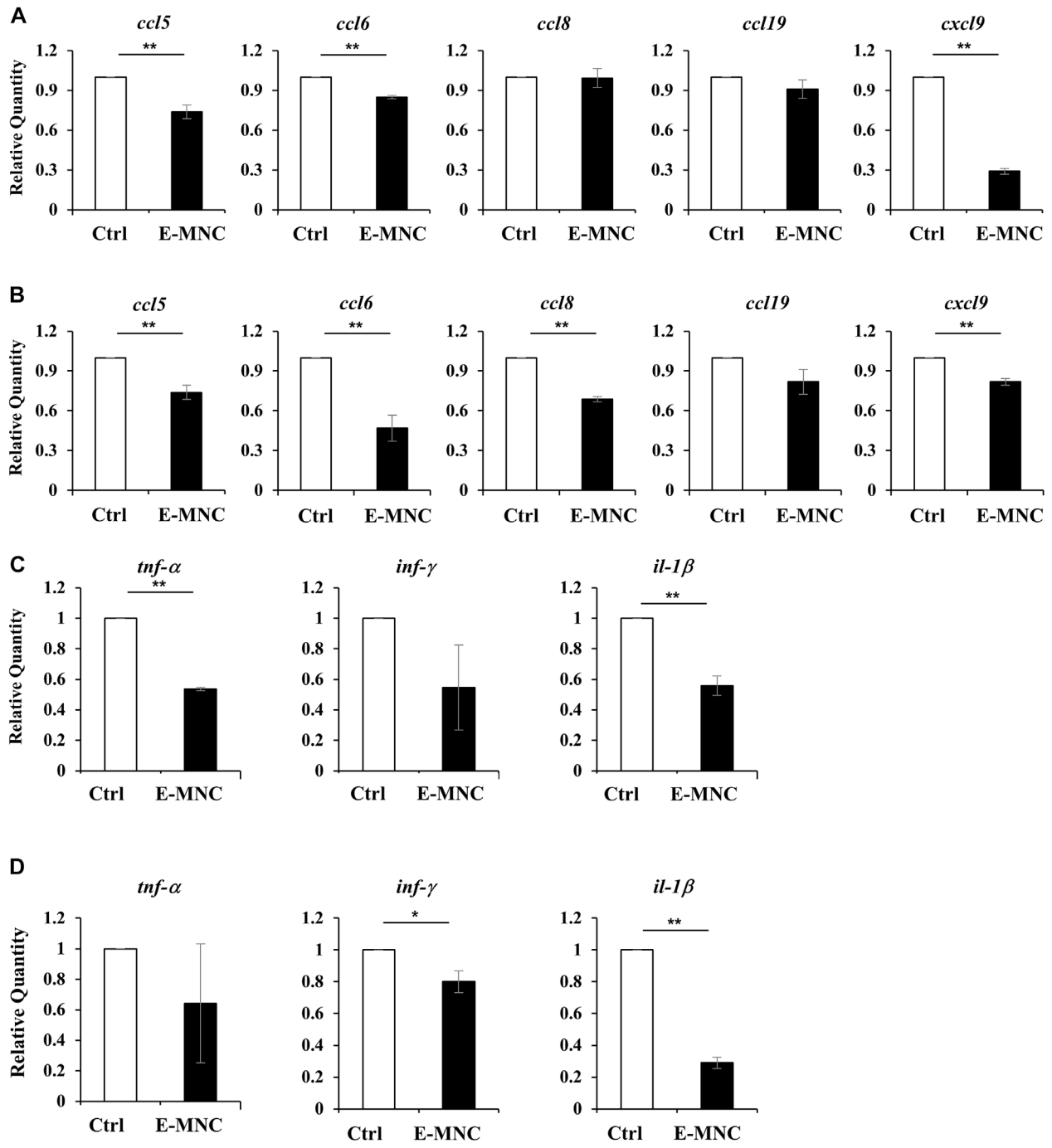

FIGURE 8
Gene expression in submandibular glands in the initial post-transplantation stage. **(A,B)** mRNA expression of the inflammatory chemokines *ccl5*, *ccl6*, *ccl8*, *ccl19*, and *cxcl9* in non-treated glands (Ctrl) and E-MNC–treated glands (E-MNC) at 1 day **(A)** and 3 days **(B)** post-transplantation (**$p < 0.01$). **(C,D)** Expression of the pro-inflammatory genes *tnf-α*, *inf-γ*, and *il-1β* in non-treated glands (Ctrl) and E-MNC–treated glands (E-MNC) at 1 day **(C)** and 3 days **(D)** post-transplantation (*$p < 0.05$, **$p < 0.01$). For statistical analysis, the Student's t-test was used to analyze differences between E-MNC-group and Ctrl-group.

inflammatory and immunomodulatory properties. Additionally, the results of flow cytometric analyses showed that E-MNCs obtained from NOD mice at the onset of pSS acquired an anti-inflammatory and immunoregulatory profile following 5G-culture, similar to those of CB6F1 mice. These results suggest that this culture system could overcome the inherent limitations of autologous cell therapy in patients with autoimmune diseases such as SS and that E-MNCs ultimately generated using this culture system may be useful as a therapeutic agent. Thus, the use of E-MNCs, which does not require long-term cell expansion, is a simple and direct approach with low invasiveness that takes advantage of a readily available source (blood).

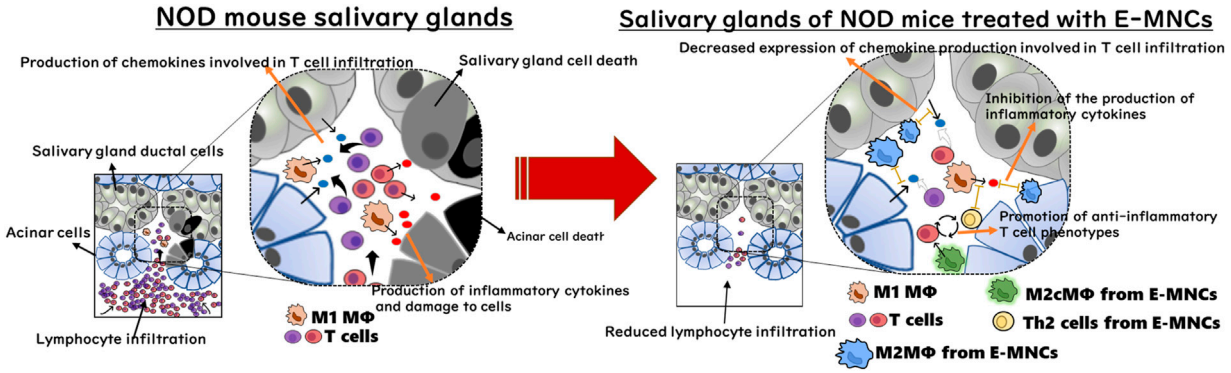

FIGURE 9
Diagram of the cellular mechanism of E-MNC transplantation at the onset of SS in NOD mice. E-MNCs function in a paracrine manner to inhibit chemotaxis of pathogenic T cells and improve the tissue microenvironment via the immunomodulatory effects of M2 macrophages and/or Th2 cells among E-MNCs during the initial stage after transplantation.

With regard to inhibition of disease development, we found that E-MNC treatment inhibited the infiltration of $CD4^+$ T cells at 4 and 8 weeks post-transplantation and reduced the area of lymphocyte infiltration (focus score area) at 12 weeks to approximately 58% of that of non-treated SGs. These phenomena indicate that transplanted E-MNCs directly suppress the infiltration of inflammatory cells and were not involved in the pathogenesis of pSS. As mentioned above, E-MNCs were enriched in M2 macrophages and Th2 cells. Typical M2 macrophages have the capacity to potently suppress $CD4^+$ T cell proliferation via the release of IL-10 (Salminen, 2010). Interestingly, a histological study of lip SGs from pSS patients showed that the number of $CXCR3^+$/$CD163^+$ M2 macrophages was inversely correlated with the severity of inflammatory lesions, demonstrating that M2 macrophages play an anti-inflammatory role in pSS lesions (Aota et al., 2018; Ushio et al., 2018). Similarly, this study revealed that the proliferation of $CD206^+$ M2 macrophage after E-MNC treatment was followed by suppression of $CD4^+$ T cell proliferation in the submandibular glands. Considered collectively, these data suggest that among E-MNCs, M2 macrophages and/or supporting cells such as Th2 cells contribute to the prevention of lymphocyte infiltration in the initial stage of pSS.

With regard to the cellular function of E-MNCs, human E-MNCs have been shown to potently suppress the activation of T cells among PBMNCs in culture, and mouse E-MNCs exhibit downregulation of mRNA expression of chemokines associated with T cell chemotaxis after transplantation (Huang et al., 2019; Chen et al., 2022). These data suggest that E-MNCs affect pathogenic T cells in a paracrine manner and improve the local inflammatory environment in injured SGs. In contrast, we found that transplanted E-MNCs gradually migrate from the interlobular space to the parenchyma over time. However, interestingly, $CD206^+$ M2 macrophages were derived from not only E-MNCs but also from the host cells could be observed in treated glands from 1day post-transplantation. As mentioned above, $CCR4^+$/$CCR6^-$ Th2 cells were also enriched in E-MNCs. Th2 cells are known to produce anti-inflammatory cytokines such as IL-4, IL-10, IL-13, and TGF-β (Young et al., 2000; Wegmann, 2009; Iwaszko et al., 2021; Kokubo et al., 2022). Moreover, galectin3 produced by macrophages plays a major role in the activation of M2 polarization via IL-4 signaling in Th2 cells (MacKinnon et al., 2008; Sperandio et al., 2009; Espinosa Gonzalez et al., 2022). Therefore, M2 macrophages and Th2 cells among E-MNCs might function in cooperation with self-induced host M2 macrophages. These findings led us to conclude that E-MNCs act in a paracrine manner to inhibit the chemotaxis of pathogenic T cells and improve the tissue microenvironment via immunomodulatory functions of M2 macrophages and/or Th2 cells among E-MNCs during the initial post-transplantation stages (Figure 9). However, the data in this study are still limited due to the lack of quantitative analysis at the protein level of chemokines such as CCL5, CCL6, CCL8, CCL19, and CXCL9, which are remarkably induced by pathogenic T cells at the disease initiation. During the development of SS-like disease, multiple chemokines function in a coordinated manner, with these chemokine-ligand families exhibiting different phases of gene expression (Nguyen CQ et al., 2009). Therefore, there may be no apparent differences in protein level of each chemokine because the changes in their mRNA expressions are relatively small (within one to three times). Overall changes in each chemokine production must be involved in the migration of pathogenic T cells. To resolve such limitations, further investigation on dynamic expression analysis of chemokine, chemokine receptor and cytokine gene responses in the pathological condition after E-MNC treatment may be required.

Msr1, an important phagocytic receptor in M2 macrophages, is involved in the elimination of apoptotic cells (Geske et al., 2002; Todt et al., 2008; Zhang et al., 2019; Zheng et al., 2022). Therefore, Msr1-expressing M2 macrophages among E-MNCs might contribute to alleviation of the inflammatory microenvironment and the activation of tissue regeneration. Indeed, the EGF concentration in saliva significantly increased after E-MNC treatment. EGF promotes the growth of salivary epithelial cells and inhibits apoptotic cell death (Azuma et al., 2018; Cho et al., 2021). It has been shown that the concentration of EGF increases in SGs of NOD mice with pSS-like disease following administration of MSCs (Khalili et al., 2012). Furthermore, as we and other groups

demonstrated in a previous study (Masuda et al., 2011; Tsukada et al., 2013; I et al., 2019) using a CFU assay and immunocytochemistry (uptake of AcLDL and binding of ILB), E-MNCs function both directly and indirectly in promoting angiogenesis during tissue regeneration. Data from microarray analyses also suggested that E-MNCs are involved in anti-inflammatory processes, angiogenesis, and the clearance of apoptotic cells. Some cells among E-MNCs must directly ameliorate the inflammatory microenvironment in injured SGs to facilitate tissue regeneration.

5 Conclusion

In conclusion, this study demonstrated that E-MNC therapy partially prevents the development of pSS-like disease in mice and preserves saliva secretion. E-MNCs can be produced using a readily available and minimally invasive source of cells in a short period of time. This therapy can be easily performed for SS patients in the clinic. However, the associated cellular mechanisms and therapeutic conditions need to be investigated in greater detail for future clinical applications. For example, this study did not focus on pathogenic B cells, which predominate in the chronic inflammatory stage of SS. Another limitation of the present study is that we employed a single transplantation to the submandibular glands using a specific dose, but tailored regimens that maximize the efficacy of E-MNC treatment should be developed. Therefore, further investigations employing proper clinical models of SS are needed. Overall, this study found that the immunomodulatory effects of E-MNCs could be part of a therapeutic strategy targeting the early stages of pSS.

Data availability statement

The original contributions presented in the study are included in the article/Supplementary Material, further inquiries can be directed to the corresponding author.

Ethics statement

The studies involving human participants were reviewed and approved by The Ethics Committee of Nagasaki University Graduate School of Biomedical Sciences. The patients/participants provided their written informed consent to participate in this study. The animal study was reviewed and approved by The Animal Care and Use Committee of Nagasaki University.

Author contributions

MS, IA, and YS contributed to conception and design of the study. KH, JR and TI contributed to experimental activity and data acquisition. KH, TY, RH and MI contributed to establish the methodology for culture. JR and TI contributed to establish the methodology for cell transplantation. TI and YS wrote the draft of the manuscript. ST provided contribution in supervision and paper editing. MS and IA helped in the interpretation of the data, reviewed the manuscript. YS provided contribution in experimental data design, production, curation, paper writing and editing, funding acquisition and research project administration.

Funding

This work was supported by JSPS KAKENHI grant numbers 20K10142 and 22H03276.

Acknowledgments

We thank Ms. Naomi Sakashita (Nagasaki University) and Ms. Mika Nishihara (CellAxia Inc.) for providing technical assistance with the experiments.

Conflict of interest

Author MS was employed by CellAxia Inc.

The remaining authors declare that the research was conducted in the absence of any commercial or financial relationships that could be construed as a potential conflict of interest.

Publisher's note

Supplementary material

The Supplementary Material for this article can be found online at: https://www.frontiersin.org/articles/10.3389/fbioe.2023.1144624/full#supplementary-material

References

Abughanam, G., Elkashty, O. A., Liu, Y., Bakkar, M. O., and Tran, S. D. (2019). Mesenchymal stem cells extract (MSCsE)-Based therapy alleviates xerostomia and keratoconjunctivitis sicca in sjogren's syndrome-like disease. *Int. J. Mol. Sci.* 20 (19), 4750. doi:10.3390/ijms20194750

Agata, H., Asahina, I., Watanabe, N., Ishii, Y., Kubo, N., Ohshima, S., et al. (2010). Characteristic change and loss of *in vivo* osteogenic abilities of human bone marrow stromal cells during passage. *Tissue Eng. Part A* 16 (2), 663–673. doi:10.1089/ten.TEA.2009.0500

Agata, H., Sumita, Y., Hidaka, T., Iwatake, M., Kagami, H., and Asahina, I. (2019). Intra-bone marrow administration of mesenchymal stem/stromal cells is a promising approach for treating osteoporosis. *Stem Cells Int.* 1, 10. doi:10.1155/2019/4214281

Aota, K., Yamanoi, T., Kani, K., Nakashiro, K. I., Ishimaru, N., and Azuma, M. (2018). Inverse correlation between the number of CXCR3+ macrophages and the severity of inflammatory lesions in sjögren's syndrome salivary glands: A pilot study. *J. Oral Pathol. Med.* 47 (7), 710–718. doi:10.1111/jop.12756

Asahina, I., Kagami, H., Agata, H., Honda, M. J., Sumita, Y., Inoue, M., et al. (2021). Clinical outcome and 8-year follow-up of alveolar bone tissue engineering for severely atrophic alveolar bone using autologous bone marrow stromal cells with platelet-rich plasma and β-tricalcium phosphate granules. *J. Clin. Med.* 10 (22), 5231. doi:10.3390/jcm10225231

Azuma, N., Katada, Y., and Sano, H. (2018). Deterioration in saliva quality in patients with sjögren's syndrome: Impact of decrease in salivary epidermal growth factor on the severity of intraoral manifestations. *Inflamm. Regen.* 9, 6. doi:10.1186/s41232-018-0062-0

Both, T., Dalm, V. A., van Hagen, P. M., and van Daele, P. L. (2017). Reviewing primary sjögren's syndrome: Beyond the dryness - from pathophysiology to diagnosis and treatment. *Int. J. Med. Sci.* 14 (3), 191–200. doi:10.7150/ijms.17718

Brito-Zerón, P., Retamozo, S., Gheitasi, H., and Ramos-Casals, M. (2016). Treating the underlying pathophysiology of primary sjögren syndrome: Recent advances and future prospects. *Drugs* 76 (17), 1601–1623. doi:10.1007/s40265-016-0659-z

Chang, W. L., Lee, W. R., Kuo, Y. C., and Huang, Y. H. (2021). Vitiligo: An autoimmune skin disease and its immunomodulatory therapeutic intervention. *Front. Cell Dev. Biol.* 14 (9), 797026. doi:10.3389/fcell.2021.797026

Chen, Y., Hu, M., Wang, S., Wang, Q., Lu, H., Wang, F., et al. (2022). Nano-delivery of salvianolic acid B induces the quiescence of tumor-associated fibroblasts via interfering with TGF-β1/Smad signaling to facilitate chemo- and immunotherapy in desmoplastic tumor. *Int. J. Pharm.* 25, 121953. doi:10.1016/j.ijpharm.2022.121953

Cho, J. M., Yoon, Y. J., Lee, S., Kim, D., Choi, D., Kim, J., et al. (2021). Retroductal delivery of epidermal growth factor protects salivary progenitors after irradiation. *J. Dent. Res.* 100 (8), 883–890. doi:10.1177/0022034521999298

Chu, F., Shi, M., Lang, Y., Chao, Z., Jin, T., Cui, L., et al. (2021). Adoptive transfer of immunomodulatory M2 macrophages suppresses experimental autoimmune encephalomyelitis in C57BL/6 mice via blockading NF-κB pathway. *Clin. Exp. Immunol.* 204 (2), 199–211. doi:10.1111/cei.13572

Clément, F., Grockowiak, E., Zylbersztejn, F., Fossard, G., Gobert, S., and Maguer-Satta, V. (2017). Stem cell manipulation, gene therapy and the risk of cancer stem cell emergence. *Stem Cell Investig.* 25 (4), 67. doi:10.21037/sci.2017.07.03

Cong, Y., Tang, X., Wang, D., Zhang, Z., Huang, S., Zhang, X., et al. (2022). Umbilical cord mesenchymal stem cells alleviate Sjögren's syndrome and related pulmonary inflammation through regulating Vγ4+ IL-17+ T cells. *Ann. Transl. Med.* 10 (10), 594. doi:10.21037/atm-22-1855

Du, Q., Tsuboi, N., Shi, Y., Ito, S., Sugiyama, Y., Furuhashi, K., et al. (2016). Transfusion of CD206+ M2 macrophages ameliorates antibody-mediated glomerulonephritis in mice. *Am. J. Pathol.* 186 (12), 3176–3188. doi:10.1016/j.ajpath.2016.08.012

Elghanam, G. A., Liu, Y., Khalili, S., Fang, D., and Tran, S. D. (2017). Compact bone-derived multipotent mesenchymal stromal cells (MSCs) for the treatment of sjogren's-like disease in NOD mice. *Methods Mol. Biol.* 1553, 25–39. doi:10.1007/978-1-4939-6756-8_3

Espinosa Gonzalez, M., Volk-Draper, L., Bhattarai, N., Wilber, A., and Ran, S. (2022). Th2 cytokines IL-4, IL-13, and IL-10 promote differentiation of pro-lymphatic progenitors derived from bone marrow myeloid precursors. *Stem Cells Dev.* 31 (11-12), 322–333. doi:10.1089/scd.2022.0004

Genç, D., Bulut, O., Günaydin, B., Göksu, M., Düzgün, M., Dere, Y., et al. (2022). Dental follicle mesenchymal stem cells ameliorated glandular dysfunction in Sjögren's syndrome murine model. *PLoS One* 17 (5), e0266137. doi:10.1371/journal.pone.0266137

Geske, F. J., Monks, J., Lehman, L., and Fadok, V. A. (2002). The role of the macrophage in apoptosis: Hunter, gatherer, and regulator. *Int. J. Hematol.* 76 (1), 16–26. doi:10.1007/BF02982714

Gong, B., Zheng, L., Huang, W., Pu, J., Pan, S., Liang, Y., et al. (2020). Murine embryonic mesenchymal stem cells attenuated xerostomia in Sjögren-like mice via improving salivary gland epithelial cell structure and secretory function. *Int. J. Clin. Exp. Pathol.* 13 (5), 954–963.

Hall, B. E., Zheng, C., Swaim, W. D., Cho, A., Nagineni, C. N., Eckhaus, M. A., et al. (2010). Conditional overexpression of TGF-β1 disrupts mouse salivary gland development and function. *Lab. Invest.* 90 (4), 543–555. doi:10.1038/labinvest.2010.5

Huang, J., Yue, H., Jiang, T., Gao, J., Shi, Y., Shi, B., et al. (2019). IL-31 plays dual roles in lung inflammation in an OVA-induced murine asthma model. *Biol. Open* 15 (1), bio036244. doi:10.1242/bio.036244

I, T., Sumita, Y., Yoshida, T., Honma, R., Iwatake, M., Raudales, J. L. M., et al. (2019). Anti-inflammatory and vasculogenic conditioning of peripheral blood mononuclear cells reinforces their therapeutic potential for radiation-injured salivary glands. *Stem Cell Res. Ther.* 10 (1), 304. doi:10.1186/s13287-019-1414-7

Iwaszko, M., Biały, S., and Bogunia-Kubik, K. (2021). Significance of interleukin (IL)-4 and IL-13 in inflammatory arthritis. *Cells* 10 (11), 3000. doi:10.3390/cells10113000

Jonsson, M. V., Delaleu, N., Brokstad, K. A., Berggreen, E., and Skarstein, K. (2006). Impaired salivary gland function in NOD mice: Association with changes in cytokine profile but not with histopathologic changes in the salivary gland. *Arthritis Rheum.* 54 (7), 2300–2305. doi:10.1002/art.21945

Khalili, S., Faustman, D. L., Liu, Y., Sumita, Y., Blank, D., Peterson, A., et al. (2014). Treatment for salivary gland hypofunction at both initial and advanced stages of sjögren-like disease: A comparative study of bone marrow therapy versus spleen cell therapy with a 1-year monitoring period. *Cytotherapy* 16 (3), 412–423. doi:10.1016/j.jcyt.2013.10.006

Khalili, S., Liu, Y., Kornete, M., Roescher, N., Kodama, S., Peterson, A., et al. (2012). Mesenchymal stromal cells improve salivary function and reduce lymphocytic infiltrates in mice with Sjögren's-like disease. *PLoS One* 7 (6), e38615. doi:10.1371/journal.pone.0038615

Kokubo, K., Onodera, A., Kiuchi, M., Tsuji, K., Hirahara, K., and Nakayama, T. (2022). Conventional and pathogenic Th2 cells in inflammation, tissue repair, and fibrosis. *Front. Immunol.* 9 (13), 945063. doi:10.3389/fimmu.2022.945063

Kuroshima, S., Nakajima, K., Sasaki, M., I, T., Sumita, Y., Asahara, T., et al. (2019). Systemic administration of quality- and quantity-controlled PBMNCs reduces bisphosphonate-related osteonecrosis of jaw-like lesions in mice. *Stem Cell Res. Ther.* 10 (1), 209. doi:10.1186/s13287-019-1308-8

Liu, O., Xu, J., Wang, F., Jin, W., Zanvit, P., Wang, D., et al. (2021). Adipose-mesenchymal stromal cells suppress experimental Sjögren syndrome by IL-33-driven expansion of ST2+ regulatory T cells. *iScience* 24 (5), 102446. doi:10.1016/j.isci.2021.102446

MacKinnon, A. C., Farnworth, S. L., Hodkinson, P. S., Henderson, N. C., Atkinson, K. M., Leffler, H., et al. (2008). Regulation of alternative macrophage activation by galectin-3. *J. Immunol.* 180, 2650–2658. doi:10.4049/jimmunol.180.4.2650

Masuda, H., Alev, C., Akimaru, H., Ito, R., Shizuno, T., Kobori, M., et al. (2011). Methodological development of a clonogenic assay to determine endothelial progenitor cell potential. *Circ. Res.* 24 (1), 20–37. doi:10.1161/CIRCRESAHA.110.231837

Misuno, K., Tran, S. D., Khalili, S., Huang, J., Liu, Y., and Hu, S. (2014). Quantitative analysis of protein and gene expression in salivary glands of Sjogren's-like disease NOD mice treated by bone marrow soup. *PLoS One* 29 (1), e87158. doi:10.1371/journal.pone.0087158

Nemeth, K., Leelahavanichkul, A., Yuen, P., Mayer, B., Parmelee, A., Doi, K., et al. (2009). Bone marrow stromal cells attenuate sepsis via prostaglandin E2-dependent reprogramming of host macrophages to increase their interleukin-10 production. *Nat. Med.* 15 (1), 42–49. doi:10.1038/nm.1905

Nguyen, C. Q., Sharma, A., Lee, B. H., She, J. X., McIndoe, R. A., and Peck, A. B. (2009). Differential gene expression in the salivary gland during development and onset of xerostomia in Sjögren's syndrome-like disease of the C57BL/6.NOD-Aec1Aec2 mouse. *Arthritis Res. Ther.* 11 (2), R56. doi:10.1186/ar2676

Nocturne, G., and Mariette, X. (2013). Advances in understanding the pathogenesis of primary Sjögren's syndrome. *Nat. Rev. Rheumatol.* 9 (9), 544–556. doi:10.1038/nrrheum.2013.110

Norozi, F., Ahmadzadeh, A., Shahrabi, S., Vosoughi, T., and Saki, N. (2016). Mesenchymal stem cells as a double-edged sword in suppression or progression of solid tumor cells. *Tumour Biol.* 37 (9), 11679–11689. doi:10.1007/s13277-016-5187-7

Ramos-Casals, M., Brito-Zerón, P., Sisó-Almirall, A., Bosch, X., and Tzioufas, A. G. (2012). Topical and systemic medications for the treatment of primary Sjögren's syndrome. *Nat. Rev. Rheumatol.* 1 (7), 399–411. doi:10.1038/nrrheum.2012.53

Salminen, A. (2010). Immunosuppressive network promotes immunosenescence associated with aging and chronic inflammatory conditions. *J. Mol. Med. Berl.* 99 (11), 1553–1569. doi:10.1007/s00109-021-02123-w

Shi, B., Qi, J., Yao, G., Feng, R., Zhang, Z., Wang, D., et al. (2018). Mesenchymal stem cell transplantation ameliorates Sjögren's syndrome via suppressing IL-12 production by dendritic cells. *Stem Cell Res. Ther.* 9 (1), 308. doi:10.1186/s13287-018-1023-x

Shirakawa, K., Endo, J., Kataoka, M., Katsumata, Y., Yoshida, N., Yamamoto, T., et al. (2018). IL (Interleukin)-10-STAT3-Galectin-3 Axis is essential for osteopontin-producing reparative macrophage polarization after myocardial infarction. *Circulation* 138 (18), 2021–2035. doi:10.1161/CIRCULATIONAHA.118.035047

Sperandio, M., Gleissner, C. A., and Ley, K. (2009). Glycosylation in immune cell trafficking. *Immunol. Rev.* 230 (1), 97–113. doi:10.1111/j.1600-065X.2009.00795.x

Sumita, Y., Iwamoto, N., Seki, M., Yoshida, T., Honma, R., Iwatake, M., et al. (2020). Phase 1 clinical study of cell therapy with effective-mononuclear cells (E-MNC) for radiogenic xerostomia (first-in-human study) (FIH study on E-MNC therapy for radiogenic xerostomia). *Med. Baltim.* 99 (26), e20788. doi:10.1097/MD.0000000000020788

Sumita, Y., Liu, Y., Khalili, S., Maria, O. M., Xia, D., Key, S., et al. (2010). Bone marrow-derived cells rescue salivary gland function in mice with head and neck irradiation. *Int. J. Biochem. Cell Biol.* 43 (1), 80–87. doi:10.1016/j.biocel.2010.09.023

Sun, T., Liu, S., Yang, G., Zhu, R., Li, Z., Yao, G., et al. (2022). Mesenchymal stem cell transplantation alleviates Sjögren's syndrome symptoms by modulating Tim-3 expression. *Int. Immunopharmacol.* 111, 109152. doi:10.1016/j.intimp.2022.109152

Todt, J. C., Hu, B., and Curtis, J. L. (2008). The scavenger receptor SR-A I/II (CD204) signals via the receptor tyrosine kinase Mertk during apoptotic cell uptake by murine macrophages. *J. Leukoc. Biol.* 84 (2), 510–518. doi:10.1189/jlb.0307135

Tsukada, S., Kwon, S. M., Matsuda, T., Jung, S. Y., Lee, J. H., Lee, S. H., et al. (2013). Identification of mouse colony-forming endothelial progenitor cells for postnatal neovascularization: A novel insight highlighted by new mouse colony-forming assay. *Stem Cell Res. Ther.* 4 (1), 20. doi:10.1186/scrt168

Ushio, A., Arakaki, R., Otsuka, K., Yamada, A., Tsunematsu, T., Kudo, Y., et al. (2018). CCL22-Producing resident macrophages enhance T cell response in sjögren's syndrome. *Front. Immunol.* 9, 2594. doi:10.3389/fimmu.2018.02594

Wegmann, M. (2009). Th2 cells as targets for therapeutic intervention in allergic bronchial asthma. *Expert Rev. Mol. Diagn* 9 (1), 85–100. doi:10.1586/14737159.9.1.85

Yao, G., Qi, J., Liang, J., Shi, B., Chen, W., Li, W., et al. (2019). Mesenchymal stem cell transplantation alleviates experimental Sjögren's syndrome through IFN-β/IL-27 signaling axis. *Theranostics* 9 (26), 8253–8265. doi:10.7150/thno.37351

Young, D. A., Lowe, L. D., Booth, S. S., Whitters, M. J., Nicholson, L., Kuchroo, V. K., et al. (2000). IL-4, IL-10, IL-13, and TGF-beta from an altered peptide ligand-specific Th2 cell clone down-regulate adoptive transfer of experimental autoimmune encephalomyelitis. *J. Immunol.* 164 (7), 3563–3572. doi:10.4049/jimmunol.164.7.3563

Zhang, Q. Z., Su, W. R., Shi, S. H., Wilder-Smith, P., Xiang, A. P., Wong, A., et al. (2010). Human gingiva-derived mesenchymal stem cells elicit polarization of m2 macrophages and enhance cutaneous wound healing. *Stem Cells* 18 (10), 1856–1868. doi:10.1002/stem.503

Zhang, Z., Jiang, Y., Zhou, Z., Huang, J., Chen, S., Zhou, W., et al. (2019). Scavenger receptor A1 attenuates aortic dissection via promoting efferocytosis in macrophages. *Biochem. Pharmacol.* 168, 392–403. doi:10.1016/j.bcp.2019.07.027

Zheng, Z. Y., Feng, C. H., Xie, G., Liu, W. L., Zhu, X. L., Zhao, X., et al. (2022). Fatty acids derived from apoptotic chondrocytes fuel macrophages FAO through MSR1 for facilitating BMSCs osteogenic differentiation. *Redox Biol.* 53, 102326. doi:10.1016/j.redox.2022.102326

frontiers | Frontiers in Bioengineering and Biotechnology

TYPE Review
PUBLISHED 26 May 2023
DOI 10.3389/fbioe.2023.1149662

OPEN ACCESS

EDITED BY
Yuan Yin,
Fourth Military Medical University, China

REVIEWED BY
Dali Zheng,
Fujian Medical University, China
Geza Tamas Szabo,
Semmelweis University, Hungary

*CORRESPONDENCE
Fang Jin,
jinfang@fmmu.edu.cn
Meng Li,
119340881@qq.com

†These authors have contributed equally to this work

RECEIVED 22 January 2023
ACCEPTED 19 May 2023
PUBLISHED 26 May 2023

CITATION
Zhang Y, Liu J, Liu S, Yu L, Liu S, Li M and Jin F (2023), Extracellular vesicles in oral squamous cell carcinoma: current progress and future prospect.
Front. Bioeng. Biotechnol. 11:1149662.
doi: 10.3389/fbioe.2023.1149662

Extracellular vesicles in oral squamous cell carcinoma: current progress and future prospect

Yanqi Zhang[1,2†], Jianing Liu[1,2†], Shiyu Liu[2], Lu Yu[3], Siying Liu[1], Meng Li[2,4*] and Fang Jin[1*]

[1]Department of Orthodontics, School of Stomatology, The Fourth Military Medical University, Xi'an, China, [2]State Key Laboratory of Military Stomatology, National Clinical Research Center for Oral Diseases, Shaanxi International Joint Research Center for Oral Diseases, Center for Tissue Engineering, School of Stomatology, The Fourth Military Medical University, Xi'an, China, [3]Department of Periodontology, Shandong Key Laboratory of Oral Tissue Regeneration, Shandong Engineering Laboratory for Dental Materials and Oral Tissue Regeneration, Shandong Provincial Clinical Research Center for Oral Diseases, School and Hospital of Stomatology, Cheeloo College of Medicine, Shandong University, Jinan, Shandong, China, [4]Department of Prosthodontics, School of Stomatology, The Fourth Military Medical University, Xi'an, China

Oral squamous cell carcinoma (OSCC) is the most aggressive oral and maxillofacial malignancy with a high incidence and low survival rate. OSCC is mainly diagnosed by tissue biopsy, which is a highly traumatic procedure with poor timeliness. Although there are various options for treating OSCC, most of them are invasive and have unpredictable therapeutic outcomes. Generally, early diagnosis and noninvasive treatment cannot be always satisfied simultaneously in OSCC. Extracellular vesicles (EVs) are involved in intercellular communication. EVs facilitate disease progression and reflect the location and status of the lesions. Therefore, EVs are relatively less invasive diagnostic tools for OSCC. Furthermore, the mechanisms by which EVs are involved in tumorigenesis and tumor treatment have been well studied. This article dissects the involvement of EVs in the diagnosis, development, and treatment of OSCC, providing new insight into the treatment of OSCC by EVs. Different mechanisms, such as inhibiting EV internalization by OSCC cells and constructing engineered vesicles, with potential applications for treating OSCC will be discussed in this review article.

KEYWORDS

oral squamous cell carcinoma, extracellular vesicles, diagnosis, tumorigenesis, treatment

1 Introduction

Oral squamous cell carcinoma (OSCC) is a malignant tumor mainly originating from squamous epithelial cells. In 2018, there were 354,864 new cases and 177,384 deaths of OSCC (Bray et al., 2018). OSCC is usually diagnosed in advanced stages, which leads to a poor prognosis. Researchers attempted to find new methods for early diagnosis of OSCC. Currently, the main treatment of OSCC is still surgery combined with chemotherapy, and the main chemotherapy regimen includes 5-fluorouracil (5-FU) and cisplatin (Longley et al., 2003). However, 5-year survival remained low, mainly due to chemoresistance (Epstein et al., 2012; Chi et al., 2015). Therefore, it is crucial to improve the diagnostic approach and treatment method in OSCC.

EVs have been a main focus of research in recent years. They are membrane-derived vesicles secreted by different cells and widely found in body fluids. According to their biogenesis and releasing mode, EVs can be divided into microvesicles, exosomes, and

apoptotic bodies. They carry DNA, RNA, protein, miRNA, and other substances (Doyle and Wang, 2019) (Figure 1). EVs widely exist in tumor microenvironment (TME) and participate in cellular communication. EVs have the potential to be used for minimally invasive diagnosis because they are involved in tumorigenesis and they contain is a biologic sample from tumor cells. EVs exist in various body fluids and are easy to obtain. In addition, EVs regulate cell function by delivering their vesicular substances, thus participating in the development of OSCC (van Niel et al., 2022). More and more attention has been recently paid to the role of EVs in tumorigenesis (Brinton et al., 2015; Bebelman et al., 2018; Urabe et al., 2020). EVs are involved in many important processes in OSCC (Kaiser, 2016), such as angiogenesis and epithelial-mesenchymal transformation (EMT). Tumor-associated macrophages (TAM) are the main cell in TME and promote tumor development. EVs can regulate the phenotypic transition of macrophages. EVs are internalized by macrophages, and their signaling molecules regulate the polarization of macrophages.

In this review, we have discussed how EVs are involved in the diagnosis and development of OSCC. By understanding the role of EVs in the development of OSCC, it would be possible to design more effective therapeutic regimens. Moreover, by modifying the surface characteristics and contents of EVs, their targeting ability and treatment efficiency can improve (Herrmann et al., 2021). Therefore, producing manipulated EVs is a promising method for treating OSCC. So far, few review articles comprehensively analyzed the efficacy of EVs in the diagnosis, tumorigenesis, and treatment of OSCC, and most of them only analyzed some of these topics. Therefore, we summarized the role of EVs in the development, diagnosis, and treatment of OSCC. In addition, whether EVs can improve the survival rate of OSCC patients is also discussed.

2 The applications of EVs in the diagnosis and prognosis of OSCC

EVs contain several types of biological molecules, including proteins, lipids, DNA, and RNA, which play important roles in the development and progression of OSCC. Particularly, they are involved in several biological processes such as proliferation, apoptosis, DNA repair, metabolism, angiogenesis, and immune response (Becker et al., 2016; Ciardiello et al., 2016; Almeria et al., 2019; Kalluri and LeBleu, 2020). Some constituents of EVs are upregulated and others are downregulated to contribute to tumor cell proliferation and invasion. Non-coding RNAs, including miRNA, lncRNA, and circ RNA, along with proteins, have been increasingly investigated as diagnostic and prognostic markers for OSCC. Apart from tissue specimens, diagnostic EVs are most often collected from body fluids, such as saliva and serum, or cell culture supernatants. Body fluid-derived EVs can be easily used for minimally invasive early diagnosis and prognosis (Li et al., 2021).

2.1 RNAs in EVs as diagnostic markers for OSCC

Exosomal RNAs are heavily involved in the interaction between tumor cells and TME (Table 1). Carcinoma-derived exosomal RNAs can promote TME remodeling, and exosomal RNAs originating

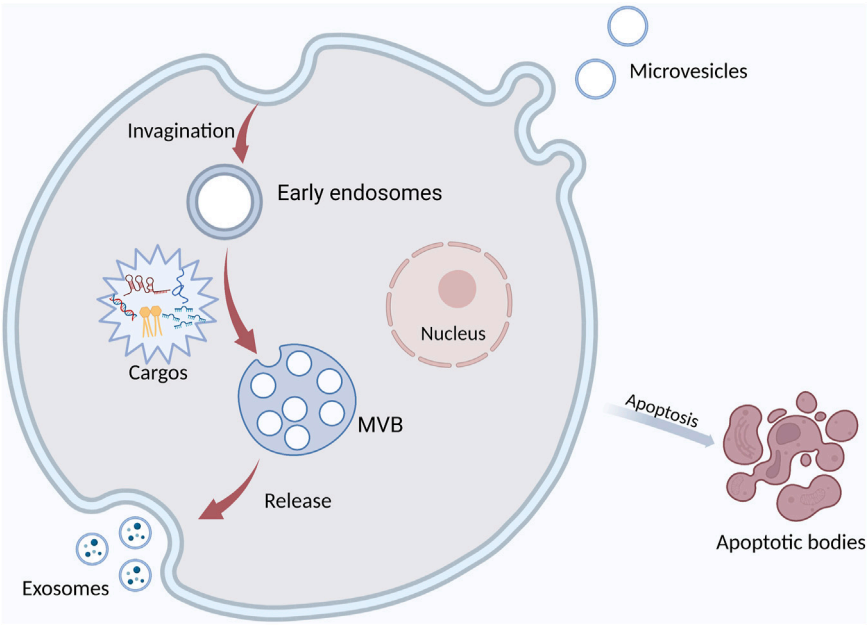

FIGURE 1
The formation and secretion of EVs. Extracellular vesicles are mainly classified into three main types: exosomes, microvesicles, and apoptotic bodies. Exosomes are formed by the fusion of multivesicular bodies (MVBs) with the plasma membrane, MVs form directly from the plasma membrane to the outward bud, and apoptotic bodies are released by the cells after apoptosis. It contains DNA, miRNA, protein, and other cargos.

from TME can also affect tumor cell behavior. By regulating tumor cell-TME crosstalk, exosomal RNAs can facilitate tumorigenesis, tumor growth, and metastasis (Fang et al., 2020; Tan et al., 2020; Forder et al., 2021; Lu et al., 2021; Villegas-Pineda et al., 2021; Zhao et al., 2022). Therefore, RNAs in EVs have increasingly received attention for OSCC diagnosis.

2.1.1 Correlation between EV-derived miRNAs and OSCC

miRNAs, also known as small non-coding RNAs, have 19–24 nucleotides and post-transcriptionally regulate gene expression in several physiological and pathological processes (Lu et al., 2021). Circulatory miRNAs exist in three forms: free circulating miRNAs, exosomal miRNAs, and conjugated with argonaute proteins (Ago2) (Sahu and Routray, 2021). Free miRNAs in saliva, serum, and plasma can accelerate the less-invasiveness diagnosis of OSCC and improve patients' compliance compared with conventional methods like tissue biopsy and mucosal scraping. Therefore, they received significant attention as a diagnostic method for oral cancer in recent years (He L. et al., 2020). Exosomes contain complex payloads encapsulated by a lipid bilayer, which improves the stability of miRNAs and allows them to resist nucleases (Sahu and Routray, 2021). Recent studies have elucidated that exosomes are deeply involved in the regulation of intercellular communication (Kalluri and LeBleu, 2020). Exosomal miRNAs modulate various disease progression by delivering signaling molecules and miRNAs. Oncogenic miRNAs (oncomiRs) and tumor-suppressing miRNAs (TS-miRNAs) are two subtypes of miRNAs that can be distinguished based on their regulatory roles in oncogenesis (Chen and Huang, 2021).

Exosomal miRNAs with differential expression in OSCC cells and normal cells have been the focus of research in recent years. Salivary exosomes from OSCC patients and exosomes derived from OSCC tissues had significantly higher levels of miR-24-3p compared with normal controls. The ROC curve revealed that the area under the curve (AUC) for salivary exosomes was 0.738 (He L. et al., 2020). Therefore, miR-24-3p in salivary exosomes can potentially help the early diagnosis of OSCC (He L. et al., 2020). As a potential diagnostic biomarker, miR-30a was significantly overexpressed in exosomes and OSCC tissues, with an AUC value of 0.812. A high level of miR-30a also predicted shorter recurrence-free survival (He T. et al., 2021). Similarly, miR-210 had significantly higher levels in plasma-derived EVs from OSCC patients than in plasma-derived EVs from control samples (AUC = 0.951) (Bigagli et al., 2021). miR-365 was expressed in OSCC cell lines and transferred into EVs produced by OSCC cell lines (Coon et al., 2020). Similar to miR-365, miR-23a-3p was significantly upregulated in OSCC cell lines (SCC-9 and CAL-27). Intriguingly, exosomes derived from OSCC cell lines contained higher levels of miR-23a-3p compared with OSCC cells. miR-23a-3p-rich tumor-derived exosomes (TEX) can induce macrophage polarization toward the M2 subtype, associated with tumor growth and invasion (Cai and Qiao, 2019). A miRNA array confirmed that compared with conjugated normal cells, oncogenic miR-155 and miR-21 were upregulated by two to five folds in exosomes derived from primary OSCC cells. They promote cell proliferation and invasion by downregulating PTEN and Bcl-6 tumor suppressor genes in OSCC cells (Chen and Huang, 2021). miR-21-5p is the most abundant microRNA (miR) in EVs released from OSCC cells. miR-21-5p promotes tumor cell stemness and migration (Chen et al., 2019). Two key oncomiRs, miR-342-3p and miR-1246, are highly expressed in OSCC-derived exosomes. They were transferred to HOC313-P cell and enhanced its motility by exosomes derived from HOC313-LM cell, a type of human OSCC cell line with high metastatic capacity (Sakha et al., 2016). miR-302b-3p and miR-517b-3p were only detected in salivary EVs from OSCC patients. miR-512-3p and miR-412-3p had higher expression levels in OSCC patients (Gai et al., 2018). In addition, the oxygen concentration in TME can affect the contents of OSCC-derived exosomes. OSCC-derived exosomes can enhance the metastasis and invasiveness of OSCC cells under hypoxic conditions (Li and Zhu, 2016). miRNA sequencing explains how exosomes from OSCCs in normoxic and hypoxic environments differently express miRNAs. Of 108 differentially expressed miRNAs in OSCCs, miR-21 exhibited the greatest difference. It was upregulated in OSCCs and induced EMT, which is needed for tumor migration and invasion. Exosomal miR-21 level may be used as a diagnostic marker in OSCC (Li and Zhu, 2016). Various onco-miRNAs are upregulated in OSCC-derived EVs, which can serve as diagnostic markers.

Although exosomal miRNAs have several advantages as OSCC biomarkers, their application is still controversial because the sensitivity of isolation methods alters the composition of exosomes. Furthermore, smoking, alcohol abuse, and HPV infection can upregulate exosomal miRNAs in the serum samples of healthy participants. Moreover, exosomal miRNAs can be upregulated in other malignant tumors like breast cancer, bladder cancer, hepatocellular carcinoma, and Hodgkin's lymphoma (He L. et al., 2020).

On the other hand, exosomal miR-126, a TS-miRNA, is downregulated in OSCC. miR-126 downregulates epidermal growth factor-like domain multiple 7 (EGFL7), a tumor-suppressor in OSCC, thereby regulating vascular endothelial growth factor (VEGF), Notch, and Wnt signaling pathways. (Chen and Huang, 2021). Previously, it was found that miR-101-3p has significantly higher expression in normal tissues compared with adjacent malignant tissues. Similarly, it was shown that miR-101-3p is downregulated in several OSCC cell lines such as CAL27, SCC9, and TCA8113 (Xie et al., 2019a, 101-3). According to *in-vitro* and *in-vivo* experiments, exosomes transfer miR-101-3p from hBMSCs to OSCC cells to prevent OSCC progression (Xie et al., 2019a). Although TS-miRNAs have not yet been investigated comprehensively, they are promising for both diagnosis and treatment of OSCC.

2.1.2 The value of other non-coding exosomal RNAs in the diagnosis of OSCC

It is worth noting that other exosomal non-coding RNAs always function through interaction with miRNAs. Bioinformatics analysis revealed that exosomal circ_0000199, a circRNA originating from the end of an RNA molecule, sponges particular miRNAs, such as miR-145-5p and miR-29b-3p, to upregulate oncoproteins in OSCC cells. Researchers found that exosomal circ_0000199 expression is associated with TNM stage, tumor size, and lymphatic metastasis and that circ_0000199 overexpression shortens the survival of OSCC patients (HR 3.57; 95% CI 2.48-6.24, $p = 0.0035$) (Luo et al., 2020). M1 macrophage-derived exosomal lncRNA HOTTIP can decrease proliferation, induce apoptosis, and enhance M1 phenotype differentiation in head and neck squamous cell carcinomas (HNSCC) (Jiang et al., 2022). Exosomal lncRNA LBX1-AS1 is released by RBPJ-OE macrophages. It competes with miR-182-5p

to prevent the growth of tumor cells by regulating Forkhead Box O (FOXO) expression (Ai et al., 2021, 1). lncRNA Lnc-CAF is remarkably upregulated in HSC3 cell-derived exosomes. It can be absorbed by cancer-associated fibroblasts (CAFs) to upregulate Lnc-CAF. This forms a positive feedback loop and causes Lnc-CAF co-expression with IL-3, which promotes OSCC growth (Ding et al., 2018). Similar to miRNAs, other non-coding RNAs can help in the early detection of OSCC. However, there are only a few studies investigating the role of other types of exosomal non-coding RNAs in OSCC. circ IGHG is highly expressed in OSCC and induces EMT, suggesting a promising potential for theranostics, but still, further studies are needed (Liu et al., 2021).

2.2 Cargo proteins and surface markers of EVs are indicators of OSCC

Previous articles have reviewed several proteins used as hallmarks of OSCC prognosis (Sasahira and Kirita, 2018); nevertheless, exosomal proteins are extensively diverse and our knowledge about their functions is rapidly growing. Intriguingly, it was unfolded that PTEN, a crucial tumor suppressor protein for angiogenesis, is downregulated by miR-130b-3p in OSCC cells; however, PTEN mRNA level did not significantly change compared with adjacent healthy tissues (Yan et al., 2021). It has been suggested that PTEN and PDCD4 both downregulate STAT3 (Chen et al., 2019). STAT3 silencing reduced miR-21-5p level (Chen et al., 2019), which has been introduced as an oncomiR in previous sections. SWATH-MS analysis between healthy, OSCC_NLNM, and OSCC_LNM groups, showed that small proline-rich protein 3 (SPRR3) is significantly upregulated in the salivary small extracellular vesicles (S/SEVs) of OSCC-free participants (Fontana et al., 2021). Recently findings indicated how low expression of SPRR3 is involved in OSCC progression (Yu et al., 2020). In addition, the SWATH-MS analysis uncovered that some proteins (like lipocalin-2, LCN2, and S100) related to anti-microbial defense and inflammatory response are enriched in the S/SEVs of OSCC patients with lymph node metastasis (Fontana et al., 2021). Other studies also unveiled that they can serve as diagnostic and prognostic biomarkers of OSCC (Raffat et al., 2018; Rahimi et al., 2020). Laminin-332 was upregulated in EVs produced by OSCC cell lines (LN1-1) and in plasma EVs derived from OSCC patients with lymph node metastasis. After being absorbed by lymphatic endothelial cells (LECs), Laminin-332 promotes LEC migration and tube formation (Wang et al., 2019). ApoA1, CXCL7, PF4V1, and F13A1 have potential application as novel circulating biomarkers of OSCC with LNM (Li L. et al., 2019). CKLF-like MARVEL transmembrane domain-containing 6 (CMTM6) was highly expressed in OSCC specimens. Besides, it was revealed that exosomal CMTM6 can be transferred to macrophages and regulate macrophage polarization (Pang et al., 2021). HSP90α and HSP90β, as molecular chaperones, were markedly increased in EVs from metastatic cell lines and predicted poor prognosis of OSCC (Ono et al., 2018). Matrix metallopeptidases (MMPs) facilitate OSCC metastasis by degrading ECMs (Khan et al., 2020). MMP9 was strongly upregulated in exosomes from tumor cells (Qadir et al., 2018). Mechanistically, these results imply that proteins in EVs can serve as useful biomarkers of OSCC progression and metastasis. Apart from cargo proteins in EVs, some surface markers can also help with diagnosis. Despite CD63, CD81, and CD9 are downregulated in patients with oral cancer (OC) (Zlotogorski-Hurvitz et al., 2016). It was unveiled that life expectancy after surgery was correlated with the plasma level of exosomal CD63 (Rodríguez Zorrilla et al., 2019). Centrosomal protein (CEP55) was found on tumor-derived exosomes in HNCC, but not in primary human oral keratinocytes (Qadir et al., 2018). However, the specific mechanisms by which CD molecules and other transmembrane proteins are involved in OSCC progression remain unclear and further studies are warranted.

Taken together, these biomarkers have great potential for the diagnosis and prognosis of OSCC. Although our information about exosomal proteins, especially about exosomal surface proteins, is limited. CD markers lack stability and enough specificity. Future studies on exosomal proteins are needed to improve early diagnosis and prognosis in OSCC.

3 The role of EVs in the development of OSCC

Since the constituents of EVs can be used as diagnostic markers in OSCC, EVs may be involved in the development of OSCC. Herein, we review key components of OSCC development (Figure 2), such as TAM, polarization, angiogenesis, and EMT, and enumerate the role of EVs in these processes. In addition, we also elucidate the mechanism by which EVs promote chemotherapy resistance in OSCC and more comprehensively dissect the role of EVs in OSCC development.

3.1 The role of EVs to regulate TAM subtypes in OSCC

TME supports the growth of tumor cells. TME is composed of immune cells, stromal cells, extracellular matrix, and other components. The interaction between tumor cells and TME is crucial for tumor growth (Joyce and Pollard, 2009). TAMs are the main cells in TME and contribute to tumor development to varying degrees (Ruffell et al., 2012; Coussens et al., 2013; Mantovani et al., 2017). Recent studies have indicated that TAMs include M1 (classically activated macrophage) and M2 (alternatively activated macrophage) subtypes (Laviron and Boissonnas, 2019). OSCC cells and macrophages can release EVs that regulate TME. M1 macrophages have been described as the pro-inflammatory phenotype and play an important role in anti-microbial defense. M2 macrophages have been described as the anti-inflammatory phenotype and facilitate post-inflammatory tissue repair (Baig et al., 2020).

3.1.1 EVs regulateM1 macrophage activation

Cancer cells release various EVs (Akers et al., 2013; Doyle and Wang, 2019). Several products of cancer cells can regulate macrophage polarization through the paracrine mechanism. EVs released by cancer cells can be internalized by macrophages and modulate the phenotypes of macrophages (Bellmunt et al., 2019; Baig et al., 2020). Many studies have suggested that M1 macrophages are antitumor phenotypes (Ai et al., 2021). M1 exosomal lncRNA HOTTIP inhibits HNSCC progression by competitively absorbing miRNA-19a-3p and miRNA-19b-3p and activating TLR5/NF-κB

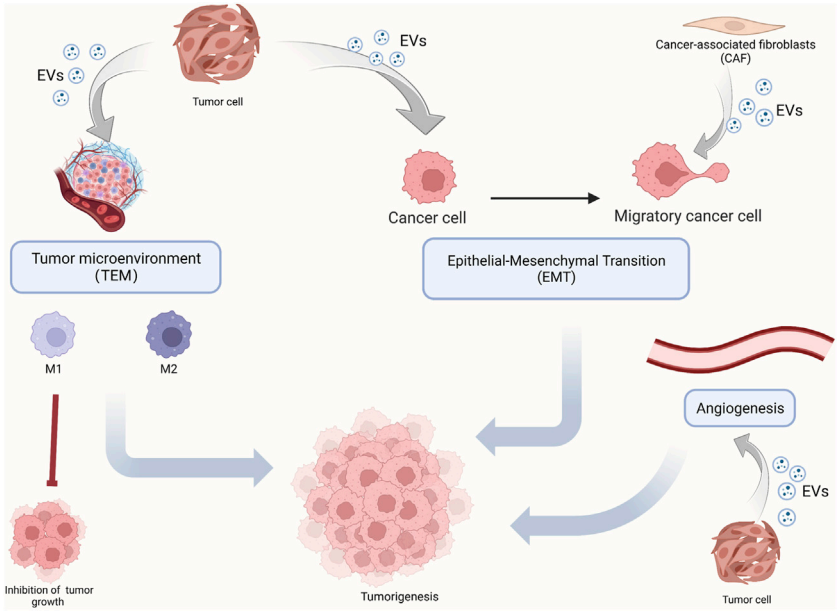

FIGURE 2
The role of EVs in OSCC tumorigenesis. OSCC tumorigenesis mainly includes the polarization of macrophages in the tumor microenvironment, epithelium-mesenchymal transformation, and angiogenesis. EVs carry molecular signals which play a regulating role.

signaling pathway (Jiang et al., 2022). miRNA-9 is a key miRNA for tumor growth, metastasis, immunity, and radiosensitivity. Exosomes secreted by HPV + HNSCC contain miRNA-9, which downregulates PPARδ in macrophages, thereby inducing M1 polarization and increasing radiosensitivity in HNSCC (Tong et al., 2020). Recent studies have shown that M1-like cells also promote tumor development. The high invasiveness of M1-like TAM has been associated with the aggressive characteristics of some cancers. Similarly, M1-like TAM promoted tumor cell migration in OSCC (Gao et al., 2018; He Y. et al., 2020; Oshi et al., 2020). OSCC cells secrete EVs containing THBS1 that promotes macrophage polarization into M1-like cells. M1-like macrophages secrete IL-6, which activates Jak/STAT3 pathway in OSCC cells and promotes EMT, OSCC stemness, and THBS1 transcription (Xiao et al., 2018; You et al., 2022). In conclusion, the positive feedback loop between M1-like TAM and OSCC cells regulates EMT and cancer stemness (You et al., 2022). THBS1 is the most abundant protein secreted by OSCC. It is a multifunctional protein and an effective regulator of macrophage activation (Pal et al., 2016). In summary, M1-like macrophages are no longer considered the tumor-resistant phenotype, and they can promote tumor progression in certain circumstances.

3.1.2 The role of EVs in M2-type macrophages activation

EVs provide a new method of information exchange between cells. Tumor cells interact with other cells in the TME by miRNA-riched exosomes (Brinton et al., 2015). TEM is mainly composed of macrophages, whose function can be regulated by OSCC-derived exosomes. M2-like macrophages promote tumor development (Baig et al., 2020). Endoplasmic reticulum stress was positively correlated with poor survival in OSCC patients. Many studies showed that programmed cell death-ligand 1 (PD-L1) prevents T cell activation and contributes to tumor immune escape (Xie F. et al., 2019; Daassi et al., 2020). Studies have shown that endoplasmic reticulum stress enhances PD-L1-rich exosome secretion by OSCC cells, thereby promoting M2 polarization of macrophages. M2-like macrophages impair the cytotoxic response of $CD8^+$ T cell immune response and promote tumorigenesis (Yuan et al., 2022). CMTM6 is a key regulator of immune response in cancer. OSCC cells can release CMTM6-rich exosomes to activate ERK1/2 signaling pathway in macrophages, induce an M2-like phenotype, and promote tumor progression (Pang et al., 2021). The study also proved that CMTM6 deletion can reduce the proliferation and migration of OSCC cells, providing a new idea for treating OSCC.

3.2 Cargos in EVs to regulate angiogenesis of OSCC

EVs contain proteins, DNA, and miRNA. They precisely regulate tumor cell communication with neighboring cells and distant cells. Tumor cells can use EVs to reprogram signaling pathways in target cells and promote angiogenesis (Qadir et al., 2018). EVs can carry tumor antigens and specific proteins involved in vesicle formation and transportation (Baietti et al., 2012). Angiogenesis is essential for tumor development. Neovascularization provides oxygen supply and nutrients for the tumor cells. Increased angiogenesis and upregulation of VEGF reduce the overall survival rate of patients with OSCC (Kyzas et al., 2005). Therefore, understanding the mechanism of angiogenesis helps the targeted therapy in OSCC. Among 45 OSCC patients, higher levels of circulating microparticles (MPs) were significantly associated with tumor size, lymph node

metastasis classification, vascular density, and VEGF expression. Circulating MPs isolated from OSCC patients can be internalized by human umbilical vein endothelial cells (HUVEC) and promote endothelial cell proliferation, migration, invasion, angiogenesis, and expression of pro-angiogenic factors (Ren et al., 2016). Studies have shown that EVs isolated from HNSCC cells can induce angiogenesis. EPHB2 carried by EVs can promote angiogenesis by inducing ephrin reverse signal transduction, thereby promoting tumor cell survival and metastasis (Sato et al., 2019). Many studies have shown that miRNAs carried by EVs can regulate angiogenesis in HNSCC (Panvongsa et al., 2022). AS a tumor suppressor gene, PTEN plays an important role in tumorigenesis. Exosomes carrying miRNA-130B-3P can promote angiogenesis by downregulating PTEN expression (Yan et al., 2021). OSCC-derived exosomes carry miRNA-221, which downregulates PIK3R1 and promotes HUVEC migration and duct formation (He S. et al., 2021). Many studies attempted to inhibit angiogenesis, thereby preventing OSCC development (Rosenberger et al., 2019). It has been suggested that exosomes of human deciduous stem cells carry miRNA100-5P and miRNA-1246, which inhibit angiogenesis (Liu P. et al., 2022).

3.3 The involvement of EVs in EMT of OSCC

EMT is a critical process in tumorigenesis. EMT is characterized by reduced expression of cell adhesion molecules and transformation of the cytoskeleton from keratin to vimentin. Epithelial cells are closely connected; however, mesenchymal cells have different morphologies, providing a higher invasion and migration capacity (Yeung and Yang, 2017). EMT is divided into three types. Type three EMT has been a research hotspot in recent years, as it is related to tumorigenesis. Identification and inhibition of key molecules in EMT is an important prerequisite for controlling tumor development. Tumor-derived exosomes (TDEs) can promote EMT, thereby enhancing invasion and migration capacity (Syn et al., 2016). CAFs also play a critical role in EMT. Many studies have shown that CAFs can interact with tumor cells via exosomes, and exosomal miRNAs can participate in oncogenesis (Yang et al., 2017). Transcription factors can directly modulate gene expression in EMT. Changes in RNA expression can also regulate EMT. The initiation and progression of EMT need different signaling pathways, and these pathways interact with each other as a network (Lamouille et al., 2014). As a bidirectional regulatory process, the interaction between EVs and tumor cells markedly differs based on the constituents of EVs. For instance, fibroblasts transfer exosomal miRNA-34a-5p to OSCC cells and may be involved in OSCC progression via the AKT/GSK-3β/β-catenin/Snail signaling pathway. These findings can help the treatment of OSCC. miRNA-34a-5p/AXL axis inhibitors may treat OSCC (Li et al., 2018). Currently, many studies are investigating EMT-based interventions to inhibit tumorigenesis.

3.4 EVs participates in the chemoresistance of OSCC

Chemoresistance can markedly undermine the efficacy of cisplatin and 5-FU, as the main chemotherapeutic agents for OSCC (Longley et al., 2003).

EVs can impair chemosensitivity and induce chemoresistance in OSCC through various mechanisms, thereby lowering the survival rate among OSCC patients. The constituents of exosomes, drug efflux by EVs, changes in vesicular pH, the anti-apoptotic signal transmitted by EVs, regulation of DNA repair mechanisms, immune response, and induction of cancer stemness and EMT by EVs are all involved in such outcomes (Law et al., 2021).

Many studies have shown that miRNAs mediate chemoresistance in tumor cells (Chen et al., 2014a; Chen et al., 2014b). OSCC cells with 5-FU resistance secreted APCDD1L-AS1-rich exosomes, which targeted miRNA-1224-5p and regulated miR-1224-5p/nuclear receptor binding SET domain protein 2 (NSD2) to induce 5-FU resistance (Li et al., 2021c). EMT enhances chemoresistance (Wang et al., 2016). Cells with acquired chemoresistance (cisRes90-OSCC) release exosomal miRNA-155, which targets FOXO3a and regulates EMT in OSCC cells (Kirave et al., 2020). Studies have shown that cisplatin-resistant cell lines (HSC-3-R, SCC-9-R) can transfer miRNA-21a to OSCC cells through exosomes. miRNA-21a induces cisplatin resistance by targeting PTEN and programmed cell death 4 (PDCD4) (Liu et al., 2017). Stromal cells such as macrophages can modulate the sensitivity of tumor cells to chemotherapeutic agents. It has been shown that macrophage-derived exosomes can reduce the sensitivity of OSCC cells to chemotherapeutic agents by activating the AKT/GSK-3β signaling pathway (Tomita et al., 2020).

4 EVs in multiple forms provide new ideas for OSCC treatment

The combination of surgery and chemotherapy is the most common and efficient therapeutic approach for patients with OSCC. In addition to chemotherapy resistance, which is common in OSCC, chemotherapeutics also cause major side effects, such as bone marrow depression, nephrotoxicity, gastrointestinal discomfort, skin and tongue lesions, and severe weight loss (Wang et al., 2015; Huang et al., 2020). Therefore, alternative therapeutic approaches are needed.

EVs from other cells may modulate some pathophysiological processes such as macrophage polarization, angiogenesis, and EMT through paracrine mechanism (Ohno et al., 2013; Kamerkar et al., 2017). Recently, inhibiting the ability of OSCC cells to endocytose EVs from TME has demonstrated satisfactory therapeutic efficacy (Fujiwara et al., 2018; Sasabe et al., 2022) (Figure 3).

4.1 Naturally derived EVs function as a double-edged sword

Mesenchymal stem cells (MSCs) can either suppress or promote immune response (Li et al., 2012; Liang et al., 2021). MSC-derived EVs can be used in cancer treatment. miR-16 from MSC-derived EVs can inhibit breast cancer growth by downregulating VEGF and subsequent angiogenesis (Lee et al., 2013). Similarly, exosomes derived from human exfoliated deciduous teeth (SHEDs) can attenuated angiogenesis in OSCC. A xenograft transplantation model indicated that miR-100-5p and miR-1246 carried by SHED-Exos can inhibited angiogenesis (Liu P. et al., 2022).

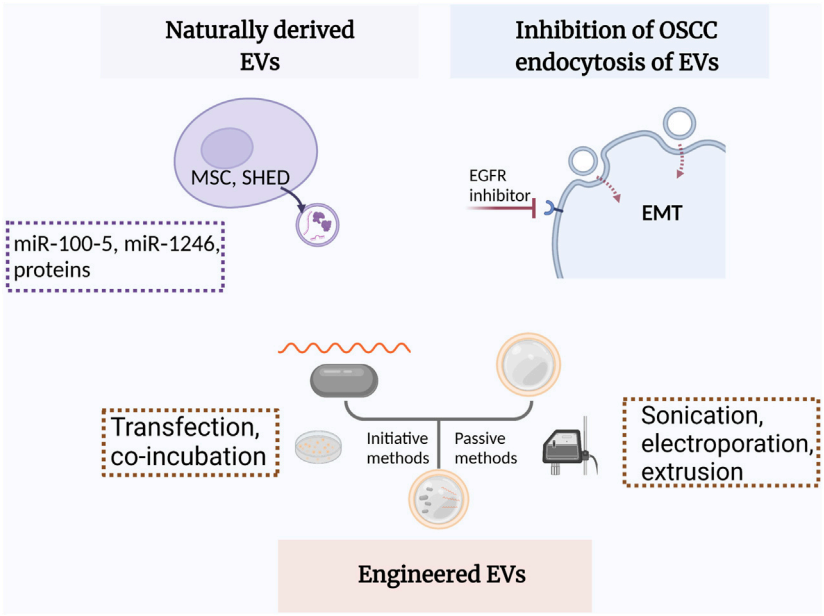

FIGURE 3
Schematic illustration of EVs applied in OSCC treatment. MSC, mesenchymal stem cells; SHEDs, stem cells of human exfoliated deciduous teeth; EGFR, epidermal growth factor receptor; EMT, epithelial-mesenchymal transition.

However, MSC derived EVs are regarded as a double-edged sword due to promoting tumor progression. More studies are needed to overcome this issue.

4.2 Engineered EVs as a novel platform supplementary for targeted treatment in OSCC

Nanotechnology, particularly the development of different types of nanoparticles such as liposomes and biomimetic nanoparticles, has considerably improved the targeted treatment of tumors (Zhang et al., 2020). After being modified through initiative (transfection and co-incubation) or passive methods (freeze–thaw cycles, sonication, electroporation, and extrusion), nanoparticles can be loaded with chemotherapeutic agents, specific miRNAs, or other cargoes (Ebnoether and Muller, 2020; Zhang et al., 2021).

Modified EVs applied in other diseases can be similarly used for treating OSCC. Engineered EVs are now extensively used as drug carriers. We have previously constructed engineered neutrophil-derived apoptotic bodies (eNABs) loaded with hexyl 5-aminolevulinate hydrochloride (HAL) to ameliorate cardiac infarction (Bao et al., 2022). We also produced chimeric apoptotic bodies (cABs) preloaded with microRNA-21 to modulate inflammatio (Dou et al., 2020). As cancer immunotherapeutic drug carriers, dendritic cell-derived exosomes (DCs-Exo) loaded with antigens have been used for treating malignant melanoma (Nikfarjam et al., 2020). For specifically targeting cancer cells and preventing rapid clearance of drugs, specialized exosomes were constructed using iEXO-OXA platform and MSC-derived exosomes with superficial alteration with oxaliplatin (OXA) (Zhou et al., 2021) Through surface modification, CD44 facilitates lipid-mimetic-chains-grafted HA-modified EVs penetration into tumoral tissues and DOX delivery to tumor cells (Liu et al., 2019). Future improvements in EV design can improve the targeted therapy of OSCC. Different sources of biomimetic EVs have been used in previous studies to improve the efficiency of engineered EVs. Intriguingly, engineered bovine milk exosomes linked to doxorubicin via a special bond were packed with endoperoxides and chlorin e6 (Ce6) through a series of reactions. Producing exosomes by this method can overcome the low efficiency and ethical issues caused by using natural vesicles (Zhang et al., 2020).

In addition to promoting the selective uptake of therapeutic EVs by tumor cells, it is feasible to inhibit EVs endocytosis by phagocytic cells. Both upregulation of CD47 (Mathieu et al., 2019) and downregulation of integrins α6β4 and αvβ5 on the surface of exosomes can prevent tumor cell metastasis (Hoshino et al., 2015).

Although much experience has been provided about engineered EVs in other cancers, few studies have been conducted in OSCC. Some researchers have found that the constituents of EVs can inhibit OSCC growth. Exosomal miR-34a-5p targets AXL, thereby inhibiting the proliferation and motility of OSCC cells through AKT/GSK-3β/β-catenin/Snail signaling pathway. But miR-34a-5p has low expression in OSCC cells. It suggests that EVs can be loaded with inhibitors of the miR-34a-5p/AXL axis to treat OSCC (Li, 2018). In fact, some miRs are enriched in exosomes to function efficiently. For instance, γδT cells infected with lenti-miR138 virus can produce miR-138-rich γδTDEs, which can be used in the treatment of OSCC. miR-138 targets PD-1 and CTLA-4 in $CD8^+$ T cells and promotes anti-tumor immunity (L et al., 2019). Apart from miRs, some onco-miR inhibitors can be transported by EVs. Exosomes transfected with calcium chloride, a miR-155 suppressor, can upregulate FOXO3a and induce mesenchymal-epithelial

TABLE 1 Exosomal RNA biomarkers related to diagnosis and prognosis of OSCC.

Biomolecules	Molecules	Origin	Findings	Ref(s)
OncomiRs				
	miR-24-3p	OSCC patients	Elevate in salivary exosomes of OSCC patients (AUC = 0.738)	He et al. (2020a)
	miR-23a-3p	SCC-9 and CAL-27	OSCC cells derived exosomes enriched than OSCC cells	Cai and Qiao (2019)
	miR-155, miR-21	serum samples of OSCC patients	upregulated in exosomes derived from primary tumor cells from OSCC patients than paired normal cells	Chen and Huang (2021)
	miR-342-3p, miR-1246	HOC313-LM	express high in exosomes and promote its motility	Sakha et al. (2016)
	miR-30a	OSCC patients	a positive relation between the expression in exosomes and tissues of OSCC patients (AUC = 0.812)	He et al. (2021b)
	miR-302b-3p, miR-517b-3p	Saliva of OSCC patients	only discovered in EVs from OSCC patients saliva but healthy controls	Gai et al. (2018)
	miR-512-3p, miR-412-3p	OSCC patients	increase in comparison with the paired	Gai et al. (2018)
	miR-210	plasma of OSCC patients	express higher than normal samples with AUC of 0.9513	Bigagli et al. (2021)
	miR-365	SCC25, CAL27	exist in OSCC cell lines and extracellular vesicles	Coon et al. (2020)
	miR-21	SCC-9, CAL-27	drive recipient cells toward EMT, advantageous for tumor migration and invasion	Li and Zhu (2016)
TSmiRs				
	miR-126	serum exosomes of OSCC patients	suppress angiogenesis, lymphangiogenesis and tumorigenesis by targeting EGFL7	Chen and Huang (2021)
	miR-101-3p	CAL27, SCC9, TCA8113	suppress OSCC progression	Xie et al. (2019a)
Others				
	circ_0000199	OSCC cells from human sample	elevate in OSCC patients, associated with TNM stage, tumor size, lymphatic metastasis	Luo et al. (2020)
	lncRNA HOTTIP	FaDu, CNE-2Z, Hep-2	inhibit HNSCC proliferation through M1 polarization	Jiang et al. (2022)
	lncRNA ADAMTS9-AS	CAL-27, SCC-9	interect with miRs to regulate EMT and AKT signalling pathway and suppresses tumor growth, invasion and metastasis	Zhou et al. (2021)
	lncRNA LBX1-AS1	THP-1, SCC-4, CAL-27	inhibit tumor progression by regulate downstream FOXO expression	Ai et al. (2021)
	lncRNA FLJ22447	HSC-3	ingested by stromal CAFs to upregulate Lnc-CAF in turn, and co-express with IL-3 to promote OSCC growth	Ding et al. (2018)

transformation (MET) in cisplatin-resistant OSCC spheroids and *in vivo*, thereby reversing chemoresistance (Sayyed et al., 2021).

As mentioned previously, exosomes play a crucial role in the development of OSCC. Identifying the mechanism of exosome uptake can be promising in the treatment of OSCC. Epithelial growth factor receptor (EGFR) inhibition and knockdown both can inhibit exosome uptake by OSCC cells, thereby impeding OSCC invasion and progression. Similarly, OSCC development is influenced by the inhibitor of micropinocytosis (EIPA) (Sasabe et al., 2022). For example, cetuximab is assumed to be a therapeutic antibody for OSCC because it blocks EMT in EGFR-rich OSCC-EVs (Fujiwara et al., 2018).

Although most researchers believe that EVs are biocompatible even when administered repeatedly, their effects on other cells are still unclear. There are still many challenges, such as purification issues and immune properties, to be addressed before the clinical application of engineered EVs (Ketabat et al., 2019). Still, more progress in the field of engineered EVs is needed before their clinical application in OSCC.

5 The challenges for EVs in OSCC

5.1 The challenges for EVs in experimental research of OSCC

Currently, EVs can be classified by their origins, including cell culture-derived EVs, body fluid-derived EVs, and tissue-derived EVs (Ti-EVs). Cells lose their heterogeneity after several *in-vitro* passages, which can mask their original biological characteristics.

In particular, a two-dimensional (2D) cultural environment can barely stimulate the *in-vivo* microenvironment (Jensen and Teng, 2020). Furthermore, EVs extracted at a specific time obscured the temporal nature of their actions, which could not reflect the course of the disease. In addition, EVs cannot be easily purified from the body fluid, and they are commonly contaminated with various proteins, such as serum proteins. However, Ti-EVs contain less impurities than body fluid-derived EVs. Studies have shown that Ti-EVs promote the development and metastasis of tumors (Costa-Silva et al., 2015; Hoshino et al., 2015; Liu and Cao, 2016). As mentioned previously, TEM-derived EVs are involved in the development of OSCC by regulating macrophage polarization, angiogenesis, and EMT (Xie et al., 2019b). Therefore, more attention should be paid to Ti-EVs in the future stage. There are still some challenges to be solved in the extraction of Ti-EVs, such as its challenges regarding their isolation and purification. It is necessary to develop standardized extraction methods, characterization methods, and titer evaluation methods to improve the reliability of Ti-EV (Li et al., 2021).

5.2 The challenges in the use of EVs for diagnosing OSCC

As previously mentioned, EVs can carry substances that contribute to the development and resistance of OSCC, making them novel diagnostic tools for OSCC (Han et al., 2018). Due to their presence in various body fluids, EVs are easy to acquire. Particularly, salivary EVs can be obtained at different stages of OSCC, without causing any discomfort to patients. This accelerates the use of EVs for diagnosing OSCC, following its progression, and developing more effective treatment methods.

However, there are still many problems to be solved before using EV as a new diagnostic method. The first problem is the lack of uniform diagnostic criteria. The contents of EVs derived from various cells are different. For instance, EVs derived from tumor parenchyma and those derived from immune cells in TEM are different (Liu P. et al., 2022). Secondly, most articles focus on the role of a single molecule. However, EVs have a variety of markers on their surface and carry various signaling molecules. Whether a single molecule or a combination of multiple molecules can be used as a diagnostic method needs to be clarified in the future. This also suggests that EVs can simultaneously target several signaling pathways.

Recently, some studies have shown that nano-flow cytometer (nFCM) can be used to detect DNA in EVs, which can be a more comprehensive method to determine the source of EVs for tumor diagnosis (Liu H. et al., 2022). In addition, it has been reported that microfluidic devices can be used to analyze and characterize single EVs to determine their exact physiological effects. It can become a new method of minimally invasive diagnosis of diseases (Bordanaba-Florit et al., 2021).

5.3 The challenges in the use of EVs for treating OSCC

EVs are increasingly recognized as a promising drug delivery system due to their unique physiological characteristics, including excellent biocompatibility, biodegradability, non-immunogenicity, and targeted delivery (Ha et al., 2016). However, EVs from various sources have their advantages and limitations. For instance, immune cell-derived EVs are highly targeted but not lethal; MSC-derived EVs have only anti-inflammatory and regenerative properties, and macrophage-derived EVs can regulate TEM and stimulate T cell activation. Therefore, engineering EVs, which can enhance their advantages and improve their limitations, has received much attention. Engineered EVs can be modified in an active or passive manner to enhance their therapeutic effects (Zhang et al., 2021). For example, car-T through the chimeric antigen receptor, improves the targeting specificity of T cells. Therefore, EVs can from car-T cells may become a new method of tumor treatment.

There are several challenges associated with EV-based treatment, including: 1) time-consuming and low-yield extraction process through ultra-centrifugation. 2) low efficiency of drug loading. 3) short duration of action *in vivo*. These issues necessitate further research and development, with a focus on constructing more effective engineered EVs.

6 Conclusion

EVs have emerged as a significant players in the diagnosis, development, drug resistance, and treatment of OSCC, and the precise mechanisms remain incompletely understood. This article aimed to review the involvement of EVs in the diagnosis, prognosis, tumorigenesis, drug resistance, and treatment of OSCC and outline the challenges associated with the use of EVs.

Recent studies indicated that EVs can be used as new diagnostic tools. As EVs can be easily obtained from saliva, blood, and other body fluids, the identification of their content is the least invasive diagnostic method. EVs are involved in many processes during OSCC development. They can regulate TAM polarization and promote or inhibit tumor development. EVs can also interact with tumor cells to promote angiogenesis, which is essential during tumorigenesis. Furthermore, EVs promote EMT, thereby facilitating tumor progression and invasion. EVs are also involved in drug resistance, leading to poor prognosis in OSCC. This article discussed natural EVs and engineered EVs. It also explained how to inhibit OSCC development by inhibiting EV endocytosis by tumor cells. Engineered vesicles can improve the treatment of OSCC.

In summary, EVs play a crucial role in the pathogenesis and progression of OSCC. Standardizing the diagnostic pattern and producing engineered vesicles for treating OSCC require more attention in the future. By addressing these challenges, we can accelerate the clinical translation of this promising biotechnology.

Author contributions

YZ and FJ contributed to the conception and design of the study. YZ and JL designed and wrote the whole manuscript sections. YZ and JL designed all Figures of the manuscript. All authors contributed to the article and approved the submitted version.

Funding

This research was funded by the National Natural Science Foundation of China (grant number 82170988), the National Key Research and Development Program of China (2022YFA11044003), and Chinese Stomatological Association Youth Clinical Research Foundation for Orthodontics (grant number CSA-02020-01).

Acknowledgments

The authors would like to express their gratitude to EditSprings (https://www.editsprings.cn) for the expert linguistic services provided.

Conflict of interest

The authors declare that the research was conducted in the absence of any commercial or financial relationships that could be construed as a potential conflict of interest.

Publisher's note

All claims expressed in this article are solely those of the authors and do not necessarily represent those of their affiliated organizations, or those of the publisher, the editors and the reviewers. Any product that may be evaluated in this article, or claim that may be made by its manufacturer, is not guaranteed or endorsed by the publisher.

References

Ai, Y., Wei, H., Wu, S., Tang, Z., Li, X., and Zou, C. (2021). Exosomal LncRNA LBX1-AS1 derived from RBPJ overexpressed-macrophages inhibits oral squamous cell carcinoma progress via miR-182-5p/FOXO3. *Front. Oncol.* 11, 605884. doi:10.3389/fonc.2021.605884

Akers, J. C., Gonda, D., Kim, R., Carter, B. S., and Chen, C. C. (2013). Biogenesis of extracellular vesicles (EV): Exosomes, microvesicles, retrovirus-like vesicles, and apoptotic bodies. *J. Neurooncol* 113, 1–11. doi:10.1007/s11060-013-1084-8

Almeria, C., Weiss, R., Roy, M., Tripisciano, C., Kasper, C., Weber, V., et al. (2019). Hypoxia conditioned mesenchymal stem cell-derived extracellular vesicles induce increased vascular tube formation *in vitro*. *Front. Bioeng. Biotechnol.* 7, 292. doi:10.3389/fbioe.2019.00292

Baietti, M. F., Zhang, Z., Mortier, E., Melchior, A., Degeest, G., Geeraerts, A., et al. (2012). Syndecan–syntenin–ALIX regulates the biogenesis of exosomes. *Nat. Cell Biol.* 14, 677–685. doi:10.1038/ncb2502

Baig, M. S., Roy, A., Rajpoot, S., Liu, D., Savai, R., Banerjee, S., et al. (2020). Tumor-derived exosomes in the regulation of macrophage polarization. *Inflamm. Res.* 69, 435–451. doi:10.1007/s00011-020-01318-0

Bao, L., Dou, G., Tian, R., Lv, Y., Ding, F., Liu, S., et al. (2022). Engineered neutrophil apoptotic bodies ameliorate myocardial infarction by promoting macrophage efferocytosis and inflammation resolution. *Bioact. Mater.* 9, 183–197. doi:10.1016/j.bioactmat.2021.08.008

Bebelman, M. P., Smit, M. J., Pegtel, D. M., and Baglio, S. R. (2018). Biogenesis and function of extracellular vesicles in cancer. *Pharmacol. Ther.* 188, 1–11. doi:10.1016/j.pharmthera.2018.02.013

Becker, A., Thakur, B. K., Weiss, J. M., Kim, H. S., Peinado, H., and Lyden, D. (2016). Extracellular vesicles in cancer: Cell-to-Cell mediators of metastasis. *Cancer Cell* 30, 836–848. doi:10.1016/j.ccell.2016.10.009

Bellmunt, À. M., López-Puerto, L., Lorente, J., and Closa, D. (2019). Involvement of extracellular vesicles in the macrophage-tumor cell communication in head and neck squamous cell carcinoma. *PLoS ONE* 14, e0224710. doi:10.1371/journal.pone.0224710

Bigagli, E., Locatello, L. G., Di Stadio, A., Maggiore, G., Valdarnini, F., Bambi, F., et al. (2021). Extracellular vesicles miR-210 as a potential biomarker for diagnosis and survival prediction of oral squamous cell carcinoma patients. *J. Oral Pathol. Med.* 51, 350. doi:10.1111/jop.13263

Bordanaba-Florit, G., Royo, F., Kruglik, S. G., and Falcón-Pérez, J. M. (2021). Using single-vesicle technologies to unravel the heterogeneity of extracellular vesicles. *Nat. Protoc.* 16, 3163–3185. doi:10.1038/s41596-021-00551-z

Bray, F., Ferlay, J., Soerjomataram, I., Siegel, R. L., Torre, L. A., and Jemal, A. (2018). Global cancer statistics 2018: GLOBOCAN estimates of incidence and mortality worldwide for 36 cancers in 185 countries. *CA A Cancer J. Clin.* 68, 394–424. doi:10.3322/caac.21492

Brinton, L. T., Sloane, H. S., Kester, M., and Kelly, K. A. (2015). Formation and role of exosomes in cancer. *Cell. Mol. Life Sci.* 72, 659–671. doi:10.1007/s00018-014-1764-3

Cai, J., and Qiao, B. (2019). Oral squamous cell carcinoma-derived exosomes promote M2 subtype macrophage polarization mediated by exosome-enclosed miR-29a-3p. *Am. J. Physiol. Cell Physiol.* 316, C731–C740. doi:10.1152/ajpcell.00366.2018

Chen, C.-M., and Huang, C.-C. (2021). Exosome-derived microRNAs in oral squamous cell carcinomas impact disease prognosis. *Oral Oncol.* 120, 105402. doi:10.1016/j.oraloncology.2021.105402

Chen, J.-H., Wu, A. T. H., Bamodu, O. A., Yadav, V. K., Chao, T.-Y., Tzeng, Y.-M., et al. (2019). Ovatodiolide suppresses oral cancer malignancy by down-regulating exosomal mir-21/STAT3/β-catenin cargo and preventing oncogenic transformation of normal gingival fibroblasts. *Cancers (Basel)* 12, E56. doi:10.3390/cancers12010056

Chen, W., Cai, Y., Lv, M., Chen, L., Zhong, S., Ma, T., et al. (2014a). Exosomes from docetaxel-resistant breast cancer cells alter chemosensitivity by delivering microRNAs. *Tumor Biol.* 35, 9649–9659. doi:10.1007/s13277-014-2242-0

Chen, W., Liu, X., Lv, M., Chen, L., Zhao, J., Zhong, S., et al. (2014b). Exosomes from drug-resistant breast cancer cells transmit chemoresistance by a horizontal transfer of MicroRNAs. *PLoS ONE* 9, e95240. doi:10.1371/journal.pone.0095240

Chi, A. C., Day, T. A., and Neville, B. W. (2015). Oral cavity and oropharyngeal squamous cell carcinoma-an update: Oral and Oropharyngeal Cancer Update. *CA A Cancer J. Clin.* 65, 401–421. doi:10.3322/caac.21293

Ciardiello, C., Cavallini, L., Spinelli, C., Yang, J., Reis-Sobreiro, M., de Candia, P., et al. (2016). Focus on extracellular vesicles: New Frontiers of cell-to-cell communication in cancer. *Int. J. Mol. Sci.* 17, 175. doi:10.3390/ijms17020175

Coon, J., Kingsley, K., and Howard, K. M. (2020). miR-365 (microRNA): Potential biomarker in oral squamous cell carcinoma exosomes and extracellular vesicles. *Int. J. Mol. Sci.* 21, E5317. doi:10.3390/ijms21155317

Costa-Silva, B., Aiello, N. M., Ocean, A. J., Singh, S., Zhang, H., Thakur, B. K., et al. (2015). Pancreatic cancer exosomes initiate pre-metastatic niche formation in the liver. *Nat. Cell Biol.* 17, 816–826. doi:10.1038/ncb3169

Coussens, L. M., Zitvogel, L., and Palucka, A. K. (2013). Neutralizing tumor-promoting chronic inflammation: A magic bullet? *Science* 339, 286–291. doi:10.1126/science.1232227

Daassi, D., Mahoney, K. M., and Freeman, G. J. (2020). The importance of exosomal PDL1 in tumour immune evasion. *Nat. Rev. Immunol.* 20, 209–215. doi:10.1038/s41577-019-0264-y

Ding, L., Ren, J., Zhang, D., Li, Y., Huang, X., Hu, Q., et al. (2018). A novel stromal lncRNA signature reprograms fibroblasts to promote the growth of oral squamous cell carcinoma via LncRNA-CAF/interleukin-33. *Carcinogenesis* 39, 397–406. doi:10.1093/carcin/bgy006

Dou, G., Tian, R., Liu, X., Yuan, P., Ye, Q., Liu, J., et al. (2020). Chimeric apoptotic bodies functionalized with natural membrane and modular delivery system for inflammation modulation. *Sci. Adv.* 6, eaba2987. doi:10.1126/sciadv.aba2987

Doyle, L., and Wang, M. (2019). Overview of extracellular vesicles, their origin, composition, purpose, and methods for exosome isolation and analysis. *Cells* 8, 727. doi:10.3390/cells8070727

Ebnoether, E., and Muller, L. (2020). Diagnostic and therapeutic applications of exosomes in cancer with a special focus on head and neck squamous cell carcinoma (HNSCC). *IJMS* 21, 4344. doi:10.3390/ijms21124344

Epstein, J. B., Thariat, J., Bensadoun, R.-J., Barasch, A., Murphy, B. A., Kolnick, L., et al. (2012). Oral complications of cancer and cancer therapy: From cancer treatment to survivorship. *CA A Cancer J. Clin.* 62, 400–422. doi:10.3322/caac.21157

Fang, Z., Xu, J., Zhang, B., Wang, W., Liu, J., Liang, C., et al. (2020). The promising role of noncoding RNAs in cancer-associated fibroblasts: An overview of current status and future perspectives. *J. Hematol. Oncol.* 13, 154. doi:10.1186/s13045-020-00988-x

Fontana, S., Mauceri, R., Novara, M. E., Alessandro, R., and Campisi, G. (2021). Protein cargo of salivary small extracellular vesicles as potential functional signature of oral squamous cell carcinoma. *Int. J. Mol. Sci.* 22, 11160. doi:10.3390/ijms222011160

Forder, A., Hsing, C.-Y., Trejo Vazquez, J., and Garnis, C. (2021). Emerging role of extracellular vesicles and cellular communication in metastasis. *Cells* 10, 3429. doi:10.3390/cells10123429

Fujiwara, T., Eguchi, T., Sogawa, C., Ono, K., and Murakami, J. S. (2018). Ibaragi Carcinogenic epithelial-mesenchymal transition initiated by oral cancer exosomes is inhibited by anti-EGFR antibody cetuximab. *Oral Oncol.* 86. 251, doi:10.1016/j.oraloncology.2018.09.030

Gai, C., Camussi, F., Broccoletti, R., Gambino, A., Cabras, M., Molinaro, L., et al. (2018). Salivary extracellular vesicle-associated miRNAs as potential biomarkers in oral squamous cell carcinoma. *BMC Cancer* 18, 439. doi:10.1186/s12885-018-4364-z

Gao, S., Hu, J., Wu, X., and Liang, Z. (2018). PMA treated THP-1-derived-IL-6 promotes EMT of SW48 through STAT3/ERK-dependent activation of Wnt/β-catenin signaling pathway. *Biomed. Pharmacother.* 108, 618–624. doi:10.1016/j.biopha.2018.09.067

Ha, D., Yang, N., and Nadithe, V. (2016). Exosomes as therapeutic drug carriers and delivery vehicles across biological membranes: Current perspectives and future challenges. *Acta Pharm. Sin. B* 6, 287–296. doi:10.1016/j.apsb.2016.02.001

Han, Y., Jia, L., Zheng, Y., and Li, W. (2018). Salivary exosomes: Emerging roles in systemic disease. *Int. J. Biol. Sci.* 14, 633–643. doi:10.7150/ijbs.25018

He, L., Cheng, B., and Xia, J. (2020a). Salivary exosomal miR-24-3p serves as a potential detective biomarker for oral squamous cell carcinoma screening. *Biomed. Pharmacother.* 121, 109553. doi:10.1016/j.biopha.2019.109553

He, S., Zhang, W., Li, X., Wang, J., Chen, X., Chen, Y., et al. (2021a). Oral squamous cell carcinoma (OSCC)-derived exosomal MiR-221 targets and regulates phosphoinositide-3-kinase regulatory subunit 1 (PIK3R1) to promote human umbilical vein endothelial cells migration and tube formation. *Bioengineered* 12, 2164–2174. doi:10.1080/21655979.2021.1932222

He, T., Guo, X., Li, X., Liao, C., Wang, X., and He, K. (2021b). Plasma-derived exosomal microRNA-130a serves as a noninvasive biomarker for diagnosis and prognosis of oral squamous cell carcinoma. *J. Oncol.* 2021, 5547911. doi:10.1155/2021/5547911

He, Y., Du, J., and Dong, Z. (2020b). Myeloid deletion of phosphoinositide-dependent kinase-1 enhances NK cell-mediated antitumor immunity by mediating macrophage polarization. *OncoImmunology* 9, 1774281. doi:10.1080/2162402X.2020.1774281

Herrmann, I. K., Wood, M. J. A., and Fuhrmann, G. (2021). Extracellular vesicles as a next-generation drug delivery platform. *Nat. Nanotechnol.* 16, 748–759. doi:10.1038/s41565-021-00931-2

Hoshino, A., Costa-Silva, B., Shen, T.-L., Rodrigues, G., Hashimoto, A., Tesic Mark, M., et al. (2015). Tumour exosome integrins determine organotropic metastasis. *Nature* 527, 329–335. doi:10.1038/nature15756

Huang, Z., Zhang, Q., Wang, Y., Chen, R., Wang, Y., Huang, Z., et al. (2020). Inhibition of caspase-3-mediated GSDME-derived pyroptosis aids in noncancerous tissue protection of squamous cell carcinoma patients during cisplatin-based chemotherapy. *Am. J. Cancer Res.* 10, 4287–4307.

Jensen, C., and Teng, Y. (2020). Is it time to start transitioning from 2D to 3D cell culture? *Front. Mol. Biosci.* 7, 33. doi:10.3389/fmolb.2020.00033

Jiang, H., Zhou, L., Shen, N., Ning, X., Wu, D., Jiang, K., et al. (2022). M1 macrophage-derived exosomes and their key molecule lncRNA HOTTIP suppress head and neck squamous cell carcinoma progression by upregulating the TLR5/NF-κB pathway. *Cell Death Dis.* 13, 183. doi:10.1038/s41419-022-04640-z

Joyce, J. A., and Pollard, J. W. (2009). Microenvironmental regulation of metastasis. *Nat. Rev. Cancer* 9, 239–252. doi:10.1038/nrc2618

Kaiser, J. (2016). Malignant messengers. *Science* 352, 164–166. doi:10.1126/science.352.6282.164

Kalluri, R., and LeBleu, V. S. (2020). The biology, function, and biomedical applications of exosomes. *Science* 367, eaau6977. doi:10.1126/science.aau6977

Kamerkar, S., LeBleu, V. S., Sugimoto, H., Yang, S., Ruivo, C. F., Melo, S. A., et al. (2017). Exosomes facilitate therapeutic targeting of oncogenic KRAS in pancreatic cancer. *Nature* 546, 498–503. doi:10.1038/nature22341

Ketabat, F., Pundir, M., Mohabatpour, F., Lobanova, L., Koutsopoulos, S., Hadjiiski, L., et al. (2019). Controlled drug delivery systems for oral cancer treatment—current status and future perspectives. *Pharmaceutics* 11, 302. doi:10.3390/pharmaceutics11070302

Khan, T., Relitti, N., Brindisi, M., Magnano, S., Zisterer, D., Gemma, S., et al. (2020). Autophagy modulators for the treatment of oral and esophageal squamous cell carcinomas. *Med. Res. Rev.* 40, 1002–1060. doi:10.1002/med.21646

Kirave, P., Gondaliya, P., Kulkarni, B., Rawal, R., Garg, R., Jain, A., et al. (2020). Exosome mediated miR-155 delivery confers cisplatin chemoresistance in oral cancer cells via epithelial-mesenchymal transition. *Oncotarget* 11, 1157–1171. doi:10.18632/oncotarget.27531

Kyzas, P. A., Cunha, I. W., and Ioannidis, J. P. A. (2005). Prognostic significance of vascular endothelial growth factor immunohistochemical expression in head and neck squamous cell carcinoma: A meta-analysis. *Clin. Cancer Res.* 11, 1434–1440. doi:10.1158/1078-0432.CCR-04-1870

Lamouille, S., Xu, J., and Derynck, R. (2014). Molecular mechanisms of epithelial–mesenchymal transition. *Nat. Rev. Mol. Cell Biol.* 15, 178–196. doi:10.1038/nrm3758

Laviron, M., and Boissonnas, A. (2019). Ontogeny of tumor-associated macrophages. *Front. Immunol.* 10, 1799. doi:10.3389/fimmu.2019.01799

Law, Z.-J., Khoo, X. H., Lim, P. T., Goh, B. H., Ming, L. C., Lee, W.-L., et al. (2021). Extracellular vesicle-mediated chemoresistance in oral squamous cell carcinoma. *Front. Mol. Biosci.* 8, 629888. doi:10.3389/fmolb.2021.629888

Lee, J.-K., Park, S.-R., Jung, B.-K., Jeon, Y.-K., Lee, Y.-S., Kim, M.-K., et al. (2013). Exosomes derived from mesenchymal stem cells suppress angiogenesis by down-regulating VEGF expression in breast cancer cells. *PLOS ONE* 8, e84256. doi:10.1371/journal.pone.0084256

Li, C., Zhou, Y., Liu, J., Su, X., Qin, H., Huang, S., et al. (2019b). Potential markers from serum-purified exosomes for detecting oral squamous cell carcinoma metastasis. *Cancer Epidemiol. Biomarkers Prev.* 28, 1668. doi:10.1158/1055-9965.EPI-18-1122

Li, L., Lu, S., Liang, X., Cao, B., Wang, S., Jiang, J., et al. (2019a). δTDEs: An efficient delivery system for miR-138 with anti-tumoral and immunostimulatory roles on oral squamous cell carcinoma. *Mol. Ther. Nucleic acids* 14. doi:10.1016/j.omtn.2018.11.009

Li, L., and Zhu, G. (2016). Exosomes derived from hypoxic oral squamous cell carcinoma cells deliver miR-21 to normoxic cells to elicit a prometastatic phenotype. *Cancer Res.* 76, 1770–1780. doi:10.1158/0008-5472.CAN-15-1625

Li, S., Man, Q., Gao, X., Lin, H., Wang, J., Su, F., et al. (2021). Tissue-derived extracellular vesicles in cancers and non-cancer diseases: Present and future. *J Extracell. Vesicle* 10, e12175. doi:10.1002/jev2.12175

Li, S., Shi, Z., Fu, S., Li, Q., Li, B., Sang, L., et al. (2021c). Exosomal-mediated transfer of APCDD1L-AS1 induces 5-fluorouracil resistance in oral squamous cell carcinoma via miR-1224-5p/nuclear receptor binding SET domain protein 2 (NSD2) axis. *Bioengineered* 12, 7177–7193. doi:10.1080/21655979.2021.1979442

Li, W., Ren, G., Huang, Y., Su, J., Han, Y., Li, J., et al. (2012). Mesenchymal stem cells: A double-edged sword in regulating immune responses. *Cell Death Differ.* 19, 1505–1513. doi:10.1038/cdd.2012.26

Li, Y.-Y. (2018). Cancer-associated fibroblasts contribute to oral cancer cells proliferation and metastasis via exosome-mediated paracrine miR-34a-5p. *EBioMedicine* 36, 209–220. doi:10.1016/j.ebiom.2018.09.006

Li, Y., Tao, Y., Gao, S., Li, P., Zheng, J., Zhang, S., et al. (2018). Cancer-associated fibroblasts contribute to oral cancer cells proliferation and metastasis via exosome-mediated paracrine miR-34a-5p. *EBioMedicine* 36, 209–220. doi:10.1016/j.ebiom.2018.09.006

Liang, W., Chen, X., Zhang, S., Fang, J., Chen, M., Xu, Y., et al. (2021). Mesenchymal stem cells as a double-edged sword in tumor growth: Focusing on MSC-derived cytokines. *Cell Mol. Biol. Lett.* 26, 3. doi:10.1186/s11658-020-00246-5

Liu, H., Tian, Y., Xue, C., Niu, Q., Chen, C., and Yan, X. (2022a). Analysis of extracellular vesicle DNA at the single-vesicle level by nano-flow cytometry. *J Extracell. Vesicle* 11, e12206. doi:10.1002/jev2.12206

Liu, J., Jiang, X., Zou, A., Mai, Z., Huang, Z., Sun, L., et al. (2021). circIGHG-induced epithelial-to-mesenchymal transition promotes oral squamous cell carcinoma progression via miR-142-5p/IGF2BP3 signaling. *Cancer Res.* 81, 344–355. doi:10.1158/0008-5472.CAN-20-0554

Liu, J., Ye, Z., Xiang, M., Chang, B., Cui, J., Ji, T., et al. (2019). Functional extracellular vesicles engineered with lipid-grafted hyaluronic acid effectively reverse cancer drug resistance. *Biomaterials* 223, 119475. doi:10.1016/j.biomaterials.2019.119475

Liu, P., Zhang, Q., Mi, J., Wang, S., Xu, Q., Zhuang, D., et al. (2022b). Exosomes derived from stem cells of human deciduous exfoliated teeth inhibit angiogenesis *in vivo* and *in vitro* via the transfer of miR-100-5p and miR-1246. *Stem Cell Res. Ther.* 13, 89. doi:10.1186/s13287-022-02764-9

Liu, T., Chen, G., Sun, D., Lei, M., Li, Y., Zhou, C., et al. (2017). Exosomes containing miR-21 transfer the characteristic of cisplatin resistance by targeting PTEN and PDCD4 in oral squamous cell carcinoma. *Acta Biochimica Biophysica Sinica* 49, 808–816. doi:10.1093/abbs/gmx078

Liu, Y., and Cao, X. (2016). Organotropic metastasis: Role of tumor exosomes. *Cell Res.* 26, 149–150. doi:10.1038/cr.2015.153

Longley, D. B., Harkin, D. P., and Johnston, P. G. (2003). 5-Fluorouracil: Mechanisms of action and clinical strategies. *Nat. Rev. Cancer* 3, 330–338. doi:10.1038/nrc1074

Lu, Y., Zheng, Z., Yuan, Y., Pathak, J. L., Yang, X., Wang, L., et al. (2021). The emerging role of exosomes in oral squamous cell carcinoma. *Front. Cell Dev. Biol.* 9, 628103. doi:10.3389/fcell.2021.628103

Luo, Y., Liu, F., Guo, J., and Gui, R. (2020). Upregulation of circ_0000199 in circulating exosomes is associated with survival outcome in OSCC. *Sci. Rep.* 10, 13739. doi:10.1038/s41598-020-70747-y

Mantovani, A., Marchesi, F., Malesci, A., Laghi, L., and Allavena, P. (2017). Tumour-associated macrophages as treatment targets in oncology. *Nat. Rev. Clin. Oncol.* 14, 399–416. doi:10.1038/nrclinonc.2016.217

Mathieu, M., Martin-Jaular, L., Lavieu, G., and Théry, C. (2019). Specificities of secretion and uptake of exosomes and other extracellular vesicles for cell-to-cell communication. *Nat. Cell Biol.* 21, 9–17. doi:10.1038/s41556-018-0250-9

Nikfarjam, S., Rezaie, J., Kashanchi, F., and Jafari, R. (2020). Dexosomes as a cell-free vaccine for cancer immunotherapy. *J. Exp. Clin. Cancer Res.* 39, 258. doi:10.1186/s13046-020-01781-x

Ohno, S., Takanashi, M., Sudo, K., Ueda, S., Ishikawa, A., Matsuyama, N., et al. (2013). Systemically injected exosomes targeted to EGFR deliver antitumor microRNA to breast cancer cells. *Mol. Ther.* 21, 185–191. doi:10.1038/mt.2012.180

Ono, K., Eguchi, T., Sogawa, C., Calderwood, S. K., Futagawa, J., Kasai, T., et al. (2018). HSP-enriched properties of extracellular vesicles involve survival of metastatic oral cancer cells. *J. Cell Biochem.* 119, 7350–7362. doi:10.1002/jcb.27039

Oshi, M., Tokumaru, Y., Asaoka, M., Yan, L., Satyananda, V., Matsuyama, R., et al. (2020). M1 Macrophage and M1/M2 ratio defined by transcriptomic signatures resemble only part of their conventional clinical characteristics in breast cancer. *Sci. Rep.* 10, 16554. doi:10.1038/s41598-020-73624-w

Pal, S. K., Nguyen, C. T. K., Morita, K., Miki, Y., Kayamori, K., Yamaguchi, A., et al. (2016). THBS1 is induced by TGFB1 in the cancer stroma and promotes invasion of oral squamous cell carcinoma. *J. Oral Pathol. Med.* 45, 730–739. doi:10.1111/jop.12430

Pang, X., Wang, S., Zhang, M., Jiang, J., Fan, H., Wu, J., et al. (2021). OSCC cell-secreted exosomal CMTM6 induced M2-like macrophages polarization via ERK1/2 signaling pathway. *Cancer Immunol. Immunother.* 70, 1015–1029. doi:10.1007/s00262-020-02741-2

Panvongsa, W., Pegtel, D. M., and Voortman, J. (2022). More than a bubble: Extracellular vesicle microRNAs in head and neck squamous cell carcinoma. *Cancers* 14, 1160. doi:10.3390/cancers14051160

Qadir, F., Aziz, M. A., Sari, C. P., Ma, H., Dai, H., Wang, X., et al. (2018). Transcriptome reprogramming by cancer exosomes: Identification of novel molecular targets in matrix and immune modulation. *Mol. Cancer* 17, 97. doi:10.1186/s12943-018-0846-5

Raffat, M. A., Hadi, N. I., Hosein, M., Mirza, S., Ikram, S., and Akram, Z. (2018). S100 proteins in oral squamous cell carcinoma. *Clin. Chim. Acta* 480, 143–149. doi:10.1016/j.cca.2018.02.013

Rahimi, S., Roushandeh, A. M., Ahmadzadeh, E., Jahanian-Najafabadi, A., and Roudkenar, M. H. (2020). Implication and role of neutrophil gelatinase-associated lipocalin in cancer: lipocalin-2 as a potential novel emerging comprehensive therapeutic target for a variety of cancer types. *Mol. Biol. Rep.* 47, 2327–2346. doi:10.1007/s11033-020-05261-5

Ren, J. G., Zhang, W., Liu, B., Man, Q. W., Xiong, X. P., Li, C., et al. (2016). Clinical significance and roles in angiogenesis of circulating microparticles in oral cancer. *J. Dent. Res.* 95, 860–867. doi:10.1177/0022034516641037

Rodríguez Zorrilla, S., Pérez-Sayans, M., Fais, S., Logozzi, M., Gallas Torreira, M., and García García, A. (2019). A pilot clinical study on the prognostic relevance of plasmatic exosomes levels in oral squamous cell carcinoma patients. *Cancers (Basel)* 11, E429. doi:10.3390/cancers11030429

Rosenberger, L., Ezquer, M., Lillo-Vera, F., Pedraza, P. L., Ortúzar, M. I., González, P. L., et al. (2019). Stem cell exosomes inhibit angiogenesis and tumor growth of oral squamous cell carcinoma. *Sci. Rep.* 9, 663. doi:10.1038/s41598-018-36855-6

Ruffell, B., Affara, N. I., and Coussens, L. M. (2012). Differential macrophage programming in the tumor microenvironment. *Trends Immunol.* 33, 119–126. doi:10.1016/j.it.2011.12.001

Sahu, S., and Routray, S. (2021). Assessing the analytical efficacy of TEX in diagnosing oral cancer using a systematic review approach. *J. Oral Pathol. Med.* 50, 123–128. doi:10.1111/jop.13126

Sakha, S., Muramatsu, T., Ueda, K., and Inazawa, J. (2016). Exosomal microRNA miR-1246 induces cell motility and invasion through the regulation of DENND2D in oral squamous cell carcinoma. *Sci. Rep.* 6, 38750. doi:10.1038/srep38750

Sasabe, E., Tomomura, A., Liu, H., Sento, S., Kitamura, N., and Yamamoto, T. (2022). Epidermal growth factor/epidermal growth factor receptor signaling blockage inhibits tumor cell-derived exosome uptake by oral squamous cell carcinoma through macropinocytosis. *Cancer Sci.* 113, 609. doi:10.1111/cas.15225

Sasahira, T., and Kirita, T. (2018). Hallmarks of cancer-related newly prognostic factors of oral squamous cell carcinoma. *Int. J. Mol. Sci.* 19, 2413. doi:10.3390/ijms19082413

Sato, S., Vasaikar, S., Eskaros, A., Kim, Y., Lewis, J. S., Zhang, B., et al. (2019). EPHB2 carried on small extracellular vesicles induces tumor angiogenesis via activation of ephrin reverse signaling. *JCI Insight* 4, e132447. doi:10.1172/jci.insight.132447

Sayyed, A. A., Gondaliya, P., Mali, M., Pawar, A., Bhat, P., Khairnar, A., et al. (2021). MiR-155 inhibitor-laden exosomes reverse resistance to cisplatin in a 3D tumor spheroid and xenograft model of oral cancer. *Mol. Pharm.* 18, 3010–3025. doi:10.1021/acs.molpharmaceut.1c00213

Syn, N., Wang, L., Sethi, G., Thiery, J.-P., and Goh, B.-C. (2016). Exosome-Mediated metastasis: From epithelial–mesenchymal transition to escape from immunosurveillance. *Trends Pharmacol. Sci.* 37, 606–617. doi:10.1016/j.tips.2016.04.006

Tan, S., Xia, L., Yi, P., Han, Y., Tang, L., Pan, Q., et al. (2020). Exosomal miRNAs in tumor microenvironment. *J. Exp. Clin. Cancer Res.* 39, 67. doi:10.1186/s13046-020-01570-6

Tomita, R., Sasabe, E., Tomomura, A., and Yamamoto, T. (2020). Macrophage-derived exosomes attenuate the susceptibility of oral squamous cell carcinoma cells to chemotherapeutic drugs through the AKT/GSK-3β pathway. *Oncol. Rep.* 44, 1905. doi:10.3892/or.2020.7748

Tong, F., Mao, X., Zhang, S., Xie, H., Yan, B., Wang, B., et al. (2020). HPV + HNSCC-derived exosomal miR-9 induces macrophage M1 polarization and increases tumor radiosensitivity. *Cancer Lett.* 478, 34–44. doi:10.1016/j.canlet.2020.02.037

Urabe, F., Kosaka, N., Ito, K., Kimura, T., Egawa, S., and Ochiya, T. (2020). Extracellular vesicles as biomarkers and therapeutic targets for cancer. *Am. J. Physiology-Cell Physiology* 318, C29–C39. doi:10.1152/ajpcell.00280.2019

van Niel, G., Carter, D. R. F., Clayton, A., Lambert, D. W., Raposo, G., and Vader, P. (2022). Challenges and directions in studying cell–cell communication by extracellular vesicles. *Nat. Rev. Mol. Cell Biol.* 23, 369–382. doi:10.1038/s41580-022-00460-3

Villegas-Pineda, J. C., Lizarazo-Taborda, M. D. R., de-Arellano, A. R., and Pereira-Suárez, A. L. (2021). Exosomal miRNAs and lncRNAs: The modulator keys of cancer-associated fibroblasts in the genesis and progression of malignant neoplasms. *Front. Cell Dev. Biol.* 9, 717478. doi:10.3389/fcell.2021.717478

Wang, J., Wei, Q., Wang, X., Tang, S., Liu, H., Zhang, F., et al. (2016). Transition to resistance: An unexpected role of the EMT in cancer chemoresistance. *Genes and Dis.* 3, 3–6. doi:10.1016/j.gendis.2016.01.002

Wang, S.-H., Liou, G.-G., Liu, S.-H., Chang, J. S., Hsiao, J.-R., Yen, Y.-C., et al. (2019). Laminin γ2-enriched extracellular vesicles of oral squamous cell carcinoma cells enhance *in vitro* lymphangiogenesis via integrin α3-dependent uptake by lymphatic endothelial cells. *Int. J. Cancer* 144, 2795–2810. doi:10.1002/ijc.32027

Wang, Z.-Q., Liu, K., Huo, Z.-J., Li, X.-C., Wang, M., Liu, P., et al. (2015). A cell-targeted chemotherapeutic nanomedicine strategy for oral squamous cell carcinoma therapy. *J. Nanobiotechnol* 13, 1–10. doi:10.1186/s12951-015-0116-2

Xiao, M., Zhang, J., Chen, W., and Chen, W. (2018). M1-like tumor-associated macrophages activated by exosome-transferred THBS1 promote malignant migration in oral squamous cell carcinoma. *J. Exp. Clin. Cancer Res.* 37, 143. doi:10.1186/s13046-018-0815-2

Xie, C., Du, L.-Y., Guo, F., Li, X., and Cheng, B. (2019a). Exosomes derived from microRNA-101-3p-overexpressing human bone marrow mesenchymal stem cells suppress oral cancer cell proliferation, invasion, and migration. *Mol. Cell Biochem.* 458, 11–26. doi:10.1007/s11010-019-03526-7

Xie, C., Ji, N., Tang, Z., Li, J., and Chen, Q. (2019b). The role of extracellular vesicles from different origin in the microenvironment of head and neck cancers. *Mol. Cancer* 18, 83. doi:10.1186/s12943-019-0985-3

Xie, F., Xu, M., Lu, J., Mao, L., and Wang, S. (2019c). The role of exosomal PD-L1 in tumor progression and immunotherapy. *Mol. Cancer* 18, 146. doi:10.1186/s12943-019-1074-3

Yan, W., Wang, Y., Chen, Y., Guo, Y., Li, Q., and Wei, X. (2021). Exosomal miR-130b-3p promotes progression and tubular formation through targeting PTEN in oral squamous cell carcinoma. *Front. Cell Dev. Biol.* 9, 616306. doi:10.3389/fcell.2021.616306

Yang, F., Ning, Z., Ma, L., Liu, W., Shao, C., Shu, Y., et al. (2017). Exosomal miRNAs and miRNA dysregulation in cancer-associated fibroblasts. *Mol. Cancer* 16, 148. doi:10.1186/s12943-017-0718-4

Yeung, K. T., and Yang, J. (2017). Epithelial-mesenchymal transition in tumor metastasis. *Mol. Oncol.* 11, 28–39. doi:10.1002/1878-0261.12017

You, Y., Tian, Z., Du, Z., Wu, K., Xu, G., Dai, M., et al. (2022). 回路M1-like tumor-associated macrophages cascade a mesenchymal/stem-like phenotype of oral squamous cell carcinoma via the IL6/Stat3/THBS1 feedback loop. *J. Exp. Clin. Cancer Res.* 41, 10. doi:10.1186/s13046-021-02222-z

Yu, L., Yang, Z., Liu, Y., Liu, F., Shang, W., Shao, W., et al. (2020). Identification of SPRR3 as a novel diagnostic/prognostic biomarker for oral squamous cell carcinoma via RNA sequencing and bioinformatic analyses. *PeerJ* 8, e9393. doi:10.7717/peerj.9393

Yuan, Y., Jiao, P., Wang, Z., Chen, M., Du, H., Xu, L., et al. (2022). Endoplasmic reticulum stress promotes the release of exosomal PD-L1 from head and neck cancer cells and facilitates M2 macrophage polarization. *Cell Commun. Signal* 20, 12. doi:10.1186/s12964-021-00810-2

Zhang, M., Liang, J., Yang, Y., Liang, H., Jia, H., and Li, D. (2020). Current trends of targeted drug delivery for oral cancer therapy. *Front. Bioeng. Biotechnol.* 8, 618931. doi:10.3389/fbioe.2020.618931

Zhang, X., Zhang, H., Gu, J., Zhang, J., Shi, H., Qian, H., et al. (2021). Engineered extracellular vesicles for cancer therapy. *Adv. Mater.* 33, 2005709. doi:10.1002/adma.202005709

Zhao, S., Mi, Y., Zheng, B., Wei, P., Gu, Y., Zhang, Z., et al. (2022). Highly-metastatic colorectal cancer cell released miR-181a-5p-rich extracellular vesicles promote liver metastasis by activating hepatic stellate cells and remodelling the tumour microenvironment. *J. Extracell. Vesicles* 11, e12186. doi:10.1002/jev2.12186

Zhou, S., Zhu, Y., Li, Z., Zhu, Y., He, Z., and Zhang, C. (2021). Exosome-derived long non-coding RNA ADAMTS9-AS2 suppresses progression of oral submucous fibrosis via AKT signalling pathway. *J. Cell Mol. Med.* 25, 2262–2273. doi:10.1111/jcmm.16219

Zlotogorski-Hurvitz, A., Dayan, D., Chaushu, G., Salo, T., and Vered, M. (2016). Morphological and molecular features of oral fluid-derived exosomes: Oral cancer patients versus healthy individuals. *J. Cancer Res. Clin. Oncol.* 142, 101–110. doi:10.1007/s00432-015-2005-3

frontiers | Frontiers in Bioengineering and Biotechnology

TYPE Original Research
PUBLISHED 31 May 2023
DOI 10.3389/fbioe.2023.1189010

OPEN ACCESS

EDITED BY
Hai Zhang,
University of Washington, United States

REVIEWED BY
Serkan Yaman,
Turkish Biotechnology Institute, Türkiye
Zhaoting Li,
University of Wisconsin-Madison,
United States

*CORRESPONDENCE
Tingming Fu,
futm@njucm.edu.cn
Shaoguang Li,
drlishaoguang@163.com

†These authors share first authorship

RECEIVED 18 March 2023
ACCEPTED 22 May 2023
PUBLISHED 31 May 2023

CITATION
Li S, Wang Y, Wang S, Xie J, Fu T and Li S (2023), *In situ* gelling hydrogel loaded with berberine liposome for the treatment of biofilm-infected wounds. *Front. Bioeng. Biotechnol.* 11:1189010. doi: 10.3389/fbioe.2023.1189010

In situ gelling hydrogel loaded with berberine liposome for the treatment of biofilm-infected wounds

Sipan Li[1†], Yongan Wang[1†], Siting Wang[1†], Jianjun Xie[1], Tingming Fu[1*] and Shaoguang Li[2*]

[1]School of Pharmacy, Nanjing University of Chinese Medicine, Nanjing, China, [2]Microsurgery Department of Senior Department of Orthopedics, The Fourth Medical Center of PLA General Hospital, Beijing, China

Background: In recent years, the impact of bacterial biofilms on traumatic wounds and the means to combat them have become a major research topic in the field of medicine. The eradication of biofilms formed by bacterial infections in wounds has always been a huge challenge. Herein, we developed a hydrogel with the active ingredient berberine hydrochloride liposomes to disrupt the biofilm and thereby accelerate the healing of infected wounds in mice.

Methods: We determined the ability of berberine hydrochloride liposomes to eradicate the biofilm by means of studies such as crystalline violet staining, measuring the inhibition circle, and dilution coating plate method. Encouraged by the *in vitro* efficacy, we chose to coat the berberine hydrochloride liposomes on the Poloxamer range of *in-situ* thermosensitive hydrogels to allow fuller contact with the wound surface and sustained efficacy. Eventually, relevant pathological and immunological analyses were carried out on wound tissue from mice treated for 14 days.

Results: The final results show that the number of wound tissue biofilms decreases abruptly after treatment and that the various inflammatory factors in them are significantly reduced within a short period. In the meantime, the number of collagen fibers in the treated wound tissue, as well as the proteins involved in healing in the wound tissue, showed significant differences compared to the model group.

Conclusion: From the results, we found that berberine liposome gel can accelerate wound healing in *Staphylococcus aureus* infections by inhibiting the inflammatory response and promoting re-epithelialization as well as vascular regeneration. Our work exemplifies the efficacy of liposomal isolation of toxins. This innovative antimicrobial strategy opens up new perspectives for tackling drug resistance and fighting wound infections.

KEYWORDS

wound infection, biofilm, liposomes, berberine, temperature-sensitive gel, *Staphylococcus aureus*

Abbreviations: BH-Lip, Berberine liposome; CAZ-Lip, Ceftazidime liposome; CIP-Lip, Ciprofloxacin liposome; CK14, cytokeratin 14; EPS, Extracellular polymeric substances; FISH, Fluorescent *in situ* hybridization; VEGF, Vascular endothelial growth factor.

1 Introduction

It has been reported that more than 10 million people are infected by disease-causing bacteria each year, and death from bacterial infections is the second leading cause of death worldwide (Hu et al., 2017). Wounds caused by various natural and human factors are the main route of bacterial invasion, making wound infections account for 60%–80% of human bacterial infections. In our daily life, wound infections are often caused by delayed wound treatment or poor antibacterial properties of therapeutic drugs. Moreover, chronic wounds have become one of the major global health problems due to an aging population and the increasing prevalence of diseases such as diabetes and obesity. The main reason why infectious diseases are difficult to deal with was thought to be the bacterial resistance caused by the overuse of antibiotics (Turner et al., 2019; Huemer et al., 2020; LaPlante et al., 2022). However, recent studies have shown that another major reason for the failure of many wound infection treatments is the formation of biofilms, which are difficult for many antimicrobial agents to penetrate (Roy et al., 2020; Lin et al., 2021; Rubio-Canalejas et al., 2022).

In nature, the vast majority of bacteria exist as a biofilm rather than as plankton (Sharahi et al., 2019). Bacterial communities tend to attach to the surfaces they come in contact with and encase themselves in self-produced extracellular polymeric substances (EPS), and the bacterial aggregates resulting from this community activity of bacteria are referred to as biofilms. The main component of the EPS is water and also includes lipids, polysaccharides, proteins, etc., which shapes a good habitat for the bacteria to communicate with the external environment and also protects them from the immune system (Zhou et al., 2018; Yan and Bassler, 2019; Jiang et al., 2021). In other words, biofilms provide a natural protective barrier for bacterial communities, and it is this protective effect of the biofilm on the bacteria that makes the eradication of the bacteria so tough. The ability of biofilms to protect themselves is as virulent as it is extremely difficult to completely remove them from the infected wound. Therefore, there is an urgent need to develop a new therapeutic strategy to combat biofilms on wounds. Scheme 1.

In the past decade, liposomes have become a hot research topic as drug carriers, since their lipid-like bilayer structure has good biocompatibility and the ability to encapsulate drugs (Chang and Yeh, 2012; Forier et al., 2014; Scriboni et al., 2019; Kluzek et al., 2022). We recently combined artificially designed liposomes with berberine to enable the berberine liposomes (BH-Lip) to target biofilms and promote drug release, which has played a very good role in the eradication of *Staphylococcus aureus* (*S. aureus*) biofilms (Xie et al., 2022). Moreover, it was found that liposomes can not only encapsulate drugs but also can sequester bacterial toxins. The synthetic liposomes with a high concentration of cholesterol (66 mol% cholesterol) as a decoy effectively bind protein toxins secreted by many bacterial pathogens, thus protecting the host cells from the toxins (Henry et al., 2015). The outstanding antibacterial and cytoprotective functions of berberine liposome provide the possibility for its application in infected wounds.

As a typical biocompatible wound dressing, hydrogels exhibit superior characteristics similar to the natural extracellular matrix and has been extensively applied in the treatment of wound infections (Liu et al., 2020), inhibition of post-surgery tumor recurrence (Li et al., 2022a), prevention of postoperative adhesion (Zhou et al., 2022). Compared with conventional preformed hydrogels, temperature-sensitive *in situ* gelling hydrogels have the property of undergoing a self-solution to gel phase transition with temperature changes at the drug application site and are considered promising materials for wound dressings (Yan et al., 2019; Zhang et al., 2019; Park et al., 2022). Poloxamer series gels are widely recognized for their good flowability, short gelling time, and excellent drug compatibility (Wang et al., 2019; Yang et al., 2020; Liang et al., 2021; Zhang et al., 2021). Recently, Li et al., (2022b) developed an injectable *in situ* gel for the peri-tumoural administration of primary and metastatic tumours by using Pluronic F127. Peng et al. (2022) designed a Poloxamer 407 and

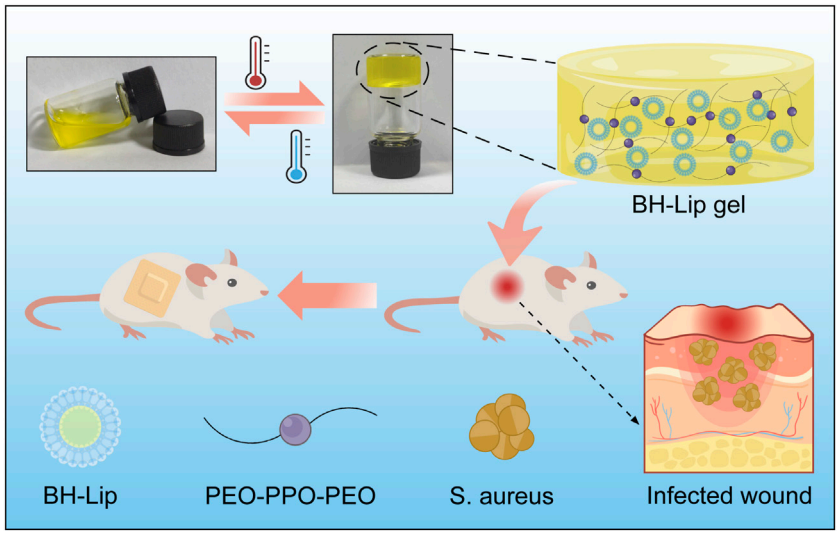

SCHEME 1
Schematic diagram of the formation of berberine liposomal thermosensitive *in situ* gel and its promotion of wound healing in *S. aureus* infections.

hyaluronic acid thermosensitive hydrogel encapsulated Ginsenoside Rg3 to promote skin wound healing. In this study, *in situ* gelling hydrogel loaded with berberine hydrochloride liposome (BH-Lip gel) was used to treat skin wounds of mice infected with *S. aureus*. According to the results of *in vivo* experiments, the hydrogel loaded with BH-Lip greatly eradicated the biofilm on the wound and promoted wound healing. This multifunctional thermosensitive hydrogel with simple preparation and low-cost design by us has a broad development prospect and is expected to be used clinically for the treatment of wound infection caused by bacteria.

2 Materials and methods

2.1 Materials

BH was purchased from Liangwei Biotechnology Co., Ltd. (Nanjing, China). HSPC, 1, 2-distearoyl-sn-glycerol-3-phosphoethanolamine-N-[methoxy (polyethylene glycol)-2000] (DSPE-PEG2000), and cholesterol were purchased from AVT (Shanghai) Pharmaceutical Tech Co., Ltd. *S. aureus* (ATCC25923), Poloxamer 407, and Poloxamer 188 were purchased from Solarbio Science Technology Co., Ltd. (Beijing, China). ELISA kits were purchased from Nanjing YIFEIXUE Biotechnology Co., Ltd. All other reagents were commercially purchased and were not further purified.

2.2 Preparation of blank liposome

The protocol for the preparation of liposomes was slightly modified from the previous study (Xie et al., 2022). The components of the liposomes were Hydrogenated Soybean Phosphatidylcholine (HSPC), cholesterol, and DSPE-PEG_{2000}. Initially, HSPC, cholesterol, and DSPE-PEG_{2000} were dispersed in an eggplant flask containing chloroform at a molar ratio of 45:50:5 and gently shaken until completely dissolved. Then the organic solvent was removed in a rotary vacuum evaporator at 60°C. After the solvent was completely evaporated, the lipid film was formed. Then a citric acid buffer (50×10^{-3} M citric acid, 23.8×10^{-3} M sodium citrate) was added as a hydration medium to form a lipid suspension at a concentration of 5 mg/mL. Next, the liposomes were sonicated for 5 min in an ultrasonic cell disruption apparatus. Finally, the suspension was extruded through a polycarbonate membrane (Whatman plc, Buckinghamshire, United Kingdom) with a pore size of 0.2 μm for 6 times at a temperature higher than the lipid transition temperature (60°C), and then extruded through a polycarbonate membrane with a pore size of 0.1 μm for 11 times to obtain liposomes of uniform particle size. Determination of liposome size distribution using dynamic light scattering (Zetasizer Nano ZS90; Malvern Panalytic, Malvern, United Kingdom).

2.3 Preparation of antibiotic liposomes

The pH gradient method was used to prepare berberine liposomes. First, the blank liposome suspension obtained by the above method was mixed with berberine hydrochloride solution (1 mg/mL) at a volume ratio of 2:1. Then 595×10^{-3} mM $NaHCO_3$ solution was slowly added to adjust the pH of the external phase to 7.0, and dilute the berberine hydrochloride concentration to 200 μg/mL with PBS. Finally, the mixed solution was incubated in a water bath at 60°C for 20 min and then subjected to rapid cooling, and the obtained BH-Lip solution was stored at 4°C. Liposomes containing ciprofloxacin or ceftazidime were prepared using the same method as BH-Lip, with the difference that ciprofloxacin hydrochloride aqueous solution or ceftazidime aqueous solution was used instead of berberine hydrochloride solution.

2.4 Antibacterial test process

The drug sensitivity test followed the standard method of CLSL (Clinical And Laboratory Standards Institute) with minor adjustments for the determination of minimum inhibitory concentration (MIC) using the micro broth dilution method (Nicolosi et al., 2015). Firstly, the concentration of *S. aureus* was adjusted to 10^6 CFU/mL with TSB liquid medium (10^8 CFU/mL at OD_{600} = 0.4 abs). and then 100 μL of the above-mentioned bacterial solution with a concentration of 10^6 CFU/mL was added to 100 μL of BH-Lip solution which was serially diluted 2 times, and one column of the 96-well plate was used as the negative control (100 μL of bacterial solution mixed with 100 μL of TSB), and the other column was used as the blank control (diluted the drug solution with sterile PBS). After incubation at 37°C for 24 h, the absorbance at 600 nm was measured using an enzyme marker, and the MIC of the drug was determined by calculating the inhibition rate.

2.5 Determination of the inhibition circle

For the determination of the inhibition circle, the culture was diluted to 10^6 CFU/mL, and 100 μL was pipetted onto TSA agar plates using a micropipette. Then 4 wells were punched on the agar plate with a hole puncher (6 mm diameter) and 50 μL of the solution was added dropwise to each well and incubate the agar plate at 37°C for 18–24 h to observe the range of the inhibition circle.

2.6 Determination of biofilm eradication effectiveness

The eradication rate of BH-Lip on the biofilm of *S. aureus* was determined by the crystalline violet staining method. Firstly, the bacterial concentration was adjusted to 10^6 CFU/mL by TSB, and then the bacterial solution with proper concentration was added to columns 2 to 11 of the 96-well plate (the middle 6 wells in each column were added 200 μL of bacterial solution), and the remaining wells were sealed with 200 μL of sterile PBS, and then left at 37°C for incubated for 24 h to form biofilms. BH-Lip solution was diluted to 200, 100, 50, 25, and 12.5 μg/mL respectively, 200 μL of each concentration of BH-Lip was added to the well and incubated with biofilm at 37°C for 24 h. 200 μL of sterile PBS to the negative control group. After reaching the incubation time, the supernatant was aspirated and discarded, the biofilm was washed with sterile PBS several times. 200 μL of methanol was added to each well, and after fixation for 15 min, the residual methanol was

allowed to evaporate for 30 min at room temperature. 200 μL of 0.1% crystalline violet was added to each well and incubated for 30 min, the crystalline violet solution was then aspirated and discarded, and the biofilm was washed several times with sterile PBS and dried at room temperature. 200 μL of 30% glacial acetic acid solution was added to each well to dissolve the crystalline violet, 100 μL of each well was aspirated and the absorbance was measured at 595 nm with a microplate reader to calculate the biofilm eradication rate. The Ceftazidime liposomes (CAZ-Lip) and Ciprofloxacin liposomes (CIP-Lip) eradication experiments for *S. aureus* biofilms were performed as described above.

2.7 Preparation of *in-situ* thermosensitive hydrogel

The *in-situ* thermosensitive hydrogels were prepared using a cold dissolution method (Khallaf et al., 2022). For the blank gel, a certain mass of Poloxamer 407 (P407) and Poloxamer 188 (P188) was dissolved in cold deionized water (4°C–8°C) to a concentration of 23% for P407 and 3% for P188, stirred continuously for 1 h in an ice water bath, and then placed under refrigeration at 4°C overnight to ensure complete dissolution. The BH gel (BH concentration of 200 μg/mL), BH-Lip gel (BH-Lip concentration of 200 μg/mL), and Lip gel (2 mg/mL) were prepared by mixing the blank gel with the corresponding substance (BH, BH-lip or blank Lip).

2.8 Measurement of gelation temperature and time

The gelling temperature was measured using the vial tilt method (Fathalla et al., 2017). A 2 mL sample was added to the vial, and the vial was put into a water bath where the water temperature was increased from 25°C to 45°C at a rate of 1°C/min. During this period, the temperature at which the sample changed from solution to gel was recorded (each gel was measured three times and the average was taken as the result). After the phase transition temperature of the gel was determined, 150 μL of the sample was pipetted onto a hot aluminum pan that maintains the phase transition temperature, and then the pan was tilted by 90° and the time for the gel to stop flowing was recorded in seconds (repeat the test three times, and take the average value).

2.9 *In vitro* antibacterial activity of thermosensitive hydrogel

The antibacterial performance of hydrogels was evaluated using the colony counting method. Firstly, 500 μL of hydrogel was aspirated in sterile centrifuge tubes, then 500 μL of 10^6 CFU/mL of *S. aureus* solution was added sequentially and incubated at a constant temperature of 37°C for 24 h. Finally, 100 μL of the incubated suspension after 10^3-fold gradient dilution were pipetted onto TSA agar plates and incubated at 37°C for 18–20 h to observe the growth of colonies. The inhibition of *S. aureus* by the gels at different periods was performed in 24-well plates. 500 μL of gel was pipetted with 500 μL of 10^6 CFU/mL of bacterial solution in a 24-well plate (6 wells of each gel were taken as a parallel control), and a mixture of 500 μL of PBS solution and 500 μL of 10^6 CFU/mL of bacterial solution was used as a control. Following, the 24-well plates were incubated in a thermostat (37°C) for 0 h, 6 h, 12 h, and 24 h, and then 4 wells were randomly selected for each group until the corresponding time. 10 μL of the mixed solution was added dropwise to the agar plates and incubated in a thermostat (37°C) for 18–24 h to observe the antimicrobial effect, and the remaining solution was used for absorbance measurement.

2.10 *In vivo* antibacterial effect and wound healing properties

In vivo S. aureus infection experiments were performed using male BALB/c mice (6–8 weeks). Mice were randomly divided into 6 groups, and two symmetrical circular wounds were cut on the back of each mouse except the blank group using a 6-mm diameter punch. Infective wounds were prepared by dropping 100 μL of *S. aureus* solution (10^7 CFU/mL) into the wound. The day of infection was recorded as day 0, and the drug administration was started on the first day after infection (150 μL of saline as the control in the model group and 150 μL of gel in the other four groups) and continued for 13 days. During the treatment period, the body weight and wound area of each mouse were measured and recorded every other day.

On day 5, three mice in each group were randomly selected to be euthanized. A portion of wound tissue was homogenized and centrifuged at 5,000 × g at 4°C for 10 min, and the supernatant was collected for the determination of interleukin 1β (IL-1β), interleukin 6 (IL-6), and tumor necrosis factor-α (TNF-α). Some tissue homogenates were serially diluted 10^3 folds with PBS, and 100 μL of the diluted homogenates were pipetted onto TSA agar to quantify bacterial colonies. Another portion of the tissue was fixed with *in situ* hybridization fixative and used for fluorescence *in situ* hybridization (FISH) experiments. On day 14 of treatment, all mice were euthanized and a portion of the wound tissue was taken for IL-1β, IL-6, and TNF-α, while the rest of the wound tissue was used for H&E and Masson's staining and immunofluorescence for cytokeratin 14 (CK14), Vascular endothelial growth factor (VEGF) and protein F4/80.

2.11 Statistical analysis

All the data in this study were statistically analyzed by One-way ANOVA (intergroup comparisons) and Student's t-test (intragroup comparisons). The values were presented as mean ± standard deviation (SD), $p < 0.05$ was considered statistically significant ($^*p < 0.05$, $^{**}p$, $^{***}p < 0.01$).

3 Results

3.1 Berberine-loaded liposomes successfully inhibited *S. aureus* and eradicated biofilm

As shown in Figure 1A, all liposomes had a uniform particle size of 100 nm with typical bilayer vesicle structures, and the loading of

10.3389/fbioe.2023.1189010

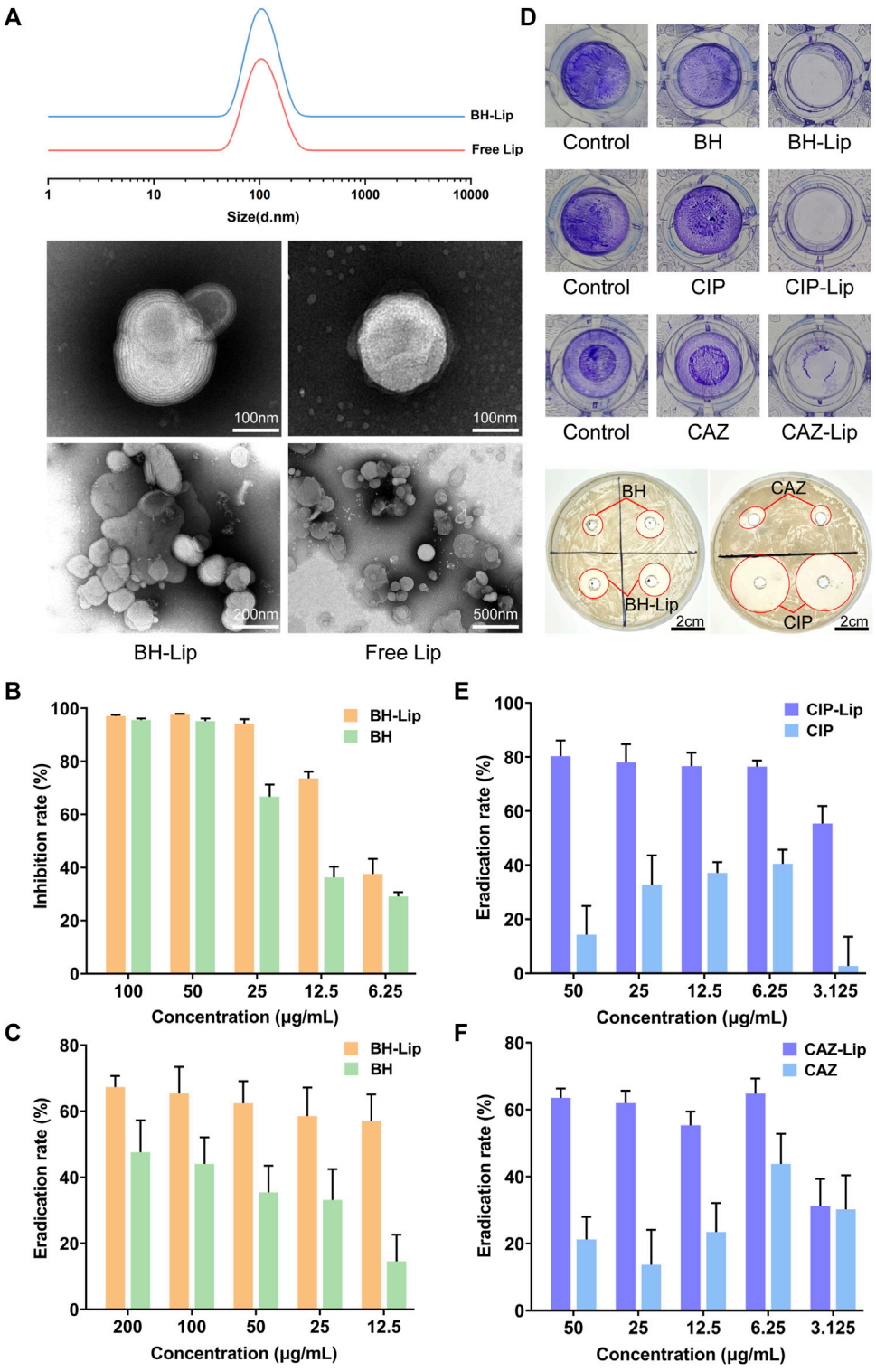

FIGURE 1
The particle size of BH-Lip and Free Lip and their TEM images **(A)**. Inhibition of planktonic *S. aureus* by BH-Lip. (*n* = 6/group) **(B)**. The eradication rate of BH-Lip (*n* = 5/group) **(C)**. Difference between the administered group and the control group after crystalline violet staining and the circle of inhibition of the different drugs **(D)**. The eradication rate of CIP-Lip (*n* = 5/group) **(E)**. The eradication rate of CAZ-Lip (*n* = 5/group) **(F)**.

berberine did not affect the size and structure of liposomes. The particle size and zeta potential of the free liposome and the BH-Lip did not change significantly over 21 days, indicating the good stability of the nanoparticles (Supplementary Figure S1; Supplementary Table S1). The inhibition rate for planktonic *S. aureus* was almost 100% when the concentration of free

10.3389/fbioe.2023.1189010

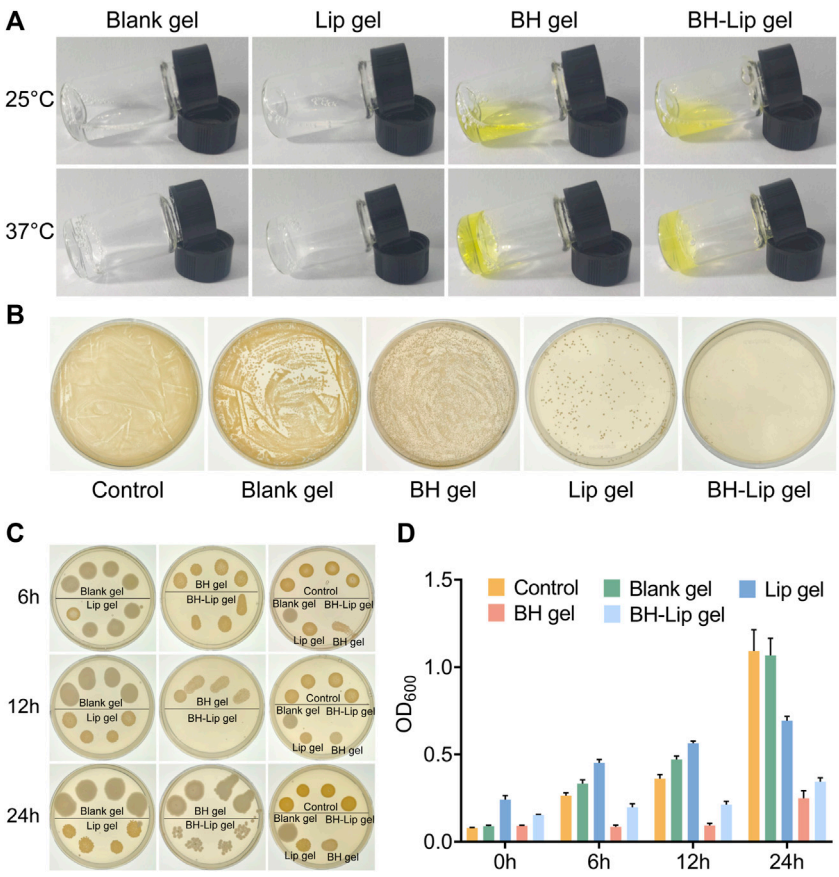

FIGURE 2
Four temperature-sensitive gels at phase change temperature **(A)**. The inhibition effect of four gels on *S. aureus* was verified by dilution coated plate method (diluted 10^3 times, n = 3/group) **(B)**. Antimicrobial effect of four gels against *S. aureus* after incubation of 6, 12, and 24 h **(C)**. Absorbance of the four gels after incubation with *S. aureus* at different periods (n = 6/group) **(D)**.

berberine was 50 μg/mL, while the inhibition rate of berberine liposomes against *S. aureus* was significantly higher than that of free berberine at lower concentration (Figure 1B). The biofilm eradication rates of the liposome-encapsulated berberine were higher than that of the free drug, which demonstrated that the liposomes as carriers fully exploited their ability to penetrate the biofilm, allowing berberine to be more fully targeted to bacteria inside the biofilm.

The biofilm eradication rate of 50 μg/mL BH-Lip was about 60%, which did not decrease significantly with the decrease in concentration. In contrast, the biofilm eradication rate of free berberine solution was significantly lower than that of liposomes, which was only about half of that of liposomes (Figure 1C). Ciprofloxacin and cephradine, two widely used antibiotics, did not remove biofilms, especially at high concentrations, indicating the resistance of biofilms to antibiotics, which is consistent with previous reports. However, both of them showed efficient biofilm removal ability when encapsulated in liposomes (Figures 1D–F). Considering the biofilm eradication stability of berberine and its liposomes, we selected berberine as the model for *in vitro* and *in vivo* experiments in subsequent experiments.

3.2 *In vitro* experiments showed that *in-situ* thermosensitive hydrogel loaded with liposome could inhibit *S. aureus* and its biofilm

As shown in Figure 2A, all four temperature-sensitive gels are liquid with the good flow at room temperature. After being heated in a 37°C water bath they rapidly transform into semi-solid gels. After repeated testing, all four gels have good gel-forming properties and the process of gel formation typically takes less than 1 min, allowing them gelling *in situ*. In addition, the gel-loaded drugs were released slowly *in vitro* and stabilized at 36 h. Finally, the cumulative release rate was about 70% (Supplementary Figure S2). Poloxamer, the material used to form the gels, is a (PEO-PPO-PEO) triblock copolymer consisting of a hydrophobic chain poly (propylene oxide) (PPO) and a hydrophilic chain poly (ethylene oxide) (PEO) (Bodratti and Alexandridis, 2018; Zarrintaj et al., 2020). When the temperature rises to the phase transition temperature of the system, Poloxamer can self-assemble into a micelle structure through hydrophobic interactions between PPO and PEO, then the micelles build up on each other, exhibiting a reversible sol-gel transition and form a network structure (Chatterjee et al., 2019; Russo and Villa, 2019).

10.3389/fbioe.2023.1189010

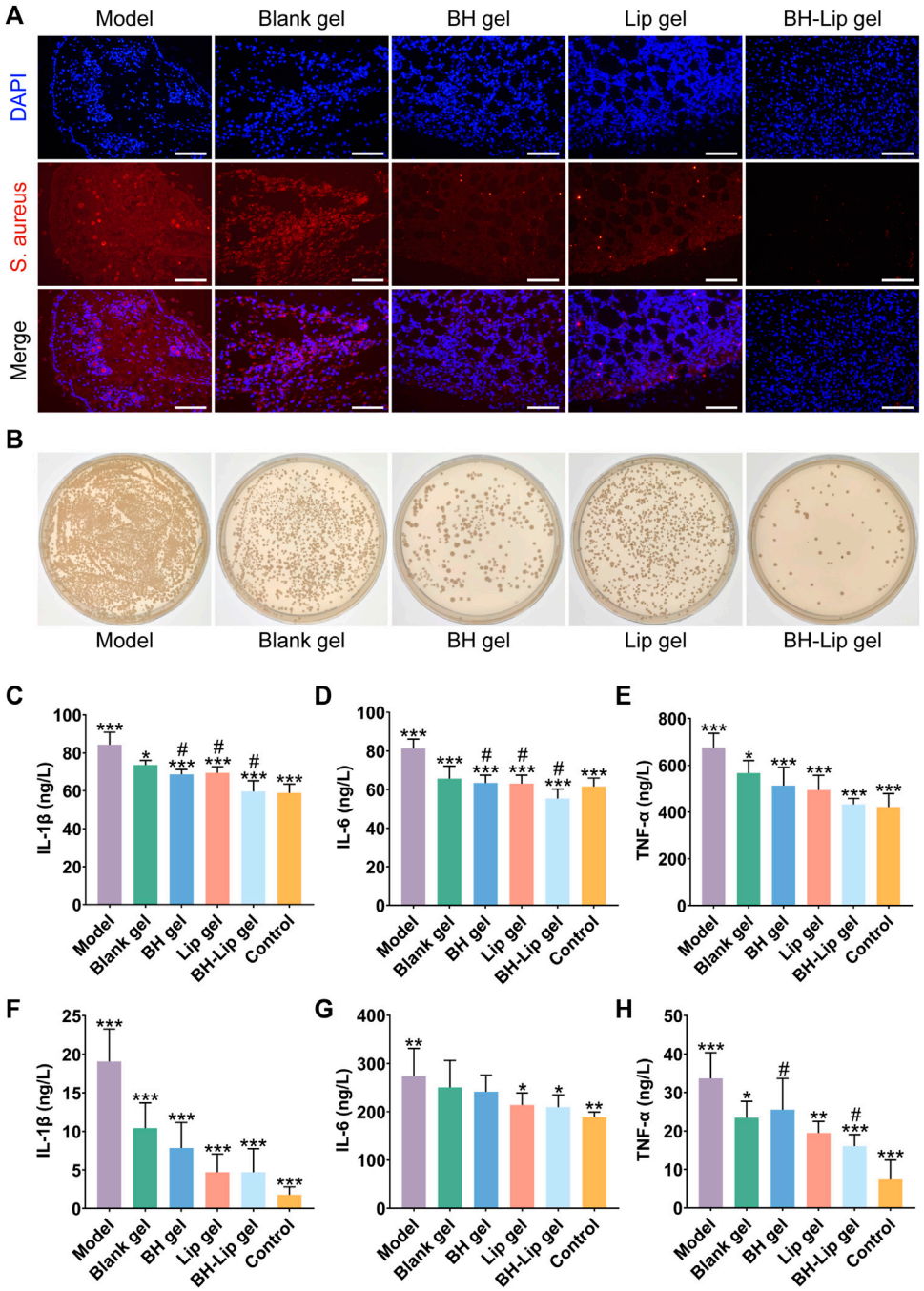

FIGURE 3
FISH analysis of wound tissue from different groups of mice (Scale bar = 50 μm). The wound tissue of *S. aureus* was labeled by a specific ribosomal RNA (rRNA) FISH probe (Red). The nuclear region of the bacteria was stained (blue) after DAPI (4′,6-diamidino-2-phenylindole) counterstaining **(A)**. Comparison of the number of viable bacteria in the wound tissues after treatment with the four different gels by dilution coating plate method (diluted 10^3 times, n = 3/group) **(B)**. Quantitative analysis of IL-1β, IL-6, and TNF-α levels in wound tissue on day 5 after treatment (***$p < 0.01$, *$p < 0.05$ when compared with the model group, $^{\#}p < 0.05$ when compared with the BH-Lip gel group, n = 6/group) **(C,D,E)**. Quantitative analysis of IL-1β, IL-6, and TNF-α levels in wound tissue on day 14 after treatment (***p, **$p < 0.01$, *$p < 0.05$ when compared with the model group, $^{\#}p < 0.05$ when compared with the BH-Lip gel group, n = 6/group) **(F,G,H)**.

The four gels differed significantly in their inhibition of *S. aureus*, with the BH-Lip gel showing the best performance. The blank gel showed almost no inhibition effect, and the Lip gel had a slightly stronger inhibition effect than the BH gel (Figure 2B). We then examined the inhibition effect exerted by the four gels at different times. The results showed that the BH-Lip gel was still the most effective regardless of the period and showed the strongest efficacy at 12 h. BH gel is unable to target bacteria as stably as BH-Lip gel, which also highlights the characteristics of liposomes as carriers to improve the effectiveness of antibacterial drugs (Figures 2C, D).

3.3 *In-situ* thermosensitive hydrogel loaded with liposome have anti-inflammatory and antibacterial effects *in vivo*

Encouraged by the *in vitro* efficacy, we further conducted *in vivo* trials for the treatment of wound infections, and explored the effect of BH-Lip temperature-sensitive gel on the removal of biofilm from infected wounds. We used fluorescent *in situ* hybridization (FISH) to locate the bacteria and their biofilm on the wound utilizing a gene probe. This technique has the advantage of rapid identification of pathogens and more visualization of the results (Frickmann et al., 2017; Prudent and Raoult, 2019; Wu et al., 2019). As shown in Figure 3A, fluorescence images of *S. aureus* were obtained by FISH of the wound tissue after 5 days of administration (the red fluorescence shows hybridization of specific probes targeting *S. aureus* rRNA and blue fluorescence represents the nucleus). The model group showed the most intense red fluorescence signal, which was concentrated in a regional distribution, highly similar to the high density of the biofilm and the clustered nature of the contact surface. Therefore, it could be judged that the model of the biofilm of *S. aureus* colonizing the wound was successfully constructed.

The red fluorescence intensity of the blank gel group was slightly lower than that of the model group but much greater than that of the remaining three groups, indicating that the blank gel alone was unable to exert an antibacterial effect, which is also consistent with the results of previous *in vitro* experiments. The red fluorescence intensity of the BH-gel, Lip-gel, and BH-Lip gel groups decreased in turn, and the difference between the BH-gel and Lip-gel groups was not significant, while the BH-Lip gel group had a clear difference from the other groups and the red fluorescence signal was already almost invisible, indicating that BH-Lip gel successfully exerted its drug effect *in vivo* after 5 days of treatment. We further investigated the antimicrobial effect of the gel on the wound using the dilution coating plate method (Figure 3B). Interestingly, the BH gel group had fewer colonies than the Lip gel group, which is different from the previous results of the *in vitro* dilution coating plate method. There is no doubt that the BH-Lip gel group had the lowest number of colonies compared to the other groups and showed the best results.

The expression levels of three inflammatory factors, IL-Iβ, IL-6, and TNF-α, were considerably lower in the BH gel, Lip gel, and BH-Lip gel groups than in the model group 5 days after administration. The level of the three inflammatory factors in the BH-Lip gel group, which had the strongest anti-inflammatory effect, was reduced to a level close to that of the blank group, and its expression levels of IL-1β and IL-6 were significantly different from those of the BH gel and Lip gel groups. The difference between the blank gel group and the model group was not as prominent as in the other groups, indicating that blank gel had a smaller effect on inflammation abatement (Figures 3C–E).

We also measured the expression levels of the three inflammatory factors in tissues 14 days after administration (Figures 3F–H), and found that the expression levels of IL-1β and TNF-α decreased in all groups compared to the pre-treatment period of days 0–5. Overall, the organism was in a continuous dynamic balance of inflammation levels during the transition from the early to the late phase of treatment. However, the difference was that the level of elimination of the three inflammatory factors was generally stronger in the Lip gel group than in the BH-gel group during the late phase of treatment, which was a novel finding.

3.4 BH-lip hydrogel promoted wound healing by eliminating inflammation and accelerating angiogenesis

To determine whether BH-Lip gel can accelerate healing of infected wounds, we established a full-layer skin resection model in mice and continued treatment for 13 days (Figure 4A). As shown in Figure 4B, the wound was regularly rounded (approximately 6 mm in diameter) on day 0 of molding and emerged with golden yellow bacterial aggregates that were highly adherent after 24 h of infection. After 13 days of treatment, the wound healing in different groups is shown in Figure 4C. It can be seen that the BH-Lip gel group had the best healing effect on day 13, while the BH gel group and Lip gel group also had some effect on wound healing. After quantification of the wound area by ImageJ software (Figure 4D), it was easy to see that the three gel groups with significant healing (Lip gel, BH gel, and BH-Lip gel) had a lower wound shrinkage rate on day 5 than on the other days. When analyzed together with the three inflammatory factors measured on the fifth day of treatment, it was found that the fifth day was the time when the inflammation subsided. Thus, the degree of remission of inflammatory factors was proportional to the degree of wound healing and the drug-laden gel further promoted subsequent wound healing by reducing the inflammatory factors on the wound. During these 13 days, the trend in body weight change was normal in all mice (Figure 4E).

As shown in Figure 5A, images of cross-sections of wound tissue from different groups after H&E staining and Masson staining were used to further assess wound healing. The BH gel group, Lip gel group, and BH-Lip gel group were covered with a continuous and thick epidermal layer. The regenerated dermis (red arrows) was significantly thicker in these three groups relative to the model and blank gel groups, with the BH-Lip gel group first and the Lip gel group slightly thicker than the BH gel group (Figure 5D). The Masson staining reflects the degree of collagen deposition during the wound healing phase, and the intensity of the blue staining represents the number and maturity of collagen fibers. The BH-Lip gel group had the most closely packed collagen fibers, the darkest blue color, and far more new hair follicles than the other groups, followed by the Lip group, while the BH gel group was inferior to the above two groups. These pathological results were also consistent with the trend of the H&E staining results (Figure 5E), demonstrating that BH-Lip gel can promote wound healing and tissue regeneration.

It has been reported that the rate of wound healing is closely related to the degree of re-epithelialization (Guan et al., 2021). Keratin is the structural protein of epidermal cells and they form extremely fine microfilaments that build an extensive intracellular meshwork. Keratin promotes keratin-forming cells and maintains their integrity in the epithelium, with epidermal cells expressing different keratins depending on the degree of differentiation (Pan et al., 2013; Konop et al., 2021; Qiang et al., 2021). In contrast, cytokeratin 14 (CK14), a type of keratin, is a marker for basal keratin-forming cells and is essential for wound re-epithelialization

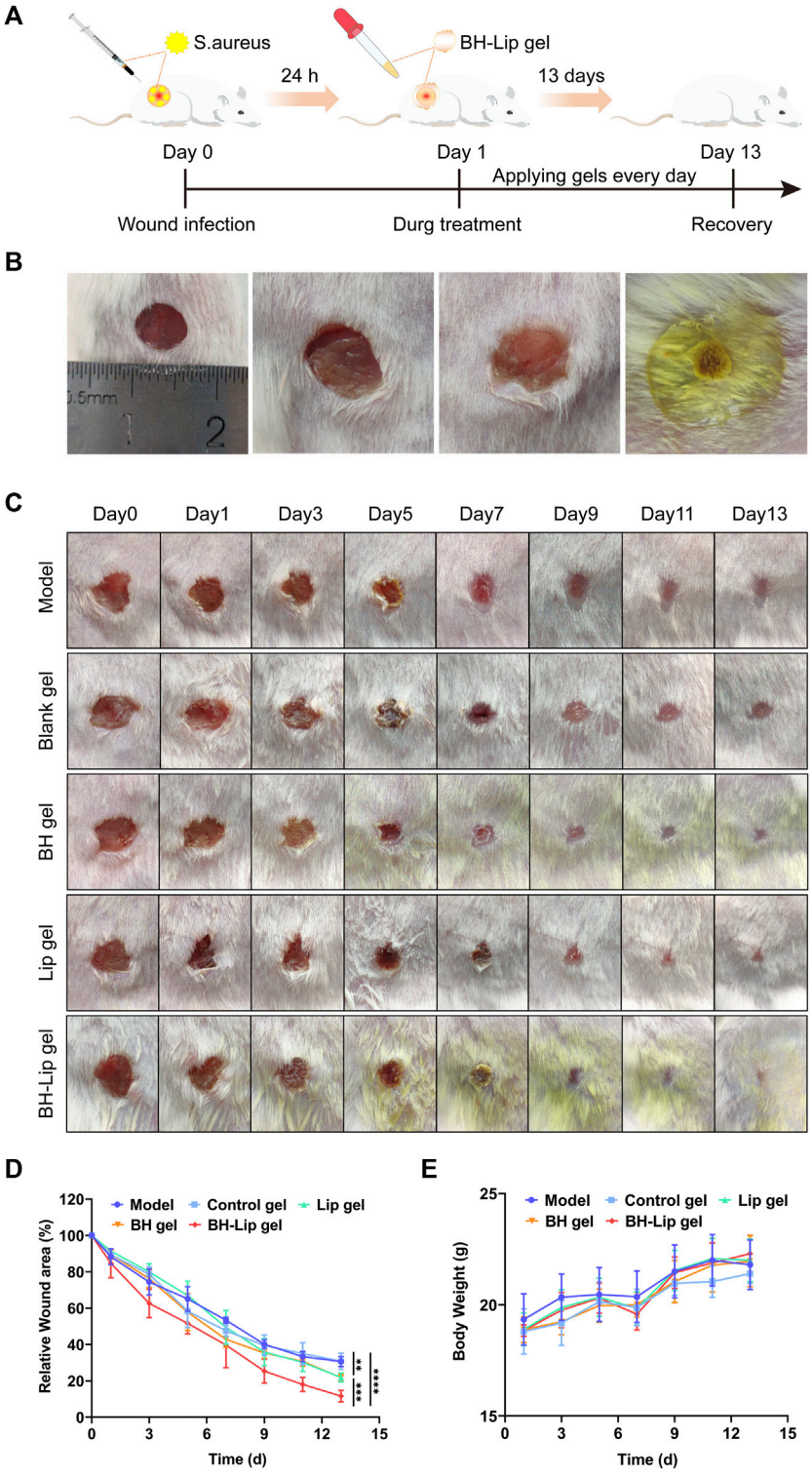

FIGURE 4
Experimental schematic of BH-Lip gel-mediated enhanced wound healing effect in the *S. aureus* infection model **(A)**. Comparison of the appearance of the wound before and after infection, molding day 0 (left), molding day 1 (middle two pictures), and gel forming rapidly on the wound surface (right) **(B)**. Wound healing after treatment in different groups on days 0, 1, 3, 5, 7, 9, 11, and 13 **(C)**. Quantification of wound healing area (****$p < 0.01$ when comparing the BH-Lip gel group with the model group, ***$p < 0.01$ when comparing the Lip gel group and the BH gel group with the BH-Lip group, **$p < 0.01$ when comparing the Lip gel group and the BH gel group with the model group, $n = 5$/group) **(D)**. Weight of mice over 14 days ($n = 5$/group) **(E)**.

(Cheng et al., 2020). As shown in Figure 5B, in the BH-Lip gel group, both the new hair follicle and the wound gap were filled with CK14-forming cells (red fluorescence), and keratinocytes continued to migrate from the dermis to the epidermis and formed a thick spine layer in the stacked epidermis, such a phenomenon was also present in the Lip gel group as well as the BH gel group. However, in the

10.3389/fbioe.2023.1189010

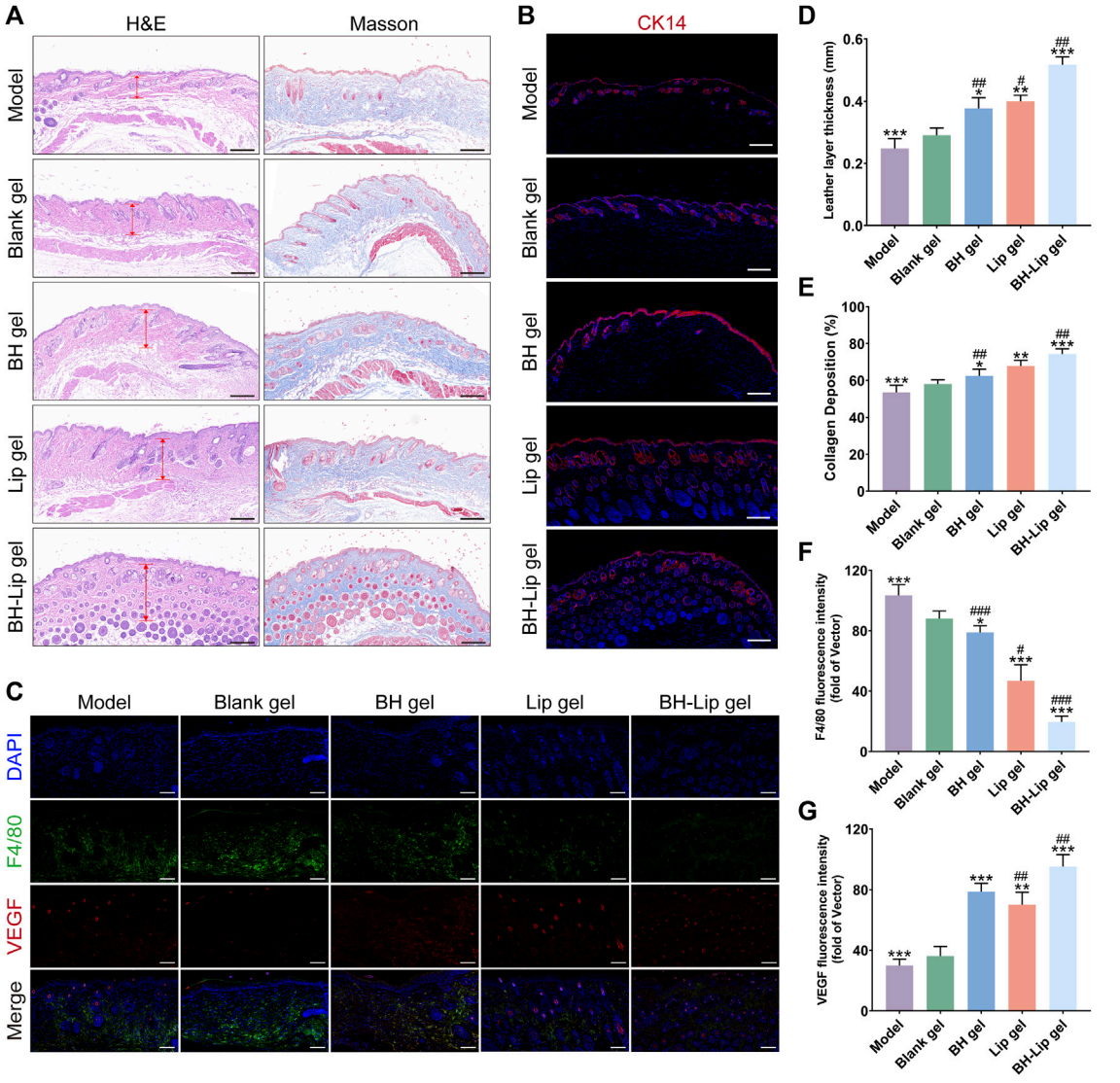

FIGURE 5
H&E and Masson staining of wound tissues of different groups (Scale bar = 200 μm) **(A)**. Immunofluorescence staining of CK14 (red) for the wounds at days 14 (Scale bar = 200 μm), cells were stained with CK14 and nuclei were re-stained with blue DAPI **(B)**. Immunofluorescence staining of F4/80 (green) and VEGF (red) for the wounds at day 14 (Scale bar = 100 μm) **(C)**. Quantification of the length of the new leather layer of the wound (***p, **$p < 0.01$, *$p < 0.05$ when compared with the model group, ##$p < 0.01$, #$p < 0.05$ when compared with the BH-Lip gel group, n = 6/group) **(D)**. Maturity of collagen fibers in different groups (***p, **$p < 0.01$, *$p < 0.05$ when compared with the model group, ##$p < 0.01$ when compared with the BH-Lip gel group, n = 6/group) **(E)**. Quantification of F4/80 fluorescence intensity (***$p < 0.01$, *$p < 0.05$ when compared with the model group, ###$p < 0.01$, #$p < 0.05$ when compared with the BH-Lip gel group, n = 6/group) **(F)**. Quantification of VEGF fluorescence intensity (***p, **$p < 0.01$ when compared with the model group, ##$p < 0.01$ when compared with the BH-Lip gel group, n = 6/group) **(G)**.

blank gel group and the model group, the expression of CK14 was relatively low, the cell proliferation rate was not as fast as the other three groups, and the re-epithelialization was not mature enough, which fully indicates that the re-epithelialization in the BH-Lip gel group was far ahead, and the drug effectively played the role of promoting the proliferation and migration of keratinocytes.

F4/80 is a cell surface glycoprotein, the expression of F4/80 changes markedly during the maturation and activation of macrophages (Biguetti et al., 2018). From another perspective, the level of F4/80 expression is to some extent proportional to the level of inflammation in the tissue (Zhou et al., 2018; Yang et al., 2020). Compared to the Lip gel and BH-Lip groups, intense green fluorescence was detected in the model and blank gel groups, indicating that there was still excessive inflammation in the tissues, which was not conducive to wound healing. the fluorescence intensity of F4/80 in the Lip gel group was significantly different from that of the BH-Lip gel group and much greater than that of the BH gel group, and we judge that it could be that drugs induce an inflammatory response in the organism and that liposomes, as affinity carriers, have a similar composition to that of cell membranes, thus well avoiding the irritation of drugs (Figures 5C, F). VEGF is a key factor in the formation of new blood vessels, and continuous treatment with BH-Lip gel promoted the secretion of VEGF (red fluorescence) in the

wound, which in the case of a high number of new blood vessels, led to the proliferation of granulation tissue in the wound and the ability of the tissue to fibrosis was enhanced (Yao et al., 2020). In conclusion, immunofluorescence staining analysis showed that BH-Lip gel promoted healing by increasing the rate of wound re-epithelialization and angiogenesis (Figures 5C, G).

4 Discussion

There are many treatments for biofilm-related wounds, but scientists and medical professionals have yet to find the most effective and efficient combination of treatments. Current treatments fall into three main categories: mechanical debridement, antibiotics, and anti-biofilm/biofilm-destroying agents such as QS blockers. However, none of the three categories on its own will provide adequate treatment. Mechanical debridement, such as surgery, often cannot completely remove biofilms because the EPS matrix penetrates deep into tissue structures. Any residue will quickly restore the biofilm. In addition, debridement needs to be carried out continuously, and only 25% of the wounds with irregular debridement can heal, while 83% of the wounds with weekly debridement can heal. Antibiotic treatment alone is also not sufficient, because biofilms have many resistance mechanisms.

In this work, we have developed a multilayer liposome with a particle size of approximately 100 nm that can be loaded with berberine hydrochloride, ceftazidime, and ciprofloxacin, antibiotics that target delivery of drugs to penetrate the bacterial biofilm to fight the bacteria within the membrane. For better application in infected wounds, we have taken advantage of the temperature-sensitive properties of the Poloxamer series of gels to combine drug-containing liposomes with the gels to allow the drug to reach the biofilm deep within the wound and thus take full effect.

On the one hand, *in vitro* experiments have shown that these antibiotic-containing liposomes are not only effective against Gram-positive bacteria (*S. aureus*), but also against Gram-negative bacteria (*Pseudomonas aeruginosa*), which confirms the advantages of liposomes as drug carriers for targeted delivery. In addition, we found that the absorbance of the BH gels after co-incubation with the bacteria did not correspond to the inhibition effect on agar plates, which we speculate may be related to the environment (liquid or solid) in which the gels release the drug and need to be further investigated. We also found that Lip-gel showed a stronger inhibition effect than BH-gel *in vitro* and that the antibacterial and anti-inflammatory effects exerted in the *in vivo* experiments were significant, and that the inhibition effect exerted by the blank liposomes is not negligible and has some value for future research.

On the other hand, the *in vivo* results showed that BH-Lip gel not only fights the biofilm on the wound but also plays a role in promoting wound healing. In general, wound healing goes through four stages: coagulation, inflammatory response, cell proliferation, and tissue remodeling, and the regulation of inflammation is crucial in the wound healing process. BH-Lip gel is effective in shortening the inflammatory phase of the wound, accelerating angiogenesis and collagen deposition after the inflammation has subsided (after the 5th day of administration), thus promoting wound healing. One of the crucial mechanisms of wound treatment is the regulation of the macrophage M1/M2 balance. Macrophages in trauma have both phagocytic and secretory functions. During the period of wound infection, M1-type macrophages can phagocytose and remove exogenous foreign bodies and necrotic cells, while in the stage of trauma recovery, M2-type macrophages can regulate wound repair by releasing various cytokines (Kobashi et al., 2020; Tang et al., 2023). The anti-inflammatory effect of BH-Lip gel could be interpreted as the pharmacological activity of berberine, which was able to regulate inflammation by inducing macrophages to differentiate from M1 to M2 type, and reducing the production of TNF-α, IL-6 and then improve the local inflammatory environment and promote lipid clearance and metabolism (Ehteshamfar et al., 2020).

5 Conclusion

Colonization of wounds by bacterial biofilm is one of the major causes of obstruction of infected wound healing. There are various clinical treatments for wound infections, such as surgical debridement (Wormald et al., 2020), ultrasound therapy (Lyu et al., 2021), negative pressure therapy (Iheozor-Ejiofor et al., 2018), the use of appropriate dressings and the use of antibiotics (Hu et al., 2022; Zhou et al., 2022). However, due to the misuse of antibiotics, a large number of common bacteria have developed resistance and the biofilm has a complex internal structure and multiple mechanisms of resistance to external stimuli, making it highly resistant to both immune responses and antimicrobial drugs. Because biofilms are difficult to remove completely, new therapeutic strategies to combat biofilms are now urgently needed.

Berberine, a bright yellow isoquinoline alkaloid existing in a variety of natural plants, has been widely studied and reported for its antibacterial effects. Berberine has antibacterial mechanisms such as inhibition of bacterial division, disruption of bacterial structure and interference with bacterial metabolism (Bhatia et al., 2021). However, its clinical application is limited by its poor solubility properties and short residence time in tissues (Wang et al., 2017). In this study, an *in-situ* temperature-sensitive hydrogel loaded with berberine liposomes was developed and applied to the treatment of infected wounds in mice, which led to a slower release of the drug and enhanced drug retention time in the body. The results showed that berberine liposome and its hydrogel could significantly inhibit *S. aureus* and eradicate biofilm *in vitro*. When the BH-Lip comes into contact with the biofilm, it can effectively penetrate the biofilm structure and release berberine directly into the biofilm-embedded cells. This effect is related to the high content of cholesterol in liposomes which attracts bacterial pore-forming toxins and the release of drugs resulting from pore-forming. This function of liposomes can be attributed to the good fusion of liposomes on bacterial biofilms. α-Hemolysin, which is secreted by *S. aureus*, forms small pores that primarily affect the intracellular ion balance. α-Hemolysin binding depends on the presence of certain lipid and/or liquid-ordered lipid microdomains within the liposomes, which is consistent with the composition of host cell plasmalemma (Pornpattananangkul et al., 2011; Jiang et al., 2021). Therefore, liposomes can act as decoys to isolate bacterial toxins and thus achieve the purpose of protecting host cells. *In vivo* experiments showed that the thermosensitive hydrogels containing berberine liposome could significantly remove bacterial biofilms from wounds, inhibit inflammatory factors and promote wound recovery. In conclusion, current research confirmed that hydrogel-mediated BH-Lip could be considered as an effective nanomaterial and that BH-lip gel promoted wound healing by eliminating inflammation and

accelerating angiogenesis. This temperature-sensitive hydrogel we have developed can be applied to biomedical applications, including targeted drug delivery, tissue adhesion, and tissue engineering. Our study provides an effective management method for biofilm-associated wound infections and is expected to play a greater role in clinical practice.

Data availability statement

The raw data supporting the conclusion of this article will be made available by the authors, without undue reservation.

Ethics statement

The animal study was reviewed and approved by the Ethical Committee for Animal Experiment of Nanjing University of Chinese Medicine.

Author contributions

All authors listed have made a substantial, direct, and intellectual contribution to the work and approved it for publication.

Funding

This work was funded by a project of the National Natural Science Foundation of China (81873013).

Acknowledgments

The schematic diagram Material for this article is provided by www.freepik.com, www.figdraw.com, and scidraw. io. We also thank the Experiment Center for Science and Technology, Nanjing University of Chinese Medicine.

Conflict of interest

The authors declare that the research was conducted in the absence of any commercial or financial relationships that could be construed as a potential conflict of interest.

Publisher's note

All claims expressed in this article are solely those of the authors and do not necessarily represent those of their affiliated organizations, or those of the publisher, the editors and the reviewers. Any product that may be evaluated in this article, or claim that may be made by its manufacturer, is not guaranteed or endorsed by the publisher.

Supplementary material

The Supplementary Material for this article can be found online at: https://www.frontiersin.org/articles/10.3389/fbioe.2023.1189010/full#supplementary-material

References

Bhatia, E., Sharma, S., Jadhav, K., and Banerjee, R. (2021). Combinatorial liposomes of berberine and curcumin inhibit biofilm formation and intracellular methicillin resistant *Staphylococcus aureus* infections and associated inflammation. *J. Mater. Chem. B* 9 (3), 864–875. doi:10.1039/d0tb02036b

Biguetti, C. C., Vieira, A. E., Cavalla, F., Fonseca, A. C., Colavite, P. M., Silva, R. M., et al. (2018). CCR2 contributes to F4/80+Cells migration along intramembranous bone healing in maxilla, but its deficiency does not critically affect the healing outcome. *Front. Immunol.* 9, 1804. doi:10.3389/fimmu.2018.01804

Bodratti, A. M., and Alexandridis, P. (2018). Formulation of poloxamers for drug delivery. *J. Funct. biomaterials* 9 (1), 11. doi:10.3390/jfb9010011

Chang, H. I., Yeh, M. K., and Ming-Yen, C. (2012). Clinical development of liposome-based drugs: Formulation, characterization, and therapeutic efficacy. *Int. J. Nanomedicine* 7, 49–60. doi:10.2147/ijn.S26766

Chatterjee, S., Hui, P. C. L., Kan, C. W., and Wang, W. (2019). Dual-responsive (pH/temperature) Pluronic F-127 hydrogel drug delivery system for textile-based transdermal therapy. *Sci. Rep.* 9, 11658. doi:10.1038/s41598-019-48254-6

Cheng, L., Cai, Z., Ye, T., Yu, X., Chen, Z., Yan, Y., et al. (2020). Injectable polypeptide-protein hydrogels for promoting infected wound healing. *Adv. Funct. Mater.* 30 (25), 2001196. doi:10.1002/adfm.202001196

Ehteshamfar, S. M., Akhbari, M., Afshari, J. T., Seyedi, M., Nikfar, B., Shapouri-Moghaddam, A., et al. (2020). Anti-inflammatory and immune-modulatory impacts of berberine on activation of autoreactive T cells in autoimmune inflammation. *J. Cell. Mol. Med.* 24 (23), 13573–13588. doi:10.1111/jcmm.16049

Fathalla, Z. M. A., Vangala, A., Longman, M., Khaled, K. A., Hussein, A. K., El-Garhy, O. H., et al. (2017). Poloxamer-based thermoresponsive ketorolac tromethamine *in situ* gel preparations: Design, characterisation, toxicity and transcorneal permeation studies. *Eur. J. Pharm. Biopharm.* 114, 119–134. doi:10.1016/j.ejpb.2017.01.008

Forier, K., Raemdonck, K., De Smedt, S. C., Demeester, J., Coenye, T., and Braeckmans, K. (2014). Lipid and polymer nanoparticles for drug delivery to bacterial biofilms. *J. Control. Release* 190, 607–623. doi:10.1016/j.jconrel.2014.03.055

Frickmann, H., Zautner, A. E., Moter, A., Kikhney, J., Hagen, R. M., Stender, H., et al. (2017). Fluorescence *in situ* hybridization (FISH) in the microbiological diagnostic routine laboratory: A review. *Crit. Rev. Microbiol.* 43 (3), 263–293. doi:10.3109/1040841x.2016.1169990

Guan, Y., Niu, H., Liu, Z., Dang, Y., Shen, J., Zayed, M., et al. (2021). Sustained oxygenation accelerates diabetic wound healing by promoting epithelialization and angiogenesis and decreasing inflammation. *Sci. Adv.* 7 (35), eabj0153. doi:10.1126/sciadv.abj0153

Henry, B. D., Neill, D. R., Becker, K. A., Gore, S., Bricio-Moreno, L., Ziobro, R., et al. (2015). Engineered liposomes sequester bacterial exotoxins and protect from severe invasive infections in mice. *Nat. Biotechnol.* 33 (1), 81–88. doi:10.1038/nbt.3037

Hu, D., Li, H., Wang, B., Ye, Z., Lei, W., Jia, F., et al. (2017). Surface-adaptive gold nanoparticles with effective adherence and enhanced photothermal ablation of methicillin-resistant *Staphylococcus aureus* biofilm. *Acs Nano* 11 (9), 9330–9339. doi:10.1021/acsnano.7b04731

Hu, H., Zhong, D., Li, W., Lin, X., He, J., Sun, Y., et al. (2022). Microalgae-based bioactive hydrogel loaded with quorum sensing inhibitor promotes infected wound healing. *Nano Today* 42, 101368. doi:10.1016/j.nantod.2021.101368

Huemer, M., Mairpady Shambat, S., Brugger, S. D., and Zinkernagel, A. S. (2020). Antibiotic resistance and persistence-Implications for human health and treatment perspectives. *Embo Rep.* 21 (12), e51034. doi:10.15252/embr.202051034

Iheozor-Ejiofor, Z., Newton, K., Dumville, J. C., Costa, M. L., Norman, G., and Bruce, J. (2018). Negative pressure wound therapy for open traumatic wounds. *Cochrane Database Syst. Rev.* 7, CD012522. doi:10.1002/14651858.CD012522.pub2

Jiang, L., Zhu, Y., Luan, P., Xu, J., Ru, G., Fu, J. G., et al. (2021a). Bacteria-anchoring hybrid liposome capable of absorbing multiple toxins for antivirulence therapy of *Escherichia coli* infection. *Acs Nano* 15 (3), 4173–4185. doi:10.1021/acsnano.0c04800

Jiang, Y., Liu, Y., Zhang, X., Gao, H., Mou, L., Wu, M., et al. (2021b). Biofilm application in the microbial biochemicals production process. *Biotechnol. Adv.* 48, 107724. doi:10.1016/j.biotechadv.2021.107724

Khallaf, A. M., El-Moslemany, R. M., Ahmed, M. F., Morsi, M. H., and Khalafallah, N. M. (2022). Exploring a novel fasudil-phospholipid complex formulated as liposomal thermosensitive *in situ* gel for glaucoma. *Int. J. Nanomedicine* 17, 163–181. doi:10.2147/ijn.S342975

Kluzek, M., Oppenheimer-Shaanan, Y., Dadosh, T., Morandi, M. I., Avinoam, O., Raanan, C., et al. (2022). Designer liposomic nanocarriers are effective biofilm eradicators. *Acs Nano* 16 (10), 15792–15804. doi:10.1021/acsnano.2c04232

Kobashi, S., Terashima, T., Katagi, M., Nakae, Y., Okano, J., Suzuki, Y., et al. (2020). Transplantation of M2-deviated microglia promotes recovery of motor function after spinal cord injury in mice. *Mol. Ther.* 28 (1), 254–265. doi:10.1016/j.ymthe.2019.09.004

Konop, M., Rybka, M., and Drapala, A. (2021). Keratin biomaterials in skin wound healing, an old player in modern medicine: A mini review. *Pharmaceutics* 13 (12), 2029. doi:10.3390/pharmaceutics13122029

LaPlante, K. L., Dhand, A., Wright, K., and Lauterio, M. (2022). Re-establishing the utility of tetracycline-class antibiotics for current challenges with antibiotic resistance. *Ann. Med.* 54 (1), 1686–1700. doi:10.1080/07853890.2022.2085881

Li, Z., Ding, Y., Liu, J., Wang, J., Mo, F., Wang, Y., et al. (2022a). Depletion of tumor associated macrophages enhances local and systemic platelet-mediated anti-PD-1 delivery for post-surgery tumor recurrence treatment. *Nat. Commun.* 13 (1), 1845. doi:10.1038/s41467-022-29388-0

Li, Z., Mo, F., Wang, Y., Li, W., Chen, Y., Liu, J., et al. (2022b). Enhancing Gasdermin-induced tumor pyroptosis through preventing ESCRT-dependent cell membrane repair augments antitumor immune response. *Nat. Commun.* 13 (1), 6321. doi:10.1038/s41467-022-34036-8

Liang, Y., He, J., and Guo, B. (2021). Functional hydrogels as wound dressing to enhance wound healing. *Acs Nano* 15 (8), 12687–12722. doi:10.1021/acsnano.1c04206

Lin, Y. K., Yang, S. C., Hsu, C. Y., Sung, J. T., and Fang, J. Y. (2021). The antibiofilm nanosystems for improved infection inhibition of microbes in skin. *Molecules* 26 (21), 6392. doi:10.3390/molecules26216392

Liu, W., Wenbin, O. Y., Zhang, C., Wang, Q., Pan, X., Huang, P., et al. (2020). Synthetic polymeric antibacterial hydrogel for methicillin-resistant Staphylococcus aureus-infected wound healing: Nanoantimicrobial self-assembly, drug- and cytokine-free strategy. *Acs Nano* 14 (10), 12905–12917. doi:10.1021/acsnano.0c03855

Lyu, W., Ma, Y., Chen, S., Li, H., Wang, P., Chen, Y., et al. (2021). Flexible ultrasonic patch for accelerating chronic wound healing. *Adv. Healthc. Mater.* 10 (19), 2100785. doi:10.1002/adhm.202100785

Nicolosi, D., Cupri, S., Genovese, C., Tempera, G., Mattina, R., and Pignatello, R. (2015). Nanotechnology approaches for antibacterial drug delivery: Preparation and microbiological evaluation of fusogenic liposomes carrying fusidic acid. *Int. J. Antimicrob. Agents* 45 (6), 622–626. doi:10.1016/j.ijantimicag.2015.01.016

Pan, X., Hobbs, R. P., and Coulombe, P. A. (2013). The expanding significance of keratin intermediate filaments in normal and diseased epithelia. *Curr. Opin. Cell. Biol.* 25 (1), 47–56. doi:10.1016/j.ceb.2012.10.018

Park, S. H., Kim, R. S., Stiles, W. R., Jo, M., Zeng, L., Rho, S., et al. (2022). Injectable thermosensitive hydrogels for a sustained release of iron nanochelators. *Adv. Sci.* 9 (15), 2200872. doi:10.1002/advs.202200872

Peng, X., Ding, C., Zhao, Y., Hao, M., Liu, W., Yang, M., et al. (2022). Poloxamer 407 and hyaluronic acid thermosensitive hydrogel-encapsulated Ginsenoside Rg3 to promote skin wound healing. *Front. Bioeng. Biotechnol.* 10, 831007. doi:10.3389/fbioe.2022.831007

Pornpattananangkul, D., Zhang, L., Olson, S., Aryal, S., Obonyo, M., Vecchio, K., et al. (2011). Bacterial toxin-triggered drug release from gold nanoparticle-stabilized liposomes for the treatment of bacterial infection. *J. Am. Chem. Soc.* 133 (11), 4132–4139. doi:10.1021/ja111110e

Prudent, E., and Raoult, D. (2019). Fluorescence *in situ* hybridization, a complementary molecular tool for the clinical diagnosis of infectious diseases by intracellular and fastidious bacteria. *Fems Microbiol. Rev.* 43 (1), 88–107. doi:10.1093/femsre/fuy040

Qiang, L., Yang, S., Cui, Y. H., and He, Y. Y. (2021). Keratinocyte autophagy enables the activation of keratinocytes and fibroblasts and facilitates wound healing. *Autophagy* 17 (9), 2128–2143. doi:10.1080/15548627.2020.1816342

Roy, S., Santra, S., Das, A., Dixith, S., Sinha, M., Ghatak, S., et al. (2020). *Staphylococcus aureus* biofilm infection compromises wound healing by causing deficiencies in granulation tissue collagen. *Ann. Surg.* 271 (6), 1174–1185. doi:10.1097/sla.0000000000003053

Rubio-Canalejas, A., Baelo, A., Herbera, S., Blanco-Cabra, N., Vukomanovic, M., and Torrents, E. (2022). 3D spatial organization and improved antibiotic treatment of a Pseudomonas aeruginosa-Staphylococcus aureus wound biofilm by nanoparticle enzyme delivery. *Front. Microbiol.* 13, 959156. doi:10.3389/fmicb.2022.959156

Russo, E., and Villa, C. (2019). Poloxamer hydrogels for biomedical applications. *Pharmaceutics* 11 (12), 671. doi:10.3390/pharmaceutics11120671

Scriboni, A. B., Couto, V. M., de Morais Ribeiro, L. N., Freires, I. A., Groppo, F. C., de Paula, E., et al. (2019). Fusogenic liposomes increase the antimicrobial activity of vancomycin against *Staphylococcus aureus* biofilm. *Front. Pharmacol.* 10, 1401. doi:10.3389/fphar.2019.01401

Sharahi, J. Y., Azimi, T., Shariati, A., Safari, H., Tehrani, M. K., and Hashemi, A. (2019). Advanced strategies for combating bacterial biofilms. *J. Cell. Physiology* 234 (9), 14689–14708. doi:10.1002/jcp.28225

Tang, Q., Xue, N., Ding, X., Tsai, K. H. Y., Hew, J. J., Jiang, R., et al. (2023). Role of wound microbiome, strategies of microbiota delivery system and clinical management. *Adv. Drug Deliv. Rev.* 192, 114671. doi:10.1016/j.addr.2022.114671

Turner, N. A., Sharma-Kuinkel, B. K., Maskarinec, S. A., Eichenberger, E. M., Shah, P. P., Carugati, M., et al. (2019). Methicillin-resistant *Staphylococcus aureus*: An overview of basic and clinical research. *Nat. Rev. Microbiol.* 17 (4), 203–218. doi:10.1038/s41579-018-0147-4

Wang, C., Wang, M., Xu, T., Zhang, X., Lin, C., Gao, W., et al. (2019). Engineering bioactive self-healing antibacterial exosomes hydrogel for promoting chronic diabetic wound healing and complete skin regeneration. *Theranostics* 9 (1), 65–76. doi:10.7150/thno.29766

Wang, Y., Shou, J. W., Li, X. Y., Zhao, Z. X., Fu, J., He, C. Y., et al. (2017). Berberine-induced bioactive metabolites of the gut microbiota improve energy metabolism. *Metabolism-Clinical Exp.* 70, 72–84. doi:10.1016/j.metabol.2017.02.003

Wormald, J. C. R., Wade, R. G., Dunne, J. A., Collins, D. P., and Jain, A. (2020). Hydrosurgical debridement versus conventional surgical debridement for acute partial-thickness burns. *Cochrane Database Syst. Rev.* 2020 (9), CD012826. doi:10.1002/14651858.CD012826.pub2

Wu, Y. K., Cheng, N. C., and Cheng, C. M. (2019). Biofilms in chronic wounds: Pathogenesis and diagnosis. *Trends Biotechnol.* 37 (5), 505–517. doi:10.1016/j.tibtech.2018.10.011

Xie, J., Meng, Z., Han, X., Li, S., Ma, X., Chen, X., et al. (2022). Cholesterol microdomain enhances the biofilm eradication of antibiotic liposomes. *Adv. Healthc. Mater.* 11 (8), 2101745. doi:10.1002/adhm.202101745

Yan, J., and Bassler, B. L. (2019). Surviving as a community: Antibiotic tolerance and persistence in bacterial biofilms. *Cell. Host Microbe* 26 (1), 15–21. doi:10.1016/j.chom.2019.06.002

Yan, X., Fang, W. W., Xue, J., Sun, T. C., Dong, L., Zha, Z., et al. (2019). Thermoresponsive *in situ* forming hydrogel with sol-gel irreversibility for effective methicillin-resistant *Staphylococcus aureus* infected wound healing. *Acs Nano* 13 (9), 10074–10084. doi:10.1021/acsnano.9b02845

Yang, J., Chen, Z., Pan, D., Li, H., and Shen, J. (2020a). Umbilical cord-derived mesenchymal stem cell-derived exosomes combined pluronic F127 hydrogel promote chronic diabetic wound healing and complete skin regeneration. *Int. J. Nanomedicine* 15, 5911–5926. doi:10.2147/ijn.S249129

Yang, L., Guo, J., Yu, N., Liu, Y., Song, H., Niu, J., et al. (2020b). Tocilizumab mimotope alleviates kidney injury and fibrosis by inhibiting IL6 signaling and ferroptosis in UUO model. *Life Sci.* 261, 118487. doi:10.1016/j.lfs.2020.118487

Yao, C. H., Chen, K. Y., Cheng, M. H., Chen, Y. S., and Huang, C. H. (2020). Effect of genipin crosslinked chitosan scaffolds containing SDF-1 on wound healing in a rat model. *Mater. Sci. Eng. C-Materials Biol. Appl.* 109, 110368. doi:10.1016/j.msec.2019.110368

Zarrintaj, P., Ramsey, J. D., Samadi, A., Atoufi, Z., Yazdi, M. K., Ganjali, M. R., et al. (2020). Poloxamer: A versatile tri-block copolymer for biomedical applications. *Acta Biomater.* 110, 37–67. doi:10.1016/j.actbio.2020.04.028

Zhang, T., Chen, S., Dou, H., Liu, Q., Shu, G., Lin, J., et al. (2021). Novel glucosamine-loaded thermosensitive hydrogels based on poloxamers for osteoarthritis therapy by intra-articular injection. *Mater. Sci. Eng. C-Materials Biol. Appl.* 118, 111352. doi:10.1016/j.msec.2020.111352

Zhang, Y., Yu, J., Ren, K., Zuo, J., Ding, J., and Chen, X. (2019). Thermosensitive hydrogels as scaffolds for cartilage tissue engineering. *Biomacromolecules* 20 (4), 1478–1492. doi:10.1021/acs.biomac.9b00043

Zhou, J., Zhang, H., Fareed, M. S., He, Y., Lu, Y., Yang, C., et al. (2022). An injectable peptide hydrogel constructed of natural antimicrobial peptide J-1 and ADP shows anti-infection, hemostasis, and antiadhesion efficacy. *Acs Nano* 16 (5), 7636–7650. doi:10.1021/acsnano.1c11206

Zhou, K., Li, C., Chen, D., Pan, Y., Tao, Y., Qu, W., et al. (2018a). A review on nanosystems as an effective approach against infections of *Staphylococcus aureus*. *Int. J. Nanomedicine* 13, 7333–7347. doi:10.2147/ijn.S169935

Zhou, Y., Que, K. T., Zhang, Z., Yi, Z. J., Zhao, P. X., You, Y., et al. (2018b). Iron overloaded polarizes macrophage to proinflammation phenotype through ROS/acetyl-p53 pathway. *Cancer Med.* 7 (8), 4012–4022. doi:10.1002/cam4.1670

frontiers | Frontiers in Bioengineering and Biotechnology

TYPE Original Research
PUBLISHED 07 July 2023
DOI 10.3389/fbioe.2023.1226065

OPEN ACCESS

EDITED BY
Xianqi Li,
Matsumoto Dental University, Japan

REVIEWED BY
Xiangxiang Hu,
The Ohio State University, United States
Dengfeng Peng,
Shenzhen University, China
Jiachi Zhang,
Lanzhou University, China

*CORRESPONDENCE
Bing Li,
libing-1975@163.com
Xiuping Wu,
77wxp@163.com

†These authors share first authorship

RECEIVED 20 May 2023
ACCEPTED 29 June 2023
PUBLISHED 07 July 2023

CITATION
Zhang Z, Zong M, Liu J, Ren J, Liu X, Zhang R, Cui J, Sun L, Song H, Zhang Y, Li B and Wu X (2023), Biosafety evaluation of $BaSi_2O_2N_2$:Eu^{2+}/PDMS composite elastomers.
Front. Bioeng. Biotechnol. 11:1226065.
doi: 10.3389/fbioe.2023.1226065

Biosafety evaluation of $BaSi_2O_2N_2$:Eu^{2+}/PDMS composite elastomers

Zheyuan Zhang[1,2†], Mingrui Zong[1,2†], Jinrong Liu[1,2], Jianing Ren[1,2], Xiaoming Liu[1,2], Ran Zhang[1,2], Jiayu Cui[1,2], Lingxiang Sun[1,2], Hao Song[3], Yanjie Zhang[3], Bing Li[1,2*] and Xiuping Wu[1,2*]

[1]School and Hospital of Stomatology, Shanxi Medical University, Taiyuan, Shanxi, China, [2]Shanxi Province Key Laboratory of Oral Diseases Prevention and New Materials, Taiyuan, Shanxi, China, [3]Research Institute of Photonics, Dalian Polytechnic University, Dalian, Liaoning, China

In recent years, mechanoluminescent (ML) materials have shown great potential in stress sensing, mechanical energy collection and conversion, so they have attracted wide attention in the field of stomatology. In the early stage of this study, $BaSi_2O_2N_2$:Eu^{2+} ML phosphors were synthesized by two-step high temperature solid state method, and then mixed with Polydimethylsiloxane (PDMS) in different proportions to obtain $BaSi_2O_2N_2$:Eu^{2+}/PDMS ML composites with different mass fractions (10%,20%,30%,40%,50%). Then its biosafety was evaluated by Cell Counting Kit-8 (CCK-8), Calcein-AM/PI fluorescence staining, hemolysis, oral mucosal irritation, acute and subacute systemic toxicity tests. The experimental results show that the biosafety of $BaSi_2O_2N_2$:Eu^{2+}/PDMS ML composite elastomers with different mass fraction is in line with the existing standards, and other related properties can be further studied.

KEYWORDS

mechanoluminescent, $BaSi_2O_2N_2$:Eu^{2+}, polydimethylsiloxane, composite, biosafety

1 Introduction

In recent years, a unique luminescence phenomenon—mechanoluminescent (ML) has attracted widespread attention (Wang et al., 2022), which first originated in 1605″Advancement of Learning" (Jha and Chandra, 2014). ML in a broad sense refers to all luminescence phenomena generated by various mechanical effects such as friction, extrusion, etc. In a narrow sense, it refers specifically to the luminescence caused by elastic deformation, plastic deformation or fracture deformation (Bai et al., 2021; Fujio et al., 2022). Since mechanical interactions permeate all aspects of life, ML could theoretically provide new solutions to challenging problems in biology, optoelectronics, and energy and environmental sciences (Xiong et al., 2021; Zhuang and Xie, 2021). In addition, it has received a lot of attention in dental materials science because of its demonstrated potential in stress sensing, mechanical energy harvesting and conversion (Shin et al., 2022).

Temporomandibular disorders (TMD) is one of the common diseases in oral clinic, and its pathogenic factors are various, including joint, masticatory muscle, occlusal and psychological disorders (Li and Leung, 2021), so it has always been an important and difficult point in the process of clinical diagnosis and treatment. Occlusal abnormalities are often considered by clinicians as a potential factor in TMD (Manfredini et al., 2017), and the relationship between them has always been concerned and controversial. Some scholars believe that the position of the condyle during apical malocclusion (intercuspalocclusion, ICO) determines the balance of the masticatory system, while the abnormal occlusal relationship may destroy this phenomenon, change the functional position of the

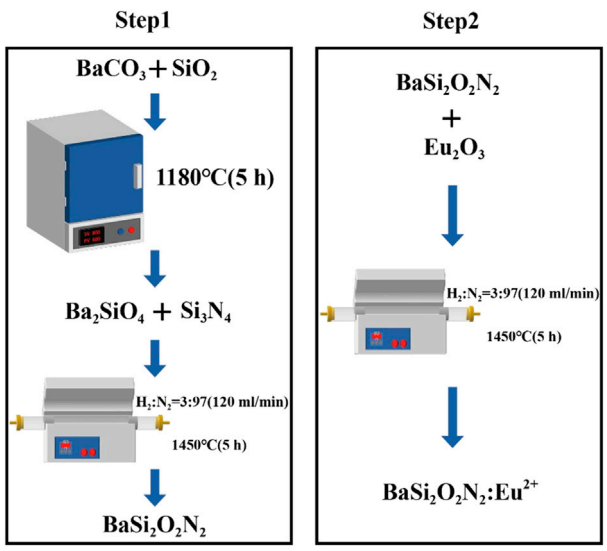

FIGURE 1
Synthesis of $BaSi_2O_2N_2:Eu^{2+}$ phosphors.

mandible and the relationship between the condyle and the articular fossa, and then increase the risk of TMD (Ohrbach et al., 2020). Occlusal splint is a common and effective method for the treatment of abnormal occlusal function (Wieckiewicz et al., 2015). It is found that after stable occlusal splint treatment, abnormal muscle and joint activity in patients with TMD are significantly reduced, abnormal occlusal contact and mandibular movement are improved, and symptoms such as limited opening and joint pain are greatly solved (Al-Moraissi et al., 2020). However, some studies have shown that the existing occlusal materials have some shortcomings, such as high water absorption and solubility, easy to be affected by saliva and can not accurately reflect the actual occlusal situation (Grymak et al., 2022). Therefore, it is necessary to look for an alternative material which can provide accurate occlusal detection function and better comprehensive performance.

The emergence of ML materials provides a new idea for optimizing occlusal detection and analysis in oral clinic and realizing occlusal visualization. ML materials have good physical and chemical stability, and the luminous intensity is proportional to the stress (Bai et al., 2022). Among them, the nitrogen oxide fluorescent material $BaSi_2O_2N_2:Eu^{2+}$ (BSON:Eu^{2+}) shows super ML (Seibald et al., 2012). After mechanical stimulation such as pressing and stretching, the green ML can last for tens of seconds. Because the material type is nitrogen oxide and the preparation process has no pollution to the environment (Yun et al., 2016), it can be mixed with flexible matrix polydimethylsiloxane (PDMS), which is widely used in clinic, to prepare ML composite elastomer, so as to establish the relationship between mechanical force and optical signal.

In this study, $BaSi_2O_2N_2:Eu^{2+}$ phosphors were synthesized by two-step high temperature solid state method to further improve their luminous intensity, and then mixed with PDMS to prepare a series of $BaSi_2O_2N_2:Eu^{2+}$/PDMS composite elastomers with different mass fraction. Medical biomaterials related to oral cavity need to be strictly tested by relevant regulatory agencies before they are used in clinic, in order to minimize the adverse effects caused by direct contact with tissues, including *in vitro* cell tests, animal tests and so on (Xie et al., 2017). Therefore, according to the ISO7405/ISO10993 standard, the biological safety of $BaSi_2O_2N_2:Eu^{2+}$/PDMS composite elastomer was preliminarily evaluated by Cell Counting Kit-8 (CCK-8) cytotoxicity test, Calcein-AM/PI fluorescence staining, hemolysis test, oral mucosal irritation test, subacute and acute systemic toxicity test, in order to explore the possibility of its clinical application and provide experimental basis for future clinical application.

2 Experimental sections

2.1 Preparation of materials

2.1.1 Preparation of $BaSi_2O_2N_2:Eu^{2+}$ phosphors

As shown in Figure 1, $BaSi_2O_2N_2:Eu^{2+}$ phosphors was prepared by two-step high temperature solid state method.

Step one: first, $BaCO_3$ and SiO_2 are ground and mixed and placed in a 1180°C box muffle furnace, sintered for 5 h and cooled, and Ba_2SiO_4 is obtained after re-grinding. Then add Si_3N_4, put it into a high temperature tube furnace after grinding and put into the reducing atmosphere with H_2/N_2 ratio of 3/97 (atmosphere flow rate is 120 mL/min). After sintering at 1450°C for 5 h, $BaSi_2O_2N_2$ is obtained by cooling grinding.

Step two: add metal oxide Eu_2O_3 on the basis of the first step, grind it in a high temperature tube furnace and put it into a reducing atmosphere with a H_2/N_2 ratio of 3/97 (120 mL/min), sintering at 1450°C for 5 h, cooling and grinding to obtain $BaSi_2O_2N_2:Eu^{2+}$ phosphors, which is put into a sealed bag for subsequent performance characterization and testing.

2.1.2 Preparation of $BaSi_2O_2N_2:Eu^{2+}$/PDMS composite elastomers

The core content of the process is to mix the luminescent material of the powder with the organic matrix. The organic matrix selected in this experiment is PDMS (composed of the main body and curing agent, the mixing ratio is 10:1). $BaSi_2O_2N_2:Eu^{2+}$ phosphors and PDMS were weighed at the mass ratio of 10%、20%、30%、40%、50%, mixed and stirred to get the ML complex, which was left for a period of time to eliminate bubbles, and then cured at room temperature for 24 h to obtain the target $BaSi_2O_2N_2:Eu^{2+}$/PDMS composite elastomer.

2.1.3 Preparation of ML occlusal splint

The initial model of the occlusal plate was coated on the single jaw plaster tooth model, then the silicone rubber was coated on the outer layer, and the single jaw plaster dental mold covered with the splint was stripped off after the silicone rubber was cured. $BaSi_2O_2N_2:Eu^{2+}$/PDMS was injected into the silicone rubber, then the silicone rubber was covered with a single jaw plaster dental mold, and then cured at 80°C for 1 h.

2.2 Characterization

X-ray diffractometer (XRD) is used to observe the phase structure and crystal structure of $BaSi_2O_2N_2:Eu^{2+}$, and then field-emission

scanning electron microscopy (FESEM) is usually used to detect the micro-morphology and observe the distribution of particles. The prepared ML composite elastomer was irradiated under ultraviolet lamp for 3–5 min, then in a completely dark environment, simulated tooth bite force was applied to it after the afterglow disappeared completely, and its ML Phenomenon was observed.

2.3 Preparation of the specimens and extracts

The material samples were uniformly made into long 4 mm, wide 5 mm and 1 mm thick, and the $BaSi_2O_2N_2$:Eu^{2+}/PDMS ML composite elastomers were washed in anhydrous ethanol for 20 min, then washed with distilled water, routinely sterilized, dried and sterilized by high pressure steam. Put it in normal saline (the ratio of the surface area of the specimen to the extraction medium is 6 cm^2/mL) and put it in a water bath at 37°C for 72 h.

2.4 Biosafety tests

2.4.1 Cytotoxicity test

2.4.1.1 CCK-8 assay

L929 fibroblasts were resuscitated and passaged for 2–3 times, then Dulbecco's modified Eagle medium (DMEM) culture medium containing 10% embryonic bovine serum was used to make single cell suspension (2.5×10^4 cells/mL) and inoculated on 24-well plate (400 μL/well). Then the cells were incubated in a cell incubator of 37°C and 5%CO_2 for 24 h. After observing the adhesion of the cells, the original medium was discarded and a new medium was added. The $BaSi_2O_2N_2$:Eu^{2+}/PDMS composite elastomers with the same specifications and different mass fractions (the experimental group) were clamped into a 24-well plate with ophthalmic tweezers, while the control group only added DMEM medium. Three 24-well plates were inoculated under the same conditions and cultured in cell incubator for 1, 3 and 5 days.

On the first, third and fifth day, 24-well plates were taken out, and the morphology of cells was observed under inverted microscope. 40 μL WST-8 solution was added to each well, and then transferred to 96-well plate (100 μL/well) after 1.5 h of incubation. The oplical densiy (OD) of each well was measured at 450 nm wavelength by enzyme-linked immunosorbent assay (Elisa), and the cell survival rate was calculated.

$$\textbf{Cell Viability}\,(\%) = (\textbf{material group} - \textbf{blank group})/ \times (\textbf{control group} - \textbf{blank group})$$

2.4.1.2 Calcein-AM/PI fluorescence staining

Calcein-AM/PI double staining method was used to stain living cells and dead cells, in which Calcein-AM only stained living cells because it could easily penetrate the living cell membrane, hydrolyze in the cytoplasm and emit strong green fluorescence, while PI only stained dead cells because it could not pass through the living cell membrane and could pass through the disordered region of the dead cell membrane to reach the nucleus and embedded into the DNA double helix of the cell to produce red fluorescence. The method of culturing cells and adding materials was the same as 2.4.1.1.24-well plates were taken out on the first, third and fifth day, respectively, and the morphology of cells was observed under inverted microscope. 100 μL Calcein-AM was added to each 10 mL medium, and 20 min–25 min was incubated at 37°C. After that, 20–200 μL PI solution was added to each 10 mL medium, and 5 min was stained at room temperature. Finally, live cells (yellow-green fluorescence) and dead cells (red fluorescence) were detected by fluorescence microscope at 490 ± 10 nm; in addition, only dead cells could be observed in 545 nm.

2.4.2 Oral mucosa irritation test

The subjects were 25 healthy golden gophers aged about 5 months, and every 5 gophers were set as an experimental group. There was no abnormality in bilateral buccal mucosa. The buccal mucosa of one side of each golden gopher was sutured with medical sutures to fix the $BaSi_2O_2N_2$:Eu^{2+}/PDMS composite elastomers of the same size, and the contralateral buccal mucosa was used as a blank control without any treatment. Every day after operation, whether the specimen fell off, whether the mucosa around the specimen was abnormal, such as hyperemia, swelling and erosion, and whether the animals had signs of poisoning and death were observed. Two weeks later, the golden gophers were killed under excessive anesthesia, and the specimens were removed. The mucosa and surrounding tissues of the contact and contralateral parts were embedded, fixed and sliced, and stained with hematoxylin-eosin (HE) for histopathological observation.

2.4.3 Subacute systemic toxicity test

60 healthy SD rats weighing about 130 g were randomly divided into 6 groups (5 experimental groups, 1 control group, half male and half female). They adapted to the laboratory environment 7 days in advance and had to fast overnight without water before the experiment. The rats in the experimental group were perfused with $BaSi_2O_2N_2$:Eu^{2+}/PDMS composite elastomers extract (10%、20%、30%、40%、50%) with the dose of 50 mL/kg, while the rats in the control group were perfused with the same dose of normal saline. Once a day for 28 days, and then observed for 7 days. During this period, the signs of poisoning and death were observed, and the food utilization rate and relative growth rate of body weight were calculated by measuring weekly food consumption and weight gain of rats. At the end of the experiment, the animals were killed under excessive anesthesia, and the important tissues and organs were selected for dissection to observe the abnormal changes of each tissue and organ.

$$\textbf{relative growth rate of body weight}\,(\%) = \textbf{weight gain}\,(\textbf{g})/ \textbf{initial weight}\,(\textbf{g}) \times 100\%$$

$$\textbf{food utilization rate}\,(\%) = \textbf{weight growth}\,(\textbf{g})/ \textbf{total food consumption}\,(\textbf{g}) \times 100\%$$

2.4.4 Acute systemic toxicity test

60 healthy C57 mice with about 17 g were randomly divided into 6 groups (5 experimental groups, 1 control group, half male and half female). The mice in the experimental group were intravenously injected with $BaSi_2O_2N_2$:Eu^{2+}/PDMS composite elastomers extract (10%, 20%, 30%, 40%, 50%) at the dose of 50 mL/kg every day,

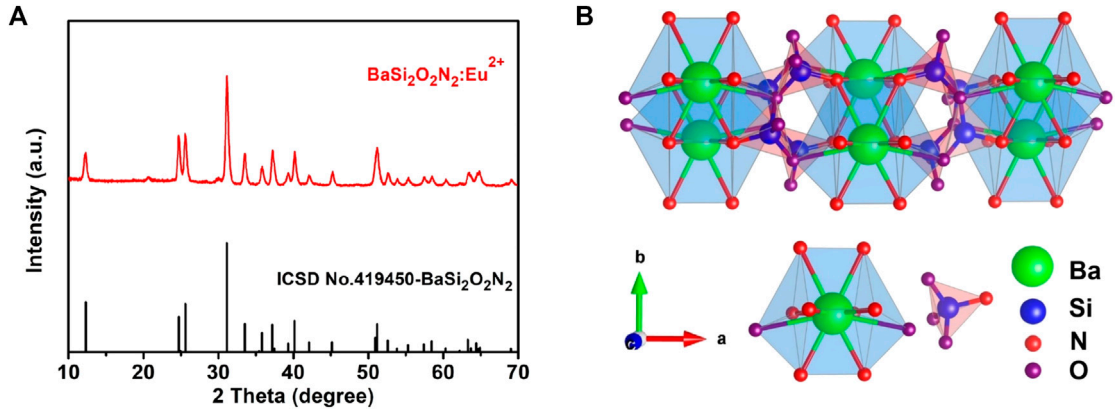

FIGURE 2
XRD patterns of $BaSi_2O_2N_2:Eu^{2+}$ **(A)** and Crystal structure of $BaSi_2O_2N_2$ **(B)**.

while the control group was injected with the same dose of normal saline. The symptoms of collapse, cyanosis, dyspnea, abdominal irritation, diarrhea and tremor were observed immediately after injection. The general behavior, clinical toxic symptoms and death were observed at 4, 24, 48 and 72 h after injection. at the same time, the experimental mice were weighed and recorded, and the body weight changes of mice were monitored. 72 h later, the animals were killed under excessive anesthesia, and the important tissues and organs were dissected to observe the abnormal changes of each tissue and organ.

2.4.5 Hemolysis test

Heart puncture took 6-week-old New Zealand rabbit whole blood 10mL, add 2% potassium oxalate normal saline solution 0.5 mL anticoagulation, and then add normal saline diluted at 4:5. The experimental group was 5 g of different mass fraction of $BaSi_2O_2N_2$:Eu^{2+}/PDMS composite elastomers (10%, 20%, 30%, 40%, 50%), respectively, adding 10 mL 0.9% normal saline, the negative control group was 10 mL 0.9% normal saline, and the positive control group (complete hemolysis) was 10 mL distilled water. The test tube was placed in a 37°C water bath for 30 min (3 parallel samples in each group). Diluted fresh anticoagulant rabbit blood 0.2 mL was added and kept warm for 60 min. The supernatant OD value of the supernatant was measured by spectrophotometer 576 nm and the hemolysis rate was calculated after centrifugation at 758 *g* for 5 min.

$$\textit{Hemolysis rate}\ (\%) = \left[(OD_X - OD_Z) \,/\, (OD_Y - OD_Z) \right] \times 100\%$$

in which OD_X is the experimental group ($BaSi_2O_2N_2:Eu^{2+}$/PDMS composite elastomers with different mass fractions), OD_Y is the positive control group (10 mL distilled water), and OD_Z is the negative control group (10 mL 0.9% saline).

3 Results and discussion

3.1 Characterization

Figure 2A is the X-ray diffraction pattern of $BaSi_2O_2N_2:Eu^{2+}$ phosphor and $BaSi_2O_2N_2$ matrix prepared by two-step high temperature solid state method. From the diagram, we can see that all the diffraction peaks of $BaSi_2O_2N_2:Eu^{2+}$ prepared by this method are consistent with the standard data of $BaSi_2O_2N_2$ crystal (ICSD number 419450). No other impurity phases are found. Eu^{2+} ions are effectively doped into the $BaSi_2O_2N_2$ matrix lattice to form $BaSi_2O_2N_2:Eu^{2+}$ phosphors. Figure 2B shows the crystal structure of $BaSi_2O_2N_2$ with space group Pbcn. $BaSi_2O_2N_2$ is formed by periodic stratification of $(Si_2O_2N_2)^{2-}$ anions and Ba^{2+} cations. Ba^{2+} cations exist at only one crystal site, which coordinates with eight O atoms and two long N atoms to form a cube structure; $(Si_2O_2N_2)^{2-}$ anions are composed of high-density $SiON_3$ tetrahedrons with a common vertex.

Figures 3A, B are FESEM images of phosphors with different magnification respectively, showing clear layered structure of $BaSi_2O_2N_2$, smooth surface, good particle dispersion and cubic phase consistent with crystal structure. Therefore, $BaSi_2O_2N_2:Eu^{2+}$ phosphors were synthesized by two-step high temperature solid state method, which laid a foundation for the preparation of ML composite elastomers.

The ML occlusal splint emits cyan fluorescence after being stressed in the dark environment. It can be seen from Figures 4A–D that different parts of the dentition produce ML after stress. This phenomenon can guide us to find the site of abnormal occlusion as soon as possible and carry out the next step of targeted treatment.

3.2 Cytotoxicity test

3.2.1 CCK-8 assay

After 1, 3 and 5 days of culture, the cells in each group were observed under inverted microscope, and the growth and morphology of cells in the blank control group and each experimental group were normal. The OD values and cell viability of each group were shown in Figure 5. The cell viability of each group was more than 90%, and the cytotoxicity grade (CTG) was 0. There was no significant difference between the experimental group and the blank control group and between different experimental groups ($p > 0.05$). The results showed that different mass fractions of $BaSi_2O_2N_2:Eu^{2+}$/PDMS composite elastomers had no cytotoxicity.

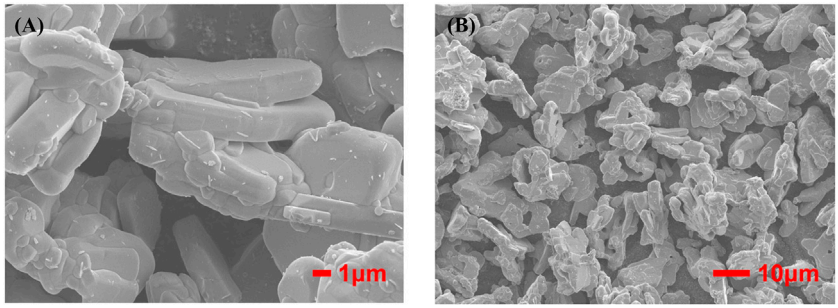

FIGURE 3
High **(A)** and low **(B)** magnification FESEM images of $BaSi_2O_2N_2:Eu^{2+}$.

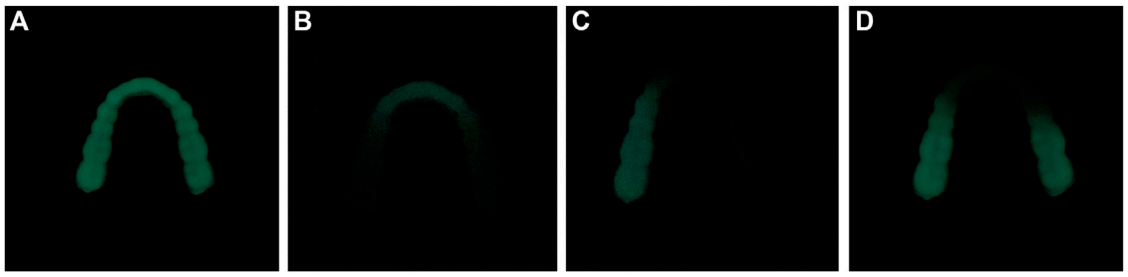

FIGURE 4
ML in different parts of dentition. **(A)** ML of the whole dentition **(B)** ML of anterior teeth **(C)** ML of left posterior teeth **(D)** ML of bilateral posterior teeth.

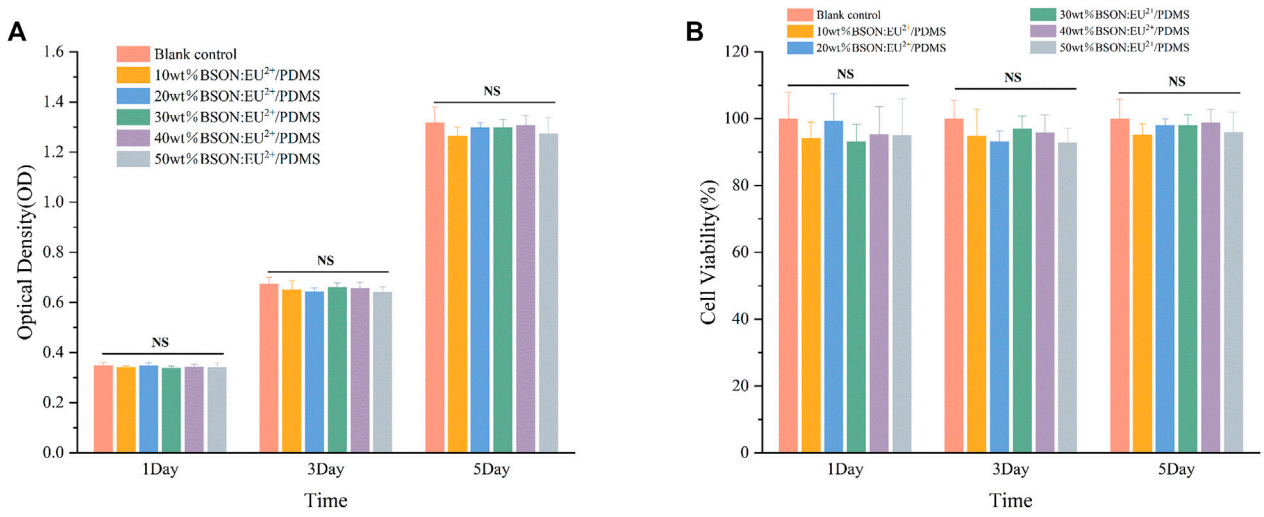

FIGURE 5
OD values **(A)** and cell viability **(B)** of each group.

3.2.2 Calcein-AM/PI fluorescence staining

As shown in Figure 6, after Calcein-AM/PI fluorescence staining, most of the cells in the experimental group and control group showed green on the first, third and fifth day, and the cells survived well and the morphology was normal, which indicated that the mass ratio of 10%、20%、30%、40%、50% $BaSi_2O_2N_2:Eu^{2+}$/PDMS composite elastomers did not cause obvious harm to the cell activity.

The main methods of cytotoxicity assessment include CCK-8 assay and Calcein-AM/PI fluorescence staining to evaluate whether

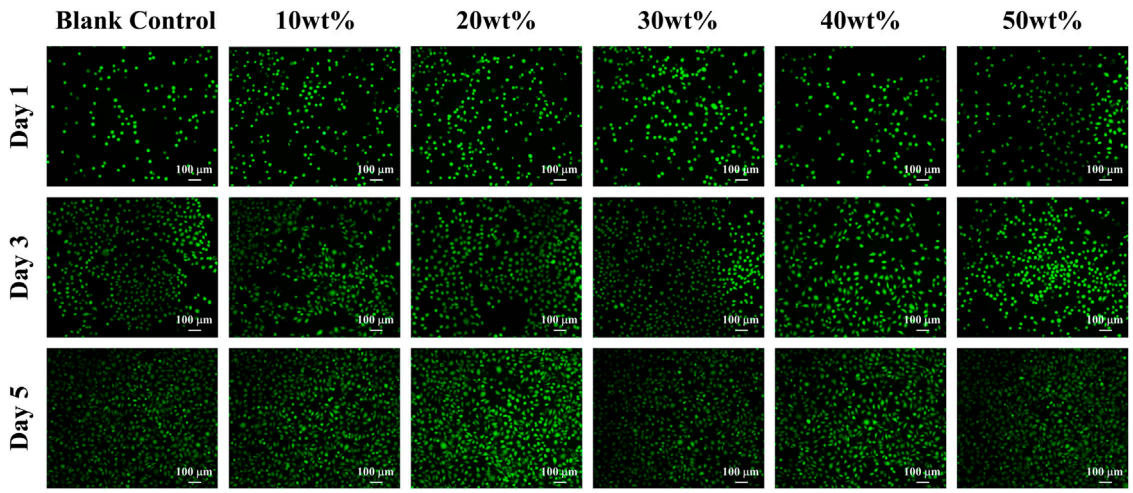

FIGURE 6
Calcein-AM/PI fluorescence staining of each group.

the cytocompatibility of materials meets the needs of biomaterials by measuring the effects of toxic substances on the morphological number, metabolic activity and proliferation of cultured cells (Cai et al., 2019; Sun et al., 2022; Dzedulionyte et al., 2023). Lmur929 fibroblasts were selected in the above two experiments, which have the advantages of strong reproductive ability, sensitivity to changes in environmental factors, and timely response to toxic substances in the materials (Lendahl et al., 2022).

The CCK-8 method is based on WST-8 (2-(2-methoxy-4-nitrophenyl)-3-(4-nitrophenyl)-5-(2-methoxy-4-disulfonated phenyl)-2H-tetrazolium monosodium salt) in the presence of electronic carrier 1-methoxy-5-methylphenazinonium sulfate dimethyl ester (1-MethoxyPMS), which is reduced by dehydrogenase in mitochondria to orange-yellow methyl Zan products with high water solubility. The more cells proliferate, the faster the color, the darker the color; the greater the cytotoxicity, the lighter the color (Kawano et al., 2019). For the same cells, the color is directly proportional to the number of living cells, and the absorbance at 450 nm wavelength can be measured by enzyme-linked immunosorbent assay (Elisa), which can indirectly reflect the activity of cells. In addition, according to the 10993–5 standard of the International Organization for Standardization, the cell survival rate is more than 90%, indicating that the material has no cytotoxicity.

The principle of Calcein-AM/PI fluorescence staining experiment is that Calcein-AM can only stain living cells, because it can easily penetrate the living cell membrane, hydrolyze in the cytoplasm and emit strong green fluorescence; PI only staining dead cells, because it can not pass through the living cell membrane, can pass through the disordered region of the dead cell membrane to reach the nucleus, and embedded into the DNA double helix of the cell to produce red fluorescence (Xue et al., 2019; Ke et al., 2020). It is worth mentioning that the premise of effective staining is that the changes in the activity of the corresponding cell model are physical and biochemical characteristics such as changes in esterase activity and plasma membrane integrity, and cytotoxic events that do not affect these cell characteristics may not be accurately evaluated by this method.

3.3 Oral mucosa irritation test

During the experiment, it was observed that the specimens of all groups of golden gophers were in good retention, normal behavior and mental state, without any abnormal conditions or adverse reactions. In addition, no adverse reactions such as redness, swelling, erosion and ulcer were found at the contact site of the specimen and its surrounding tissue.

Figure 7 shows the histological observation of oral mucosa in the experimental groups and the control group. The microscopic observation shows that compared with the blank control group, the cell morphology and structure of buccal mucosa and its surrounding tissue in each experimental group are normal, there is no epithelial hyperplasia, and the cells are well-delaminated and uniformly arranged. There is no inflammatory.

Cell infiltration in connective tissue, no hyperkeratosis, granular layer changes or other adverse changes. As the occlusal splint has been in direct contact with the oral mucosa for a long time, there is a certain degree of dissolution in the process (Reyes-Sevilla et al., 2018), so it is required that the material itself and tissue contact will not produce toxic substances. Oral mucosal irritation test is used to evaluate the irritation of materials to oral mucosa by suturing and fixing biomaterials in animals. In this experiment, after the buccal mucosa of golden gophers were exposed to $BaSi_2O_2N_2:Eu^{2+}$/PDMS composite elastomers with different mass fraction, no abnormal reaction of color, morphology and texture was observed in the buccal mucosa and its surrounding tissue, indicating that all of them had good biosafety.

3.4 Subacute systemic toxicity test: oral route

During the experiment, it was observed that the behavior and mental state of all SD rats were normal, and there were no abnormal conditions or adverse reactions. According to the daily body weight

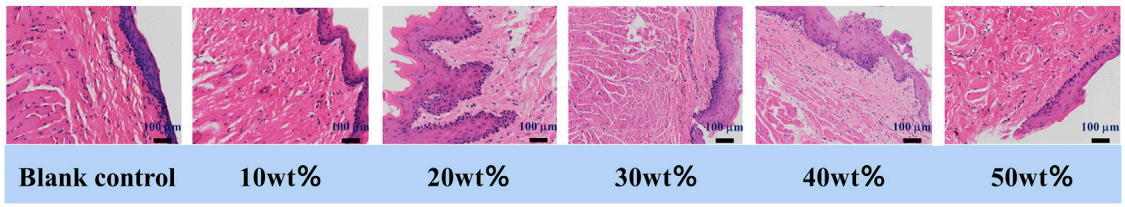

FIGURE 7
Histological observation of the oral mucosa.

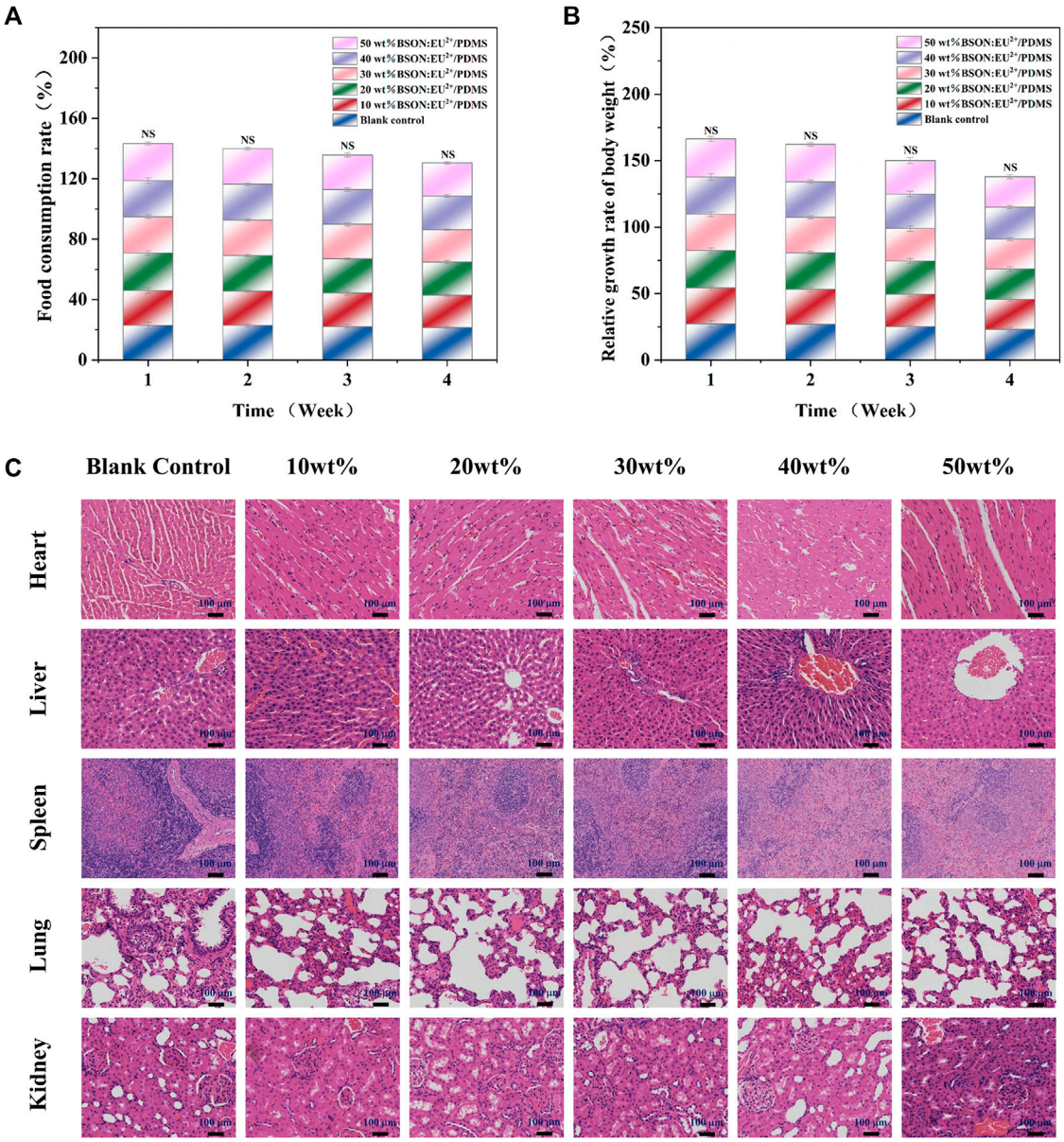

FIGURE 8
The relative growth rate of body weight **(A)** and food utilization rate **(B)** of SD rats and HE staining for the subacute systemic toxicity test of each group **(C)**.

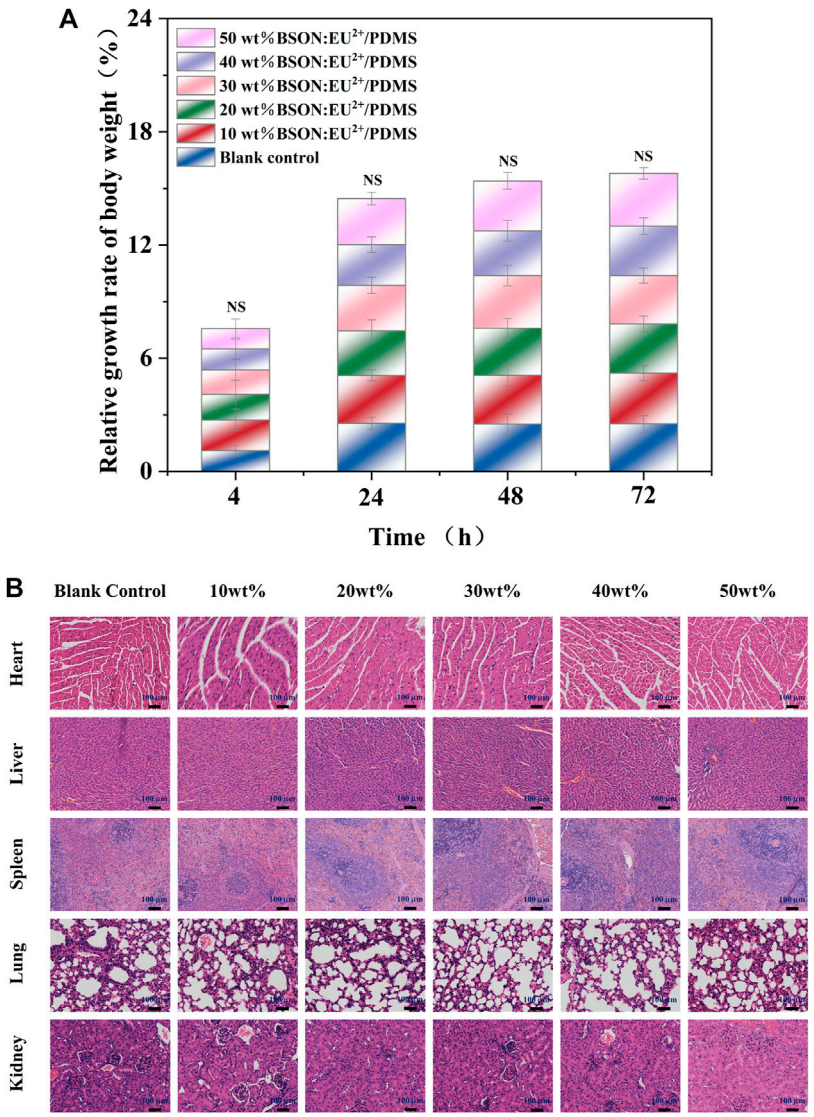

FIGURE 9
The relative growth rate of body weight of C57 mice **(A)** and HE staining for the acute systemic toxicity test of each group **(B)**.

changes and food consumption, the relative growth rate of body weight and food utilization rate could be calculated (Figures 8A, B). There was no significant difference between the experimental group and the control group and between different experimental groups by test of variance. In addition, compared with the control group, the important organs of the experimental group were normal in shape and size, and there were no abnormal changes; histopathological examination (Figure 8C) showed no pathological changes such as atrophy, degeneration or pigmentation, and no inflammatory cell infiltration.

Occlusal splint is in contact with human teeth and periodontal tissue for a long time and bears a variety of long-term stress. Its chemical composition and small substances may enter the human body along with the digestive tract, resulting in toxic effects and harm to tissues and organs of the whole body. Therefore, through the method of intragastric administration, we can ensure that enough drugs enter the digestive tract, simulate the way of toxic substances into the human body to a large extent, and evaluate the biosafety of the materials by observing the clinical symptoms and histological manifestations of animals (Okado et al., 2015).

3.5 Acute systemic toxicity test

After injection of material extract, there were no symptoms such as collapse, dyspnea, cyanosis, diarrhea and tremor. Within 72 h, the mice in the experimental group and control group moved freely, had a normal appetite, and had no clinical toxic symptoms or death. There was no significant difference in the relative growth rate of body weight of C57 mice between the experimental group and the control group and between different experimental groups (Figure 9A). There were no abnormal pathological changes such as inflammatory cell infiltration in the tissues and organs of mice in the experimental group (Figure 9B). The acute systemic toxicity test is different from the

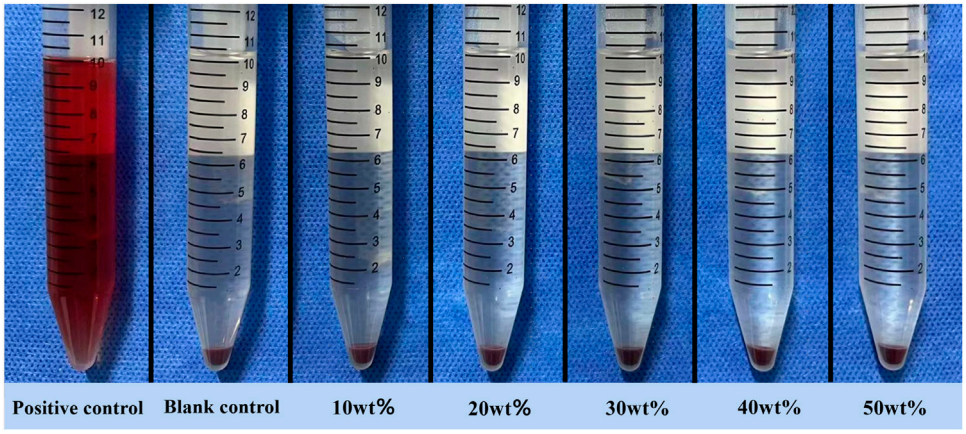

FIGURE 10
Hemolysis test supernatant.

TABLE 1 OD values of the hemolysis test.

Groups	OD value			Average OD value	Hemolysis ratio (%)
	1	2	3		
Positive control	1.3425	1.3902	1.2843	1.3390	-
Blank control	0.0196	0.0212	0.0187	0.0198	-
10 wt%BSON:EU^{2+}/PDMS	0.0314	0.0303	0.0313	0.0310	0.8465
20 wt%BSON:EU^{2+}/PDMS	0.0295	0.0329	0.0314	0.0313	0.8667
30 wt%BSON:EU^{2+}/PDMS	0.0311	0.0318	0.0291	0.0307	0.8213
40 wt%BSON:EU^{2+}/PDMS	0.0325	0.0316	0.0293	0.0311	0.8566
50 wt%BSON:EU^{2+}/PDMS	0.0301	0.0316	0.0295	0.0304	0.8010

mucosal irritation test, which is not to detect the effect on the contact site, but to evaluate whether the material is potentially toxic to the whole body tissues and organs. If more than one mouse is abnormal during the experiment, such as dyspnea or even death or significant weight loss (more than 2 g), the material is proved to be toxic (Pillai et al., 2017). In this experiment, no abnormality was found in mice, and there was no death or weight loss in mice, indicating that the material has good biological safety.

3.6 Hemolysis test

The experimental results are obvious (Figure 10). A large number of red blood cells in the positive control group were destroyed until the supernatant was red, while the supernatant in the negative control group and each experimental group was clear and transparent, and almost no red blood cells were destroyed. The hemolysis rate of each experimental group was less than 5% (Table 1). There was no significant difference between the experimental group and the control group and each experimental group by variance test.

The principle of hemolysis test is that if the test material is toxic, it will destroy the erythrocyte membrane and release hemoglobin in red blood cells. According to ISO10993-4, if the hemolysis rate of the material is less than 5%, it is proved to be non-toxic and meets the standard of biomedical application (Liu et al., 2022). In this experiment, the hemolysis rate of each experimental group is far less than the standard value, indicating that the material has good blood compatibility.

4 Conclusion

The ML phosphor $BaSi_2O_2N_2:Eu^{2+}$, was prepared by two-step high temperature solid state method, and then mixed with matrix PDMS to obtain ML composite elastomer—$BaSi_2O_2N_2:Eu^{2+}$/PDMS. The biocompatibility of $BaSi_2O_2N_2:Eu^{2+}$/PDMS composite elastomers with different mass fractions (10%, 20%, 30%, 40%, 50%) was evaluated by CCK-8 assay and Calcein-AM/PI fluorescence staining at the cellular level, acute and subacute systemic toxicity test, oral mucosal irritation test and hemolysis test. The results showed that the biosafety of different mass fractions of $BaSi_2O_2N_2:Eu^{2+}$/PDMS

composite elastomers met the current standards, and other properties could be tested in the next step. For example, elasticity, wear resistance, solubility, stability and so on, select the best quality ratio, with a view to clinical application, to provide a more efficient method for occlusal visualization.

Data availability statement

The original contributions presented in the study are included in the article/supplementary material, further inquiries can be directed to the corresponding authors.

Ethics statement

The animal study was reviewed and approved by Laboratory Animal Center, Shanxi Medical University (Authorization Number KQDW-2023-002).

Author contributions

ZZ designed the structure and content, assembled the literature and wrote this review. MZ, JL, JR, XL, RZ, JC, LS, HS, YZ, BL, and XW provided suggestions and revised this review. All authors contributed to the article and approved the submitted version.

Funding

This work was supported by Shanxi Province Science and Technology Innovation Key Talent Team (202204051002034), Central guide local science and technology development funds (transfer of scientific and technological achievements) project (YDZJSX 2021C011), Shanxi Province Key R&D Program (202102130501002) and Key country-specific science and technology cooperation projects of Shanxi Provincial Science and Technology Department (202204041101004).

Conflict of interest

The authors declare that the research was conducted in the absence of any commercial or financial relationships that could be construed as a potential conflict of interest.

Publisher's note

References

Al-Moraissi, E. A., Farea, R., Qasem, K. A., Al-Wadeai, M. S., Al-Sabahi, M. E., and Al-Iryani, G. M. (2020). Effectiveness of occlusal splint therapy in the management of temporomandibular disorders: Network meta-analysis of randomized controlled trials. *Int. J. Oral Maxillofac. Surg.* 49 (8), 1042–1056. doi:10.1016/j.ijom.2020.01.004

Bai, Y., Guo, X., Tian, B., Liang, Y., Peng, D., and Wang, Z. (2022). Self-charging persistent mechanoluminescence with mechanics storage and visualization activities. *Adv. Sci. (Weinheim, Baden-Wurttemberg, Ger.* 9 (28), e2203249. doi:10.1002/advs.202203249

Bai, Y., Zheng, Z., Wu, L., Kong, Y., Zhang, Y., and Xu, J. (2021). Construction of a novel mechanoluminescent phosphor Li(2)MgGeO(4):xMn(2+) by defect control. *Dalton Trans.* 50 (25), 8803–8810. doi:10.1039/d1dt01125a

Cai, L., Qin, X., Xu, Z., Song, Y., Jiang, H., Wu, Y., et al. (2019). Comparison of cytotoxicity evaluation of anticancer drugs between real-time cell analysis and CCK-8 method. *ACS Omega* 4 (7), 12036–12042. doi:10.1021/acsomega.9b01142

Dzedulionyte, K., Fuxreiter, N., Schreiber-Brynzak, E., Zukauskaite, A., Sackus, A., Pichler, V., et al. (2023). Pyrazole-based lamellarin O analogues: Synthesis, biological evaluation and structure-activity relationships. *RSC Adv.* 13 (12), 7897–7912. doi:10.1039/d3ra00972f

Fujio, Y., Xu, C. N., and Terasaki, N. (2022). Flexible mechanoluminescent SrAl(2)O(4):Eu film with tracking performance of CFRP fracture phenomena. *Sensors (Basel)* 22 (15), 5476. doi:10.3390/s22155476

Grymak, A., Waddell, J. N., Aarts, J. M., Ma, S., and Choi, J. J. E. (2022). Evaluation of wear behaviour of various occlusal splint materials and manufacturing processes. *J. Mech. Behav. Biomed. Mater.* 126, 105053. doi:10.1016/j.jmbbm.2021.105053

Jha, P., and Chandra, B. P. (2014). Survey of the literature on mechanoluminescence from 1605 to 2013. *Luminescence* 29 (8), 977–993. doi:10.1002/bio.2647

Kawano, M., Hokazono, E., Osawa, S., Sato, S., Tateishi, T., Manabe, M., et al. (2019). A novel assay for triglycerides using glycerol dehydrogenase and a water-soluble formazan dye, WST-8. *Ann. Clin. Biochem.* 56 (4), 442–449. doi:10.1177/0004563219830715

Ke, X., Li, M., Wang, X., Liang, J., Wang, X., Wu, S., et al. (2020). An injectable chitosan/dextran/β -glycerophosphate hydrogel as cell delivery carrier for therapy of myocardial infarction. *Carbohydr. Polym.* 229, 115516. doi:10.1016/j.carbpol.2019.115516

Lendahl, U., Muhl, L., and Betsholtz, C. (2022). Identification, discrimination and heterogeneity of fibroblasts. *Nat. Commun.* 13 (1), 3409. doi:10.1038/s41467-022-30633-9

Li, D. T. S., and Leung, Y. Y. (2021). Temporomandibular disorders: Current concepts and controversies in diagnosis and management. *Diagn. (Basel)* 11 (3), 459. doi:10.3390/diagnostics11030459

Liu, X., Yan, J., Wu, X., Wu, X., Zhang, Y., and Li, B. (2022). Biosafety evaluation of Li2Si2O5whisker-reinforced glass-ceramics. *Biomed. Mater. (Bristol, Engl.* 17 (2), 025011. doi:10.1088/1748-605x/ac4e65

Manfredini, D., Lombardo, L., and Siciliani, G. (2017). Temporomandibular disorders and dental occlusion. A systematic review of association studies: End of an era? *J. oral rehabilitation* 44 (11), 908–923. doi:10.1111/joor.12531

Ohrbach, R., Slade, G. D., Bair, E., Rathnayaka, N., Diatchenko, L., Greenspan, J. D., et al. (2020). Premorbid and concurrent predictors of TMD onset and persistence. *Eur. J. Pain* 24 (1), 145–158. doi:10.1002/ejp.1472

Okado, N., Sugi, M., Ueda, M., Mizuhashi, F., Lynch, B. S., Vo, T. D., et al. (2015). Safety evaluation of AMP deaminase from Aspergillus oryzae. *Food Chem. Toxicol.* 86, 342–350. doi:10.1016/j.fct.2015.11.001

Pillai, G. K. G., Bharate, S. S., Awasthi, A., Verma, R., Mishra, G., Singh, A. T., et al. (2017). Antidiabetic potential of polyherbal formulation DB14201: Preclinical development, safety and efficacy studies. *J. Ethnopharmacol.* 197, 218–230. doi:10.1016/j.jep.2016.07.062

Reyes-Sevilla, M., Kuijs, R. H., Werner, A., Kleverlaan, C. J., and Lobbezoo, F. (2018). Comparison of wear between occlusal splint materials and resin composite materials. *J. Oral Rehabil.* 45 (7), 539–544. doi:10.1111/joor.12636

Seibald, M., Rosenthal, T., Oeckler, O., Fahrnbauer, F., Tucks, A., Schmidt, P. J., et al. (2012). Unexpected luminescence properties of Sr(0.25)Ba(0.75)Si2O2N2:Eu(2+)-a narrow blue emitting oxonitridosilicate with cation ordering. *Chemistry* 18 (42), 13446–13452. doi:10.1002/chem.201201953

Shin, H. G., Timilsina, S., Sohn, K. S., and Kim, J. S. (2022). Digital image correlation compatible mechanoluminescent skin for structural health monitoring. *Adv. Sci. (Weinh).* 9 (11), e2105889. doi:10.1002/advs.202105889

Sun, H., Gao, K., Yi, Z., Han, C., Liu, Z., Wang, Q., et al. (2022). Cytotoxicity and bonding property of bioinspired nacre-like ceramic-polymer composites. *Front. Bioeng. Biotechnol.* 10, 913899. doi:10.3389/fbioe.2022.913899

Wang, W., Tasset, A., Pyatnitskiy, I., Mohamed, H. G., Taniguchi, R., Zhou, R., et al. (2022). Ultrasound triggered organic mechanoluminescence materials. *Adv. Drug Deliv. Rev.* 186, 114343. doi:10.1016/j.addr.2022.114343

Wieckiewicz, M., Boening, K., Wiland, P., Shiau, Y. Y., and Paradowska-Stolarz, A. (2015). Reported concepts for the treatment modalities and pain management of temporomandibular disorders. *J. Headache Pain* 16, 106. doi:10.1186/s10194-015-0586-5

Xie, H., Cao, T., Rodriguez-Lozano, F. J., Luong-Van, E. K., and Rosa, V. (2017). Graphene for the development of the next-generation of biocomposites for dental and medical applications. *Dent. Mater* 33 (7), 765–774. doi:10.1016/j.dental.2017.04.008

Xiong, P., Peng, M., and Yang, Z. (2021). Near-infrared mechanoluminescence crystals: A review. *iScience* 24 (1), 101944. doi:10.1016/j.isci.2020.101944

Xue, H., Hu, L., Xiong, Y., Zhu, X., Wei, C., Cao, F., et al. (2019). Quaternized chitosan-Matrigel-polyacrylamide hydrogels as wound dressing for wound repair and regeneration. *Carbohydr. Polym.* 226, 115302. doi:10.1016/j.carbpol.2019.115302

Yun, Y. J., Kim, J. K., Ju, J. Y., Choi, S. K., Park, W. I., Jung, H. K., et al. (2016). Eu(2+)-Activated phase-pure oxonitridosilicate phosphor in a Ba-Si-O-N system via facile silicate-assisted routes designed by first-principles thermodynamic simulation. *Inorg. Chem.* 55 (17), 8750–8757. doi:10.1021/acs.inorgchem.6b01278

Zhuang, Y., and Xie, R. J. (2021). Mechanoluminescence rebrightening the prospects of stress sensing: A review. *Adv. Mater* 33 (50), e2005925. doi:10.1002/adma.202005925

frontiers | Frontiers in Bioengineering and Biotechnology

TYPE Original Research
PUBLISHED 10 July 2023
DOI 10.3389/fbioe.2023.1223339

OPEN ACCESS

EDITED BY
Xing Wang,
Shanxi Medical University, China

REVIEWED BY
Yonghui Ding,
Northwestern University, United States
Xiangxiang Hu,
The Ohio State University, United States

*CORRESPONDENCE
Zhisheng Zhang,
zzshospital@163.com
Qianju Wu,
qianjuwu@163.com

†These authors have contributed equally to this work

RECEIVED 16 May 2023
ACCEPTED 30 June 2023
PUBLISHED 10 July 2023

CITATION
Li R, Li S, Zhang Y, Jin D, Lin Z, Tao X, Chen T, Zheng L, Zhang Z and Wu Q (2023), Titanium surfaces with biomimetic topography and copper incorporation to modulate behaviors of stem cells and oral bacteria.
Front. Bioeng. Biotechnol. 11:1223339.
doi: 10.3389/fbioe.2023.1223339

Titanium surfaces with biomimetic topography and copper incorporation to modulate behaviors of stem cells and oral bacteria

Ruiying Li[1†], Shuigen Li[1†], Yi Zhang[1], Di Jin[1], Zhiming Lin[1], Xian Tao[1], Tianlai Chen[1], Liyuan Zheng[1], Zhisheng Zhang[1*] and Qianju Wu[1,2*]

[1]Stomatological Hospital of Xiamen Medical College, Xiamen Key Laboratory of Stomatological Disease Diagnosis and Treatment, Xiamen, Fujian, China, [2]Shanghai Ninth People's Hospital, School of Medicine, Shanghai Jiao Tong University, Xiamen, China

Purpose: Insufficient osseointegration and implant-associated infection are major factors in the failure of Ti-based implants, thus spurring scientists to develop multifunctional coatings that are better suited for clinical requirements. Here, a new biomimetic micro/nanoscale topography coating combined with antibacterial copper was simultaneously designed for Ti-based implant surfaces by adopting a hybrid approach combining plasma electrolytic oxidation and hydrothermal treatment.

Results: The biological interactions between this biofunctionalized material interface and stem cells promoted cellular adhesion and spreading during initial attachment and supported cellular proliferation for favorable biocompatibility. Bone marrow mesenchymal stem cells (BMMSCs) on the coating displayed enhanced cellular mineral deposition ability, higher alkaline phosphatase activity, and upregulated expression of osteogenic-related markers without the addition of osteoinductive chemical factors, which improved osseointegration. More interestingly, this new coating reduced the viability of oral pathogens (*Fusobacterium nucleatum* and *Porphyromonas gingivalis*)—the primary causes of implant-associated infections as indicated by damage of cellular structures and decreased population. This is the first study investigating the antibacterial property of dental implants modified by a hybrid approach against oral pathogens to better mimic the oral environment.

Conclusion: These findings suggest that biofunctionalization of the implant coating by surface modification methods and the incorporation of antibacterial copper (Cu) offer superior osteogenesis capability and effective antibacterial activity, respectively. These strategies have great value in orthopedic and dental implant applications.

KEYWORDS

dental implants, copper, biocompatibility, antibacterial performance, osteogenesis

Introduction

Titanium (Ti) and its alloys have superior biocompatibility and desired mechanical properties in the field of clinical dental implantation (Haugen and Chen, 2022). Although Ti-based products occupy a large percentage of the dental market, limited osseointegration is a continuous challenge that restricts application of Ti-based dental implants. Peri-implantitis is an inflammatory reaction that is one issue in the inherent non-antibacterial characteristics of Ti-based dental implants. Another issue is the different degrees of loss in supporting bone surrounding the dental implant (Kloss et al, 2022). Hence, a new generation of orthopedic and dental implants with both antibacterial ability and osteoinductivity are desirable for better clinical outcomes. Thus, various modification approaches have been investigated (Mei et al, 2014; Bessa et al, 2022). Of these, plasma electrolytic oxidation (PEO) technology has attracted considerable attention recently due to its convenience and effectiveness. It is a relatively new technology in the field of Ti-based materials and can achieve favorable biological effects (Zhao et al, 2009; Al-Dulaijan and Balhaddad, 2022). Through PEO, a relatively rough and firmly adherent porous titania coating can be prepared on Ti-based implants. This coating contains anatase and rutile together with bioactive elements such as calcium (Ca) and phosphorus (P) originating from selective electrolytes. Numerous studies have demonstrated that a calcium/phosphate-rich titania coating fabricated by PEO could improve the biological performance of implants, thus making them potential candidates in dental applications (Krzakala et al, 2013; Zhou et al, 2013; Huang et al, 2022).

The oral environment is abundant with microorganisms and surgery can compromise host defenses and consequently facilitate bacterial attack (Zhang et al, 2013). PEO-modified dental implants offer inadequate antibacterial properties that restrict its application on a larger scale (Dias Corpa Tardelli et al, 2021). Hence, it is critical to equip dental implants with antibacterial properties to restrain initial bacterial adhesion and biofilm formation. Thus, strategies including the delivery or incorporation of antibacterial inorganic elements such as copper (Cu) or silver (Ag) into the surface of biomedical implants could be a simple and effective way to achieve this goal. In contrast to antibiotics, copper ions are non-specific bactericides that can act against a broad spectrum of bacterial species (Goudouri et al, 2014). They are essential trace elements in the human body, and studies have demonstrated that they play significant biological roles including the ability to enhance cell activity and proliferation of osteoblastic lineages and promote angiogenesis. These features make copper ions more biologically functional than silver ions (Ag^+).

Hydrothermal treatment is an effective approach to loading inorganic ions and regulate surface chemical elements (Li et al, 2014). A hybrid approach that combines PEO and hydrothermal treatment to generate bioactive coatings on Ti-based implant surfaces is still in the early stages of development. Therefore, in the present work, we prepared a novel coating on Ti-based implant surfaces while simultaneously introducing the antibacterial copper by combining plasma electrolytic oxidation and hydrothermal treatment. Moreover, the interactions of this coating with oral microorganisms were assessed to address the design of Ti-based dental and orthopedic implants to better meet clinical requirements.

Material and methods

Abbreviation; day (d), hour (h), minute (min)

Fabrication of materials

Grade 1 pure Ti plates with purity of >99.85 wt% were cut into foils with dimensions of $1 \times 1 \times 0.1$ cm^3 or $2 \times 2 \times 0.1$ cm^3 for further use followed by acid cleaning in 5 wt% oxalic acid solution (100°C, 2 h) to obtain a homogeneous clean surface. A titania coating was then fabricated on a Ti surface via PEO in calcium/phosphate containing electrolyte, and the prepared samples were used as the control TiO_2 group. In the experimental group, the hydrothermal method was employed to incorporate copper ions into the prepared TiO_2 coating. It is indeed that the potential cytotoxicity of copper ions should be taken into consideration. As a consequence, a primary research on the role of copper ions with different concentrations for the biological activities of BMMSCs was performed in our previous work in order to optimize the experimental design (Wu et al, 2014). We found the concentrations of copper ranging from 1 nM to 1 μM turned out to show no significant cytotoxic effect for BMMSCs. Moreover, the concentration of 1 μM significantly upregulated the expressions of osteogenic genes of BMMSCs. On the basis of our foundation, 1 μM was chosen to modify the implant surface. Each PEO-pretreated Ti plate was placed in the Teflon-lined reaction vessel containing 1 μM $CuCl_2$ aqueous solution for 1 h at 200°C. Afterward, the Ti plate was gently rinsed with ultrapure water and dried naturally. The final prepared specimen was named Cu-TiO_2 (Scheme 1).

Surface characterization analysis

Field-emission scanning electron microscopy (FE-SEM; S-4800, HITACHI, Japan) was used to determine the surface topographies of samples, and the phase components were studied by an X-ray diffractometer (XRD; D/Max, Rigaku, Tokyo, Japan) fitted with a Cu Kα (λ = 1.541 Å) source ranging from 15° to 80° with a glancing angle of 1°. X-ray photoelectron spectroscopy (XPS; PHI 5802, Physical Electronics Inc., Eden Prairie, MN) with an Mg Kα (1,253.6 eV) source was used for the analysis of surface chemical compositions and states of different coatings.

Ion release detection

The samples of TiO_2 and Cu-TiO_2 were soaked in 10 mL Dulbecco's Modified Eagle's Medium (DMEM, Gibco, United States) and incubated at 37°C for 1, 4, 7, and 14 d. At each time point, the liquid extract was collected, and the concentrations of Ca/P/Cu ions released were tested by inductively coupled plasma mass spectrometry (ICP-MS; Nu Instruments, Wrexham, UK).(Yan et al, 2022).

Contact angle measurement

Contact angle measurements were performed to detect the surface wettability of samples under room temperature with atmospheric relative humidity of 30% by a contact angle instrument (Automatic Contact Angle Meter Model SL200B, Solon Information Technology Co., Ltd., China). The contact angles of five ultrapure water droplets were analyzed on each group repeatedly, and the results were expressed as mean ± SD.

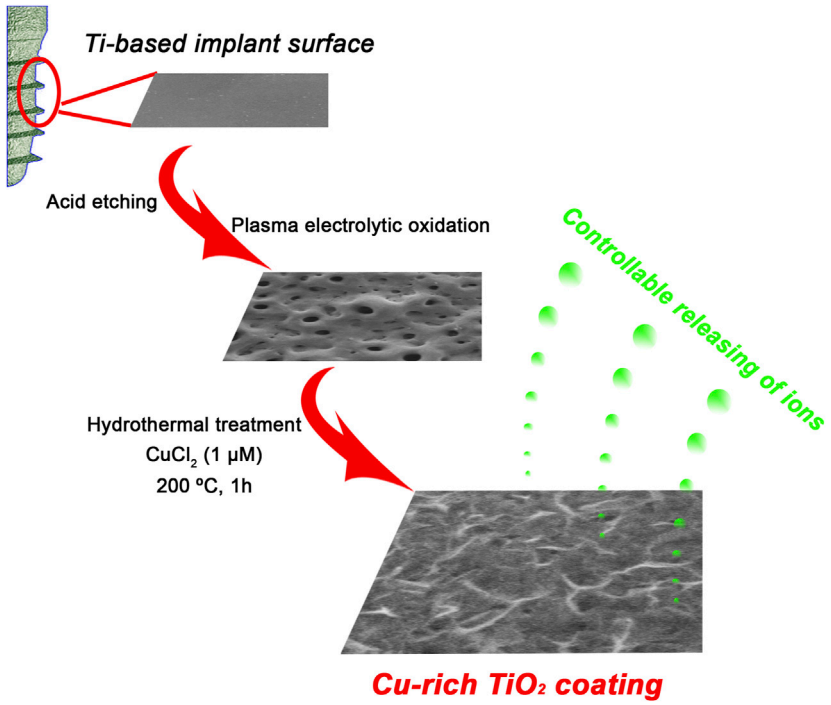

SCHEME 1
Schematic illustration for fabrication procedures of a bioactive Cu-TiO_2 coating on Ti surface using plasma electrolytic oxidation (PEO) and hydrothermal treatment together.

Isolation and culture of bone marrow mesenchymal stem cells (BMMSCs)

BMMSCs derived from Wistar rats were isolated and cultured according to previously published procedures.(Wu et al, 2022). Briefly, both ends of the rat femurs were removed and the bone was then quickly rinsed out by Dulbecco's Modified Eagle's Medium (DMEM, Gibco, United States) with 10% fetal bovine serum (FBS, Gibco, United States) and 200 U/mL heparin (Sigma, United States). The primary cells were cultured under 5% CO_2 and 37°C in DMEM supplemented with 10% FBS, 100 U/mL penicillin, and 100 U/mL streptomycin in an incubator. Non-adherent cells were removed, and the culture medium was renewed every 2-3 d. Cells were sub-cultured when they reached 80%–90% confluence, and passage 2–4 of BMMSCs were employed in the following *in vitro* experiments.

Cell adhesion and morphology observation

Cell counting was performed to detect the adhered cells on each sample at the initial seeding period of 4 h. Cells at the density of 4.0×10^4 cells/well were seeded onto samples and incubated at 37°C for 4 h. The non-adhered cells were removed by PBS, and remaining cells were fixed in 4% paraformaldehyde for 30 min at 4°C and subsequently stained with DAPI (Sigma, United States) for 5 min at room temperature. The cell number was determined in five random fields at ×200 magnification of each sample with immunofluorescence microscopy (Olympus, Japan).

To detect the morphology of stem cells, samples were fixed and treated with 0.1% Triton X-100 and then blocked with 1% BSA for 30 min. Finally, the cytoskeletons were stained by incubating with Phalloidin-TRITC (Sigma, United States), and the cell nuclei were contrast-labeled by DAPI (Sigma, United States) visualized using immunofluorescence microscopy (Olympus, Japan).

Cell proliferation

The cell proliferation activity of the BMMSCs seeded on each sample was tested by MTT metabolic assay as previously described.(Wu et al, 2014). Initially, 2.0×10^4 cells per mL were seeded onto each sample placed in 24-well plates for culture. At d 1, 4, and 8, the MTT solution (5 mg/mL) was added into the wells and incubated at 37°C for 4 h to form formazan, which was then dissolved in dimethyl sulfoxide (DMSO). Finally, the absorbance was measured at 490 nm with an ELX Ultra Microplate Reader (Bio-Tek, United States). The experiments were run in triplicate.

Osteogenic potential estimation

To investigate whether Cu-doped TiO_2 coating could enhance the potential activity of osteogenic differentiation of BMMSCs seeded on implant surface, mineral deposition assay, alkaline phosphate (ALP) activity, and real-time quantitative polymerase chain reaction (RT-qPCR) assays were performed.

Cell mineral deposition assays were performed at d 14 by alizarin red S (ARS) assay. BMMSCs cultured on each sample were fixed in 95% alcohol for 15 min, immersed in 0.1% ARS solution (Sigma) for 30 min, and then washed with PBS three times before observation, moreover, the quantitative analysis was also carried out. For the ALP activity assay, BMMSCs cultured on each sample for 14 d were fixed with 4% paraformaldehyde and stained with an ALP kit (Beyotime, China). Quantitative ALP

TABLE 1 The sequences of specific primers for real-time PCR operation.

Gene	Prime sequence (F, forward; R, reverse)	Product size (bp)	Accession number
OCN	F: TCAACAATGGACTTGGAGCCC	161	NM_013414.1
	R: GCAACACATGCCCTAAACGG		
OPN	F: CAAGCGTGGAAACACACAGCC	165	NM_012881.2
	R: GGCTTTGGAACTCGCCTGACTG		
BMP-2	F: ATGGGTTTGTGGTGGAAGTG	167	NM_017178.1
	R: TGTTTGTGGAGTGGATGTC		
β-Actin	F: AGGGAGTGATGGTTGGAATG	107	NM_031004.2
	R: GATGATGCCGTGTTCTATCG		

analysis was performed by measurement of optical density (OD) at 405 nm after incubation with p-nitrophenyl phosphate (pNPP) (Sigma, United States). The activity levels were normalized to total protein and presented as OD values at 405 nm per milligram of total protein.

For real-time quantitative polymerase chain reaction (RT-qPCR) assays, total RNA was extracted from BMMSCs seeded on each sample by using Trizol reagent (Invitrogen, United States). The real-time PCR operation was performed via a Bio-Rad real-time PCR system (Bio-Rad, United States), and the comparative ΔΔCt method was employed to calculate the relative expression of osteogenic genes such as osteocalcin (OCN), osteopontin (OPN), and bone morphogenetic protein-2 (BMP-2). The β-actin housekeeping gene was treated for normalization. The purified specific primers were synthesized commercially (Shengong, China) and the sequences are shown in Table 1. All experiments were run in triplicate.

Anti-oral pathogens assay

For the sake of better mimicking the oral environment, two selective bacteria, *Fusobacterium nucleatum* (Fn, ATCC25586, Gram-negative bacteria) and *Porphyromonas gingivalis* (Pg, ATCC33277, Gram-positive bacteria) were utilized to test the antimicrobial activity of each sample against oral pathogens. SEM were used to evaluate anti-oral pathogens ability of the prepared Cu-TiO_2 coating. First, each sample was sterilized by 75 v/v% ethanol solution, and then a bacterial solution with the concentration of 10^7 CFU/mL of Fn, was introduced onto the surface. After incubation under standard anaerobic conditions of 80% N_2, 10% H_2, and 10% CO_2 at 37°C for 1 d, the samples were rinsed with phosphate buffered saline (PBS) three times, fixed in 3% glutaraldehyde, and dehydrated in a series of ethanol solutions (from 30 to 100 v/v%) for 10 min, followed by drying in hexamethyldisilizane (HMDS). Finally, the morphology of Fn on each sample were observed by SEM (SEM, S-3400, HITACHI, Japan).

For fluorescence staining, the viability of bacteria (Fn and Pg) on samples was investigated using a LIVE/DEAD BaclightTM Bacterial Viability Kit (Life Technologies, United States). The samples were incubated with the bacteria-containing medium (10^7 CFU/mL) followed by rinsing with PBS. SYTO 9 and propidium iodide (PI) dyes were used to label the live and dead bacteria in green or red, respectively, for 15 min in darkness, and then the samples were examined with a confocal laser scanning microscope (CLSM, Leica, Germany).

Statistical analysis

All statistical comparisons were measured via *t*-tests and analyzed by the SAS 8.2 software package (Cary, United States). The data acquired were represented as mean ± standard deviation (SD), and $p < 0.01$ was considered statistically significant and defined compared to the control TiO_2 group.

Results

Materials characterization

The surface morphology of the PEO-treated and subsequent hydrothermally treated Ti plates was observed by FE-SEM. In Figure 1A, the surface of Ti after PEO treatment presented a rough and porous topography—there were numerous micron-sized holes distributed uniformly. The PEO-treated coating on Ti surface was mainly composed of anatase TiO_2 with typical diffraction peaks (2θ = 25.2°, 38.0°, 48.1°, 53.8°, 62.8°, etc.), A small peak at 2θ = 27.4° could also be observed as the indicator of rutile phase according to the XRD (Figure 2A). After the hydrothermal treatment in copper-containing aqueous solution, the low magnification topography of the coating surface was not transformed significantly (Figure 1C) nor was the phase component; a unique nanopetal-like topography emerged on the TiO_2 coating at high magnification (Figure 1D), whereas the PEO-treated Ti displayed a relatively smooth surface morphology (Figure 1B).

XPS analysis (Figures 2B, C) showed that oxygen (O), titanium (Ti), calcium (Ca) and phosphorus (P) could be detected from the PEO-treated Ti surface. Moreover, Cu with a content of 1.8 wt% was also detected from the sample treated with the hydrothermal treatment in $CuCl_2$ aqueous solution; there were some losses of Ca and P during the hydrothermal treatment. Further high

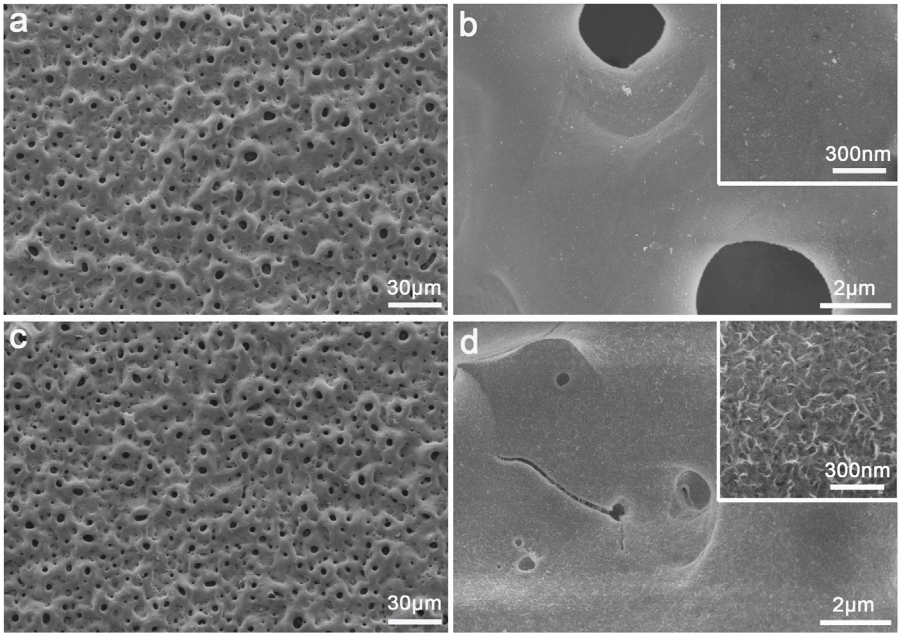

FIGURE 1
Surface morphology of the plasma electrolytic oxidized TiO_2 coating **(A–B)** and Cu-TiO_2 coating **(C–D)** observed by SEM at low and high magnifications together with the insets showing the corresponding higher-magnification pictures.

resolution XPS analysis was conducted for the Cu-TiO_2 sample. Figure 2D shows that three peaks were consistent with the predominant ones at 347.1 eV and 350.6 eV corresponding to Ca 2p in Ca_3 $(PO_4)_2$; another at 347.5 eV was assigned to Ca 2p in $CaHPO_4$. P 2p (Figure 2E) had two peaks at 133.5 eV and 132.4 eV consistent with the P–O bonds in PO_4^{3-} and HPO_4^{2-}. The double peaks of Cu 2p located at 952.6 eV and 932.7 eV were attributed to the Cu $2p_{1/2}$ and Cu $2p_{3/2}$ in $CuTiO_3$, respectively (Figure 2F). Figures 2G–I showed the release profiles of Ca, P, and Cu ions from each sample immersed in DMEM. Over 14 d, Ca and P ions were released from each sample in a sustained way. It existed statistic difference for the releasing amount of Ca ion between two groups, however, the amount of P ion for these two groups were similar without statistic difference. For Cu-TiO_2 groups, the copper ions could also be released in a slow and sustained way, and at each time point, the releasing amount of Cu-TiO_2 was remarkably higher than the TiO_2 group.

Surface wettability

The water contact angles of samples TiO_2 and Cu-TiO_2 are displayed in Figure 3. The surface of Cu-TiO_2 became more hydrophilic than that of TiO_2 after the hydrothermal treatment, thus leading to a diminishing contact angle likely due to the generation of micro/nanostructured surface with copper incorporation. These surface changes altered the surface topography and chemical composition serving as two factors for material wettability. Moreover, it is widely accepted that hydrophilic surfaces can improve bioactivity and promote cell attachment, spreading, and proliferation.

Cell adhesion, spreading and proliferation

The biological responses of BMMSCs on two different coatings at the initial adhesion period were detected by immunofluorescence microscopy (Figures 4A–C). To investigate adhesion, cells attached onto both samples were detected after rinsing with PBS to remove non-adhered cells after 4 h of culture. The results reveal that the number of adherent cells on the Cu-TiO_2 coating was significantly higher than the TiO_2 coating control group. The quantitative data acquired by counting stained cellular nuclei suggests more adhesive cells on the Cu-TiO_2 than TiO_2 group with a statistically significant difference ($p < 0.01$, Figure 4B). This is consistent with Figure 4A.

Cytoskeletons were visualized by labelling to observe the cellular morphology of seeded BMMSCs (Figure 4C). The BMMSCs on sample TiO_2 seemed to be round based on the lack of the noticeable filopodia extensions, while more pronounced filopodia extensions (indicated by red arrows) and extraordinary cellular elongation were apparent on the Cu-TiO_2 surface under the same culture conditions. Mitosis phase cells (indicated by blue arrows) could be observed on each sample, thus suggesting that both surfaces were favorable for the initial adhesion and spreading of BMMSCs with no cytotoxicity.

The MTT assay was performed to determine the proliferation and vitality of BMMSCs cultured on the coatings (Figure 4D). Cell proliferation increased with time, and there was no significant difference between the two groups, demonstrating that the approaches of surface modification seen here did not adversely affect the viability of stem cells. The fabricated Cu-TiO_2 implant coating possessed excellent biocompatibility.

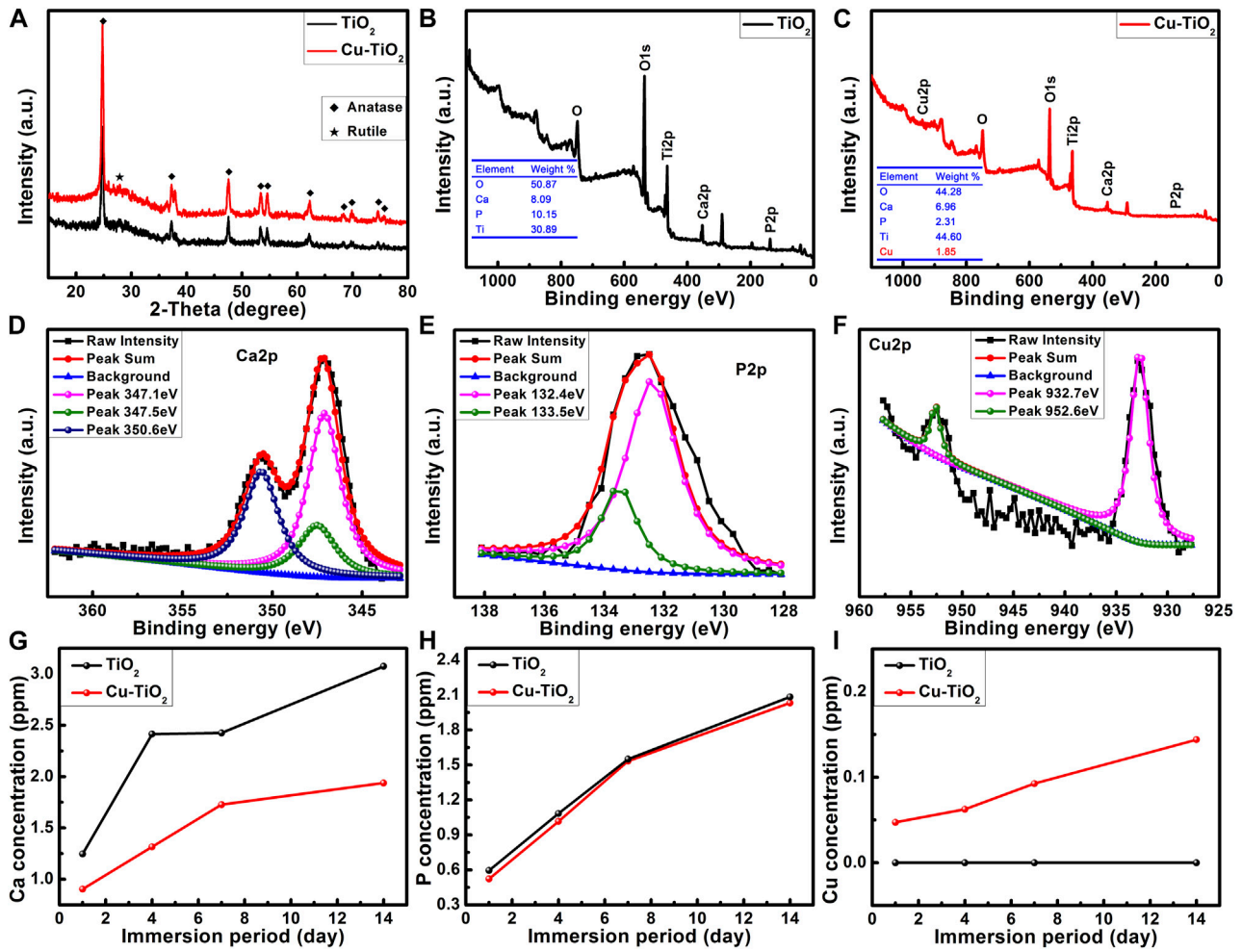

FIGURE 2
XRD patterns **(A)** and surface XPS full spectra **(B–C)** of samples TiO_2 and Cu-TiO_2 accompanied by the high-resolution XPS spectra of Ca 2p **(D)**, P 2p **(E)**, and Cu 2p **(F)** from sample Cu-TiO_2 surface as well as the release profiles of Ca, P, and Cu ions within 14 d **(G–I)**.

Osteogenic differentiation activity

Alizarin red S staining was conduct to determine the cell mineral deposition ability. As illustrated in pictures, Cu-TiO_2 was higher than the other group, together with a statistic difference (Figure 5A). Additionally, ALP staining showed more extensive positive areas on the Cu-TiO_2 sample, which was further verified by the quantitative analysis (Figure 5B). Furthermore, the RT-PCR analysis showed that the expression of selected osteogenic differentiation markers, including OCN, OPN, and BMP-2, were upregulated after 14 d of culture on the Cu-TiO_2 coating (Figure 5C), thus indicating the promotion of osteogenetic differentiation potential of BMMSCs.

Anti-oral pathogens assay

Fn and Pg were used to test the antimicrobial activity of each sample against oral pathogens. Figure 6 shows the typical morphology of Fn introduced on the two groups. Numerous bacteria were present on the surface of the TiO_2 group (blue arrow in Figure 6A), and most of them displayed an intact cellular structure (red arrow in Figure 6A), thus suggesting strong biological activity. The amount of Fn on the Cu-TiO_2 coating was reduced *versus* the former group. Damage to cellular structures was observed, which indicated that Fn was reduced in terms of survival on the Cu-TiO_2 coating (as shown in Figure 6B).

Figure 7 shows representative results of the live and dead assay for Fn and Pg after cultivation on the samples, respectively. The live bacteria with intact membranes were visualized in green fluorescence, and the dead ones with damaged membranes fluoresced in red due to the differences in spectral characteristics and the ability to penetrate healthy bacterial cells of SYTO 9 and PI. The amounts of dead bacteria of Fn and Pg were obviously pronounced while less vital ones were detected from the Cu-TiO_2 coating than that on control group, especially for the population of Fn, showing its effective performance in killing the adhered oral bacteria.

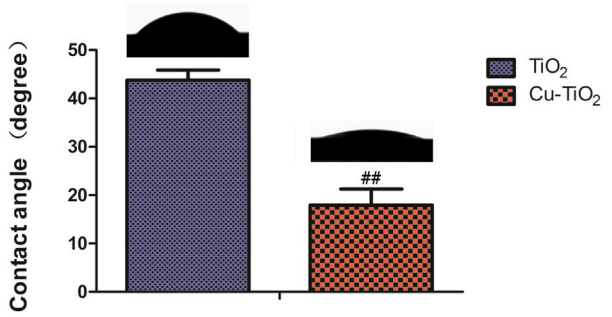

FIGURE 3
Contact angle measurement on different samples accompanied by corresponding typical ultrapure water droplet images. Notes: ##$p < 0.01$ vs. TiO_2 group.

Discussion

A micron-sized structure was obtained on the Ti surface via the PEO process. This nanopetal-like topography was seen after the incorporation of copper ions by a hydrothermal method. More interestingly, the appearance of petal-like nanostructures is similar to the cross-section of tooth enamel after acid etching, i.e., the most highly mineralized tissue in the human body (Cassari et al, 2023; Wu et al, 2023). This result suggests that this nanometer topography plays a significant role in regulating the cells' fate and micro/nanostructure from the biomimetic aspect and could possess excellent biological properties and enhanced stem cell functions (Wang et al, 2018; Bunz et al, 2022; Celesti et al, 2022). Our results showed that the Cu-TiO_2 group with biomimetic micro/nanostructure was more hydrophilic. BMMSCs exhibit higher adhesion activity and more extensive cell spreading during the initial attachment period, and the trend of cell proliferation on two groups increased regardless of whether copper was incorporated or not during the culture period of 8 d, thus confirming excellent cytocompatibility of Cu-TiO_2 coating. We further evaluated the osteogenic activity of stem cells on different samples and discovered that the mineral deposition ability and ALP activity of BMMSCs on Cu-TiO_2 was improved. Moreover, the level of gene expression for selective osteogenic markers were all upregulated (OCN, OPN, and BMP-2), which were consistent with the results of ARS and ALP activity. Hence, this biofunctionalized surface is likely beneficial for guiding osteogenic differentiation of stem cells, which is critical for osseointegration (Li et al, 2023).

In the oral environment, more than 500 microbial strains play different roles in the oral biofilm formation and peri-implantitis (Brunetti et al, 2023; Ye et al, 2023). Many studies have demonstrated that there is a higher risk of pathogens colonization on the susceptible implant surface during the initial 6 h after surgery (Jin et al, 2019; Agarwalla et al, 2022), thus making the antimicrobial effects on the first day vital to clinical success. Hence, two representatives of oral pathogens (Gram-negative Fn and Gram-positive Pg), which are actively implicated in implant-associated infection, were immobilized onto the coatings for 1 d for antibacterial analysis. The Cu-TiO_2 implant coating reduced the viability of bacterial species *versus* the control group, thus demonstrating its antibacterial properties. As a non-specific biocidal agent, copper can strongly destroy a broad spectrum of bacterial and

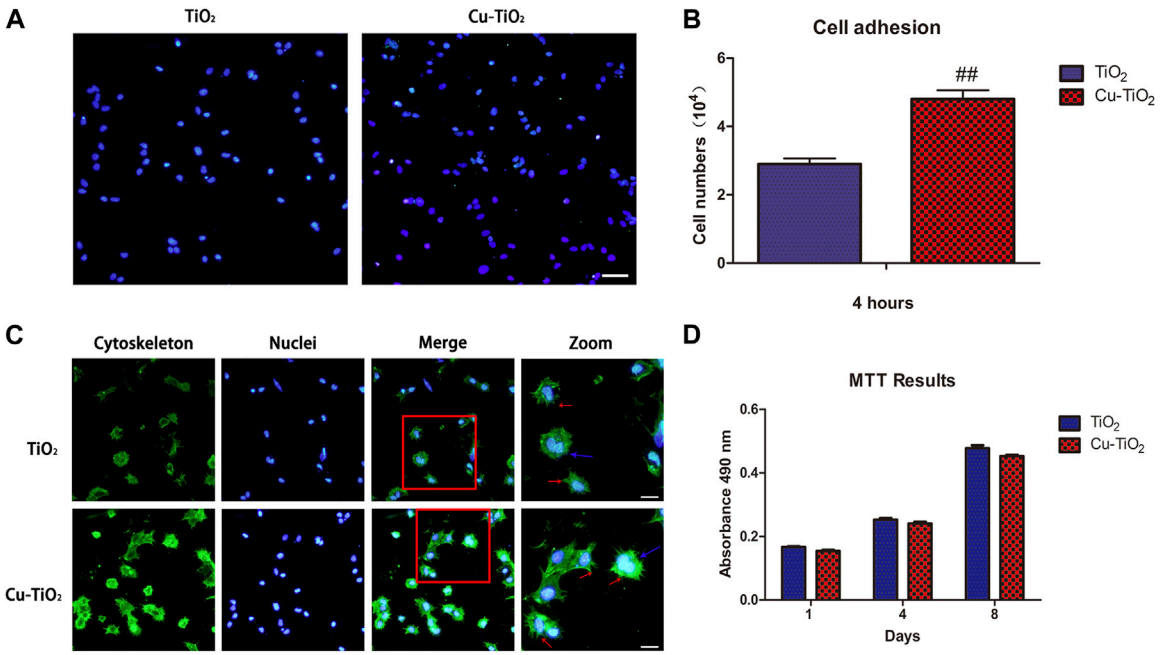

FIGURE 4
Cell initial adhesion, spreading, and proliferation ability evaluation. **(A)** Image of adherent cells with immunofluorescence microscopy (scale bar = 100 μm) together with the adhesion data **(B)**; **(C)** Immunofluorescence of cell spreading: The actin filaments (cytoskeleton) were labelled in green, and blue represented cell nuclei (scale bar = 100 μm); **(D)** MTT assay showed the proliferation ability of BMMSCs. All experiments were performed in triplicate. Notes: ## indicates $p < 0.01$ *versus* TiO_2 group.

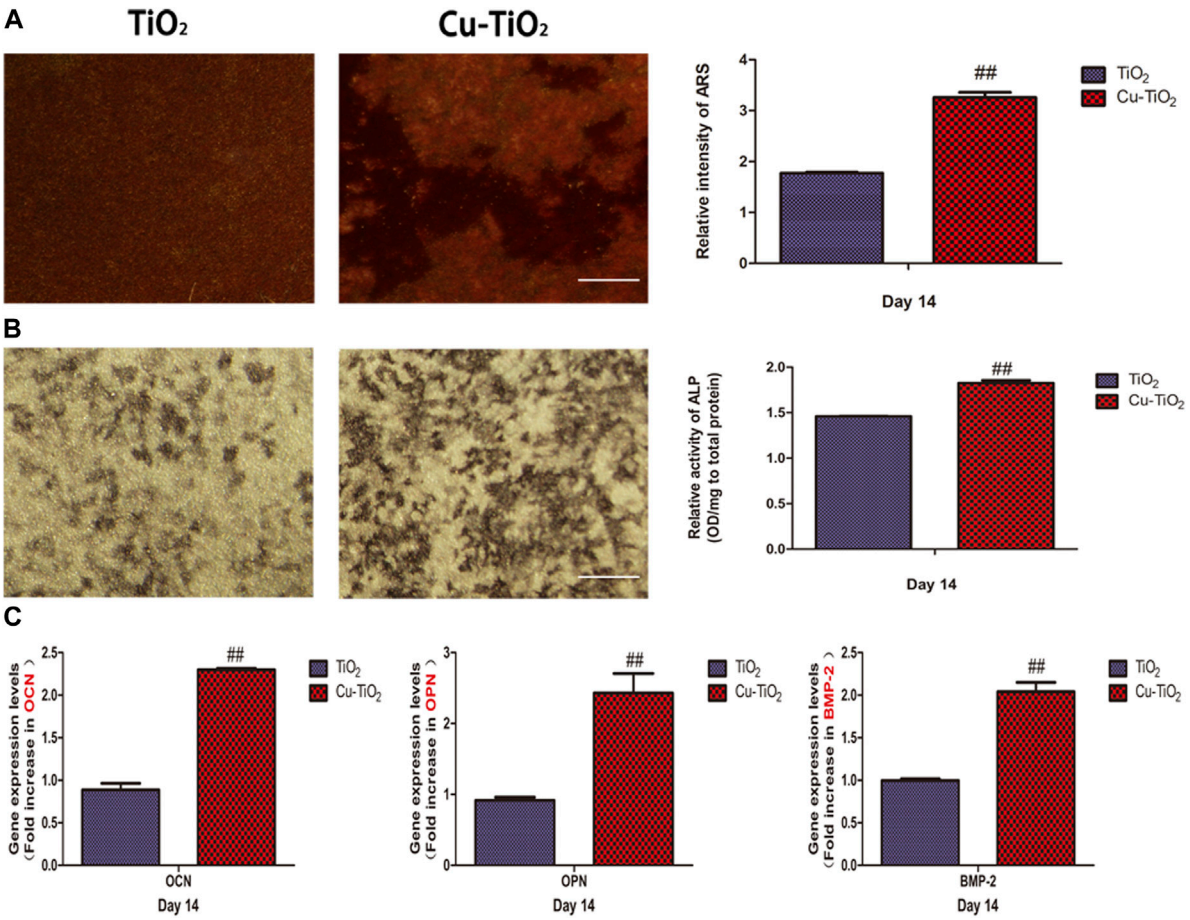

FIGURE 5
Mineral deposition assay **(A)** and alkaline phosphatase (ALP) activity **(B)** together with the expression levels of osteogenesis-related genes [**(C)**, OCN; OPN; BMP-2] for BMMSCs seeded on the TiO_2 and Cu-TiO_2 coating. All experiments were performed in triplicate. Notes: ## indicates $p < 0.01$ vs. TiO_2 group. Scale bar = 75 μm.

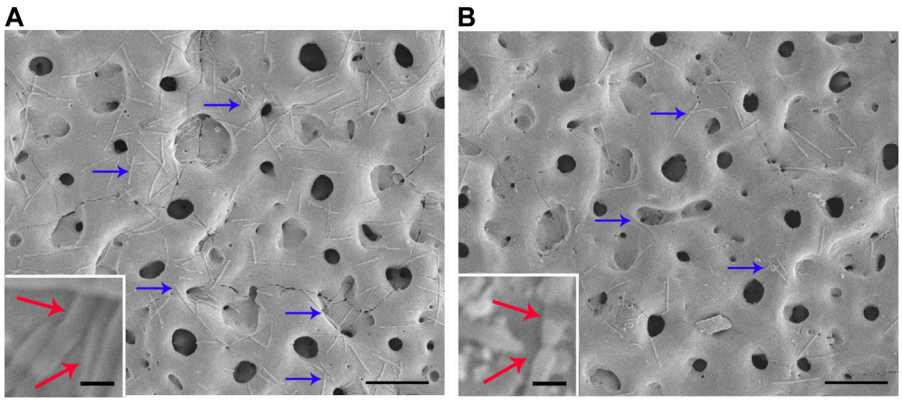

FIGURE 6
Typical photographs of Fn cultured on TiO_2 coating **(A)** and Cu-TiO_2 coating **(B)** by SEM. All experiments were performed in triplicate. Scale bar = 10 μm for the original pictures (right), and scale bar = 1 μm for the inset (left).

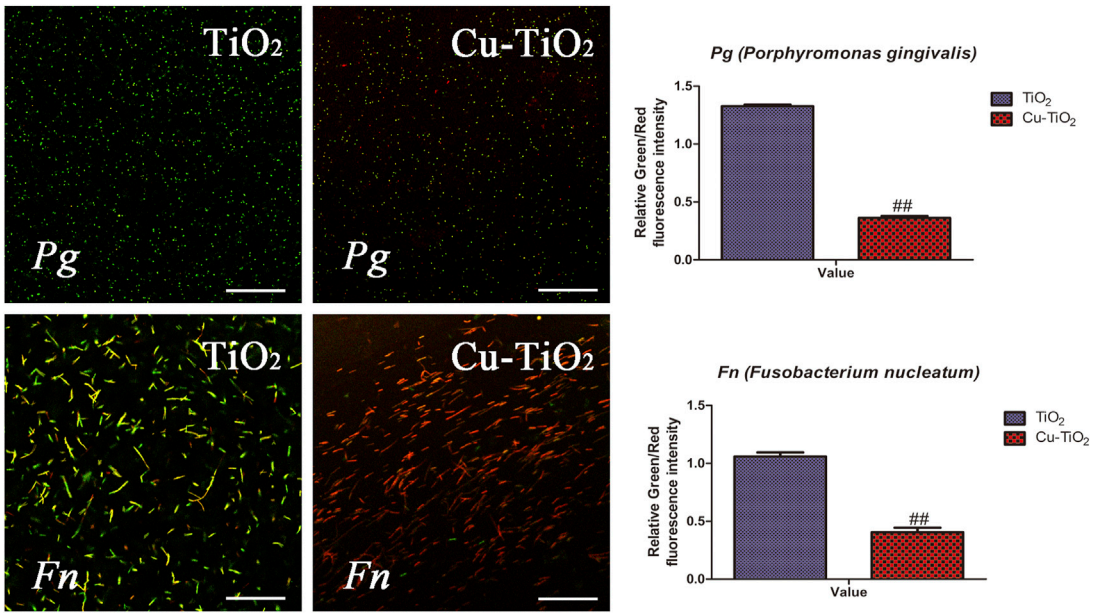

FIGURE 7
Typical confocal images of Fn (*F. nucleatum*, the upper row) and Pg (*P. gingivalis*, the bottom row) cultured on each sample for 1 d. The green fluorescence indicated live bacteria, and the dead ones are in red, together with the results of quantification. All experiments were performed in triplicate. Scale bar = 75 μm.

fungal species (Hameed et al, 2022). The most accepted mechanism behind the antibacterial property is that copper could damage the activity of respiratory enzymes and destroy the integrity of bacterial membranes, thus disordering the biochemical processes leading to cell lysis or even cell death. However, the biological responses of cells to copper ions tend to show a concentration dependence on account of the potential cytotoxicity. The burst release and excessive doses of copper ions from implant's surface are detrimental to cell function, which makes it critical to study this issue. Our time-releasing data indicate that the concentration of copper released accumulates to ~0.15 ppm at 14 d, which is much less than the reported threshold of toxic concentration for human cells, thus making it possible to reduce the toxicity of copper and balance bacteria killing while supporting cell functions (Wu et al, 2023). Sufficient stem cell attachment and pronounced cell spreading could occupy more exposed space on the biomaterial surface against pathogens, thus helping to reduce the possibility of infection. To the best of our knowledge, there are no reports investigating the performance of implants incorporating antibacterial copper by this hybrid approach against oral pathogens. The approach described here is practical and valid, and can prevent implant-associated infections.

Biomaterials with hierarchical micro/nanotopographies can enhance the osteogenic activity of stem cells by imitating the natural hybrid structure of bone extracellular matrix (Santos-Coquillat et al, 2019; Sobolev et al, 2019; Vu et al, 2019). The proper amount of copper ions delivered in a controllable way of sustained release from the surface could induce some positive changes in the adjacent microenvironment and further regulate the biological responses of stem cells. Thus, the enhancement of cellular activities could be ascribed to the synergistic effect of the hierarchical surface topography and the bioactive copper element.

Conclusion

A novel biomimetic micro/nanoscale topography coating incorporating antibacterial copper on a Ti-based implant surface was prepared via the hybrid approach combining PEO and hydrothermal treatment. The biological performance of this biofunctionalized implant surface could promote initial adhesion, proliferation, and further enhance osteogenic differentiation of stem cells. Its effectiveness in reducing the viability of oral pathogens such as Fn and Pg was demonstrated. Thus, the coating provides cytocompatibility, osteoinduction, and antibacterial properties. This study suggests that the biofunctionalization of implant coating and the incorporation of antibacterial copper could be achieved simultaneously to better meet clinical requirements with value in orthopedic and dental implant applications.

Data availability statement

The raw data supporting the conclusion of this article will be made available by the authors, without undue reservation.

Ethics statement

The animal study was reviewed and approved by the Institutional Animal Care and Use Committee of Ninth People's Hospital, Shanghai Jiao Tong University (SH9H-2020-A116-1).

Author contributions

Conceptualization, RL and SL; methodology, YZ and ZL; validation, DJ; investigation, XT; resources, TC; data analysis, LZ; writing editing, ZZ; funding acquisition and supervision, QW. All authors contributed to the article and approved the submitted version.

Funding

The present work is supported by Xiamen medical and health guiding project of Xiamen Science and Technology Bureau (3502Z20224ZD1332 and 3502Z20184063) of China.

Conflict of interest

The authors declare that the research was conducted in the absence of any commercial or financial relationships that could be construed as a potential conflict of interest.

Publisher's note

References

Agarwalla, S. V., Ellepola, K., Sorokin, V., Ihsan, M., Silikas, N., Neto, A. C., et al. (2022). Antimicrobial-free graphene nanocoating decreases fungal yeast-to-hyphal switching and maturation of cross-kingdom biofilms containing clinical and antibiotic-resistant bacteria. *Biomater. Biosyst.* 8, 100069. doi:10.1016/j.bbiosy.2022.100069

Al-Dulaijan, Y. A., and Balhaddad, A. A. (2022). Prospects on tuning bioactive and antimicrobial denture base resin materials: A narrative review. *Polym. (Basel)* 15 (1), 54. doi:10.3390/polym15010054

Bessa, L. J., Botelho, J., Machado, V., Alves, R., and Mendes, J. J. (2022). Managing oral health in the context of antimicrobial resistance. *Int. J. Environ. Res. Public Health* 19 (24), 16448. doi:10.3390/ijerph192416448

Brunetti, G., Valentini, E., Berlutti, F., Calvani, P., Raponi, F., Antonelli, G., et al. (2023). The effect of the electromagnetic field on metabolic-active bacterial biofilm experimentallyinduced on titanium dental implants. *New Microbiol.* 46 (2), 202–206.

Bunz, O., Steegmann, M. C., Benz, K., Testrich, H., Quade, A., Naumova, E. A., et al. (2022). Human gingival fibroblast adhesion and proliferation on hydroxyapatite-coated zirconia abutment surfaces. *Mater. (Basel)* 15 (10), 3625. doi:10.3390/ma15103625

Cassari, L., Zamuner, A., Messina, G. M. L., Marsotto, M., Chang, H. C., Coward, T., et al. (2023). Strategies for the covalent anchoring of a BMP-2-mimetic peptide to PEEK surface for bone tissue engineering. *Mater. (Basel)* 16 (10), 3869. doi:10.3390/ma16103869

Celesti, C., Gervasi, T., Cicero, N., Giofre, S. V., Espro, C., Piperopoulos, E., et al. (2022). Titanium surface modification for implantable medical devices with anti-bacterial adhesion properties. *Mater. (Basel)* 15 (9), 3283. doi:10.3390/ma15093283

Dias Corpa Tardelli, J., Lima da Costa Valente, M., Theodoro de Oliveira, T., and Candido Dos Reis, A. (2021). Influence of chemical composition on cell viability on titanium surfaces: A systematic review. *J. Prosthet. Dent.* 125 (3), 421–425. doi:10.1016/j.prosdent.2020.02.001

Goudouri, O. M., Kontonasaki, E., Lohbauer, U., and Boccaccini, A. R. (2014). Antibacterial properties of metal and metalloid ions in chronic periodontitis and peri-implantitis therapy. *Acta Biomater.* 10 (8), 3795–3810. doi:10.1016/j.actbio.2014.03.028

Hameed, H. A., Hasan, H. A., Luddin, N., Husein, A., Ariffin, A., and Alam, M. K. (2022). Osteoblastic cell responses of copper nanoparticle coatings on Ti-6Al-7Nb alloy using electrophoretic deposition method. *Biomed. Res. Int.* 2022, 1–11. doi:10.1155/2022/3675703

Haugen, H. J., and Chen, H. (2022). Is there a better biomaterial for dental implants than titanium?-A review and meta-study analysis. *J. Funct. Biomater.* 13 (2), 46. doi:10.3390/jfb13020046

Huang, T., Wang, H., Zhang, Z., Feng, K., and Xiang, L. (2022). Incorporation of inorganic elements onto titanium-based implant surfaces by one-step plasma electrolytic oxidation: An efficient method to enhance osteogenesis. *Biomater. Sci.* 10 (23), 6656–6674. doi:10.1039/d2bm00818a

Jin, J., Fei, D., Zhang, Y., and Wang, Q. (2019). Functionalized titanium implant in regulating bacteria and cell response. *Int. J. Nanomedicine* 14, 1433–1450. doi:10.2147/IJN.S193176

Kloss, F. R., Kammerer, P. W., and Kloss-Brandstatter, A. (2022). Risk factors for complications following staged alveolar ridge augmentation and dental implantation: A retrospective evaluation of 151 cases with allogeneic and 70 cases with autogenous bone blocks. *J. Clin. Med.* 12 (1), 6. doi:10.3390/jcm12010006

Krzakala, A., Kazek-Kesik, A., and Simka, W. (2013). Application of plasma electrolytic oxidation to bioactive surface formation on titanium and its alloys. *RSC Adv.* 3 (43), 19725–19743. doi:10.1039/C3RA43465F

Li, J., Zhang, W., Qiao, Y., Zhu, H., Jiang, X., Liu, X., et al. (2014). Chemically regulated bioactive ion delivery platform on a titanium surface for sustained controlled release. *J. Mater. Chem. B* 2 (3), 283–294. doi:10.1039/c3tb21102a

Li, J., Zhao, J., Xu, Y., Xu, A., and He, F. (2023). Titanium surface interacting with blood clot enhanced migration and osteogenic differentiation of bone marrow mesenchymal stem cells. *Front. Bioeng. Biotechnol.* 11, 1136406. doi:10.3389/fbioe.2023.1136406

Mei, S., Wang, H., Wang, W., Tong, L., Pan, H., Ruan, C., et al. (2014). Antibacterial effects and biocompatibility of titanium surfaces with graded silver incorporation in titania nanotubes. *Biomaterials* 35 (14), 4255–4265. doi:10.1016/j.biomaterials.2014.02.005

Santos-Coquillat, A., Mohedano, M., Martinez-Campos, E., Arrabal, R., Pardo, A., and Matykina, E. (2019). Bioactive multi-elemental PEO-coatings on titanium for dental implant applications. *Mater Sci. Eng. C Mater Biol. Appl.* 97, 738–752. doi:10.1016/j.msec.2018.12.097

Sobolev, A., Valkov, A., Kossenko, A., Wolicki, I., Zinigrad, M., and Borodianskiy, K. (2019). Bioactive coating on Ti alloy with high osseointegration and antibacterial Ag nanoparticles. *ACS Appl. Mater Interfaces* 11 (43), 39534–39544. doi:10.1021/acsami.9b13849

Vu, A. A., Robertson, S. F., Ke, D., Bandyopadhyay, A., and Bose, S. (2019). Mechanical and biological properties of ZnO, SiO(2), and Ag(2)O doped plasma sprayed hydroxyapatite coating for orthopaedic and dental applications. *Acta Biomater.* 92, 325–335. doi:10.1016/j.actbio.2019.05.020

Wang, H., Zhang, X., Wang, H., Zhang, J., Li, J., Ruan, C., et al. (2018). Enhancing the osteogenic differentiation and rapid osseointegration of 3D printed Ti6Al4V implants via nano-topographic modification. *J. Biomed. Nanotechnol.* 14 (4), 707–715. doi:10.1166/jbn.2018.2551

Wu, N., Gao, H., Wang, X., and Pei, X. (2023). Surface modification of titanium implants by metal ions and nanoparticles for biomedical application. *ACS Biomater. Sci. Eng.* 9, 2970–2990. doi:10.1021/acsbiomaterials.2c00722

Wu, Q., Hu, L., Yan, R., Shi, J., Gu, H., Deng, Y., et al. (2022). Strontium-incorporated bioceramic scaffolds for enhanced osteoporosis bone regeneration. *Bone Res.* 10 (1), 55. doi:10.1038/s41413-022-00224-x

Wu, Q. J., Li, J. H., Zhang, W. J., Qian, H. X., She, W. J., Pan, H. Y., et al. (2014). Antibacterial property, angiogenic and osteogenic activity of Cu-incorporated TiO2 coating. *J. Mater. Chem. B* 2 (39), 6738–6748. doi:10.1039/c4tb00923a

Yan, R., Li, J., Wu, Q., Zhang, X., Hu, L., Deng, Y., et al. (2022). Trace element-augmented titanium implant with targeted angiogenesis and enhanced osseointegration in osteoporotic rats. *Front. Chem.* 10, 839062. doi:10.3389/fchem.2022.839062

Ye, M., Liu, W., Cheng, S., and Yan, L. (2023). Efficacy of Adjunctive Chlorhexidine in non-surgical treatment of Peri-Implantitis/Peri-Implant Mucositis: An updated systematic review and meta-analysis. *Pak J. Med. Sci.* 39 (2), 595–604. doi:10.12669/pjms.39.2.7253

Zhang, W., Wang, G., Liu, Y., Zhao, X., Zou, D., Zhu, C., et al. (2013). The synergistic effect of hierarchical micro/nano-topography and bioactive ions for enhanced osseointegration. *Biomaterials* 34 (13), 3184–3195. doi:10.1016/j.biomaterials.2013.01.008

Zhao, L., Chu, P. K., Zhang, Y., and Wu, Z. (2009). Antibacterial coatings on titanium implants. *J. Biomed. Mater Res. B Appl. Biomater.* 91 (1), 470–480. doi:10.1002/jbm.b.31463

Zhou, J., Li, B., Lu, S., Zhang, L., and Han, Y. (2013). Regulation of osteoblast proliferation and differentiation by interrod spacing of Sr-ha nanorods on microporous titania coatings. *ACS Appl. Mater. Interfaces* 5 (11), 5358–5365. doi:10.1021/am401339n

frontiers | Frontiers in Bioengineering and Biotechnology

TYPE Original Research
PUBLISHED 21 August 2023
DOI 10.3389/fbioe.2023.1258030

OPEN ACCESS

EDITED BY
Xing Wang,
Shanxi Medical University, China

REVIEWED BY
Xiangning Liu,
Jinan University, China
Qianju Wu,
Xiamen Stomatological Hospital, China
Xiangkai Zhang,
Shanghai Jiao Tong University, China

*CORRESPONDENCE
Shilei Zhang,
leinnymd@hotmail.com
Kaili Lin,
linkaili@sjtu.edu.cn,
lklecnu@aliyun.com
Yong Zhang,
zhangyong1362@163.com
Jinyang Wu,
wujinyang7029@foxmail.com

†These authors have contributed equally to this work and share first authorship

RECEIVED 13 July 2023
ACCEPTED 09 August 2023
PUBLISHED 21 August 2023

CITATION
Zhang C, Zhou Z, Liu N, Chen J, Wu J, Zhang Y, Lin K and Zhang S (2023), Osteogenic differentiation of 3D-printed porous tantalum with nano-topographic modification for repairing craniofacial bone defects.
Front. Bioeng. Biotechnol. 11:1258030.
doi: 10.3389/fbioe.2023.1258030

Osteogenic differentiation of 3D-printed porous tantalum with nano-topographic modification for repairing craniofacial bone defects

Chuxi Zhang[1†], Zhongwei Zhou[2†], Nian Liu[1], Jiangping Chen[1], Jinyang Wu[1*], Yong Zhang[1*], Kaili Lin[1*] and Shilei Zhang[1*]

[1]Shanghai Key Laboratory of Stomatology and Shanghai Research Institute of Stomatology, Department of Oral and Cranio-Maxillofacial Surgery, National Clinical Research Center, Shanghai Ninth People's Hospital, College of Stomatology, Shanghai Jiao Tong University School of Medicine, Shanghai, China, [2]Ningxia Key Laboratory of Oral Diseases Research, Department of Oral and Maxillofacial Surgery, General Hospital of Ningxia Medical University, Institute of Medical Sciences, Yinchuan, Ningxia, China

Introduction: Congenital or acquired bone defects in the oral and cranio-maxillofacial (OCMF) regions can seriously affect the normal function and facial appearance of patients, and cause great harm to their physical and mental health. To achieve good bone defect repair results, the prosthesis requires good osteogenic ability, appropriate porosity, and precise three-dimensional shape. Tantalum (Ta) has better mechanical properties, osteogenic ability, and microstructure compared to Ti6Al4V, and has become a potential alternative material for bone repair. The bones in the OCMF region have unique shapes, and 3D printing technology is the preferred method for manufacturing personalized prosthesis with complex shapes and structures. The surface characteristics of materials, such as surface morphology, can affect the biological behavior of cells. Among them, nano-topographic surface modification can endow materials with unique surface properties such as wettability and large surface area, enhancing the adhesion of osteoblasts and thereby enhancing their osteogenic ability.

Methods: This study used 3D-printed porous tantalum scaffolds, and constructed nano-topographic surface through hydrothermal treatment. Its osteogenic ability was verified through a series of *in vitro* and *in vivo* experiments.

Results: The porous tantalum modified by nano-topographic surface can promote the proliferation and osteogenic differentiation of BMSCs, and accelerate the formation of new bone in the Angle of the mandible bone defect of rabbits.

Discussion: It can be seen that 3D-printed nano-topographic surface modified porous tantalum has broad application prospects in the repair of OCMF bone defects.

KEYWORDS

oral and cranio-maxillofacial, tantalum, three-dimensional printing, alkali-heat-treatment, nano-topography, osteogenesis

1 Introduction

Oral and cranio-maxillofacial surgery (OCMS) is a surgical specialty that concentrates on the treatment of lesions in the oral, maxillofacial, facial, or head and neck areas (Bell, 2010) with complex anatomy, important physiological functions, and aesthetic requirements (Kim J.-W. et al., 2016; Rachmiel et al., 2017). In fact, congenital or acquired defects and malformations in the craniomaxillofacial (CMF) region (Rudman et al., 2011; Seok et al., 2016; Oh, 2018), especially bone defects, stemmed from traffic accidents, sports injuries, congenital malformations, tumor resection, surgical accidents and periodontal diseases not only severely affect the normal function and facial appearance, but also brings harm to the physical and mental health of patients.

However, the reconstruction of CMF bone defects is extremely challenging in the global medical system due to its stringent requirements in shape and high risk of postoperative infection in the selection of repairing materials. An ideal material needs to satisfy several conditions. Firstly, the restoration with high biocompatibility is required to prevent from any adverse reactions such as immune rejection in the human body, and the material is supposed to provide mechanical support for the defect area with excellent mechanical performance. Appropriate surface properties and porosity are also needed to simulate the composition, structure and performance of biological bone tissue, while the specific pore size and porosity are conducive to the generation of fresh and orderly vascular systems throughout the defect spaces, facilitating the transfer of nutrients and cells to the newborn bones. In addition, the induction and conduction of bones are instrumental in inducing the mesenchymal cells adjacent tissue to differentiate into osteoblasts or facilitating the crawling of nearby bone tissue (Gundu et al., 2022).

Among all bone defect implant materials used in clinical, metal materials have strong plasticity and can be adjusted appropriately during surgery to achieve better surgical results, and Ti6Al4V is currently the most widely used metal implant material. Huang et al. (2022) demonstrated through cell experiments that tantalum scaffolds with the same structure have better osteogenic ability than Ti6Al4V scaffolds. Fan et al. (2021) tested the biomechanical properties of tantalum and titanium scaffolds in reconstructing bone defects, proving that tantalum scaffolds outperform titanium scaffolds in terms of compression and deformation, and have biomechanical properties closer to bone scaffolds. In addition, the research of Schildhauer et al. (2006) proved that tantalum scaffold has lower *Staphylococcus aureus* adhesion than titanium alloy. The above studies have shown that tantalum has better mechanical properties, osteogenic ability, and microstructure compared to titanium alloys, making it a potential substitute material for bone repair. Tantalum has been widely applied in orthopedics such as hip, knee arthroplasty and spine surgery as a new type of biomedical implant material, which is stable within the pH and voltage ranges *in vivo*. However, tantalum is generally biologically inert in the human body and encounters limitations in inducing the formation of new bones indicating that directly integration with the surrounding bone is impractical. Clinically, it will take 3–6 months to ensure the sufficient osseointegration if necessary. Therefore, how to promote osseointegration and shorten the time has been heated debated for tantalum.

The surface characteristics of materials, such as surface morphology and surface chemistry are strongly relevant to the biological behavior of cells and deeply influenced the performance (Ponche et al., 2010). It has been reported (Vitte et al., 2004) that the long-term adhesion of cells is associated with the surface morphology of materials, especially the roughness, while short-term adhesion is mainly controlled by surface chemistry.

Most cells in the body (except blood cells) adhere to the extracellular matrix (ECM), while the bone-forming and degrading cells, i.e., osteoblasts and osteoclasts in the bone tissue attach to and grow on the ECM, which consists of proteins and calcium phosphate-rich mineral proteoglycans. Only when cells adhere normally can they continue to grow and differentiate (Anselme et al., 2010). The first interaction between the cell and the material surface will determine the binding quality of the tissue-implant interface, and the surface will be covered with water and proteins after a few seconds of contact between the material and the body fluid by which the cells sense the surface characteristics of the ECM. Cells adhere with the help of physicochemical interactions such as ionic force and van der Waals force firstly, and then by various biomolecules. The most critical part in this process is the surface receptor also called integrin, which is a transmembrane molecule interacting with the ECM outside the cell and the cytoskeleton molecules and adhesion sites inside in order to transfer the information between the both sides. Therefore, signals are transmitted from the ECM to the nucleus through the biochemical signal transduction pathways for the sake of protein aggregation and phosphorylation (Siebers et al., 2005). It seems reasonable to regulate the differentiation of stem cells by modifying the extracellular environment.

Nano-technology is widely used in surface modification of implants (Manivasagam et al., 2022). Due to the unique surface properties of nanomaterials such as wettability, large surface area, proteins will attach to the nano-surface and form a protein layer, acting as a biological medium for the interaction between the nanomaterials and cells (Zhang et al., 2020). The unique surface properties of nano biomaterials increase protein adhesion. The enhanced protein adsorption layer continues to increase the cell adhesion through signal recognition triggered by integrin and ultimately affect subsequent cell reactions, such as cell migration and osteoblastic differentiation (Huang et al., 2016). After the nanomaterials are overlapped by albumin, laminin, or collagen, the adhesion of osteoblasts to the nanomaterials is significantly enhanced. In addition, the adsorption kinetics of proteins vary with different chemical and physical properties. Specific types of proteins can better adhere to the surface of the nanomaterials, selectively mediating the adhesion of osteoblasts (Webster et al., 2000).

Researchers have developed many methods to prepare the nano-topographic surface, such as thin film deposition, physical and chemical vapor deposition, chemical etching, nanoimprinting, photolithography, electron beam or nanosphere lithography, etc. (Babuska et al., 2022). Among these methods, alkali heat treatment enables to significantly improve in the hydrophilicity of the material surface (Kim H. S. et al., 2016), which facilitates the interaction of cells with the implant surface. Moreover, alkali heat-treated metallic tantalum effectively induces extracellular bone matrix

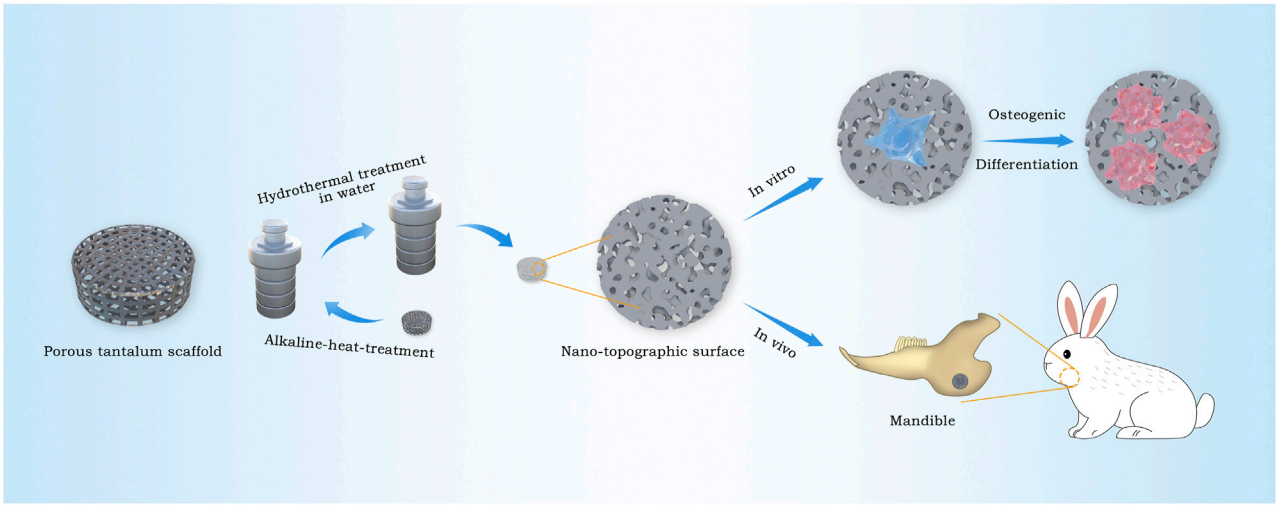

FIGURE 1
Schematic illustration for the construction procedure of nano-topographic surface tantalum scaffold and its application of osteogenic effects *in vitro* and vivo.

mineralization by rapid hydroxyapatite deposition in simulated body fluids (Miyazaki et al., 2000).

Finished biomaterials processed by slicing are not adequate for the anatomical structure of bone defects and the demands of defects with critical sizes and maxillofacial aesthetics, and they are mostly used for skull repair (Jardini et al., 2014). The development of 3D printing technology has largely solved these challenges, thus providing a new direction for the treatment of maxillofacial bone defects (Jones, 2012).

In this work, 3D printing technology is used to produce porous tantalum scaffolds, then nano-morphology on the surface of the scaffolds is constructed by alkali heat treatment with NaOH solution and the following hydrothermal treatment in deionized water in order to realize the rapid bone integration, high compatibility with the elastic modulus of human bones, and satisfy personalized demands. The surface characteristics of 3D-printed porous tantalum scaffolds modified in nano-topographic are systematically analyzed. Further research about the biological reaction *in vitro* and the ability of bone integration *in vivo* of nano-topographic modified 3D-printed porous tantalum scaffold were studied by co culturing rat bone marrow stem cells (BMSCs) *in vitro* and repairing the bone defect of the rabbit mandible angle *in vivo* (Figure 1).

2 Materials and methods

2.1 Materials

The samples are prepared by Ningxia Dongfang Zhizao Technology Co., Ltd., and the preparation method is as follows. Firstly, the scaffold model is constructed by Geomagic Studio 2014 (Geomagic Inc., Morrisville, NC, United States), and 3D printed by Huashu FS271M laser printer (Huanan Farsoon High Technology Co., Ltd., China) using Tantalum medical powder with an average particle size of 15–53 μm. Every layer of the porous scaffolds was processed by laser selective melting.

The scaffold with a diameter of 10 mm, a thickness of 2 mm is used for *in vitro* cell experiments, while the one with a diameter of 6 mm, a thickness of 2 mm is prepared for *in vivo* animal experiments. The pore size of these two types is 400–500 μm, and the porosity is 70%–80% with <20 GPa elastic modulus. All samples were ultrasonically cleaned in acetone, anhydrous ethanol and distilled water for 15 min.

To construct nano-topographic surface, the 3D-printed porous tantalum scaffolds were immersed in a 5 mmol/L NaOH solution and subjected to hydrothermal treatment at 80°C for 6 h in a Teflon-lined autoclave. After thoroughly cleaned with deionized water using ultrasonic cleaner, the samples were wet oxidized at 200°C for 4 h in deionized water (Wang et al., 2018). The samples obtained before and after the hydrothermal treatment were labeled as Ta-3D and Ta-nano respectively, where the 3D samples were used as controls. Autoclaving steam sterilization (0.21 MPa, 134°C) was performed prior to *in vitro* and *in vivo* studies.

2.2 Methods

2.2.1 Surface characterization of the samples

The surface morphology of the prepared samples was observed by a scanning electron microscope (SEM, Hitachi SU8220, Japan). The chemical phases on the surface of two groups of materials were identified by X-ray diffractometry (XRD, Buker D8 advance, Germany) using a Cu Kαx-ray source with a 2θ scan range of 20°–60° and a scan rate of 2°/min. The compositions of the samples were analyzed by energy dispersive x-ray spectrometry (EDS, EBSD X-MAXN, OXFORD, Britain). The surface wettability of the material is measured by a contact angle meter (SL200KS, SOLON TECH, China).

2.2.2 *In vitro* experiments

2.2.2.1 Rat BMSCs separation and culture

Male rats at 3 weeks of age were selected to extract BMSCs cells. The rats were cervically dislocated and placed in 70% ethanol for immersion. The executed rats were placed supine on a dissecting board, a skin augmentation was made on the abdomen with forceps, a small incision about 1 cm long was made with sterile dissecting scissors, and the skin of the limbs and feet were peeled from the wound to expose the lower abdomen and legs. The foot was removed by making an incision from below the ankle joint, and an incision was made along the iliac bone at the hip bone to separate the femoral head from the hip bone, and an incision was made in the middle of the hip bone to separate the two iliac bones. Using vascular forceps and small scissors, the muscles of the femur, tibia and ilium were carefully removed. After separating all bones, they are placed in Phosphate buffer solution (PBS) and moved to the ultra-clean bench for the remaining separation steps. Prepare Petri dishes containing 10 mL of prepared α-MEM medium (Shanghai BasalMedia Technologies Co., Ltd., Shanghai, China) (containing 10% fetal bovine serum (FBS, Gibco, United States), 1% penicillin and streptomycin double antibodies). Make small incisions of approximately 1–2 mm both proximal and distal to the bone, aspirate 3 mL of the configured α-MEM medium with a 5 mL syringe, rinse the bone, flush the rinse solution into the Petri dish, and wash the bone cavity thoroughly with the syringe at least three times until the bone appears white, indicating that all bone marrow has been flushed. The medium was incubated in an incubator at 37°C and 5% CO_2. Primary BMSCs cells were cultured for 72 h. Fresh medium was added to remove non-adherent cells, and the remaining adherent cells were mainly bone marrow mesenchymal stem cells. After that, the medium was changed every 2 days until the cell fusion reached 80% and the cells were ready for passaging. BMSCs cells of three to five generations were selected for the following experiments.

2.2.2.2 Cell adhesion observation

In a 48-well plate, BMSCs cells were inoculated onto each sample at a density of 2×10^4/well. After 24 h of incubation, the cells were rinsed twice with PBS, then fixed for 24 h at 4°C by adding 4% paraformaldehyde, and rinsed three times with PBS. The cells were then dried in a vacuum freeze dryer (CoolSafePro110-4, LABOGENE, Denmark) for 24 h. After gold spraying, the morphology and adhesion of cells on the surface of porous metallic tantalum material were observed by scanning electron microscopy at 3.0 kV.

2.2.2.3 Cell live/dead assay

The toxicity of different samples to cells was studied by live/dead staining. Ta-3D and Ta-nano porous materials were spread on 48-well plates, where 4 wells of each material. BMSCs were seeded on the materials at a density of 1×10^4 cells/well, and they were cultured for 3 days. Staining was performed with Calcein/PI cell activity and cytotoxicity assay kit (Shanghai Maokang Biotechnology Co., Ltd., Shanghai, China) and the observation and counting are carried out under fluorescent microscope.

2.2.2.4 Cell proliferation

BMSCs were inoculated at a cell density of 5,000 cells/well on each group of material, and 0.5 mL of α-MEM complete medium was added to each well. And they were incubated for 1/4/7 days. At each time point, the medium was removed and, and the samples were washed 2–3 times with PBS and transferred to a new 48-well plate with sterilized forceps, and 0.5 mL of α-MEM complete medium containing 10% CCK8(Cell Counting Kit-8, Dojindo Laboratories, Japen) reagent was added to each well. Away from light, the plate was incubated for 2 h in the incubator, and then transferred to a 96-well plate with 100 μL per well. The absorbance OD value was determined at 450 nm in an enzyme marker.

2.2.2.5 The alkaline phosphate (ALP) activity assay

Ta-3D and Ta-nano porous materials were spread in two 48-well plates with 4 wells per material, and BMSCs were seeded on the material at a density of 2×10^4 cells/well. After 4 and 7 days of incubation, the material was rinsed 2–3 times with PBS, transferred to a new 48-well plate. After covering the materials with 0.5–1 mL per well 1% TritonX-100 (Beyotime, China) for 30–40 min, the lysate was then transferred to a 15 mL centrifuge tube using a micropipette and centrifuged at 12,000 rpm/min for 10 min at 4°C to obtain the supernatant. ALP activity was determined using the ALP kit (JianCheng Bioengineering Institute, Nanjing, China) and total protein concentration was determined using the BCA protein assay kit (Beyotime, China), and all operations were performed on ice. The AKP standard curve was used for calculation of the assay results.

2.2.2.6 Alkaline phosphatase staining assay

Ta-3D and Ta-nano porous scaffolds were spread in 48-well plates, 4 wells of each material, for a total of 2 plates. BMSCs were seeded on the materials with a density of 2×10^4 cells/well. Due to the dark color of the scaffolds, alkaline phosphatase activity staining purple was difficult to develop, so the cells were cultured for 4 and 7 days, and then after complete digestion of the cells from the scaffolds using 0.25% trypsin digestion solution (Gibco, United States), they were transferred to new 48-well plates and cultured for another 24 h. The intracellular ALP was characterized using the BCIP/NBT alkaline phosphatase color development kit (Beyotime, China). The surface was observed and photographed using a stereomicroscope.

2.2.2.7 Alizarin red staining (ARS) Assay

Alizarin red staining was used to assess the extent of ECM mineralization. BMSCs were seeded on the materials at a density of 1×10^4 cells/well. The 0.2% ascorbic acid, 1% sodium β-glycerophosphate and 0.01% dexamethasone were added to complete α-MEM medium to prepare osteogenic induction medium. When the cell fusion of BMSCs reached 50%–70%, the α-MEM culture medium was aspirated and the osteogenic induction medium was added, and the medium was changed every 2 days to induce the deposition of calcium salts on the cell surface and the formation of calcium nodules. The BMSCs were cultured for 21 days on the surface of each of the two groups of samples, and then fixed with 4% paraformaldehyde for 60 min. After staining with alizarin red staining solution (2%, pH 8.3) (Beyotime, China) for 10 min, the excess dye was washed 3–5 times with phosphate buffer, and then observed and photographed under a body view microscope.

2.2.2.8 Quantitative Real-Time PCR

The expression levels of osteogenic genes were analyzed using fluorescence real-time quantitative PCR to examine the expression

TABLE 1 Primer sequences utilized for RT-PCR.

Gene	Primers (F = forward; R = reverse)
GAPDH	F:5′-GAAGGTGAAGGTCGGAGTC-3′
	R:5′-GAAGATGGTGATGGGATTTC-3′
ALP	F: 5′-TATGTCTGGAACCGCACTGAAC-3′
	R: 5′-CACTAGCAAGAAGAAGCCTTTGG-3′
BMP-2	F: 5′-GAAGCCAGGTGTCTCCAAGAG-3′
	R: 5′-GTGGATGTCCTTTACCGTCGT-3′
BSP	F: 5′-AGAAAGAGCAGCACGGTTGAGT-3′
	R: 5′-GACCCTCGTAGCCTTCATAGCC-3′
COL-1	F: 5′-GCCTCCCAGAACATCACCTA-3′
	R: 5′-GCAGGGACTTCTTGAGGTTG-3′

of ALP, BMP-2, BSP and COL-1. BMSCs were seeded on the materials at a density of 2×10^4 cells/well and cultured for 4 and 7 days. Total RNA was extracted using Trizol reagent (Invitrogen, United States). cDNA was then synthesized by Prime-Script™ RT kit (Takara Bio, Japan). The real-time PCR procedure was performed by using SYBR green PCR reaction mix (Roche, Basel, Switzerland) on the Light Cycler® 96 Real-Time PCR System (Roche, Switzerland). All the above experiments were performed on ice. All expression levels of target genes were normalized to GAPDH and related genes were quantified using the $2^{-\Delta\Delta CT}$ method. The primers are listed in Table 1.

2.2.2.9 Western blot analysis

Osteogenic protein expression (COL-1) in BMSCs was assessed using Western blot. BMSCs were seeded on the materials at a density of 2×10^4 cells/well and cultured for 7 days. Cells on the scaffold were treated with RIPA buffer containing protease and phosphatase inhibitors (Shanghai Epizyme Biomedical Technology Co., Ltd, China) on ice, and the lysate was transferred to a 1.5 mL EP tube and centrifuged at 4°C. The total protein in the supernatant denatured with protein loading buffer (Shanghai Epizyme Biomedical Technology Co., Ltd, China) was separated by SDS-PAGE, and then transferred to Polyvinylidene fluoride (PVDF) membrane (Millipore, United States). The membrane was blocked in 5% BSA dissolved in TBST at room temperature for 1 h, and then incubated overnight with primary antibodies at 4°C. After rinsing three times in TBST, the membrane was incubated at room temperature in a second antibody conjugated with fluorescence for 1 h. Protein bands detected using an infrared laser imaging system (Odyssey,United States). β-Actin serves as a reference for this study.

2.2.3 *In Vivo* studies

2.2.3.1 Animal Surgical Implantation

Eight healthy adult male New Zealand white rabbits were randomly divided into four groups, while the experimental group was named Ta-nano group, and the control group was called Ta-3D group. Three and 6 weeks were selected as the sample time point with four rabbits in each group at each time point. Porous tantalum prostheses were implanted in the mandibles of the rabbits, and both mandibular angles were operated on. After palpating the lower edge of the mandible and the mandibular angle, the skin and subcutaneous tissue were incised from front to back parallel to the lower edge of the mandible, approximately 3 mm above the lower edge of the mandible and at the anterior edge of the occlusal muscle, layer by layer, with an incision length of approximately 3–4 cm. According to the requirements of critical bone defect size of rabbit mandible described in the literature (Schmitz and Hollinger, 1986; Manju et al., 2018), this study chose to construct the 6 mm circular bone defect at the Angle of the mandible of rabbit. Bilateral standardized 6 mm diameter circular holes were made to create experimental defects with a stripper while drilling. Carefully embed the sterilized material into the circular hole so that the material fits closely to the bone defect area. After implantation, the wound was closed by suturing in layers. Every rabbit was reared for 2 and 4 weeks and injected with calcein and alizarin red (dose: 10 mg/kg) in the gluteus maximus muscle for fluorescent labeling, respectively. Rabbits in each group were euthanized and harvested at 3 weeks and 6 weeks after implantation.

2.2.3.2 Micro-CT Analysis

The bone tissue samples were fixed in 4% paraformaldehyde for 24–48 h, and it was scanned by micro-CT (Quantum GX2 micro-CT, PerkinElmer, United States), and images and statistics were obtained using its accompanying automated bone analysis software (VAccuCT™, PerkinElmer, United States).

2.2.3.3 Histological evaluation

After dehydration with an ethanol gradient and dethermalization with a series of mixtures of Technovit 7,200 resin and ethanol, samples were infiltrated in light-cured Technovit 7,200 resin, infiltrated for 3 days, and then placed in a light-cured embedding machine for 10 h. Finally, slices were cut into 300 μm size using a hard tissue slicer (E3000CP/400CS; EXACT Verteriebs, Germany) and grounded to 30–50 μm on a hard tissue grinder. Fluorescently labeled sections were observed under a laser confocal microscope (Leica, Germany) to study dynamic osteogenic information in porous implants. Van Gieson staining of the sections was performed to assess the bone growth in porous implants. Slides were rinsed with dehydrated alcohol and then observed under a optical microscope. The volume of osteogenesis within the tantalum metal porous material was calculated by ImageJ software (National Institutes of Health, United States).

2.2.4 Statistics

Data were presented as mean (MD) ± standard deviation (SD). Statistical analysis was performed using *t*-test by SPSS 22.0 statistical package. The value was statistically significant only when $p < 0.05$.

3 Results and discussion

3.1 Surface characterization

Figure 2A shows three-dimensional printed porous tantalum scaffolds. The surface morphology of the porous metallic tantalum materials in the Ta-3D and Ta-nano groups was observed by SEM (Figure 2B). The Ta-3D and Ta-nano porous tantalum metal

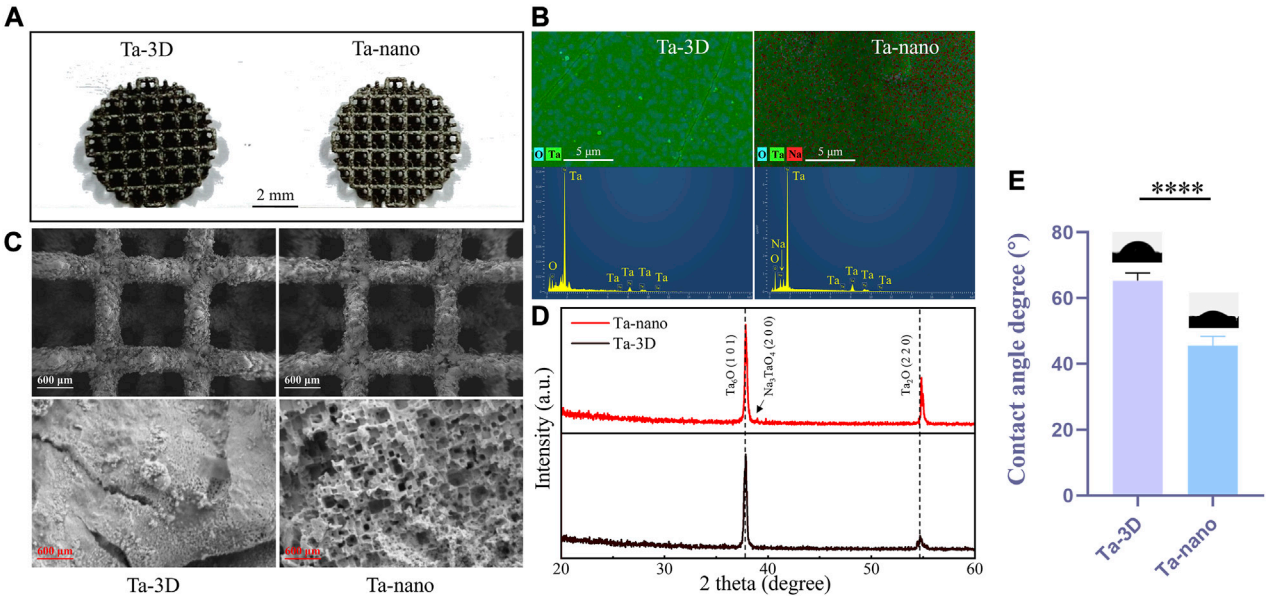

FIGURE 2
Structure and surface characterization of 3D printed porous tantalum scaffolds. **(A)** 3D-printed porous tantalum scaffolds. **(B)** SEM images of surface morphology of Ta-3D group and Ta-nano group porous tantalum scaffolds. **(C)** EDS layered image and EDS analysis of Ta-3D and Ta-nano. **(D)** XRD patterns of Ta-3D and Ta-nano. **(E)** The water contact angles of Ta-3D and Ta-nano.

materials show the same 3D structure and similar original micron-level surface morphology at the ×30 low-magnification SEM images, which indicate that the metal powder has melted sufficiently and there is almost no Ta powder remaining on the surface of the scaffold. The porous tantalum scaffold is a regular square lattice-like structure with a side length of 1.35 mm. Under the high magnification SEM image at 30k×, the surface of the porous tantalum scaffold in the Ta-3D group is relatively flat, while the porous tantalum metal material in the Ta-nano group shows a microporous nano-topographic surface structure.

The surface chemical elemental composition of the prepared samples was further evaluated by EDS X-ray spectrometer analysis (Figure 2C), and the EDS spectra of the unprocessed tantalum metal scaffolds of Ta-3D group showed significant peaks for Ta as well as O elemental peaks. Moreover, the EDS results of the nano-surface modified tantalum metal of Ta-nano group revealed the presence of Na in addition to Ta and O.

XRD patterns of the unprocessed Ta and nanomodified porous tantalum scaffolds was shown in Figure 2D. It can be seen from the figure that the material surfaces are dominated by Ta-O oxides, which may be due to the generation of Ta_6O/Ta_2O oxide layer on the material surface during the laser melting. Besides, a peak corresponding to sodium tantalate (Na_3TaO_4) appears in the Ta-nano group due tp the reaction between Ta and the NaOH solution used in the alkali thermal operation.

The wettability of the material surface was tested using a contact angle meter. The results of the contact angle measurement are as follows (Figure 2E): the average contact angle of Ta-3D group is about 65.769°, while the average contact angle of Ta-nano group is about 42.483°. It can be seen that the nano surface modification significantly improves the wettability of tantalum metal. The wettability of biomaterials is a key characteristic that affects the initial protein adsorption and a series of subsequent cell-material interactions. Good wettability can improve the adsorption of osteoblast protein on the implant surface and increase the time of implant exposure to the cell Integrin binding domain, thereby enhancing the attachment, adhesion and further development of osteoblast precursors on the implant surface, thus accelerating bone integration (Ghezzi et al., 2021).

3.2 Cell adhesion

The cell morphology and adhesion of BMSCs cells cultured on porous tantalum scaffolds in the Ta-3D and Ta-nano groups for 1 day was shown in Figure 3. BMSCs cells were fully spread and adhered in both scaffold grids as seen in the 50 × SEM images. A small number of cell pseudopods were observed to adhere to the scaffold grids in the porous tantalum scaffolds of Ta-3D group. In the Ta-nano group, BMSCs cells were clearly stretched and more fully extended, with more filamentous pseudopods and lamellar footprints, indicating that the cells were more extended and adherent. As the first step in the interaction between cells and materials, cell adhesion is the foundation of cell anchoring and a prerequisite for cell diffusion and proliferation on the surface of implants (Su et al., 2022). The biological effect of surface structures on cells is determined by their sizes and it is more likely to interact between structures of the similar size; that is, micrometer-scale structures are similar in size to individual cells (tens of micrometers), while nanoscale structures formed after surface modification are almost identical to organelles, biomolecules, etc. in size, thus providing better contact guidance (Miyoshi and Adachi, 2014; Zhu et al., 2019).

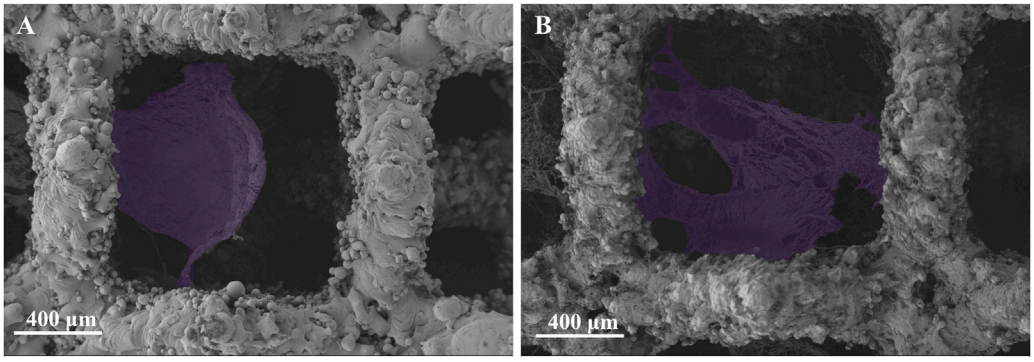

FIGURE 3
SEM images of the adherent BMSCs (purple) on Ta-3D and Ta-nano surfaces after 1 day of culture. [**(A)**: Ta-3D, **(B)** Ta-nano].

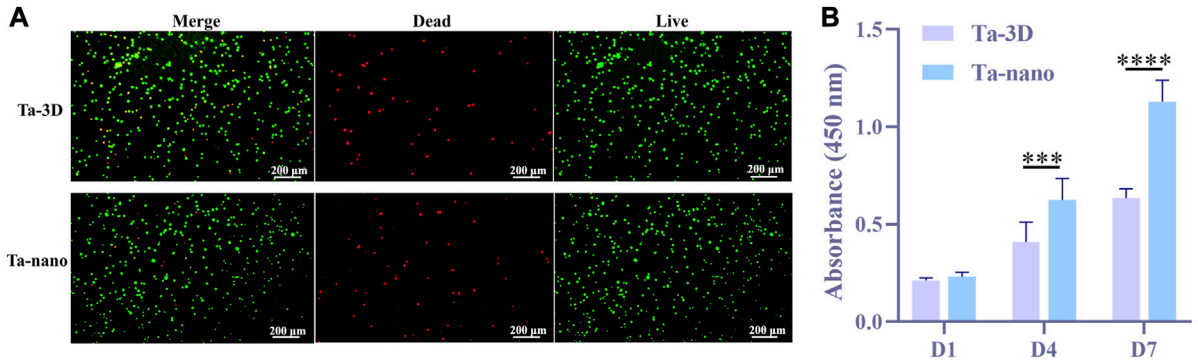

FIGURE 4
Cytotoxicity and cell proliferation. **(A)** Fluorescence images of live/dead staining after BMSCs were cultured on the surface of two samples for 3 days. **(B)** CCK-8 results showed the proliferation of BMSCs in Ta-3D and Ta-nano.P

3.3 Cell viability and proliferation

The BMSCs cells were cultured on porous tantalum scaffolds of Ta-3D group and Ta-nano group for 3 days and then stained for live-dead staining, and the results of live-dead staining are shown in Figure 4A. Both groups were covered with a large number of living cells (showing green fluorescence) and a very few dead cells (showing red fluorescence), which proved that both groups had no obvious toxicity and good biocompatibility.

After suffering from the bone defects resulting from pathological injuries, the self-repair of bone relies mainly on the amount of the cells rather than the volume. Therefore, a sufficient supply of cells (including MSCs and bone progenitor cells, etc.) is critical for effective bone regeneration (Li et al., 2022). CCK-8 was utilized to evaluate the adhesion and proliferation of BMSCs cells after 1/4/7 days of culturing on both groups of materials (Figure 4B). Figure 5 shows that there was no statistically significant difference between the two groups in day 1, but as the culturing time increased to 4 and 7 days, the proliferation activity of BMSCs on porous tantalum scaffolds in the Ta-nano group was significantly higher than that in the Ta-3D group, as the gap became more pronounced with increasing time, indicating that the nano-topographic surface structure enhance the proliferation of bone marrow mesenchymal stem cells indeed. This may be due to the fact that nanostructures are similar in size to Organelles and biomolecules, and cells can directly interact with them to form nanostructured matrices, which play a crucial role in stimulating cell proliferation (Babuska et al., 2022). Miyoshi and Adachi (2014) believes that nanostructures play a role as direct constraints of Integrin, which acts as a molecular link for transmission of a force between ECM and the actin filaments. The most characteristic way of Actin regulating cell proliferation is the tension stimulation of Actin Cytoskeleton involved in the Rho ROCK (Rho related protein kinase) pathway and the resulting Integrin aggregation pathway, which increases the activity of extracellular signal regulated kinase (ERK) and induces cell Cyclin D1 through ERK dependence, leading to enhanced cell growth (Assoian and Klein, 2008).

3.4 Osteogenic differentiation of BMSCs

The ALP activity values of both groups increased with time, and the ALP osteogenic activity values on day 4 were slightly higher in the Ta-nano group than in the Ta-3D group, but there was no

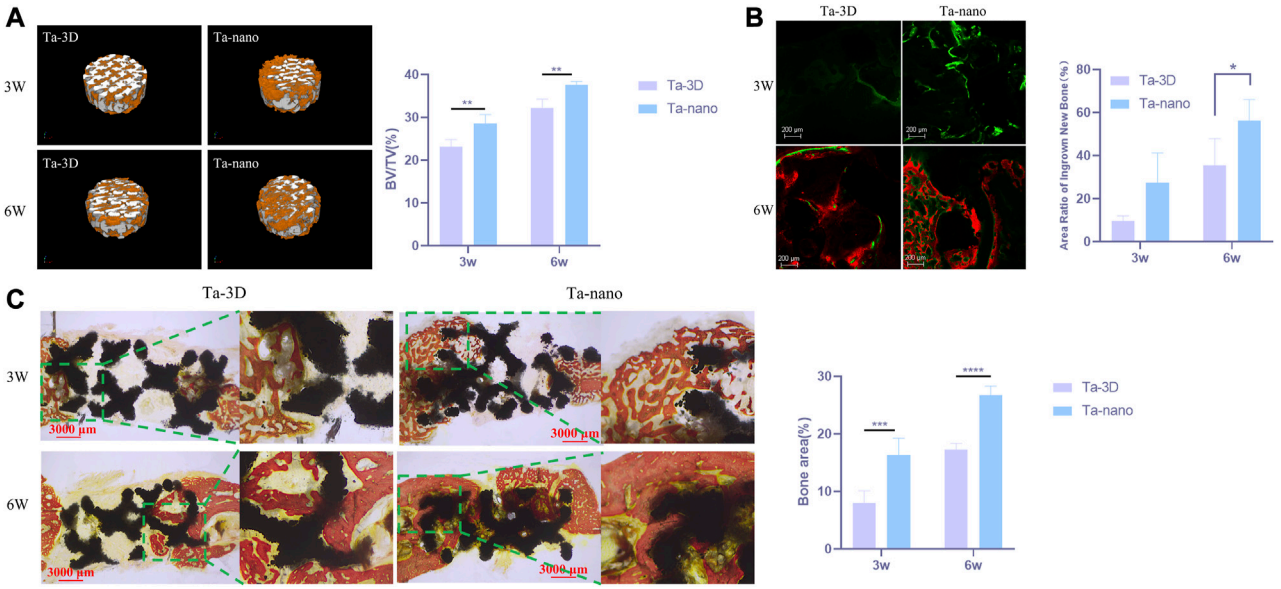

FIGURE 5
Capacity of New Bone Formation *In Vivo*. **(A)** Right: Micro-CT three-dimensional reconstruction of two groups of materials. Left: Percentage of the regenerated bone volume (BV) to the total volume (TV) according to the micro-CT images. **(B)** Fluorescent staining of porous scaffolds of new bone formation. The bone-formation fronts at the second, fourth week are marked by a green label from calcein green and red label from alizarin red respectively. **(C)** Histological section images of the Ta-3D and Ta-nano and percentage of osteogenic area of two groups of materials.P

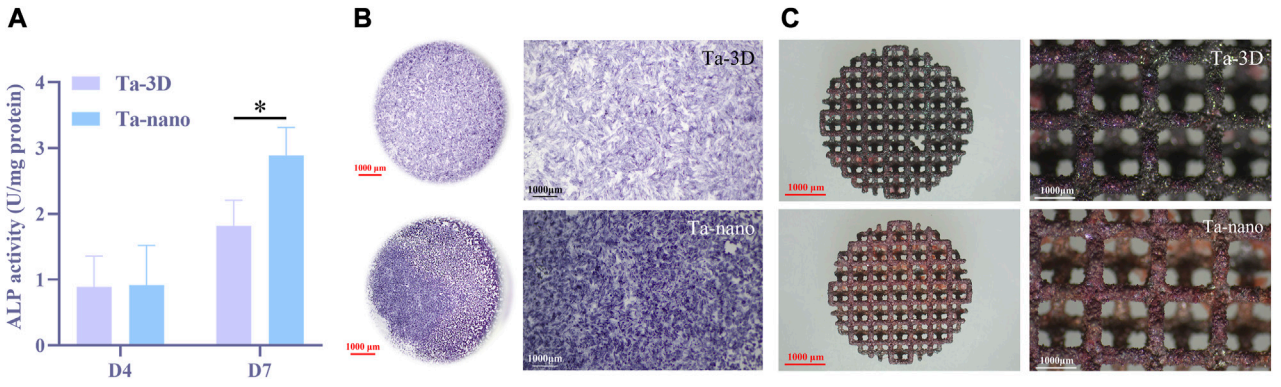

FIGURE 6
Osteogenic Differentiation of BMSCs. **(A)** ALP activity of BMSCs cells cultured on two groups of porous tantalum scaffolds on the 4 days and 7 days. **(B)** Representative staining ALP of BMSCs cells cultured on two groups of porous tantalum scaffolds on 7 days. **(C)** Representative staining ARS of BMSCs cells cultured on two groups of porous tantalum scaffolds on 21 days.

statistically significant difference between the two groups, while it could be seen that BMSCs incubated on the surface of the Ta-nano porous tantalum scaffold exhibited significantly better ALP activity than the Ta-3D group material without surface modification up to day 7, as shown in Figure 6A.

Figure 6B shows the representative images of ALP staining results on day 7 for two different groups of samples, respectively. Obviously, ALP staining level of the Ta-nano group is higher than that of the Ta-3D group without surface modification, which proves that the ALP osteogenic activity of the Ta-nano group is stronger than that of the porous tantalum scaffold without modification, which is consistent with the results of quantitative experiments.

ALP is an enzymatic protein secreted by osteoblasts whose active site consists of zinc-containing homodimeric metalloenzymes (Bremner and Beattie, 1995) which enables to hydrolyze a variety of phosphate compounds and release the inorganic phosphate (Pi) into the extracellular matrix (Farley et al., 1994). Besides, matrix vesicles also contain other calcium-dependent proteins which requires Pi to initiate crystalline nucleation of extracellular matrix calcium deposits, resulting in the formation of hydroxyapatite (Balcerzak et al., 2003). Consequently, the early expression of ALP of cells serves as one of the characteristic early markers of osteoblast differentiation, and the semi quantitative and staining results of ALP showed that nano

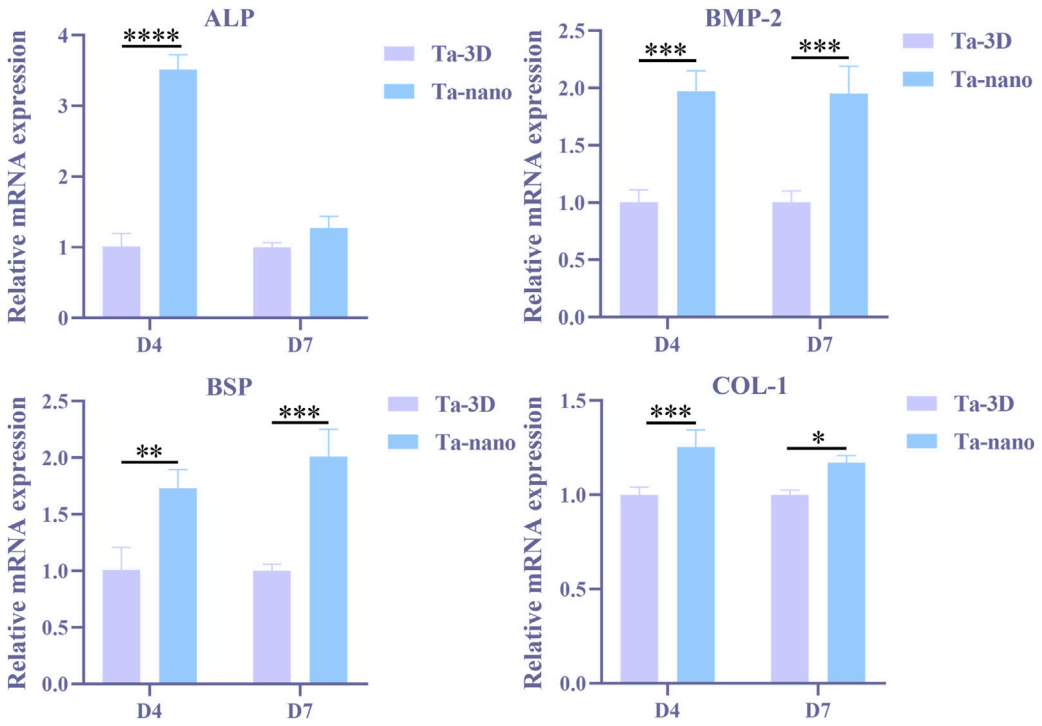

FIGURE 7
Osteogenic gene expressions (ALP, BMP-2, BSP and COL-1) of BMSCs on different samples at day 4/7 determined using RT-PCR.

surface modification contributed to the early osteogenic differentiation of BMSCs.

After culturing BMSCs cells on porous tantalum scaffolds of Ta-3D and Ta-nano groups for 21 days, the degree of mineralization of the extracellular matrix was further assessed by alizarin red staining. As can be seen from Figure 6C, red mineral compounds were observed on both groups of materials covering the internal lattices and surfaces of both scaffolds, and more mineralized nodules could be observed on the surface of porous tantalum scaffolds in the Ta-nano group. Alizarin red staining allows for the detection of calcium deposits and calcified nodules in cultured cells. The osseointegration of the implanted prosthesis with the surrounding bone *in vivo* consists of promoting the adsorption of biomolecules, recruiting BMSCs to adhere, differentiating into osteoblasts, and initiating the secretion of bone ECM, thus enhancing the early bone regeneration (Walmsley et al., 2015). Mineralization of the extracellular matrix is one of the processes of osteogenesis and implies late osteoblast differentiation. The BMSCs on the scaffolds of the Ta-nano group exhibited higher mineralization capacity, indicating that nano-topographic surface modification significantly enhanced osteogenic differentiation and mineralization of the cells.

3.5 Osteogenic gene/protein expression of BMSCs

Quantitative real-time quantitative PCR was performed to detect the expression of osteogenic genes, such as ALP, BSP, BMP-2 and COL-1 in BMSCs cultured on both groups of materials for 4 and 7 days, as shown in Figure 7. The expression of BMP-2, BSP and COL-1 was significantly increased in BMSCs cells of the Ta-nano group on days 4 and 7 compared to the Ta-3D group ($p < 0.05$). On the day 4, the amount of ALP gene expression was evidently higher in the Ta-nano group than in the Ta-3D group ($p < 0.05$), whereas no significant difference in ALP expression was observed between the Ta-3D and Ta-nano groups at day 7. Western blot analysis was used to detect the expression of COL-1 proteins in BMSCs cultured for 7 days, as shown in Supplementary Figure S1. The protein band grayscale of the Ta-nano group was deepened compared to the Ta-3D group, indicating a higher expression of COL-1, which was consistent with the gene expression result of RT-PCR. Compared with the differences in gene and protein expression between the two groups, it can be concluded that the nano-topographic surface can promote osteogenic differentiation of BMSCs.

The phenotype of osteoblasts is acquired in two stages. In the first stage, the cells proliferate and the matrix matures. Specific factors associated with the osteoblast phenotype, such as ALP, can be detected within 10 days of cell proliferation and matrix maturation or during 10–15 days. In the second phase of osteoblast phenotype acquisition, matrix mineralization, late osteogenic markers such as osteocalcin (OCN) are produced after 10–15 days or 25–30 days. Finally, multiple anabolic signaling pathways are actively involved in regulating bone formation, such as the BMP, Wnt and Runx2 pathways. RT-PCR results showed that ALP expression in nano-topographic surface modified porous tantalum material was higher than in the unprocessed group at day 4, while the difference in expression at day 7 was not significant. ALP is the most widely recognized biochemical marker representing osteoblast activity, and it is a

typical protein for osteoblast phenotype and it is a typical protein product of osteoblast phenotype and osteoclast differentiation. In general, the appearance of ALP activity is an early phenotypic marker of osteoblastogenesis (Stein et al., 1990). The expression of BSP, COL-1 and BMP-2 in nano-topographic surface modified porous tantalum material was higher than that of the Ta-3D group in BMSCs cells cultured for 4 and 7 days. Bone sialoprotein (BSP), which appears after ALP expression, localizes to the mineralized matrix, and BSP helps nucleation of hydroxyapatite mineralization and promotes calcium admixture and formation of mineralized nodules (Gordon et al., 2007), which represents a phenotypic marker of osteoblast differentiation in the middle and late stages and is essential for initiation of bone mineralization and promotion of adhesion of osteoblasts to the mineralized matrix. Type I collagen (COL-1) is an extracellular matrix protein that stimulates osteoblast adhesion and differentiation (Mizuno and Kuboki, 2001) and is a mid-stage marker of osteogenic differentiation of bone marrow mesenchymal stem cells. Nano-topographic surface modification significantly promoted the type I collagen (COL-1) synthesis. Bone morphogenetic protein (BMP) plays an important role in bone formation and osteoblast differentiation by stimulating ALP activity and synthesis of proteoglycan, type I collagen, fibronectin and osteocalcin (An et al., 2016), and BMP-2 is an important growth factor that promotes the differentiation of BMSCs into osteoblasts and further boosts the osseointegration one of them. Therefore, nano-topographic surface modification serves to upregulate the expression of relevant osteogenic genes and enhance bone regeneration in both early and late stages of osteoblast differentiation and bone formation.

3.6 Capacity of new bone formation *In Vivo*

Micro-CT indicated that both groups of porous tantalum scaffolds at two time points were well integrated with the surrounding bone without infection or bone resorption, and the restorations did not dislodge and shift. The 3D reconstructed image of the cylindrical implant of the bone defect is shown in Figure 5A, which is approximately 2 mm high and 6 mm in diameter, from which it can be visualized that the amount of new bone around the restorations increased obviously with time. Afterwards, the volumes of the tissue area and bone tissue in this region were quantitatively analyzed for each material, and the bone volume fraction of each material showed that at both the third and sixth week, the amount of new bone production was significantly higher in the Ta-nano group than in the Ta-3D group, as shown in Figure 5A.

There was new bone formation around the material in both the Ta-3D and Ta-nano groups according to the fluorescence labeling results, where the width, brightness and fluorescence distribution area of the fluorescence strip around the restoration scaffold in the Ta-nano group were better than those in the Ta-3D group, which proved that there was more new bone formation (Figure 5B).

VG staining of histological sections at 3 and 6 weeks of restoration implantation (Figure 5C) showed that new bone production was already visible within the porous tantalum scaffold 3 weeks after the defect repair, while more bone production within the porous scaffold in the Ta-nano group. As the healing period was extended to 6 weeks, the amount of newly formed bone within the material increased significantly in both groups, and the nano-modified group remained superior to the unprocessed Ta-3D group. Histomorphometric analysis further confirmed the histological observations, showing a higher percentage of osteogenic area in the Ta-nano group at both time points.

Moreover, more new bone growth into the porous tantalum scaffold in the nano-topographic surface modified group was observed from the calcium xanthophyll-alizarin red double fluorescent labeling and Van Gieson staining experiments of rabbit mandibular defect implantation. Calcein and alizarin red were injected at 2/4 weeks postoperatively, and green and red fluorescence were observed in samples reared for 3 and 6 weeks, indicating that new bone production had already started at 2 weeks postoperatively.

In summary, the interface between cells and nanomaterials plays an important role in the physiological function of cells. Therefore, nano modification of the material surface to simulate natural bone structure and biological environment effectively enhances the osteogenic ability.

4 Conclusion

The 3D-printed porous tantalum scaffolds with microporous-like nano-topographic surface were prepared by alkali heat and water heat treatment. According to the cellular experiments, the nano-topographic surface modification by 3D printing enhances the adhesion and osteogenic differentiation of bone marrow mesenchymal stem cells. The *in vivo* experiments demonstrated that nano-topographic surface modification of 3D-printed prosthesis facilitates early and rapid osseointegration. A preliminary experimental validation was conducted for the application of nano-topographic surface modified porous tantalum prosthesis in the repair of bone defects in the jaws, which provides a theoretical and experimental basis for further clinical applications subsequently.

Data availability statement

The raw data supporting the conclusion of this article will be made available by the authors, without undue reservation.

Ethics statement

The animal study was approved by Shanghai Ninth People's Hospital. The study was conducted in accordance with the local legislation and institutional requirements.

Author contributions

CZ: Formal analysis, Investigation, Methodology, Visualization, Writing–original draft. ZZ: Methodology, Writing–original draft, Conceptualization, Resources. NL: Methodology, Writing–original draft. JC: Methodology, Writing–original draft. JW: Formal analysis, Resources, Writing–review and editing. YZ: Writing–review and editing, Supervision. KL: Conceptualization, Resources, Supervision, Writing–review and editing, Validation. SZ: Conceptualization,

Resources, Supervision, Writing–review and editing, Project administration.

The reviewer XZ declared a shared affiliation with the authors to the handling editor at the time of review.

Funding

This work was supported by the Fundamental Research Funds for the Central Universities (YG2023LC05), the National Clinical Research Center for Oral Diseases (NCRCO202106), and Shanghai Science and Technology Committee (20S31902200 and 20XD1433400), Shanghai Ninth People's Hospital, Shanghai Jiao Tong University School of Medicine (JS22A03).

Conflict of interest

The authors declare that the research was conducted in the absence of any commercial or financial relationships that could be construed as a potential conflict of interest.

Publisher's note

Supplementary material

The Supplementary Material for this article can be found online at: https://www.frontiersin.org/articles/10.3389/fbioe.2023.1258030/full#supplementary-material

References

An, J., Yang, H., Zhang, Q., Liu, C., Zhao, J., Zhang, L., et al. (2016). Natural products for treatment of osteoporosis: the effects and mechanisms on promoting osteoblast-mediated bone formation. *Life Sci.* 147, 46–58. doi:10.1016/j.lfs.2016.01.024

Anselme, K., Ponche, A., and Bigerelle, M. (2010). Relative influence of surface topography and surface chemistry on cell response to bone implant materials. Part 2: biological aspects. *Proc. Inst. Mech. Eng. Part H. J. Eng. Med.* 224, 1487–1507. doi:10.1243/09544119JEIM901

Assoian, R. K., and Klein, E. A. (2008). Growth control by intracellular tension and extracellular stiffness. *Trends Cell Biol.* 18, 347–352. doi:10.1016/j.tcb.2008.05.002

Babuska, V., Kasi, P. B., Chocholata, P., Wiesnerova, L., Dvorakova, J., Vrzakova, R., et al. (2022). Nanomaterials in bone regeneration. *Appl. Sci.* 12, 6793. doi:10.3390/app12136793

Balcerzak, M., Hamade, E., Zhang, L., Pikula, S., Azzar, G., Radisson, J., et al. (2003). The roles of annexins and alkaline phosphatase in mineralization process. *Acta Biochim. Pol.* 50, 1019–1038. doi:10.18388/abp.2003_3629

Bell, R. B. (2010). Computer planning and intraoperative navigation in cranio-maxillofacial surgery. *Oral Maxillofac. Surg. Clin. North Am.* 22, 135–156. doi:10.1016/j.coms.2009.10.010

Bremner, I., and Beattie, J. H. (1995). Copper and zinc metabolism in health and disease: speciation and interactions. *Proc. Nutr. Soc.* 54, 489–499. doi:10.1079/pns19950017

Fan, H., Deng, S., Tang, W., Muheremu, A., Wu, X., He, P., et al. (2021). Highly porous 3D printed tantalum scaffolds have better biomechanical and microstructural properties than titanium scaffolds. *Biomed. Res. Int.* 2021, 1–8. doi:10.1155/2021/2899043

Farley, J. R., Hall, S. L., Tanner, M. A., and Wergedal, J. E. (1994). Specific activity of skeletal alkaline phosphatase in human osteoblast-line cells regulated by phosphate, phosphate esters, and phosphate analogs and release of alkaline phosphatase activity inversely regulated by calcium. *J. Bone Min. Res.* 9, 497–508. doi:10.1002/jbmr.5650090409

Ghezzi, B., Lagonegro, P., Attolini, G., Rotonda, P. M., Cornelissen, C., Ponraj, J. S., et al. (2021). Hydrogen plasma treatment confers enhanced bioactivity to silicon carbide-based nanowires promoting osteoblast adhesion. *Mat. Sci. Eng. C. Mat. Biol. Appl.* 121, 111772. doi:10.1016/j.msec.2020.111772

Gordon, J. A. R., Tye, C. E., Sampaio, A. V., Underhill, T. M., Hunter, G. K., and Goldberg, H. A. (2007). Bone sialoprotein expression enhances osteoblast differentiation and matrix mineralization *in vitro*. *Bone* 41, 462–473. doi:10.1016/j.bone.2007.04.191

Gundu, S., Varshney, N., Sahi, A. K., and Mahto, S. K. (2022). Recent developments of biomaterial scaffolds and regenerative approaches for craniomaxillofacial bone tissue engineering. *J. Polym. Res.* 29, 73. doi:10.1007/s10965-022-02928-4

Huang, B., Yuan, Y., Li, T., Ding, S., Zhang, W., Gu, Y., et al. (2016). Facilitated receptor-recognition and enhanced bioactivity of bone morphogenetic protein-2 on magnesium-substituted hydroxyapatite surface. *Sci. Rep.* 6, 24323. doi:10.1038/srep24323

Huang, G., Pan, S. T., and Qiu, J. X. (2022). The osteogenic effects of porous Tantalum and Titanium alloy scaffolds with different unit cell structure. *Colloids Surfaces B Biointerfaces* 210, 112229. doi:10.1016/j.colsurfb.2021.112229

Jardini, A. L., Larosa, M. A., Filho, R. M., Zavaglia, C. A. D. C., Bernardes, L. F., Lambert, C. S., et al. (2014). Cranial reconstruction: 3D biomodel and custom-built implant created using additive manufacturing. *J. Cranio-Maxillofacial Surg.* 42, 1877–1884. doi:10.1016/j.jcms.2014.07.006

Jones, N. (2012). Science in three dimensions: the print revolution. *Nature* 487, 22–23. doi:10.1038/487022a

Kim, H. S., Kim, Y. J., Jang, J. H., and Park, J. W. (2016a). Surface engineering of nanostructured titanium implants with bioactive ions. *J. Dent. Res.* 95, 558–565. doi:10.1177/0022034516638026

Kim, J.-W., Kim, D.-Y., Ahn, K.-M., and Lee, J.-H. (2016b). Surgical implications of anatomical variation in anterolateral thigh flaps for the reconstruction of oral and maxillofacial soft tissue defects: focus on perforators and pedicles. *J. Korean Assoc. Oral Maxillofac. Surg.* 42, 265. doi:10.5125/jkaoms.2016.42.5.265

Li, M., Yin, S., Lin, M., Chen, X., Pan, Y., Peng, Y., et al. (2022). Current status and prospects of metal-organic frameworks for bone therapy and bone repair. *J. Mat. Chem. B* 10, 5105–5128. doi:10.1039/d2tb00742h

Manivasagam, V. K., Perumal, G., Arora, H. S., and Popat, K. C. (2022). Enhanced antibacterial properties on superhydrophobic micro-nano structured titanium surface. *J. Biomed. Mat. Res. - Part A* 110, 1314–1328. doi:10.1002/jbm.a.37375

Manju, V., Anitha, A., Menon, D., Iyer, S., Nair, S. V., and Nair, M. B. (2018). Nanofibrous yarn reinforced HA-gelatin composite scaffolds promote bone formation in critical sized alveolar defects in rabbit model. *Biomed. Mat.* 13, 065011. doi:10.1088/1748-605X/aadf99

Miyazaki, T., Kim, H. M., Miyaji, F., Kokubo, T., Kato, H., and Nakamura, T. (2000). Bioactive tantalum metal prepared by NaOH treatment. *J. Biomed. Mat. Res.* 50, 35–42. doi:10.1002/(sici)1097-4636(200004)50:1<35:aid-jbm6>3.0.co;2-8

Miyoshi, H., and Adachi, T. (2014). Topography design concept of a tissue engineering scaffold for controlling cell function and fate through actin cytoskeletal modulation. *Tissue Eng. Part b. Rev.* 20, 609–627. doi:10.1089/ten.TEB.2013.0728

Mizuno, M., and Kuboki, Y. (2001). Osteoblast-related gene expression of bone marrow cells during the osteoblastic differentiation induced by type I collagen. *J. Biochem.* 129, 133–138. doi:10.1093/oxfordjournals.jbchem.a002824

Oh, J. (2018). Recent advances in the reconstruction of cranio-maxillofacial defects using computer-aided design/computer-aided manufacturing. *Maxillofac. Plast. Reconstr. Surg.* 40, 2. doi:10.1186/s40902-018-0141-9

Ponche, A., Bigerelle, M., and Anselme, K. (2010). Relative influence of surface topography and surface chemistry on cell response to bone implant materials. Part 1: physico-chemical effects. *Proc. Inst. Mech. Eng. Part H. J. Eng. Med.* 224, 1471–1486. doi:10.1243/09544119JEIM900

Rachmiel, A., Shilo, D., Blanc, O., and Emodi, O. (2017). Reconstruction of complex mandibular defects using integrated dental custom-made titanium implants. *Br. J. Oral Maxillofac. Surg.* 55, 425–427. doi:10.1016/j.bjoms.2017.01.006

Rudman, K., Hoekzema, C., and Rhee, J. (2011). Computer-assisted innovations in craniofacial surgery. *Facial Plast. Surg.* 27, 358–365. doi:10.1055/s-0031-1283054

Schildhauer, T. A., Robie, B., Muhr, G., and Köller, M. (2006). Bacterial adherence to tantalum versus commonly used orthopedic metallic implant materials. *J. Orthop. Trauma* 20, 476–484. doi:10.1097/00005131-200608000-00005

Schmitz, J. P., and Hollinger, J. O. (1986). The critical size defect as an experimental model for craniomandibulofacial nonunions. *Clin. Orthop. Relat. Res.* 205, 299–308. doi:10.1097/00003086-198604000-00036

Seok, H., Kim, M.-K., and Kim, S.-G. (2016). Reconstruction of partial maxillectomy defect with a buccal fat pad flap and application of 4-hexylresorcinol: a case report. *J. Korean Assoc. Oral Maxillofac. Surg.* 42, 370. doi:10.5125/jkaoms.2016.42.6.370

Siebers, M. C., Ter Brugge, P. J., Walboomers, X. F., and Jansen, J. A. (2005). Integrins as linker proteins between osteoblasts and bone replacing materials. A critical review. *Biomaterials* 26, 137–146. doi:10.1016/j.biomaterials.2004.02.021

Stein, G. S., Lian, J. B., and Owen, T. A. (1990). Relationship of cell growth to the regulation of tissue-specific gene expression during osteoblast differentiation. *FASEB J.* 4, 3111–3123. doi:10.1096/fasebj.4.13.2210157

Su, Z., Zhang, J., Tan, P., Zhu, S., and Jiang, N. (2022). Selective polyetheretherketone implants combined with graphene cause definitive cell adhesion and osteogenic differentiation. *Int. J. Nanomedicine* 17, 5327–5338. doi:10.2147/ijn.s380345

Vitte, J., Benoliel, A. M., Pierres, A., Bongrand, P., and Curtis, A. S. G. (2004). Is there a predictable relationship between surface physical-chemical properties and cell behaviour at the interface? *Eur. Cells Mat.* 7, 52–63. doi:10.22203/eCM.v007a06

Walmsley, G. G., McArdle, A., Tevlin, R., Momeni, A., Atashroo, D., Hu, M. S., et al. (2015). Nanotechnology in bone tissue engineering. *Nanomedicine Nanotechnol. Biol. Med.* 11, 1253–1263. doi:10.1016/j.nano.2015.02.013

Wang, H., Zhang, X., Wang, H., Zhang, J., Li, J., Ruan, C., et al. (2018). Enhancing the osteogenic differentiation and rapid osseointegration of 3D printed Ti6Al4V implants via nano-topographic modification. *J. Biomed. Nanotechnol.* 14, 707–715. doi:10.1166/jbn.2018.2551

Webster, T. J., Ergun, C., Doremus, R. H., Siegel, R. W., and Bizios, R. (2000). Specific proteins mediate enhanced osteoblast adhesion on nanophase ceramics. *J. Biomed. Mat. Res.* 51, 475–483. doi:10.1002/1097-4636(20000905)51:3<475:aid-jbm23>3.0.co;2-9

Zhang, T., Gao, Y., Cui, W., Li, Y., Xiao, D., and Zhou, R. (2020). Nanomaterials-based cell osteogenic differentiation and bone regeneration. *Curr. Stem Cell Res. Ther.* 16, 36–47. doi:10.2174/1574888x15666200521083834

Zhu, M., Ye, H., Fang, J., Zhong, C., Yao, J., Park, J., et al. (2019). Engineering high-resolution micropatterns directly onto titanium with optimized contact guidance to promote osteogenic differentiation and bone regeneration. *ACS Appl. Mat. Interfaces* 11, 43888–43901. doi:10.1021/acsami.9b16050

frontiers | Frontiers in Bioengineering and Biotechnology

TYPE Review
PUBLISHED 27 September 2023
DOI 10.3389/fbioe.2023.1267128

OPEN ACCESS

EDITED BY
Xing Wang,
Shanxi Medical University, China

REVIEWED BY
María Coronada Fernández Calderón,
Biomaterials and Nanomedicine (CIBER-BBN), Spain
Kui Xu,
Anhui University of Chinese Medicine, China

*CORRESPONDENCE
Shunli Chu,
chusl@jlu.edu.cn

RECEIVED 26 July 2023
ACCEPTED 14 September 2023
PUBLISHED 27 September 2023

CITATION
Zhai S, Tian Y, Shi X, Liu Y, You J, Yang Z, Wu Y and Chu S (2023), Overview of strategies to improve the antibacterial property of dental implants.
Front. Bioeng. Biotechnol. 11:1267128.
doi: 10.3389/fbioe.2023.1267128

Overview of strategies to improve the antibacterial property of dental implants

Shaobo Zhai, Ye Tian, Xiaolu Shi, Yang Liu, Jiaqian You, Zheng Yang, Yuchuan Wu and Shunli Chu*

Jilin Provincial Key Laboratory of Tooth Development and Bone Remodeling, Hospital of Stomatology, Jilin University, Changchun, China

The increasing number of peri-implant diseases and the unsatisfactory results of conventional treatment are causing great concern to patients and medical staff. The effective removal of plaque which is one of the key causes of peri-implant disease from the surface of implants has become one of the main problems to be solved urgently in the field of peri-implant disease prevention and treatment. In recent years, with the advancement of materials science and pharmacology, a lot of research has been conducted to enhance the implant antimicrobial properties, including the addition of antimicrobial coatings on the implant surface, the adjustment of implant surface topography, and the development of new implant materials, and significant progress has been made in various aspects. Antimicrobial materials have shown promising applications in the prevention of peri-implant diseases, but meanwhile, there are some shortcomings, which leads to the lack of clinical widespread use of antimicrobial materials. This paper summarizes the research on antimicrobial materials applied to implants in recent years and presents an outlook on the future development.

KEYWORDS

dental implant, antibacterial property, surface modification, coatings, surface topography

1 Introduction

With the development of implant materials and technologies, dental implants have become the choice of more and more patients with missing teeth as they can not only better meet the aesthetic requirements without damaging the adjacent teeth, but also maintain a high success rate while maximizing the restoration the patient's masticatory function. In recent years, the number of dental implants worldwide has increased exponentially, and the global implant market is expected to reach $13.01 billion by 2023 (Alghamdi and Jansen, 2020). However, with the popularity of dental implants, the number of those who suffer from peri-implant diseases is also increasing, causing a great deal of distress to patients and doctors. Peri-implant disease is defined as inflammatory damage that occurs in the soft and hard tissues surrounding the dental implants, including peri-implant mucositis and peri-implantitis. A recent study reported that dental implants have a 10-year survival rate of 96.4% (Howe et al., 2019). However, 54.7% of patients suffer from peri-implant mucositis and 22.1% of patients suffer from peri-implantitis during an average of 23.3 years after receiving dental implants treatment (Renvert et al., 2018). Another study showed that 47% of implant treatment failures are related to peri-implantitis (Amer and Sukumaran, 2021). So peri-implant diseases largely determine whether the implant treatment can be successful.

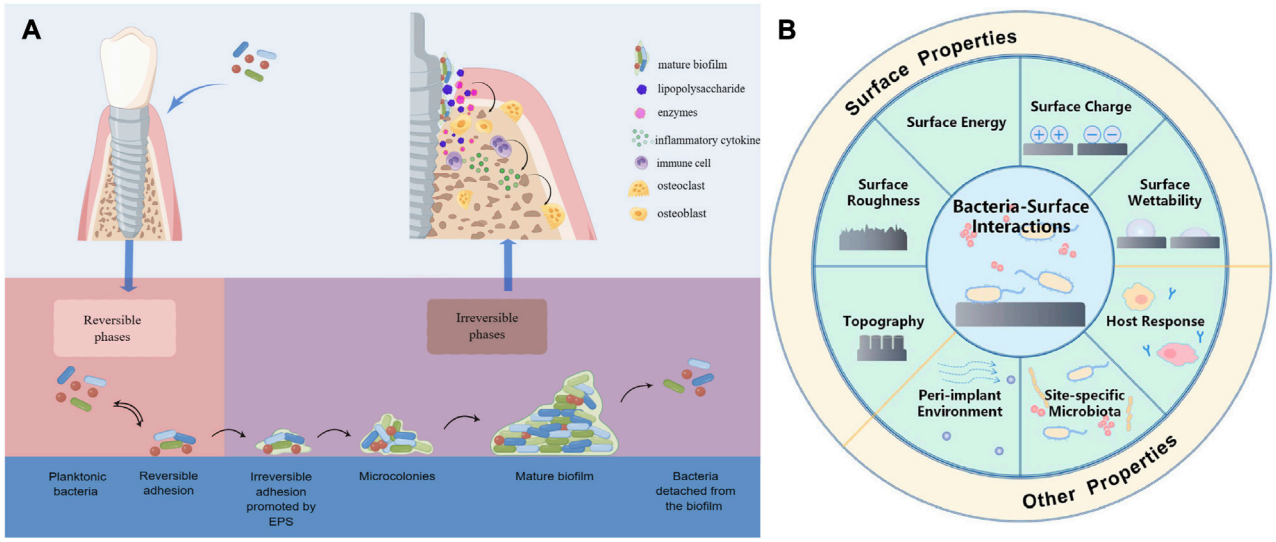

FIGURE 1
(A) Schematic presentation of biofilm formation process and bacteria secreting lipopolysaccharides and enzymes that act on osteoblasts and immune cells to cause them to secrete inflammatory factors that promote osteoclast formation, leading to bone resorption. **(B)** Schematic presentation of the various factors affecting bacterial adhesion. Reproduced with permission from (Ma et al., 2022). Copyright (2022) Frontiers Media.

Peri-implantitis is a pathological condition that occurs in the supporting tissues around dental implants and is characterized by peri-implant mucosal inflammation and progressive supporting bone loss, which, combined with its early onset and non-linear and accelerated pattern of progression, can eventually lead to the failure of dental implants without intervention and treatment (Fu and Wang, 2020). It is well known that plaque colonized on the implant is the initial factor of peri-implantitis and that microorganisms have a significant role in the occurrence and progression of peri-implantitis through formation of biofilm. After the implant surface is exposed to the oral environment, bacteria begin to adhere and colonize to the conditional film formed by salivary components on the surface of the implant and form a biofilm (Chen et al., 2021; Ardhani et al., 2022). The maturation of the biofilm undergoes the following phases: (1) cells reversibly attach to the surface; (2) extracellular polymeric substance (EPS) secreted by cells promote the irreversible attachment to the surface; (3) cells that attach to the surface replicate and form microcolonies of tens to hundreds of micrometers; (4) with the replication of cells and the accumulation of EPS, mature biofilms with three-dimensional structures are formed; (5) some cells detach from the biofilm and disperse into the surrounding liquid environment, absorbing on the surface and generating new biofilm (Renner and Weibel, 2011) (Figure 1A). After biofilm is formed, it is difficult for us to remove it by conventional methods because the bacteria in the biofilm have stronger resistance to the body's defense mechanisms as well as to antimicrobial drugs compared planktonic bacteria (Del Pozo, 2018). Therefore, therapeutic approaches that intervene bacterial adhesion and biofilm formation are expected to be one of the effective ways to prevent peri-implant diseases in the future.

There are many factors that influence the interaction between bacteria and the surface, including the bacteria associated factors, the surface properties of the materials, and environmental factors (Figure 1B). Surface modification of the implant is one of the effective ways to reduce bacterial adhesion, and the surface properties of the implant are critical to the adhesion of the tissue as well as the formation of biofilm. Bacteria are able to perceive chemical signals and surface-associated mechanical signals, according to research conducted *in vivo* and *in vitro*, so different implant surface properties can have different effects on bacterial adhesion, physiology, and formation of biofilm (Renner and Weibel, 2011; Bermejo et al., 2019). For example, *Streptococcus* salivarius (S. salivarius) is specifically bound to the tongue but not to the teeth by microvilli structures on the tongue surface, whereas the binding site of *Streptococcus* mutans (S. mutans) is opposite to that of S. salivarius (Beachey, 1981). The majority of oral implant materials are presently constructed of pure titanium (Ti) and titanium alloys (Ti_6Al_4V), as the metal Ti have a range of desirable qualities, including good biocompatibility, corrosion resistance, and osseointegration ability (Delgado-Ruiz and Romanos, 2018). However, the conventional Ti implants that are utilized in clinical practice lack excellent antibacterial properties, and in recent years, researchers have been working to develop new implant materials with better antibacterial properties, such as Zirconia, alloys, *etc.*, or by changing the surface properties of the implant to obtain better antimicrobial properties, such as surface topography (surface roughness, contour shape, *etc.*), chemical composition, surface wettability, surface energy, surface charge, *etc.* This paper presents a comprehensive summary of the research on implant surface modification and antimicrobial materials used to enhance the antibacterial properties of implants in recent years to provide a theoretical basis for future prevention of peri-implant diseases.

2 Antimicrobial coatings

Researchers have made extensive research on the addition of coatings with antimicrobial properties on the surface of implants to

resist bacterial adhesion, colonization, migration, and biofilm formation. The coatings commonly used to enhance the antimicrobial properties of implant surfaces include some metallic elements, antibiotics, antimicrobial peptides, chlorhexidine, synthetic polymers and so on.

2.1 Metal elements

Some metallic materials have excellent antimicrobial activity and are widely used for enhancing the antimicrobial properties of implant surfaces. The most commonly used metallic materials are silver, copper and zinc.

As the most potent antimicrobial metal element, silver (Ag) has broad-spectrum antibacterial properties and little toxicity to human beings (Lampé et al., 2019). It can provide anti-microbial action both in Ag^+ form and through directly "contact killing". The antimicrobial power of Ag is mainly expressed by the form of Ag^+. Ag^+ is able to enter the cytoplasm of bacteria and exert its antimicrobial action by interfering with the function of a variety of proteins and enzymes and restraining the synthesis of nucleic acids and proteins, leading to bacterial death, and Ag nanomaterials also function as antimicrobials by releasing Ag^+ (Eliaz and Metoki, 2017; Wei et al., 2020; Liu et al., 2023). Another significant mechanism by which Ag kills bacteria is direct contact killing. Ag disrupts bacterial cell walls and cytoplasm membranes through contact with bacteria, which results in leakage of cytoplasmic and essential cellular substances and ultimately leads to the death of bacteria (Bui et al., 2019). In addition, Ag nanoparticles (Ag NPs) are able to provide stimulation of soft tissue integration and osteogenesis, which makes them a desirable choice for surface modification of dental implants. A study showed that nano-Ag coating prepared on pure Ti using microwave-assisted synthesis significantly inhibited the aggregation of *S. aureus* (*Staphylococcus aureus*) on the surface (CFUs of on nano-Ag-coated Ti disks and control Ti disks are 30 ± 15.1 and 168.3 ± 32.9, respectively), *in vivo* and *In vitro*, they exhibited good antibacterial properties and no significant cytotoxic effects were observed (Odatsu et al., 2020). Li et al. prepared a time-dependent and self-adjusting antimicrobial coating by incorporating Ag nanoparticles as antibacterial agents deeply into the bottom of TiO_2 NTs prepared on pure Ti surface through centrifuge. The Ag NPs can automatically convert to an immobile state from the free state, in the early phase, the coating released Ag ions exhibiting strong "release bactericidal" activity, and gradually changed to "contact bactericidal" activity. This special design meets the antimicrobial requirements of the implant at different times after implantation and effectively resists both planktonic and immobilized bacteria (Li B. et al., 2019). Ag has excellent antimicrobial properties, but the extensive use of silver antimicrobial agents and the increasing resistance of bacteria have led to the emergence of silver-resistant bacteria. There are several reports on bacterial antimicrobial resistance to ionic Ag, and it is generally believed that bacteria resist the antimicrobial effect by eliminating Ag(I) through efflux pumps or by reducing it to less toxic Ag (0) oxidation state. There are fewer studies on bacterial resistance to AgNPs. There is no definite conclusion on the mechanism of its resistance, and some scholars believe that its resistance originates from the production of flagellin, which can lead to the aggregation of AgNPs, thus eliminating its antibacterial effect (Stabryla et al., 2021). Some scholars believe that its resistance is not related to the aggregation of AgNPs, and its resistance mechanism may be enhanced or mediated by flagellum-based motility (Panáček et al., 2018). However, it is certain that bacteria repeatedly exposed to sub-inhibitory concentrations of AgNPs can acquire stable resistance. In addition, there are concerns about toxicity due to the accumulation of metal ions, and more research is needed to identify the optimal Ag concentration required to kill bacteria and the mechanisms by which bacteria develop resistance, in order to rationalize the use of Ag antimicrobials and reduce the development of resistance.

Copper (Cu) is an essential trace element for human body with well recognized antibacterial and antiviral properties, capable of inactivating a wide range of bacteria and viruses, such as *S. aureus*, *E. coli* (*Escherichia coli*), SARS-CoV-2, influenza, *etc.* (Li et al., 2016; Aissou et al., 2023), and Cu NPs also have osteogenic and angiogenic properties (Burghardt et al., 2015). Compared to Ag, this metal is cheaper and more readily available, providing an effective antimicrobial effect over a wider range of temperatures and humidity, and also has “contact killing” mechanism. Cu induces the production of reactive oxygen species (ROS) through Fenton-like reactions, which result in damage to lipids, proteins, DNA, and cell membranes. Cu ions can enter bacteria through membrane channels and repress the synthesis of relevant enzymes and activity of bacterial DNA and interfere with the metabolism of bacteria (Figure 2). Cu nanoparticles (CuNPs) in Ti implants could release Cu ions to suppress the activity of bacteria (Wang et al., 2019; Aissou et al., 2023). Jannesari et al. have demonstrated that Cu ions and its superoxide can exert excellent antibacterial properties by suppressing the respiration of bacteria and causing DNA breakdown (Jannesari et al., 2020). Moreover, Cu has also been found to be the most effective metal to prevent the biofilm formation of *E. coli*, *S. aureus*, *P. aeruginosa* (*Pseudomonas aeruginosa*), etc (Gugala et al., 2017). Xia et al. reported the modification of Ti implants by co-implantation of C/Cu nanoparticles using plasma immersion ion implantation and deposition (PIIID) technique. While showing excellent corrosion resistance and mechanical properties, the antimicrobial properties of the modified implants were significantly enhanced, with the C/Cu-Ti surfaces achieving 90% and 100% inhibition against *S. aureus* and *E. coli*, respectively (Xia et al., 2020). van Hengel et al. used plasma electrolytic oxidation (PEO) to incorporate different proportions of Cu and/or Ag NPs into Ti dioxide layer prepared on Ti-6Al-4V surface. The modified implants exhibited strong antimicrobial activity, and in an *ex vivo* model using murine femora, all bacteria were eradicated by the functionalized implants with 25% Cu and 75% Ag NPs, and the implants containing just Cu NPs enhanced the metabolic activity of pre-osteoblastic MC3T3-E1 cells (van Hengel et al., 2020). Peri-implantitis induces ROS production, and the accumulation of excess ROS disrupts redox microenvironmental balance, inducing biofilm formation and immune disorders. Cu^{2+} induces ROS production while killing bacteria, further exacerbating redox imbalance and immune disorders, and ultimately impeding infection clearance and tissue repair, which is a cause for our concern. With this consideration, Xu et al. designed a luteolin (LUT)-loaded copper (Cu^{2+})-doped hollow mesoporous organosilica nanoparticle system (Lut@Cu-HN), which utilized LUT to scavenge excess ROS to prevent Cu^{2+} from exacerbating the redox imbalance and

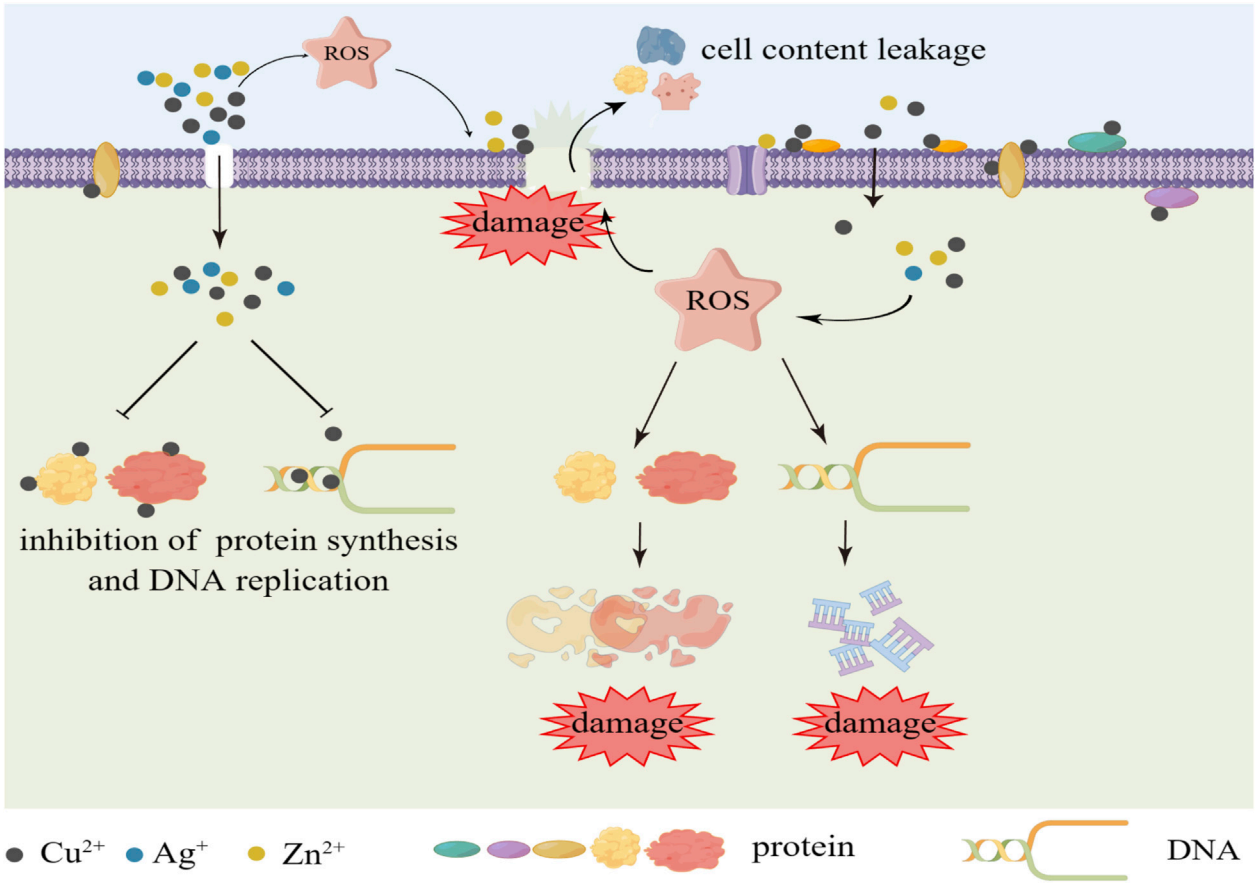

FIGURE 2
Schematic presentation of the bactericidal mechanism of Cu ion, Ag ion and Zn ion.

reducing the immunotoxicity of Cu^{2+}, and showed excellent antimicrobial and immunomodulatory activities in in vitro and *in vivo* experiments (Xu et al., 2023). Therefore, while focusing on the bactericidal effect, we should also pay more attention to the balance of the microenvironment around the implant and the regulation of immune homeostasis.

Zinc (Zn), as an essential trace element, also has desirable antimicrobial properties and has been widely applied in oral treatment as an effective antibacterial agent. Although its antibacterial activity is weaker than that of Ag and Cu, it has many advantages as an antibacterial agent, such as high safety, low side effects, and long-lasting antibacterial effect. Zn ions can interact with cell membranes, disrupt bacterial cell membranes and intracellular proteins, inhibit the activity of related enzymes, and produce multiple antibacterial effects on bacteria (Li et al., 2013; Almoudi et al., 2018). The antimicrobial mechanisms of Zn oxide include photocatalytic antibacterial mechanism and contact sterilization mechanisms causing surface damage to bacteria by interacting with the bacterial membrane, as well as inducing the production of ROS, which ultimately results in death of bacteria (Xie et al., 2011; Liu W. et al., 2014; Memarzadeh et al., 2015). In addition, Zn can affect the function of osteoclasts and osteoblasts, reducing bone resorption and promoting bone formation (He et al., 2023). Zhang et al. prepared a macroporous Ti dioxide coating by micro-arc oxidation (MAO), and introduced Zn into the modified Ti surface by hydrothermal treatment to prepare a novel TiO_2/ZnO micro/nanostructured coating, followed by a simple heat treatment to improve its cytocompatibility, and the Zn-doped TiO_2 coating exhibited a powerful inhibitory ability against *S. aureus*, which could reach an antibacterial rate of 96.1% ± 3.3% (Zhang et al., 2018). However, efficient antimicrobial activity is usually accompanied by cytotoxicity, and enriched Zn^{2+} on the surface can also be detrimental to angiogenic and osteogenic on the implant surface. Therefore, a balance between antibiotic activity accompanied by a certain degree of cytotoxicity and angiogenic and osteogenic needs to be achieved. Wang et al. applied Ti plasma immersion ion implantation (Ti-PIII) to modify carbon fiber reinforced polyetheretherketone (CFRPEEK), then hybrid polydopamine (PDA) @ZnO NPs was modified onto CFRPEEK via PDA-assisting covalent immobilization, and pro-angiogenic Endothelin-1 (EDN1) was further doped onto the surface to balance the adverse effects of antimicrobials on osteointegration. *In vitro* and *in vivo* experiments showed that the modified surface exhibited excellent bactericidal ability against *S. aureus* and *E. coli*, while effectively promoting angiogenesis and osteogenesi (Wang X. et al., 2023).

In addition to Ag, Cu, and Zn, metallic elements such as cerium, gallium, zirconium, and bismuth have also been explored for surface

modification of implants. Some non-metallic materials such as fluorine, silicon, graphene, and hydroxyapatite have also been explored as antimicrobial materials or carriers of antimicrobial materials to improve the antimicrobial properties of implants. Koopaie et al. demonstrated that the addition of zirconium, silicon, and fluorine to the surface of SLA-treated γ-TiAl significantly improved its antimicrobial activity against Actinobacillus actinomycetemcomitans (AA), Eikenella corrodens (EC) (Koopaie et al., 2020). Jang et al. also demonstrated that graphene oxide coating deposited on zirconium oxide surface significantly inhibited the adhesion and biofilm formation of S. mutans (Jang et al., 2021). While each antibacterial agent or element presents its distinctive antibacterial properties, it also has its strengths and weaknesses. For example, Ag NPs may cause cytotoxicity by producing ROS, releasing free Ag + ions, transporting across the blood-brain barrier, and inflammation (Noronha et al., 2017), the aggregation of Zn could induce mammalian cells cytotoxicity, and ZnO NPs may lead to damage of DNA and apoptosis or necrosis of cells (Kononenko et al., 2017). The toxicity can be reduced by decreasing the dose of the corresponding metal ion, and in addition, the use of multiple antibacterial agents or elements in combination has been explored in order to achieve the desirable antibacterial effect, as well as excellent osteogenic properties and biocompatibility. Li et al. simultaneously implanted different ratios of Zn and Ag ions into titanium nitride (TiN) on Ti alloy surface by plasma immersion ion implantation (PIII) system and obtained good antibacterial ability while the inhibitory effect of adhesion and proliferation of fibroblast-like cells by Ag was compensated as the ratio of Zn increased (Li L. et al., 2019). Therefore, the use of a variety of antimicrobial agents to exert synergistic antimicrobial effects, improve the biocompatibility of surface, and develop better drug controlled release system may be one of the important development directions in the future.

2.2 Polymers

Polymeric layers have attracted much attention for antibacterial properties and the enhancement of bioactivity and effective control of potent drugs release, and different polymers have been used by researchers as surface coatings for implants to improve their antibacterial properties. Some polymers can produce coatings on the surface of implants that prevent bacterial adhesion, called antifouling polymers. These polymer coatings, which reduce the adhesion of proteins and bacteria rather than directly killing the bacteria in contact, include mainly hydrophilic and amphoteric polymers. These two polymers can provide antifouling effects by creating a hydrated layer on the surface to prevent adsorption of proteins. The antiadhesion capacity of the surface modified by polymers varies with the length of the chains, the inherent characteristics of the polymer, and the homogeneity and density of the polymer (Liu L. et al., 2014; Chen et al., 2021). The hydrophilic polymer polyethylene glycol (PEG), as one of the most widely used polymers, is often used for surface modification of implants because of its good antifouling properties, and its hydrophilic, flexible chains are essential to prevent protein and bacterial adhesion (Mas-Moruno et al., 2019; Pranjali et al., 2019; Buwalda et al., 2020). Skovdal et al. developed an ultra-dense poly(ethylene glycol) (udPEG) coating that was applied to Ti surfaces and demonstrated that the coating substantially reduced the adhesion of *Staphylococcus* epidermidis (S. epidermidis) both *in vivo* and *in vitro* and increased the efficacy of vancomycin. In a mice model, the coating effectively improved the therapeutic outcome of implant-associated infections in mice (Skovdal et al., 2018). Nishida et al. prepared a polymer coating containing the zwitterionic monomer, carboxymethyl betaine (CMB), on the Ti alloy surface, and the modified Ti alloy showed great potential as an implant surface modification material by strongly inhibiting protein adsorption and doubling the amount of calcium deposition (Nishida et al., 2017). Although the anti-adhesive property of PEG can favorably inhibit the adhesion of bacteria, it also reduces the tissue cells adhesion on the implant surface, which is detrimental for implant to integrate with the surrounding tissues, which can be addressed by the addition of RGD (one of the integrin-binding peptide sequences) (Mas-Moruno et al., 2019). Buxadera-Palomero et al. demonstrated by comparing three methods of preparing PEG coatings on Ti surfaces that the immobilization of RGD improved the adhesion of fibroblasts without affecting the adhesion inhibition of *Streptococcus* sanguinis (S. sanguinis) and *Lactobacillus* salivarius (L. salivarius) (Buxadera-Palomero et al., 2017).

In addition, there are polymers such as chitosan, polylactic acid, cellulose, and hydrogels that are often used as carriers of antimicrobial drugs and are used as modifying materials for implant surfaces. Chitosan, as a natural and sustainably sourced polysaccharide with antimicrobial properties that are effective against a wide range of target organisms and no toxicity, is widely used in tissue engineering, drug delivery and promoting healing. This may be related to the fact that chitosan bears cations that can interact with anions on the cell surface, inhibiting bacterial biosynthesis and interfering with their substance transport (Levengood and Zhang, 2014; Mishra et al., 2015; Palla-Rubio et al., 2019; Valverde et al., 2019; Rahayu et al., 2022). Chitin, chitosan are polymers with innate antimicrobial activities. Their abundance and multiple functional groups allow them to be modified to enhance their intrinsic antimicrobial activities. In addition, some polymers that are not antimicrobial have been functionalized with specific groups such as quaternary ammonium or guanidium groups and/or combined with Ag nanoparticles to produce antimicrobial properties (Haktaniyan and Bradley, 2022).

2.3 Antibiotics

Despite the proven disadvantages of antibiotics, such as microbial resistance, short drug duration of action, uncontrolled release and so on, they still have a significant role for management of infections, and applying antibiotics to implant surfaces is an effective strategy to improve their antimicrobial properties and reduce their side effects. For example, gentamicin (Baro et al., 2002; Laurent et al., 2008; Govindan and Girija, 2014; Diefenbeck et al., 2016; Albright et al., 2021; Nichol et al., 2021; Sang et al., 2021), vancomycin (Zhang L. et al., 2014), minocycline (Lv et al., 2014), tobramycin (Brohede et al., 2009; Zhou et al., 2018), amoxicillin, cefthiophene and other antibiotics have been explored to prepare an antibacterial coating.

He et al. constructed an antimicrobial coating composed of gentamicin (GS) and polyacrylic acid (PAA) by layer-by-layer assembly (LBL) technique. The modified Ti exhibited outstanding antibacterial activity against *S. aureus* and *E. coli* and the release of gentamicin was slow and sustained during 11 days following an initial burst release in the first 24 h (He et al., 2020). In a mouse experiment, Stavrakis et al. demonstrated that the release of vancomycin from the PEG-PPS polymer coating was in a controlled manner and that *S. aureus* in implants containing vancomycin was reduced 139-fold and local concentration of the drug remained above the lowest inhibitory concentration of bacteria for 7 days postoperatively (Stavrakis et al., 2019). Wongsuwan et al. successfully developed a minocycline-loaded niosomes coating by thin-film hydration, which was applied to the implant surface by layer-by-layer spraying, and the modified implants showed satisfactory antibacterial efficacy against Porphyromonas gingivalis (P. gingivalis) and the drug release was maintained for more than a week (Wongsuwan et al., 2020). The application of various new materials and technologies has shown promising applications by improving the antibacterial efficacy of antibiotics, extending the duration of drug action, and reducing the side effects associated with systemic administration, but there is no consensus on the best treatment modality for the prevention of peri-implant infections with antibiotic-laden coatings. In addition, there are concerns about toxicity and bacterial resistance, so further research is needed regarding their use in dental implants (Esteves et al., 2022).

2.4 Antimicrobial peptides

Antibiotics are prone to induce drug resistance, which greatly limits its application, the emergence of antimicrobial peptides (AMPs) has provided a new approach to solve this problem (Zhang E. et al., 2021). AMPs are a class of short amphiphilic peptides having broad-spectrum antimicrobial properties, which are positively charged and can bind negatively charged bacteria by electrostatic attraction and interact with their cell membranes, leading to bacterial death (Lozeau et al., 2018; Sun et al., 2018). Studies have shown that AMPs can also enter the cytoplasm to act on intracellular targets (DNA, RNA, proteins, etc.), killing bacteria from the inside and affecting gene expression (Geng et al., 2018; Wang and Tang, 2019). Because of their specific antibacterial mechanism, the bacteria are hardly to develop drug resistance. Researchers have used different methods to coat antimicrobial peptides on the implant surface to prevent bacterial colonization, such as adsorption, binding, electrospinning, and chemical binding (Garaicoa et al., 2020; Tiwari et al., 2021). Yazici et al. designed an engineered chimeric peptide that coated peptide Tet127 on the microporous calcium phosphate on the surface of Ti nanotubes by self-assembly, and implants with the coating significantly reduced the adhesion of S. mutans and *E. coli*, and showed good osteointegration properties (Yazici et al., 2019). Cheng et al. prepared a new composite coating on the surface of smooth Ti containing the antimicrobial peptide Nal-P-113 and graphene oxide, which exhibited slow and sustained drug release *in vitro* and showed good antimicrobial performance against both P. gingivalis and S. mutans with no significant cytotoxicity against human gingival fibroblasts (Cheng et al., 2022). In a recent study, Fischer et al. coimmobilized the laminin-derived peptide LamLG3 and the antimicrobial peptide GL13K on the Ti surface, which exhibited antibiofilm activity against *Streptococcus* gordonii (S. gordonii) and was able to promote hemidesmosome formation, proliferation, and mechanical attachment of orally derived keratinocytes, while having no significant effect on fibroblast proliferation, showing the potential to reduce dental implant infection and failure rate (Fischer et al., 2020). In addition, Nie et al. found that the immobilization of KR-12 peptide on Ti surface using PEG as spacer showed better bactericidal efficiency than the surface without spacer (Nie et al., 2017). Therefore suitable spacers, properties of AMPs such as density, flexibility, *etc.*, are factors to be considered when we further optimize the antimicrobial effect of AMP-functionalized surfaces. In addition, the view that bacteria are unlikely to have evolved resistance to AMPs is increasingly being questioned due to their inherent survival strategies and evolutionary pressure. The relatively short history of their use has also meant that their clinical use has been inadequate and the mechanisms of their resistance have been poorly studied. It is possible for bacteria to develop resistance through mechanisms such as inactivation of AMPs, restrict access to AMPs, removal of AMPs, biofilm formation, *etc.* However, there is a wide variety of AMPs, and their functions are highly specific and synergistic. Accordingly, the acquisition of resistance by pathogenic bacteria is subject to evolutionary constraints, such as functional compatibility and fitness trade-offs. Therefore, we should conduct more research on the mechanisms by which bacteria acquire resistance to AMPs and their evolutionary constraints, and find techniques to exploit these constraints, such as applying AMP cocktails to minimize the efficacy of resistance selection or incorporating nanomaterials to maximize the cost of AMP resistance (Chen et al., 2022).

2.5 Chlorhexidine and other organic coatings

As a widely used antibacterial drug, chlorhexidine (CHX) has excellent antibacterial ability against both Gram-negative and Gram-positive bacteria and is generally applied for local disinfection and cleaning during oral care and oral surgery (Zheng et al., 2022). The cationic CHX molecule attracts to the surface of negatively charged bacterial cells and interacts with the cell membrane to disrupt its integrity, causing the cell contents to flow out, thus exerting its bacteria-inhibiting effects. As its concentration increases, it exerts a bactericidal effect by forming complexes with phosphorylated compounds, such as adenosine triphosphate and nucleic acids, which cause cytoplasmic coagulation and precipitation. In addition, the cationic character of the CHX molecule allows it to adhere to most negatively charged oral surfaces and interfere with the adhesion of bacteria (Poppolo Deus and Ouanounou, 2022). Garner et al. developed a CHX-hexametaphosphate coating for Ti surfaces and investigated its antimicrobial properties using a multispecies biofilm model, and determined its cytocompatibility with human mesenchymal stem cells (MSCs). The coating showed a significant reduction in multispecies biofilm formation within 72 h and had excellent cytocompatibility, allowing MSCs to perform their functions and

differentiate into osteoblasts normally (Garner et al., 2021). Matos et al. prepared multifunctional CHX-doped thin films on pure Ti using the glow discharge plasma approach, where the release of CHX peaked at day 8 and maintained a slow release for 22 days. The modified surface exhibited significant inhibition of S. sanguinis biofilm growth and had good cytocompatibility (Matos et al., 2020).

In addition, some other organic antimicrobial agents have also shown great clinical value, such as totarol, rhamnolipids, chlorophenol, polyhexamethylene biguanidine, *etc.* Xu et al. used totarol, a natural antimicrobial agent, as a coating on Ti surfaces and silicon wafers, which showed that the totarol coating produced an efficient killing and inhibiting effect on S. gordonii and mixed oral bacterial biofilms. Its anti-adhesive and biofilm inhibitory effects persisted after 24 days of saliva incubation (Xu et al., 2020). Tambone et al. adsorbed rhamnolipids onto the Ti surface by physical adsorption and demonstrated that the coating had good antibacterial activity against *S. aureus* and S. epidermidis for up to 72 h, and the coated Ti samples showed no cytotoxicity (Tambone et al., 2021). These organic antimicrobial agents exerted antibacterial effect while avoiding the development of antibiotic resistance, and are promising agents for reducing the adhesion of bacteria and the formation of biofilms on Ti surfaces.

2.6 Natural product

The problem of increasing bacterial resistance to conventional antibiotics has prompted the search for new antimicrobial products. In recent years, there has been a growing interest in natural antimicrobial products that can effectively inhibit bacterial colonization and biofilm formation and are less likely to cause the development of bacterial resistance, making them promising alternatives or supplements to current synthetic antibiotics. For example, Fernández-Babiano et al. demonstrated that Carvacrol was able to exert a favorable antimicrobial effect against S. sanguinis and S. mutans, reducing the formation of biofilm (Fernández-Babiano et al., 2022). Alonso-Español et al. demonstrated the inhibitory effect of Curcumin and Xanthohumol on multi-species biofilms on the surface of implants containing *Actinomyces* naeslundii (A. naeslundii), *Streptococcus* oralis (S. oralis), Veillonella parvula (V. parvula), *Fusobacterium* nucleatum (F. nucleatum), Aggregatibacter actinomycetemcomitans (A. actinomycetemcomitans) and P. gingivalis (Alonso-Español et al., 2023). In addition, natural products such as propoli (Navarro-Pérez et al., 2021), Colocasia antiquorum var. esculenta (CA) varnish (Shin et al., 2022), nasturtium officinale extract (Tabesh et al., 2022) and Rosmarinus officinalis extract (Günther et al., 2022) also have been studied for their antimicrobial effects. Some natural products have been explored for use as antimicrobial coatings on implant surfaces to prevent the development of peri-implantitis. Córdoba et al. functionalized Ti surfaces by covalently grafting phytate (IP6) directly onto Ti surfaces through Ti-O-P bonds without the use of cross-linker molecules. The obtained Ti-IP6 surface significantly reduced the adhesion of S. sanguinis and induced the gene expression of osteogenic markers, suggesting that it has a good antibacterial property and osteogenic potential (Córdoba et al., 2016). Gomez-Florit et al. successfully grafted quercitrin onto Ti surface, prepared quercitrin-nanocoating, and explored its antimicrobial properties with S. mutans, and tested its anti-inflammatory properties and potential to promote soft tissue regeneration with human gingival fibroblasts. The results showed that quercitrin-nanocoating significantly reduced the initial adhesion of S. mutans and biofilm formation, while increasing the attachment of human gingival fibroblasts and decreasing the expression of related inflammatory factors, indicating the value of the coating in the promotion of soft tissue integration and the prevention of peri-implantitis (Gomez-Florit et al., 2016). Natural antimicrobial products have outstanding antimicrobial properties and various efficacies, showing good application prospects, but most of them have complex compositions and various targets, so the dosage and specific mechanisms of various natural products need to be further explored.

2.7 Trigger-responsive antimicrobial coatings

The application of a trigger responsive release systems allows the release of the drug to occur only when needed, greatly increasing the drug utilization and enhancing the antimicrobial activity and specificity of the coating (Skovdal et al., 2018). Such coatings can initiate the release of drugs by responding to variations of the local microenvironment or biomolecular concentration induced by bacterial infection (Figure 3). For instance, bacterial infection causes changes such as decrease in pH of the local microenvironment, increase in temperature, and so on. Lee et al. prepared a pH-responsive cinnamaldehyde-TiO_2 nanotube coating (TNT-CIN) by silylation, hydroxylation, anodic oxidation, and Schiff base reaction, which showed better drug release in low pH condition, good anti-inflammatory, osteogenic, and anti-bacterial abilities, and the viability and number of P. gingivalis and S. mutans on the surface were significantly lower than those of uncoated TNT (Lee et al., 2022). Choi et al. used copolymers made up of 2-hydroxyethyl methacrylate and diethylene glycol methyl ether methacrylate to prepare a multi-layered temperature-responsive polymer brush (MLTRPB) coating on a Ti surface, which triggered a significant release of antibiotics from the coating at 38°C–40 °C, the local temperature that may be reached during infection. The coating showed good antimicrobial efficacy in both *in vitro* and *in vivo* experiments (Choi et al., 2022). In addition, certain specific enzymes released by bacteria during infection can also act as triggers. Li et al. loaded ciprofloxacin (CIP) into mesoporous polydopamine (MPDA) nanoparticles (MDPA@CIP), anchored them to the Ti surface, and covered them with a hyaluronic acid-catechol (HAc) coating. Bacterial hyaluronidase secreted by bacteria can accelerate the degradation of HAc, which allows the on-demand release of antimicrobial drugs at the site of infection and enables functional Ti to exhibit good antimicrobial ability (Li D. et al., 2023). Materials responsive to bacterial metabolites are beneficial to adaptive antimicrobial systems and precision medicine, allowing drug exposure or release to occur only when and where it is needed and reducing the misuse of antimicrobials and the development of bacterial resistance. Changes in the microenvironment of infection and the concentration of biomolecules can also help us detect bacterial infections and monitor bacterial growth, reflecting the extent of the infection in

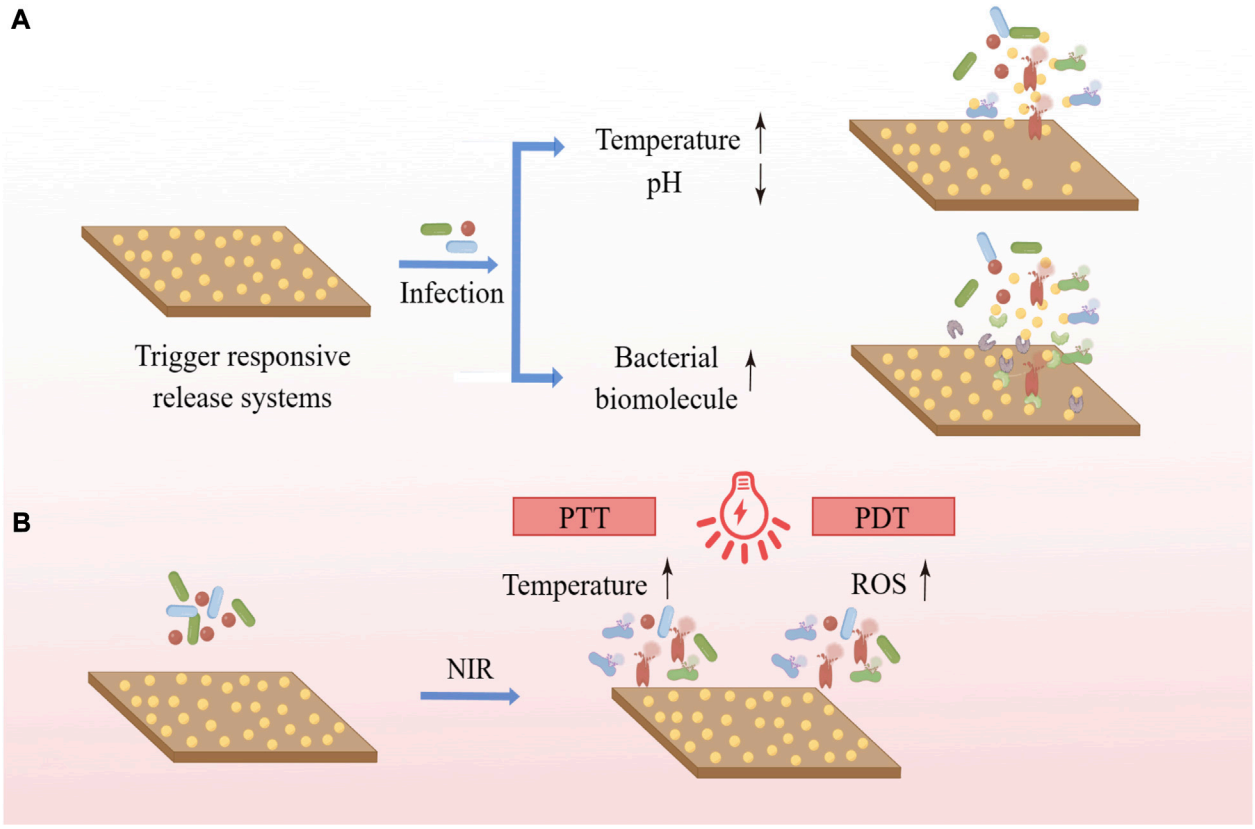

FIGURE 3
(A) Trigger responsive coatings respond to changes in the local microenvironment or biomolecule concentration caused by bacterial infection to initiate the release of the cargo. **(B)** PTT uses photothermal agents to convert light energy into heat, and PDT uses photosensitizers to trigger photochemical reactions such as the production of ROS to exert antimicrobial effects.

time to better prevent the occurrence of disease. Therefore, a stimulus-responsive antimicrobial system with both monitoring and therapeutic functions is worthy of further research (Wang et al., 2022).

Near infrared (NIR) irradiation-based photothermal therapy (PTT) and photodynamic therapy (PDT) are increasingly of interest due to their low invasiveness and good region-selectivity, having been extensively investigated in areas ranging from cancer treatment to infection relief. PTT uses photothermal agents to convert light energy into heat, while PDT uses photosensitizers to trigger photochemical reactions such as the production of ROS for treatment (Ghimire and Song, 2021) (Figure 4). In the presence of light, polydopamine (PDA), $MoSe_2$, MnO_2, TiO_2, ZnO, IR780 phosphorus, graphene oxide and indocyanine green (ICG) can increase local temperature and/or produce ROS, which can kill bacteria (Kubiak et al., 2021). Chai et al. synthesized molybdenum diselenide ($MoSe_2$) on the surface of porous Ti dioxide layers prepared by micro-arc oxidation on Ti implants using a hydrothermal method, electrostatically bonding chitosan (CHI) to $MoSe_2$ nanosheets to improve their biocompatibility. The TiO_2 coating introduced with $MoSe_2$ has good photothermal and photodynamic capabilities and shows excellent antibacterial properties under 808 nm NIR light irradiation due to the synergistic effect of high temperature and ROS (Chai et al., 2021). The photothermal and photodynamic antibacterial strategies can exert good antibacterial effects and do not cause antibiotic resistance. At the same time, it can precisely control the irradiation site, time and dose, and is easy to operate without being affected by the surrounding environment. However, the penetration of light into soft and hard tissues is limited and prolonged infrared irradiation is harmful, while short-term temperature increase and ROS production are not sufficient to effectively cure recurrent bacterial infections, which is why its application on implant surfaces requires further research.

2.8 Methods of constructing coatings

Coatings are formed by the attachment or diffusion of antimicrobial agents or bioactive elements to the substrate, or by changes in surface properties to improve the antimicrobial as well as soft/hard tissue integration capabilities of the surface. A variety of ways have been developed to construct implant surface coatings, the earliest of which was plasma spraying (Claes et al., 1976), a thermal spraying coating process that uses high temperatures to melt and spray powders on surfaces to produce a high-quality coating. People usually use powders such as Ti, hydroxyapatite, *etc.*, for surface modification of implants to improve their osseointegration. In order to enhance the antimicrobial activity, various antibiotics have been used in combination with calcium phosphate for surface

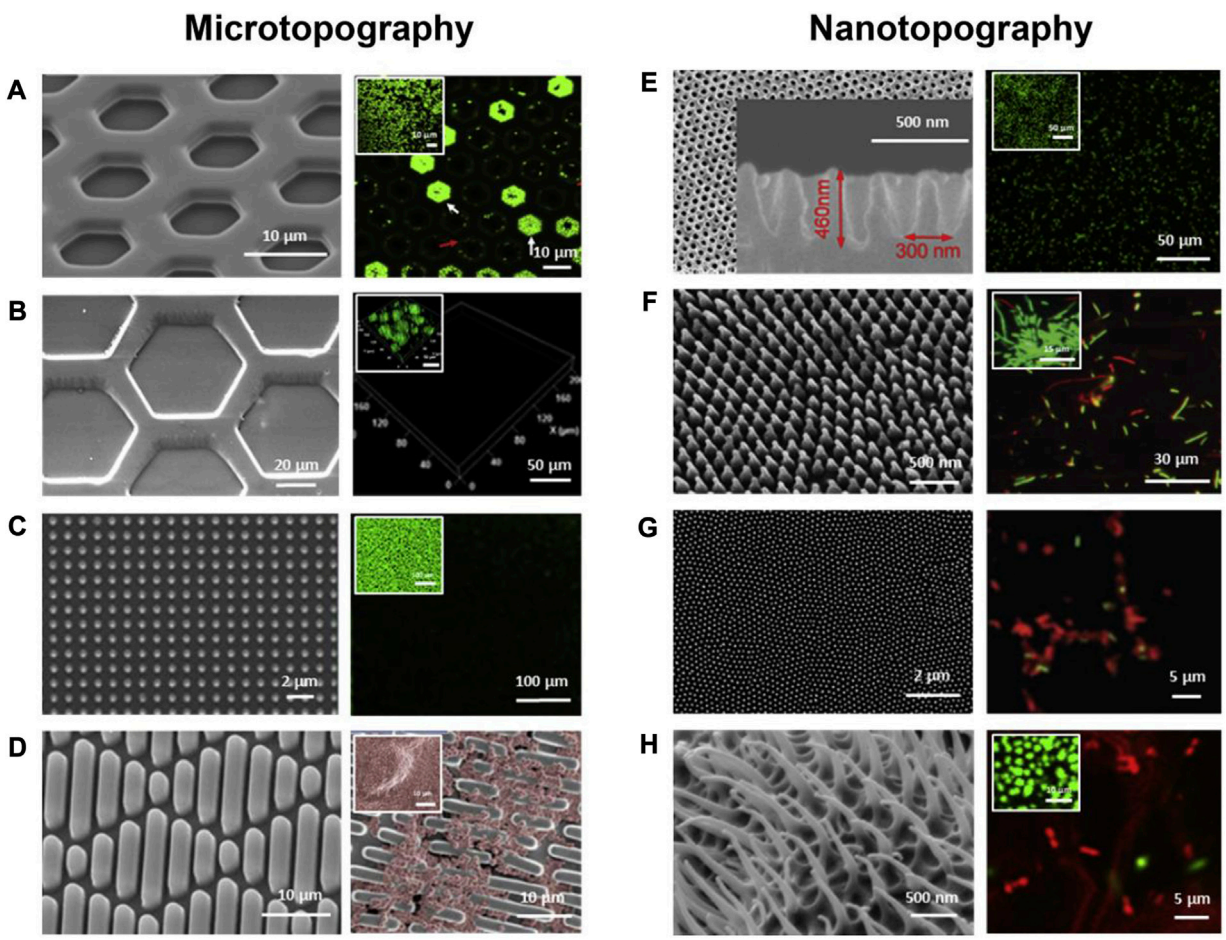

FIGURE 4
SEM images (left) and fluorescent microscopic images (right) of bacterial attachment on micron- and nano-scale topographies and the small images show cell attachment on flat control surfaces. **(A)** Hexagonal PDMS pits; **(B)** Hexagonal PDMS pillars; **(C)** Micropillars; **(D)** Sharklet™; **(E)** Parabolic nanostructures; **(F)** Nanopillars; **(G)** Cicada wings; **(H)** Gecko skins. Green represents live cells **(A–C, E–H)** and red represents dead cells **(E–H)**. The red color shows the live cells **(D)**. Reproduced with permission from (Lee et al., 2021). Copyright (2020) Elsevier.

modification of implants, such as cephalothin (Ke et al., 2017), streptomycin (Li et al., 2015), gentamicin (Govindan and Girija, 2014), and tetracycline (Ratier et al., 2001). However, extremely high temperatures make it difficult to incorporate organic compounds into the coatings in the plasma spraying technique, and the antibiotics are released too quickly to maintain antimicrobial capacity. Therefore, attempts have been made to introduce metal ions and nanoparticles with antimicrobial properties into the coatings, such as Ag (Ruan et al., 2009; Ke et al., 2019), Zn (Vu et al., 2019), *etc.* These coatings have shown good antimicrobial capabilities, but Ti alloys with plasma-sprayed hydroxyapatite have weak bonding strengths, and doubtful long-term stability after implantation, so better materials and techniques still need to be explored. In addition, Metal Ions Implantation (MII) is also a well-researched technique. The antimicrobial effects of many metal elements have been known, such as Ag (Tan et al., 2023), Cu(Wu L. et al., 2022), Zn (Li X. et al., 2019), cerium, *etc.*, which have been loaded into implants to improve the antimicrobial properties of implants. In addition to the improvement in antimicrobial properties, the technique also provides a significant improvement in the corrosion and abrasion resistance of the modified surface, which has led to its widespread application. The sol-gel method has attracted attention for its ability to produce coatings with high purity and homogeneity with relatively low temperatures, and it can be used to prepare a variety of metal oxide materials, as well as a number of coatings, films, and fibers that are difficult to melt with conventional processes, which is a commonly used technique for deposition of HA films on implants (Chai et al., 1998). Good antimicrobial properties can be obtained by replacing the calcium ions of HA with metal ions that have antimicrobial effects or replacing its hydroxyl ions with fluoride ions in the sol-gel method (Batebi et al., 2018). In addition, micro-arc oxidation (MAO), sputtering deposition, and Layer-by-Layer (LBL) self-assembly have also been used to construct surface coatings to improve the antimicrobial and osteointegration capabilities of implants.

3 Surface topography

Various approaches that rely on the addition of chemical agents to the surface face two challenges: safety and long-term

antimicrobial efficacy. Therefore, more attention has been paid to modifying the physical properties of the implant surface to improve the antimicrobial performance. Because it does not consume drugs, physical modification of the surface allows for more long-term effectiveness, less adverse effects on surrounding tissues, and does not need to worry about causing drug resistance of bacteria, so it is considered to be a more promising approach than chemical modification (Wu et al., 2018). Surface topography, an important parameter of the physical properties of the surface, includes surface roughness as well as profile shape (Ardhani et al., 2022). The effects of implant surface roughness and microscopic profile shape on bacterial adhesion and activity have been extensively studied.

3.1 Surface roughness

The most commonly used parameters to describe the characteristics of surface topography are the root-mean-square surface roughness (Rrms) as well as average surface roughness (Ra), which represents the root-mean-square and average deviation of height values from the mean line, respectively (Wu et al., 2018). A slightly rough surface is more conducive to osseointegration, and to obtain better surface properties, the implant surface is usually treated to improve cell adhesion and reduce bacterial adhesion. Commonly used methods include sandblasting, acid etching, large particle sandblasting acid etching (SLA), anodic oxidation, and fluoride treatment (Yeo, 2014; Han et al., 2017). Of these methods, large particle sandblasting acid etching is one of the most popular ways, which can increase surface roughness, enlarging the surface area for osteoblasts to attach, which is beneficial to osseointegration and interfacial stress distribution (Wang et al., 2020). However, an increasing in roughness will also increase the adhesion of bacteria while improving osseointegration because the rough surface provides more attachment sites and "shelters" for bacteria to resist shear forces (Robinson et al., 1996; Teughels et al., 2006). On the contrary, mirror polished surfaces have good resistance to bacterial adhesion and biofilm formation, yet such flat surfaces are detrimental to the adhesion of surrounding tissues (Guo et al., 2021). However, some researchers have obtained different results. In one study, Pacha-Olivenza et al. investigated the adhesion and proliferation of human gingival fibroblasts and bacterial strains: A. actinomycetemcomitans, S. sanguinis and S. mutans on the surface of Ti disks with different surface treatments: machined (Mach), nitrided (TiN), lightly acid etched (AEn), strongly acid etched (AEt) and sandblasted/acid etched (SB + AE). The results showed that smooth surfaces are more favorable for adhesion and proliferation of fibroblasts, and the overall race between cells and bacteria for surfaces also favored smoother surfaces (Mach, TiN and AEn) compared to rougher surfaces (Aet and SB + AE) (Pacha-Olivenza et al., 2019). In addition, there are also some researchers suggesting that increased surface roughness does not affect or even inhibit bacterial adhesion (Rizzello et al., 2011; Bagherifard et al., 2015; Liu et al., 2016; Lüdecke et al., 2016). The contradictory results may be due to the differences in materials and bacterial strains used, and the lack of a comprehensive analysis of the distribution of surface microtopography, profile shape, *etc.* Ra and Rrms can only describe the height of surface features, but not their lateral size, shape, spacing, *etc.* Surfaces with the same Ra and Rrms values may have different surface features, and these parameters can have a significant impact on bacterial adhesion, so we need more parameters for comprehensive analysis of surface morphology data. Stout et al. proposed a set of 14 roughness parameters for the comprehensive analysis of surfaces, called "Birmingham 14". Crawford et al. suggested that at least RMS surface roughness (Sq), summit density (Sds), developed area ratio (Sdr) is required to study the relationship between surface roughness and bacterial adhesion (Crawford et al., 2012). However, more accurate and concise schemes for characterizing surface topography still need to be further explored. In addition, the interaction between bacteria and surfaces changes over time. Han et al. obtained different surface roughnesses on zirconia surfaces by different surface treatments with Ra values of: 0.17 ± 0.03 μm (untreated), 0.56 ± 0.05 μm (grit-blasting), 1.47 ± 0.04 μm (HF-etching), 1.48 ± 0.05 μm (grit-blasting followed by HF-etching). It is interesting to note that the highest number of P. gingivalis was found on the two surfaces with the highest Ra value (the last two groups) at 24 h. However, after 72 h, the amount of biofilm on the two surfaces with the most bacteria became the lowest. The authors speculate that this change may be related to their high hydrophilicity and low surface energy. Thus, the effect of surface roughness on the adhesion of bacteria may be diminished after biofilm maturation (Han et al., 2017).

In general, it is believed that bacterial adhesion and biofilm formation are more likely to occur when the surface roughness exceeds the Ra threshold of 0.2 μm, whereas Ra values below 0.2 μm do not lead to a further decrease in bacterial adhesion (Bollen et al., 1997). Nano roughness has been proposed to be suitable for preventing the adhesion of microorganisms. The reason is that most bacteria, as well as P. gingivalis, have a length of about 1.51 μm and a diameter of about 1 μm. On surfaces with topographical features at the micrometric scale, which is similar in size to bacterial cells, cells tend to position themselves to maximize their contact area with the surface, whereas on surfaces with topographical features at the submicrometric and nanometric ranges, which are much smaller than bacterial cells, cells inhibit adhesion by reducing the contact area between the cells and the surface (Amoroso et al., 2006; Feng et al., 2015; Mukaddam et al., 2021). Various studies have revealed that micro/nanostructures are not of particularly high or low roughness, having different roughness levels according to the surface patterns (Huang et al., 2017; Kunrath et al., 2020). The same is true for surface energy, wettability, *etc.* There is a study in which the water contact angle on a microsurface was found to increase with the increase of roughness until a plateau stage is reached (Giljean et al., 2011). These can have an impact on the interaction between bacteria and the surface, and thus on the adhesion of bacteria to the surface.

3.2 Patterned surface topography

The surfaces of various plants and animals in nature have natural anti-fouling and antibacterial properties, such as shark skin (Sakamoto et al., 2014; Chien et al., 2020; Chien et al., 2021; Zhang H. et al., 2023), worm skin (Hayes et al., 2016), lotus leaves (Latthe et al., 2014; Jiang et al., 2020), butterfly wings (Bixler and Bhushan, 2014), cicada wings (Hazell et al., 2018; Shahali et al., 2019; Mo et al., 2020; Liu et al., 2022), dragonfly wings (Bhadra et al., 2015; Mathew et al., 2023), *etc.*, which suggest that specific nano/micron-scale structures have antibacterial effects. Inspired by nature, various

specific patterns have been prepared on artificial materials to study the interaction between bacteria and surfaces as well as to design surfaces with antimicrobial properties. The animal topography most widely reported for biomedical surfaces modification is sharkskin, where the microscopic shape of the surface and the distribution of denticles (diamond-shaped scales that cover the animal's outer surface) give it very outstanding anti-fouling and self-cleaning properties (Liu et al., 2020). Surfaces with the ability to prevent bacterial adhesion have been developed mimicking shark skin with topographic features of rectangular shape with a height of 3 μm, width of 2 μm, and length of 4–16 μm, arranged periodically in a diamond shape, with a distance of 2 μm between adjacent features (Damodaran and Murthy, 2016). The distribution, shape, and size of topographic patterns affect bacterial adhesion. Vadillo-Rodríguez et al. prepared surfaces with topographical features having different shapes and sizes using polydimethylsiloxane (PDMS), which include protruding and receding circular and square features and parallel channels and ridges, with micrometer-scale lateral dimensions (spacing and length/width) and nanoscale heights, to evaluate the effect of nanoscale roughness on bacterial adhesion and biofilm formation. The results showed that all surface patterns significantly inhibited bacterial adhesion and biofilm formation, and that the bacterial cells actively chose their initial locations for adhesion, favoring those geometrical locations that maximized the cell-surface contact points/areas, including square corners and convex walls of recessed surface features. This study suggests that we can control the initial location of attachment of adherent cells by the particular geometry of the features (Vadillo-Rodríguez et al., 2018). Many topographic features have been shown to have an inhibitory effect on the formation of biofilms, such as honeycombs (Vasudevan et al., 2014; Yang et al., 2015; Gu et al., 2016; Liao et al., 2021; Li S. et al., 2023), irregular micro pits (Jeong et al., 2017), line patterns (Lee and Pascall, 2018; Wu et al., 2020; Damiati et al., 2022; Sorzabal-Bellido et al., 2022), ridges (Zhang B. et al., 2014; Perera-Costa et al., 2014; Lu et al., 2016), cylindrical wells (Fontelo et al., 2020; Xiao et al., 2020), square pillars (Hou et al., 2011; Halder et al., 2014; Ge et al., 2015; Valle et al., 2015; Ge et al., 2019), hexagonal pillars (Chang et al., 2018; Pingle et al., 2018). Although the patterns, materials, and strains used vary, most patterns inhibit bacterial adherence more significantly at a smaller size.

3.3 Micron- and nano-scale topographies used for implants

Various micro/nanostructure topographies have been developed for surface modification of implants to enhance their antimicrobial properties (Figure 4). The influence of surface topography on the bacterial attachment is largely dependent on the size. Generally speaking, micron-scale topographies are not bactericidal, but can influence bacteria-surface interactions to prevent the adhesion of bacteria and impede the formation of biofilms. In contrast, many nanoscale topographies can disrupt bacterial cell membranes directly to provide a bactericidal action. For instance, nanopillars work similarly to a "bed of nails" that disrupt the cell membrane of bacteria in contact with them (Khalid et al., 2020; Lee et al., 2021).

Titanium nanotubes (TNTs) are highly ordered nanotubular structures fabricated on Ti surfaces, which are easy to fabricate, can be obtained in specified sizes by changing their design parameters, have good biocompatibility and antibacterial properties, and are widely used for surface modification of Ti. Camargo et al. prepared Ti dioxide nanotubes with diameters of 100 nm and 150 nm by anodic oxidation of Ti oxide. After 30 days of bacterial incubation, the structured surface of Ti dioxide nanotubes showed significant resistance to P. gingivalis and dense spirochetes of dental tartar (Camargo et al., 2021). Peng et al. prepared arrays of Ti oxide nanotubes with diameters of 30 nm and 80 nm, respectively, on Ti substrates by a two-step anodic oxidation method, and compared with the control group, it was observed that the surface roughness of Ti dioxide nanotubes increased, the water contact angle decreased, and the adhesion and colonization ability of S. epidermidis on its surface was significantly reduced (Peng et al., 2013). The antibacterial mechanism of TNTs may include: mutual repulsion of negative charge of TNTs and negative bacterial surface charge; stretching of bacterial membranes by nanotubular structures leading to cell membrane rupture and bacterial death; and high surface roughness of nanostructures increasing surface hydrophilicity and preventing attachment of hydrophobic bacteria (Li et al., 2019e). There are also different nanopatterns that are available to reduce bacterial attachment besides nanotubes. Kim et al. generated a surface consisting of 50–100 μm micropores and 25–30 nm nanopores by nitriding and anodic oxidation on the surface of Ti discs, and this surface significantly inhibited the adhesion of P. gingivalis and S. mutans, showing excellent antibacterial activity (Kim et al., 2021). In addition, many other nanostructured surfaces such as nanogrooves (Ferraris et al., 2017), nanopillars (Yi et al., 2018; Wang S. et al., 2023), and biomimetic micro/nanostructured surfaces (Elbourne et al., 2017; Ye et al., 2019; Mo et al., 2020; Zhang Y. et al., 2023) have been shown to have good antibacterial properties.

In addition to their antimicrobial effects, nanostructures can also influence the interaction of the surface with cells and tissues. It has been shown that some nanostructures also have the ability to facilitate the migration, adhesion, and growth of cells. A study by Wu et al. found that Ti dioxide nanotube arrays can affect the type of adsorbed proteins and change their conformation; improve adhesion of macrophages and induce polarization T lymphocytes; promote repairment-related cells adhesion and filopodia formation; and induce osteogenic differentiation and blood vessel formation (Wu B. et al., 2022). Ferraris et al. showed that the nanogrooves can drive the alignment of gingival fibroblasts, while the keratin nanofibers deposited can increase cell adhesion and proliferation, through respectively a topographical and a chemical stimulus (Ferraris et al., 2017). Surfaces with host cell coverage are largely resistant to the colonization of bacteria because of the " race for surface " principle (Gristina, 1987). Mezey et al. also demonstrated in a previous study that mesenchymal stem cells (MSCs) possess inherent antibacterial properties (Mezey and Nemeth, 2015). Therefore, while focusing on their antimicrobial effect, we should also take into account the affinity of the surface topography for the host tissue and cells. Currently, the topography that prevents bacterial colonization and facilitates tissue integration has not been well studied, and more attention should be devoted to this aspect.

At the same time, there are a large number of studies using the combination of surface topography and antibacterial agents to

obtain antifouling and antibacterial properties and inhibit the formation of biofilm. Dolid et al. prepared a surface with shark skin topography and coated the micropatterned surfaces with a peptide (DOPA-Phe(4F)-Phe(4F)-Arg-Gly-Asp) coating and tested the adhesion of *E. coli* and S. epidermidis under static conditions and in dynamic experiments, and the results showed that the micropatterned surfaces with peptide coatings in both cases had better anti-adhesive effects than the other three groups (smooth surfaces; smooth surfaces with coatings; micropatterned surfaces) (Dolid et al., 2020). In addition to biomedical surfaces, nanotubes, mesoporous structures, *etc.*, are also commonly used to load antimicrobial agents to promote the synergistic effect of surface topography and antimicrobial drugs. Nanotubes have the ability to load, store, and release bactericidal agents in addition to their excellent anti-microbial adhesion properties. Antibiotics, antimicrobial peptides, and metal nanoparticles can be combined with Ti nanotubes to exert good antimicrobial effects (Li et al., 2017; Arkusz et al., 2020; Mansoorianfar et al., 2020). Ti dioxide nanotubes doped with hydroxyapatite (HA), selenium (Se), and silver (Ag) compounds (Ag_2SepTNT) were prepared on the surface of Ti alloy (Ti_6Al_4V) by Staats et al. The modified surface showed good antimicrobial effects against S. epidermidis (Staats et al., 2022). In addition, the surface topography design promotes the separation of bacterial cells and delays their biofilm formation, which can improve the susceptibility of bacteria to antibiotics and reduce their drug resistance (Khalid et al., 2020).

3.4 Methods for improving surface topography

Sandblasting and acid etching technology is one of the most commonly used surface modification methods in commercial implants and is considered a safe and effective treatment. Sandblasting involves the projection of particles of various diameters to the surface to remove surface contaminants and obtain a roughened surface that improves the strength between the implant and the bone, increasing the osseointegration. Acid etching is the process of treating a surface using a strong acid such as HCl, HNO3, or H2SO4 to obtain microscopic pits that improve cell adhesion and osseointegration. People usually perform acid etching after sandblasting, and the whole process is considered as the reference surface treatment, called sandblasting and large grit acid etching (SLA) (Accioni et al., 2022). The ideal surface can be obtained by adjusting the parameters such as the type and size of abrasive, as well as the type and concentration of acid, and the treated surfaces obtained a better osseointegration and the SLA-treated zirconia surfaces had less biofilm formation than the pure Ti surfaces (Roehling et al., 2017). Anodic Oxidation is also one of the more commonly used methods to improve the surface morphology of implants by preparing uniform nanotube structures on Ti surfaces (Shin and Lee, 2008). The obtained nanotube structures have higher roughness and hydrophilicity and increased surface area, which can improve soft and hard tissue integration and reduce bacterial adherence (Li et al., 2019d; Pan et al., 2021). In addition, Ti dioxide nanotubes have the ability to generate ROS via photocatalysis and to be used as carriers loaded with antimicrobial drugs to exert antimicrobial effects (Podporska-Carroll et al., 2015; Fathi et al., 2019). Laser ablation technology uses a laser source to melt metals to obtain micron and nanostructures, which has the advantage of being able to maintain mechanical properties and reduce the risk of contamination. The surface roughness of the treated Ti is altered and ideal osseointegration as well as antimicrobial capacity is achieved through its high hydrophobicity (Hu et al., 2018). Alkaline heat (AH) treatment and acid-alkali treatment are also used to form micro- and nanoscale rough surfaces on Ti surfaces, and both result in modified surfaces with good antimicrobial properties (Zhang and Liu, 2015; Zhong et al., 2022). In addition, the antimicrobial properties of biomimetic topography have received much attention in recent years, and a series of methods to generate biomimetic topography have been explored, such as metal assisted chemical etching, hydrothermal synthesis, nanoimprint lithography, electron beam lithography, *etc.*

4 Intrinsic antibacterial materials

Pure Ti or Ti alloy (Ti_6Al_4V) has always been a popular material for implants due to its good biocompatibility, outstanding mechanical properties and high resistance to corrosion. However, pure Ti lacks favorable antimicrobial properties whereas various surface modifications are rarely used clinically due to limitations in safety, coating degradation and drug resistance, which has led to the development of alternative materials for implants with better antimicrobial properties.

4.1 Alloys

The lack of antimicrobial properties of pure Ti and Ti_6Al_4V, the most popular materials used for implants, is a major disadvantage. Ag, Cu and Zn are often added as antimicrobial reagents to the implant surface by a variety of surface modification methods (e.g., magnetron sputtering, plasma spraying, and plasma immersion ion implantation) to improve the antimicrobial properties of the implant, but these surface materials are gradually depleted and do not have a long-term antimicrobial effect. As a result, antimicrobial alloys have been developed to replace antimicrobial coatings and to provide good antimicrobial properties throughout the implant rather than just on the surface.

Cu and Ag are the most commonly used metallic elements added into alloys as antimicrobial agents. Cu which is an essential trace element for living organisms has become a widely used alloying element because of its outstanding properties such as promoting fracture healing, being antibacterial and protecting the cardiovascular system (Ren et al., 2015). As an element with strong biological activity, Cu has powerful bactericidal and cytotoxic effects. Liu et al. found that when the submerged concentration of Cu was higher than 0.036 mg/L (much lower than the daily intake recommended by the World Health Organization), the antibacterial rate could reach more than 99% (Liu J. et al., 2014). This goes some way to demonstrating the safety of Ti alloys containing Cu. In a recent study, Yang et al. developed Ti-Cu sintered alloys (3 wt% and 5 wt% Cu, i.e., Ti-3Cu and Ti-5Cu) and evaluated their antimicrobial activity against S. mutans and P. gingivalis. It was revealed that the Ti-Cu alloys showed time-

dependent antibacterial activity against both bacteria. The antimicrobial activity of the Ti-Cu alloy was correlated with the release of Cu^{2+} and the production of ROS. At different time points, Ti-5Cu released higher concentrations of Cu^{2+} than Ti-3Cu and also showed better antibacterial activity. 70% and 57% antibacterial activity against P. gingivalis and 78% and 63% antibacterial activity against S. mutans at 72h for Ti-5Cu and Ti-3Cu respectively (Yang et al., 2023). Zhang et al. evaluated the antibacterial and osteogenic properties of a series of hydrogen fluoride (HF) etching + anodised Ti-Cu alloy with different Cu contents (3 wt%, 5 wt% and 7 wt% Cu). The Ti-Cu alloys were shown to have strong antimicrobial properties and good biocompatibility and osteogenic ability. It was also concluded that the antibacterial rate was higher and more stable when the Cu content was ≥5% (Zhang W. et al., 2021). In the case of Ti-Cu alloys, however, the antimicrobial ability did not always correlate positively with the amount of Cu. It is also related to the form of Cu present in the alloy, and the amount of Ti_2Cu phase in the alloy is closely related to the antibacterial strength of the alloy (Fowler et al., 2019). Therefore, researchers can increase the content of Ti_2Cu to improve its antibacterial ability by different treatments rather than continuously increasing the content of Cu in the alloy. In addition to Ti-Cu alloys, Ti-6Al-4V-xCu alloys, Ti-Zr-Cu alloys and others have also been investigated. For example, Xu et al. suggested that Ti-6Al-4V-5Cu has superior corrosion resistance and cell viability than Ti-6Al-4V, as well as exhibiting outstanding antibacterial ability, the antimicrobial activity of which may be associated with the bactericidal effect of the large amount of Ti_2Cu precipitation (Xu et al., 2021).

Ag which has good antimicrobial properties and the ability to resist the formation of biofilm has been used for thousands of years as an antibacterial agent. Similar to Ti-Cu alloys, the antimicrobial ability of Ti-Ag alloys is also correlated closely with the amount of Ag. For example, Maharubin et al. developed Ti-Ag alloys containing various Ag contents (0.5 wt%-2 wt% Ag) and evaluated the antimicrobial activity against Gram-negative (*P. aeruginosa*) and Gram-positive (*S. aureus*) strains. 92% biofilm inhibition was achieved for *P. aeruginosa* and 93% for *S. aureus* after 3 h on the 1% Ag alloy. For the 1.5% Ag alloy, the inhibition rates were 99.96% and 99.7%, respectively, while the continued increase in Ag content did not result in a significant increase in antibacterial performance. Therefore, the antibacterial ability enhanced with increasing Ag content, but was not linearly correlated and higher concentrations of Ag may be harmful to mammalian cells (Maharubin et al., 2019). Nakajo et al. also demonstrated that Ti-Ag alloys do not affect bacteria when the Ag content is higher than 30 wt% Ag (Nakajo et al., 2014). Similar to Ti-Cu alloys, the antimicrobial ability of Ti-Ag alloys is also dependent on the content of their Ti_2Ag phase (Chen et al., 2016). In addition, good antibacterial activity has been obtained by adding Ag to the Ti-Nb alloy Ti-Nb-Zr (Ou et al., 2017; Cai et al., 2021). They suggest that the deposition of the Ag-rich phase is the main reason for its antimicrobial properties, but the presence of the Ti_2Ag phase increases the Young's modulus of the material, which is detrimental to the matching of Young's modulus between the human skeleton and the metallic material, so how to balance Young's modulus and antimicrobial efficacy is also a challenge for the development of antimicrobial Ti alloys.

4.2 Ceramics

Ceramics are excellent candidates for implant materials owing to their biocompatibility, wear resistance and chemical stability, as well as their excellent aesthetic properties. A variety of ceramic materials have been studied to explore their potential as implant materials, including alumina (Flamant et al., 2016), tricalcium phosphate (TCP) (Kawamura et al., 2003), hydroxyapatite (HA) (Ichikawa et al., 1998), silicon nitride (Zhou et al., 2021), zirconium oxide (Dantas et al., 2021), bioglass (Fu et al., 2018), *etc.*

As a bioceramic, zirconia is a promising material for implants with a wide range of applications in dentistry. There are already zirconia dental implants on the market, however, zirconia dental implants are still lacking in research to be a popular choice. It has been found that zirconia implants exhibit a repulsive effect on bacteria and inhibit biofilm formation due to hydrophobicity and electrical conductivity, therefore, zirconia is more resistant to bacterial adhesion and biofilm formation than Ti (Karygianni et al., 2013; Nascimento et al., 2016; Hanawa, 2020; Oda et al., 2020). Roehling et al. compared the formation of biofilms on the surfaces of pure Ti and zirconia using three-species biofilm of P. gingivalis, F. nucleatum, S. sanguinis and human plaque samples in an anaerobic flow chamber model, demonstrating that after 72 h of incubation, the thickness of the three-species biofilm and human plaque on the surface of zirconia implants was significantly lower than that of pure Ti, but the quality and metabolism of the biofilms did not show significantly difference (Roehling et al., 2017). Another *in vivo* study also demonstrated that during experimental plaque accumulation, the total number of bacteria around the Ti implants and the counts of Tannerella forsythia (T. forsythia) and Prevotella intermedia (P. intermedia) were higher than in the zirconia implants and produced a stronger inflammatory response (Clever et al., 2019). However, some studies have come to a different conclusion, for example, when Siddiqui et al. evaluated the growth of oral early colonising bacteria and mammalian host cells on commercial pure Ti and zirconium oxide surfaces, in which they found no significant difference in the bacterial counts of Streptococcal strains adhering to commercial pure Ti and zirconium oxide surfaces after 1 or 3 days (Siddiqui et al., 2019). The reasons for this variation may be as diverse as the experimental set-up, the strain, the surface treatment, *etc.* Therefore, more research is still needed on the performance of zirconia implants. In addition, silicon nitride showed better osseointegration and anti-infection properties than Ti and polyether ether ketone (PEEK) in experiments conducted by Webster et al. in rats (Webster et al., 2012). Combined with the remarkable mechanical properties, silicon nitride is considered to be an attractive ceramic implant material (Rahaman and Xiao, 2018). Ceramic materials are of great interest for their chemical stability, biocompatibility, mechanical properties and antimicrobial properties, but certain properties such as brittleness and low ductility significantly limit their clinical applications. Therefore, researchers should focus on improving the physicochemical properties of these materials while improving their antimicrobial properties through various modification methods.

5 Summaries and perspectives

With the increasing number of patients receiving dental implants, peri-implant disease has become a major concern.

While exploring and optimizing the treatment of peri-implant disease, efforts have been made to enhance the antibacterial ability of the implants through different methods. The efforts of many researchers have made great progress in improving the antimicrobial property of implants, but each method has its own inherent drawbacks, which greatly restrict the application.

The coating of implants with materials with excellent antimicrobial properties, such as antimicrobial metal elements, antibiotics, and antimicrobial peptides, has achieved good antimicrobial results, but the safety and long-term effectiveness of the coatings are challenged by the release of metal ions from the implant surface, the rapid consumption and uncontrolled release of drugs, and the resistance to antibiotics. Therefore, more research is needed in the future to develop safer and more effective antimicrobial agents and better controlled release systems to improve the safety and long-term effectiveness of the coating, and the development of material science, manufacturing technology and pharmacology will bring more possibilities for the application of antimicrobial coatings.

Adjusting surface topography for antimicrobial purposes avoids the limitations of chemical modification because it does not consume drugs and relies solely on its surface topography to improve antimicrobial properties, showing promise for long-lasting and safe antimicrobial surfaces, and a variety of techniques have been devised to create surface features and apply them to the design and study of antimicrobial surfaces. However, surface modifications that do not change the surface chemistry at all are practically non-existent, and the contact antimicrobial effect of surface features diminishes with the coverage of conditioned films and the adhesion of bacteria, and it lacks resistance to biofilms that have formed on the surface as well as to uncontacted bacteria. Therefore, dynamic surface features which enable the removal of formed biofilms and stimulus response profiles which enable the reduction of potential toxicity are all worthy directions to be explored.

Implant materials with antimicrobial properties are promising, but are not currently widely used in clinical practice. It is expensive and time-consuming to change the entire implant materials, and many implant materials have shown good antimicrobial properties but have not been well studied in terms of mechanical properties and biocompatibility, so we need to explore these aspects more in the future.

Many materials have only been proven to have antibacterial effects *in vitro*, but not *in vivo*, and few of them have been tested in clinical trials. The peri-implantitis model used in the experiments could not simulate the *in vivo* scenario very well, and most of the experiments only selected specific strains of bacteria, which is a huge difference from the complex microbial environment in the human oral cavity, and the influence of different materials and topographic features on different microorganisms, as well as on the interspecies interaction, need to be studied in more depth. Many experiments have also used only Ti discs as a substitute for implants, which ignores the possible influence of the macroscopic shape of the implant on peri-implant disease and osseointegration. Therefore, the results obtained in the experiments are full of uncertainty as to what results can be obtained in the clinical setting. Before entering clinical trials, we need to build more experimental models that are closer to real-world scenarios to validate these results.

The various methods used to improve the antimicrobial performance of implants require continued efforts by researchers to optimize them. Combining different strategies for synergistic antimicrobial activity is of great attraction, such as the combination of antimicrobial coatings and surface topography that prevent surface adhesion of bacteria and improve the bactericidal effect of antimicrobial agents. The combination of different antimicrobial modalities can reinforce each other to achieve better antimicrobial effects. In addition, while improving the antimicrobial effect of the implant, the improvement of the biocompatibility and mechanical properties of the material should not be neglected. Materials which can improve the antimicrobial performance of the implant, promote the integration of the soft and hard tissues of the host, and match the mechanical properties with the bone tissue are the future directions to be explored.

Author contributions

SZ: Investigation, Conceptualization, Writing–original draft. YT: Visualization, Writing–review and editing. XS: Visualization, Writing–review and editing: YL: Visualization, Writing–review and editing. JY: Investigation, Writing–review and editing. ZY: Supervision, Writing–review and editing. YW: Supervision, Writing–review and editing. SC: Funding acquisition, Writing–review and editing.

Funding

The author(s) declare financial support was received for the research, authorship, and/or publication of this article. Financial support from the Scientific Research Project of Jilin Provincial Department of Education, China (JJKH20231291KJ), and the Science and Technology Development Plan of Jilin Province supports the project, China (20230203065SF).

Acknowledgments

We are very grateful to SC for critical reading of the manuscript and helpful comments. We also thank Figdraw (www.figdraw.com, (accessed on 20 June 2023)) for the assistance in creating Figure 1A, Figure 2 and Figure 3.

Conflicts of interest

The authors declare that the research was conducted in the absence of any commercial or financial relationships that could be construed as a potential conflict of interest.

Publisher's note

References

Accioni, F., Vázquez, J., Merinero, M., Begines, B., and Alcudia, A. (2022). Latest trends in surface modification for dental implantology: innovative developments and analytical applications. *Pharmaceutics* 14 (2), 455. doi:10.3390/pharmaceutics14020455

Aissou, T., Jann, J., Faucheux, N., Fortier, L.-C., Braidy, N., and Veilleux, J. (2023). Suspension plasma sprayed copper-graphene coatings for improved antibacterial properties. *Appl. Surf. Sci.* 639, 158204. doi:10.1016/j.apsusc.2023.158204

Albright, V., Penarete-Acosta, D., Stack, M., Zheng, J., Marin, A., Hlushko, H., et al. (2021). Polyphosphazenes enable durable, hemocompatible, highly efficient antibacterial coatings. *Biomaterials* 268, 120586. doi:10.1016/j.biomaterials.2020.120586

Alghamdi, H. S., and Jansen, J. A. (2020). The development and future of dental implants. *Dent. Mater J.* 39 (2), 167–172. doi:10.4012/dmj.2019-140

Almoudi, M. M., Hussein, A. S., Abu Hassan, M. I., and Mohamad Zain, N. (2018). A systematic review on antibacterial activity of zinc against Streptococcus mutans. *Saudi Dent. J.* 30 (4), 283–291. doi:10.1016/j.sdentj.2018.06.003

Alonso-Español, A., Bravo, E., Ribeiro-Vidal, H., Virto, L., Herrera, D., Alonso, B., et al. (2023). The antimicrobial activity of Curcumin and Xanthohumol on bacterial biofilms developed over dental implant surfaces. *Int. J. Mol. Sci.* 24 (3), 2335. doi:10.3390/ijms24032335

Amer, S., and Sukumaran, A. (2021). "Peri-implantitis revisited," in *Current concepts in dental implantology*. Editors G. Dragana and V. Marko (Rijeka: IntechOpen), 13.

Amoroso, P. F., Adams, R. J., Waters, M. G., and Williams, D. W. (2006). Titanium surface modification and its effect on the adherence of Porphyromonas gingivalis: an *in vitro* study. *Clin. Oral Implants Res.* 17 (6), 633–637. doi:10.1111/j.1600-0501.2006.01274.x

Ardhani, R., Diana, R., and Pidhatika, B. (2022). How Porphyromonas gingivalis navigate the map: the effect of surface topography on the adhesion of Porphyromonas gingivalis on biomaterials. *Mater. (Basel)* 15 (14), 4988. doi:10.3390/ma15144988

Arkusz, K., Paradowska, E., Nycz, M., Mazurek-Popczyk, J., and Baldy-Chudzik, K. (2020). Evaluation of the antibacterial activity of Ag- and Au-nanoparticles loaded TiO_2 nanotubes. *J. Biomed. Nanotechnol.* 16 (9), 1416–1425. doi:10.1166/jbn.2020.2979

Bagherifard, S., Hickey, D. J., de Luca, A. C., Malheiro, V. N., Markaki, A. E., Guagliano, M., et al. (2015). The influence of nanostructured features on bacterial adhesion and bone cell functions on severely shot peened 316L stainless steel. *Biomaterials* 73, 185–197. doi:10.1016/j.biomaterials.2015.09.019

Baro, M., Sánchez, E., Delgado, A., Perera, A., and Evora, C. (2002). *In vitro-in vivo* characterization of gentamicin bone implants. *J. Control Release* 83 (3), 353–364. doi:10.1016/s0168-3659(02)00179-7

Batebi, K., Abbasi Khazaei, B., and Afshar, A. (2018). Characterization of sol-gel derived silver/fluor-hydroxyapatite composite coatings on titanium substrate. *Surf. Coatings Technol.* 352, 522–528. doi:10.1016/j.surfcoat.2018.08.021

Beachey, E. H. (1981). Bacterial adherence: adhesin-receptor interactions mediating the attachment of bacteria to mucosal surfaces. *J. Infect. Dis.* 143 (3), 325–345. doi:10.1093/infdis/143.3.325

Bermejo, P., Sánchez, M. C., Llama-Palacios, A., Figuero, E., Herrera, D., and Sanz Alonso, M. (2019). Biofilm formation on dental implants with different surface micro-topography: an *in vitro* study. *Clin. Oral Implants Res.* 30 (8), 725–734. doi:10.1111/clr.13455

Bhadra, C. M., Truong, V. K., Pham, V. T., Al Kobaisi, M., Seniutinas, G., Wang, J. Y., et al. (2015). Antibacterial titanium nano-patterned arrays inspired by dragonfly wings. *Sci. Rep.* 5, 16817. doi:10.1038/srep16817

Bixler, G. D., and Bhushan, B. (2014). Rice- and butterfly-wing effect inspired self-cleaning and low drag micro/nanopatterned surfaces in water, oil, and air flow. *Nanoscale* 6 (1), 76–96. doi:10.1039/c3nr04755e

Bollen, C. M., Lambrechts, P., and Quirynen, M. (1997). Comparison of surface roughness of oral hard materials to the threshold surface roughness for bacterial plaque retention: a review of the literature. *Dent. Mater* 13 (4), 258–269. doi:10.1016/s0109-5641(97)80038-3

Brohede, U., Forsgren, J., Roos, S., Mihranyan, A., Engqvist, H., and Strømme, M. (2009). Multifunctional implant coatings providing possibilities for fast antibiotics loading with subsequent slow release. *J. Mater Sci. Mater Med.* 20 (9), 1859–1867. doi:10.1007/s10856-009-3749-6

Bui, V. D., Mwangi, J. W., and Schubert, A. (2019). Powder mixed electrical discharge machining for antibacterial coating on titanium implant surfaces. *J. Manuf. Process.* 44, 261–270. doi:10.1016/j.jmapro.2019.05.032

Burghardt, I., Lüthen, F., Prinz, C., Kreikemeyer, B., Zietz, C., Neumann, H. G., et al. (2015). A dual function of copper in designing regenerative implants. *Biomaterials* 44, 36–44. doi:10.1016/j.biomaterials.2014.12.022

Buwalda, S., Rotman, S., Eglin, D., Moriarty, F., Bethry, A., Garric, X., et al. (2020). Synergistic anti-fouling and bactericidal poly(ether ether ketone) surfaces via a one-step photomodification. *Mater Sci. Eng. C Mater Biol. Appl.* 111, 110811. doi:10.1016/j.msec.2020.110811

Buxadera-Palomero, J., Calvo, C., Torrent-Camarero, S., Gil, F. J., Mas-Moruno, C., Canal, C., et al. (2017). Biofunctional polyethylene glycol coatings on titanium: an *in vitro*-based comparison of functionalization methods. *Colloids Surf. B Biointerfaces* 152, 367–375. doi:10.1016/j.colsurfb.2017.01.042

Cai, D., Zhao, X., Yang, L., Wang, R., Qin, G., Chen, D.-f., et al. (2021). A novel biomedical titanium alloy with high antibacterial property and low elastic modulus. *J. Mater. Sci. Technol.* 81, 13–25. doi:10.1016/j.jmst.2021.01.015

Camargo, S. E. A., Xia, X., Fares, C., Ren, F., Hsu, S. M., Budei, D., et al. (2021). Nanostructured surfaces to promote osteoblast proliferation and minimize bacterial adhesion on titanium. *Mater. (Basel)* 14 (16), 4357. doi:10.3390/ma14164357

Chai, C. S., Gross, K. A., and Ben-Nissan, B. (1998). Critical ageing of hydroxyapatite sol-gel solutions. *Biomaterials* 19 (24), 2291–2296. doi:10.1016/s0142-9612(98)90138-7

Chai, M., An, M., and Zhang, X. (2021). Construction of a TiO(2)/MoSe(2)/CHI coating on dental implants for combating Streptococcus mutans infection. *Mater Sci. Eng. C Mater Biol. Appl.* 129, 112416. doi:10.1016/j.msec.2021.112416

Chang, Y. R., Weeks, E. R., and Ducker, W. A. (2018). Surface topography hinders bacterial surface motility. *ACS Appl. Mater Interfaces* 10 (11), 9225–9234. doi:10.1021/acsami.7b16715

Chen, M., Zhang, E., and Zhang, L. (2016). Microstructure, mechanical properties, bio-corrosion properties and antibacterial properties of Ti-Ag sintered alloys. *Mater Sci. Eng. C Mater Biol. Appl.* 62, 350–360. doi:10.1016/j.msec.2016.01.081

Chen, X., Han, J., Cai, X., and Wang, S. (2022). Antimicrobial peptides: sustainable application informed by evolutionary constraints. *Biotechnol. Adv.* 60, 108012. doi:10.1016/j.biotechadv.2022.108012

Chen, Z., Wang, Z., Qiu, W., and Fang, F. (2021). Overview of antibacterial strategies of dental implant materials for the prevention of peri-implantitis. *Bioconjug Chem.* 32 (4), 627–638. doi:10.1021/acs.bioconjchem.1c00129

Cheng, Q., Lu, R., Wang, X., and Chen, S. (2022). Antibacterial activity and cytocompatibility evaluation of the antimicrobial peptide Nal-P-113-loaded graphene oxide coating on titanium. *Dent. Mater J.* 41 (6), 905–915. doi:10.4012/dmj.2022-094

Chien, H.-W., Chen, X.-Y., and Tsai, W.-P. (2021). Poly(methyl methacrylate)/titanium dioxide (PMMA/TiO2) nanocomposite with shark-skin structure for preventing biofilm formation. *Mater. Lett.* 285, 129098. doi:10.1016/j.matlet.2020.129098

Chien, H. W., Chen, X. Y., Tsai, W. P., and Lee, M. (2020). Inhibition of biofilm formation by rough shark skin-patterned surfaces. *Colloids Surf. B Biointerfaces* 186, 110738. doi:10.1016/j.colsurfb.2019.110738

Choi, S., Lee, H., Hong, R., Jo, B., and Jo, S. (2022). Application of multi-layered temperature-responsive polymer brushes coating on titanium surface to inhibit biofilm associated infection in orthopedic surgery. *Polym. (Basel)* 15 (1), 163. doi:10.3390/polym15010163

Claes, L., Hutzschenreuter, P., Pohler, O., Lechner, V., and Strutz, R. (1976). The dependence of the removal torque of a leg screw a screw surface and implantation time (author's transl). *Arch. Orthop. Unfallchir* 85 (2), 155–159. doi:10.1007/bf00415453

Clever, K., Schlegel, K. A., Kniha, H., Conrads, G., Rink, L., Modabber, A., et al. (2019). Experimental peri-implant mucositis around titanium and zirconia implants in comparison to a natural tooth: part 2-clinical and microbiological parameters. *Int. J. Oral Maxillofac. Surg.* 48 (4), 560–565. doi:10.1016/j.ijom.2018.10.017

Córdoba, A., Hierro-Oliva, M., Pacha-Olivenza, M., Fernández-Calderón, M. C., Perelló, J., Isern, B., et al. (2016). Direct covalent grafting of phytate to titanium surfaces through Ti-O-P bonding shows bone stimulating surface properties and decreased bacterial adhesion. *ACS Appl. Mater Interfaces* 8 (18), 11326–11335. doi:10.1021/acsami.6b02533

Crawford, R. J., Webb, H. K., Truong, V. K., Hasan, J., and Ivanova, E. P. (2012). Surface topographical factors influencing bacterial attachment. *Adv. Colloid Interface Sci.* 179-182, 142–149. doi:10.1016/j.cis.2012.06.015

Damiati, L. A., Tsimbouri, M. P., Hernandez, V. L., Jayawarna, V., Ginty, M., Childs, P., et al. (2022). Materials-driven fibronectin assembly on nanoscale topography enhances mesenchymal stem cell adhesion, protecting cells from bacterial virulence factors and preventing biofilm formation. *Biomaterials* 280, 121263. doi:10.1016/j.biomaterials.2021.121263

Damodaran, V. B., and Murthy, N. S. (2016). Bio-inspired strategies for designing antifouling biomaterials. *Biomater. Res.* 20, 18. doi:10.1186/s40824-016-0064-4

Dantas, T., Padrão, J., da Silva, M. R., Pinto, P., Madeira, S., Vaz, P., et al. (2021). Bacteria co-culture adhesion on different texturized zirconia surfaces. *J. Mech. Behav. Biomed. Mater* 123, 104786. doi:10.1016/j.jmbbm.2021.104786

Del Pozo, J. L. (2018). Biofilm-related disease. *Expert Rev. Anti Infect. Ther.* 16 (1), 51–65. doi:10.1080/14787210.2018.1417036

Delgado-Ruiz, R., and Romanos, G. (2018). Potential causes of titanium particle and ion release in implant dentistry: A systematic review. *Int. J. Mol. Sci.* 19 (11), 3585. doi:10.3390/ijms19113585

Diefenbeck, M., Schrader, C., Gras, F., Mückley, T., Schmidt, J., Zankovych, S., et al. (2016). Gentamicin coating of plasma chemical oxidized titanium alloy prevents implant-related osteomyelitis in rats. *Biomaterials* 101, 156–164. doi:10.1016/j.biomaterials.2016.05.039

Dolid, A., Gomes, L. C., Mergulhão, F. J., and Reches, M. (2020). Combining chemistry and topography to fight biofilm formation: fabrication of micropatterned surfaces with a peptide-based coating. *Colloids Surf. B Biointerfaces* 196, 111365. doi:10.1016/j.colsurfb.2020.111365

Elbourne, A., Crawford, R. J., and Ivanova, E. P. (2017). Nano-structured antimicrobial surfaces: from nature to synthetic analogues. *J. Colloid Interface Sci.* 508, 603–616. doi:10.1016/j.jcis.2017.07.021

Eliaz, N., and Metoki, N. (2017). Calcium phosphate bioceramics: A review of their history, structure, properties, coating technologies and biomedical applications. *Mater. (Basel)* 10 (4), 334. doi:10.3390/ma10040334

Esteves, G. M., Esteves, J., Resende, M., Mendes, L., and Azevedo, A. S. (2022). Antimicrobial and antibiofilm coating of dental implants-past and new perspectives. *Antibiot. (Basel)* 11 (2), 235. doi:10.3390/antibiotics11020235

Fathi, M., Akbari, B., and Taheriazam, A. (2019). Antibiotics drug release controlling and osteoblast adhesion from Titania nanotubes arrays using silk fibroin coating. *Mater Sci. Eng. C Mater Biol. Appl.* 103, 109743. doi:10.1016/j.msec.2019.109743

Feng, G., Cheng, Y., Wang, S. Y., Borca-Tasciuc, D. A., Worobo, R. W., and Moraru, C. I. (2015). Bacterial attachment and biofilm formation on surfaces are reduced by small-diameter nanoscale pores: how small is small enough? *NPJ Biofilms Microbiomes* 1, 15022. doi:10.1038/npjbiofilms.2015.22

Fernández-Babiano, I., Navarro-Pérez, M. L., Pérez-Giraldo, C., and Fernández-Calderón, M. C. (2022). Antibacterial and antibiofilm activity of Carvacrol against oral pathogenic bacteria. *Metabolites* 12 (12), 1255. doi:10.3390/metabo12121255

Ferraris, S., Truffa Giachet, F., Miola, M., Bertone, E., Varesano, A., Vineis, C., et al. (2017). Nanogrooves and keratin nanofibers on titanium surfaces aimed at driving gingival fibroblasts alignment and proliferation without increasing bacterial adhesion. *Mater Sci. Eng. C Mater Biol. Appl.* 76, 1–12. doi:10.1016/j.msec.2017.02.152

Fischer, N. G., Moussa, D. G., Skoe, E. P., De Jong, D. A., and Aparicio, C. (2020). Keratinocyte-specific peptide-based surfaces for hemidesmosome upregulation and prevention of bacterial colonization. *ACS Biomater. Sci. Eng.* 6 (9), 4929–4939. doi:10.1021/acsbiomaterials.0c00845

Flamant, Q., Caravaca, C., Meille, S., Gremillard, L., Chevalier, J., Biotteau-Deheuvels, K., et al. (2016). Selective etching of injection molded zirconia-toughened alumina: towards osseointegrated and antibacterial ceramic implants. *Acta Biomater.* 46, 308–322. doi:10.1016/j.actbio.2016.09.017

Fontelo, R., Soares da Costa, D., Reis, R. L., Novoa-Carballal, R., and Pashkuleva, I. (2020). Bactericidal nanopatterns generated by block copolymer self-assembly. *Acta Biomater.* 112, 174–181. doi:10.1016/j.actbio.2020.06.003

Fowler, L., Janson, O., Engqvist, H., Norgren, S., and Öhman-Mägi, C. (2019). Antibacterial investigation of titanium-copper alloys using luminescent Staphylococcus epidermidis in a direct contact test. *Mater Sci. Eng. C Mater Biol. Appl.* 97, 707–714. doi:10.1016/j.msec.2018.12.050

Fu, J. H., and Wang, H. L. (2020). Breaking the wave of peri-implantitis. *Periodontol. 2000* 84 (1), 145–160. doi:10.1111/prd.12335

Fu, L., Xie, L., Fu, W., Hu, S., Zhang, Z., Leifer, K., et al. (2018). Ultrastrong translucent glass ceramic with nanocrystalline, biomimetic structure. *Nano Lett.* 18 (11), 7146–7154. doi:10.1021/acs.nanolett.8b03220

Garaicoa, J. L., Bates, A. M., Avila-Ortiz, G., and Brogden, K. A. (2020). Antimicrobial prosthetic surfaces in the oral cavity-A perspective on creative approaches. *Microorganisms* 8 (8), 1247. doi:10.3390/microorganisms8081247

Garner, S. J., Dalby, M. J., Nobbs, A. H., and Barbour, M. E. (2021). A novel chlorhexidine-hexametaphosphate coating for titanium with antibiofilm efficacy and stem cell cytocompatibility. *J. Mater Sci. Mater Med.* 32 (12), 139. doi:10.1007/s10856-021-06616-5

Ge, X., Leng, Y., Lu, X., Ren, F., Wang, K., Ding, Y., et al. (2015). Bacterial responses to periodic micropillar array. *J. Biomed. Mater Res. A* 103 (1), 384–396. doi:10.1002/jbm.a.35182

Ge, X., Ren, C., Ding, Y., Chen, G., Lu, X., Wang, K., et al. (2019). Micro/nano-structured TiO(2) surface with dual-functional antibacterial effects for biomedical applications. *Bioact. Mater* 4, 346–357. doi:10.1016/j.bioactmat.2019.10.006

Geng, H., Yuan, Y., Adayi, A., Zhang, X., Song, X., Gong, L., et al. (2018). Engineered chimeric peptides with antimicrobial and titanium-binding functions to inhibit biofilm formation on Ti implants. *Mater Sci. Eng. C Mater Biol. Appl.* 82, 141–154. doi:10.1016/j.msec.2017.08.062

Ghimire, A., and Song, J. (2021). Anti-Periprosthetic infection strategies: from implant surface topographical engineering to smart drug-releasing coatings. *ACS Appl. Mater Interfaces* 13 (18), 20921–20937. doi:10.1021/acsami.1c01389

Giljean, S., Bigerelle, M., Anselme, K., and Haidara, H. (2011). New insights on contact angle/roughness dependence on high surface energy materials. *Appl. Surf. Sci.* 257 (22), 9631–9638. doi:10.1016/j.apsusc.2011.06.088

Gomez-Florit, M., Pacha-Olivenza, M. A., Fernández-Calderón, M. C., Córdoba, A., González-Martín, M. L., Monjo, M., et al. (2016). Quercitrin-nanocoated titanium surfaces favour gingival cells against oral bacteria. *Sci. Rep.* 6, 22444. doi:10.1038/srep22444

Govindan, R., and Girija, E. K. (2014). Drug loaded phosphate glass/hydroxyapatite nanocomposite for orthopedic applications. *J. Mater Chem. B* 2 (33), 5468–5477. doi:10.1039/c4tb00549j

Gristina, A. G. (1987). Biomaterial-centered infection: microbial adhesion versus tissue integration. *Science* 237 (4822), 1588–1595. doi:10.1126/science.3629258

Gu, H., Lee, S. W., Buffington, S. L., Henderson, J. H., and Ren, D. (2016). On-demand removal of bacterial biofilms via shape memory activation. *ACS Appl. Mater Interfaces* 8 (33), 21140–21144. doi:10.1021/acsami.6b06900

Gugala, N., Lemire, J. A., and Turner, R. J. (2017). The efficacy of different anti-microbial metals at preventing the formation of, and eradicating bacterial biofilms of pathogenic indicator strains. *J. Antibiot. (Tokyo)* 70 (6), 775–780. doi:10.1038/ja.2017.10

Günther, M., Karygianni, L., Argyropoulou, A., Anderson, A. C., Hellwig, E., Skaltsounis, A. L., et al. (2022). The antimicrobial effect of Rosmarinus officinalis extracts on oral initial adhesion *ex vivo*. *Clin. Oral Investig.* 26 (6), 4369–4380. doi:10.1007/s00784-022-04400-5

Guo, T., Gulati, K., Arora, H., Han, P., Fournier, B., and Ivanovski, S. (2021). Race to invade: understanding soft tissue integration at the transmucosal region of titanium dental implants. *Dent. Mater* 37 (5), 816–831. doi:10.1016/j.dental.2021.02.005

Haktaniyan, M., and Bradley, M. (2022). Polymers showing intrinsic antimicrobial activity. *Chem. Soc. Rev.* 51 (20), 8584–8611. doi:10.1039/d2cs00558a

Halder, P., Nasabi, M., Jayasuriya, N., Shimeta, J., Deighton, M., Bhattacharya, S., et al. (2014). An assessment of the dynamic stability of microorganisms on patterned surfaces in relation to biofouling control. *Biofouling* 30 (6), 695–707. doi:10.1080/08927014.2014.914177

Han, A., Tsoi, J. K.-H., Matinlinna, J. P., and Chen, Z. (2017). Influence of grit-blasting and hydrofluoric acid etching treatment on surface characteristics and biofilm formation on zirconia. *Coatings* 7 (8), 130. doi:10.3390/coatings7080130

Hanawa, T. (2020). Zirconia versus titanium in dentistry: A review. *Dent. Mater J.* 39 (1), 24–36. doi:10.4012/dmj.2019-172

Hayes, M. J., Levine, T. P., and Wilson, R. H. (2016). Identification of nanopillars on the cuticle of the aquatic larvae of the drone fly (Diptera: syrphidae). *J. Insect Sci.* 16 (1), 36. doi:10.1093/jisesa/iew019

Hazell, G., Fisher, L. E., Murray, W. A., Nobbs, A. H., and Su, B. (2018). Bioinspired bactericidal surfaces with polymer nanocone arrays. *J. Colloid Interface Sci.* 528, 389–399. doi:10.1016/j.jcis.2018.05.096

He, L.-J., Hao, J.-C., Dai, L., Zeng, R.-C., and Li, S.-Q. (2020). Layer-by-layer assembly of gentamicin-based antibacterial multilayers on Ti alloy. *Mater. Lett.* 261, 127001. doi:10.1016/j.matlet.2019.127001

He, T., Chen, H., Liu, P., Shi, H., Xu, X., Feng, C., et al. (2023). One-step co-doping of ZnO and Zn2+ in osteoinductive calcium phosphate ceramics with synergistic antibacterial activity for regenerative repair of infected bone defect. *J. Mater. Sci. Technol.* 163, 168–181. doi:10.1016/j.jmst.2023.04.032

Hou, S., Gu, H., Smith, C., and Ren, D. (2011). Microtopographic patterns affect *Escherichia coli* biofilm formation on poly(dimethylsiloxane) surfaces. *Langmuir* 27 (6), 2686–2691. doi:10.1021/la1046194

Howe, M. S., Keys, W., and Richards, D. (2019). Long-term (10-year) dental implant survival: A systematic review and sensitivity meta-analysis. *J. Dent.* 84, 9–21. doi:10.1016/j.jdent.2019.03.008

Hu, X., Xu, R., Yu, X., Chen, J., Wan, S., Ouyang, J., et al. (2018). Enhanced antibacterial efficacy of selective laser melting titanium surface with nanophase calcium phosphate embedded to TiO(2) nanotubes. *Biomed. Mater* 13 (4), 045015. doi:10.1088/1748-605X/aac1a3

Huang, Q., Yang, Y., Zheng, D., Song, R., Zhang, Y., Jiang, P., et al. (2017). Effect of construction of TiO(2) nanotubes on platelet behaviors: structure-property relationships. *Acta Biomater.* 51, 505–512. doi:10.1016/j.actbio.2017.01.044

Ichikawa, T., Hirota, K., Kanitani, H., Miyake, Y., and Matsumoto, N. (1998). *In vitro* adherence of Streptococcus constellatus to dense hydroxyapatite and titanium. *J. Oral Rehabil.* 25 (2), 125–127. doi:10.1046/j.1365-2842.1998.00216.x

Jang, W., Kim, H. S., Alam, K., Ji, M. K., Cho, H. S., and Lim, H. P. (2021). Direct-deposited graphene oxide on dental implants for antimicrobial activities and osteogenesis. *Int. J. Nanomedicine* 16, 5745–5754. doi:10.2147/ijn.S319569

Jannesari, M., Akhavan, O., Madaah Hosseini, H. R., and Bakhshi, B. (2020). Graphene/CuO(2) nanoshuttles with controllable release of oxygen nanobubbles promoting interruption of bacterial respiration. *ACS Appl. Mater Interfaces* 12 (32), 35813–35825. doi:10.1021/acsami.0c05732

Jeong, W. S., Kwon, J. S., Lee, J. H., Uhm, S. H., Ha Choi, E., and Kim, K. M. (2017). Bacterial attachment on titanium surfaces is dependent on topography and chemical changes induced by nonthermal atmospheric pressure plasma. *Biomed. Mater* 12 (4), 045015. doi:10.1088/1748-605X/aa734e

Jiang, R., Hao, L., Song, L., Tian, L., Fan, Y., Zhao, J., et al. (2020). Lotus-leaf-inspired hierarchical structured surface with non-fouling and mechanical bactericidal performances. *Chem. Eng. J.* 398, 125609. doi:10.1016/j.cej.2020.125609

Karygianni, L., Jähnig, A., Schienle, S., Bernsmann, F., Adolfsson, E., Kohal, R. J., et al. (2013). Initial bacterial adhesion on different yttria-stabilized tetragonal zirconia implant surfaces *in vitro*. *Mater. (Basel)* 6 (12), 5659–5674. doi:10.3390/ma6125659

Kawamura, H., Ito, A., Muramatsu, T., Miyakawa, S., Ochiai, N., and Tateishi, T. (2003). Long-term implantation of zinc-releasing calcium phosphate ceramics in rabbit femora. *J. Biomed. Mater Res. A* 65 (4), 468–474. doi:10.1002/jbm.a.10524

Ke, D., Robertson, S. F., Dernell, W. S., Bandyopadhyay, A., and Bose, S. (2017). Effects of MgO and SiO(2) on plasma-sprayed hydroxyapatite coating: an *in vivo* study in rat distal femoral defects. *ACS Appl. Mater Interfaces* 9 (31), 25731–25737. doi:10.1021/acsami.7b05574

Ke, D., Vu, A. A., Bandyopadhyay, A., and Bose, S. (2019). Compositionally graded doped hydroxyapatite coating on titanium using laser and plasma spray deposition for bone implants. *Acta Biomater.* 84, 414–423. doi:10.1016/j.actbio.2018.11.041

Khalid, S., Gao, A., Wang, G., Chu, P. K., and Wang, H. (2020). Tuning surface topographies on biomaterials to control bacterial infection. *Biomater. Sci.* 8 (24), 6840–6857. doi:10.1039/d0bm00845a

Kim, H. S., Ji, M. K., Jang, W. H., Alam, K., Kim, H. S., Cho, H. S., et al. (2021). Biological effects of the novel mulberry surface characterized by micro/nanopores and plasma-based graphene oxide deposition on titanium. *Int. J. Nanomedicine* 16, 7307–7317. doi:10.2147/ijn.S311872

Kononenko, V., Repar, N., Marušič, N., Drašler, B., Romih, T., Hočevar, S., et al. (2017). Comparative *in vitro* genotoxicity study of ZnO nanoparticles, ZnO macroparticles and ZnCl(2) to MDCK kidney cells: size matters. *Toxicol Vitro* 40, 256–263. doi:10.1016/j.tiv.2017.01.015

Koopaie, M., Bordbar-Khiabani, A., Kolahdooz, S., Darbandsari, A. K., and Mozafari, M. (2020). Advanced surface treatment techniques counteract biofilm-associated infections on dental implants. *Mater. Res. Express* 7 (1), 015417. doi:10.1088/2053-1591/ab6a57

Kubiak, B., Radtke, A., Topolski, A., Wrzeszcz, G., Golińska, P., Kaszkowiak, E., et al. (2021). The composites of PCL and tetranuclear titanium(IV)-oxo complexes as materials exhibiting the photocatalytic and the antimicrobial activity. *Int. J. Mol. Sci.* 22 (13), 7021. doi:10.3390/ijms22137021

Kunrath, M. F., Dos Santos, R. P., de Oliveira, S. D., Hubler, R., Sesterheim, P., and Teixeira, E. R. (2020). Osteoblastic cell behavior and early bacterial adhesion on macro-micro-and nanostructured titanium surfaces for biomedical implant applications. *Int. J. Oral Maxillofac. Implants* 35 (4), 773–781. doi:10.11607/jomi.8069

Lampé, I., Beke, D., Biri, S., Csarnovics, I., Csik, A., Dombrádi, Z., et al. (2019). <p>Investigation of silver nanoparticles on titanium surface created by ion implantation technology</p>. *Int. J. Nanomedicine* 14, 4709–4721. doi:10.2147/ijn.S197782

Latthe, S. S., Terashima, C., Nakata, K., and Fujishima, A. (2014). Superhydrophobic surfaces developed by mimicking hierarchical surface morphology of lotus leaf. *Molecules* 19 (4), 4256–4283. doi:10.3390/molecules19044256

Laurent, F., Bignon, A., Goldnadel, J., Chevalier, J., Fantozzi, G., Viguier, E., et al. (2008). A new concept of gentamicin loaded HAP/TCP bone substitute for prophylactic action: *in vitro* release validation. *J. Mater Sci. Mater Med.* 19 (2), 947–951. doi:10.1007/s10856-007-0163-9

Lee, J., and Pascall, M. A. (2018). Effect of micro-pattern topography on the attachment and survival of foodborne microorganisms on food contact surfaces. *food contact surfaces* 38 (1), e12379. doi:10.1111/jfs.12379

Lee, S. W., Phillips, K. S., Gu, H., Kazemzadeh-Narbat, M., and Ren, D. (2021). How microbes read the map: effects of implant topography on bacterial adhesion and biofilm formation. *Biomaterials* 268, 120595. doi:10.1016/j.biomaterials.2020.120595

Lee, Y., Huang, J., Bing, Z., Yuan, K., Yang, J., Cai, M., et al. (2022). pH-responsive cinnamaldehyde-TiO(2) nanotube coating: fabrication and functions in a simulated diabetes condition. *J. Mater Sci. Mater Med.* 33 (9), 63. doi:10.1007/s10856-022-06683-2

Levengood, S. L., and Zhang, M. (2014). Chitosan-based scaffolds for bone tissue engineering. *J. Mater Chem. B* 2 (21), 3161–3184. doi:10.1039/c4tb00027g

Li, B., Ma, J., Wang, D., Liu, X., Li, H., Zhou, L., et al. (2019a). Self-adjusting antibacterial properties of Ag-incorporated nanotubes on micro-nanostructured Ti surfaces. *Biomater. Sci.* 7 (10), 4075–4087. doi:10.1039/c9bm00862d

Li, D., Wang, D., He, Y., Tao, B., Liu, X., Yang, Y., et al. (2023a). A HAase/NIR responsive surface on titanium implants for treating bacterial infection and improving osseointegration. *J. Mater. Sci. Technol.* 143, 93–106. doi:10.1016/j.jmst.2022.09.029

Li, L., Li, Q., Zhao, M., Dong, L., Wu, J., and Li, D. (2019b). Effects of Zn and Ag ratio on cell adhesion and antibacterial properties of Zn/Ag coimplanted TiN. *ACS Biomater. Sci. Eng.* 5 (7), 3303–3310. doi:10.1021/acsbiomaterials.9b00248

Li, M., Lin, D., and Zhu, L. (2013). Effects of water chemistry on the dissolution of ZnO nanoparticles and their toxicity to *Escherichia coli*. *Environ. Pollut.* 173, 97–102. doi:10.1016/j.envpol.2012.10.026

Li, Q., Zhou, G., Yu, X., Wang, T., Xi, Y., and Tang, Z. (2015). Porous deproteinized bovine bone scaffold with three-dimensional localized drug delivery system using chitosan microspheres. *Biomed. Eng. Online* 14, 33. doi:10.1186/s12938-015-0028-2

Li, S., Liu, H., Siddiqui, M. A., Li, Y., Wang, H., Zhang, S. Y., et al. (2023b). Corrosion behavior and bio-functions of the ultrafine-grained Ti6Al4V-5Cu alloy with a dual-phase honeycomb shell structure in simulated body fluid. *ACS Biomater. Sci. Eng.* 9 (5), 2362–2375. doi:10.1021/acsbiomaterials.2c01316

Li, T., Wang, N., Chen, S., Lu, R., Li, H., and Zhang, Z. (2017). Antibacterial activity and cytocompatibility of an implant coating consisting of TiO₂ nanotubes combined with a GL13K antimicrobial peptide. *Int. J. Nanomedicine* 12, 2995–3007. doi:10.2147/ijn.S128775

Li, X., Qi, M., Sun, X., Weir, M. D., Tay, F. R., Oates, T. W., et al. (2019c). Surface treatments on titanium implants via nanostructured ceria for antibacterial and anti-inflammatory capabilities. *Acta Biomater.* 94, 627–643. doi:10.1016/j.actbio.2019.06.023

Li, Y., Li, B., Song, Y., Ma, A., Li, C., Zhang, X., et al. (2019d). Improved osteoblast adhesion and osseointegration on TiO₂ nanotubes surface with hydroxyapatite coating. *Dent. Mater J.* 38 (2), 278–286. doi:10.4012/dmj.2018-118

Li, Y., Liu, L., Wan, P., Zhai, Z., Mao, Z., Ouyang, Z., et al. (2016). Biodegradable Mg-Cu alloy implants with antibacterial activity for the treatment of osteomyelitis: *in vitro* and *in vivo* evaluations. *Biomaterials* 106, 250–263. doi:10.1016/j.biomaterials.2016.08.031

Li, Y., Yang, Y., Li, R., Tang, X., Guo, D., Qing, Y., et al. (2019e). <p>Enhanced antibacterial properties of orthopedic implants by titanium nanotube surface modification: a review of current techniques</p>. *Int. J. Nanomedicine* 14, 7217–7236. doi:10.2147/ijn.S216175

Liao, Y., Zhou, Z., Dai, S., Jiang, L., Yang, P., Zhao, A., et al. (2021). Cell-friendly photo-functionalized TiO(2) nano-micro-honeycombs for selectively preventing bacteria and platelet adhesion. *Mater Sci. Eng. C Mater Biol. Appl.* 123, 111996. doi:10.1016/j.msec.2021.111996

Liu, J., Li, F., Liu, C., Wang, H., Ren, B., Yang, K., et al. (2014a). Effect of Cu content on the antibacterial activity of titanium-copper sintered alloys. *Mater Sci. Eng. C Mater Biol. Appl.* 35, 392–400. doi:10.1016/j.msec.2013.11.028

Liu, L., Ercan, B., Sun, L., Ziemer, K. S., and Webster, T. J. (2016). Understanding the role of polymer surface nanoscale topography on inhibiting bacteria adhesion and growth. *ACS Biomater. Sci. Eng.* 2 (1), 122–130. doi:10.1021/acsbiomaterials.5b00431

Liu, L., Li, W., and Liu, Q. (2014b). Recent development of antifouling polymers: structure, evaluation, and biomedical applications in nano/micro-structures. *Wiley Interdiscip. Rev. Nanomed Nanobiotechnol* 6 (6), 599–614. doi:10.1002/wnan.1278

Liu, Q., Brookbank, L., Ho, A., Coffey, J., Brennan, A. B., and Jones, C. J. (2020). Surface texture limits transfer of *S. aureus*, T4 bacteriophage, influenza B virus and human coronavirus. *PLoS One* 15 (12), e0244518. doi:10.1371/journal.pone.0244518

Liu, W., Su, P., Chen, S., Wang, N., Ma, Y., Liu, Y., et al. (2014c). Synthesis of TiO2 nanotubes with ZnO nanoparticles to achieve antibacterial properties and stem cell compatibility. *Nanoscale* 6 (15), 9050–9062. doi:10.1039/c4nr01531b

Liu, X. H., Ren, Y. M., Fan, D. Y., Huang, S., Ma, Y. S., Ding, J. P., et al. (2023). Shining light on multidrug-resistant bacterial infections: rational design of multifunctional organosilver-based AIEgen probes as light-activated theranostics for combating biofilms and liver abscesses. *Adv. Funct. Mater.* doi:10.1002/adfm.202304974

Liu, Z., Yi, Y., Wang, S., Dou, H., Fan, Y., Tian, L., et al. (2022). Bio-Inspired self-adaptive nanocomposite array: from non-antibiotic antibacterial actions to cell proliferation. *ACS Nano* 16 (10), 16549–16562. doi:10.1021/acsnano.2c05980

Lozeau, L. D., Rolle, M. W., and Camesano, T. A. (2018). A QCM-D study of the concentration- and time-dependent interactions of human LL37 with model mammalian lipid bilayers. *Colloids Surf. B Biointerfaces* 167, 229–238. doi:10.1016/j.colsurfb.2018.04.016

Lu, N., Zhang, W., Weng, Y., Chen, X., Cheng, Y., and Zhou, P. (2016). Fabrication of PDMS surfaces with micro patterns and the effect of pattern sizes on bacteria adhesion. *Food Control.* 68, 344–351. doi:10.1016/j.foodcont.2016.04.014

Lüdecke, C., Roth, M., Yu, W., Horn, U., Bossert, J., and Jandt, K. D. (2016). Nanorough titanium surfaces reduce adhesion of *Escherichia coli* and *Staphylococcus aureus* via nano adhesion points. *Colloids Surf. B Biointerfaces* 145, 617–625. doi:10.1016/j.colsurfb.2016.05.049

Lv, H., Chen, Z., Yang, X., Cen, L., Zhang, X., and Gao, P. (2014). Layer-by-layer self-assembly of minocycline-loaded chitosan/alginate multilayer on titanium substrates to inhibit biofilm formation. *J. Dent.* 42 (11), 1464–1472. doi:10.1016/j.jdent.2014.06.003

Ma, Y. D., Yan, J., Yan, T. T., Wang, Q., Bao, Z. F., and Yi, Z. (2022). Biological properties of Cu-bearing and Ag-bearing titanium-based alloys and their surface modifications: A review of antibacterial aspect. *Front. Mater.* 9. doi:10.3389/fmats.2022.999794

Maharubin, S., Hu, Y., Sooriyaarachchi, D., Cong, W., and Tan, G. Z. (2019). Laser engineered net shaping of antimicrobial and biocompatible titanium-silver alloys. *Mater Sci. Eng. C Mater Biol. Appl.* 105, 110059. doi:10.1016/j.msec.2019.110059

Mansoorianfar, M., Khataee, A., Riahi, Z., Shahin, K., Asadnia, M., Razmjou, A., et al. (2020). Scalable fabrication of tunable titanium nanotubes via sonoelectrochemical process for biomedical applications. *Ultrason. Sonochem* 64, 104783. doi:10.1016/j.ultsonch.2019.104783

Mas-Moruno, C., Su, B., and Dalby, M. J. (2019). Multifunctional coatings and nanotopographies: toward cell instructive and antibacterial implants. *Adv. Healthc. Mater* 8 (1), e1801103. doi:10.1002/adhm.201801103

Mathew, A., Hasan, J., Singamneni, S., and Yarlagadda, P. K. D. V. (2023). Nanospikes on customized 3D-printed titanium implant surface inhibits bacterial colonization. *Adv. Eng. Mater.* 25 (8), 2201306. doi:10.1002/adem.202201306

Matos, A. O., de Almeida, A. B., Beline, T., Tonon, C. C., Casarin, R. C. V., Windsor, L. J., et al. (2020). Synthesis of multifunctional chlorhexidine-doped thin films for titanium-based implant materials. *Mater Sci. Eng. C Mater Biol. Appl.* 117, 111289. doi:10.1016/j.msec.2020.111289

Memarzadeh, K., Sharili, A. S., Huang, J., Rawlinson, S. C., and Allaker, R. P. (2015). Nanoparticulate zinc oxide as a coating material for orthopedic and dental implants. *J. Biomed. Mater Res. A* 103 (3), 981–989. doi:10.1002/jbm.a.35241

Mezey, É., and Nemeth, K. (2015). Mesenchymal stem cells and infectious diseases: smarter than drugs. *Immunol. Lett.* 168 (2), 208–214. doi:10.1016/j.imlet.2015.05.020

Mishra, S. K., Ferreira, J. M., and Kannan, S. (2015). Mechanically stable antimicrobial chitosan-PVA-silver nanocomposite coatings deposited on titanium implants. *Carbohydr. Polym.* 121, 37–48. doi:10.1016/j.carbpol.2014.12.027

Mo, S., Mehrjou, B., Tang, K., Wang, H., Huo, K., Qasim, A. M., et al. (2020). Dimensional-dependent antibacterial behavior on bioactive micro/nano polyetheretherketone (PEEK) arrays. *Chem. Eng. J.* 392, 123736. doi:10.1016/j.cej.2019.123736

Mukaddam, K., Astasov-Frauenhoffer, M., Fasler-Kan, E., Marot, L., Kisiel, M., Meyer, E., et al. (2021). Effect of a nanostructured titanium surface on gingival cell adhesion, viability and properties against P. gingivalis. *Mater. (Basel)* 14 (24), 7686. doi:10.3390/ma14247686

Nakajo, K., Takahashi, M., Kikuchi, M., Takada, Y., Okuno, O., Sasaki, K., et al. (2014). Inhibitory effect of Ti-Ag alloy on artificial biofilm formation. *Dent. Mater J.* 33 (3), 389–393. doi:10.4012/dmj.2013-334

Nascimento, C., Pita, M. S., Santos Ede, S., Monesi, N., Pedrazzi, V., Albuquerque Junior, R. F., et al. (2016). Microbiome of titanium and zirconia dental implants abutments. *Dent. Mater* 32 (1), 93–101. doi:10.1016/j.dental.2015.10.014

Navarro-Pérez, M. L., Vadillo-Rodríguez, V., Fernández-Babiano, I., Pérez-Giraldo, C., and Fernández-Calderón, M. C. (2021). Antimicrobial activity of a novel Spanish propolis against planktonic and sessile oral Streptococcus spp. *Sci. Rep.* 11 (1), 23860. doi:10.1038/s41598-021-03202-1

Nichol, T., Callaghan, J., Townsend, R., Stockley, I., Hatton, P. V., Le Maitre, C., et al. (2021). The antimicrobial activity and biocompatibility of a controlled gentamicin-releasing single-layer sol-gel coating on hydroxyapatite-coated titanium. *Bone Jt. J.* 103-b (3), 522–529. doi:10.1302/0301-620x.103b3.Bjj-2020-0347.R1

Nie, B. e., Long, T., Li, H., Wang, X., and Yue, B. (2017). A comparative analysis of antibacterial properties and inflammatory responses for the KR-12 peptide on titanium and PEGylated titanium surfaces. *RSC Adv.* 7 (55), 34321–34330. doi:10.1039/C7RA05538B

Nishida, M., Nakaji-Hirabayashi, T., Kitano, H., Saruwatari, Y., and Matsuoka, K. (2017). Titanium alloy modified with anti-biofouling zwitterionic polymer to facilitate formation of bio-mineral layer. *Colloids Surf. B Biointerfaces* 152, 302–310. doi:10.1016/j.colsurfb.2017.01.018

Noronha, V. T., Paula, A. J., Durán, G., Galembeck, A., Cogo-Müller, K., Franz-Montan, M., et al. (2017). Silver nanoparticles in dentistry. *Dent. Mater* 33 (10), 1110–1126. doi:10.1016/j.dental.2017.07.002

Oda, Y., Miura, T., Mori, G., Sasaki, H., Ito, T., Yoshinari, M., et al. (2020). Adhesion of streptococci to titanium and zirconia. *PLoS One* 15 (6), e0234524. doi:10.1371/journal.pone.0234524

Odatsu, T., Kuroshima, S., Sato, M., Takase, K., Valanezhad, A., Naito, M., et al. (2020). Antibacterial properties of nano-Ag coating on healing abutment: an *in vitro* and clinical study. *Antibiot. (Basel)* 9 (6), 347. doi:10.3390/antibiotics9060347

Ou, K.-L., Weng, C.-C., Lin, Y.-H., and Huang, M.-S. (2017). A promising of alloying modified beta-type titanium-niobium implant for biomedical applications: microstructural characteristics, *in vitro* biocompatibility and antibacterial performance. *J. Alloys Compd.* 697, 231–238. doi:10.1016/j.jallcom.2016.12.120

Pacha-Olivenza, M., Tejero, R., Fernández-Calderón, M. C., Anitua, E., Troya, M., and González-Martín, M. L. (2019). Relevance of topographic parameters on the adhesion and proliferation of human gingival fibroblasts and oral bacterial strains. *Biomed. Res. Int.* 2019, 1–13. doi:10.1155/2019/8456342

Palla-Rubio, B., Araújo-Gomes, N., Fernández-Gutiérrez, M., Rojo, L., Suay, J., Gurruchaga, M., et al. (2019). Synthesis and characterization of silica-chitosan hybrid materials as antibacterial coatings for titanium implants. *Carbohydr. Polym.* 203, 331–341. doi:10.1016/j.carbpol.2018.09.064

Pan, C., Liu, T., Zhang, Z., Zhang, X., Qiao, X., Hu, Y., et al. (2021). Preparation of chitosan-Zn2+ complex coating on polydopamine-modified TiO2 nanotubes to enhance osteoblast behaviors. *Mater. Lett.* 282, 128665. doi:10.1016/j.matlet.2020.128665

Panáček, A., Kvítek, L., Smékalová, M., Večeřová, R., Kolář, M., Röderová, M., et al. (2018). Bacterial resistance to silver nanoparticles and how to overcome it. *Nat. Nanotechnol.* 13 (1), 65–71. doi:10.1038/s41565-017-0013-y

Peng, Z., Ni, J., Zheng, K., Shen, Y., Wang, X., He, G., et al. (2013). Dual effects and mechanism of TiO2 nanotube arrays in reducing bacterial colonization and enhancing C3H10T1/2 cell adhesion. *Int. J. Nanomedicine* 8, 3093–3105. doi:10.2147/ijn.S48084

Perera-Costa, D., Bruque, J. M., González-Martín, M. L., Gómez-García, A. C., and Vadillo-Rodríguez, V. (2014). Studying the influence of surface topography on bacterial adhesion using spatially organized microtopographic surface patterns. *Langmuir* 30 (16), 4633–4641. doi:10.1021/la5001057

Pingle, H., Wang, P. Y., Thissen, H., and Kingshott, P. (2018). Controlled attachment of *Pseudomonas aeruginosa* with binary colloidal crystal-based topographies. *Small* 14 (14), e1703574. doi:10.1002/smll.201703574

Podporska-Carroll, J., Panaitescu, E., Quilty, B., Wang, L., Menon, L., and Pillai, S. C. (2015). Antimicrobial properties of highly efficient photocatalytic TiO2 nanotubes. *Appl. Catal. B Environ.* 176-177, 70–75. doi:10.1016/j.apcatb.2015.03.029

Poppolo Deus, F., and Ouanounou, A. (2022). Chlorhexidine in dentistry: pharmacology, uses, and adverse effects. *Int. Dent. J.* 72 (3), 269–277. doi:10.1016/j.identj.2022.01.005

Pranjali, P., Meher, M. K., Raj, R., Prasad, N., Poluri, K. M., Kumar, D., et al. (2019). Physicochemical and antibacterial properties of PEGylated zinc oxide nanoparticles dispersed in peritoneal dialysis fluid. *ACS Omega* 4 (21), 19255–19264. doi:10.1021/acsomega.9b02615

Rahaman, M., and Xiao, W. (2018). Silicon nitride bioceramics in healthcare. *Int. J. Appl. Ceram. Technol.* 15 (4), 861–872. doi:10.1111/ijac.12836

Rahayu, D. P., De Mori, A., Yusuf, R., Draheim, R., Lalatsa, A., and Roldo, M. (2022). Enhancing the antibacterial effect of chitosan to combat orthopaedic implant-associated infections. *Carbohydr. Polym.* 289, 119385. doi:10.1016/j.carbpol.2022.119385

Ratier, A., Gibson, I. R., Best, S. M., Freche, M., Lacout, J. L., and Rodriguez, F. (2001). Setting characteristics and mechanical behaviour of a calcium phosphate bone cement containing tetracycline. *Biomaterials* 22 (9), 897–901. doi:10.1016/s0142-9612(00)00252-0

Ren, L., Wong, H. M., Yan, C. H., Yeung, K. W., and Yang, K. (2015). Osteogenic ability of Cu-bearing stainless steel. *J. Biomed. Mater Res. B Appl. Biomater.* 103 (7), 1433–1444. doi:10.1002/jbm.b.33318

Renner, L. D., and Weibel, D. B. (2011). Physicochemical regulation of biofilm formation. *MRS Bull.* 36 (5), 347–355. doi:10.1557/mrs.2011.65

Renvert, S., Lindahl, C., and Persson, G. R. (2018). Occurrence of cases with peri-implant mucositis or peri-implantitis in a 21-26 years follow-up study. *J. Clin. Periodontol.* 45 (2), 233–240. doi:10.1111/jcpe.12822

Rizzello, L., Sorce, B., Sabella, S., Vecchio, G., Galeone, A., Brunetti, V., et al. (2011). Impact of nanoscale topography on genomics and proteomics of adherent bacteria. *ACS Nano* 5 (3), 1865–1876. doi:10.1021/nn102692m

Robinson, F. G., Knoernschild, K. L., Sterrett, J. D., and Tompkins, G. R. (1996). Porphyromonas gingivalis endotoxin affinity for dental ceramics. *J. Prosthet. Dent.* 75 (2), 217–227. doi:10.1016/s0022-3913(96)90102-x

Roehling, S., Astasov-Frauenhoffer, M., Hauser-Gerspach, I., Braissant, O., Woelfler, H., Waltimo, T., et al. (2017). *In vitro* biofilm formation on titanium and zirconia implant surfaces. *J. Periodontol.* 88 (3), 298–307. doi:10.1902/jop.2016.160245

Ruan, H., Fan, C., Zheng, X., Zhang, Y., and Chen, Y. (2009). *In vitro* antibacterial and osteogenic properties of plasma sprayed silver-containing hydroxyapatite coating. *Chin. Sci. Bull.* 54 (23), 4438–4445. doi:10.1007/s11434-009-0175-6

Sakamoto, A., Terui, Y., Horie, C., Fukui, T., Masuzawa, T., Sugawara, S., et al. (2014). Antibacterial effects of protruding and recessed shark skin micropatterned surfaces of polyacrylate plate with a shallow groove. *FEMS Microbiol. Lett.* 361 (1), 10–16. doi:10.1111/1574-6968.12604

Sang, S., Yang, C., Chai, H., Yuan, X., Liu, W., and Zhang, X. (2021). The sulfonated polyetheretherketone with 3D structure modified by two bio-inspired methods shows osteogenic and antibacterial functions. *Chem. Eng. J.* 420, 130059. doi:10.1016/j.cej.2021.130059

Shahali, H., Hasan, J., Mathews, A., Wang, H., Yan, C., Tesfamichael, T., et al. (2019). Multi-biofunctional properties of three species of cicada wings and biomimetic fabrication of nanopatterned titanium pillars. *J. Mater Chem. B* 7 (8), 1300–1310. doi:10.1039/c8tb03295e

Shin, S. J., Moon, S. H., Kim, H. J., Oh, S. H., and Bae, J. M. (2022). Oral microbiome using Colocasia antiquorum var. esculenta extract varnish in a mouse model with oral gavage of P. gingivalis ATCC 53978. *Med. Kaunas.* 58 (4), 506. doi:10.3390/medicina58040506

Shin, Y., and Lee, S. (2008). Self-organized regular arrays of anodic TiO2 nanotubes. *Nano Lett.* 8 (10), 3171–3173. doi:10.1021/nl801422w

Siddiqui, D. A., Jacob, J. J., Fidai, A. B., and Rodrigues, D. C. (2019). Biological characterization of surface-treated dental implant materials in contact with mammalian host and bacterial cells: titanium versus zirconia. *RSC Adv.* 9 (55), 32097–32109. doi:10.1039/c9ra06010c

Skovdal, S. M., Jørgensen, N. P., Petersen, E., Jensen-Fangel, S., Ogaki, R., Zeng, G., et al. (2018). Ultra-dense polymer brush coating reduces Staphylococcus epidermidis biofilms on medical implants and improves antibiotic treatment outcome. *Acta Biomater.* 76, 46–55. doi:10.1016/j.actbio.2018.07.002

Sorzabal-Bellido, I., Barbieri, L., Beckett, A. J., Prior, I. A., Susarrey-Arce, A., Tiggelaar, R. M., et al. (2022). Effect of local topography on cell division of Staphylococcus spp. *Nanomater. (Basel)* 12 (4), 683. doi:10.3390/nano12040683

Staats, K., Pilz, M., Sun, J., Boiadjieva-Scherzer, T., Kronberger, H., Tobudic, S., et al. (2022). Antimicrobial potential and osteoblastic cell growth on electrochemically modified titanium surfaces with nanotubes and selenium or silver incorporation. *Sci. Rep.* 12 (1), 8298. doi:10.1038/s41598-022-11804-6

Stabryla, L. M., Johnston, K. A., Diemler, N. A., Cooper, V. S., Millstone, J. E., Haig, S. J., et al. (2021). Role of bacterial motility in differential resistance mechanisms of silver nanoparticles and silver ions. *Nat. Nanotechnol.* 16 (9), 996–1003. doi:10.1038/s41565-021-00929-w

Stavrakis, A. I., Zhu, S., Loftin, A. H., Weixian, X., Niska, J., Hegde, V., et al. (2019). Controlled release of vancomycin and tigecycline from an orthopaedic implant coating prevents *Staphylococcus aureus* infection in an open fracture animal model. *Biomed. Res. Int.* 2019, 1–9. doi:10.1155/2019/1638508

Sun, H., Hong, Y., Xi, Y., Zou, Y., Gao, J., and Du, J. (2018). Synthesis, self-assembly, and biomedical applications of antimicrobial peptide-polymer conjugates. *Biomacromolecules* 19 (6), 1701–1720. doi:10.1021/acs.biomac.8b00208

Tabesh, M., Sh, M. E., Etemadi, M., Naddaf, F., Heidari, F., and Alizargar, J. (2022). The antibacterial activity of nasturtium officinale extract on common oral pathogenic bacteria. *Niger. J. Clin. Pract.* 25 (9), 1466–1475. doi:10.4103/njcp.njcp_1887_21

Tambone, E., Bonomi, E., Ghensi, P., Maniglio, D., Ceresa, C., Agostinacchio, F., et al. (2021). Rhamnolipid coating reduces microbial biofilm formation on titanium implants: an *in vitro* study. *BMC Oral Health* 21 (1), 49. doi:10.1186/s12903-021-01412-7

Tan, X., Wang, Z., Yang, X., Yu, P., Sun, M., Zhao, Y., et al. (2023). Enhancing cell adhesive and antibacterial activities of glass-fibre-reinforced polyetherketoneketone through Mg and Ag PIII. *Regen. Biomater.* 10, rbad066. doi:10.1093/rb/rbad066

Teughels, W., Van Assche, N., Sliepen, I., and Quirynen, M. (2006). Effect of material characteristics and/or surface topography on biofilm development. *Clin. Oral Implants Res.* 17 (2), 68–81. doi:10.1111/j.1600-0501.2006.01353.x

Tiwari, A., Sharma, P., Vishwamitra, B., and Singh, G. (2021). Review on surface treatment for implant infection via gentamicin and antibiotic releasing coatings. *Coatings* 11 (8), 1006. doi:10.3390/coatings11081006

Vadillo-Rodríguez, V., Guerra-García-Mora, A. I., Perera-Costa, D., Gónzalez-Martín, M. L., and Fernández-Calderón, M. C. (2018). Bacterial response to spatially organized microtopographic surface patterns with nanometer scale roughness. *Colloids Surf. B Biointerfaces* 169, 340–347. doi:10.1016/j.colsurfb.2018.05.038

Valle, J., Burgui, S., Langheinrich, D., Gil, C., Solano, C., Toledo-Arana, A., et al. (2015). Evaluation of surface microtopography engineered by direct laser interference for bacterial anti-biofouling. *Macromol. Biosci.* 15 (8), 1060–1069. doi:10.1002/mabi.201500107

Valverde, A., Pérez-Álvarez, L., Ruiz-Rubio, L., Pacha Olivenza, M. A., García Blanco, M. B., Díaz-Fuentes, M., et al. (2019). Antibacterial hyaluronic acid/chitosan multilayers onto smooth and micropatterned titanium surfaces. *Carbohydr. Polym.* 207, 824–833. doi:10.1016/j.carbpol.2018.12.039

van Hengel, I. A. J., Tierolf, M., Valerio, V. P. M., Minneboo, M., Fluit, A. C., Fratila-Apachitei, L. E., et al. (2020). Self-defending additively manufactured bone implants bearing silver and copper nanoparticles. *J. Mater Chem. B* 8 (8), 1589–1602. doi:10.1039/c9tb02434d

Vasudevan, R., Kennedy, A. J., Merritt, M., Crocker, F. H., and Baney, R. H. (2014). Microscale patterned surfaces reduce bacterial fouling-microscopic and theoretical analysis. *Colloids Surf. B Biointerfaces* 117, 225–232. doi:10.1016/j.colsurfb.2014.02.037

Vu, A. A., Robertson, S. F., Ke, D., Bandyopadhyay, A., and Bose, S. (2019). Mechanical and biological properties of ZnO, SiO(2), and Ag(2)O doped plasma sprayed hydroxyapatite coating for orthopaedic and dental applications. *Acta Biomater.* 92, 325–335. doi:10.1016/j.actbio.2019.05.020

Wang, M., and Tang, T. (2019). Surface treatment strategies to combat implant-related infection from the beginning. *J. Orthop. Transl.* 17, 42–54. doi:10.1016/j.jot.2018.09.001

Wang, Q., Zhou, P., Liu, S., Attarilar, S., Ma, R. L., Zhong, Y., et al. (2020). Multi-scale surface treatments of titanium implants for rapid osseointegration: A review. *Nanomater. (Basel)* 10 (6), 1244. doi:10.3390/nano10061244

Wang, S., Liu, Z., Wang, L., Xu, J., Mo, R., Jiang, Y., et al. (2023a). Superhydrophobic mechano-bactericidal surface with photodynamic antibacterial capability. *ACS Appl. Mater Interfaces* 15 (1), 723–735. doi:10.1021/acsami.2c21310

Wang, X., Dong, H., Liu, J., Qin, G., Chen, D., and Zhang, E. (2019). *In vivo* antibacterial property of Ti-Cu sintered alloy implant. *Mater Sci. Eng. C Mater Biol. Appl.* 100, 38–47. doi:10.1016/j.msec.2019.02.084

Wang, X., Pan, L., Zheng, A., Cao, L., Wen, J., Su, T., et al. (2023b). Multifunctionalized carbon-fiber-reinforced polyetheretherketone implant for rapid osseointegration under infected environment. *Bioact. Mater* 24, 236–250. doi:10.1016/j.bioactmat.2022.12.016

Wang, X., Shan, M., Zhang, S., Chen, X., Liu, W., Chen, J., et al. (2022). Stimuli-responsive antibacterial materials: molecular structures, design principles, and biomedical applications. *Adv. Sci. (Weinh)* 9 (13), e2104843. doi:10.1002/advs.202104843

Webster, T. J., Patel, A. A., Rahaman, M. N., and Sonny Bal, B. (2012). Anti-infective and osteointegration properties of silicon nitride, poly(ether ether ketone), and titanium implants. *Acta Biomater.* 8 (12), 4447–4454. doi:10.1016/j.actbio.2012.07.038

Wei, X., Li, Q., Wu, C., Sun, T., and Li, X. (2020). Preparation, characterization and antibacterial mechanism of the chitosan coatings modified by Ag/ZnO microspheres. *J. Sci. Food Agric.* 100 (15), 5527–5538. doi:10.1002/jsfa.10605

Wongsuwan, N., Dwivedi, A., Tancharoen, S., and Nasongkla, N. (2020). Development of dental implant coating with minocycline-loaded niosome for antibacterial application. *J. Drug Deliv. Sci. Technol.* 56, 101555. doi:10.1016/j.jddst.2020.101555

Wu, B., Tang, Y., Wang, K., Zhou, X., and Xiang, L. (2022a). Nanostructured titanium implant surface facilitating osseointegration from protein adsorption to osteogenesis: the example of TiO(2) NTAs. *Int. J. Nanomedicine* 17, 1865–1879. doi:10.2147/ijn.S362720

Wu, L., Tan, J., Chen, S., and Liu, X. (2022b). Catalyst-enhanced micro-galvanic effect of Cu3N/Cu-bearing NiTi alloy surface for selective bacteria killing. *Chem. Eng. J.* 447, 137484. doi:10.1016/j.cej.2022.137484

Wu, S., Zhang, B., Liu, Y., Suo, X., and Li, H. (2018). Influence of surface topography on bacterial adhesion: A review (review). *Biointerphases* 13 (6), 060801. doi:10.1116/1.5054057

Wu, Y., Wu, W., Zhao, W., and Lan, X. (2020). Revealing the antibacterial mechanism of copper surfaces with controllable microstructures. *Surf. Coatings Technol.* 395, 125911. doi:10.1016/j.surfcoat.2020.125911

Xia, C., Ma, X., Zhang, X., Li, K., Tan, J., Qiao, Y., et al. (2020). Enhanced physicochemical and biological properties of C/Cu dual ions implanted medical titanium. *Bioact. Mater* 5 (2), 377–386. doi:10.1016/j.bioactmat.2020.02.017

Xiao, K., Cao, X., Chen, X., Hu, H., and Wu, C. (2020). Bactericidal efficacy of nanopatterned surface tuned by topography. *J. Appl. Phys.* 128 (6). doi:10.1063/5.0010343

Xie, Y., He, Y., Irwin, P. L., Jin, T., and Shi, X. (2011). Antibacterial activity and mechanism of action of zinc oxide nanoparticles against Campylobacter jejuni. *Appl. Environ. Microbiol.* 77 (7), 2325–2331. doi:10.1128/aem.02149-10

Xu, D., Wang, T., Lu, Z., Wang, Y., Sun, B., Wang, S., et al. (2021). Ti-6Al-4V-5Cu synthesized for antibacterial effect *in vitro* and *in vivo* via contact sterilization. *J. Mater. Sci. Technol.* 90, 133–142. doi:10.1016/j.jmst.2021.03.007

Xu, D., Zhu, W., Ding, C., Mei, J., Zhou, J., Cheng, T., et al. (2023). Self-homeostasis immunoregulatory strategy for implant-related infections through remodeling redox balance. *ACS Nano* 17 (5), 4574–4590. doi:10.1021/acsnano.2c10660

Xu, Z., Krajewski, S., Weindl, T., Loeffler, R., Li, P., Han, X., et al. (2020). Application of totarol as natural antibacterial coating on dental implants for prevention of peri-implantitis. *Mater Sci. Eng. C Mater Biol. Appl.* 110, 110701. doi:10.1016/j.msec.2020.110701

Yang, H.-L., Zou, L., Juaim, A. N., Ma, C.-X., Zhu, M.-Z., Xu, F., et al. (2023). Copper release and ROS in antibacterial activity of Ti-Cu alloys against implant-associated infection. *Rare Met.* 42 (6), 2007–2019. doi:10.1007/s12598-022-02242-4

Yang, M., Ding, Y., Ge, X., and Leng, Y. (2015). Control of bacterial adhesion and growth on honeycomb-like patterned surfaces. *Colloids Surf. B Biointerfaces* 135, 549–555. doi:10.1016/j.colsurfb.2015.08.010

Yazici, H., Habib, G., Boone, K., Urgen, M., Utku, F. S., and Tamerler, C. (2019). Self-assembling antimicrobial peptides on nanotubular titanium surfaces coated with calcium phosphate for local therapy. *Mater Sci. Eng. C Mater Biol. Appl.* 94, 333–343. doi:10.1016/j.msec.2018.09.030

Ye, J., Deng, J., Chen, Y., Yang, T., Zhu, Y., Wu, C., et al. (2019). Cicada and catkin inspired dual biomimetic antibacterial structure for the surface modification of implant material. *Biomater. Sci.* 7 (7), 2826–2832. doi:10.1039/c9bm00082h

Yeo, I. S. (2014). Reality of dental implant surface modification: a short literature review. *Open Biomed. Eng. J.* 8, 114–119. doi:10.2174/1874120701408010114

Yi, G., Yuan, Y., Li, X., and Zhang, Y. (2018). ZnO nanopillar coated surfaces with substrate-dependent superbactericidal property. *Small* 14 (14), e1703159. doi:10.1002/smll.201703159

Zhang, B., Luo, Y., Pearlstein, A. J., Aplin, J., Liu, Y., Bauchan, G. R., et al. (2014a). Fabrication of biomimetically patterned surfaces and their application to probing plant-bacteria interactions. *ACS Appl. Mater Interfaces* 6 (15), 12467–12478. doi:10.1021/am502384q

Zhang, E., and Liu, C. (2015). Effect of surface treatments on the surface morphology, corrosion property, and antibacterial property of Ti-10Cu sintered alloy. *Biomed. Mater* 10 (4), 045009. doi:10.1088/1748-6041/10/4/045009

Zhang, E., Zhao, X., Hu, J., Wang, R., Fu, S., and Qin, G. (2021a). Antibacterial metals and alloys for potential biomedical implants. *Bioact. Mater* 6 (8), 2569–2612. doi:10.1016/j.bioactmat.2021.01.030

Zhang, H., Shi, K., Liu, J., and Xie, G. (2023a). One-step preparation of titanium sharkskin bionic antibacterial surface. *Ceram. Int.* 49 (8), 11950–11959. doi:10.1016/j.ceramint.2022.12.044

Zhang, L., Yan, J., Yin, Z., Tang, C., Guo, Y., Li, D., et al. (2014b). Electrospun vancomycin-loaded coating on titanium implants for the prevention of implant-associated infections. *Int. J. Nanomedicine* 9, 3027–3036. doi:10.2147/ijn.S63991

Zhang, R., Liu, X., Xiong, Z., Huang, Q., Yang, X., Yan, H., et al. (2018). Novel micro/nanostructured TiO2/ZnO coating with antibacterial capacity and cytocompatibility. *Ceram. Int.* 44 (8), 9711–9719. doi:10.1016/j.ceramint.2018.02.202

Zhang, W., Zhang, S., Liu, H., Ren, L., Wang, Q., and Zhang, Y. (2021b). Effects of surface roughening on antibacterial and osteogenic properties of Ti-Cu alloys with different Cu contents. *J. Mater. Sci. Technol.* 88, 158–167. doi:10.1016/j.jmst.2021.01.067

Zhang, Y., Cui, J., Chen, K. Y., Kuo, S. H., Sharma, J., Bhatta, R., et al. (2023b). A smart coating with integrated physical antimicrobial and strain-mapping functionalities for orthopedic implants. *Sci. Adv.* 9 (18), eadg7397. doi:10.1126/sciadv.adg7397

Zheng, T. X., Li, W., Gu, Y. Y., Zhao, D., and Qi, M. C. (2022). Classification and research progress of implant surface antimicrobial techniques. *J. Dent. Sci.* 17 (1), 1–7. doi:10.1016/j.jds.2021.08.019

Zhong, J., Li, X., Yao, Y., Zhou, J., Cao, S., Zhang, X., et al. (2022). Effect of acid-alkali treatment on serum protein adsorption and bacterial adhesion to porous titanium. *J. Mater Sci. Mater Med.* 33 (2), 20. doi:10.1007/s10856-022-06646-7

Zhou, H., Yang, S., Wei, D., Liang, C., Yang, Q., Yang, H., et al. (2021). Development of hydrofluoric acid-cleaned silicon nitride implants for periprosthetic infection eradication and bone regeneration enhancement. *Mater Sci. Eng. C Mater Biol. Appl.* 127, 112241. doi:10.1016/j.msec.2021.112241

Zhou, W., Jia, Z., Xiong, P., Yan, J., Li, M., Cheng, Y., et al. (2018). Novel pH-responsive tobramycin-embedded micelles in nanostructured multilayer-coatings of chitosan/heparin with efficient and sustained antibacterial properties. *Mater Sci. Eng. C Mater Biol. Appl.* 90, 693–705. doi:10.1016/j.msec.2018.04.069

frontiers | Frontiers in Bioengineering and Biotechnology

TYPE Mini Review
PUBLISHED 29 September 2023
DOI 10.3389/fbioe.2023.1234758

OPEN ACCESS

EDITED BY
Xing Wang,
Shanxi Medical University, China

REVIEWED BY
Mieszko Wieckiewicz,
Wroclaw Medical University, Poland
Lin Ling Zhang,
Sichuan University, China

*CORRESPONDENCE
Rui Wang,
w_rui@jlu.edu.cn

RECEIVED 05 June 2023
ACCEPTED 20 September 2023
PUBLISHED 29 September 2023

CITATION
Qu S, Ma X, Yu S and Wang R (2023), Chitosan as a biomaterial for the prevention and treatment of dental caries: antibacterial effect, biomimetic mineralization, and drug delivery. *Front. Bioeng. Biotechnol.* 11:1234758. doi: 10.3389/fbioe.2023.1234758

Chitosan as a biomaterial for the prevention and treatment of dental caries: antibacterial effect, biomimetic mineralization, and drug delivery

Shanlin Qu[1,2], Xiaolin Ma[1,2], Shuo Yu[1,2] and Rui Wang[1,2]*

[1]Hospital of Stomatology, Jilin University, Changchun, China, [2]Jilin Provincial Key Laboratory of Tooth Development and Bone Remodeling, Changchun, China

Dental caries is a chronic, progressive disease caused by plaque, influenced by multiple factors and can damage the hard tissues of the teeth. In severe cases, it can also lead to the onset and development of other oral diseases, seriously affecting patients' quality of life. The creation of effective biomaterials for the prevention and treatment of dental caries has become one of the relentless goals of many researchers, with a focus on inhibiting the production of cariogenic plaque and retaining beneficial bacteria, guiding and promoting the reconstruction of dental hard tissues, and delaying the progression of existing caries. Chitosan is a natural cationic polymer extracted from the shells of crustaceans and shellfish. Since its discovery, chitosan has shown to have various biological functions such as antibacterial, biomimetic mineralization, drug delivery, *etc.*, making it one of the most promising biopolymers for new caries prevention and materials of prostheses. Therefore, this article provides an overview of the anti-caries applications of chitosan, which mainly covers the basic research on the application of chitosan in caries prevention and treatment since 2010, with a focus on categorizing and summarizing the following characteristics of chitosan as a caries prevention material, including its antibacterial effect, biomimetic mineralization effect and delivery ability of caries prevention drugs and vaccines. It also explores the limitations of current research on chitosan as a caries prevention biomaterial and the difficulties that need to be focused on and overcome in the future to provide theoretical reference for the clinical implementation of chitosan as a caries prevention biomaterial.

KEYWORDS

chitosan, dental caries, antibacterial, biomimetic mineralization, drug delivery

1 Introduction

Chitosan is the only positively charged polysaccharide in nature, a cationic polymer derived mainly from the chitin exoskeleton of marine crustaceans such as crabs and shrimps (Shoueir et al., 2021). Since its discovery by Rouget in 1859 (Raafat and Sahl, 2009), chitosan has attracted much attention and shown great promise in medicine and bioengineering. The components of chitosan are 2-acetamido-2-deoxy-β-d-glucopyranose and 2-amino-2-deoxy-β-d-glucopyranose. The lower the proportion of 2-acetamido-2-deoxy-β-d-glucopyranose, the higher the degree of deacetylation (DD) of chitosan, and the more

free-amino groups it has, which is strongly related to the biological functions of chitosan, including its ability to carry drugs, bioadhesive characteristics, and antibacterial activity (Ali and Ahmed, 2018; Shoueir et al., 2021). Therefore, chitosan is also known as an amino polysaccharide. Additionally, the molecular weight (MW) of chitosan, which typically ranges from 10 to 1000 kDa (Yang et al., 2022), is another crucial factor that influences its biological activity (Raafat and Sahl, 2009). In addition to its unique biological activity, the biocompatibility, biodegradability and low cytotoxicity (Paradowska-Stolarz et al., 2021) of green-sourced chitosan are more conducive to expanding its application pathways in the fields of food, medicine and pharmaceuticals, in line with the concept of "green economy" (Mazur et al., 2022), and have significant and valuable research value.

Dental caries is a persistent, progressive disease that eats away at the hard tissues of the teeth. Severe caries can also lead to other oral diseases, such as pulpitis and periapical periodontitis (Galler et al., 2021; Huang et al., 2022), which can seriously damage the soft and hard structures of the oral cavity and are irreversible. Due to the uniqueness of the anatomical structure of the tooth's hard tissue, its susceptibility to caries and the uncontrollability of each individual dietary habits, the global incidence of dental caries has remained high for many years, despite continuous improvements in socio-economic status and quality of life (Bernabe et al., 2020). Bacteria play a significant and critical role in the pathophysiology of dental caries. When they adhere to the tooth surface and interact constantly, they can form plaque, a complex ecological community with a largely stable microenvironment. At the same time, bacteria can ferment carbohydrates in the oral cavity to meet their own energy needs, and the acidic by-products of this process can lead to demineralization of tooth hard tissue (Sheiham and James, 2015). When there are high levels of sugars in the mouth, plaque continues to metabolize the sugars and produce acid, leaving the tooth surface in an irreversible state of demineralization for a prolonged period of time, gradually eroding the integrity of the tooth hard tissue. In essence, it is the disruption of the dynamic balance between dental minerals and oral bacteria that leads to the development of dental caries (Pitts et al., 2017; Krol et al., 2023). At present, the prevention and treatment of dental caries base on the following techniques: blocking or regulating the progression of dental caries by removing or managing the pathogens and restoring the balance of the oral microbiota; restoring the structure and function of teeth in response to the damage that caries has caused to their integrity (Cheng et al., 2022). Chitosan, as a relatively new natural polymer in dental applications (Yamakami et al., 2022), has been widely studied and confirmed for its anti-caries effects, mainly through the development of anti-caries products or clinical adjuvant treatment technologies, such as antibacterial, biomimetic mineralization and dentin binding, anti-caries drug delivery, with broad application prospects (Figure 1). As the first article we have learned about the anti-caries effect of chitosan, this article aims to provide a comprehensive overview of the anti-caries research of chitosan, summarize the research progress in the anti-caries mechanism of chitosan in recent years, and attempt to analyze the potential applications of chitosan in the future and the shortcomings of current research, providing theoretical reference for further researches and breakthroughs in chitosan anti-caries materials and clinical implementation.

2 Materials and methods

We searched the PubMed/MEDLINE and Web of Science databases for the most recent information on the use and mechanism of chitosan in caries prevention. The articles included are original peer-reviewed papers and reviews published since 2010, and papers without evident scientific backgrounds and prominent practical aspects were excluded. The search strategy for this article is shown in Figure 2.

3 The antibacterial effect of chitosan

3.1 Chitosan and its related materials inhibit oral cariogenic bacteria

At present, the antibacterial effect of chitosan has been preliminarily confirmed by a large number of experiments, and many studies have shown that chitosan has the ability to limit the growth of certain oral bacteria (Table 1), such as *Streptococcus mutans* (*S.mutans*) and *Porphyromonas gingivalis* (*P.gingivalis*). Because of this property, chitosan has been chosen

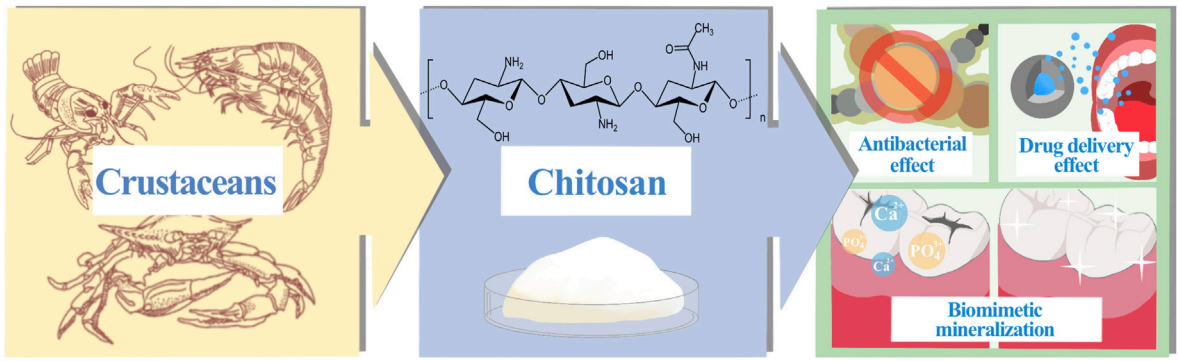

FIGURE 1
Crustacean-derived chitosan and its use in caries prevention.

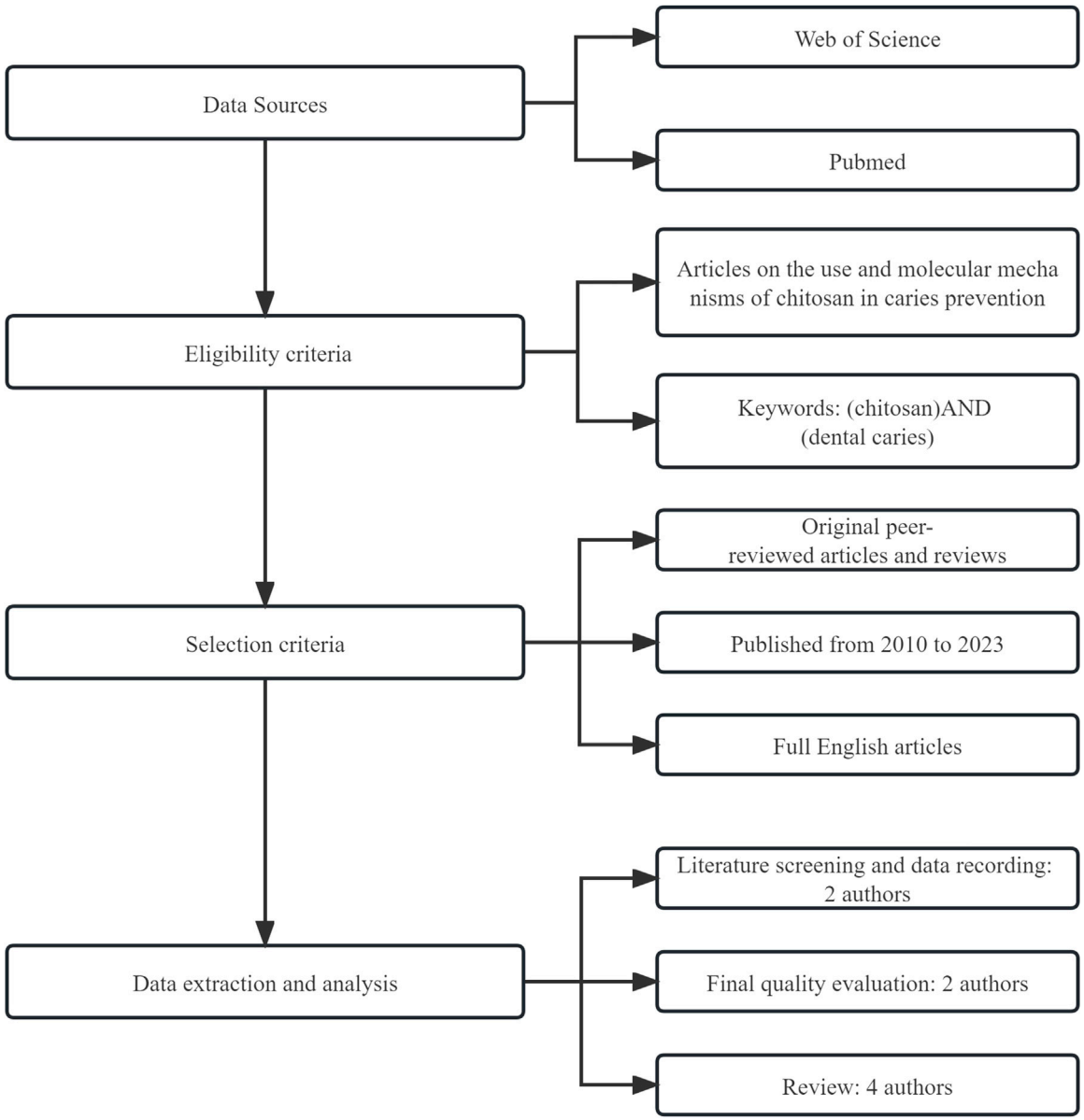

FIGURE 2
Article retrieval flowchart.

by many researchers as a raw material for the development of oral health products. Evidence suggests that chitosan-containing products may have a significant therapeutic benefit in inhibiting plaque growth. For example, some researchers have developed a water-soluble chitosan mouthwash based on chitosan glucosamine. According to *in vitro* tests, the mouthwash has antibacterial properties equal to or better than other commercial mouthwashes, achieving 99.99% antibacterial activity by acting on all test strains for 20 s. Similar antibacterial properties have also been observed in *in vivo* experiments (Chen and Chung, 2012). Chewing chitosan chewing gum can also reduce the number of mutans streptococci in a person's saliva, helping to prevent tooth decay (Khamverdi et al., 2021). Chitosan can also combine with other antibacterial materials or therapies to enhance the original antibacterial activity. One of the most effective ways to increase the antibacterial activity of chitosan is to modify it with metal ions (Ma et al., 2017). For example, compared to individual zinc oxide nanoparticles or chitosan, the antibacterial activity of chitosan-coated zinc oxide nanocomposites is dramatically increased (Javed et al., 2020). In addition, chitosan from a green source can reduce the cytotoxicity of metal ions (Maluin and Katas, 2022). Another promising antibacterial strategy is the combination of chitosan with photodynamic therapy (PDT). The ability of cationic chitosan to penetrate dense bacterial biofilms encapsulated in the extracellular matrix makes it a viable delivery vehicle for photosensitizers. Chitosan also has a physical inactivation effect on germs and can have synergistic antibacterial effects when

TABLE 1 Antibacterial effects of chitosan with different molecular weights on some common oral bacteria (high molecular weight chitosan: HMW, low molecular weight chitosan: LMW, chitosan hydrolysate: CTSNs).

Chitosan	MW (kDa)	DD	Bacteria	Antibacterial effect	Ref.
HMW	624	>75%	*P.gingivalis*	MIC = 1 mg/mL	Costa et al. (2012)
				MBC = 5 mg/mL	
			T.forsythensis	MIC = 1 mg/mL	
				MBC = 5 mg/mL	
			P. buccae	MIC = 3 mg/mL	
				MBC = 7 mg/mL	
			A.actinomycetemcomitans	MIC = 5 mg/mL	
				MBC = 7 mg/mL	
			P. intermedia	MIC = 1 mg/mL	
				MBC = 5 mg/mL	
			S. mutans	MIC = 3 mg/mL	
				MBC = 5 mg/mL	
LMW	107	between 75% and 85%	*P.gingivalis*	MIC = 1 mg/mL	
				MBC = 3 mg/mL	
			T.forsythensis	MIC = 3 mg/mL	
				MBC = 7 mg/mL	
			P. buccae	MIC = 1 mg/mL	
				MBC = 3 mg/mL	
			A.actinomycetemcomitans	MIC = 3 mg/mL	
				MBC = 7 mg/mL	
			P. intermedia	MIC = 3 mg/mL	
				MBC = 7 mg/mL	
			S. mutans	MIC = 5 mg/mL	
				MBC = 7 mg/mL	
CTSNs	6.650	It is hydrolyzed from high molecular weight chitosan with a degree of deacetylation of 95% and the DD after hydrolysis is unknown	*S. mutans*	IC_{50} = 150 μg/mL	Lee and Park (2015)
			MRSA	IC_{50} = 230 μg/mL	
CTSNs-P	7.783		*S. mutans*	IC_{50} = 200 μg/mL	
			MRSA	IC_{50} = 220 μg/mL	
CTSNs-B	5.452		*S. mutans*	IC_{50} = 190 μg/mL	
			MRSA	IC_{50} = 240 μg/mL	
CTSNs-S	3.510		*S. mutans*	IC_{50} = 170 μg/mL	
			MRSA	IC_{50} = 210 μg/mL	

combined with PDT (Guo et al., 2023). Based on sub-MIC concentrations of emodin-chitosan nanoparticles, antibacterial photodynamic treatment showed a significant reduction in *S. mutans* and ROS generation (Pourhajibagher et al., 2022). The proliferation of planktonic *S. mutans* and the development of biofilms can be significantly suppressed by antibacterial PDT mediated by chitosan and Photoditazine® (de Souza et al., 2020).

3.2 Chitosan's antibacterial mechanism and current limitations

In relevant studies on the antibacterial mechanism of chitosan, the properties of MW and DD have been widely emphasized. The following principles, which are generally accepted by many experts, can outline the antibacterial hypothesis of chitosan based on the

research already available: Firstly, several researchers have shown that low MW chitosan polymer chains are more flexible when binding to bacteria, which is an important factor in bacterial inactivation (Benhabiles et al., 2012); Secondly, low MW chitosan has the ability to pass through cell membranes, alter the shape of DNA and prevent the formation of biological macromolecules necessary for bacterial life (Sun et al., 2017; Khattak et al., 2019); In addition, chitosan with a higher level of deacetylation can carry more positive-charges through protonation, allowing it to adhere firmly to the surface of bacteria and have a better antibacterial effect (Sun et al., 2017); Furthermore, according to some researchers, chitosan may reduce bacterial pathogenicity by interfering with the production of virulence factors or molecules that facilitate intercellular communication by some pathogenic bacteria (Bano et al., 2017). However, according to some related researches, the above arguments may not fully capture the mechanism of action of chitosan on caries pathogens. Costa et al. (Costa et al., 2012) have determined the minimum inhibitory concentration (MIC) and minimum bactericidal concentration (MBC) of high MW chitosan (DD>75%, a MW of 624 kDa) and low MW chitosan (DD between 75% and 85%, a MW of 107 kDa) against various Gram-positive and Gram-negative bacteria. Interestingly, in this study, high MW chitosan and low MW chitosan showed different antibacterial effects on different bacteria, and the high MW chitosan even showed a lower MIC and MBC compared to the low MW chitosan for some bacteria, such as *S. mutans*, which is entirely inconsistent with previous conclusions. A similar conclusion in another experiment showed that high MW chitosan appeared to have more effective anti-caries pathogen properties than low MW chitosan (Abedian et al., 2020). Other academics noted that the disruption of cell walls or membranes is directly related to the antibacterial activity of chitosan. High MW chitosan has a greater inhibitory effect than low MW chitosan on mature *S. mutans* biofilm due to the interaction between its high positive-charge and the negative-charge of cell membranes, causing cell membrane disruption (Costa et al., 2013). However, the high positive-charge of this chitosan may be associated with its DD, and this study did not elucidate the specific reason. Although high MW chitosan has antibacterial properties, some researchers have hypothesized that its application is restricted by the low solubility caused by the high degree of polymerization. Several researchers have used chitosan enzymes to hydrolyze high MW chitosan (95% DD, 200 kDa) to produce various low MW chitosan hydrolysates with average MW ranging from 3.0 to 8.0 kDa and to study their biological functions. The results showed that many low MW chitosan can interfere with extracellular matrix development and bacterial growth by blocking the activity of dextransucrase (DSase), a critical point in the *S.mutans* polysaccharide production pathway. Although the exact process is unknown, it may be related to the electrostatic interaction between some *S.mutans* components and the hydrolyzed amino monosaccharides (Lee and Park, 2015). In conclusion, MW and DD affect antibacterial efficacy and applicability of chitosan. The antibacterial mechanism is not yet fully defined and the antibacterial effect may vary due to different charged molecular configurations on the surface of microbes (Bellich et al., 2016). Due to the specific nature of the oral microenvironment, it is impossible to generalize the results of previous comparable antibacterial tests. But it is undeniable that chitosan has significant antimicrobial activity.

Acid-producing and acid-tolerant bacteria in dental plaque can release acid on the surface of teeth and form a dense extracellular matrix to achieve high acid retention (Bowen et al., 2018). *S.mutans* is one of the typical representative strains of acid producing and acid resistant bacteria in plaque and has been extensively investigated by many scientists. *S.mutans* has been repeatedly cited over the years for its crucial role in promoting bacterial copolymerization and adhesion, plaque formation, the creation of an acidic microenvironment and the development of dental caries. It is one of the primary target bacteria chosen in several studies and the development of materials for caries prevention and antibacterial agents. Due to its greater capacity to absorb dietary carbohydrates, convert them into a number of acidic compounds, and maintain its homeostasis and proper growth in low pH conditions, *S. mutans* is of great concern (Lemos et al., 2019). However, the diversity of the internal microbiota in cariogenic plaque has been revealed in recent years thanks to the development of second-generation sequencing and metagenomic technology. The previous idea has been replaced by a new one, which suggests that multiple microorganisms acting together within the complex and diverse biofilm of dental plaque cause dental caries, rather than just the action of *S. mutans* alone (Simon-Soro and Mira, 2015; Sanz et al., 2017). Therefore, preventing and treating dental caries is not just a matter of monitoring and suppressing specific strains of bacteria. In recent years, the concept of caries prevention and treatment has shifted from widespread eradication of biofilms to targeted elimination of cariogenic plaque, retention of beneficial bacteria and maintenance of the ecological balance and stability of the oral microbiota. Therefore, at this stage, it would be pointless to blindly investigate the antibacterial function of chitosan. The antibacterial activity of chitosan may not be a "unique selling point" in terms of applicability to caries prevention, but rather a "bonus point".

4 Biomimetic mineralization effect of chitosan

4.1 Chitosan's guiding and mineralizing effect on enamel

Chitosan also has great potential in guiding and organizing the biomimetic mineralization of dental hard tissues (Table 2). Chitosan can inhibit demineralization of enamel and prevent the release of mineral ions, which is directly related to the barrier chitosan can create on the surface of teeth to prevent the infiltration of organic acids (Stamford Arnaud et al., 2010). In addition, demineralized enamel has a negative surface charge due to the significant loss of calcium ions, and chitosan has an affinity for demineralized enamel due to its positive-charge, which helps the adhesion and penetration into enamel of chitosan. Besides, for the long-term and stable occurrence of remineralization beneath the enamel surface, chitosan can prevent spontaneous precipitation on the enamel surface and encourage the ions necessary for mineralization to enter the deep lesion area of the enamel (Zhang et al., 2018a; Nimbeni et al., 2021). The carboxyl and hydroxyl groups of the chitosan chain can prevent the spontaneous precipitation of calcium phosphate

TABLE 2 Research on chitosan in guiding and promoting biomimetic mineralization of dental hard tissues.

Chitosan related preparations	Main function	Ref
chitosan/calcium phosphate hybrid microgel	It can assist in the nucleation and growth of calcium phosphate on the surface of dental enamel models, promote remineralization of dental caries lesions and has good adhesion and antibacterial activity	Simeonov et al. (2019)
Fluorinated chitosan and its derivatives	Effectively inhibits the release of phosphate ions on the surface of hydroxyapatite, with an effect comparable to that of sodium fluoride	Rahayu et al. (2022)
Experimental-resin-based materials doped with carboxymethyl chitosan and calcium phosphate microfillers	Effectively induces biomimetic mineralization of collagen fibrils in dentin, effectively improving the durability of the resin-dentin bond	Huang et al. (2019)
Crosslinked chitosan-nanoparticles	Collagen fibers resistance to collagenase significantly increased	Kishen et al. (2016)

by chelating calcium ions, which is essential for stabilizing ACP and promoting the production of its precursors (Chen et al., 2015; Hashmi et al., 2019). Based on the above properties, some scientists have developed a series of chitosan products to help remineralize tooth enamel and dental caries lesions. Simeonov et al. (2019) created a chitosan/calcium phosphate hybrid microgel using chitosan as a template for calcium phosphate deposition. On demineralized tooth specimens, the amorphous low crystalline calcium phosphate in the chitosan microgel can redissolve into ions and then deposite at the caries site to facilitate the nucleation and growth of calcium phosphate on the enamel model surface and promote the remineralization of caries lesions. Chitosan and modified chitosan (N-(2 (2,6-diaminohexanamide)-chitosan) have been fluorinated by using ion-interaction and have shown a strong inhibitory effect on the release of phosphate ions from the surface of hydroxyapatite. Fluorinated chitosan has a comparable effect to sodium fluoride but contains less fluoride ions, suggesting that it can reduce the dosage of fluoride required for treatment. It also has higher antibacterial activity and very low cytotoxicity (Rahayu et al., 2022).

4.2 Chitosan's guiding and mineralizing effect on dentin

In addition to promoting enamel remineralization, chitosan could also contribute to stabilization and direction of the biomimetic mineralization of dentin. Because the process of ACP conversion to apatite, which occurs spontaneously, is easily influenced by the pH of the solution (43), the early formation of apatite can easily prevent the penetration of minerals, which is not conducive to the occurrence of deep tissue remineralization and significantly reduces the mechanical stability of dentin. By chelating calcium ions, chitosan and its derivatives can prevent the early precipitation of ACP, which helps the deep collagen fibers to capture mineral ions and promote mineralization (Li et al., 2023). Type I collagen fibers are the main component of the dentin collagen matrix and have a unique physical structure that resembles a 'gate' allowing only molecules with a molecular weight of less than 6 kDa to enter while preventing molecules with a molecular weight of more than 40 kDa from entering (Price et al., 2009). This property has led some researchers to hypothesize that high MW carboxymethyl chitosan could blocked out of the collagen fibers and ACP could infiltrate into the collagen fibers through electrostatic interactions, which stimulates mineralization inside the collagen fibers and improves the mechanical properties of dentin, as well as inhibiting early crystallization and mineralization outside the fibers and stabilizing mineral precursors (Huang et al., 2019). In addition to increasing mineralization within collagen fibers, protecting collagen from degradation by collagenase is also the key to promoting biomimetic mineralization. Studies have shown that chitosan forms a cross-link with dentin type I collagen after carbodiimide cross-linking treatment to protect collagen and block the binding site of collagenase, preventing collagen destruction. Chitosan can also directly block collagenase in the absence of cross-linking agents (Kishen et al., 2016).

Some researchers have suggested that the addition of chitosan and its derivatives to resin-based materials or adhesives can increase the strength and stability of dentin bonds due to the intriguing biomimetic mineralization properties of these substances. The experimental resin for remineralization can suppress crystallization by releasing carboxymethyl chitosan while continuously releasing calcium and phosphorus ions to promote biomimetic mineralization of dentin (Huang et al., 2019). According to the research by Zhang et al. (2022) remineralization of the resin-dentin interface and improved permeability of hydrophobic monomers to the dentin matrix could be demonstrated following treatment with carboxymethyl chitosan solution, suggesting the potential for a novel type of indirect pulp capping agent. In recent years, external demineralization of dentin fibers has emerged as a new method for improving the stability of resin-dentin bonds. This method increases the durability of the dentin bond while preserving the integrity of the hydroxyapatite in the collagen fibers and preventing collagenase degradation. Pretreatment of the dentin bonding interface with chitosan (MW > 40 kDa) prior to bonding, according to Gu et al. (2019), is beneficial for the stability of the internal minerals of the dentin collagen and may also protect the collagen in the hybrid layer from protease activity. Chitosan has the potential to dramatically improve the integrity of the dentin bonding interface, as demonstrated by the significant reduction in water permeability of the resin-dentin hybrid layer and its antibacterial effect on three individual bacterial biofilms.

TABLE 3 Chitosan drug delivery system for anti-caries agents.

Chitosan drug delivery system	Delivery forms	Administration routes	Types of drugs	Anti-caries agents	Main function	Ref
Carboxymethyl chitosan nanogel	Nanogel	Enamel coating	Protein, minerals	Chimeric lysin ClyR and amorphous calcium phosphate	It can significantly reduce the colony count and biofilm activity of *Streptococcus* mutans and reduce enamel surface demineralization	Zhu et al. (2021)
An experimental adhesive resin with chitosan	Powder	Incorporating into resin	Antibiotic	Triclosan	It has long-term antibacterial activity and stability and can inhibit the formation and growth of *S.mutans* biofilm	Schauenberg Machado et al. (2019)
Chitosan-coated cellulose acetate phthalate-poloxamer enamel adhesive device	Nanocomposites	Enamel coating	Antibiotic	Minocycline	With superior mucosal and dental adhesion properties, it can achieve 8 h of continuous drug release and inhibit *S.mutans* biofilm	Singh et al. (2022)
Chitosan nanoparticles	Nanoparticles	Not mentioned	Metal ions, minerals	Zn–Nb bioglass-ceramic	Chitosan helps to form a strong bond between the composite material and tooth tissue, helping the composite material to maintain stability during ion release and remineralization processes to prevent secondary caries	Uskokovic et al. (2021)
Mucoadhesive electrospun chitosan-based nanofiber mats	Nanofiber	Adhesion to buccal mucosa	Plant active ingredients	Garcinia mangostana extract	It has good mucosal adhesion and releases antibacterial agents to inhibit *S.mutans* and *S.sanguis*	Samprasit et al. (2015)
Dual oral tissue adhesive chitosan nanofiber membranes	Nanofiber	Adhesion to oral hard tissue and soft tissue	Peptide	Antimicrobial Peptides	It has good tissue adhesion properties and can achieve pH-responsive drug delivery, inhibiting the activity of bacterial biofilms	Boda et al. (2020)
Chitosan hydrogel	Hydrogel	Enamel coating	Peptide	Amelogenin-derived peptide	It has pH-responsive properties and can release active ingredients in specific microenvironments, providing a dual caries-preventive effect of antibacterial and promoting remineralization of carious lesions	Ren et al. (2019); Ren et al. (2018)
Chitosan hydrogel	Hydrogel	Enamel coating	Protein	Amelogenin	The pH-responsive properties of chitosan can effectively release active ingredients, achieve antibacterial effects, promote remineralization of demineralized enamel and effectively prevent the occurrence of secondary caries	Ruan et al. (2013)
Chitosan/DNA complexes liposome nanoparticles	Conjugates	Vaccination of the nasal mucosa	DNA	Anti-caries DNA vaccine pGJA-P/VAX	It can effectively achieve nasal mucosal delivery of caries prevention vaccines, with high transfection rate and residence time, achieving long-term mucosal immunity	Chen et al. (2013)

5 The drug delivery effect of chitosan

With a focus on prolonging the exposure of drugs to the oral environment, reducing drug loss and ensuring sustained drug release, chitosan has great application value in the delivery of various biological macromolecules or drugs. Chitosan can achieve drug delivery in a variety of forms, the most typical of which include composite materials such as films, microspheres, nanoparticles, nanofibers and nanocomposites (Ali and Ahmed, 2018). Besides, chitosan can also improve the clinical operability of some biosynthetic materials, such as injectable chitosan hydrogels (Zhu et al., 2019). As a biological macromolecule with antibacterial properties, chitosan can be used as a carrier for antibacterial drugs, while enhancing their ability to fight bacteria (Patil and Jobanputra, 2015). In addition, the positively charged amino groups carried by chitosan greatly assist in the attraction of the substance to the surface of mucous membranes or teeth, keeping the materials close to the tissue surface during the drug release process. Chitosan can deliver a range of anticaries substances, such as antibacterial metal ions, minerals, antibiotics, proteins, DNA, *etc.* However, some scientists have suggested that due to the influence of chitosan's own properties (high hydrophilicity, high positive-charge, *etc.*), the encapsulation and slow release effects of chitosan hydrogels on cationic, hydrophobic or macromolecular substances are not ideal (Peers et al., 2020). Based on the above biological properties of chitosan, drug delivery systems related to chitosan mainly have the following administration routes, such as oral soft and hard tissue adhesion, mucosal delivery, enamel or dentin coating, *etc.* Some chitosan materials also achieve similar effects when incorporated into dental pulp sealants, solutions, scaffolds, restorations, adhesives

or resins. Relevant research on chitosan for the delivery and prevention of caries-related agents is detailed in Table 3.

5.1 Chitosan can serve as an effective vehicle for anticaries drugs

Chitosan carriers can achieve successful delivery of traditional antibacterial or mineralizing drugs. For instance, some researchers use carboxymethyl chitosan nanogel to carry the antibacterial chimeric lysin ClyR and ammonium chloride phosphate (ACP), which can achieve the dual anti-caries effect of antibacterial and mineralization promoting, and the effect is similar to that of chlorhexidine. The abundant carboxymethyl groups in carboxymethyl chitosan help to maintain the stability of ACP(52). Additionally, chitosan can significantly prolong the retention and efficacy of drugs. Schauenberg Machado et al. (2019) incorporated chitosan loaded with triclosan into the experimental resin, which further improved the antibacterial effect of triclosan, and this antibacterial effect can extended to 6 months with the help of chitosan. Besides, the positive-charge carried by chitosan gives it an affinity with the surface of oral soft and hard tissues, which helps to improve the retention and duration of the drug at the site of action. Research has shown that the chitosan-coated enamel bonding tool can deliver medication continuously for 24 h, slow the growth of *S.mutans* over time and adhere strongly to the tooth surface (Singh et al., 2022). Other researchers have used thiol-chitosan as mucosal adhesion polymers to create electrospun nanofibre mats (Samprasit et al., 2015), which generate disulfide bonds with mucus matrix glycoproteins by thiol groups to achieve strong adhesion between mats and mucous membranes (Frigaard et al., 2022). Antibacterial tests have shown that the mats has strong and sustained inhibition of *S.mutans* and *S. sanguinis in vitro*, as well as a reduction in the oral microbiota in the subjects' bodies. Furthermore, other researchers have used chitosan as a matrix carrying bio-ceramic particles because the expandability of chitosan in physiological dentin solution and the electrostatic interaction between positively charged amino carried by chitosan and negatively charged silica and dentin collagen can form a close bond between the composite and tooth tissue, helping the composite to maintain stability during ion release and remineralization to prevent secondary caries (Uskokovic et al., 2021).

5.2 Chitosan has pH-responsive property

The available sugars in the plaque consumption environment on the tooth surface can lower the pH of the plaque microenvironment and, after reaching a certain level, enter the plateau stage, leading to demineralization of the tooth surface. When most of the available sugars in the environment consumed up, the pH rises and returns to the neutral state, and the enamel on the tooth surface enters the remineralization phase. The amount of sugar in the environment directly impact how long the platform period lasts. When the environment contains high levels of readily available sugars, dental caries develops because plaque continues to produce acid and the tooth surface remains in a hardly reversible state of demineralization for a prolonged period. In essence, the key to the cariogenic properties of plaque is the sustained low pH caused by high sugar levels (Zhang et al., 2018b). As a cationic polymer, chitosan contains many amino groups that can protonate in acidic conditions, causing chitosan to dissolve. However, in neutral and alkaline conditions, the solubility of chitosan is significantly reduced due to deprotonation (Jin et al., 2020). Therefore, chitosan has a pH-responsive property that also provides a very interesting entry point for its application of the prevention and treatment of dental caries. Based on this property, some scientists have developed a series of pH-responsive chitosan nanomaterials to target the inhibition and removal of cariogenic plaque. Chitosan-modified antibacterial nanomaterials can release antibacterial drugs by protonating the nanomaterials in an acidic environment (Boda et al., 2020), which has the effect of specific eliminating pathogenic plaque; in addition, the ability of chitosan nanomaterials with positive-charge due to protonation to bind with the negatively charged bacterial surfaces is enhanced in an acidic environment, making the antibacterial effect of nanomaterials in an acidic environment stronger than that in a neutral environment (Xu et al., 2022).

Apatite dissolves to release calcium and phosphorus ions when the pH of the tooth hard tissue falls below the threshold due to bacterial acid production. When the pH returns to neutral, the environmental mineral ions can redeposit on the tooth surface and promote mineralization and repair of tooth hard tissue. The pH of the dental microenvironment is critical to the repair of dental hard tissue. Even if a mineralizer is present in the environment, mineralization is difficult to achieve at low pH value. Therefore, selectively controlling the release of mineral ions using pH differences caused by tooth surface pathology and the physiological environment is beneficial for improving the retention rate of drugs in the oral cavity and achieving long-term drug stability. Researchers have developed several chitosan nanocomposites that are rich in remineralizing agents. Highly charged amino groups carried by chitosan can competitively capture hydrogen ions from acidic environments to form a positively charged protective layer that inhibits the process of pH decrease and prevents further penetration of organic acids and demineralization of tooth surfaces; in addition, chitosan interacts electrostatically to maintain stability and prevent degradation until the environment becomes neutral with biological macromolecules that regulate the synthesis of hydroxyapatite, such as amelogenin and its derived peptide. In neutral environment, chitosan has a weak positive-charge and low solubility and dissociates from the biological macromolecules it carries, promoting remineralization of enamel (Ruan et al., 2013; Ren et al., 2018; Ren et al., 2019).

5.3 Chitosan effectively promotes mucosal delivery and antigen transfection of vaccines to prevent caries

Chitosan can effectively transport anti-caries vaccines in addition to anti-caries drugs. Chitosan offers new perspectives and approaches for vaccine delivery and improving antigen transfection efficiency, although the debate about anti-caries

vaccine research is ongoing. Positive-charge chitosan can protect DNA and promote its absorption by compressing DNA into nanocomposites. It can also deliver vaccines by attaching to the mucosal surface and altering epithelial permeability (Li et al., 2016). Some researchers have combined chitosan and anionic liposomes to develop a novel anti-caries DNA vaccine delivery nanoparticle with pH-responsive release and mucosal adhesion properties. Vaccine delivery can achieve through the nasal mucosa, which helps to prolong the vaccine retention time and enhance the nasal mucosal immune response (Chen et al., 2013). In addition, chitosan has a stimulatory effect on humoral and cell-mediated immune responses, so that it can be used not only as a delivery system but also as an immunostimulatory adjuvant for vaccine antigens. Bi et al. (2019) chose two adjuvant mixtures of chitosan-Pam_3CSK_4 (a TLR2 agonist) and chitosan-monophosphoryl lipid A (MPL, a TLR4 agonist) as immune response enhancers to increase and prolong the immune response induced by the recombinant *S. mutans* PAc protein. According to the experimental results, chitosan-Pam_3CSK_4 or chitosan-MPL can significantly increase the titer of PAc-specific antibodies in serum and saliva compared to Pac alone, which can reduce the severity of dental caries. However, some researchers have suggested that chitosan and its derivatives as vaccine adjuvants or delivery systems requires close attention to the potential cytotoxicity caused by their high surface positive-charges, efficacy and safety, and immune tolerance, which need a further assessment (Khademi et al., 2018).

6 Summary and prospect

In general, the anti-caries applications of chitosan can be summarized as follows: 1) Chitosan can effectively inhibit the development of biofilms and the growth of bacteria linked to caries, but the level of its antibacterial activity depends on the MW and DD of chitosan. The amino group carried by chitosan is the key to its antibacterial action, which can promote chitosan binding and even penetrate cell membranes, damaging bacterial genetic materials and biomacromolecules; The combination of chitosan and its derivatives with other antibacterial composite materials or methods can significantly improve the antibacterial effect on the original basis; 2) Chitosan can act as a reservoir for calcium and phosphorus ion deposition, which aids in the remineralization of enamel caries sites. In addition, high molecular weight chitosan and its derivatives with a molecular weight greater than 40 kDa can act as inhibitors of extracellular dentin collagen mineralization, promoting the orderly formation of mineralized crystals inside collagen and reducing collagenase's activity to break it down; 3) Chitosan can serve as an efficient drug delivery vehicle for remineralizing or antibacterial agents, which helps to increase medication bioavailability, lower dosages, and preserve long-term treatment efficacy. In addition, the amino groups carried by chitosan are protonated in acidic environments, altering its solubility and conformation, giving it significant pH-responsive properties, further extending its application in the prevention and treatment of dental caries.

Chitosan has limited applications, mainly due to its poor solubility in water or other organic solvents. However, chitosan has a high potential for chemical modification due to a number of amino groups it carries (Abd El-Hack et al., 2020). Many scientists have modified chitosan in various ways to improve its physical and chemical properties. In addition to increasing solubility, modified chitosan has antimicrobial effects, improves drug absorption or has chelating properties. Furthermore, it is important to note that the majority of products used in the prevention and treatment of dental caries are liquid or semi-solid (Ahmadian et al., 2018) and rely on the coating of the hard tissues of the teeth to increase the convenience of application. Although chitosan has an affinity for the tooth surface, high concentrations of chitosan may limit the ability of the substance to spread over the tooth surface due to its high viscosity caused by the network of sugar chains created by chitosan's hydrogen bonding and hydrophobic interactions (Calero et al., 2010; Pichaiaukrit et al., 2019). Studies have also shown that although the addition of chitosan derivatives to dental restorative materials or adhesives can help reduce bacterial accumulation at the repair interface and the likelihood of secondary caries, the resulting reduction in the mechanical properties of the composite material poses a significant challenge to the clinical implementation of chitosan (Stenhagen et al., 2019). Finally, it is critical to focus on the potential degradation of chitosan and its derivatives by salivary lysozyme and the potential effects of this lysozyme degradation (Wang et al., 2021). It is necessary to conduct scientifically designed animal and clinical studies to verify the role of chitosan *in vivo*. Although many researchers have developed anti-caries chitosan-based products, more supportive research is needed before these can be used in a clinical setting.

Author contributions

SQ: conceptualization, visualization, and writing—original draft preparation. XM: conceptualization and writing—review and editing. SY: writing–original draft preparation. RW: supervision, validation, and writing—review and editing. All authors contributed to the article and approved the submitted version.

Funding

This research was funded by "Jilin Health Research Project, 2021JK02."

Conflict of interest

The authors declare that the research was conducted in the absence of any commercial or financial relationships that could be construed as a potential conflict of interest.

Publisher's note

References

Abd El-Hack, M. E., El-Saadony, M. T., Shafi, M. E., Zabermawi, N. M., Arif, M., Batiha, G. E., et al. (2020). Antimicrobial and antioxidant properties of chitosan and its derivatives and their applications: A review. *Int. J. Biol. Macromol.* 164, 2726–2744. doi:10.1016/j.ijbiomac.2020.08.153

Abedian, Z., Jenabian, N., Moghadamnia, A. A., Zabihi, E., Pourbagher, R., and Rajabnia, M. (2020). Antibacterial activity of high-molecular-weight and low-molecular-weight chitosan upon oral pathogens. *Int. J. Infect. Dis.* 101, 46–47. doi:10.1016/j.ijid.2020.09.154

Ahmadian, E., Shahi, S., Yazdani, J., Dizaj, S. M., and Sharifi, S. (2018). Local treatment of the dental caries using nanomaterials. *Biomed. Pharmacother.* 108, 443–447. doi:10.1016/j.biopha.2018.09.026

Ali, A., and Ahmed, S. (2018). A review on chitosan and its nanocomposites in drug delivery. *Int. J. Biol. Macromol.* 109, 273–286. doi:10.1016/j.ijbiomac.2017.12.078

Bano, I., Ghauri, M. A., Arshad, M., Yasin, T., and Younus, M. (2017). Bioactivity of variant molecular weight chitosan against drug-resistant bacteria isolated from human wounds. *Microb. Drug Resist.* 23 (8), 958–965. doi:10.1089/mdr.2016.0211

Bellich, B., D'Agostino, I., Semeraro, S., Gamini, A., and Cesaro, A. (2016). The good, the bad and the ugly" of chitosans. *Mar. Drugs* 14 (5), 99. doi:10.3390/md14050099

Benhabiles, S., Salah, R., Lounici, H., Drouiche, N., Goosen, M. F. A., and Mameri, N. (2012). Antibacterial activity of chitin, chitosan and its oligomers prepared from shrimp shell waste. *Food Hydrocoll.* 29 (1), 48–56. doi:10.1016/j.foodhyd.2012.02.013

Bernabe, E., Marcenes, W., Hernandez, C. R., Bailey, J., Abreu, L. G., Alipour, V., et al. (2020). Global, regional, and national levels and trends in burden of oral conditions from 1990 to 2017: A systematic analysis for the global burden of disease 2017 study. *J. Dent. Res.* 99 (4), 362–373. doi:10.1177/0022034520908533

Bi, Y., Xu, Q., Su, L., Xu, J., Liu, Z., Yang, Y., et al. (2019). The combinations chitosan-pam(3)Csk(4) and chitosan-monophosphoryl lipid A: promising immune-enhancing adjuvants for anticaries vaccine pac. *Infect. Immun.* 87 (12), e00651-19. doi:10.1128/iai.00651-19

Boda, S. K., Fischer, N. G., Ye, Z., and Aparicio, C. (2020). Dual oral tissue adhesive nanofiber membranes for ph-responsive delivery of antimicrobial peptides. *Biomacromolecules* 21 (12), 4945–4961. doi:10.1021/acs.biomac.0c01163

Bowen, W. H., Burne, R. A., Wu, H., and Koo, H. (2018). Oral biofilms: pathogens, matrix, and polymicrobial interactions in microenvironments. *Trends Microbiol.* 26 (3), 229–242. doi:10.1016/j.tim.2017.09.008

Calero, N., Munoz, J., Ramirez, P., and Guerrero, A. (2010). Flow behaviour, linear viscoelasticity and surface properties of chitosan aqueous solutions. *Food Hydrocoll.* 24 (6-7), 659–666. doi:10.1016/j.foodhyd.2010.03.009

Chen, C-Y., and Chung, Y-C. (2012). Antibacterial effect of water-soluble chitosan on representative dental pathogens Streptococcus mutans and lactobacilli brevis. *J. Appl. Oral Sci.* 20 (6), 620–627. doi:10.1590/s1678-77572012000600006

Chen, L., Zhu, J., Li, Y., Lu, J., Gao, L., Xu, H., et al. (2013). Enhanced nasal mucosal delivery and immunogenicity of anti-caries DNA vaccine through incorporation of anionic liposomes in chitosan/DNA complexes. *Plos One* 8 (8), e71953. doi:10.1371/journal.pone.0071953

Chen, Z., Cao, S., Wang, H., Li, Y., Kishen, A., Deng, X., et al. (2015). Biomimetic remineralization of demineralized dentine using scaffold of cmc/acp nanocomplexes in an *in vitro* tooth model of deep caries. *Plos One* 10 (1), e0116553. doi:10.1371/journal.pone.0116553

Cheng, L., Zhang, L., Yue, L., Ling, J., Fan, M., Yang, D., et al. (2022). Expert consensus on dental caries management. *Int. J. Oral Sci.* 14 (1), 17. doi:10.1038/s41368-022-00167-3

Costa, E. M., Silva, S., Pina, C., Tavaria, F. K., and Pintado, M. M. (2012). Evaluation and insights into chitosan antimicrobial activity against anaerobic oral pathogens. *Anaerobe* 18 (3), 305–309. doi:10.1016/j.anaerobe.2012.04.009

Costa, E. M., Silva, S., Tavaria, F. K., and Pintado, M. M. (2013). Study of the effects of chitosan upon Streptococcus mutans adherence and biofilm formation. *Anaerobe* 20, 27–31. doi:10.1016/j.anaerobe.2013.02.002

de Souza, C. M., Garcia, M. T., de Barros, P. P., Pedroso, L. L. C., Ward, R., Strixino, J. F., et al. (2020). Chitosan enhances the antimicrobial photodynamic inactivation mediated by Photoditazine® against Streptococcus mutans. *Photodiagnosis Photodyn. Ther.* 32, 102001. doi:10.1016/j.pdpdt.2020.102001

Frigaard, J., Jensen, J. L., Galtung, H. K., and Hiorth, M. (2022). The potential of chitosan in nanomedicine: an overview of the cytotoxicity of chitosan based nanoparticles. *Front. Pharmacol.* 13, 880377. doi:10.3389/fphar.2022.880377

Galler, K. M., Weber, M., Korkmaz, Y., Widbiller, M., and Feuerer, M. (2021). Inflammatory response mechanisms of the dentine-pulp complex and the periapical tissues. *Int. J. Mol. Sci.* 22 (3), 1480. doi:10.3390/ijms22031480

Gu, L. S., Cai, X., Guo, J. M., Pashley, D. H., Breschi, L., Xu, H. H. K., et al. (2019). Chitosan-based extrafibrillar demineralization for dentin bonding. *J. Dent. Res.* 98 (2), 186–193. doi:10.1177/0022034518805419

Guo, W., Li, Y., Wang, S., Wang, Y., Li, C., Jin, Y., et al. (2023). Photodynamic nano hydroxyapatite with biofilm penetration capability for dental plaque eradication and prevention of demineralization. *Colloids surfaces B, Biointerfaces* 225, 113242. doi:10.1016/j.colsurfb.2023.113242

Hashmi, A., Zhang, X., and Kishen, A. (2019). Impact of dentin substrate modification with chitosan-hydroxyapatite precursor nanocomplexes on sealer penetration and tensile strength. *J. Endod.* 45 (7), 935–942. doi:10.1016/j.joen.2019.03.021

Huang, F., Cheng, L., Li, J., and Ren, B. (2022). Nanofibrous scaffolds for regenerative endodontics treatment. *Front. Bioeng. Biotechnol.* 10, 1078453. doi:10.3389/fbioe.2022.1078453

Huang, Z., Qi, Y., Zhang, K., Gu, L., Guo, J., Wang, R., et al. (2019). Use of experimental-resin-based materials doped with carboxymethyl chitosan and calcium phosphate microfillers to induce biomimetic remineralization of caries-affected dentin. *J. Mech. Behav. Biomed. Mater.* 89, 81–88. doi:10.1016/j.jmbbm.2018.09.008

Javed, R., Rais, F., Fatima, H., ul Haq, I., Kaleem, M., Naz, S. S., et al. (2020). Chitosan encapsulated zno nanocomposites: fabrication, characterization, and functionalization of bio-dental approaches. *Mater. Sci. Eng. C-Materials Biol. Appl.* 116, 111184. doi:10.1016/j.msec.2020.111184

Jin, T., Wu, D., Liu, X-M., Xu, J-T., Ma, B-J., Ji, Y., et al. (2020). Intra-articular delivery of celastrol by hollow mesoporous silica nanoparticles for ph-sensitive anti-inflammatory therapy against knee osteoarthritis. *J. Nanobiotechnology* 18 (1), 94. doi:10.1186/s12951-020-00651-0

Khademi, F., Taheri, R-A., Avarvand, A. Y., Vaez, H., Momtazi-Borojeni, A. A., and Soleimanpour, S. (2018). Are chitosan natural polymers suitable as adjuvant/delivery system for antituberculosis vaccines? *Microb. Pathog.* 121, 218–223. doi:10.1016/j.micpath.2018.05.035

Khamverdi, Z., Farhadian, F., Khazaei, S., and Adabi, M. (2021). Efficacy of chitosan-based chewing gum on reducing salivary S. Mutans counts and salivary ph: A randomised clinical trial. *Acta Odontol. Scand.* 79 (4), 268–274. doi:10.1080/00016357.2020.1836392

Khattak, S., Wahid, F., Liu, L-P., Jia, S-R., Chu, L-Q., Xie, Y-Y., et al. (2019). Applications of cellulose and chitin/chitosan derivatives and composites as antibacterial materials: current state and perspectives. *Appl. Microbiol. Biotechnol.* 103 (5), 1989–2006. doi:10.1007/s00253-018-09602-0

Kishen, A., Shrestha, S., Shrestha, A., Cheng, C., and Goh, C. (2016). Characterizing the collagen stabilizing effect of crosslinked chitosan nanoparticles against collagenase degradation. *Dent. Mater. official Publ. Acad. Dent. Mater.* 32 (8), 968–977. doi:10.1016/j.dental.2016.05.005

Krol, D. M., Whelan, K., and SECTION ON ORAL HEALTH (2023). Maintaining and improving the oral health of young children. *Pediatrics* 151 (1), e2022060417. doi:10.1542/peds.2022-060417

Lee, C. G., and Park, J. K. (2015). Comparison of inhibitory activity of bioactive molecules on the dextransucrase from Streptococcus mutans. *Appl. Microbiol. Biotechnol.* 99 (18), 7495–7503. doi:10.1007/s00253-015-6693-z

Lemos, J. A., Palmer, S. R., Zeng, L., Wen, Z. T., Kajfasz, J. K., Freires, I. A., et al. (2019). The biology of Streptococcus mutans. *Microbiol. Spectr.* 7 (1). doi:10.1128/microbiolspec.GPP3-0051-2018

Li, H., Lu, Y., Xiang, J., Jiang, H., Zhong, Y., and Lu, Y. (2016). Enhancement of immunogenic response and protection in model rats by cstm nanoparticles anticaries DNA vaccine. *Nanomedicine* 11 (11), 1407–1416. doi:10.2217/nnm-2016-0012

Li, Z., Zeng, Y., Ren, Q., Ding, L., Han, S., Hu, D., et al. (2023). Mineralization promotion and protection effect of carboxymethyl chitosan biomodification in biomimetic mineralization. *Int. J. Biol. Macromol.* 234, 123720. doi:10.1016/j.ijbiomac.2023.123720

Ma, Z., Garrido-Maestu, A., and Jeong, K. C. (2017). Application, mode of action, and *in vivo* activity of chitosan and its micro- and nanoparticles as antimicrobial agents: A review. *Carbohydr. Polym.* 176, 257–265. doi:10.1016/j.carbpol.2017.08.082

Maluin, F. N., and Katas, H. (2022). Chitosan functionalization of metal- and carbon-based nanomaterials as an approach toward sustainability tomorrow. *Nanotoxicology* 16 (4), 425–449. doi:10.1080/17435390.2022.2090025

Mazur, M., Ndokaj, A., Bietolini, S., Nissi, V., Dus-Ilnicka, I., and Ottolenghi, L. (2022). Green dentistry: organic toothpaste formulations. A literature review. *Dent. Med. Problems* 59 (3), 461–474. doi:10.17219/dmp/146133

Nimbeni, S. B., Nimbeni, B. S., and Divakar, D. D. (2021). Role of chitosan in remineralization of enamel and dentin: A systematic review. *Int. J. Clin. Pediatr. Dent.* 14 (4), 562–568. doi:10.5005/jp-journals-10005-1971

Paradowska-Stolarz, A., Wieckiewicz, M., Owczarek, A., and Wezgowiec, J. (2021). Natural polymers for the maintenance of oral health: review of recent advances and perspectives. *Int. J. Mol. Sci.* 22 (19), 10337. doi:10.3390/ijms221910337

Patil, A. G., and Jobanputra, A. H. (2015). Rutin-chitosan nanoparticles: fabrication, characterization and application in dental disorders. *Polymer-Plastics Technol. Eng.* 54 (2), 202–208. doi:10.1080/03602559.2014.935425

Peers, S., Montembault, A., and Ladaviere, C. (2020). Chitosan hydrogels for sustained drug delivery. *J. Control. Release* 326, 150–163. doi:10.1016/j.jconrel.2020.06.012

Pichaiaukrit, W., Thamronganansku, N., Siralertmukul, K., and Swasdison, S. (2019). Fluoride varnish containing chitosan demonstrated sustained fluoride release. *Dent. Mater. J.* 38 (6), 1036–1042. doi:10.4012/dmj.2018-112

Pitts, N. B., Zero, D. T., Marsh, P. D., Ekstrand, K., Weintraub, J. A., Ramos-Gomez, F., et al. (2017). Dental caries. *Nat. Rev. Dis. Prim.* 3, 17030–17116. doi:10.1038/nrdp.2017.30

Pourhajibagher, M., Keshavarz Valian, N., and Bahador, A. (2022). Theranostic nanoplatforms of emodin-chitosan with blue laser light on enhancing the anti-biofilm activity of photodynamic therapy against Streptococcus mutans biofilms on the enamel surface. *BMC Microbiol.* 22 (1), 68. doi:10.1186/s12866-022-02481-6

Price, P. A., Toroian, D., and Lim, J. E. (2009). Mineralization by inhibitor exclusion. *J. Biol. Chem.* 284 (25), 17092–17101. doi:10.1074/jbc.M109.007013

Raafat, D., and Sahl, H-G. (2009). Chitosan and its antimicrobial potential - a critical literature survey. *Microb. Biotechnol.* 2 (2), 186–201. doi:10.1111/j.1751-7915.2008.00080.x

Rahayu, D. P., Draheim, R., Lalatsa, A., and Roldo, M. (2022). Harnessing the antibacterial properties of fluoridated chitosan polymers against oral biofilms. *Pharmaceutics* 14 (3), 488. doi:10.3390/pharmaceutics14030488

Ren, Q., Ding, L., Li, Z., Wang, X., Wang, K., Han, S., et al. (2019). Chitosan hydrogel containing amelogenin-derived peptide: inhibition of cariogenic bacteria and promotion of remineralization of initial caries lesions. *Archives Oral Biol.* 100, 42–48. doi:10.1016/j.archoralbio.2019.02.004

Ren, Q., Li, Z., Ding, L., Wang, X., Niu, Y., Qin, X., et al. (2018). Anti-biofilm and remineralization effects of chitosan hydrogel containing amelogenin-derived peptide on initial caries lesions. *Regen. Biomater.* 5 (2), 69–76. doi:10.1093/rb/rby005

Ruan, Q., Zhang, Y., Yang, X., Nutt, S., and Moradian-Oldak, J. (2013). An amelogenin-chitosan matrix promotes assembly of an enamel-like layer with a dense interface. *Acta Biomater.* 9 (7), 7289–7297. doi:10.1016/j.actbio.2013.04.004

Samprasit, W., Kaomongkolgit, R., Sukma, M., Rojanarata, T., Ngawhirunpat, T., and Opanasopit, P. (2015). Mucoadhesive electrospun chitosan-based nanofibre mats for dental caries prevention. *Carbohydr. Polym.* 117, 933–940. doi:10.1016/j.carbpol.2014.10.026

Sanz, M., Beighton, D., Curtis, M. A., Cury, J. A., Dige, I., Dommisch, H., et al. (2017). Role of microbial biofilms in the maintenance of oral health and in the development of dental caries and periodontal diseases. Consensus report of group 1 of the joint efp/orca workshop on the boundaries between caries and periodontal disease. *J. Clin. Periodontology* 44, S5-S11–S11. doi:10.1111/jcpe.12682

Schauenberg Machado, A. H., Garcia, I. M., da Motta, AdS., Branco Leitune, V. C., and Collares, F. M. (2019). Triclosan-loaded chitosan as antibacterial agent for adhesive resin. *J. Dent.* 83, 33–39. doi:10.1016/j.jdent.2019.02.002

Sheiham, A., and James, W. P. T. (2015). Diet and dental caries: the pivotal role of free sugars reemphasized. *J. Dent. Res.* 94 (10), 1341–1347. doi:10.1177/0022034515590377

Shoueir, K. R., El-Desouky, N., Rashad, M. M., Ahmed, M. K., Janowska, I., and El-Kemary, M. (2021). Chitosan based-nanoparticles and nanocapsules: overview, physicochemical features, applications of a nanofibrous scaffold, and bioprinting. *Int. J. Biol. Macromol.* 167, 1176–1197. doi:10.1016/j.ijbiomac.2020.11.072

Simeonov, M., Gussiyska, A., Mironova, J., Nikolova, D., Apostolov, A., Sezanova, K., et al. (2019). Novel hybrid chitosan/calcium phosphates microgels for remineralization of demineralized enamel - a model study. *Eur. Polym. J.* 119, 14–21. doi:10.1016/j.eurpolymj.2019.07.005

Simon-Soro, A., and Mira, A. (2015). Solving the etiology of dental caries. *Trends Microbiol.* 23 (2), 76–82. doi:10.1016/j.tim.2014.10.010

Singh, A., Jain, P., Khan, R., Anwer, M. K., Ansari, M. J., Aqil, M., et al. (2022). Development and quality evaluation of chitosan-coated cellulose acetate phthalate-poloxamer enamel adhesive device for the treatment of dentin carious lesion. *Int. J. Polym. Mater. Polym. Biomaterials* 71 (17), 1345–1358. doi:10.1080/00914037.2021.1963722

Stamford Arnaud, T. M., de Barros Neto, B., and Diniz, F. B. (2010). Chitosan effect on dental enamel de-remineralization: an *in vitro* evaluation. *J. Dent.* 38 (11), 848–852. doi:10.1016/j.jdent.2010.06.004

Stenhagen, I. S. R., Rukke, H. V., Dragland, I. S., and Kopperud, H. M. (2019). Effect of methacrylated chitosan incorporated in experimental composite and adhesive on mechanical properties and biofilm formation. *Eur. J. Oral Sci.* 127 (1), 81–88. doi:10.1111/eos.12584

Sun, Z., Shi, C., Wang, X., Fang, Q., and Huang, J. (2017). Synthesis, characterization, and antimicrobial activities of sulfonated chitosan. *Carbohydr. Polym.* 155, 321–328. doi:10.1016/j.carbpol.2016.08.069

Uskokovic, V., Abuna, G., Ferreira, P., Wu, V. M., Gower, L., Pires-de-Souza, F. C. P., et al. (2021). Synthesis and characterization of nanoparticulate niobium- and zinc-doped bioglass-ceramic/chitosan hybrids for dental applications. *J. Sol-Gel Sci. Technol.* 97 (2), 245–258. doi:10.1007/s10971-020-05442-5

Wang, J., Liu, Z., Ren, B., Wang, Q., Wu, J., Yang, N., et al. (2021). Biomimetic mineralisation systems for *in situ* enamel restoration inspired by amelogenesis. *J. Mater. Science-Materials Med.* 32 (9), 115. doi:10.1007/s10856-021-06583-x

Xu, X., Fan, M., Yu, Z., Zhao, Y., Zhang, H., Wang, J., et al. (2022). A removable photothermal antibacterial "warm paste" target for cariogenic bacteria. *Chem. Eng. J.* 429, 132491. doi:10.1016/j.cej.2021.132491

Yamakami, S. A., Faraoni, J. J., Lia, N. S. N. D., Regula, F. B., Ohyama, H., and Palma-Dibb, R. G. (2022). Effect of an experimental chitosan/casein gel on demineralized enamel under a cariogenic challenge. *Dent. Med. Problems* 59 (4), 531–538. doi:10.17219/dmp/146038

Yang, Z., Liu, W., Liu, H., Li, R., Chang, L., Kan, S., et al. (2022). The applications of polysaccharides in dentistry. *Front. Bioeng. Biotechnol.* 10, 970041. Epub 2022/08/09. doi:10.3389/fbioe.2022.970041

Zhang, J., Lynch, R. J. M., Watson, T. F., and Banerjee, A. (2018a). Remineralisation of enamel white spot lesions pre-treated with chitosan in the presence of salivary pellicle. *J. Dent.* 72, 21–28. doi:10.1016/j.jdent.2018.02.004

Zhang, Q., Guo, J., Huang, Z., and Mai, S. (2022). Promotion effect of carboxymethyl chitosan on dental caries via intrafibrillar mineralization of collagen and dentin remineralization. *Materials* 15 (14), 4835. doi:10.3390/ma15144835

Zhang, Y., Wang, X., Li, H., Ni, C., Du, Z., and Yan, F. (2018b). Human oral microbiota and its modulation for oral health. *Biomed. Pharmacother.* 99, 883–893. doi:10.1016/j.biopha.2018.01.146

Zhu, N., Chatzistavrou, X., Ge, L., Qin, M., Papagerakis, P., and Wang, Y. (2019). Biological properties of modified bioactive glass on dental pulp cells. *J. Dent.* 83, 18–26. doi:10.1016/j.jdent.2019.01.017

Zhu, Y., Yan, J., Mujtaba, B. M., Li, Y., Wei, H., and Huang, S. (2021). The dual anti-caries effect of carboxymethyl chitosan nanogel loaded with chimeric lysin clyr and amorphous calcium phosphate. *Eur. J. Oral Sci.* 129 (3), e12784. doi:10.1111/eos.12784

frontiers | Frontiers in Bioengineering and Biotechnology

TYPE Original Research
PUBLISHED 20 October 2023
DOI 10.3389/fbioe.2023.1272527

OPEN ACCESS

EDITED BY
Yuan Yin,
Fourth Military Medical University, China

REVIEWED BY
Han Qin,
Chongqing Medical University, China
Shunli Zheng,
Anhui Medical University, China

*CORRESPONDENCE
Yong Xia,
yxia@stu.edu.cn

RECEIVED 04 August 2023
ACCEPTED 02 October 2023
PUBLISHED 20 October 2023

CITATION
Chen Y, Chen Z, Zheng Z and Xia Y (2023), Bio-inspired nanocomposite coatings on orthodontic archwires with corrosion resistant and antibacterial properties. *Front. Bioeng. Biotechnol.* 11:1272527. doi: 10.3389/fbioe.2023.1272527

Bio-inspired nanocomposite coatings on orthodontic archwires with corrosion resistant and antibacterial properties

Yuming Chen, Zihan Chen, Zebin Zheng and Yong Xia*

The First Affiliated Hospital of Shantou University Medical College, Shantou, China

The corrosion resistance and antibacterial properties of fixed orthodontic devices are insufficient in the complex oral cavity, which delays tooth movement and causes enamel demineralization. To overcome the challenges, this research constructs a series of polydopamine-graphene oxide (PDA-GO) nanocoatings on representative NiTi archwires via self-assembly. The morphology, chemical structure, and multifunctional properties of coatings showed tunability dependent on the PDA/GO ratio. Optimized PDA-GO coatings with uniform and dense characteristics prolonged the diffusion path for the corrosive medium and reduced Ni dissolution in NiTi alloys. Meanwhile, the applied coatings endowed NiTi alloys with antibacterial activity against *Streptococcus mutans* due to the surface structures and inherent properties of PDA-GO. *In vitro* cytotoxicity tests further verified their good biocompatibility. This bio-inspired nanocomposite coating provides a practical reference for modification of dental metal surfaces to better behave in the intraoral environment.

KEYWORDS

polydopamine-graphene oxide, NiTi alloy, corrosion resistance, antibacterial properties, orthodontic archwire

1 Introduction

Equiatomic nickel-titanium (NiTi) alloys are frequently employed in orthodontic treatment to align and level dentition. Orally placed for more than 3 months, NiTi archwires continuously interact with saliva proteins, corrosive ions, bending stress, and microorganisms (Ghazal et al., 2015; Wang et al., 2023; Zhang et al., 2023). However, they are ineffective in preventing corrosion and lack antimicrobial qualities, leading to reduced service efficiency and several clinical complications. For example, orthodontic stress intensifies the corrosion behavior of NiTi wires in saliva, further increases the friction coefficient, and prolongs treatment process (Krishnan et al., 2012). Health issues, such as cytotoxicity and allergic responses, may result from excessive Ni^{2+} release into oral cavity (Močnik et al., 2017). Additionally, orthodontic fixtures hamper oral hygiene, combined with adhered bacteria, which poses a risk of enamel demineralization and periodontal diseases (Venkatesan et al., 2020). In this regard, materials science-oriented investigations should pay more attention to the concerns and modifications of dental metals and alloys.

The past couple of decades have witnessed the booming development of nanomaterials in metallic surface design, which could meet the requirements of diverse oral treatment (Moses and Mandal, 2022). Notably, graphene oxide (GO) is suitable for orthodontic mechanical scenario because of its excellent strength and elastic deformation

(Yang et al., 2022). The large surface area and special layered structure give it unique advantages in filling pores and improving corrosion resistance of the coating (Zhou et al., 2022). GO can also endow metal surfaces with antibacterial activity through membrane damage and oxidative stress (Lee et al., 2018; Mazinani et al., 2021). However, the bonding durability on metal surface of GO remains a challenge (Han et al., 2018). Some natural compounds have been used to modify substrates to enhance long-term stability, such as mussel-inspired polydopamine (PDA) (Cheng et al., 2019). Combining biomimetic PDA with GO was reported to achieve Ti alloys with tribological properties for orthopaedic applications (Wang et al., 2019); however, the feasibility of these nanosystems as orthodontic coatings in oral environment requires emphatic investigation.

Self-assembly is an environmentally benign strategy for manufacturing multi-component coatings while preserving the substrates' mechanical properties (Sun et al., 2023; Tanaka et al., 2023). It provides a powerful method to exploit desired functionality based on intermolecular interactions (Lee et al., 2019). Herein, the PDA-GO coatings were conducted on orthodontic NiTi alloys by self-assembly technology, aiming to optimize the corrosion-resistant and antibacterial properties of intraoral orthodontic materials (Figure 1). The dose-dependent process and the regulation mechanism were investigated and discussed, which laid a considerable foundation for designing efficient fixed appliances and provided guidance for developing advanced dental alloys.

2 Materials and methods

2.1 Characterization of GO

The morphology and dimension of GO nanosheets (XFNANO Materials Tech Co., China) were detected by SEM (Zeiss Sigma 300, Germany) and AFM (Dimension Icon, Germany), respectively. Raman spectroscopy (Renishaw, United Kingdom) was used to determine the molecular structure of GO at 514 nm wavelength. The functional groups of GO were measured by XPS (Thermo Fisher K-Alpha, United States).

2.2 Fabrication and characterization of PDA-GO-coated NiTi alloys

Ni-55.75 wt% NiTi alloys ($10 \times 10 \times 2$ mm^3) and 0.019×0.025-inch NiTi archwires with a 13-mm length were obtained from Baoji Titanium

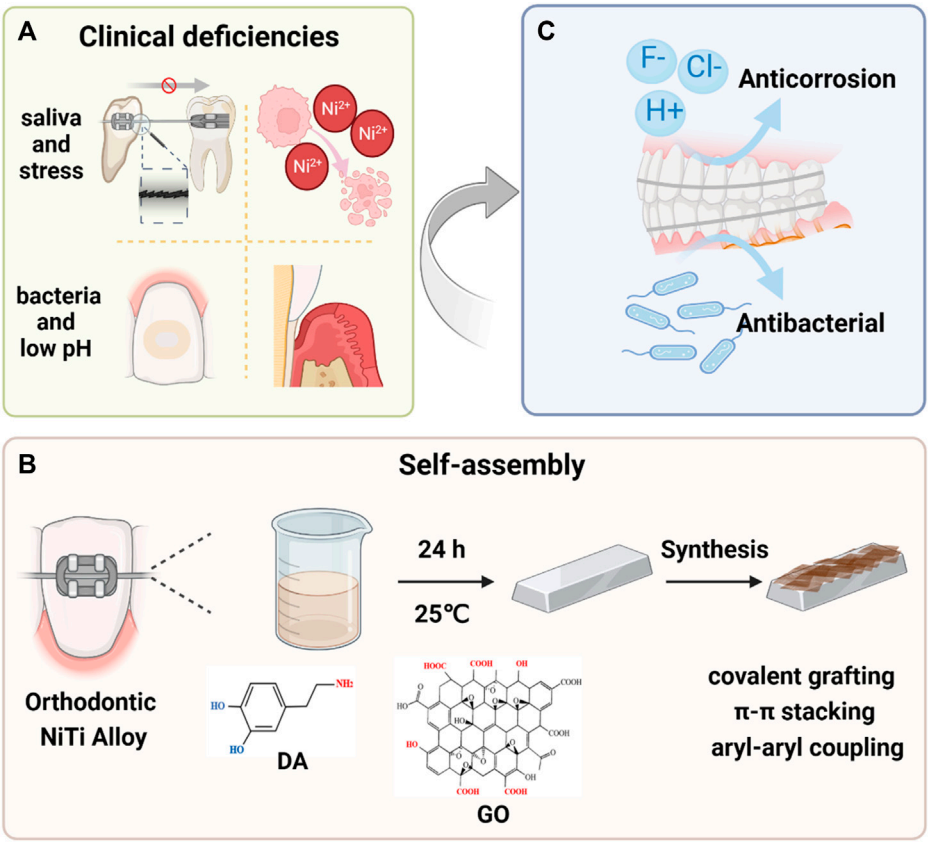

FIGURE 1
Schematic illustration of the PDA-GO modified orthodontic NiTi archwires. **(A)** Metallic fixed appliances can induce specific changes in oral environment. Stress corrosion under salivary corrosion medium impacts tooth movement and releases excess Ni^{2+}. Also, a decreased pH promotes development of bacteria-induced enamel demineralization and periodontal diseases. The most commonly used NiTi alloys have poor corrosion resistance and no antibacterial behavior, which requires modification. **(B)** The modification process and mechanisms of forming PDA-GO coatings from precursors in a self-assembly reaction. **(C)** PDA-GO coatings encourage excellent anti-corrosion performance while preventing bacterial infection.

Industry (China). The NiTi metals were ground with sandpaper, cleaned with acetone, anhydrous ethanol, and deionized water, and dried for later use. The fresh GO solution (0.2, 0.5, 1.0, 1.5, and 2.0 mg/mL) was ultrasonically dispersed and mixed with an equal volume of 2 mg/mL dopamine hydrochloride in pH 8.5 Tris-HCl buffer to prepare a co-deposition solution. A series of PDA-GO coatings were performed via the self-assembly reaction at 25 °C. After 24 h, the obtained PDA-GO-coated NiTi alloys were rinsed with distilled water and dried at 40 °C. The samples prepared by 0.2, 0.5, and 1.0 mg/mL GO were denoted as PDA-GO1, PDA-GO2, and PDA-GO3, respectively.

The surface morphology and composition of modified NiTi alloys were identified by SEM and EDS. AFM was employed to detect the three-dimensional morphology and roughness. The functional groups were characterized by FTIR. XPS characterized the element content and chemical bonds of PDA-GO-coated NiTi alloys. Mechanical stability and adhesion performance were assessed through the tape-peeling test following the ATSM D3359 standard (Yang et al., 2019). Briefly, the surface form the grid by vertical scratches and was pressed with 3 M adhesive tape, which was examined by optical imaging after the tape was pulled up.

2.3 Corrosion resistance performance

2.3.1 Stress corrosion tests

The bending stress of NiTi wire under orthodontic application was simulated using a three-point bending model. The mechanical constant applied to the archwire was 3.0-mm stress when immersed in artificial saliva at 37 °C (Liu et al., 2014). After 4 weeks, the leaching solution was collected, and the release of Ni^{2+} was detected by an inductively coupled plasma mass spectrometry (ICP-MS, Agilent 7700s, United States). After the archwire was unloaded and dried, the corrosion morphology was characterized by SEM, and the surface elements were detected by EDS.

2.3.2 Electrochemical corrosion experiments

During electrochemical tests, different NiTi samples were welded with copper wire and packaged with epoxy resin as the working electrode in a three-electrode system (Metrohm Autolab PGSTAT302N, Swiss). Prior to the potentiodynamic polarization test, the samples were kept in artificial saliva at 37 °C for 0.5 h to obtain a steady state. Tafel polarization curve scanning rate was 1.0 mV/s, voltage range was −1.5 to 1.5 V (vs. Ag/AgCl). The corrosion potential (E_{corr}) and corrosion current density (I_{corr}) were obtained by Tafel extrapolation method.

2.4 Antibacterial activity assays

2.4.1 Live/dead staining

Streptococcus mutans (*S. mutans*, ATCC25175) were incubated with different NiTi samples for 24 h. According to the Live/Dead bacterial kit (Thermo Fisher Scientific Inc., United States) instructions, each sample was stained with a mixed Brain Heart Infusion (BHI) liquid medium containing STYO9 and PI reagents and incubated for 15 min. The dead bacteria were marked as red, while the live bacteria were marked as green under confocal laser scanning microscopy (CLSM, Leica, Germany).

2.4.2 SEM

After 24 h of co-culture with *S. mutans*, the NiTi samples were washed with PBS and fixed with 2.5% glutaraldehyde for 2 h. After alcohol gradient dehydration and drying, the number and morphology of bacteria on the sample were observed by SEM. Three fields of view images were taken for each substrate.

2.4.3 Colony forming unit (CFU) counting

According to GB/T 2591 standard, 50 μL of bacterial solution (1.0×10^5 CFU/mL) was added to 24-hole plates, with three parallel samples in each group. The surface of the sample was completely immersed, covered with polyethylene film, and incubated in an anaerobic environment for 24 h. The biofilm was dissociated by ultrasonication in PBS for 3 min, and the bacterial solution was diluted in a series of gradients. 50 μL was coated on the BHI solid medium and cultured anaerobically for 24 h. The corresponding CFU values and sterilization efficiency were calculated.

2.5 Biocompatibility assessment

Based on ISO10993-12 standard, the extraction DMEM medium was obtained at 3 cm^2/mL (volume ratio of NiTi surface area to extraction liquid). To evaluate cell proliferation activity, mouse fibroblast L-929 cells were seeded in 96-well plates at a density of 5×10^3 cells/well and cultured in an incubator at 37 °C for 24 h. The cell lines present in this study were obtained from Zhongqiao Xinzhou Co., Ltd., Shanghai China. 100 μL extract from different samples was added to each well, and DMEM medium was added to the blank control group. After 1, 3, and 5 days of co-culture, the reagents were added according to the instructions of CCK-8 (Dojindo, Japan) and incubated for 1 h. The absorbance at 450 nm was measured. Live/dead staining assays were used to assess the morphology of L-929 cells. Cells were cultured with extract for 5 days and stained with a Calcein-AM/PI Double Stain Kit (Solarbio, China). Then, cells were imaged under an inverted fluorescence microscope (DMI8A, Leica). To evaluate ROS production, L-929 cells were inoculated into 6-well plates at a density of 2×10^5 cells per well, and extracts of different groups were added. After 24 h of co-culture, a diluted 100 μL DCFH-DA (Sigma-Aldrich, United States) probe was added to each well. After incubation, the fluorescence intensity was detected by flow cytometry (ThermoFisher DxFLEX, United States).

2.6 Statistical analysis

Data are represented as mean ± standard deviation, and statistical analyses were realized by GraphPad Prism. Significant differences were identified by one-way analysis of variance (ANOVA) or a two-sided unpaired Student's t-test. $p < 0.05$ indicated statistical significance.

3 Results and discussion

3.1 Characterization of GO

Characterization of nanomaterials is crucial for developing biocompatible nanocoatings. SEM reveals that the commercially

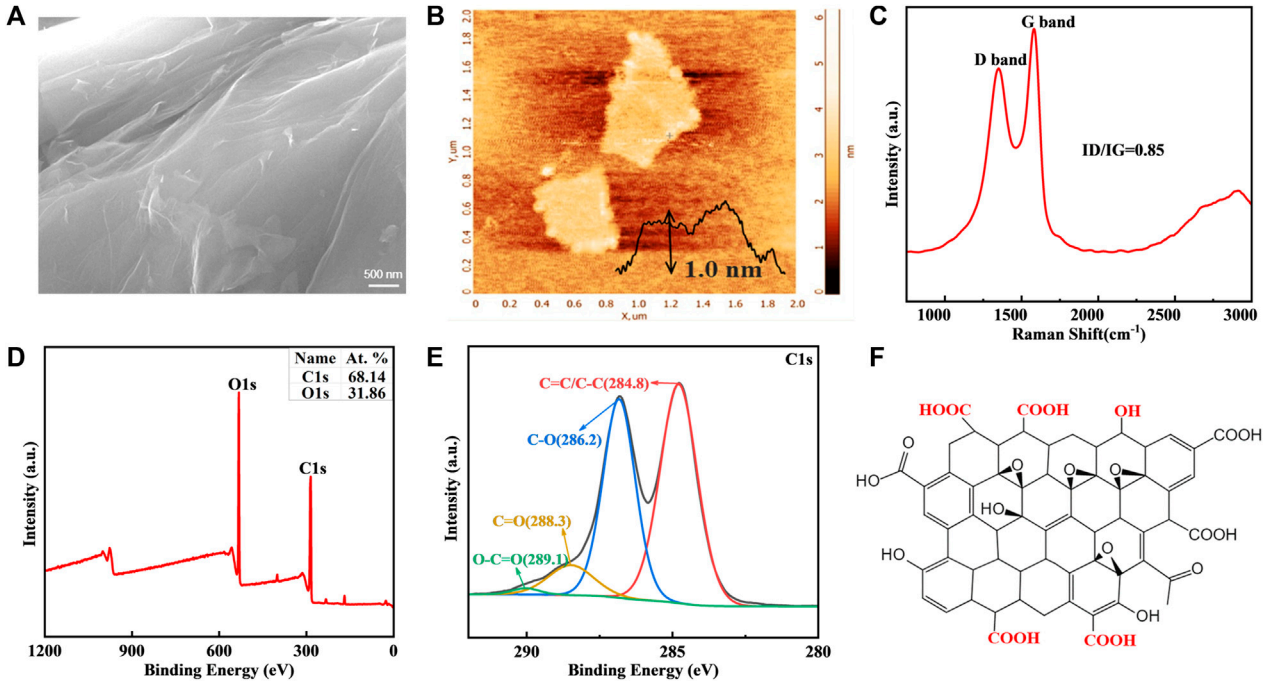

FIGURE 2
GO characteristics. **(A)** SEM image of GO. **(B)** Representative AFM image. **(C)** Raman spectra. **(D,E)** Elements and functional groups detected by XPS. **(F)** Chemical struture of GO.

obtained GO is lamellar with wrinkles on the surface (Figure 2A). The thickness of GO sheet measured by AFM is around 1.0 nm (Figure 2B). According to Raman spectra, GO has two typical peaks, D peak and G peak, which are positioned at 1,350 cm^{-1} and 1,581 cm^{-1}, respectively (Figure 2C). The ratio of their intensities is 0.85. The XPS-determined percentage of O element in GO is 31.86%, while the remainder is C element (Figure 2D). GO benefits from various hydrophilic oxygenic groups, including C-O (286.2 eV), C=O (288.3 eV), and O-C=O (289.1 eV), which provide active sites for covalent or non-covalent modification and endow it with high bioavailability (Figures 2E, F) (Hashemi et al., 2018). However, flaky GO nanosheet is easily wrinkled, and direct application will lead to poor adhesion between the coating and metal substrate (Han et al., 2018). The GO-based nanocomposite coating is more adaptable to modified NiTi archwires in orthodontic scenarios.

3.2 Coating morphology analysis

Inspired by mussel chemistry, self-polymerized PDA emanates as a versatile modifier with strong adhesion towards substrate surfaces due to the presence of catecholamine. In the self-assembly nanosystems, PDA and GO vividly serve as mortar and brick, respectively. Nanocomposites cannot be stuck on substrate at a low ratio of PDA/GO, while the fixed depositions ('brick') are limited at a high ratio (Yu et al., 2023). Based on the biomedical potential of GO, this study aims to explore the medical function of NiTi alloys in oral scenarios obtained by varying GO concentrations.

As shown in SEM images, the surface of bare NiTi sheet possessed some obvious scratches (Figure 3A). The wrinkled deposits were relatively evenly distributed when the GO solution was in the range of 0.2 mg/mL-1.0 mg/mL in the co-deposition system (Figures 3B–D). An increase in GO concentrations (1.5 and 2.0 mg/mL) resulted in agglomerated and stacked aggregates (Figures 3E, F), indicating that the excessive PDA-GO tended to form on the surface protrusions. Some uncovered areas were found in these two groups, which were not conducive to improving the following anti-corrosion performance of NiTi alloys. Therefore, 1.5 and 2.0 mg/mL were not included in the subsequent study.

Based on the SEM and AFM results, scatter deposition covered areas of the PDA-GO1 sample (0.2 mg/mL) with a roughness Rq value of about 24.99 nm (Figures 3G, H). More corrugated deposits in axial directions were observed on the surface of PDA-GO2 (0.5 mg/mL). EDS tests revealed that Ni and Ti element contents decreased compared to that of PDA-GO1, indicating that composite coating was fixed on a wider range of NiTi surface after introducing more GO. For the PDA-GO3 (1.0 mg/mL) sample, AFM displayed a uniformly pleated structure with a slightly increased Rq value, owing to more surface deposition of PDA-GO sheets. In line with our findings, Zhu et al. found that a compact lamellar PDA-GO microstructure was visible under increased GO concentration (Zhu et al., 2017). The different topographies might be attributed to the supplemented defects by appropriate proportion of PDA/GO. During the process, self-assembled PDA adsorbed certain amounts of flexible GO and cross-linked to co-deposit on the substrate (Li et al., 2023). Taken together, morphology analysis demonstrated that a greater GO concentration in a particular range provides a stable solution environment for PDA-GO to diffuse and self-assemble dense and well-arranged layers on NiTi surface.

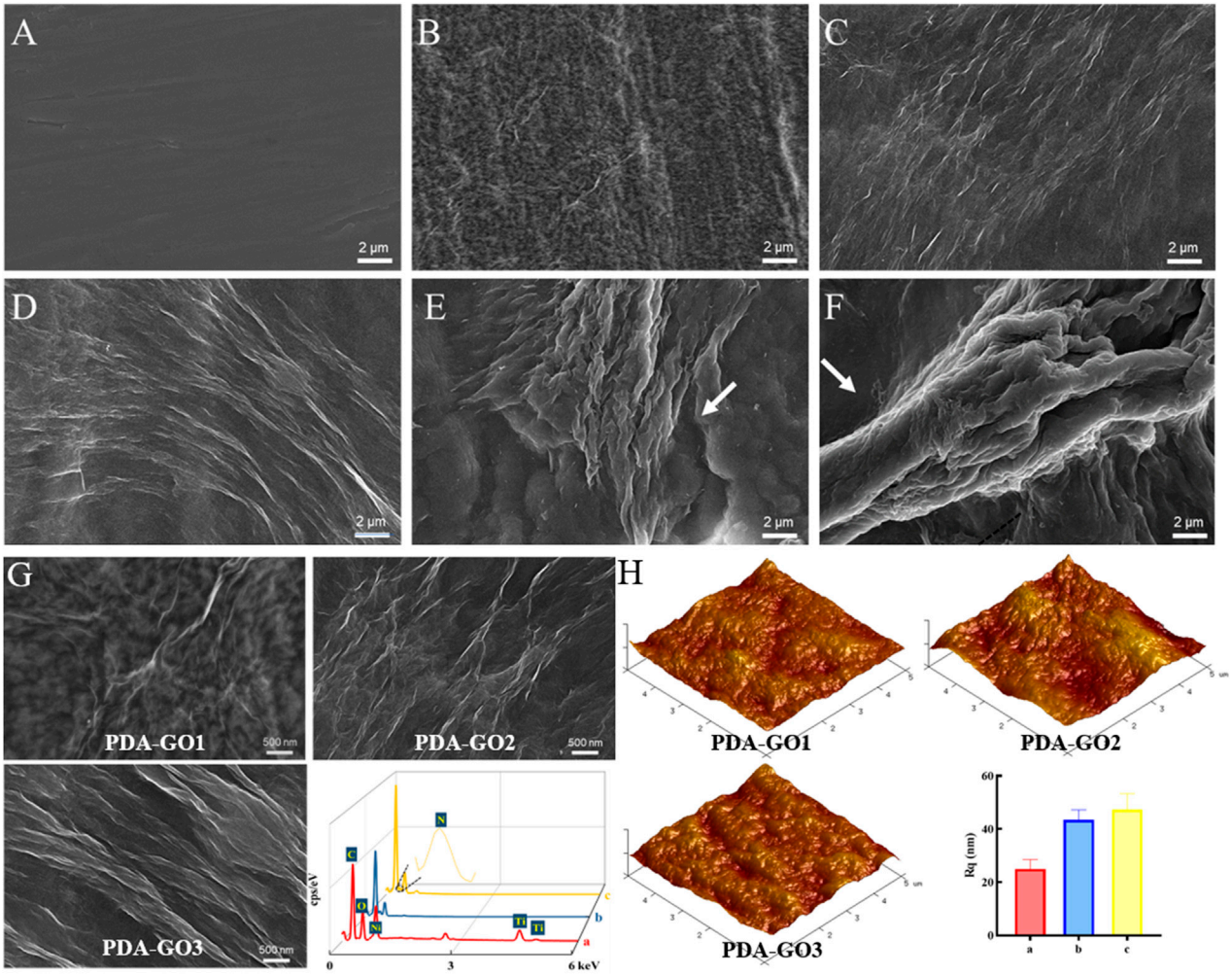

FIGURE 3
Coating morphology analysis. **(A)** SEM images of uncoated NiTi. **(B–F)** Modified NiTi assembled in DA solution with 0.2–2.0 mg/mL GO. **(G)** Enlarged SEM surface micrographs and EDS spectra of PDA-GO1, PDA-GO2, and PDA-GO3. **(H)** AFM images and roughness detection. Rq: the root mean square roughness.

3.3 Chemical structure and adhesive property

To explore the interaction between PDA and GO, we further analyzed the chemical characteristics of the as-prepared NiTi alloys. FTIR spectra suggested that PDA-GO1 had characteristic peaks at 1,737, 1,623, and 1,029 cm^{-1}, corresponding to the stretching vibration peak of C=O, C=C, and C-O, respectively (Figure 4A). The presence of these oxygen-containing functional groups and aromatic rings indicated the GO layers were successfully grafted. With the increase in GO concentration, the characteristic peak of C=O gradually decreased, suggesting that GO was partially reduced by PDA (Han et al., 2022). Compared to that of other groups, the spectrum of PDA-GO3 showed an N-H band at 1,508 cm^{-1}, which was derived from the amino group of PDA. The broad peak at 3,100–3,500 cm^{-1} may be caused by -OH (Zhao et al., 2019).

Five element peaks, including C1s, N1s, O1s, Ti2p, and Ni2p, were found on the NiTi-surface-assembled PDA-GO coatings via XPS analysis (Figure 4B). Among them, PDA-GO3 possessed the highest N content, accounting for 6.91%, with an emerged C-N peak at 285.5 eV (Figure 4C). It implied PDA covalently attached to GO on the modified NiTi surface, piling and interpenetrating the layers. Meanwhile, dense distribution of oxygenic groups offered anchoring sites for PDA-GO reaction (Chen et al., 2020). Mechanically, PDA stems from the oxidation, intramolecular cyclization and rearrangement of dopamine, serving as a stabilizer in GO reduction. GO with abundant oxygenic groups could be introduced to the surface by dopamine and may bind to NiTi alloy through π–π stacking and covalent interaction (Jia et al., 2016). Simultaneously, more GO nanosheets as oxidants promoted the nucleation and growth of the PDA film so that the composite coatings completely covered the NiTi alloy, which corresponded well with SEM observations.

Previous coatings, such as alumina, titanium dioxide, and hydroxyapatite, are easily cracked and will be partially peeled off, making them unsuitable for current clinical practice (Araujo et al., 2022). Tape-peeling test was utilized to evaluate the mechanical stability

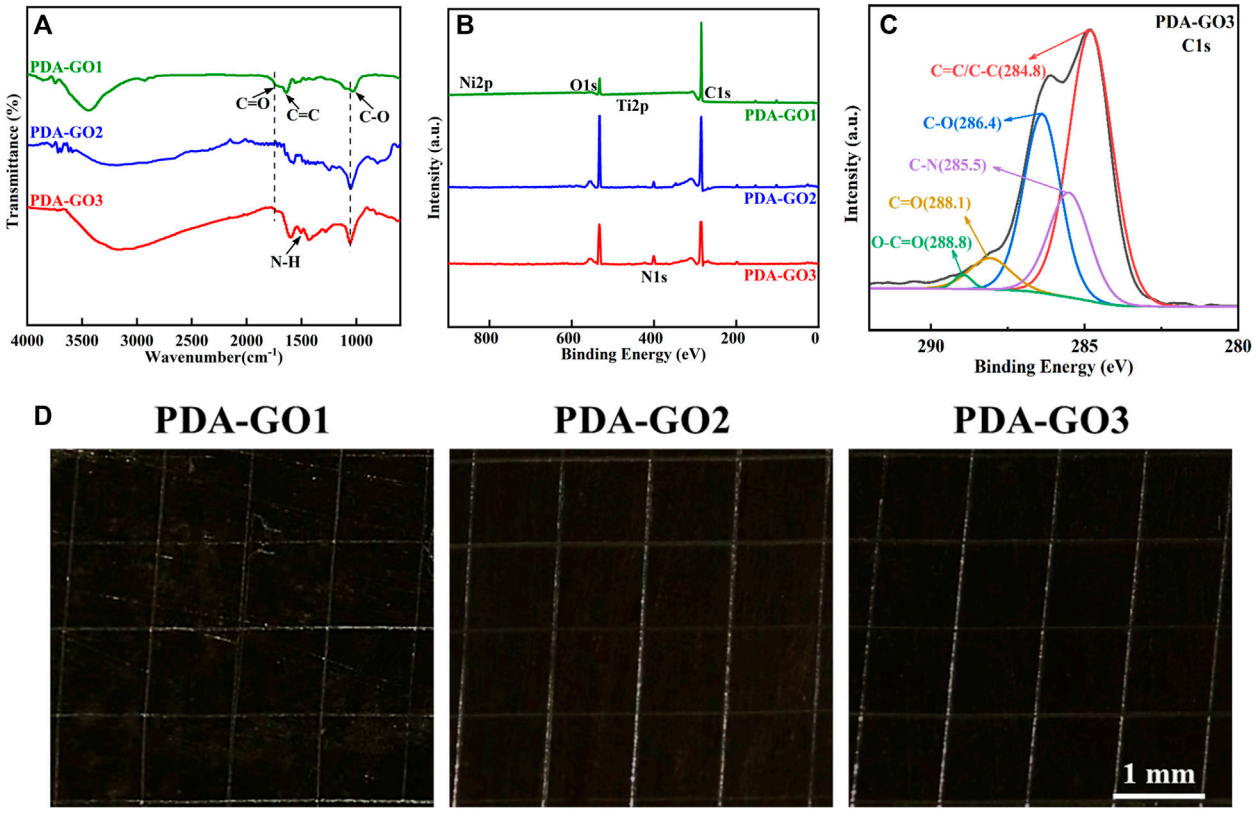

FIGURE 4
Chemical structure and adhesive property. **(A)** FTIR spectroscopic analysis. **(B)** Element compositions measured by XPS. **(C)** C1s XPS spectra of PDA-GO3. **(D)** Optical microscope images of adhesive tests.

and bonding strength according to ASTM D3359 standard (Shen et al., 2019). As shown in Figure 4D, the PDA-GO1 coating was partially detached from the substrate and the scratch area, and the area percentage was about 12.5%, while the PDA-GO2 and PDA-GO3 coatings displayed no detached or delaminated sediment. The adhesion levels between the latter coatings and the metal substrate were both regarded as 5A, which could be attributed to the compact and aligned structure during the self-assembly process (Figure 4D). This kind of excellent mechanical stability and adhesive performance of coated NiTi lays the foundation for long-term stability while correcting misplaced teeth in orthodontic treatment.

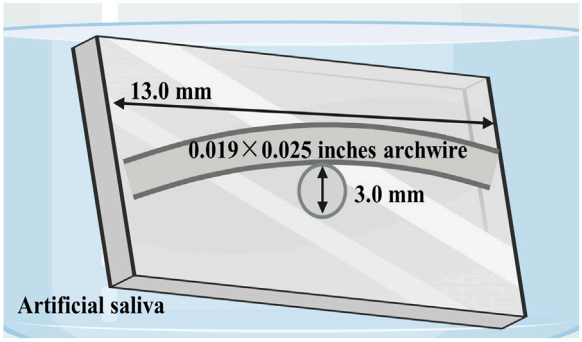

FIGURE 5
Schematic illustration of bending stress models in artificial saliva designed to simulate intraoral conditions.

3.4 Corrosion resistance performance

3.4.1 Stress corrosion tests

The oral cavity is a harsh corrosive environment for orthodontic devices, in which mechanical and chemical stresses damage their service life and orthodontic efficacy. To investigate the anti-corrosion potential of PDA-GO coated NiTi, a three-point stress model combined with an artificial saliva corrosion medium was performed, which realistically simulated the service state of archwires in the inoral cavity (Figure 5). SEM showed that corrosion pits and cracks were observed on bare NiTi, suggesting the dissolution of substrate by artificial saliva under 3-mm dislocation for 4 weeks (Figure 6A). Among the modified samples, the PDA-GO1 surface was rough with a relatively high proportion of Ni and Ti elements (Figure 6B). Under the same stress and saliva conditions, the other two samples showed a relatively intact and smooth surface with the granular products composed of calcium and phosphate from saliva, which obtained potent resistance to further development of corrosion (Figures 6C, D). GO possesses ultra-high tensile strength and elastic modulus, and maintains the integrity of its structure even if the archwires undergo

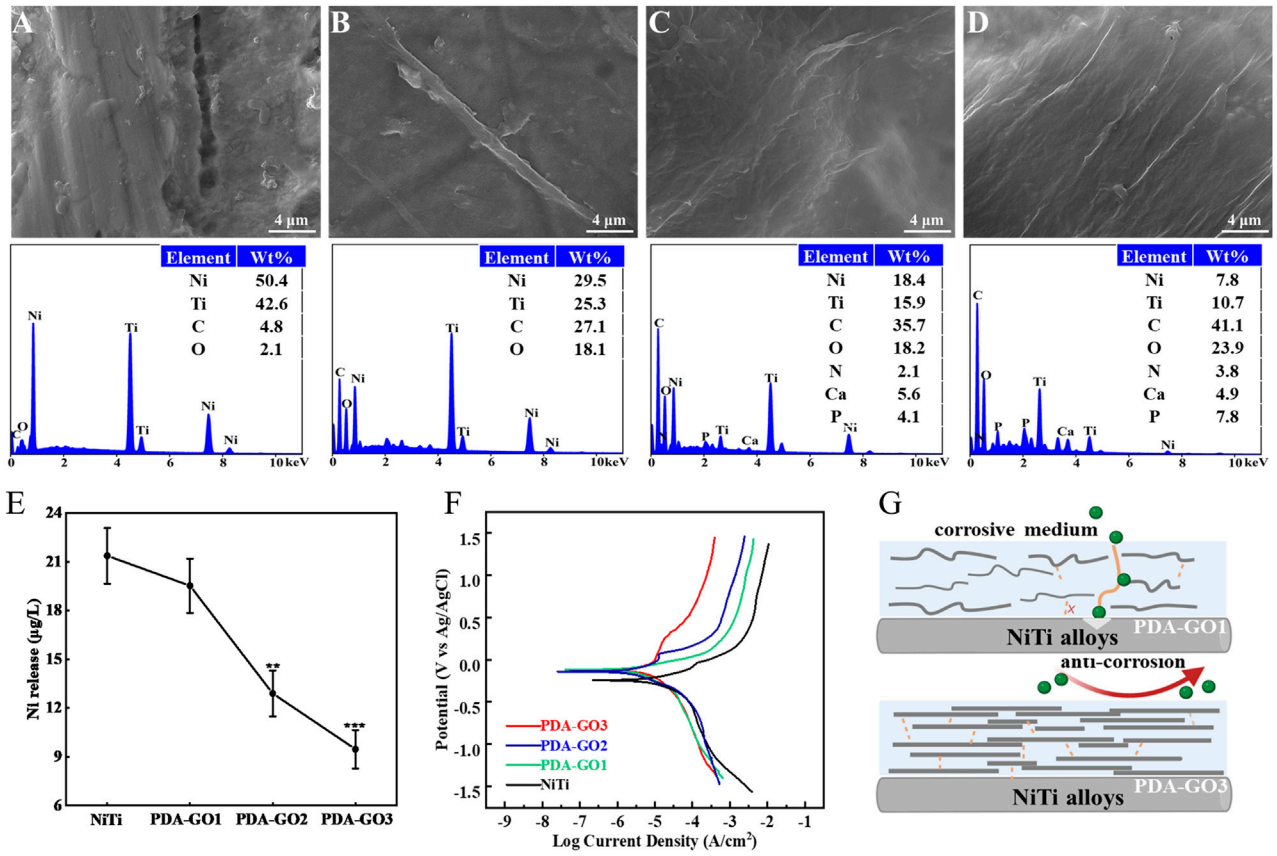

FIGURE 6
Anti-corrosive properties of PDA-GO coatings. **(A–D)** SEM morphology observations and EDS elemental tests of different substrates, including bare NiTi, PDA-GO1, PDA-GO2, and PDA-GO3, after stress corrosion. **(E)** Corresponding Ni^{2+} concentration. $^{**}p < 0.01$; $^{***}p < 0.001$ compared with NiTi group. **(F)** Representative cyclic potentiodynamic polarization curves of PDA-GO modified NiTi. **(G)** The proposed protection mechanisms during the corrosion process. Certain amounts of GO could chemically and physically bond with PDA and form a labyrinth-like superposition on NiTi surface, significantly reducing the contact area between the orthodontic appliances and corrosion medium.

stress deformation (Tasnim et al., 2017). Additionally, the binding affinity of PDA not only compensates for the GO defects through bond interactions but also firmly chelates metal ions (Zhu et al., 2022).

After 4 weeks of immersion in artificial saliva, the release of Ni^{2+} in PDA-GO2 and PDA-GO3 samples was 12.90 and 9.47 μg/L, respectively (Figure 6E). Compared with bare NiTi, PDA-GO modified NiTi exhibited remarkable anti-nickel release properties in saliva scenario. Similar results were reported in titanium dioxide-modified NiTi alloys via anodic oxidation technology, but large-scale device manufacture would be difficult (Xu et al., 2019). This research adopted self-assembly to mildly coat PDA-GO, which avoids the oxidation of considerable Ni into the coating and directly reduces Ni^{2+} dissolution. Appropriate GO sheets in PDA-GO3 were wrapped up to effectively form a close lamellar structure for mitigating serious corrosion. Accordingly, interaction of assembly and the well-dispersed morphology make PDA-GO provide stable barrier protection to intraoral stress and salivary environment.

3.4.2 Electrochemical corrosion

Electrochemical corrosion has been considered to be the main reason for Ni^{2+} dissolution in NiTi alloys (Shabalovskaya et al., 2009), which were examined under the saliva medium in the following study. For the polarization curve, the smaller I_{corr} reflects a slower corrosion rate and good corrosion resistance. As shown in Table 1 and Figure 6F, the E_{corr} of the unmodified NiTi sample was −171.70 mV, and the I_{corr} was 3.54×10^{-6} A/cm^2. In marked contrast, I_{corr} decreased in the PDA-GO coating samples. In particular, the I_{corr} of PDA-GO3 sample decreased to 5.3×10^{-7} A/cm^2, outperforming other films. The gathered data showed that PDA-GO modification made NiTi alloy have better corrosion resistance in oral corrosion medium. GO sheets were deposited on NiTi by PDA modification under the action of self-assembly, and the saliva electrolyte tended to approach the substrate through unevenness and defects between different layers (Chu et al., 2019). The PDA-GO1 coating had defects with low adhesive properties, which limited improvement in corrosion resistance. Consistent with the stress corrosion results, PDA-GO3 sample possessed the best protective performance in saliva environment, which reflected the influence of PDA/GO parameters on corrosion resistance of NiTi. Specifically, increased GO concentration contributes to orderly accumulating multiple layers during the deposition process, and more GO sheets are crosslinked to seal the NiTi surface by the interlocking effect with PDA, thereby

TABLE 1 E_{corr} and I_{corr} values calculated from potentiodynamic polarization curves.

Group	E_{corr} (mV vs. Ag/AgCl)	I_{corr} (A/cm^2)
NiTi	−171.70	3.54×10^{-6}
PDA-GO1	−140.96	2.51×10^{-6}
PDA-GO2	−109.90	1.05×10^{-6}
PDA-GO3	−104.77	5.30×10^{-7}

prolonging the diffusion path of corrosive electrolytes (such as chloride ions) into the substrate (Figure 6G) (Zhao et al., 2019). Other factors, such as the interlayer spacing and lattice structure of PDA-GO, might affect corrosion behavior of the coatings, which needs future study (Alkhouzaam et al., 2021).

3.5 Antibacterial activity

Orthodontic brackets and archwires create retention sites for bacterial growth due to their irregular surfaces; thus, proper modification is urgently desired to reduce microbial affection. *S. mutans*, the most critical cariogenic bacteria, was listed as the primary research object of antibacterial testing (Peng et al., 2022). Live/dead bacteria fluorescence staining showed that considerable green-stained live bacteria were observed on the uncoated NiTi surface, with almost no dead bacteria (Figure 7). However, the application of PDA-GO coating decreased the number of live bacteria and increased dead bacteria, exhibiting the property of effectively killing the adhered bacteria after 24 h of contact with modified NiTi.

SEM images indicated that more *S. mutans* adhered to the surface of bare NiTi, and grew in clusters with a relatively intact surface morphology (Figure 8A). In contrast, adherent bacteria decreased on the PDA-GO1, and no apparent aggregation was observed. PDA-GO2 found sporadic bacteria with changed morphology. On the surface of PDA-GO3, the integrity of *S. mutans* was destroyed at the interface in contact with the coating, as reflected in the exuded cellular content. The results revealed the concentration-dependent bactericidal potential of PDA-GO together with a decreased number of total adherent bacteria. Similarly, the number of bacteria adhered to the surface of bare NiTi was the highest in the CFU experiment (Figure 8B). The number of bacteria in the PDA-GO1 and PDA-GO2 groups gradually decreased, while the bacteria observed corresponding to PDA-GO3 were the least, showing superior antibacterial ability through interfering cell membranes (Zheng et al., 2018). According to the quantitative evaluation (Figure 8C), the antibacterial rates of each PDA-GO coating sample were 33.4%, 77.7%, and 93.1%, respectively, suggesting the tendency for more dead bacteria dependent on GO concentration.

Although efficient antibacterial coatings have been proposed, quite a few present defects, such as complex manufacturing processes or unsatisfied biocompatibility, which seriously hinder clinical applications. As an antibiotic-free antibacterial agent, the mechanism of GO includes two categories: oxidative stress and physical membrane damage such as nanoknife and encapsulation (Gao et al., 2022). It has been proposed that the more GO layers in GO composites, the stronger the oxidative stress in cells (Qiu et al., 2017; Mahmoudi et al., 2019). The increase in GO concentration may induce more PDA-GO layers with higher intracellular ROS levels, producing peroxides that affect the respiratory chain reaction, and destroy the integrity of bacterial membranes. These function cooperatively in the prominent antibacterial performance of PDA-GO3 (Figure 8D). The developed composite nano-coating optimizes the antibacterial properties of orthodontic NiTi alloys by increasing the PDA-GO component, which provides a viable preventive measure against orthodontic complications. Future research may involve elucidating how the PDA-GO alters antibacterial effects at the molecular level.

3.6 Biocompatibility properties

The biological security of GO composites needs to be highly valued for future clinical translation. To quantitatively determine the

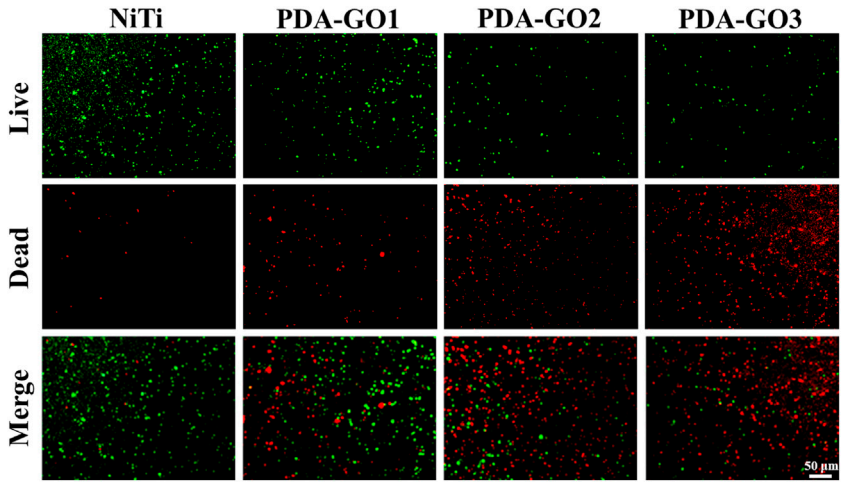

FIGURE 7
Live/dead results.

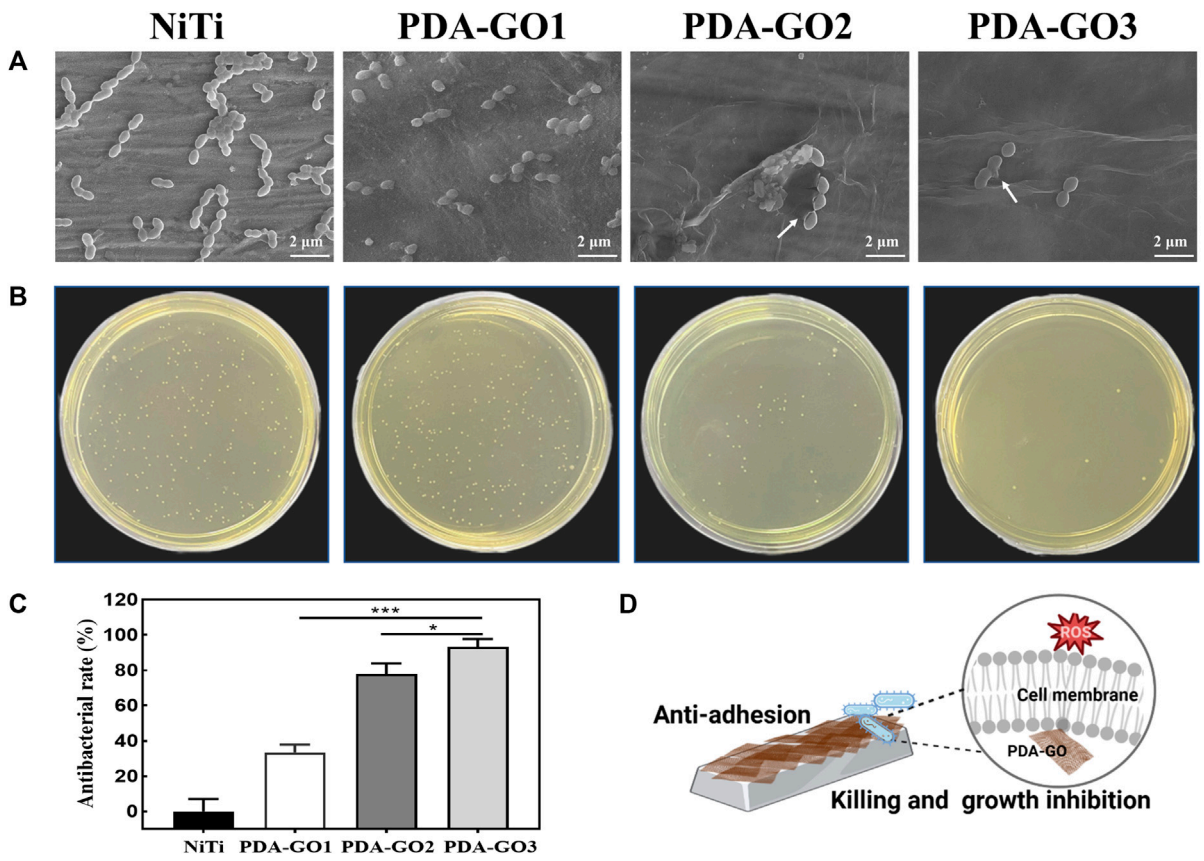

FIGURE 8
Antibacterial activity assays. **(A)** SEM analysis. **(B)** CFU results and **(C)** relative antibacterial rates. *$p < 0.05$; ***$p < 0.001$ compared with NiTi group. **(D)** The anti-adhesive and killing effect of PDA-GO coated NiTi alloys.

cytotoxicity, CCK-8 experiment was performed using L-929 cells, a common ideal *in vitro* model for detecting materials' biocompatibility (Yu et al., 2017; Nedeljkovic et al., 2022). Based on the results, the relative cell survival rate decreased with the prolongation of culture time. Notably, the cell viability in the PDA-GO3 group at 5 days significantly decreased to about 85% (Figure 9A), which was still acceptable cytotoxicity. The results qualified the modified NiTi as biosafety, with 70% viability being a mark for safe devices (Łyczek et al., 2023). Live/dead staining was carried out to further visualize the cell responses. As shown in Figure 9B, most of the extract-treated L-929 cells were green stained and alive, which was in accordance with the CCK-8 results. Cells in the PDA-GO groups presented a spindle-shaped morphology, similar to cells in the control group. Accordingly, the coatings exhibit not only great bacteriostatic effects, but also appropriate biocompatibility, which may be due to differences in the sensitivity of the cell lines used, the degree of interaction with cells, and the complexity of cellular responses (Zhao et al., 2016). Eukaryotic cells have been shown to be flexible and adaptable to different surfaces, leading to a superior survival rate (Butler et al., 2023). Bacterial membranes possess a higher population of negative intrinsic curvature lipids than mammalian cell membranes and are more likely to be damaged (Zhu et al., 2018). Antibacterial properties correlate positively with a certain range of GO concentration, but the concentration is not as high as possible in terms of biocompatibility. Thus, optimizing the bioefficacy of dental alloys requires a delicate balancing act between the cytotoxicity and bioactivity of different nanocomposite designs (Zheng et al., 2018).

GO-based nanocomposite can induce cytotoxicity through oxidative stress, and the ROS productions of different samples were also judged. PDA-GO coated NiTi stimulated cellular ROS production more than that in bare NiTi, and gradually increased with more GO concentration. From Figure 9C, the intracellular ROS level in PDA-GO3 was about 1.35 times that of the unmodified NiTi group (*$p < 0.05$). Modified NiTi remained safe for L-929 cells and met ISO 10993-5:2009 requirements for medical devices. This may be related to the fact that the amount of ROS induced is lower than the cell antioxidant threshold (Richtera et al., 2015). In addition, the phenolic hydroxyl and amino groups of PDA can interact with most molecules and proteins, enhancing the materials' affinity with cells (Liu et al., 2021). PDA-GO coatings applied in NiTi had a high guarantee of safety, but they still lacked clinical trials and long-term follow-up observation.

4 Conclusion

This study explores an effective means to optimize orthodontic NiTi archwires by preparing PDA-GO coatings. The morphology, chemical structure, and multifunctional properties are adjusted appropriately by changing the ratio of PDA/GO. PDA-GO is yarn-

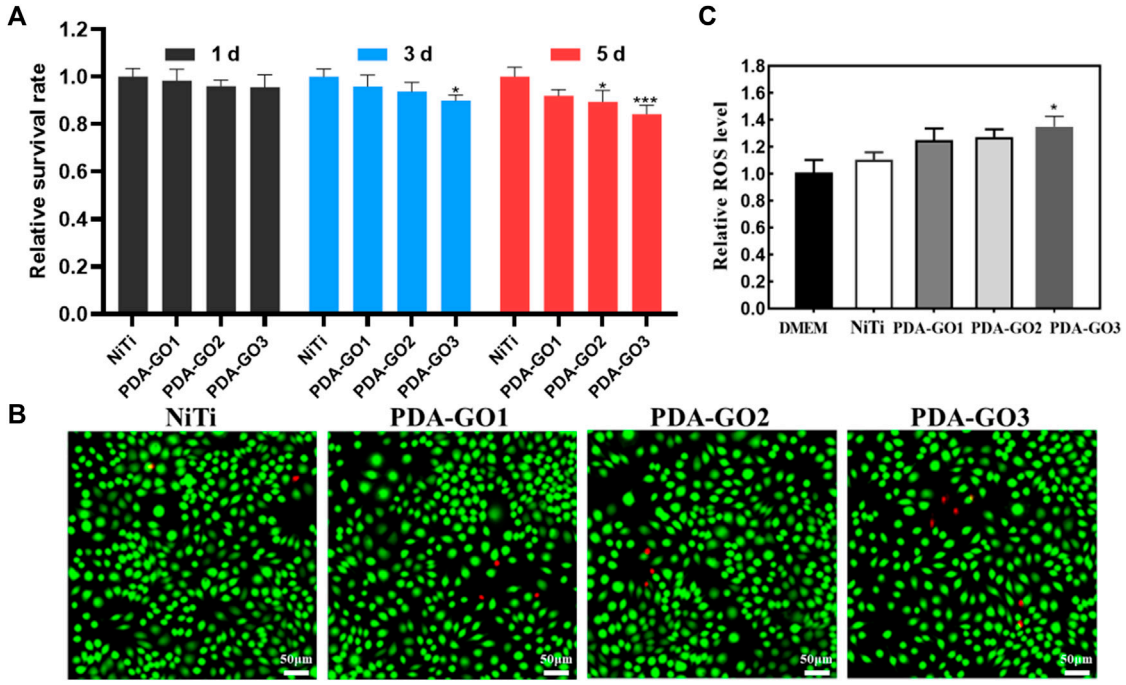

FIGURE 9
Biocompatibility assessment. **(A)** CCK-8 results. **(B)** Live/dead fluorescence staining after L-929 cells were cultured for 5 days in different NiTi extract. **(C)** Cell ROS production was evaluated and quantified. *$p < 0.05$; ***$p < 0.001$ compared with NiTi group.

wrinkled and unevenly distributed at a low GO concentration, which has limited effect on improving properties of NiTi alloys. By appropriately increasing GO concentration, a uniform and dense lamellar structure was obtained. The inherent attributes and special structure of PDA-GO endow the substrate with anti-corrosion property in oral environment and antibacterial capacity against oral cariogenic bacteria. PDA-GO nanocoatings on NiTi alloy combine manufacturing simplicity, adhesive performance, excellent corrosion resistance, reliable antibacterial, and biocompatible properties, which are potential for application as an effective and protective material for orthodontics.

Data availability statement

The raw data supporting the conclusion of this article will be made available by the authors, without undue reservation.

Author contributions

YC: Conceptualization, Formal Analysis, Methodology, Writing–original draft. ZC: Data analysis, Writing–original draft. ZZ: Validation, Writing–review and editing. YX: Conceptualization.

Funding

The authors declare that no financial support was received for the research, authorship, and/or publication of this article.

Acknowledgments

We would like to thank BioRender.com for drawing schematic diagrams.

Conflict of interest

The authors declare that the research was conducted in the absence of any commercial or financial relationships that could be construed as a potential conflict of interest.

Publisher's note

All claims expressed in this article are solely those of the authors and do not necessarily represent those of their affiliated organizations, or those of the publisher, the editors and the reviewers. Any product that may be evaluated in this article, or claim that may be made by its manufacturer, is not guaranteed or endorsed by the publisher.

References

Alkhouzaam, A., Qiblawey, H., and Khraisheh, M. (2021). Polydopamine functionalized graphene oxide as membrane nanofiller: spectral and structural studies. *Membranes*, 11. doi:10.3390/membranes11020086

Araujo, A. F., Ferreira, M. V. F., Felisberto, M. D. V., Sicupira, D. C., and Santos, L. A. (2022). Corrosion resistance of a superelastic NiTi alloy coated with graphene–based coatings. *Prog. Org. Coatings* 165, 106727. doi:10.1016/j.porgcoat.2022.106727

Butler, J., Handy, R. D., Upton, M., and Besinis, A. (2023). Review of Antimicrobial Nanocoatings in Medicine and Dentistry: mechanisms of action, biocompatibility performance, safety, and benefits compared to antibiotics. *ACS Nano* 17, 7064–7092. doi:10.1021/acsnano.2c12488

Chen, Y., Ren, B., Gao, S., and Cao, R. (2020). The sandwich-like structures of polydopamine and 8-hydroxyquinoline coated graphene oxide for excellent corrosion resistance of epoxy coatings. *J. colloid interface Sci.* 565, 436–448. doi:10.1016/j.jcis.2020.01.051

Cheng, W., Zeng, X., Chen, H., Li, Z., Zeng, W., Mei, L., et al. (2019). Versatile Polydopamine Platforms: synthesis and promising applications for surface modification and advanced nanomedicine. *ACS Nano* 13, 8537–8565. doi:10.1021/acsnano.9b04436

Chu, J. H., Tong, L. B., Zhang, J. B., Kamado, S., Jiang, Z. H., Zhang, H. J., et al. (2019). Bio-inspired graphene-based coatings on Mg alloy surfaces and their integrations of anti-corrosive/wearable performances. *Carbon* 141, 154–168. doi:10.1016/j.carbon.2018.09.047

Gao, Y., Kang, K., Luo, B., Sun, X., Lan, F., He, J., et al. (2022). Graphene oxide and mineralized collagen-functionalized dental implant abutment with effective soft tissue seal and romotely repeatable photodisinfection. *Regen. Biomater.* 9, rbac024. doi:10.1093/rb/rbac024

Ghazal, A. R., Hajeer, M. Y., Al-Sabbagh, R., Alghoraibi, I., and Aldiry, A. (2015). An evaluation of two types of nickel-titanium wires in terms of micromorphology and nickel ions' release following oral environment exposure. *Prog. Orthod.* 16, 9. doi:10.1186/s40510-015-0081-1

Han, K., Bai, Q., Zeng, Q., Sun, N., Zheng, C., Wu, W., et al. (2022). A multifunctional mussel-inspired hydrogel with antioxidant, electrical conductivity and photothermal activity loaded with mupirocin for burn healing. *Mater. Des.* 217, 110598. doi:10.1016/j.matdes.2022.110598

Han, L., Sun, H., Tang, P., Li, P., Xie, C., Wang, M., et al. (2018). Mussel-inspired graphene oxide nanosheet-enwrapped Ti scaffolds with drug-encapsulated gelatin microspheres for bone regeneration. *Biomater. Sci.* 6, 538–549. doi:10.1039/c7bm01060e

Hashemi, M., Omidi, M., Muralidharan, B., Tayebi, L., Herpin, M. J., Mohagheghi, M. A., et al. (2018). Layer-by-layer assembly of graphene oxide on thermosensitive liposomes for photo-chemotherapy. *Acta Biomater.* 65, 376–392. doi:10.1016/j.actbio.2017.10.040

Jia, Z., Shi, Y., Xiong, P., Zhou, W., Cheng, Y., Zheng, Y., et al. (2016). From Solution to Biointerface: graphene self-assemblies of varying lateral sizes and surface properties for biofilm control and osteodifferentiation. *ACS Appl. Mater. Interfaces* 8, 17151–17165. doi:10.1021/acsami.6b05198

Krishnan, V., Ravikumar, K. K., Sukumaran, K., and Kumar, K. J. (2012). *In vitro* evaluation of physical vapor deposition coated beta titanium orthodontic archwires. *Angle Orthod.* 82, 22–29. doi:10.2319/040811-251.1

Lee, H. A., Ma, Y., Zhou, F., Hong, S., and Lee, H. (2019). Material-independent surface chemistry beyond polydopamine coating. *Accounts Chem. Res.* 52, 704–713. doi:10.1021/acs.accounts.8b00583

Lee, J. H., Jo, J. K., Kim, D. A., Patel, K. D., Kim, H. W., and Lee, H. H. (2018). Nano-graphene oxide incorporated into PMMA resin to prevent microbial adhesion. *Dent. Mater* 34, e63–e72. doi:10.1016/j.dental.2018.01.019

Li, X., Wu, C., Hou, B., Wu, J., Sun, R., and Chen, M. (2023). Molecular investigation of interplay mechanism between polydopamine and graphene oxide: the effect of oxidation degree on the adsorption behavior of polydopamine. *Appl. Surf. Sci.* 611, 155759. doi:10.1016/j.apsusc.2022.155759

Liu, J.-K., Liu, I. H., Liu, C., Chang, C.-J., Kung, K.-C., Liu, Y.-T., et al. (2014). Effect of titanium nitride/titanium coatings on the stress corrosion of nickel–titanium orthodontic archwires in artificial saliva. *Appl. Surf. Sci.* 317, 974–981. doi:10.1016/j.apsusc.2014.08.132

Liu, X., Chen, W., Shao, B., Zhang, X., Wang, Y., Zhang, S., et al. (2021). Mussel patterned with 4D biodegrading elastomer durably recruits regenerative macrophages to promote regeneration of craniofacial bone. *Biomaterials* 276, 120998. doi:10.1016/j.biomaterials.2021.120998

Łyczek, J., Bończak, B., Krzymińska, I., Giżyński, K., and Paczesny, J. (2023). Gold–oxoborate nanocomposite-coated orthodontic brackets gain antibacterial properties while remaining safe for eukaryotic cells. *J. Biomed. Mater. Res. Part B Appl. Biomaterials* 111, 996–1004. doi:10.1002/jbm.b.35208

Mahmoudi, E., Ang, W. L., Ng, C. Y., Ng, L. Y., Mohammad, A. W., and Benamor, A. (2019). Distinguishing characteristics and usability of graphene oxide based on different sources of graphite feedstock. *J. colloid interface Sci.* 542, 429–440. doi:10.1016/j.jcis.2019.02.023

Mazinani, A., Nine, M. J., Chiesa, R., Candiani, G., Tarsini, P., Tung, T. T., et al. (2021). Graphene oxide (GO) decorated on multi-structured porous titania fabricated by plasma electrolytic oxidation (PEO) for enhanced antibacterial performance. *Mater. Des.* 200, 109443. doi:10.1016/j.matdes.2020.109443

Močnik, P., Kosec, T., Kovač, J., and Bizjak, M. (2017). The effect of pH, fluoride and tribocorrosion on the surface properties of dental archwires. *Mater Sci. Eng. C Mater Biol. Appl.* 78, 682–689. doi:10.1016/j.msec.2017.04.050

Moses, J. C., and Mandal, B. B. (2022). Mesoporous silk-bioactive glass nanocomposites as drug eluting multifunctional conformal coatings for improving osseointegration and bactericidal properties of metal implants. *ACS Appl. Mater Interfaces* 14, 14961–14980. doi:10.1021/acsami.2c00093

Nedeljkovic, I., Doulabi, B. Z., Abdelaziz, M., Feilzer, A. J., Exterkate, R. A. M., Szafert, S., et al. (2022). Cytotoxicity and anti-biofilm properties of novel hybrid-glass-based caries infiltrant. *Dent. Mater* 38, 2052–2061. doi:10.1016/j.dental.2022.11.018

Peng, S., Sang, T., Wang, H., Guan, Y., Deng, Y., Wang, P., et al. (2022). Bioinspired anti-demineralization enamel coating for orthodontics. *J. Dent. Res.* 101, 1620–1627. doi:10.1177/00220345221129806

Qiu, J., Geng, H., Wang, D., Qian, S., Zhu, H., Qiao, Y., et al. (2017). Layer-number dependent antibacterial and osteogenic behaviors of graphene oxide electrophoretic deposited on titanium. *ACS Appl. Mater Interfaces* 9, 12253–12263. doi:10.1021/acsami.7b00314

Richtera, L., Chudobova, D., Cihalova, K., Kremplova, M., Milosavljevic, V., Kopel, P., et al. (2015). The composites of graphene oxide with metal or semimetal nanoparticles and their effect on pathogenic microorganisms. *Materials* 8, 2994–3011. doi:10.3390/ma8062994

Shabalovskaya, S. A., Tian, H., Anderegg, J. W., Schryvers, D. U., Carroll, W. U., and Van Humbeeck, J. (2009). The influence of surface oxides on the distribution and release of nickel from Nitinol wires. *Biomaterials* 30, 468–477. doi:10.1016/j.biomaterials.2008.10.014

Shen, Y., Wu, Y., Tao, J., Zhu, C., Chen, H., Wu, Z., et al. (2019). Spraying Fabrication of Durable and Transparent Coatings for Anti-Icing Application: dynamic water repellency, icing delay, and ice adhesion. *ACS Appl. Mater Interfaces* 11, 3590–3598. doi:10.1021/acsami.8b19225

Sun, A. R., Sun, Q., Wang, Y., Hu, L., Wu, Y., Ma, F., et al. (2023). Surface modifications of titanium dental implants with strontium eucommia ulmoides to enhance osseointegration and suppress inflammation. *Biomaterials Res.* 27, 21. doi:10.1186/s40824-023-00361-2

Tanaka, H., Dotera, T., and Hyde, S. T. (2023). Programmable self-assembly of nanoplates into bicontinuous nanostructures. *ACS Nano* 17, 15371–15378. doi:10.1021/acsnano.2c11929

Tasnim, N., Kumar, A., and Joddar, B. (2017). Attenuation of the *in vitro* neurotoxicity of 316L SS by graphene oxide surface coating. *Mater Sci. Eng. C Mater Biol. Appl.* 73, 788–797. doi:10.1016/j.msec.2016.12.123

Venkatesan, K., Kailasam, V., and Padmanabhan, S. (2020). Evaluation of titanium dioxide coating on surface roughness of nickel-titanium archwires and its influence on Streptococcus mutans adhesion and enamel mineralization: a prospective clinical study. *Am. J. Orthod. Dentofac. Orthop.* 158, 199–208. doi:10.1016/j.ajodo.2019.07.019

Wang, C., Zhang, G., Li, Z., Xu, Y., Zeng, X., Zhao, S., et al. (2019). Microtribological properties of Ti6Al4V alloy treated with self-assembled dopamine and graphene oxide coatings. *Tribol. Int.* 137, 46–58. doi:10.1016/j.triboint.2019.04.030

Wang, N., Yu, J., Yan, J., and Hua, F. (2023). Recent advances in antibacterial coatings for orthodontic appliances. *Front. Bioeng. Biotechnol.* 11, 1093926. doi:10.3389/fbioe.2023.1093926

Xu, J. L., Lai, T., and Luo, J. M. (2019). Preparation and characterization of the aesthetic coating on nickel-titanium orthodontic archwire by electrophoretic deposition. *Prog. Org. Coatings* 137, 105271. doi:10.1016/j.porgcoat.2019.105271

Yang, N., Yang, T., Wang, W., Chen, H., and Li, W. (2019). Polydopamine modified polyaniline-graphene oxide composite for enhancement of corrosion resistance. *J. Hazard. Mater.* 377, 142–151. doi:10.1016/j.jhazmat.2019.05.063

Yang, P., Yu, F., Yang, Z., Zhang, X., and Ma, J. (2022). Graphene oxide modified κ-carrageenan/sodium alginate double-network hydrogel for effective adsorption of antibiotics in a batch and fixed-bed column system. *Sci. total Environ.* 837, 155662. doi:10.1016/j.scitotenv.2022.155662

Yu, P., Lei, J., Honglei, L., and Hui, C. (2017). Cell death affected by dental alloys: modes and mechanisms. *Dent. Mater. J.* 36, 82–87. doi:10.4012/dmj.2016-154

Yu, Y., Zhao, X., and Ye, L. (2023). A novel biocompatible wearable sensors based on poly (vinyl alcohol)/graphene oxide hydrogel with superior self-adhesion, flexibility and sensitivity. *Compos. Struct.* 309, 116768. doi:10.1016/j.compstruct.2023.116768

Zhang, R., Han, B., and Liu, X. (2023). Functional Surface Coatings on Orthodontic Appliances: reviews of friction reduction, antibacterial properties, and corrosion resistance. *Int. J. Mol. Sci.* 24, 6919. doi:10.3390/ijms24086919

Zhao, C., Pandit, S., Fu, Y., Mijakovic, I., Jesorka, A., and Liu, J. (2016). Graphene oxide based coatings on nitinol for biomedical implant applications: effectively promote

mammalian cell growth but kill bacteria. *RSC Adv.* 6, 38124–38134. doi:10.1039/c6ra06026a

Zhao, Z., Guo, L., Feng, L., Lu, H., Xu, Y., Wang, J., et al. (2019). Polydopamine functionalized graphene oxide nanocomposites reinforced the corrosion protection and adhesion properties of waterborne polyurethane coatings. *Eur. Polym. J.* 120, 109249. doi:10.1016/j.eurpolymj.2019.109249

Zheng, H., Ma, R., Gao, M., Tian, X., Li, Y. Q., Zeng, L., et al. (2018). Antibacterial applications of graphene oxides: structure-activity relationships, molecular initiating events and biosafety. *Sci. Bull.* 63, 133–142. doi:10.1016/j.scib.2017.12.012

Zhou, Z., Seif, A., Pourhashem, S., Silvestrelli, P. L., Ambrosetti, A., Mirzaee, M., et al. (2022). Experimental and theoretical studies toward superior anti-corrosive nanocomposite coatings of aminosilane wrapped layer-by-layer graphene Oxide@MXene/waterborne epoxy. *ACS Appl. Mater Interfaces* 14, 51275–51290. doi:10.1021/acsami.2c14145

Zhu, J., Yuan, L., Guan, Q., Liang, G., and Gu, A. (2017). A novel strategy of fabricating high performance UV-resistant aramid fibers with simultaneously improved surface activity, thermal and mechanical properties through building polydopamine and graphene oxide bi-layer coatings. *Chem. Eng. J.* 310, 134–147. doi:10.1016/j.cej.2016.10.099

Zhu, M., Liu, P., Shi, H., Tian, Y., Ju, X., Jiang, S., et al. (2018). Balancing antimicrobial activity with biological safety: bifunctional chitosan derivative for the repair of wounds with Gram-positive bacterial infections. *J. Mater Chem. B* 6, 3884–3893. doi:10.1039/c8tb00620b

Zhu, Z., Zhao, Y., Liu, Y., Wu, C., Lei, Y., Su, W., et al. (2022). Improvement of anticorrosion properties of waterborne coatings by designing a new type of modified graphene with high dispersion and low conductivity. *Prog. Org. Coatings* 173, 107188. doi:10.1016/j.porgcoat.2022.107188

frontiers | Frontiers in Bioengineering and Biotechnology

TYPE Original Research
PUBLISHED 02 November 2023
DOI 10.3389/fbioe.2023.1273318

OPEN ACCESS

EDITED BY
Jianyun Zhang,
Peking University Hospital of Stomatology, China

REVIEWED BY
Gianluca Tartaglia,
University of Milan, Italy
Zhijun Li,
Tianjin Medical University General Hospital, China

*CORRESPONDENCE
Jian Sun,
sunjianqdfy@qdu.edu.cn

RECEIVED 05 August 2023
ACCEPTED 23 October 2023
PUBLISHED 02 November 2023

CITATION
Xu Y, Li Y, Xiao W, Yue J, Xue L, Li L, Xu Z and Sun J (2023), Virtual surgical planning/3D printing assisted fibula osteoseptocutaneous flap combined with anterolateral thigh flaps for extensive composite oromandibular defects reconstruction: a retrospective study of case series.
Front. Bioeng. Biotechnol. 11:1273318.
doi: 10.3389/fbioe.2023.1273318

Virtual surgical planning/3D printing assisted fibula osteoseptocutaneous flap combined with anterolateral thigh flaps for extensive composite oromandibular defects reconstruction: a retrospective study of case series

Yaoxiang Xu[1,2,3,4], Yali Li[1], Wenlin Xiao[1,2], Jin Yue[1,2], Lingfa Xue[1,2], Li Li[1,2,3,4], Zexian Xu[1,2,3,4] and Jian Sun[1,2,3,4]*

[1]Department of Oral and Maxillofacial Surgery, The Affiliated Hospital of Qingdao University, Qingdao, China, [2]School of Stomatology, Qingdao University, Qingdao, China, [3]Dental Digital Medicine and 3D Printing Engineering Laboratory of Qingdao, Qingdao, China, [4]Shandong Provincial Key Laboratory of Digital Medicine and Computer-Assisted Surgery, Qingdao, China

Oromandibular tumors or osteoradionecrosis often lead to extensive composite defects encompassing intraoral, bone and extraoral tissues. A single flap cannot simultaneously offer sufficient bone and soft tissue. The combination of free flaps could be a prospective approach to overcome the challenge. The study aims to assess the efficacy of virtual surgical planning (VSP) and 3D printing assisted fibula osteoseptocutaneous flap (FOSCF) combined with anterolateral thigh flaps (ALT) in reconstructing extensive composite defects in the oromandibular region. A retrospective analysis was conducted on 8 patients who underwent reconstruction using FOSCFs combined with ALTs. Post-surgical excision of the lesions, we obtained mean values for the defects of intraoral soft tissue, bone, extraoral soft tissue, namely, being 42.7 cm^2, 96 mm, and 68.9 cm^2. The mean surgical procedures took 712.5 min. A total of 16 flaps were harvested and transplanted for the 8 patients, with all successfully surviving. Postoperatively, complications manifested as localized intraoral infections in 2 cases, intermuscular vein thrombosis in another 2 cases, and pulmonary infections in 2 patients. Two patients unfortunately experienced tumor recurrence, at 12 and 3 months post-operation respectively. For the surviving 6 patients, the average follow-up period was 12.2 months. Regarding patient satisfaction, one expressed dissatisfaction with the contour of the mandible, and two exhibited moderate trismus. Objective assessments identified 1 case of oral incontinence and 2 cases where external flap contractures were observed. All 8 patients experienced restoration of masticatory function and were able to consume a soft diet within a month post-surgery. VSP/3D printing assisted FOSCFs combined with ALTs can be performed safely to reconstruct the extensive composite tissue

defects in our study, with desirable esthetic and functional results, and it is a reliable option in selecting patients with defects involving multiple tissue types. However, the benefits of this method needed more cases to validate.

KEYWORDS

flap transplantation, reconstructive surgery, virtual surgical planning, multipleflap, 3D printing

1 Introduction

Extensive composite oromandibular defects are frequently caused by surgical resection of sizeable primary tumors in the head and neck region, or the result of osteoradionecrosis (ORN) post-radiotherapy. The reconstruction of such complex defects, encompassing multiple structures such as external skin, mandible, and oral mucosa presents a formidable challenge. Free flap reconstruction is the standard of care in these extensive defects, while there may not exist a single free flap capable of simultaneously offering sufficient bone stock and soft tissue. In these instances, the combination of multiple free flaps proves to be an efficacious treatment strategy (Lee et al., 2010; Weitz et al., 2015).

Selecting suitable free flap is integral to the reconstructive success and overall outcome. In contrast to iliac or scapular osteocutaneous free flaps, the FOSCF can provide longer bone segments as well as ample skin paddle for intraoral lining (Taylor et al., 2016; Liu et al., 2022). The ALT is the most useful workhorse flap employed for microsurgical reconstruction. Depending on requirements, the flap can be harvested as myocutaneous, fasciocutaneous, adipofascial, or in combination with the adjacent tissues or muscles as chimeric flaps. This versatility makes it particularly suited for the reconstruction of extensive extraoral skin defects (Hsieh et al., 2021; Ranganath et al., 2022). The advent of VSP and 3D printing marks a significant milestone for the FOSCF. The utilization of these techniques enhances the safety, accuracy, and symmetry of this surgical procedure while considerably reducing the operating time (Ritschl et al., 2021; Al-Sabahi et al., 2022; Idris et al., 2022).

Despite their advantages, multi-flap approaches for the reconstruction of composite oromandibular defects continue to be challenging and are a subject of ongoing debate. A few reports are available on the functional and aesthetic outcome of double free flap reconstructions in these defects (Lee et al., 2010; Tharakan et al., 2023). The objective of this study is to evaluate the effect of the combination of VSP/3D printing-assisted FOSCF with ALT in composite tissue defects reconstruction which could not be solved by one single flap.

2 Patients and methods

This study received approval from the Ethics Committee at the Affiliated Hospital of Qingdao University, Qingdao (ethics number, QYFYWZLL 27958). A retrospective review was conducted of 8 patients who underwent extensive composite oromandibular defects repair using the combination of VSP/3D printing-assisted FOSCF with ALT between July 2019 and December 2022 at our department.

The cohort comprised seven males and one female. All patients had undergone lesion resection, with extensive defects variably involving oral mucosa, mandible, and perioral skin areas. All defects were reconstructed using a FOSCF in combination with ALT. A two-team approach was consistently employed throughout all stages of the operation.

2.1 Preparation of the FOSCF assisted by VSP and 3D printing

All patients underwent routine preoperative three-dimensional CT scan of the mandible and fibula (SOMATOM Force CT, slice thickness 0.625 mm), in addition to lower limb CT angiography (CTA). The acquired data were input into the Mimics 17.0 software (Materialise, Leuven, Belgium) in the DICOM format. The software was used to simulate tumor excision, fibula osteotomy, mandibular reconstruction, and the design of repositioning guides. In the process, the mandibular osteotomy guide and the fibula positioning guide share the same nail track to ensure the accuracy of mandibular reconstruction. For those mandibular defects not traversing the midline, mirror technology was employed to accomplish reconstruction. However, in cases where the defects did cross the midline, a synergistic approach combining mirror and surface reconstruction techniques was adopted. Following the completion of the virtual surgery, the designed guides were materialized using an 3D printer (UltraCraft A2D, HeyGears), and subsequently sterilized with plasma. The reconstruction-team prepared the FOSCF. The skin perforator was located and the skin paddle was incised in accordance with the magnitude of the intraoral soft tissue defect. The fibula osteotomy guide was positioned, leading to the fibula being cut to the length prescribed in the virtual surgery. The distal end of the fibular artery was ligated, preserving the proximal vascular pedicle. The fibula was then contoured using the shaping guide and secured in position with miniplates. Upon completing the FOSCF preparation, the same team proceeded to harvest the ALT.

2.2 Oral lesion excision

The resection-team was tasked with the excision of the tumor at its safe boundary. According to the preoperative virtual surgical design, the mandibular osteotomy guide was positioned, followed by the segmental resection of the mandible. After the complete excision of the tumor, two sets of recipient vessels were prepared. Subsequent to the surgical procedure, patients were admitted to the intensive care unit (ICU), and tracheostomy was not a routine intervention. Patients were typically transferred back to the general ward within a period of 3–5 days postoperatively, contingent upon their stabilized condition. All patients needed nasogastric feeding for 1 week post-surgery. Subsequently, a soft or normal diet was gradually adopted. All patients except No.5 and No.8 underwent postoperative radiation therapy.

TABLE 1 Patient data.

Case no.	Age (Y)	Sex	Tumor	Location	Stage	ILD (cm)	OLD (cm)	BD (mm)	Arteries used	Veins used	Operation Time (min)	Survived/ Deceased
1	61	M	SCC	Buccal	T4N0M0	9 × 5	11 × 6	100	Facial; superior thyroid	External jugular; facial	720	Deceased (12 months, recurrence)
2	68	F	SCC	Buccal	T4N1M0	7 × 5.5	10 × 6.5	109	Facial; Contralateral facial	Facial; Contralateral facial	780	Deceased (3 months, recurrence)
3	66	M	SCC	Buccal	T4N0M0	7.5 × 4	8 × 5	76	Facial; superior thyroid	External jugular; facial	660	Survived (18 months)
4	65	M	SCC	Gum	T4N0M0	9 × 4.5	12 × 6.5	108	Facial; Lingual	Facial; internal jugular	710	Survived (15 months)
5	70	M	ORN	Buccal	/	7 × 4.5	9 × 6	78	Facial; superior thyroid	Facial; internal jugular	730	Survived (12 months)
6	48	M	SCC	Buccal	T4N0M0	8.5 × 5.5	10 × 8	80	Facial; superior thyroid	Facial; internal jugular	660	Survived (11 months)
7	45	M	SCC	Buccal	T4N1M0	12 × 6.5	14 × 9	125	Facial; superior thyroid	External jugular; internal jugular	840	Survived (10 months)
8	61	M	SCC	Mouth floor	T4N0M0	7 × 4.5	8.5 × 5	92	Facial; superior thyroid	Facial; superior thyroid	600	Survived (7 months)

ILD, inner lining defect; BD, bone defect; OLD, outer lining defect; SCC, squamous cell carcinoma; ORN, osteoradionecrosis.

Surgical and medical complications were documented. A patients satisfaction questionnaire was administered to make subjective evaluation on chewing, speech, dry mouth and facial appearance, which were divided into three grades: very satisfied, satisfied and dissatisfied. To determine objective evaluation, facial appearance, oral incontinence, speech problems, eating problems, xerostomia, and flap contracture were assessed. Each individual item was scored using a Likert scale (1 = extremely abnormal and 5 = completely normal).

3 Results

Our study comprised 8 patients including 7 males and 1 female, aged from 45 to 68 years (mean, 60.5 years). Seven of these patients presented with oral malignant tumors, all diagnosed as squamous cell carcinoma, while one patient (No.5) had osteoradionecrosis as a consequence of radiation therapy. A total of 16 flaps were prepared for 8 patients, which consisted 8 FOSCFs and 8 ALTs. Post-excision of the lesions, the dimensions of the intraoral soft tissue defects ranged from 7.5 × 4 cm to 12 × 6.5 cm (mean, 42.7 cm^2). The length of the bone defects extended from 76 mm to 125 mm (mean, 96 mm), while the extraoral soft tissue defects varied from 8 × 5 cm to 14 × 9 cm (mean, 68.9 cm^2). The anastomosis involved recipient arteries that included the facial artery, superior thyroid artery, and lingual artery. Concurrently, the recipient veins involved were the facial vein, superior thyroid vein, internal jugular vein, and external jugular vein. One case required vascular grafting. The operative duration for these procedures ranged between 600 and 840 min, with an average of approximately 712.5 min (Table 1).

Remarkably, all of the flaps survived without any vascular crises or local flap necrosis. Two cases (No.3, No.4) developed local oral infections. Additionally, intermuscular vein thrombosis in the lower limbs was observed 2 patients (No.2, No.5). Pulmonary infection was found in 2 cases (No.2, No.4). Unfortunately, 2 of the 8 patients succumbed due to tumor recurrence at 12 months and 3 months post-surgery respectively. The mean follow-up time of the remaining 6 patients was 12.2 months (range, 7 months–18 months). Patient satisfaction assessments revealed one individual (No.3) was dissatisfied with their post-operative appearance, while two (No.2, No.4) reported moderate trismus. However, the remaining patients all reported satisfaction levels above average. Objective evaluations indicated oral incontinence in 1 case (No.4) and external flap contracture in 2 cases (No.2, No.4). Impressively, all 8 patients regained masticatory function and resumed a soft diet within a month post-operation.

3.1 Case presentation

A 45-year-old male patient diagnosed with a squamous cell carcinoma on his left cheek. The tumor demonstrated regression by radiation therapy (66 Gy) 7 months ago. However, the anterior part was ulcerated and gradually formed a penetrating defect after 1 month. Histopathological examination confirmed squamous cell carcinoma, staged clinically as T4N1M0. With the assistance of VSP and 3D printing technology, the reconstruction utilising both flaps was successfully performed (Figures 1, 2).

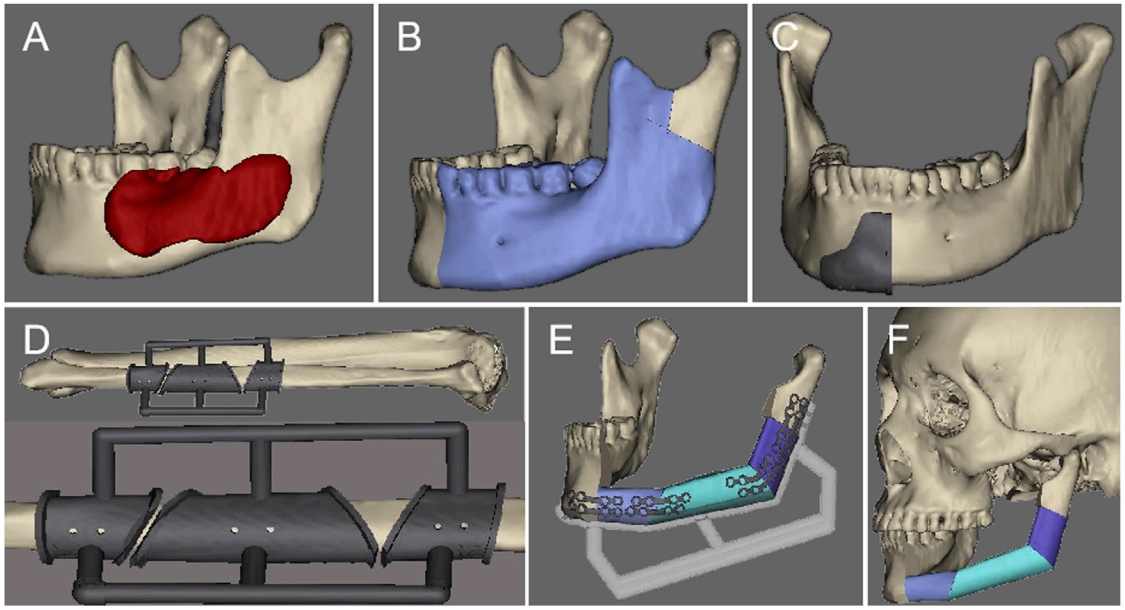

FIGURE 1
The preoperative virtual surgical design: **(A)**. Determine the range of the lesion. **(B)** Simulate the range of bone cutting. **(C)** Design the bone cutting guide. **(D)** Design the fibula osteotomy guide. **(E)** Design the fibula repositioning guide. **(F)** Restore the mandibular contour.

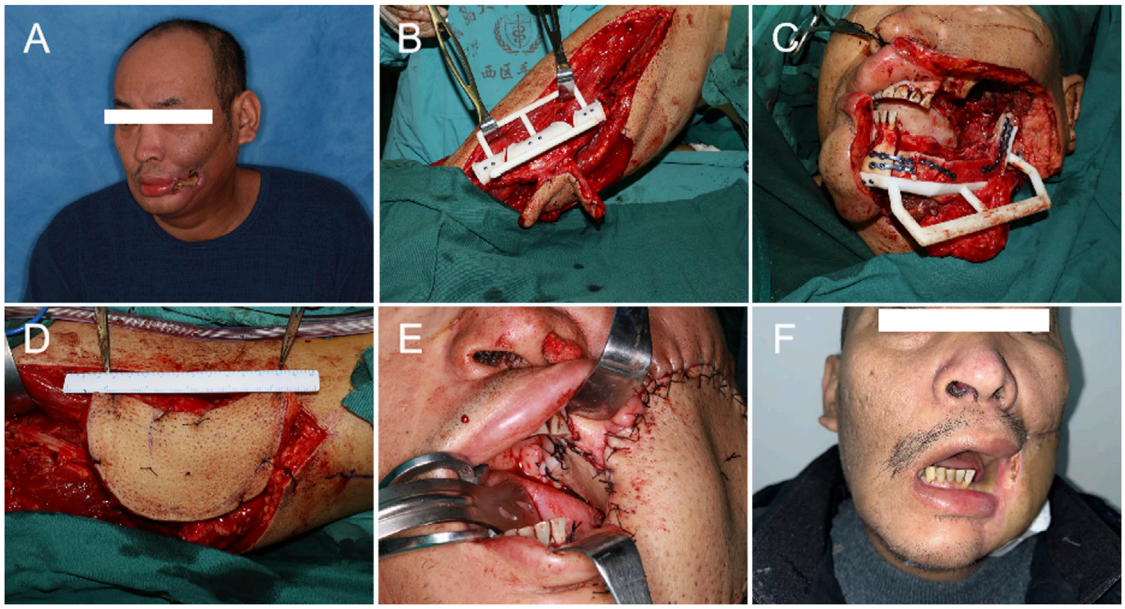

FIGURE 2
Operational procedure: **(A)**. Preoperative photo. **(B)** Fibula shaping. **(C)** Fibula positioning. **(D)** Harvest of the ALT. **(E)** The fibula osteoseptocutaneous flap was used to repair the oral soft tissue and the mandible, and the ALT was used to repair the extraoral tissues. **(F)** 6 months post-operation.

4 Discussion

Surgical removal of oral tumors or osteoradionecrosis can result in substantial composite tissue defects, presenting formidable challenges for reconstructive repair. A single flap is often insufficient to adequately address these extensive defects. Consequently, the combination of multiple flaps has emerged as an innovative therapeutic approach (Lee et al., 2010; Weitz et al., 2015; Hsieh and Bewley, 2019; Silva et al., 2019; Moratin et al., 2021; Raghuram et al., 2021; Santilli et al., 2021; Tharakan et al., 2023). The ALT can furnish sufficient tissue volume and can be fashioned into a chimeric flap with minimal impact on the donor site, rendering it an

optimal choice for repair and reconstruction of large soft tissue defects in the oromandibular region (Thomas et al., 2020). The FOSCF is exceptionally suitable for large bone tissue defects. Its accompanying skin paddle can repair tissues both inside or outside the oral cavity, and its associated muscle can effectively fill the surgical dead space (Dowthwaite et al., 2013). Therefore, for large composite tissue defects in the oromandibular region, we opt for the ALT for the repair of extraoral soft tissue defects and the FOSCF for the repair of bone and intraoral soft tissue defects. Nevertheless, surgical alternatives should be carefully considered. The fibular flap can be substituted with a reconstruction plate, iliac bone muscle flap, or scapular bone muscle flap. Soft tissue flap can be replaced with a vascularized free flap or pedicled flap, such as the forearm flap, rectus abdominis flap, or pectoralis major myocutaneous flap. However, the radial forearm flap offers limited soft tissue volume, it is difficult to fill the dead cavity effectively. Its application is further limited by the severe scarring left on the forearm, tendon exposure, and forearm mobility disorders (Ranganath et al., 2022). The rectus abdominis myocutaneous flap can deliver a satisfactory volume of soft tissue, yet it may trigger complications such as reduced abdominal wall strength and incisional hernia. While the pectoralis major flap supplies generous soft tissue, it's typically considered a backup option. The free iliac flap has insufficient bone length to adequately repair the defects. Besides, the free scapular flap cannot effectively mimic the shape of the mandibula, and has limitations in deficient bone length (Liu et al., 2022). Moreover, reconstruction plates are prone to complications like screw loosening, plate fracture, plate exposure and stress shielding.

A unique aspect of our study is the incorporation of VSP and 3D printing. VSP allows for tailoring surgical approaches, ensuring precise lesion delineation, osteotomy localization, and fibula harvest estimation. Preoperative mandibular modeling not only reduces surgical time but also ensures superior functional and aesthetic outcomes. 3D-printed guides, enhance surgical accuracy, fostering a closer match to the original mandibular structure. Shared screw tracks between the mandibular osteotomy and fibula positioning guides simplify the procedure, further minimizing trauma and operative time (Seruya et al., 2013; Schepers et al., 2015; Wu et al., 2021). Using the osteotomy guide and positioning guide, the fibula is contoured and then affixed with mini titanium plates. Shaw et al. (2004) proved that there were no significant differences in complications between miniplates and reconstruction plates, but the author also highlighted the defects of reconstruction plates, including stress shielding, interference with the vascular pedicle, and problems of metal fatigue when bending plates in the sagittal plane. In comparison, miniplates which avoid the above drawbacks are a better choice. Intermaxillary fixation was performed after surgery for 1 week, encouraging oral exercises to prevent trismus.

The vascular pedicle is severed after the recipient vessels are prepared, markedly reducing ischemic time and overall duration of the surgery. Literature indicates that when the ALT donor site width is under 8.0 cm, primary closure is feasible; for wider defects, skin grafting becomes necessary (Chen and Tang, 2003). Some reports suggest that direct suturing is feasible when the width is less than 10.0 cm (Townley et al., 2011). Studies have proposed that the ratio of flap width to thigh circumference can serve as a reliable metric for direct wound closure, with a ratio less than 16% indicating direct closure (Boca et al., 2010). In our study, we found that for one patient, the flap width was 9.0 cm, and direct suturing did not induce fascial compartment syndrome or other complications.

While the use of double flaps allows for the repair of large composite tissue defects in the oromandibular region, overcoming the limitations of a single flap or composite flap due to vascular pedicle restrictions, it demands higher provisions for neck vessels. This includes the preparation of two sets of anastomotic arteries and veins in the recipient area. In our study, it was found that arteries were relatively easier to prepare, with a total of 16 arteries prepared. The most frequently used anastomotic arteries were the facial artery and the superior thyroid artery, while the facial vein and internal jugular vein were the most commonly used anastomotic veins. Flow-through flaps, as reported in literature (Qing et al., 2015; He et al., 2021), allow the usage of only one set of recipient area vessels. However, this approach carries a significant drawback: if a vascular crisis arises, both flaps are in danger of necrosis. Therefore, we advocate for the preparation of two sets of anastomotic arteries and veins in the recipient area to mitigate such circumstances. Literature suggests that the ligated internal jugular vein can be utilized for end-to-side anastomosis, offering a method for venous anastomosis (Akazawa et al., 2019). Furthermore, it has been reported that the transverse cervical vein and superficial temporal vein can also serve as recipient area vessels (Hansen et al., 2007; Tessler et al., 2017; Wang et al., 2021).

This method affords greater flexibility and autonomy, but it involves extended operation time, high costs, considerable trauma, and numerous potential complications. It mandates superior surgical skill, restricting its broader implementation. Inexperienced medical institutions and young physicians should first master single flap reconstruction before considering advanced techniques. Without this foundation, there's a risk of increased surgical complications and irreversible outcomes. Additionally, the inclusion of 3D printing escalates treatment costs, making this approach unfeasible for institutions lacking this technology. In our study, though every flap transplantation was triumphant, five cases did confront complications. Two cases suffered from local oral infections and gradually recovered after conservative treatments. Two patients presented with intermuscular vein thrombosis in the lower limbs, which were successfully managed with oral medication, preventing the progression to potential organ embolisms such as cardiac, pulmonary, or cerebral embolism. Additionally, two cases demonstrated a pulmonary infection, which was effectively controlled with antibiotic therapy (Tharakan et al., 2023). reported postoperative complications in multi-flap surgeries to range from 26% to 50%, aligning with our findings. Earlier research indicated a 5-year survival rate for advanced head and neck cancers between 25% and 56% (Abdelmeguid et al., 2021; Mody et al., 2021). Our study, with 2 out of 8 patients succumbing to postoperative tumor recurrence, indicates a marginally superior survival rate, albeit potentially influenced by the relatively shorter follow-up duration. In summary, our study's outcomes resonate with existing literature, suggesting that this approach doesn't elevate complications or mortality rates.

It is crucial to acknowledge that patients who are candidates for this procedure are typically in the advanced stages of oral cancer. As

such, it is of utmost importance to strictly adhere to the surgical indications:

1) The presence of extensive composite tissue defects, including intraoral, mandibula, and extraoral tissue defects that are too extensive to be repaired with a single flap;
2) The patient must be in good physical health, without obvious surgical contraindications such as congestive heart failure, pulmonary dysfunction, or neck vessel thrombosis;
3) The tumor can be completely resectable without systemic metastasis of lung and bone tissues;
4) The patient must possess a strong desire to combat the disease, as a positive attitude towards treatment is crucial.

However, this study does have limitations. Denture restoration is crucial for patients' masticatory function (Sozzi et al., 2017). Found that implant survival was high and implant-supported prostheses were a reliable rehabilitation option in patients whose jaws have been reconstruction with fibula-free flap. In our surgical method, fibula was used to prepare for implant repair in the future. However, due to postoperative adjuvant radiotherapy, patients paid more attention to tumor treatment and neglected denture repair. Both function and aesthetics are critically important, yet there is a potential gap in patients' understanding of these aspects. Consequently, it's our responsibility to educate them, promoting the benefits of implant restorations to restore masticatory function. Because of the rarity of such patients, we were unable to conduct controlled studies to objectively evaluate the advantages and disadvantages of this method compared to other treatment modalities. Nonetheless, we are confident that as the number of cases increases, the effectiveness of this treatment strategy will be confirmed. Moreover, the success of the double-flap surgery heavily relies on a precise preoperative surgical design and thorough considerations. The surgical approach offers limited flexibility, and the surgical procedure cannot be changed arbitrarily during the operation, as any deviations may result in a mismatch with the original design. Should unforeseen circumstances arise intraoperatively, we are prepared to implement alternative surgical strategies. Developing methodologies to anticipate, mitigate, and adeptly respond to such occurrences will constitute a primary objective in our ongoing research endeavors.

5 Conclusion

In conclusion, VSP/3D printing assisted FOSCFs combined with ALTs offers a safe and effective avenue for reconstructing oromandibular massive composite tissue defects in the study. However, the broader benefits and efficacy of this technique necessitate further validation through an expanded patient cohort.

Data availability statement

The original contributions presented in the study are included in the article/supplementary material, further inquiries can be directed to the corresponding author.

Ethics statement

The studies involving humans were approved by the ethical committee of the Affiliated Hospital of Qingdao University. The studies were conducted in accordance with the local legislation and institutional requirements. The participants provided their written informed consent to participate in this study. Written informed consent was obtained from the individual(s) for the publication of any potentially identifiable images or data included in this article.

Author contributions

YX: Investigation, Writing–original draft. YL: Investigation, Visualization, Writing–original draft. WX: Visualization, Writing–original draft. JY: Data curation, Writing–review and editing. LX: Validation, Writing–review and editing. LL: Data curation, Writing–review and editing. ZX: Formal Analysis, Writing–review and editing. JS: Funding acquisition, Resources, Writing–review and editing.

Funding

The author(s) declare financial support was received for the research, authorship, and/or publication of this article. This research was funded by the Qingdao Medical and Health Research Program (grant number: 2021-WJZD193), the Qingdao University Affiliated Hospital Clinical Medicine + X Scientific Research Project (grant number: QDFY+X202101041), the Shandong Province Medical and Health Technology Development Plan Project (grant number: 202208020979), Qingdao Key Health Discipline Development Fund and Oral Medicine Climbing Discipline Project in Qingdao.

Acknowledgments

This study was approved by the ethical committee of the affiliated hospital of qingdao university (NO. QYFYWZLL 27958).

Conflict of interest

The authors declare that the research was conducted in the absence of any commercial or financial relationships that could be construed as a potential conflict of interest.

Publisher's note

References

Abdelmeguid, A. S., Silver, N. L., Boonsripitayanon, M., Glisson, B. S., Ferrarotto, R., Gunn, G. B., et al. (2021). Role of induction chemotherapy for oral cavity squamous cell carcinoma. *Cancer* 127, 3107–3112. doi:10.1002/cncr.33616

Akazawa, T., Sekido, M., Adachi, K., Sasaki, K., Aihara, Y., Shibuya, Y., et al. (2019). End-to-Side venous anastomosis to a ligated vein stump for free flap transfer in head and neck reconstruction. *Ann. Plast. Surg.* 83, 180–182. doi:10.1097/sap.0000000000001905

Al-Sabahi, M. E., Jamali, O. M., Shindy, M. I., Moussa, B. G., Amin, A. A., and Zedan, M. H. (2022). Aesthetic reconstruction of onco-surgical mandibular defects using free fibular flap with and without CAD/CAM customized osteotomy guide: a randomized controlled clinical trial. *BMC Cancer* 22, 1252. doi:10.1186/s12885-022-10322-y

Boca, R., Kuo, Y. R., Hsieh, C. H., Huang, E. Y., and Jeng, S. F. (2010). A reliable parameter for primary closure of the free anterolateral thigh flap donor site. *Plast. Reconstr. Surg.* 126, 1558–1562. doi:10.1097/prs.0b013e3181ef8cb7

Chen, H. C., and Tang, Y. B. (2003). Anterolateral thigh flap: an ideal soft tissue flap. *Clin. Plast. Surg.* 30, 383–401. doi:10.1016/s0094-1298(03)00040-3

Dowthwaite, S. A., Theurer, J., Belzile, M., Fung, K., Franklin, J., Nichols, A., et al. (2013). Comparison of fibular and scapular osseous free flaps for oromandibular reconstruction: a patient-centered approach to flap selection. *JAMA Otolaryngol. Head. Neck Surg.* 139, 285–292. doi:10.1001/jamaoto.2013.1802

Hansen, S. L., Foster, R. D., Dosanjh, A. S., Mathes, S. J., Hoffman, W. Y., and Leon, P. (2007). Superficial temporal artery and vein as recipient vessels for facial and scalp microsurgical reconstruction. *Plast. Reconstr. Surg.* 120, 1879–1884. doi:10.1097/01.prs.0000287273.48145.bd

He, J., Qing, L., Wu, P., Zhou, Z., Yu, F., and Tang, J. (2021). Large wounds reconstruction of the lower extremity with combined latissimus dorsi musculocutaneous flap and flow-through anterolateral thigh perforator flap transfer. *Microsurgery* 41, 533–542. doi:10.1002/micr.30754

Hsieh, F., Leow, O. Q. Y., Cheong, C. F., Hung, S. Y., and Tsao, C. K. (2021). Musculoseptocutaneous perforator of anterolateral thigh flap: a clinical study. *Plast. Reconstr. Surg.* 147, 103e–110e. doi:10.1097/prs.0000000000007471

Hsieh, T. Y., and Bewley, A. (2019). Use of multiple free flaps in head and neck reconstruction. *Curr. Opin. Otolaryngol. Head. Neck Surg.* 27, 392–400. doi:10.1097/moo.0000000000000574

Idris, S., Logan, H., Tabet, P., Osswald, M., Nayar, S., and Seikaly, H. (2022). The accuracy of 3D surgical design and simulation in prefabricated fibula free flaps for jaw reconstruction. *J. Pers. Med.* 12, 1766. doi:10.3390/jpm12111766

Lee, J. T., Hsu, H., Wang, C. H., Cheng, L. F., Sun, T. B., Huang, C. C., et al. (2010). Reconstruction of extensive composite oromandibular defects with simultaneous free anterolateral thigh fasciocutaneous and fibular osteocutaneous flaps. *J. Reconstr. Microsurg* 26, 145–151. doi:10.1055/s-0029-1242134

Liu, A. Q., Deane, E. C., Heffernan, A., Ji, Y., Durham, J. S., and Prisman, E. (2022). Patient-reported outcomes and morbidity after head and neck reconstructions: an evaluation of fibular and scapular free flaps. *Oral Oncol.* 132, 106019. doi:10.1016/j.oraloncology.2022.106019

Mody, M. D., Rocco, J. W., Yom, S. S., Haddad, R. I., and Saba, N. F. (2021). Head and neck cancer. *Lancet* 398, 2289–2299. doi:10.1016/s0140-6736(21)01550-6

Moratin, J., Horn, D., Heinemann, M., Metzger, K., Mrosek, J., Ristow, O., et al. (2021). Multiple sequential free flap reconstructions of the head and neck: a single-center experience. *Plast. Reconstr. Surg.* 148, 791e–799e. doi:10.1097/prs.0000000000008432

Qing, L., Wu, P., Liang, J., Yu, F., Wang, C., and Tang, J. (2015). Use of flow-through anterolateral thigh perforator flaps in reconstruction of complex extremity defects. *J. Reconstr. Microsurg* 31, 571–578. doi:10.1055/s-0035-1555138

Raghuram, A. C., Manfro, G., Teixeira, G. V., Cernea, C. R., Dias, F. L., Marco, M., et al. (2021). Use of single chimeric free flaps or double free flaps for complex head and neck reconstruction. *J. Reconstr. Microsurg* 37, 791–798. doi:10.1055/s-0041-1727188

Ranganath, K., Jalisi, S. M., Naples, J. G., and Gomez, E. D. (2022). Comparing outcomes of radial forearm free flaps and anterolateral thigh free flaps in oral cavity reconstruction: a systematic review and meta-analysis. *Oral Oncol.* 135, 106214. doi:10.1016/j.oraloncology.2022.106214

Ritschl, L. M., Mucke, T., Hart, D., Unterhuber, T., Kehl, V., Wolff, K. D., et al. (2021). Retrospective analysis of complications in 190 mandibular resections and simultaneous reconstructions with free fibula flap, iliac crest flap or reconstruction plate: a comparative single centre study. *Clin. Oral Investig.* 25, 2905–2914. doi:10.1007/s00784-020-03607-8

Santilli, M., D'Addazio, G., Rexhepi, I., Sinjari, B., and Filippini, A. (2021). Multiple free flap reconstruction of a complex intraoral defect after squamous cell carcinoma excision: a case report. *Med. Kaunas.* 58, 54. doi:10.3390/medicina58010054

Schepers, R. H., Raghoebar, G. M., Vissink, A., Stenekes, M. W., Kraeima, J., Roodenburg, J. L., et al. (2015). Accuracy of fibula reconstruction using patient-specific CAD/CAM reconstruction plates and dental implants: a new modality for functional reconstruction of mandibular defects. *J. Craniomaxillofac Surg.* 43, 649–657. doi:10.1016/j.jcms.2015.03.015

Seruya, M., Fisher, M., and Rodriguez, E. D. (2013). Computer-assisted versus conventional free fibula flap technique for craniofacial reconstruction: an outcomes comparison. *Plast. Reconstr. Surg.* 132, 1219–1228. doi:10.1097/prs.0b013e3182a3c0b1

Shaw, R. J., Kanatas, A. N., Lowe, D., Brown, J. S., Rogers, S. N., and Vaughan, E. D. (2004). Comparison of miniplates and reconstruction plates in mandibular reconstruction. *Head. Neck* 26, 456–463. doi:10.1002/hed.10343

Silva, A. K., Humphries, L. S., Maldonado, A. A., and Gottlieb, L. J. (2019). Chimeric vs composite flaps for mandible reconstruction. *Head. Neck* 41, 1597–1604. doi:10.1002/hed.25606

Sozzi, D., Novelli, G., Silva, R., Connelly, S. T., and Tartaglia, G. M. (2017). Implant rehabilitation in fibula-free flap reconstruction: a retrospective study of cases at 1-18 years following surgery. *J. Craniomaxillofac Surg.* 45, 1655–1661. doi:10.1016/j.jcms.2017.06.021

Taylor, G. I., Corlett, R. J., and Ashton, M. W. (2016). The evolution of free vascularized bone transfer: a 40-year experience. *Plast. Reconstr. Surg.* 137, 1292–1305. doi:10.1097/prs.0000000000002040

Tessler, O., Gilardino, M. S., Bartow, M. J., St Hilaire, H., Womac, D., Dionisopoulos, T., et al. (2017). Transverse cervical artery: consistent anatomical landmarks and clinical experience with its use as a recipient artery in complex head and neck reconstruction. *Plast. Reconstr. Surg.* 139, 745e–751e. doi:10.1097/prs.0000000000003085

Tharakan, T., Marfowaa, G., Akakpo, K., Jackson, R., Zenga, J., Puram, S. V., et al. (2023). Multiple simultaneous free flaps for head and neck reconstruction: a multi-institutional cohort. *Oral Oncol.* 136, 106269. doi:10.1016/j.oraloncology.2022.106269

Thomas, W. W., Calcagno, H. E., Azzi, J., Petrisor, D., Cave, T., Barber, B., et al. (2020). Incidence of inadequate perforators and salvage options for the anterior lateral thigh free flap. *Laryngoscope* 130, 343–346. doi:10.1002/lary.28176

Townley, W. A., Royston, E. C., Karmiris, N., Crick, A., and Dunn, R. L. (2011). Critical assessment of the anterolateral thigh flap donor site. *J. Plast. Reconstr. Aesthet. Surg.* 64, 1621–1626. doi:10.1016/j.bjps.2011.07.015

Wang, L., Ma, C. Y., Shen, Y., Fang, J., Haugen, T. W., Guo, B., et al. (2021). Transverse cervical artery anterior perforator flap for head and neck oncological reconstruction: preliminary study. *Head. Neck* 43, 3598–3607. doi:10.1002/hed.26873

Weitz, J., Kreutzer, K., Bauer, F. J., Wolff, K. D., Nobis, C. P., and Kesting, M. R. (2015). Sandwich flaps as a feasible solution for the management of huge mandibular composite tissue defects. *J. Craniomaxillofac Surg.* 43, 1769–1775. doi:10.1016/j.jcms.2015.07.038

Wu, P., Hu, L., Li, H., Feng, L., Liu, Y., Zhang, S., et al. (2021). Clinical application and accuracy analysis of 3D printing guide plate based on polylactic acid in mandible reconstruction with fibula flap. *Ann. Transl. Med.* 9, 460. doi:10.21037/atm-20-6781

frontiers | Frontiers in Bioengineering and Biotechnology

TYPE Original Research
PUBLISHED 20 December 2023
DOI 10.3389/fbioe.2023.1321495

OPEN ACCESS

EDITED BY
Yuan Yin,
Fourth Military Medical University, China

REVIEWED BY
Samuel Ebhodaghe,
University of Benin, Nigeria
Zheng Duanmu,
Beijing Information Science and Technology University, China

*CORRESPONDENCE
Marta Macarena Paz-Cortés,
mpazcor@uax.es
Javier Gil,
xavier.gil@uic.es

RECEIVED 14 October 2023
ACCEPTED 11 December 2023
PUBLISHED 20 December 2023

CITATION
Cintora-López P, Arrieta-Blanco P, Martin-Vacas A, Paz-Cortés MM, Gil J and Aragoneses JM (2023), *In vitro* analysis of the influence of the thermocycling and the applied force on orthodontic clear aligners.
Front. Bioeng. Biotechnol. 11:1321495.
doi: 10.3389/fbioe.2023.1321495

In vitro analysis of the influence of the thermocycling and the applied force on orthodontic clear aligners

Patricia Cintora-López[1], Patricia Arrieta-Blanco[1], Andrea Martin-Vacas[1], Marta Macarena Paz-Cortés[1]*, Javier Gil[2]* and Juan Manuel Aragoneses[1]

[1]Faculty of Dentistry, Alfonso X El Sabio University, Villanueva de la Cañada, Spain, [2]Faculty of Medicine and Health Sciences, Bioengineering Institute of Technology, International University of Catalunya, Barcelona, Spain

The mechanical properties of polyurethane dental aligners have been studied in an oral environment at 37°C and subjected to thermal cycling between 5°C and 55°C for long periods of time at different mechanical stresses. The aim is to determine the efficacy of the orthodontic aligner at different stress levels, the effect of thermal cycling with therapy time on tooth position correction. Sixty aligners with the same design were studied applying tensions of 0, 3 and 30 N and determining the deformation at different times from 1 to 760 h. Half of these aligners were subjected to stresses submerged in artificial saliva at 37°C and the other half were subjected to thermal cycles between 2°C and 55°C in salivary medium. Deformation was determined using a high-resolution stereo magnifier and ImageJ image analysis software. Water adsorption by the polyurethane was determined at the different test times. The results showed that in the unloaded aligners there is no appreciable deformation, but with thermal cycling there is a light shrinkage of the aligner due to the semi-crystallization process (ordering of polymeric chains) of the polyurethane. When applying loads of 3 and 30 N, creep curves with constant deformation transition zones can be seen. The transition zones decrease as the applied mechanical load increases. In addition, the significant effect of thermal cycling on the reduction of the transition zone of the aligners has been demonstrated. The transition zones are optimal for dental correction as constant stresses are exerted for tooth movement. The effect of thermal cycling shortens the constant deformation zone and reduces tooth alignment time. It was observed that the absorption of water in the aligner is constant after 1 h of immersion and does not exceed 0.4% by weight of absorbed water.

KEYWORDS

polymers, orthodontic appliances, removable, clear aligner appliances, mechanical properties, creep

1 Introduction

Orthodontic systems of clear aligners and retainers combined with digital planning systems turn out to be the present and future of orthodontics. Effective orthodontic therapy necessitates a thorough understanding of the materials for our patients, without adequate knowledge of the materials used in our patients, their properties, and biocompatibility.

Currently, the digital manufacturing method uses CAD-CAM (Computer Aided Design Computer Aided Manufacturing) technology and digital workflow protocol. The digital image is obtained either through an intraoral scanner or indirectly through buccal impressions in high-quality polyvinyl siloxane (PVS) material which are then digitally scanned to provide a digital model (.stl). Teeth movements will be planned with the digital dental model using digital CAD platforms and generating virtual sequential models with the teeth in the desired positions, planned for each stage. Printing 3D models of each virtual configuration through CAM technology involves incorporating subtractive (milling) or additive (3D printing) manufacturing techniques (Hartshorne and Wertheimer, 2022).

The performance of aligners depends on the composition of the material used for their manufacture, being directly dependent on the manufacturing process. The most widely used is the conventional vacuum thermoforming method that includes molding the thermoplastic material into physical models (Tartaglia et al., 2021). Thermoplastic Polyurethane (TPU), composed mainly of di- and tri-isocyanates and polyols, is another extremely versatile polymer with advantages such as excellent mechanical and elastomeric characteristics, chemical and abrasion resistance. TPU is the material that was one of the first to be used and has been evolving to this day. One of its advantages is that when subjected to a load, TPU changes shape but can recover, when the load is removed it elongates and recovers due to its flexibility. The material also features high tear and fracture strength (Bichu et al., 2022).

The changes suffered by orthodontic materials when they are introduced into an electrolytic medium such as the oral cavity, as well as the effect they suffer due to masticatory stress and other environmental changes, such as temperature, have been extensively studied by numerous authors in order to evaluate the effectiveness of the materials and the effect of the degradation of its components on the health of patients with orthodontic appliances. Most of these studies are carried out analyzing the effect on the components of fixed multibracketts appliances in different brands and materials (Pascual et al., 1999; Manero et al., 2003; Gil et al., 2004; Djeu et al., 2005; Keim et al., 2014; Abbate et al., 2015; Han, 2015; Li et al., 2015; Hennessy et al., 2016; Gu et al., 2017; Lanteri et al., 2018). With the increase in orthodontic treatment with aligners, it is necessary to enhance the studies in which the composition of its material is analyzed when it is introduced into the oral cavity and the degradation of its components based on various environmental stimuli to which they are subjected in the oral cavity (Eliades et al., 1999; Schuster et al., 2004; Eliades et al., 2007; Eliades et al., 2009; Gracco et al., 2009; Rossini et al., 2015; Halimi et al., 2016; Buxadera-Palomero et al., 2017; Eliades and Bisphenol, 2017; Yi et al., 2018; Francisco et al., 2022).

Invisaling® system clear aligners are thermoplastic polymers based on polyurethanes, aromatic multilayer thermoplastic polyurethane, methylphenyl diisocyanate and 1,6-hexanediol plus additives (Raghavan et al., 2017). They are characterized by having higher values of hardness and elastic modulus and index, but lower values of creep resistance compared to other materials also used as aligners. Thermoplastics have excellent aesthetics and adaptability to different shapes that are widely used for orthodontic treatment. Since Kesling in 1945 produced the first aligner made of elastic polymer (Shalish et al., 2012), there has been an important development in materials and especially in CAD-CAM manufacturing processes, thermofabrication, 3D printing, etc. that have been fundamental to improve orthodontic treatments (Kesling, 1945; Elkholy et al., 2015; Gomez et al., 2015). In 2013, Invisalign® began using SmartTrack as a material for its aligners, a multilayer polymer that provides light and constant force and superior control over tooth movement (Simon et al., 2014).

TABLE 1 Chemical composition of artificial saliva.

Chemical composition	g/dm^3
K_2HPO_4	0.20
KCI	1.20
KSCN	0.33
Na_2HPO_4	0.26
NaCl	0.70
$NaHCO_3$	1.50
Urea	1.50
Lactic acid	Until pH = 6.7

Although there are numerous studies on the biological behavior of clear aligners with different thermoplastic polymeric materials, there is no much evidence on their mechanical properties (Align Technology, 2023). Due to this lack of evidence, it is important to carry out research which analyze the behavior of clear aligners in the oral environment, and the influence of thermal cycles. The hypothesis of this research was that polyurethanes, being thermoplastic materials, would produce elongation in the aligner by exerting constant tension on its walls. Furthermore, the effect of temperature can influence the movement of polymeric chains, affecting the correction of dental position. The aim is to analyze in an artificial mouth the influence of the temperature and masticatory forces on the behavior of the clear aligner characteristics.

2 Materials and methods

The aim is to determine the creep of the aligner, i.e., the increase in deformation when applying a constant force for long periods of time. This mechanical behavior simulates the effect of stresses created on the aligner in the mouth over time and can be determined when the aligner is active. For this purpose, different forces will be applied by means of a spring calibrated with a constant force, determining the elongation increases at different times. The tests will be carried out at a constant temperature and thermocycled. In this way it will be possible to determine the effect of the variations of the temperatures on the mechanical creep behavior of the aligners (Morresi et al., 2014).

An *in vitro*, experimental transversal research was carried out. Due to the *in vitro* design of the study, the approval of the Ethics Committee was not necessary. According to the calculation of experiments, a total of 60 identical clear aligners were studied. These aligners were manufactured by Align Technologies, Inc. (Tempe, Arizona, USA) with polyurethane 1,6-hexanedial methylene diphenyl diisocyanate. The thickness of the clear aligners was 0.72 mm.

FIGURE 1
Thermocycling equipment. The thermocycles studied in artificial saliva were between 2°C and 55°C being at these temperatures for 30 s. At the different test times, the aligners were removed, and the elongation was measured.

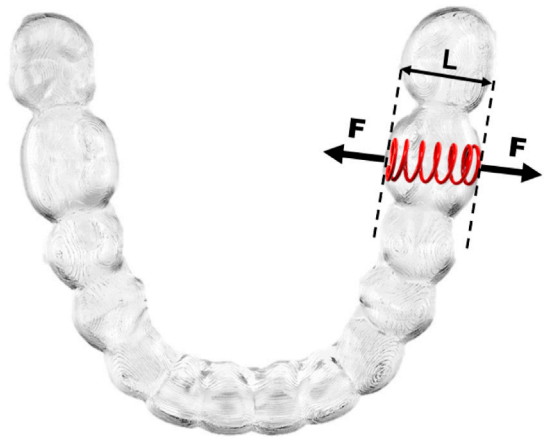

FIGURE 2
Diagram of the mechanical test performed on aligners (F: Forces; L: length).

Thirty samples were placed in an artificial saliva container at constant temperature of 37°C. The chemical composition of artificial saliva can be seen in Table 1 (Murakami et al., 1983). Thermal thermocycling was applied to 30 random samples for 600 cycles (1,200 immersions) considering in this case 20 temperature changes in the patient's mouth for 30 days. For the thermocycling study, equipment manufactured in the dental laboratory of the International University of Catalunya (UIC, Sant Cugat del Vallés, Spain) was used to control the thermal cycles by immersion in a thermostatic bath with a controlled temperature at 2°C for 30 s and another 30 s in a bath at 55°C (Figure 1).

Mechanical tests were carried out at 0 N, 3 N and 30 N applied to the first left molar (3.6). We studied 10 inserts for each were studied. The force is exerted with a calibrated spring that exerts tensile stress on the mold walls as can be seen in Figure 2. The springs are calibrated by a highly sensitive Adamel Lhomargy dynamometer (Adamel Lhomargy ST2507-E23, Saint Baldolph, France). These stresses simulate the stresses exerted by the tooth on the template. Elongations caused by applied force and/or thermal cycling were determined by observing the samples under a high-precision stereo magnification Q-star high-resolution system using ImageJ software for measurements (Bethesda Q-2022-ST18965, Maryland, USA). Two marks are made on the aligner with a diamond-tipped indenter at two points. The sample is positioned in such a way that there can be no movement and it is ensured that the electronic source is always at the same angle. ImageJ is used to determine the difference between points in the unloaded state, obtaining the distance between the points automatically, which corresponds to the initial distance.

ImageJ is the world's fastest pure Java image processing program. It can filter a 2048 × 2048 image in 0.1 s. That's 40 million pixels per second. 8-bit grayscale or indexed color, 16-bit unsigned integer, 32-bit floating-point and RGB color. Tools are provided for zooming (1:32 to 32:1) and scrolling images. All analysis and processing functions work at any magnification factor. Create rectangular, elliptical or irregular area selections. Create line and point selections. Edit selections and automatically create them using the wand tool. Draw, fill, clear, filter or measure selections. Save selections and transfer them to other images. Supports smoothing, sharpening, edge detection, median filtering and thresholding on both 8-bit grayscale and RGB color images. Interactively adjust brightness and contrast of 8, 16 and 32-bit images. Measure lengths in this case and standard deviation. Calibrate using density standards. Split a 32-bit color image into RGB or HSV components. Merge 8-bit components into a color image. Convert an RGB image to 8-bit indexed color. Apply pseudo-color palettes to grayscale images (Vallet-Regí et al., 2005).

The aligner is subjected to a constant force and the distance at different test times is determined. With the new distance the

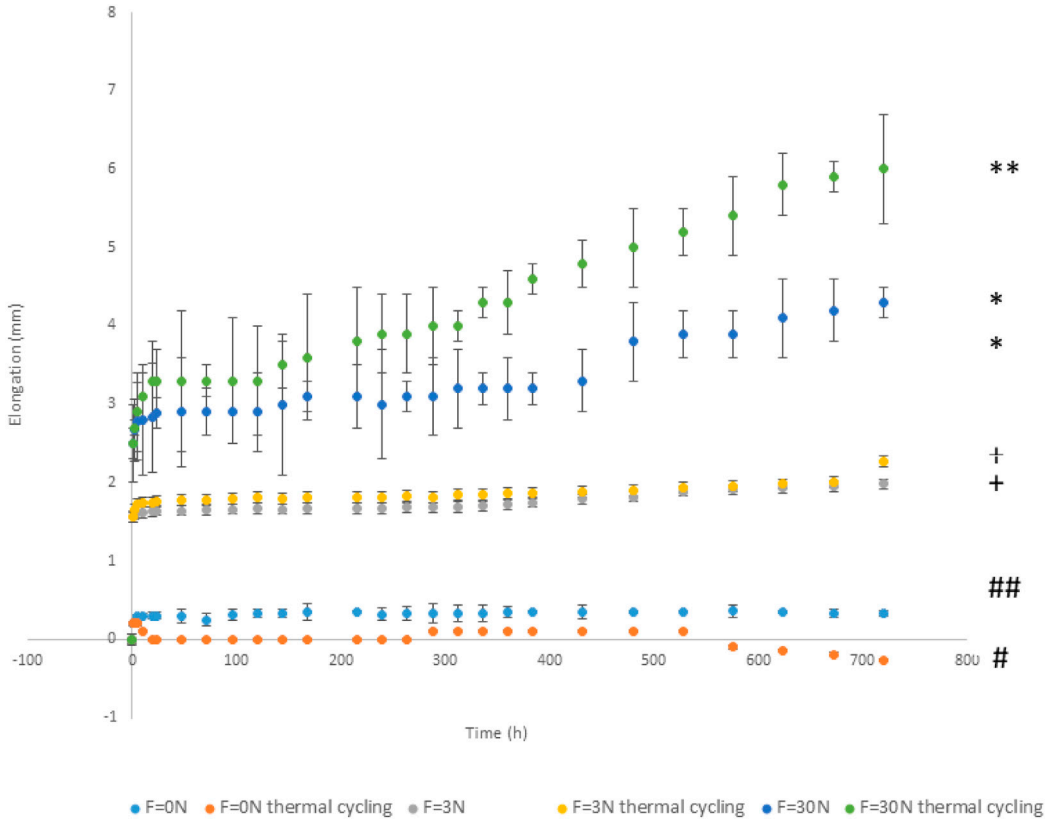

FIGURE 3
Elongation of clear aligner appliance without load and loaded at different forces without and with thermal cycling in relation to the time in hours. (Different signals indicate significance statistical differences with $p < 0.05$).

software calculates the elongation. The sensitivity of the distances calculated by the equipment and the software was 0.001 mm and has been used in different research studies that require high precision (Vallet-Regí et al., 2005; Godoy-Gallardo et al., 2016a; Herrero-Climent et al., 2023). Measurement times were: 0, 1, 2, 5, 10, 20, 24, 48, 72, 96, 120, 144, 168, 216, 240, 264, 268, 312, 336, 384, 432, 480, 528, 576, 624, 672, 720 h. The 720 h correspond to the hours of a month, the maximum application time. Elongation was calculated by determining the difference between initial separation between two points of the aligner and the distance between the same points after the experimental time has elapsed. The points are always the same and were identified by a small incision in the surrounding area (Herrero-Climent et al., 2023).

The water absorption of the clear aligners at different times without thermal cycling was studied using 20 mm × 20 mm samples. Samples were stored in a desiccator until constant weight (Initial weight = W1) was reached and then immersed in artificial saliva at 37°C for 1 min. After the different times they are dried with a cloth and weighed (Second weight = W2). They are weighed on a balance with a sensitivity of 0.00001 g (Sartorius x1000, Barcelona, Spain) and the water absorption (WA) is calculated according to the formula (Padrós et al., 2020):

$$WA = \frac{W_2 - W1}{W1} x100$$

Data were statistically analyzed using Student's t-tests with a 99.5% significance level ($p < 0.005$) and asympotics significance and Turkey multiple comparison tests to assess any statistically significant differences between sample groups. All statistical analyzes were performed using MinitabTM software (Minitab version 13.0, Minitab Inc., USA).

3 Results

Figure 3 shows the elongation values with the test time for the aligner appliance unloaded and loaded at 3 and 30N with and without thermal cycling.

The water absorption results of the artificial saliva give constant values from 5 h onwards, as can be seen in Figure 4.

4 Discussion

It can be observed that the samples that do not undergo loading and without thermal cycling, the elongations are practically negligible, and no changes in the shape of the template are

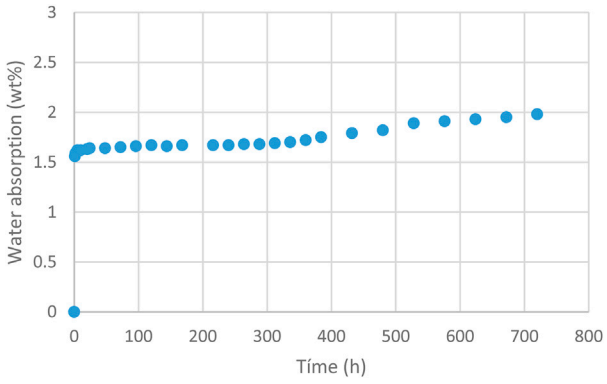

FIGURE 4
Water absorption up to 1 month.

observed. Samples without loading but which are thermally cycled show shrinkage of the template after 550 h of cycling. This shortening of the distances may be due to a partial chain folding process, called crystallisation, which decreases the distances.

The polyurethanes used are composed of two main polymeric segments: hard and soft chains. These two types of segments have different chain dynamics with repulsive interaction towards each other (Huang et al., 2012). The hard chains, with high extent of hydrogen bonding, have higher glass transition temperature (Tg) compared to soft chains and act as a physical cross-linker of soft segments. The repulsive interaction between hard and soft segments results in a decrease in crystallization of the soft segments (Lu et al., 2017). Salvekar et al. (Salvekar et al., 2017) determined for polyols composed of two different chains, their final physical and thermodynamic properties depend on the extent of phase separation, and their relative composition. To control the extent of phase separation for two different polyol chains, there are different procedures such as copolymerization with different structures, from random to block copolymers, and directed self-assembly of homopolymers with block copolymers of the same chemistry as homopolymers (Ge et al., 2012).

Some polyurethanes present shape memory property is due to the sensitivity of polyurethane to stimuli to retain an induced shape at a constant low temperature for a time: it also exhibits the ability to recover the original shape after removing the external stimulus force in the reheating process (Xie and Rousseau, 2009; Wu et al., 2017). These polymers are known for their ability to recover shape while maintaining constant stresses. In orthodontics, low and constant tensions in tempo are optimal to cause tooth movement; this same behavior is achieved with superelastic NiTi orthodontic wires (Gil and Planell, 1993; Gil et al., 2012; Gil et al., 2013; Bellini et al., 2016; Gil et al., 2018). The justification for the high shape resilience of polyetherimides is the presence of hard domains that act as physical cross-linkers to prevent chain slippage (Wu et al., 2017). The soft chains are responsible for fixing the temporary shape over a range of temperature (Tg) or crystallization temperature (Tc) (Ge et al., 2012; Wu et al., 2017). Thermal cycling below the Tg temperature will allow chain folding during heating, which reduces the dimensions of the aligner.

The materials with 3N mechanical loading show an initial deformation of the template due to the application of the load at time zero. Afterwards, a slight increase in elongation is observed with a very flat transition zone. This plateau is ideal for orthodontic treatment as the stress on the tooth does not cause an increase in elongation. At longer times, an increase in elongation is observed due to the creep of the polymeric material (Lombardo et al., 2012; Ihssen et al., 2019; Papadopoulou et al., 2019). This behavior is accentuated when thermal cycles are applied to the insole. At times longer than 600 h, a more intense increase in elongation is observed.

The insoles subjected to 30 N undergo a greater elongation than in the case of 3 N and a plateau suitable for orthodontic therapy can also be seen. After 500 h, a slight change in the slope of the deformation rate is observed. When subjected to this 30 N load and the material is thermally cycled, the plateau is reduced and from 450 h of treatment the elongation increases considerably. At high loads, as in this case, the thermal cycling has an intensifying effect on creep, which is why the treatment times under these conditions have to be shorter.

As can be seen, the aligners follow the typical creep graph, which has three stages (Espinar-Escalona et al., 2013; Iijima et al., 2015; Lombardo et al., 2015; Dalaie et al., 2021).

The first stage corresponds to a sudden increase in deformation when mechanical load is applied.

The second stage is the plateau zone which is the zone where the mechanical force exerted on the teeth is practically constant. It is called the transition phase and is the most suitable force for the correction of tooth positions. Constant, low intensity forces are the most suitable for tissue accommodation and the correct apposition and deposition of the bone that causes orthodontic movements.

The third stage is a stage of gross growth where the aligner may have lost thickness due to constant tension, which has produced a rearrangement of the polymeric chains causing a sudden increase in deformation. This stage is ineffective for any tooth movement and the aligner has ceased to perform its function.

This creep treatment occurs because polyurethane is a thermoplastic polymer, i.e., the temperature causes the polymer chains to align and can modify their shape and therefore the stresses exerted on the teeth or molars. These movements of polymer chains are produced by the effect of temperature. When the polyurethane is not mechanically loaded, the effect of temperature is the folding of chains in the so-called pseudocrystalline zones. This chain folding causes a decrease in volume, and it is for this reason that the aligner at 0N with thermal cycling up to 55°C shrinks (Lombardo et al., 2017; Dalaie et al., 2021).

The chain folding process does not occur when the polyurethane is subjected to mechanical stress as it prevents folding due to the directionality of the force exerted. For samples subjected to mechanical stress, thermal cycling facilitates the movement of the polymer chains in the direction of the stress, causing a faster creep of the aligner and reducing the plateau of the aligners, thus impairing tooth movement (Hodge et al., 1996; Godoy-Gallardo et al., 2016b; Jaggy et al., 2020).

For a given load and level of deformation, a material can be considered as symmetrical if the creep strain does not vary over time while an asymmetrical material presents a change in creep strain

rate. Previous studies reported the asymmetrical behavior of polyurethane (Kasgoz, 2021), which is related, to the general chemical nature of the polymer, for example, including interactions among the polymer chains over time, chemical bonds and others. At 25°C, this grade of polyurethane displayed an asymmetric nature at only 30 N of load, which is an extreme condition, not commonly achieved when in service. In this case, an increase in the elongation rate can be observed during the test run.

The tests were performed at thermal cycles to simulate an accelerated aged condition for this grade of polyurethane and were stipulated according to previous studies, where better ageing responses were obtained at this level of temperature (55°C) (Jia et al., 2011). As seen on Figure 3, under 30 N and thermal cycling accelerated ageing conditions all specimens tend to present an increase of elongation. Creep strain rate results in both tested temperatures did not show a creep fracture point, which demonstrate that in the aforementioned conditions, the material used did not fail even after the lengthy duration of the test. However, the aligner losses the activation to move the teeth.

The modeling of the creep behavior of polyurethanes must take into consideration two contributions: the viscoelastic behavior and the long-term behavior, i.e., the influence of time. The modeling of viscoelasticity integrates the structure-properties interactions, the share of elastic and viscous deformation in the total deformation and the relaxation coefficient. Many viscoelastic models have been developed and used by various authors in order to define the relationship between viscoelastic structure and polyurethane characteristics (Wu et al., 1994; Findley and Davis, 2013).

The best fitting model is the four-element Burger model (Wu et al., 1994; Jhao et al., 2022; Cui and Clyne, 2023), which is a simple combination of the Maxwell and Kelvin-Voigt models.

Under the condition of linear deformation, the total strain of a viscoelastic solid may be given as the sum of immediate elastic deformation of Maxwell spring (ε_{M1}), delayed elastic deformation of Maxwell dashpot (ε_{M2}) and viscous deformation of Kelvin unit (ε_K) (Eq. 1).

$$\varepsilon(t)=\varepsilon_{M1+}\varepsilon_{K+}\varepsilon_{M2} \tag{1}$$

Considering the combination of the Maxwell and Kelvin-Voight elements in the Burger model, the mathematical representation of the Burger model may be given as follows;

$$\varepsilon\,(t)=\frac{\sigma}{E_M}+\frac{\sigma}{E_K}\left[1-exp\frac{-E_K t}{\eta_K}\right]\frac{\sigma t}{\eta_M} \tag{2}$$

where E_M and η_M are the modulus and viscosity of the Maxwell spring and dashpot, respectively; E_K and η_K are the modulus and viscosity of the Kelvin spring and dashpot, respectively, and σ is the applied stress value.

From the values in Figure 4, it can be confirmed that water absorption by the polyurethane is constant from the first hours of placement, reaching values that do not exceed 0.4% wt of the polyurethane composition. Therefore, the mechanical behavior studied is not affected by water absorption but depends fundamentally on the composition of the polymer, the stresses applied and the thermal cycling of the aligner (Mima et al., 1983; Skaik et al., 2019; Cui and Clyne, 2023).

Several studies have been carried out analyzing different materials of invisible aligners for orthodontics, observing creep phenomena for all of them. Cianci C. et al. (Cianci et al., 2020) studied the compression behavior under cyclic loading of Polyethylene terephthalate-glycol (PET-G) -one of the most famous and used thermoplastic- and used as invisible aligners. It was observed for the first day of testing of the aligners that stiffening effects occur while cyclic loading progresses. It was also observed that stiffening decreases during the non-loading time between two successive sessions of test while stiffening effects are observed again when a new set of cycles is applied to the aligners. One of the results obtained was that in the case of testing with saliva saliva an higher stress recovery is observed between two subsequent loading sessions; moreover, the hygrothermal environment showed a contribution to reduce the stress accumulation effect during the test. In our case we have observed that the influence of the thermal cycles accelerates the creep processes reducing the transition straight line which is the desired one to provoke the activation of tooth alignment.

Other investigations (Lombardo et al., 2017; Albertini et al., 2022) carried out for different aligner materials show behaviors like those observed in our results, although the tests have been carried out in short periods of time (24 h) in all the polymers released a significant amount of stress during the 24-h period. Stress release was greater during the first 8 h, reaching a plateau that generally remained constant. The single-layer materials, F22 Aligner polyurethane (Sweden & Martina, Due Carrare, Padova, Italy) and Duran polyethylene terephthalate glycol-modified (SCHEU, Iserlohn, Germany), exhibited the greatest values for both absolute stress and stress decay speed. The double-layer materials, Erkoloc-Pro (Erkodent, Pfalzgrafenweiler, Germany) and Durasoft (SCHEU), exhibited very constant stress release, but at absolute values up to four times lower than the single-layer samples tested. Albertini et al. (Albertini et al., 2022) conducted studies at longer periods of time at constant temperature determining that all the materials that we tested showed a rapidity of stress decay during the first few hours of application, before reaching a plateau phase. The polyurethane showed the greatest level of final stress, with relatively constant stress release during the entire 15-day period. Further research after *in vivo* aging is necessary in order to study the real aligners' behavior during orthodontic treatment. These results show similar behaviors to those obtained without thermal cycling and as they suggest could be influenced by thermal cycling in salivary medium as in this work, we have been able to complete the research of Albertini et a (Albertini et al., 2022).

It has been possible to observe the consequences of the structural changes of semi-crystallization with the volume contractions of the aligners when the material is not subjected to mechanical loading. These results could be compared with the work of Condo et al. (CondoPazzini et al., 2018). These authors characterized the samples by means of Fourier transform infrared spectroscopy, micro-Raman spectroscopy, X-ray diffraction, tensile and indentation strength test. The results showed an increase of crystalline fraction producing an increase of hardness and hyper-plasticity.

This research work has several limitations as we have tried to simulate the oral environment in which the aligners work. However, chewing stress levels have not been considered, as well as the bacterial environment to which the aligner may be subjected. One of the limitations of this study is the determination of dental forces and occlusal forces. A good model is the study by Duanmu Zheng et al. (Duanmu et al., 2021) where they developed a biomechanical model for the analysis of occlusal stresses. Future work could use this model to develop the behavior of aligners under the conditions described in this contribution. In any case, the mechanical behavior of the aligners has

been verified and the hypothesis put forward in the study has been confirmed.

5 Conclusion

Polyurethane dental aligners have characteristic creep curves with transition zones for loads of 3 and 30 N. These plateaus, which are optimal for dental alignment, are reduced by the effect of the load and thermal cycling. It was found that the water absorption in the inserts is constant after 1 h and reaches values of 0.4% by weight of the polyurethane. It has also been confirmed that thermal cycling in the insoles without mechanical stress is susceptible to shrinkage due to semi-crystallisation processes of the polymeric material.

Data availability statement

The raw data supporting the conclusion of this article will be made available by the authors, without undue reservation.

Author contributions

PC-L: Investigation, Project administration, Writing–original draft. PA-B: Methodology, Project administration, Visualization, Writing–original draft. AM-V: Conceptualization, Investigation, Writing–review and editing. MP-C: Investigation, Methodology, Writing–review and editing. JG: Conceptualization, Investigation, Writing–original draft. JA: Data curation, Funding acquisition, Software, Writing–review and editing.

Funding

The author(s) declare financial support was received for the research, authorship, and/or publication of this article. The work was supported by the Spanish Government and the Ministry of Science and Innovation of Spain by research projects CONCEPTO PDC 2022-133628-C22 (co-funded by the European Regional Development Fund (ERDF), a way to build Europe).

Acknowledgments

The authors are grateful to the Universidad Alfonso X el sabio y el Banco de Santander for the administrative and technical support.

Conflict of interest

The authors declare that the research was conducted in the absence of any commercial or financial relationships that could be construed as a potential conflict of interest.

Publisher's note

All claims expressed in this article are solely those of the authors and do not necessarily represent those of their affiliated organizations, or those of the publisher, the editors and the reviewers. Any product that may be evaluated in this article, or claim that may be made by its manufacturer, is not guaranteed or endorsed by the publisher.

References

Abbate, G. M., Caria, M. P., Montanari, P., Mannu, C., Orrù, G., Caprioglio, A., et al. (2015). Periodontal health in teenagers treated with removable aligners and fixed orthodontic appliances. *J. Orofac. Orthop.* 76 (3), 240–250. doi:10.1007/s00056-015-0285-5

Albertini, P., Mazzanti, V., Mollica, F., Pellitteri, F., Palone, M., and Lombardo, L. (2022). Stress relaxation properties of five orthodontic aligner materials: a 14-day *in-vitro* study. *Bioengineering* 9, 349. doi:10.3390/bioengineering9080349

Align Technology (2023). Inc. INVISALIGNt presenta smart-track. Available in: http://invisalign.com.au/doctor/doc/folletos/SmartTrack_brochure.pdf August 8, 2023.

Bellini, H., Moyano, J., Gil, J., and Puigdollers, A. (2016). Comparison of the superelasticity of different nickel–titanium orthodontic archwires and the loss of their properties by heat treatment. *J.Mater.Sci. Mater. Med.* 27, 158. doi:10.1007/s10856-016-5767-5

Bichu, Y. M., Alwafi, A., Liu, X., Andrews, J., Ludwig, B., Bichu, A. Y., et al. (2022). Advances in orthodontic clear aligner materials. *Bioact. Mater* 20 (22), 384–403. doi:10.1016/j.bioactmat.2022.10.006

Buxadera-Palomero, J., Calvo, C., Torrent-Camarero, S., Gil, F. J., Mas-Moruno, C., Canal, C., et al. (2017). Biofunctional polyethylene glycol coatings on titanium: an *in vitro*-based comparison of functionalization methods. *Colloids Surfaces B Biointerfaces* 152, 367–375. doi:10.1016/j.colsurfb.2017.01.042

Cianci, C., Pappalettera, G., Renna, G., Casavola, C., Laurenziello, M., Battista, G., et al. (2020). Mechanical behavior of PET-G tooth aligners under cyclic loading. *Front. Mater.* 7. doi:10.3389/fmats.2020.00104

CondoPazzini, R. L., Cerroni, L., Pasquantonio, G., Lagana, G., Pecora, A., Mussi, V., et al. (2018). Mechanical properties of "two generations" of teeth aligners: change analysis during oral permanence. *Dent. Mater.* 37 (5), 835–842. doi:10.4012/dmj.2017-323

Cui, Y., and Clyne, T. W. (2023). Creep of particle and short fibre reinforced polyurethane rubber. *Mech. Time-Depend Mater* 27, 45–58. doi:10.1007/s11043-021-09524-x

Dalaie, K., Fatemi, S. M., and Ghaffari, S. (2021). Dynamic mechanical and thermal properties of clear aligners after thermoforming and aging. *Prog. Orthod.* 28 (1), 15. doi:10.1186/s40510-021-00362-8

Djeu, G., Shelton, C., and Maganzini, A. (2005). Outcome assessment of Invisalign and traditional orthodontic treatment compared with the American Board of Orthodontics objective grading system. *Am. J. Orthod. Dentofac. Orthop.* 128 (3), 292–298. doi:10.1016/j.ajodo.2005.06.002

Duanmu, Z., Liu, L., Deng, Q., Ren, Y., and Wang, M. (2021). Development of a biomechanical model for dynamic occlusal stress analysis. *Int. J. Oral Sci.* 13, 29. doi:10.1038/s41368-021-00133-5

Eliades, T., and Bisphenol, A. (2017). Bisphenol A and orthodontics: an update of evidence-based measures to minimize exposure for the orthodontic team and patients. *Am. J. Orthod. Dentofac. Orthop.* 152 (4), 435–441. doi:10.1016/j.ajodo.2017.08.004

Eliades, T., Eliades, G., and Watts, D. C. (1999). Structural conformation of *in vitro* and *in vivo* aged orthodontic elastomeric modules. *Eur. J. Orthod.* 21 (6), 649–658. doi:10.1093/ejo/21.6.649

Eliades, T., Gioni, V., Kletsas, D., Athanasiou, A., and Eliades, G. (2007). Oestrogenicity of orthodontic adhesive resins. *Eur. J. Orthod.* 29 (4), 404–407. doi:10.1093/ejo/cjm040

Eliades, T., Pratsinis, H., Athanasiou, A. E., Eliades, G., and Kletsas, D. (2009). Cytotoxicity and estrogenicity of Invisalign appliances. *Am. J. Orthod. Dentofac. Orthop.* 136 (1), 100–103. doi:10.1016/j.ajodo.2009.03.006

Elkholy, F., Panchaphongsaphak, T., Kilic, F., Schmidt, F., and Lapatki, B. G. (2015). Forces and moments delivered by PET-G aligners to an upper central incisor for labial and palatal translation. *J. Orofac. Orthop.* 76 (6), 460–475. doi:10.1007/s00056-015-0307-3

Espinar-Escalona, E., Llamas-Carreras, J. M., Barrera-Mora, J. M., Abalos-Lasbrucci, C., and Gil-Mur, F. J. (2013). Effect of temperature on the orthodontic clinical applications of NiTi closed-coil springs. *Med. Oral Patol. Oral Cir. Bucal* 18 (4), e721–e724. doi:10.4317/medoral.19073

Findley, W. N., and Davis, F. A. (2013). *Creep and relaxation of nonlinear viscoelastic materials*. North Holand. London: Courier Corporation.

Francisco, I., Paula, A. B., Ribeiro, M., Marques, F., Travassos, R., Nunes, C., et al. (2022). The biological effects of 3D resins used in orthodontics: a systematic review. *Bioeng. (Basel)* 3 (1), 15. doi:10.3390/bioengineering9010015

Ge, Q., Yu, K., Ding, Y., and Qi, H. J. (2012). Prediction of temperature-dependent free recovery behaviors of amorphous shape memory polymers. *Soft Matter* 8 (43), 11098–11105. doi:10.1039/C2SM26249E

Gil, F. J., Cenizo, M., Espinar, E., Rodriguez, A., Rúperez, E., and Manero, J. M. (2013). NiTi superelastic orthodontic wires with variable stress obtained by ageing treatments. *Mater. Lett.* 104, 5–7. doi:10.1016/j.matlet2013.03.135

Gil, F. J., Espinar, E., Llamas, J. M., Manero, J. M., and Ginebra, M. P. (2012). Variation of the superelastic properties and nickel release from original and reused NiTi orthodontic archwires. *J. Mech. Beh. Biomed. Mater.* 6, 113–119. doi:10.1016/j.jmbbm.2011.11.005

Gil, F. J., and Planell, J. A. (1993). Aplicaciones biomédicas del titanio y aleaciones. *Biomecánica.* 1, 34–43.

Gil, F. J., Rupérez, E., Velasco, E., Aparicio, C., and Manero, J. M. (2018). Mechanism of fracture of NiTi superelastic endodontic rotary instruments. *J. Mater. Sci. Mater. Med.* 29 (131), 131. doi:10.1007/s10856-018-6140-7

Gil, F. J., Solano, E., Peña, J., Engel, E., Mendoza, A., and Planell, J. A. (2004). Microstructural, mechanical and citotoxicity evaluation of different NiTi and NiTiCu shape memory alloys. *J. Mater Sci. Mater Med.* 15, 1181–1185. doi:10.1007/s10856-004-5953-8

Godoy-Gallardo, M., Guillem-Marti, J., Sevilla, P., Manero, J. M., Gil, F. J., and Rodriguez, D. (2016b). Anhydride-functional silane immobilized onto titanium surfaces induces osteoblast cell differentiation and reduces bacterial adhesion and biofilm formation. *Mater Sci. Eng. C Mater Biol. Appl.* 59, 524–532. doi:10.1016/j.msec.2015.10.051

Godoy-Gallardo, M., Manzanares-Céspedes, M. C., Sevilla, P., Nart, J., Manzanares, N., Manero, J. M., et al. (2016a). Evaluation of bone loss in antibacterial coated dental implants: an experimental study in dogs. *Mater Sci. Eng. C Mater Biol. Appl.* 69, 538–545. doi:10.1016/j.msec.2016.07.020

Gomez, J. P., Peña, F. M., Martínez, V., Giraldo, D. C., and Cardona, C. I. (2015). Initial force systems during bodily tooth movement with plastic aligners and composite attachments: a three-dimensional finite element analysis. *Angle Orthod.* 85 (3), 454–460. doi:10.2319/050714-330.1

Gracco, A., Mazzoli, A., Favoni, O., Conti, C., Ferraris, P., Tosi, G., et al. (2009). Short-term chemical and physical changes in invisalign appliances. *Aust. Orthod. J.* 25 (1), 34–40.

Gu, J., Tang, J. S., Skulski, B., Fields, H. W., Beck, F. M., Firestone, A. R., et al. (2017). Evaluation of Invisalign treatment effectiveness and efficiency compared with conventional fixed appliances using the Peer Assessment Rating index. *Am. J. Orthod. Dentofac. Orthop.* 151 (2), 259–266. doi:10.1016/j.ajodo.2016.06.041

Halimi, A., Benyahia, H., Bahije, L., Adli, H., Azeroual, M. F., and Zaoui, F. (2016). A systematic study of the release of bisphenol A by orthodontic materials and its biological effects. *Int. Orthod.* 14 (4), 399–417. doi:10.1016/j.ortho.2016.10.005

Han, J. Y. (2015). A comparative study of combined periodontal and orthodontic treatment with fixed appliances and clear aligners in patients with periodontitis. *J. Periodontal Implant Sci.* 45 (6), 193–204. doi:10.5051/jpis.2015.45.6.193

Hartshorne, J., and Wertheimer, M. B. (2022). Emerging insights and new developments in clear aligner therapy: a review of the literature. *AJO-DO Clin. Companion.* 2 (4), 311–324. doi:10.1016/j.xaor.2022.04.009

Hennessy, J., Garvey, T., and Al-Awadhi, E. A. (2016). A randomized clinical trial comparing mandibular incisor proclination produced by fixed labial appliances and clear aligners. *Angle Orthod.* 86 (5), 706–712. doi:10.2319/101415-686.1

Herrero-Climent, M., Punset, M., Molmeneu, M., Brizuela, A., and Gil, J. (2023). Differences between the fittings of dental prostheses produced by CAD-CAM and laser sintering processes. *J. Funct. Biomater.* 14, 67. doi:10.3390/jfb14020067

Hodge, R. M., Edward, G. H., and Simon, G. P. (1996). Water absorption and states of water in semicrystalline poly(vinyl alcohol) films. *Polymer* 37 (8), 1371–1376. doi:10.1016/0032-3861(96)81134-7

Huang, W. M., Zhao, Y., Wang, C. C., Ding, Z., Purnawali, H., Tang, C., et al. (2012). Thermo/chemo-responsive shape memory effect in polymers: a sketch of working mechanisms, fundamentals and optimization. *J. Polym. Res.* 19 (9), 9952. doi:10.1007/s10965-012-9952-z

Ihssen, B. A., Willmann, J. H., Nimer, A., and Drescher, D. (2019). Effect of *in vitro* aging by water immersion and thermocycling on the mechanical properties of PETG aligner material. *J. Orofac. Orthop.* 80 (6), 292–303. doi:10.1007/s00056-019-00192-8

Iijima, M., Kohda, N., Kawaguchi, K., Muguruma, T., Ohta, M., Naganishi, A., et al. (2015). Effects of temperature changes and stress loading on the mechanical and shape memory properties of thermoplastic materials with different glass transition behaviours and crystal structures. *Eur. J. Orthod.* 37 (6), 665–670. doi:10.1093/ejo/cjv013

Jaggy, F., Zinelis, S., Polychronis, G., Patcas, R., Schätzle, M., Eliades, G., et al. (2020). ATR-FTIR analysis and one-week stress relaxation of four orthodontic aligner materials. *Mater. (Basel)* 13 (8), 1868. doi:10.3390/ma13081868

Jhao, Y.-S., Ouyang, H., Yang, F., and Lee, S. (2022). Thermo-mechanical and creep behaviour of polylactic acid/thermoplastic polyurethane blends. *Polymers* 14, 5276. doi:10.3390/polym14235276

Jia, Y., Peng, K., Gong, X., and Zhang, Z. (2011). Creep and recovery of polypropylene/carbon nanotube composites. *Int. J. Plasticity* 27, 1239–1251. doi:10.1016/j.ijplas.2011.02.004

Kasgoz, A. (2021). Mechanical, tensile creep and viscoelastic properties of thermoplastic polyurethane/polycarbonate blends. *Fibers Polym.* 22, 295–305. doi:10.1007/s12221-021-0113-z

Keim, R. G., Gottlieb, E. L., Vogels, D. S., and Vogels, P. B. (2014). 2014 JCO study of orthodontic diagnosis and treatment procedures, Part 1: results and trends. *J. Clin. Orthod.* 48 (10), 607–630.

Kesling, H. D. (1945). The philosophy of the tooth positioning appliance. *Am. J. Orthod. Oral Surg.* 31, 297–304. doi:10.1016/0096-6347(45)90101-3

Lanteri, V., Farronato, G., Lanteri, C., Caravita, R., and Cossellu, G. (2018). The efficacy of orthodontic treatments for anterior crowding with Invisalign compared with fixed appliances using the Peer Assessment Rating Index. *Quintessence Int.* 49 (7), 581–587. doi:10.3290/j.qi.a40511

Li, W., Wang, S., and Zhang, Y. (2015). The effectiveness of the Invisalign appliance in extraction cases using the the ABO model grading system: a multicenter randomized controlled trial. *Int. J. Clin. Exp. Med.* 15 (5), 8276–8282.

Lombardo, L., Arreghini, A., Maccarrone, R., Bianchi, A., Scalia, S., and Siciliani, G. (2015). Optical properties of orthodontic aligners--spectrophotometry analysis of three types before and after aging. *Prog. Orthod.* 16, 41. doi:10.1186/s40510-015-0111-z

Lombardo, L., Marafioti, M., Stefanoni, F., Mollica, F., and Siciliani, G. (2012). Load deflection characteristics and force level of nickel titanium initial archwires. *Angle Orthod.* 82 (3), 507–521. doi:10.2319/032511-213.1

Lombardo, L., Martines, E., Mazzanti, V., Arreghini, A., Mollica, F., and Siciliani, G. (2017). Stress relaxation properties of four orthodontic aligner materials: a 24-hour *in vitro* study. *Angle Orthod.* 87 (1), 11–18. doi:10.2319/113015-813.1

Lu, H., Wang, X., Yu, K., Huang, W. M., Yao, Y., and Leng, J. (2017). A phenomenological formulation for the shape/temperature memory effect in amorphous polymers with multi-stress components. *Smart Mater Struct.* 26 (9), 095011. doi:10.1088/1361-665x/aa77b3

Manero, J. M., Gil, F. J., Padrós, E., and Planell, J. A. (2003). Applications of environmental scanning electron microscopy (ESEM) in biomaterials field. *Microsc. Res. Tech.* 61, 469–480. doi:10.1002/jemt.10358

Mima, M., Iwamoto, R., and Yoshikawa, S. (1983). Highly deacetylated chitosan and its properties. *J. Appl. Polym. Sci.* 28 (6), 1909–1917. doi:10.1002/app.1983.070280607

Morresi, A. L., D'Amario, M., Capogreco, M., Gatto, R., Marzo, G., D'Arcangelo, C., et al. (2014). Thermal cycling for restorative materials: does a standardized protocol exist in laboratory testing? A literature review. *J. Mech. Behav. Biomed. Mater* 29, 295–308. doi:10.1016/j.jmbbm.2013.09.013

Murakami, H., Kawai, T., Hisada, K., Mori, S., and Hasegawa, J. (1983). Fluid behavior of saliva in dental materials science. *Aichi Gakuin Daigaku Shigakkai Shi* 21 (4), 702–707.

Padrós, R., Punset, M., Molmeneu, M., Velasco, A. B., Herrero-Climent, M., Rupérez, E., et al. (2020). Mechanical properties of CoCr dental-prosthesis restorations made by three manufacturing processes. Influence of the microstructure and topography. *Metals* 10, 788. doi:10.3390/met10060788

Papadopoulou, A. K., Cantele, A., Polychronis, G., Zinelis, S., and Eliades, T. (2019). Changes in roughness and mechanical properties of Invisalign® appliances after one- and two-weeks use. *Mater. (Basel)* 12 (15), 2406. doi:10.3390/ma12152406

Pascual, B., Gurruchaga, M., Ginebra, M. P., Gil, F. J., Planell, J. A., and Goñi, I. (1999). Influence of the modification of P/L ratio on a new formulation of acrylic bone cement. *Biomaterials* 20 (5), 465–474. doi:10.1016/S0142-9612(98)00192-6

Raghavan, A. S., Pottipalli Sathyanarayana, H., Kailasam, V., and Padmanabhan, S. (2017). Comparative evaluation of salivary bisphenol A levels in patients wearing vacuum-formed and Hawley retainers: an *in-vivo* study. *Am. J. Orthod. Dentofac. Orthop.* 151 (3), 471–476. doi:10.1016/j.ajodo.2016.07.022

Rossini, G., Parrini, S., Castroflorio, T., Deregibus, A., and Debernardi, C. L. (2015). Efficacy of clear aligners in controlling orthodontic tooth movement: a systematic review. *Angle Orthod.* 85 (5), 881–889. doi:10.2319/061614-436.1

Salvekar, A. V., Huang, W. M., Xiao, R., Wong, Y. S., Venkatraman, S. S., Tay, K. H., et al. (2017). Water-Responsive shape recovery induced buckling in biodegradable photo-cross-linked poly(ethylene glycol) (PEG) hydrogel. *Acc. Chem. Res.* 50 (2), 141–150. doi:10.1021/acs.accounts.6b00539

Schuster, S., Eliades, G., Zinelis, S., Eliades, T., and Bradley, T. G. (2004). Structural conformation and leaching from *in vitro* aged and retrieved Invisalign appliances. *Am. J. Orthod. Dentofac. Orthop.* 126 (6), 725–728. doi:10.1016/j.ajodo.2004.04.021

Shalish, M., Cooper-Kazaz, R., Ivgi, I., Canetti, L., Tsur, B., Bachar, E., et al. (2012). Adult patients' adjustability to orthodontic appliances. Part I: a comparison between Labial, Lingual, and Invisalign™. *Eur. J. Orthod.* 34(6): 724–730. doi:10.1093/ejo/cjr086

Simon, M., Keilig, L., Schwarze, J., Jung, B. A., and Bourauel, C. (2014). Treatment outcome and efficacy of an aligner technique--regarding incisor torque, premolar derotation and molar distalization. *BMC Oral Health* 11 (14), 68. doi:10.1186/1472-6831-14-68

Skaik, A., Li Wei, X., Abusamak, I., and Iddi, I. (2019). Effects of time and clear aligner removal frequency on the force delivered by different polyethylene terephthalate glycol-modified materials determined with thin-film pressure sensors. *Am. J. Orthod. Dent. Orthop.* 155 (1), 98–107. doi:10.1016/j.ajodo.2018.03.017

Tartaglia, G. M., Mapelli, A., Maspero, C., Santaniello, T., Serafin, M., Farronato, M., et al. (2021). Direct 3D printing of clear orthodontic aligners: current state and future possibilities. *Mater. (Basel)* 14 (7), 1799. doi:10.3390/ma14071799

Vallet-Regí, M., Román, J., Padilla, S., Doadrio, J. C., and Gil, F. J. (2005). "Bioactivity and mechanical properties of SiO2-CaO-P2O5 glass-ceramics". *J. Mater. Chem.* 15, 1353–1359. doi:10.1039/b415134h

Wu, X. L., Huang, W. M., Lu, H. B., Wang, C. C., and Cui, H. P. (2017). Characterization of polymeric shape memory materials. *J. Polym. Eng.* 37 (1), 1–20. doi:10.1515/polyeng-2015-0370

Wu, Y. K., Lodoen, G. A., Anderson, J. M., Baer, E., and Hiltner, A. (1994). Creep of a poly(etherurethane urea) in an oxidative environment. *J. Biomed. Mater Res.* 28 (4), 515–522. doi:10.1002/jbm.820280414

Xie, T., and Rousseau, I. A. (2009). Facile tailoring of thermal transition temperatures of epoxy shape memory polymers. *Polym. Guildf.* 50 (8), 1852–1856. doi:10.1016/j.polymer.2009.02.035

Yi, J., Xiao, J., Li, Y., Li, X., and Zhao, Z. (2018). External apical root resorption in non-extraction cases after clear aligner therapy or fixed orthodontic treatment. *J. Dent. Sci.* 13 (1), 48–53. doi:10.1016/j.jds.2017.09.007

frontiers | Frontiers in Bioengineering and Biotechnology

TYPE Review
PUBLISHED 29 January 2024
DOI 10.3389/fbioe.2024.1291880

OPEN ACCESS

EDITED BY
Xianqi Li,
Matsumoto Dental University, Japan

REVIEWED BY
Ning Cheng,
4D Molecular Therapeutics, United States
Zhen Geng,
Shanghai University, China

*CORRESPONDENCE
Shaoxia Pan,
panshaoxia@vip.163.com
Yi Zhang,
zhangyi612@hotmail.com
Xianghui Feng,
susanf0821@163.com

†These authors have contributed equally to this work and share first authorship

RECEIVED 10 September 2023
ACCEPTED 09 January 2024
PUBLISHED 29 January 2024

CITATION
Li Y, Li X, Guo D, Meng L, Feng X, Zhang Y and Pan S (2024), Immune dysregulation and macrophage polarization in peri-implantitis. *Front. Bioeng. Biotechnol.* 12:1291880. doi: 10.3389/fbioe.2024.1291880

Immune dysregulation and macrophage polarization in peri-implantitis

Yue Li[1†], Xue Li[2†], Danni Guo[1], Lingwei Meng[1], Xianghui Feng[3*], Yi Zhang[2*] and Shaoxia Pan[1*]

[1]Department of Prosthodontics, Peking University School and Hospital of Stomatology and National Center for Stomatology and National Clinical Research Center for Oral Diseases and National Engineering Research Center of Oral Biomaterials and Digital Medical Devices and Beijing Key Laboratory of Digital Stomatology and Research Center of Engineering and Technology for Computerized Dentistry Ministry of Health and NMPA Key Laboratory for Dental Materials, Beijing, China, [2]Stem Cell and Regenerative Medicine Lab, Beijing Institute of Radiation Medicine, Beijing, China, [3]Department of Periodontology, Peking University School and Hospital of Stomatology and National Center for Stomatology and National Clinical Research Center for Oral Diseases and National Engineering Research Center of Oral Biomaterials and Digital Medical Devices and Beijing Key Laboratory of Digital Stomatology and Research Center of Engineering and Technology for Computerized Dentistry Ministry of Health and NMPA Key Laboratory for Dental Materials, Beijing, China

The term "peri-implantitis" (peri-implantitis) refers to an inflammatory lesion of the mucosa surrounding an endosseous implant and a progressive loss of the peri-implant bone that supports the implant. Recently, it has been suggested that the increased sensitivity of implants to infection and the quick elimination of supporting tissue after infection may be caused by a dysregulated peri-implant mucosal immune response. Macrophages are polarized in response to environmental signals and play multiple roles in peri-implantitis. In peri-implantitis lesion samples, recent investigations have discovered a considerable increase in M1 type macrophages, with M1 type macrophages contributing to the pro-inflammatory response brought on by bacteria, whereas M2 type macrophages contribute to inflammation remission and tissue repair. In an effort to better understand the pathogenesis of peri-implantitis and suggest potential immunomodulatory treatments for peri-implantitis in the direction of macrophage polarization patterns, this review summarizes the research findings related to macrophage polarization in peri-implantitis and compares them with periodontitis.

KEYWORDS

peri-implantitis, macrophages, polarization, immune dysregulation, periodontitis

1 Introduction

Since Brånemark first made dental implants available in the 1960s, they have been the norm for those with edentulism and missing teeth (Brånemark et al., 1969; Brånemark et al., 1977; Albrektsson, Brånemark, Hansson and Lindström, 1981). However, peri-implantitis (PI) is an increasingly serious biological complication of oral implantology. Its prevalence increases with the duration of the implant (French, Ofec and Levin, 2021; Obreja et al., 2021). The term "peri-implantitis" (PI) refers to an inflammatory lesion of the mucosa surrounding an endosseous implant and a progressive loss of the peri-implant bone that supports the implant (Renvert, Persson, Pirih and Camargo, 2018). According to reports, it affects between 5% and 37% of implants and between 11% and 53% of patients (Fransson, Lekholm, Jemt and Berglundh, 2005; Roos-Jansåker, Lindahl, Renvert and Renvert, 2006; Renvert, Roos-Jansåker, Lindahl, Renvert

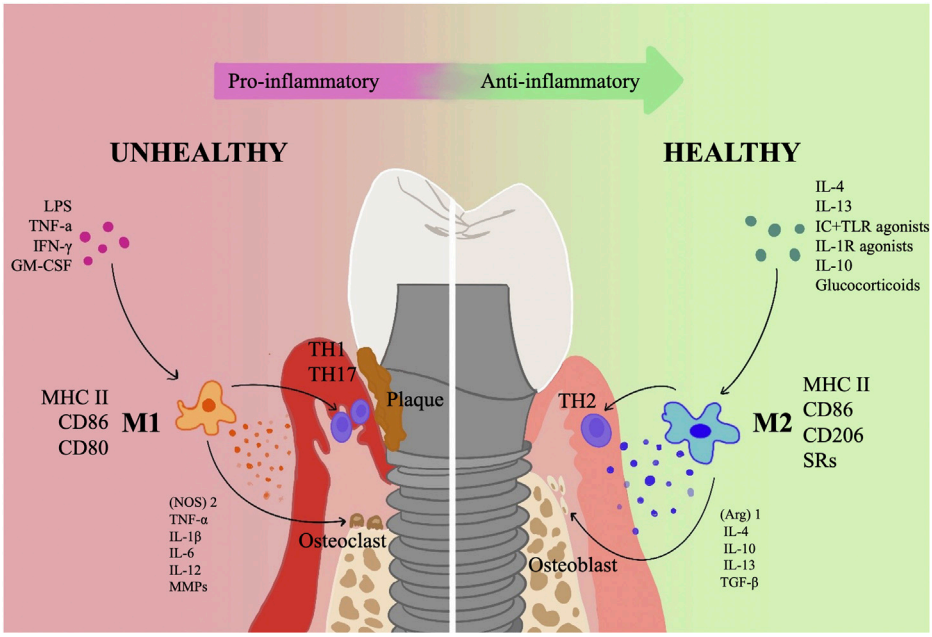

FIGURE 1
An overview of how polarized macrophages contribute to the incidence and growth of PI. The progressive and retreating phases of inflammation are dominated, respectively, by the M1 and M2 phenotypes of macrophages. M1 primarily serves a pro-inflammatory role, releasing a number of pro-inflammatory substances such (NOS)2, TNF-α, IL-1, IL-6, IL-12, and MMPs and collaborating with Th1 and Th17 cells. In addition, M1 type activates osteoclasts and causes resorption of alveolar bone; M2 type primarily functions as an anti-inflammatory, carrying out tissue repair via a variety of anti-inflammatory factors, such as (Arg)1, IL-4, IL-10, IL-13, and TGF-β, mainly synergizes with Th2 cells, and activates osteoblasts to promote bone regeneration.

and Rutger Persson, 2007; Koldsland, Scheie and Aass, 2010; Rinke, Ohl, Ziebolz, Lange and Eickholz, 2011).

Although the clinical and radiological manifestations of PI and periodontitis share many features, there are key differences in their clinical progression, histological features, and microbial composition, suggesting different pathogenesis (Carcuac and Berglundh, 2014). By using 16S pyrosequencing, Kumar et al. discovered that the peri-implant microbiome differs greatly from the periodontal microbiome with regard to both health and illness. Peri-implantitis is a microbiological heterogeneous infection predominantly brought on by Gram-negative bacteria (i.e., the dominant species are not the same in each individual) and is not as complex as periodontitis (Kumar et al., 2012).

When PI samples were compared to periodontitis samples, the region of inflammatory infiltration was more than twice as large in the PI samples, and there were also considerably more macrophages and plasma cells in the PI samples overall (Carcuac and Berglundh, 2014). In both PI and periodontitis lesions, plasma cells and lymphocytes predominate. However, PMN and macrophages take more percentage in PI than in periodontitis (Esposito et al., 1997; Gualini and Berglundh, 2003; Berglundh, Gislason, Lekholm, Sennerby and Lindhe, 2004; Berglundh, Zitzmann and Donati, 2011; Carcuac and Berglundh, 2014). The periapical tissue goes through a "self-limiting" process when the ligature is removed in which the connective tissue capsule divides the ICT from the bone in periodontitis, whereas in the peri-implant tissue, the ICT extends to the bone crest (Berglundh, Zitzmann and Donati, 2011).

Implants dysregulate the immune response in the peri-implant mucosa (PIM), as shown by the development of a mouse model of dental implants and experimental PI (Pirih et al., 2015; Koutouzis, Eastman, Chukkapalli, Larjava and Kesavalu, 2017; Tzach-Nahman, Mizraji, Shapira, Nussbaum and Wilensky, 2017; Heyman et al., 2018; Heyman et al., 2022). This "dysregulated homeostasis" or inflammatory condition of the PIM may be the cause of the implant's greater vulnerability to infection and the swift elimination of supporting tissue after infection (Carcuac and Berglundh, 2014).

Notably, Macrophages become polarized while responding to environmental signals, with M1 macrophages playing a role in bacterially-induced pro-inflammatory responses and M2 macrophages in inflammation regression and tissue repair (Yu et al., 2016; Palevski et al., 2017). Studies have shown an increase in polymorphonuclear leukocytes (PMN) and macrophages in PI lesions compared to periodontitis. Additionally, PI lesion samples revealed a notable rise in M1 macrophages (Fretwurst et al., 2020). This kind of macrophage polarization feature could partially explain the faster progression of PI in humans compared to periodontitis. It is consistent with the finding that PI advances more quickly than periodontitis because there is an increased quantity and density of PMN and macrophages (particularly M1) in the peri-implant lesions (Dionigi, Larsson, Carcuac and Berglundh, 2020). Studies on the function of macrophage polarization in the onset of PI and periodontitis have gradually risen in recent years (Figure 1). This review summarizes the research results related to macrophage polarization in PI and compares them with periodontitis in an attempt to deepen the understanding of the pathogenesis of PI and propose possible immunomodulatory therapies for PI in the direction of macrophage polarization patterns. This will improve our knowledge of, capacity to avoid, and manage PI.

2 Overview of the polarization of macrophages

Macrophages were first recognized for their phagocytic abilities. They also contributed to host-microbe equilibrium, antigen presentation, mobilization of immune defense mechanisms, and resistance to bacterial infection (Sun X. et al., 2021). Although several attempts have been made to classify macrophages, the most widely accepted classification has been the mononuclear phagocytic system (MPS). There are also other functional classifications of macrophages, for example, binary classification of inflammatory states classifies macrophages into activated macrophages and alternatively activated macrophages (AAM) (Gordon and Martinez, 2010; Sica and Mantovani, 2012; Wynn, Chawla and Pollard, 2013).

Macrophages can adjust to a variety of activation states that fall under the M1/M2 phenotypes of macrophage polarization in order to support immune activity and maintain tissue homeostasis (Martinez, Sica, Mantovani and Locati, 2008). The pro-inflammatory cytokines TNF-γ, interleukins IL-1, IL-6, and IL-12, as well as a high volume of reactive nitrogen and oxygen intermediates, are all produced by M1 macrophages after being primed by the interferon IFN-γ. These responses encourage Th1 responses with potent bactericidal and antitumor activity. IL-4 or IL-13 can prime M2 macrophages, which then express high levels of a metabolic marker called arginase (Arg) 1, the differentiation cluster CD206, and the anti-inflammatory cytokine IL-10, thereby dampening the inflammatory response to preserve tissue homeostasis, thereby attenuating the inflammatory response to maintain tissue homeostasis. The repression of parasites, stimulation of tissue remodeling, advancement of tumors, and immunomodulatory actions are all facilitated by M2 macrophages. Table 1 summaries the polarization types, characteristics and basic functions of macrophages. In summary, M1 macrophages have a role in bacterial killing and inflammation, whereas M2 macrophages are primarily involved in tissue homeostasis, suppression, inflammatory regression, and tissue healing (Morris, Singer and Lumeng, 2011; Sica and Mantovani, 2012).

The development of numerous inflammatory disorders, including infections, obesity, and cancer, is characterized by an imbalanced M1/M2 ratio (Wynn et al., 2013). Obesity, atherosclerosis, diabetes, allergies and asthma, autoimmunity, and cancer are a few examples of chronic diseases that are linked to specific macrophage polarization profiles (Sima and Glogauer, 2013). It has been proven that macrophages can become functionally polarized *in vivo*, both in healthy and unhealthy circumstances. Pregnancy, embryogenesis, and the preservation of normal conditions in particular tissues (such as the testis and fat tissue) are all included in the former. Included in the latter are cancer, vascular disease, infection, chronic inflammation, tissue healing, and metabolism (Sica and Mantovani, 2012).

3 Polarization of macrophages in periodontitis

As the sixth most common disease in the world, periodontitis is a common condition that affects many people. In its extreme stages, 10% of adult population are affected (Larsson et al., 2022). It is a chronic infectious illness characterized by microbial-related and host-mediated inflammation, which is brought on by the persistent breakdown of supportive periodontal tissues, which is started by plaque biofilm (Tonetti, Greenwell and Kornman, 2018). A considerable number of animal experiments and human studies have shown increased polarization of M1 macrophages in periodontitis (Table 2). In mice infected with Porphyromonas gingivalis (Pg), an animal investigation found that M1 macrophages dramatically expanded in the gingival tissue (Lam et al., 2014). M1 macrophages increased higher than M2 in the periodontitis group compared to the healthy control group, according to research by Yu T et al. on animals. Additionally, periodontal tissue affected by periodontitis showed an increase in the M1 inflammatory factors TNF-α and IL-1β as well as the M2 inflammatory factor IL-10 (Yu et al., 2016). Another human study showed that M1 macrophages increased in periodontitis compared to healthy controls (Higuchi, Sm, Yamashita, Ozaki and Yoshimura, 2020). However, when periodontitis worsens, the macrophage phenotype may alter. M1 is enhanced during the inflammatory phase while macrophage phenotype polarizes towards the M2 type during the recovery stage (Gonzalez et al., 2015; Viniegra et al., 2018; Zhou et al., 2019; Wu X. et al., 2020).

3.1 M1 macrophage polarization in periodontitis

Numerous M1 macrophages are present at the sites of bone degradation in chronic osteolytic disorders, such as various types of arthritis and periodontitis. These macrophages contribute significantly to disease-induced bone resorption by producing inflammatory cytokines including IL-1β and TNF-α and activating osteoclasts (Arend and Dayer, 1990; Stashenko, Jandinski, Fujiyoshi, Rynar and Socransky, 1991; Metzger, 2000; Górska et al., 2003; Andrukhov et al., 2011; Shaddox et al., 2011). Clinical outcomes may be enhanced by antagonist therapy that lowers TNF-α and IL-1β levels (Zwerina, Redlich, Schett and Smolen, 2005; McInnes and Schett, 2007). By employing IL-1β and TNF-α antagonists or knocking down the IL-1 receptor and TNF receptor, alveolar bone resorption in mice with experimental periodontitis was also decreased (Assuma, Oates, Cochran, Amar and Graves, 1998; Graves and Cochran, 2003). Additionally, gingival crevicular fluid IL-1 levels were found to be lower, IL-10 levels were higher, and bone resorption activity was lower when periodontal treatment was effective (Holmlund, Hänström and Lerner, 2004; de Lima Oliveira et al., 2012).

Matrix metalloproteinases (MMPs), which are involved in the breakdown of the extracellular matrix, are just one of the significant proteases that M1 macrophages release in addition to cytokines in the advancement of periodontal disorders (Franco, Patricia, Timo, Claudia and Marcela, 2017). MMPs are produced as a result of the inflammatory cytokines TNF-α, IL-1, and IL-6, all of which are highly expressed in diseased periodontal tissue (Stashenko et al., 1991; Irwin and Myrillas, 1998; Irwin, Myrillas, Traynor, Leadbetter and Cawston, 2002), some of these MMPs are also associated with increased M1/M2 ratios during disease (J. Yang et al., 2018).

3.2 M2 macrophage polarization in periodontitis

Widespread expression of the M2 macrophage's IL-10 in inflamed periodontal tissue is linked to tissue healing, a

TABLE 1 The polarization types, characteristics and basic functions of macrophages (Sima and Glogauer, 2013; Sun X. et al., 2021).

Phenotypes	Stimuli	Special surface receptor	Cytokines	Basic function
M1	LPS TNF-a IFN-γ GM-CSF	MHC II CD86 CD80	IL-1β	Stimulates the endothelium of vessels
				Makes lymphocytes active
				Localized deterioration of tissues
				Enhances effector cell accessibility
				Generation of IL-6
			IL-6	Activation of lymphocytes
				Increased synthesis of antibodies
				Stimulates the synthesis of acute-phase proteins
			TNF-α	Enhances the permeability of the vascular endothelium
				Enhanced fluid drainage to lymph nodes
				Enhanced entrance of IgG, complement, and cells into tissues
				Metabolite mobilization
			CXCL8/IL-8	Chemotactic factor that attracts T-cells, basophils, and polymorphonuclear neutrophils to the infection site
				Degranulates, mobilizes, and activates polymorphonuclear neutrophils
			IL-12	Triggers the activation of natural killer cells
				Stimulates the development of $CD4^+$ T cells into T-helper 1 cells
			IL-23	Stimulates the generation of interferon gamma and T-helper 17 memory T-cell proliferation
			CCL2/monocyte chemotactic protein-1	Attracts T-cells, monocytes, basophils, immature dendritic cells and natural killer cells
			CXCL9	Involved in T-cell trafficking
			CXCL10	Attracts natural killer cells and T-cells
				Signals through CXCR3
M2	IL-4 IL-13 IC + TLR/IL-1R agonists IL-10 Glucocorticoids	MHC II CD86 CD206 SRs	IL-1R antagonist	Acts as a natural antagonist of IL-1 function
			IL-10	Inhibits the production of pro-inflammatory cytokines, including granulocyte–macrophage colony-stimulating factor, TNF-α, IFN-γ, IL-2, and IL-3
			TGF-β1	Inhibits cell growth
				Anti-inflammatory
				Induces switch to IgA production
			Insulin-like growth factor-1	Stimulates fibroblast proliferation and survival
			CCL17	Attracts T-cells and macrophages
			CCL18	Attracts lymphocytes, immature dendritic cells and monocytes
			CCL22	Attracts T-helper 2 cells and other CCR4-expressing cells
			CCL24	Attracts T-helper 2 cells

reduction in periodontitis severity, and a reduction to inflammation (Lappin, MacLeod, Kerr, Mitchell and Kinane, 2001; Garlet, Martins, Fonseca, Ferreira and Silva, 2004; Garlet, 2010). In IL-10 deficient animals, which were more vulnerable to Pg-induced alveolar bone loss, its protective effect was also demonstrated (Sasaki et al., 2004). Additionally, TGF-β is

TABLE 2 Studies related to macrophage polarization in periodontitis.

Author & year	Article type	Polarization markers		Possible regulatory pathways	Results
		M1	M2		
Lam et al. (2014)	Animal study (mice)	CD86	CD206	—	Pg infection causes functional/inflammatory M1 macrophage infiltration of gingival tissue and alveolar bone resorption. M1 macrophages ($CD86^+$), but not M2 macrophages (CD206+), are the predominant macrophage phenotype in gingival infiltration
Gonzalez et al. (2015)	Animal study (Rhesus monkeys)	M1 gene profiles	M2 gene profiles	—	Age and periodontitis cause a large rise in macrophages. The M1 phenotype is the most common rise in older, particularly in tissues with periodontitis
Yu et al. (2016)	Animal study	(NOS)-2	CD206	In the setting of periodontitis, a multitude of signals, such as pro- and anti-inflammatory cytokines upregulated in the macrophages themselves, as well as M1-stimulating (IFN-γ) and M2-stimulating (IL-4) cytokines upregulated in T-helper cells, may combine to generate a macrophage phenotype	In the periodontal tissues, the periodontitis group had a 14-fold increase in M1 type, a 4-fold rise in M2 type, and an improved M1/M2 ratio ($p < 0.01$) in comparison to the control group. Increased M1 and M2 macrophage phenotypes were linked to periodontal inflammation; the transition from M2 to M1 may be a major mechanism generating periodontal tissue damage, including alveolar bone loss
Viniegra et al. (2018)	Animal study (mice)	TNF-α	IL-10	—	M2 activation, partly via direct action on osteoblasts, promotes bone repair during healing of periodontal lesions. In osteolytic illness, immunomodulation of macrophages to polarize them toward the M2 type stimulates bone growth
			TGF-β		
			CD206		
Zhou et al. (2019)	Human study	iNOS	CD206	—	The periodontitis group had considerably higher levels of TNF-α, IFN-γ, IL-6, and IL-12, along with a larger M1/M2 ratio and a greater number of M1 cells when compared to the control group
Wu et al. (2020b)	Human study	CD86	CD163	Akt2/JNK1/2/c-Jun Akt2/miR-155–5p/DET1/c-Jun	Inhibition of Akt2 promotes macrophage M2 polarization and rescues periodontitis-induced bone loss
Ahmad, Naqvi, Valverde and Naqvi (2023)	Animal (mice) and Human study	iNOS	ARG1	LncRNA MALAT1/microRNA-30b	MALAT1 functions and is expressed antagonistically with miR-30b, another non-coding RNA. MALAT1 knockdown favors the M2 phenotype, while miR-30b overexpression encourages M2 polarization
		STAT1	STAT3		
		TNF-α	CCL2		
		ARG2	IL-10		
(Wu, Wang, Chen, Wang and Gu, 2023)	Animal study (mice)	CD86	CD206	PTEN/Akt1/Akt2	M2 polarization is induced in macrophages by PTEN inhibition, while M1 polarization is promoted by PTEN overexpression. PTEN inhibitor therapy prevented alveolar bone resorption and markedly decreased the local inflammatory state in mice
(Yang et al., 2023)	Animal studu (mice)	iNOS	CD206	IL-37/NLRP3	In the gingival tissues of periodontitis-stricken mice, IL-37 markedly decreased the number of iNOS + cells while increasing the number of CD206+ cells.By preventing the activation of the NLRP3 inflammasome and facilitating the polarization of M1/M2 macrophages, IL-37 stopped the advancement of periodontitis
Li et al. (2023a)	Animal study (mice)	iNOS	Arg-1	MicoRNA-126/MEKK2	By controlling the MEKK2 signaling pathway, miR-126 inhibits macrophage M1 polarization and stops alveolar bone resorption in individuals with diabetic periodontitis

regarded as one of the most significant cytokines involved in the upkeep of the M2 phenotype, which suppresses the synthesis of endogenous NO (Vodovotz, Bogdan, Paik, Xie and Nathan, 1993), and is crucial for the recruitment of bone marrow mesenchymal stem cells (MSCs) during tissue regeneration (Fu et al., 2019). By releasing IL-4, IL-10, IL-13, and TGF-β throughout the inflammatory process, M2 macrophages counteract the M1 type macrophage response, control inflammation, and aid in tissue repair

and wound healing (Mosser and Edwards, 2008; Wynn and Vannella, 2016).

3.3 Potential pathways for macrophage polarization in the etiology of periodontitis

M1 macrophages and Th1/Th17 lymphocytes are more prevalent than M2 macrophages and Th2/Treg lymphocyte subsets in active periodontal diseases compared to both of these cell types (Cavalla and Hernandez, 2022).

Through interactions with other immune cells, it has been demonstrated that macrophage polarization plays a role in the etiology of periodontitis: (1) macrophage-PMN-monocyte crosstalk: during inflammation, M1 macrophages locally recruit PMN to clear pathogens. Monocytes emerge after PMN recruitment and are activated as M2 macrophages to remove apoptotic PMN and other debris; (2) macrophage-lymphocyte crosstalk: M1 type macrophages activated by LPS, TNF-α, and IFN-γ produce IL-23, which stimulates Th17 cell infiltration. An inflammatory amplification loop is created when a Th17 cell releases IL-17 (a pro-inflammatory cytokine that promotes PMN recruitment and activation), IL-1, IL-6, TNF-α, MMPs, and RANKL. The decoy receptor osteoprotegerin and RANKL, a significant pro-osteoclastic mediator, are necessary for the coupling of bone resorption and creation (Sima and Glogauer, 2013).

4 Relationship between implants and dysregulated immune responses in the peri-implant mucosa (PIM)

Animal experiments based on a murine implant model have shown that the titanium implant itself promoted peri-implant inflammation and dysregulated mucosal homeostasis. Langerhans cells, the primary antigen-presenting cells of the oral epithelium, were hampered in their ability to mature, which was a result of the implant's release of titanium ions. Titanium dental implants disrupted the immunological control of the PIM by impairing the growth of oral Langerhans cells (Heyman et al., 2018).

In peri-implant tissue biopsies, a reduction in inflammatory cell density was seen as healing time increased, so it is thought that the onset and regression of inflammation is a characteristic of PIM healing (Tomasi et al., 2016). This occurrence might be the PIM's transitional immunological state before it returns to a homeostatic level resembling healthy gingival tissue. However, inflammatory infiltration of the PIM had been reported in implants that did not show clinical signs related to inflammation even 6 months after implant insertion, as found in animal studies (Pongnarisorn et al., 2007). Determining whether the PIM reaches a "normal" steady state, as it does in the gingiva, is therefore uncertain, suggesting the possibility that the PIM develops an alternative immune homeostasis. Given that the peri-implant tissue is more "inflamed" than the normal gingiva based on Th17/Treg homeostasis, this theory could explain why the implant is more susceptible to infection (Heyman et al., 2022). As mentioned previously, M1 macrophages and Th1/Th17 lymphocyte subsets are more prevalent than M2 macrophages and Th2/Treg lymphocyte subsets in active periodontal diseases (Cavalla and Hernandez, 2022). Thus, although the role played by macrophage polarization in the immune dysregulation of peri-implant tissues has not been fully investigated, it can be hypothesized that its role should not be underestimated.

Additionally, utilizing a mouse dental implant model, Heyman et al. discovered that dental implants were able to promote dysbiosis of the oral microbiota and increase inflammation and bone loss in the remote teeth in addition to locally raising inflammation and bone loss. It was not entirely clear which mechanisms induced the promotion of bone loss at the remote site. The Th1 immune response, represented by IFN-γ, may yet be implicated in this process, according to findings of cytokine production and lymphocyte infiltration in the gingiva (Heyman et al., 2020). The possibility of M1 macrophages contributing is also raised by this.

5 Polarization of macrophages in peri-implantitis

Currently, there are only several studies investigating macrophage polarization in PI. No consensus has been reached.

It was reported earlier that the number of M1 macrophages present was similar between the periodontitis and PI groups, although higher than that of healthy controls (Karatas et al., 2020). M1 and M2 expression in PI samples did not show any statistically significant differences (Galarraga-Vinueza, Obreja, Khoury, et al., 2021a).

However, research from the previous 2 years revealed that PI had much more M1 macrophages than periodontitis did. In comparison to periodontitis samples, it was discovered that PI samples showed a much greater degree of inflammatory cell infiltration and a significantly higher number of M1 macrophages (Dionigi et al., 2020; Fretwurst et al., 2020). M2 macrophage counts, however, did not significantly differ between the two illnesses (Fretwurst et al., 2020). M1 macrophage levels were also noticeably greater in advanced PI cases (i.e., radiographic marginal bone loss >50% of implant length, PI severity classification (Monje et al., 2019)), and a significant association between higher M1 macrophage expression and deeper probing depth was found (Galarraga-Vinueza, Obreja, Ramanauskaite, et al., 2021b). Table 3 summarizes the literature related to macrophage polarization in human PI in recent years.

5.1 M1/M2 polarization in regulating osteoclast and osteoblast functions

It is now believed that the large number of macrophages and elevated M1 macrophages observed in PI lesions indicate a strong immune system response to local factors that increase tissue destruction. The histological data in the literature are consistent with the progression of PI disease observed in the clinic (Derks et al., 2016; Fretwurst et al., 2020). The higher expression of M1 macrophages may be associated with a "destructive" inflammatory response and significant peri-implant osteolysis in advanced PI cases (Garlet and Giannobile, 2018; Zhuang et al., 2019; Fretwurst et al., 2020).

TABLE 3 Studies related to macrophage polarization in peri-implantitis.

Author & year	Sample size		Inclusion criteria of patients with PI	Polarization markers		Results
	Number of patients with periodontitis	Number of patients with PI		M1	M2	
Fretwurst et al. (2016)	—	12	Severe peri-implant disease with indication for explantation included radiographic bone loss of more than two-third of the implant length, suppuration, mobility, or cortical bone perforations	PGM-1[1]	—	M1 macrophages were few overall in the specimens, and immunohistological analyses revealed that they concentrated in regions with higher amounts of the metals titanium and iron
Karatas et al. (2020)	15	15	2017 World Workshop (Berglundh et al., 2018)	iNOS	—	In comparison to periodontitis and PI specimens, peri-implant mucositis showed reduced iNOS expression, with no differences found in the former two
Fretwurst et al. (2020)	7	7	2017 World Workshop (Berglundh et al., 2018)	iNOS	CD206	M1 macrophage population was significantly increased in PI samples compared to periodontal disease samples ($p < 0.01$); M2 macrophage polarization showed similar levels in both ($p > 0.05$). In comparison to periodontitis specimens, the area and density of iNOS-positive cells in PI specimens were higher
Dionigi et al. (2020)	40	40	severe peri-implantitis:The subjects in this group demonstrated ≥1 implant with peri-implant bone loss ≥3 mm and a peri-implant probing pocket depth ≥7 mm, with bleeding on probing and/or suppuration (Carcuac and Berglundh, 2014)	iNOS	—	The area and density of iNOS-positive cells in PI specimens were greater than in periodontitis specimens
Galarraga-Vinueza, Obreja, Ramanauskaite, et al. (2021a)	—	20	the presence of at least one screw-type (one- or two-part) titanium implant diagnosed with peri-implantitis and indicated for surgical peri-implantitis treatment	CD80 CD68	CD206 CD68	M1>M2 ($p = 0.01$)
Galarraga-Vinueza, Obreja, Khoury, et al. (2021b)	—	14	2017 World Workshop (Berglundh et al., 2018)	CD80	CD206	M1>M2 ($p = 0.16$)

[a]Legend: PGM-1: Glucose phosphate metastase-1. World Workshop (Berglundh et al., 2018): (1) Presence of bleeding and/or suppuration on gentle probing. (2) Increased probing depth compared to previous examinations. (3) Presence of bone loss beyond crestal bone level changes resulting from initial bone remodeling. Epidemiological studies need to take into account the error of measurements in relation to assessments of bone level changes. Bone loss should be reported using thresholds exceeding the measurement error (mean 0.5 mm).

10.3389/fbioe.2024.1291880

Through the secretion of cytokines that activate osteoclast precursors and encourage Th1 responses, M1 contributes to the activation of osteoclasts. Concurrently, M1 contributes to the generation of cytokines that are thought to be important for bone resorption, including PGE2, IL-1β, TNF-α, IL-6, and IL-12. PGE2 is the most potent inducer of periodontal bone resorption among them. It also facilitates a number of detrimental processes in the alveolar bone, including reducing osteoblast viability and mineralization and promoting the development of osteoclasts (Oka et al., 2007; Ruiz-Heiland, Yong, von Bremen and Ruf, 2021). LPS stimulates M1's expression of IL-1β, and TNF-α and IL-1β together stimulate M1's synthesis of IL-1β to support osteoclast activation and differentiation (Ruiz-Heiland et al., 2021); TNF-α also causes T cells and B cells to produce RANKL (Becerra-Ruiz, Guerrero-Velázquez, Martínez-Esquivias, Martínez-Pérez and Guzmán-Flores, 2022). Furthermore, IL-6 causes osteoclasts to break down the extracellular matrix and create MMPs, which eventually results in alveolar bone resorption (Figueiredo et al., 2020).

As was previously noted, TGF-β is regarded as one of the key cytokines in the preservation of the M2 phenotype and is crucial for bone marrow MSC recruitment during tissue healing (Fu et al., 2019). M2 also expresses high levels of IL-10 (Zhou et al., 2019), which helps to partially explain its role in the formation of new bone. The excessive effects of IL-10 and IL-4 on the healing process appear to be related to the downregulation of proinflammatory cytokines and MMP as well as the stimulation of osteoblasts. M2 secretes BMP-2, which speeds up osteogenesis (Liang, Wang, Wu and Wang, 2021). To sum up, M2 secretes anti-inflammatory and repair mediators, including TGF-β, IL-4, IL-10, and vascular endothelial growth factor, which in turn suppress proinflammatory cytokines and encourage tissue regeneration and homeostasis restoration. The M2-induced local microenvironment promotes osseointegration and angiogenesis (Park, Silvin, Ginhoux and Merad, 2022).

5.2 Titanium particles and foreign body reactions in peri-implant tissues

The presence of foreign bodies is thought to be strongly associated with PI, and they cause a dysregulated immune response in the peri-implant tissues. These foreign bodies are mainly titanium and dental adhesives (Wilson et al., 2015). Successive studies have reported cases of post-implant titanium allergy or peri-implant mucosal reactive lesions, and metallic-like particles and cells suggestive of allergic reactions, such as eosinophils and PMN, have been observed histologically. Available data suggested that titanium particles were present in more than 90% of PI lesions (Shafizadeh, Amid, Mahmoum and Kadkhodazadeh, 2021). Several *in vitro* studies have confirmed that microns or nanoparticles of titanium implant alloys may be cytotoxic and enhance pro-inflammatory responses (Okuda-Shimazaki, Takaku, Kanehira, Sonezaki and Taniguchi, 2010; Cai et al., 2011; Irshad et al., 2013; Pettersson et al., 2017). A significant inflammatory reaction was seen in soft tissue biopsies near implants when titanium particles were present (Schlegel, Eppeneder and Wiltfang, 2002; Olmedo et al., 2012; Wilson et al., 2015). There was considerable evidence that debris, titanium ions, and particle shedding could lead to sterile peri-implant inflammation and implant failure (Revell, 2008).

Histological biopsies of human PI samples revealed that M1 macrophages accumulated in areas of increased titanium and iron concentrations (Fretwurst et al., 2016). It has been discovered that titanium particles cause macrophages to react similarly to LPS, and the resulting inflammatory response fuels osteoclast-mediated bone tissue destruction. *In vitro* and *in vivo* gene expression, secretome profiling, fluorescence activated cell sorting (FACS), and other analyses on macrophages revealed that M1 polarization occurs in response to titanium particles. However, all of their assays were performed during the early inflammatory phase. Inflammation regression was observed in some tissues *in vivo* after 6–8 weeks, indicating that M1 and M2 macrophages may be distributed more dynamically and intricately over time (Eger et al., 2018).

To study the impact of various titanium particle sources on macrophage polarization, Eger et al. used a mouse calvarial model (Eger, Sterer, Liron, Kohavi and Gabet, 2017). The findings demonstrated that there was no noticeable difference in M2 macrophage numbers between the experimental and control groups. However, mice exposed to titanium particles produced by machined (M) or sandblasted and acid-etched (SLA) processes had considerably more M1 macrophages (Eger et al., 2018).

In vitro macrophage cultures revealed similar results. TNF-α, IL-1β, and IL-6 mRNA expression in macrophages increased (up to a 3.5-fold rise) when TiO2 particles were added to the culture medium (Ramenzoni, Fluckiger, Attin and Schmidlin, 2021). Titanium ions in physiological solutions induced the release of IL-1β via activating inflammatory vesicles in human macrophages (Pettersson et al., 2017), and all these cytokine profiles were characteristic of M1 polarization.

In conclusion, immune dysregulation can be found in PI. The most common phenomenon is the polarization of macrophages, but related studies are still lacking. The difficulty of creating an animal model is a significant factor in the paucity of data regarding the etiology of PI. PI lesion tissue is not easily available may also be responsible for it. In addition, Regarding the indicators of M1/M2 polarization, there is currently no definite agreement in the macrophage polarization literature (Fretwurst et al., 2020). Research is still needed in the area of choosing more precise molecular markers to distinguish M1/M2 macrophages (Galarraga-Vinueza, Obreja, Ramanauskaite, et al., 2021a).

6 Immunoregulatory therapy for peri-implantitis linked to polarized macrophages

One should not undervalue the role that macrophage polarization plays in the clinical management of periodontitis and PI. It is currently thought that the major goal of macrophage polarization therapy is to get macrophages to polarize toward the M2 macrophages in order to reduce inflammation, encourage tissue repair, and produce anti-inflammatory benefits (Sun et al., 2021; Whitaker, Hernaez-Estrada, Hernandez, Santos-Vizcaino and Spiller, 2021). Promoting macrophage polarization from M1-type to M2-type by immunomodulatory therapy to promote bone regeneration has been successfully attempted in diabetic fracture

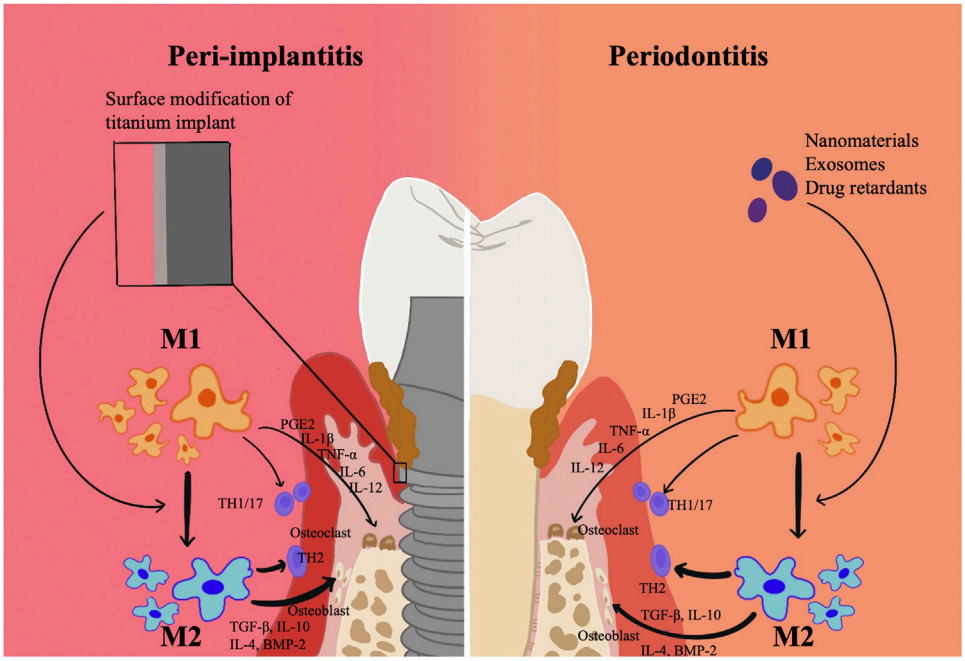

FIGURE 2
Surface modification technique of titanium related to Macrophage polarization in periodontitis and peri-implantitis. Surface modification of titanium may influence macrophage polarization. By modifying macrophage polarization, surface modification technique might reduce chronic inflammation and further increase osseointegration around the implant material.

healing models, and in bone-related diseases including osteoarthritis (OA), osteoporosis (OP), and bone defects (Whitaker et al., 2021; Wang et al., 2023). Macrophage polarization immunomodulatory therapy for periodontitis is currently a hot topic, but those therapies regarding PI are currently rare.

The current literature on regulating macrophage polarization as a therapeutic target for periodontal disease can be summarized as follows: (1) anti-cytokine therapy: when anti-TNF-α therapy was used in combination with mechanical debridement, periodontal parameters showed a tendency of improvement (Pers, Saraux, Pierre and Youinou, 2008; Mayer, Balbir-Gurman and Machtei, 2009; Ortiz et al., 2009). Therapeutic blocking of IL-1 receptors dramatically reduced local inflammatory cell infiltration, osteoclast activation, and bone resorption in an animal model of periodontitis (Assuma et al., 1998; Delima et al., 2001); (2) pharmacological treatment: when used systemically, rosiglitazone inhibited bone resorption during inflammation, increased bone regeneration during the repair of periodontitis, and polarized macrophages toward the M2 macrophages (Di Paola et al., 2006; Hassumi et al., 2009; Viniegra et al., 2018). Other drugs that affect macrophage polarization include PPARγ agonists (thiazolidinediones) (Charo, 2007; Stienstra et al., 2008; Lu et al., 2011), zoledronic acid, statins (Fujita et al., 2010), trabectedin (Germano et al., 2010); (3) cell therapy: isolated polarized M2 macrophages had the potential to initiate the regression of periodontal disease inflammation (Sima and Glogauer, 2013); (4) gene knockout: It has been shown that local injection of AKT inhibitors decreased the M1/M2 ratio and reduced alveolar bone resorption in mice with periodontitis, and that *in vitro* knockdown of Akt2 hindered M1 polarization and enhanced M2 polarization (Zhuang et al., 2019; Wu et al., 2020). The polarization of M1 macrophages was also decreased by TET1 knockdown because it prevented the NF-κB signaling pathway from being activated (Huang, Tian, Li and Xu, 2019).

Surface modification of titanium may influence macrophage polarization (Figure 2). Successfully synthesising IL-23R non-competitive antagonist nanocoatings on titanium surfaces, Pizarek et al. discovered that the coatings inhibited the IL-23/17A pathway, which is a source of inflammation, and polarized macrophages to the M2 phenotype in *vitro* cellular studies (Pizarek, Fischer and Aparicio, 2023). In a recent study, it was discovered that by modifying macrophage polarization, a surface modification technique using peptide coatings might reduce chronic inflammation and further increase osseointegration around the implant material (Bai et al., 2020). By interfering with integrin-α2β1 and integrin-αvβ3, peptide-modified titanium implants might successfully reduce peri-implant inflammation in wear particle models and induce macrophage polarization to a pro-healing M2 phenotype. With the use of tetravalent 3,4-dihydroxy-L-phenylalanine (DOPA) and Arg-Gly-Asp (RGD) sequences, this catecholic peptide with mussel-inspired structure was created. The mussel adhesion mechanism allowed for the easy apposition of this peptide to the surface of medical titanium materials, enhancing osteoblast adherence and fostering osteogenesis of titanium implants even under inflammatory circumstances (Guo et al., 2022).

In addition, MSC therapy has great potential in preventing and treating peri-implantitis. Li et al. used a hydrogel loaded with gingival-derived MSCs and injected it into the peri-implant area of a rat model of early implant placement and found that it was effective in improving epithelial closure around the implant and

TABLE 4 Materials used in Immunomodulatory therapies related to Macrophage polarization in periodontitis.

Methods	Author & year	Materials
Nanomaterials	Ni et al. (2019)	45 nm gold nanoparticles (AuNPs)
	Garapaty and Champion (2019)	ligand presentation on rods
	Wu et al. (2020a)	modified zirconia surface
	Sun et al. (2021b)	cerium@Ce6 multifunctional nanocomposite
	Wang et al. (2021)	antioxidant drug quercetin onto nano-octahedral ceria
	Yang et al. (2021)	micro/nanomesh
	Ming et al. (2023)	sericin-hydroxyapatite nanoparticles (Se-nHA NPs)
	Xiao et al. (2023)	liposome-encapsulated indocyanine green (ICG) and rapamycin drug-delivery nanoparticle (ICG-rapamycin)
	Wang et al. (2023a)	AuAg-procyanidins (AuAg-PC)
	Huangfu et al. (2023)	resveratrol (RES)-20(S)-protopanaxadiol (PPD) (RES@PPD NPs)
	Chato-Astrain et al. (2023)	dexamethasone-loaded titanium micro particles (TiP) (Dex-TiP)
Exosomes	Wang et al. (2019)	exosomes secretion of periodontal ligament cells (PDLs)
	Curtale, Rubino and Locati (2019)	MicroRNAs: Mir-146a, Mir-125a and Mir-145–5p
	Shen et al. (2020)	dPSC-ExO-chitosan hydrogel (dPSC-ExO/CS)
	Nakao et al. (2021)	exosomes secretion of gingival tissue-derived MSCs
	He, Zhang and Lin (2021)	microrNA-125A-5P
	Luo et al. (2023)	CXCR4-miR126-Exo
	Deng et al. (2023)	Bio-GelMA@Bio-EX hydrogels-Exo
Drug retardants	Zhuang et al. (2019)	controlled-release microparticles (MPS)

promoting M2 macrophage polarization. This would aid in preventing the growth of peri-implantitis (Li et al., 2023). However, the precise molecular processes and signaling pathways of interactions between epithelial cells and macrophages have not yet been clarified.

Nevertheless, the majority of inflammatory disease treatments, including those for periodontitis, are palliative and only offer temporary relief. The idea of immunomodulatory nanosystems (IMNs) may be able to solve this issue (Ahamad et al., 2021). The main IMNs for macrophage polarization-associated periodontitis include nanomaterials, exosomes, and periodontal drug retardants (Sun et al., 2021). Table 4 summarizes the immunomodulatory treatment strategies for macrophage polarization-associated periodontitis in recent years. Possible therapeutic strategies related to macrophage polarization in PI are less studied, but the current research in the periodontal field may provide some new directions for future research.

7 Conclusion

Animal experiments based on a murine implant model have shown that the titanium implant itself promoted peri-implant inflammation and dysregulated mucosal homeostasis. Titanium ions that were released from the implant acted as a mediator in this process. It is currently thought that the onset and resolution of inflammation is a characteristic of PIM healing, but it is unclear whether the PIM achieves a "normal" stable state as in the gingiva, suggesting the possibility that the PIM develops alternative immune homeostasis. The available data indicate that macrophage polarization plays a significant role in the dysregulation of peri-implant immunity, despite the fact that the mechanisms behind this dysregulation are not fully understood.

Macrophage polarization has a complex and extensive variety of roles, with M2 macrophages primarily involved in tissue homeostasis, suppression and regression of inflammation, and tissue repair, and M1 macrophages promoting bacterial death and increasing inflammation. Although studies related to macrophage polarization in PI are not sufficiently thorough, the available literature suggests that the higher expression of M1 macrophages in PI compared to periodontitis may be associated with a "destructive" inflammatory response and significant peri-implant osteolysis in patients diagnosed with advanced PI. Furthermore, macrophage polarization toward the M1 phenotype may be caused by micron- or nano-sized particles of typical titanium implant alloys.

The ability to control immune homeostasis has been tentatively shown in some studies to be a promising therapeutic strategy. This is accomplished by carefully examining the mechanisms of action of various cytokines and mediators that regulate macrophage polarization and by controlling the ratio of macrophages with different polarization phenotypes to achieve a good balance between immune defense and tissue homeostasis.

However, the need for an experimental model and an unambiguous agreement on the markers to distinguish M1 from M2 polarization, which permits careful examination of this crucial issue, still exists. For further research, more PI lesion tissue needs to be gathered. The treatment options for PI macrophage polarization are few and will likely require more research in the future.

Author contributions

YL: Methodology, Writing–original draft. XL: Methodology, Writing–original draft. DG: Writing–review and editing. LM: Writing–review and editing. XF: Writing–review and editing. YZ: Writing–review and editing. SP: Conceptualization, Funding acquisition, Methodology, Writing–original draft, Writing–review and editing.

Funding

The author(s) declare financial support was received for the research, authorship, and/or publication of this article. This work was supported by the National Key R&D Program of China (2020YFC2009000, Project No. 2020YFC2009005), and supported by Beijing Natural Science Foundation (No. 7222228), and by the National Program for Multidisciplinary Cooperative Treatment on Major Diseases (PKUSSNMP-202004).

Conflict of interest

The authors declare that the research was conducted in the absence of any commercial or financial relationships that could be construed as a potential conflict of interest.

Publisher's note

All claims expressed in this article are solely those of the authors and do not necessarily represent those of their affiliated organizations, or those of the publisher, the editors and the reviewers. Any product that may be evaluated in this article, or claim that may be made by its manufacturer, is not guaranteed or endorsed by the publisher.

References

Ahamad, N., Kar, A., Mehta, S., Dewani, M., Ravichandran, V., Bhardwaj, P., et al. (2021). Immunomodulatory nanosystems for treating inflammatory diseases. *Biomaterials* 274, 120875. doi:10.1016/j.biomaterials.2021.120875

Ahmad, I., Naqvi, R. A., Valverde, A., and Naqvi, A. R. (2023). LncRNA MALAT1/microRNA-30b axis regulates macrophage polarization and function. *Front. Immunol.* 14, 1214810. doi:10.3389/fimmu.2023.1214810

Albrektsson, T., Brånemark, P. I., Hansson, H. A., and Lindström, J. (1981). Osseointegrated titanium implants. Requirements for ensuring a long-lasting, direct bone-to-implant anchorage in man. *Acta Orthop. Scand.* 52 (2), 155–170. doi:10.3109/17453678108991776

Andrukhov, O., Ulm, C., Reischl, H., Nguyen, P. Q., Matejka, M., and Rausch-Fan, X. (2011). Serum cytokine levels in periodontitis patients in relation to the bacterial load. *J. Periodontol.* 82 (6), 885–892. doi:10.1902/jop.2010.100425

Arend, W. P., and Dayer, J. M. (1990). Cytokines and cytokine inhibitors or antagonists in rheumatoid arthritis. *Arthritis Rheum.* 33 (3), 305–315. doi:10.1002/art.1780330302

Assuma, R., Oates, T., Cochran, D., Amar, S., and Graves, D. T. (1998). IL-1 and TNF antagonists inhibit the inflammatory response and bone loss in experimental periodontitis. *J. Immunol.* 160 (1), 403–409. doi:10.4049/jimmunol.160.1.403

Bai, J., Wang, H., Chen, H., Ge, G., Wang, M., Gao, A., et al. (2020). Biomimetic osteogenic peptide with mussel adhesion and osteoimmunomodulatory functions to ameliorate interfacial osseointegration under chronic inflammation. *Biomaterials* 255, 120197. doi:10.1016/j.biomaterials.2020.120197

Becerra-Ruiz, J. S., Guerrero-Velázquez, C., Martínez-Esquivias, F., Martínez-Pérez, L. A., and Guzmán-Flores, J. M. (2022). Innate and adaptive immunity of periodontal disease. From etiology to alveolar bone loss. *Oral Dis.* 28 (6), 1441–1447. doi:10.1111/odi.13884

Benoit, M., Desnues, B., and Mege, J. L. (2008). Macrophage polarization in bacterial infections. *J. Immunol.* 181 (6), 3733–3739. doi:10.4049/jimmunol.181.6.3733

Berglundh, T., Armitage, G., Araujo, M. G., Avila-Ortiz, G., Blanco, J., Camargo, P. M., et al. (2018). Peri-implant diseases and conditions: consensus report of workgroup 4 of the 2017 world Workshop on the classification of periodontal and peri-implant diseases and conditions. *J. Periodontol.* 89 (1), S313–S318. doi:10.1002/JPER.17-0739

Berglundh, T., Gislason, O., Lekholm, U., Sennerby, L., and Lindhe, J. (2004). Histopathological observations of human periimplantitis lesions. *J. Clin. Periodontol.* 31 (5), 341–347. doi:10.1111/j.1600-051X.2004.00486.x

Berglundh, T., Zitzmann, N. U., and Donati, M. (2011). Are peri-implantitis lesions different from periodontitis lesions? *J. Clin. Periodontol.* 38 (11), 188–202. doi:10.1111/j.1600-051X.2010.01672.x

Brånemark, P. I., Adell, R., Breine, U., Hansson, B. O., Lindström, J., and Ohlsson, A. (1969). Intra-osseous anchorage of dental prostheses. I. Experimental studies. *Scand. J. Plast. Reconstr. Surg.* 3 (2), 81–100. doi:10.3109/02844316909036699

Brånemark, P. I., Hansson, B. O., Adell, R., Breine, U., Lindström, J., Hallén, O., et al. (1977). Osseointegrated implants in the treatment of the edentulous jaw. Experience from a 10-year period. *Scand. J. Plast. Reconstr. Surg. Suppl.* 16, 1–132.

Cai, K., Hou, Y., Hu, Y., Zhao, L., Luo, Z., Shi, Y., et al. (2011). Correlation of the cytotoxicity of TiO2 nanoparticles with different particle sizes on a sub-200-nm scale. *Small* 7 (21), 3026–3031. doi:10.1002/smll.201101170

Carcuac, O., and Berglundh, T. (2014). Composition of human peri-implantitis and periodontitis lesions. *J. Dent. Res.* 93 (11), 1083–1088. doi:10.1177/0022034514551754

Cavalla, F., and Hernandez, M. (2022). Polarization profiles of T lymphocytes and macrophages responses in periodontitis. *Adv. Exp. Med. Biol.* 1373, 195–208. doi:10.1007/978-3-030-96881-6_10

Charo, I. F. (2007). Macrophage polarization and insulin resistance: PPARγ in control. *Cell Metab.* 6 (2), 96–98. doi:10.1016/j.cmet.2007.07.006

Chato-Astrain, J., Toledano-Osorio, M., Alaminos, M., Toledano, M., Sanz, M., and Osorio, R. (2023). Effect of functionalized titanium particles with dexamethasone-loaded nanospheres on macrophage polarization and activity. *Dent. Mater* 40, 66–79. doi:10.1016/j.dental.2023.10.023

Curtale, G., Rubino, M., and Locati, M. (2019). MicroRNAs as molecular switches in macrophage activation. *Front. Immunol.* 10, 799. doi:10.3389/fimmu.2019.00799

Delima, A. J., Oates, T., Assuma, R., Schwartz, Z., Cochran, D., Amar, S., et al. (2001). Soluble antagonists to interleukin-1 (IL-1) and tumor necrosis factor (TNF) inhibits loss of tissue attachment in experimental periodontitis. *J. Clin. Periodontol.* 28 (3), 233–240. doi:10.1034/j.1600-051x.2001.028003233.x

de Lima Oliveira, A. P., de Faveri, M., Gursky, L. C., Mestnik, M. J., Feres, M., Haffajee, A. D., et al. (2012). Effects of periodontal therapy on GCF cytokines in generalized aggressive periodontitis subjects. *J. Clin. Periodontol.* 39 (3), 295–302. doi:10.1111/j.1600-051X.2011.01817.x

Deng, D., Li, X., Zhang, J. J., Yin, Y., Tian, Y., Gan, D., et al. (2023). Biotin-avidin system-based delivery enhances the therapeutic performance of MSC-derived exosomes. *ACS Nano* 17 (9), 8530–8550. doi:10.1021/acsnano.3c00839

Derks, J., Schaller, D., Håkansson, J., Wennström, J. L., Tomasi, C., and Berglundh, T. (2016). Peri-implantitis - onset and pattern of progression. *J. Clin. Periodontol.* 43 (4), 383–388. doi:10.1111/jcpe.12535

Dionigi, C., Larsson, L., Carcuac, O., and Berglundh, T. (2020). Cellular expression of DNA damage/repair and reactive oxygen/nitrogen species in human periodontitis and peri-implantitis lesions. *J. Clin. Periodontol.* 47 (12), 1466–1475. doi:10.1111/jcpe.13370

Di Paola, R., Mazzon, E., Maiere, D., Zito, D., Britti, D., De Majo, M., et al. (2006). Rosiglitazone reduces the evolution of experimental periodontitis in the rat. *J. Dent. Res.* 85 (2), 156–161. doi:10.1177/154405910608500208

Eger, M., Hiram-Bab, S., Liron, T., Sterer, N., Carmi, Y., Kohavi, D., et al. (2018). Mechanism and prevention of titanium particle-induced inflammation and osteolysis. *Front. Immunol.* 9, 2963. doi:10.3389/fimmu.2018.02963

Eger, M., Sterer, N., Liron, T., Kohavi, D., and Gabet, Y. (2017). Scaling of titanium implants entrains inflammation-induced osteolysis. *Sci. Rep.* 7, 39612. doi:10.1038/srep39612

Esposito, M., Thomsen, P., Mölne, J., Gretzer, C., Ericson, L. E., and Lekholm, U. (1997). Immunohistochemistry of soft tissues surrounding late failures of Brånemark implants. *Clin. Oral Implants Res.* 8 (5), 352–366. doi:10.1034/j.1600-0501.1997.080502.x

Figueiredo, L. C., Bueno-Silva, B., Nogueira, C. F. P., Valadares, L. C., Garcia, K. M. M., Filho, G., et al. (2020). Levels of gene expression of immunological biomarkers in peri-implant and periodontal tissues. *Int. J. Environ. Res. Public Health* 17 (23), 9100. doi:10.3390/ijerph17239100

Franco, C., Patricia, H. R., Timo, S., Claudia, B., and Marcela, H. (2017). Matrix metalloproteinases as regulators of periodontal inflammation. *Int. J. Mol. Sci.* 18 (2), 440. doi:10.3390/ijms18020440

Fransson, C., Lekholm, U., Jemt, T., and Berglundh, T. (2005). Prevalence of subjects with progressive bone loss at implants. *Clin. Oral Implants Res.* 16 (4), 440–446. doi:10.1111/j.1600-0501.2005.01137.x

French, D., Ofec, R., and Levin, L. (2021). Long term clinical performance of 10 871 dental implants with up to 22 years of follow-up: a cohort study in 4247 patients. *Clin. Implant Dent. Relat. Res.* 23 (3), 289–297. doi:10.1111/cid.12994

Fretwurst, T., Buzanich, G., Nahles, S., Woelber, J. P., Riesemeier, H., and Nelson, K. (2016). Metal elements in tissue with dental peri-implantitis: a pilot study. *Clin. Oral Implants Res.* 27 (9), 1178–1186. doi:10.1111/clr.12718

Fretwurst, T., Garaicoa-Pazmino, C., Nelson, K., Giannobile, W. V., Squarize, C. H., Larsson, L., et al. (2020). Characterization of macrophages infiltrating peri-implantitis lesions. *Clin. Oral Implants Res.* 31 (3), 274–281. doi:10.1111/clr.13568

Fu, X., Liu, G., Halim, A., Ju, Y., Luo, Q., and Song, A. G. (2019). Mesenchymal stem cell migration and tissue repair. *Cells* 8 (8), 784. doi:10.3390/cells8080784

Fujita, E., Shimizu, A., Masuda, Y., Kuwahara, N., Arai, T., Nagasaka, S., et al. (2010). Statin attenuates experimental anti-glomerular basement membrane glomerulonephritis together with the augmentation of alternatively activated macrophages. *Am. J. Pathol.* 177 (3), 1143–1154. doi:10.2353/ajpath.2010.090608

Galarraga-Vinueza, M. E., Obreja, K., Khoury, C., Begic, A., Ramanauskaite, A., Sculean, A., et al. (2021a). Influence of macrophage polarization on the effectiveness of surgical therapy of peri-implantitis. *Int. J. Implant Dent.* 7 (1), 110. doi:10.1186/s40729-021-00391-2

Galarraga-Vinueza, M. E., Obreja, K., Ramanauskaite, A., Magini, R., Begic, A., Sader, R., et al. (2021b). Macrophage polarization in peri-implantitis lesions. *Clin. Oral Investig.* 25 (4), 2335–2344. doi:10.1007/s00784-020-03556-2

Garapaty, A., and Champion, J. A. (2019). Shape of ligand immobilized particles dominates and amplifies the macrophage cytokine response to ligands. *PLoS One* 14 (5), e0217022. doi:10.1371/journal.pone.0217022

Garlet, G. P. (2010). Destructive and protective roles of cytokines in periodontitis: a re-appraisal from host defense and tissue destruction viewpoints. *J. Dent. Res.* 89 (12), 1349–1363. doi:10.1177/0022034510376402

Garlet, G. P., and Giannobile, W. V. (2018). Macrophages: the bridge between inflammation resolution and tissue repair? *J. Dent. Res.* 97 (10), 1079–1081. doi:10.1177/0022034518785857

Garlet, G. P., Martins, W., Jr., Fonseca, B. A., Ferreira, B. R., and Silva, J. S. (2004). Matrix metalloproteinases, their physiological inhibitors and osteoclast factors are differentially regulated by the cytokine profile in human periodontal disease. *J. Clin. Periodontol.* 31 (8), 671–679. doi:10.1111/j.1600-051X.2004.00545.x

Germano, G., Frapolli, R., Simone, M., Tavecchio, M., Erba, E., Pesce, S., et al. (2010). Antitumor and anti-inflammatory effects of trabectedin on human myxoid liposarcoma cells. *Cancer Res.* 70 (6), 2235–2244. doi:10.1158/0008-5472.Can-09-2335

Gonzalez, O. A., Novak, M. J., Kirakodu, S., Stromberg, A., Nagarajan, R., Huang, C. B., et al. (2015). Differential gene expression profiles reflecting macrophage polarization in aging and periodontitis gingival tissues. *Immunol. Invest.* 44 (7), 643–664. doi:10.3109/08820139.2015.1070269

Gordon, S., and Martinez, F. O. (2010). Alternative activation of macrophages: mechanism and functions. *Immunity* 32 (5), 593–604. doi:10.1016/j.immuni.2010.05.007

Górska, R., Gregorek, H., Kowalski, J., Laskus-Perendyk, A., Syczewska, M., and Madaliński, K. (2003). Relationship between clinical parameters and cytokine profiles in inflamed gingival tissue and serum samples from patients with chronic periodontitis. *J. Clin. Periodontol.* 30 (12), 1046–1052. doi:10.1046/j.0303-6979.2003.00425.x

Graves, D. T., and Cochran, D. (2003). The contribution of interleukin-1 and tumor necrosis factor to periodontal tissue destruction. *J. Periodontol.* 74 (3), 391–401. doi:10.1902/jop.2003.74.3.391

Gualini, F., and Berglundh, T. (2003). Immunohistochemical characteristics of inflammatory lesions at implants. *J. Clin. Periodontol.* 30 (1), 14–18. doi:10.1034/j.1600-051x.2003.300103.x

Guo, X., Bai, J., Ge, G., Wang, Z., Wang, Q., Zheng, K., et al. (2022). Bioinspired peptide adhesion on Ti implants alleviates wear particle-induced inflammation and improves interfacial osteogenesis. *J. Colloid Interface Sci.* 605, 410–424. doi:10.1016/j.jcis.2021.07.079

Hassumi, M. Y., Silva-Filho, V. J., Campos-Júnior, J. C., Vieira, S. M., Cunha, F. Q., Alves, P. M., et al. (2009). PPAR-gamma agonist rosiglitazone prevents inflammatory periodontal bone loss by inhibiting osteoclastogenesis. *Int. Immunopharmacol.* 9 (10), 1150–1158. doi:10.1016/j.intimp.2009.06.002

He, W., Zhang, N., and Lin, Z. (2021). MicroRNA-125a-5p modulates macrophage polarization by targeting E26 transformation-specific variant 6 gene during orthodontic tooth movement. *Arch. Oral Biol.* 124, 105060. doi:10.1016/j.archoralbio.2021.105060

Heyman, O., Horev, Y., Koren, N., Barel, O., Aizenbud, I., Aizenbud, Y., et al. (2020). Niche specific microbiota-dependent and independent bone loss around dental implants and teeth. *J. Dent. Res.* 99 (9), 1092–1101. doi:10.1177/0022034520920577

Heyman, O., Horev, Y., Mizraji, G., Haviv, Y., Shapira, L., and Wilensky, A. (2022). Excessive inflammatory response to infection in experimental peri-implantitis: resolution by Resolvin D2. *J. Clin. Periodontol.* 49, 1217–1228. doi:10.1111/jcpe.13631

Heyman, O., Koren, N., Mizraji, G., Capucha, T., Wald, S., Nassar, M., et al. (2018). Impaired differentiation of Langerhans cells in the murine oral epithelium adjacent to titanium dental implants. *Front. Immunol.* 9, 1712. doi:10.3389/fimmu.2018.01712

Higuchi, K., Sm, Z., Yamashita, Y., Ozaki, Y., and Yoshimura, A. (2020). Initial periodontal treatment affects nucleotide-binding domain leucine-rich repeat-containing protein 3 inflammasome priming in peripheral blood mononuclear cells. *Arch. Oral Biol.* 110, 104625. doi:10.1016/j.archoralbio.2019.104625

Holmlund, A., Hänström, L., and Lerner, U. H. (2004). Bone resorbing activity and cytokine levels in gingival crevicular fluid before and after treatment of periodontal disease. *J. Clin. Periodontol.* 31 (6), 475–482. doi:10.1111/j.1600-051X.2004.00504.x

Huang, Y., Tian, C., Li, Q., and Xu, Q. (2019). TET1 knockdown inhibits Porphyromonas gingivalis LPS/IFN-γ-Induced M1 macrophage polarization through the NF-κB pathway in THP-1 cells. *Int. J. Mol. Sci.* 20 (8), 2023. doi:10.3390/ijms20082023

Huangfu, H., Du, S., Zhang, H., Wang, H., Zhang, Y., Yang, Z., et al. (2023). Facile engineering of resveratrol nanoparticles loaded with 20(S)-protopanaxadiol for the treatment of periodontitis by regulating the macrophage phenotype. *Nanoscale* 15 (17), 7894–7908. doi:10.1039/d2nr06452a

Irshad, M., Scheres, N., Crielaard, W., Loos, B. G., Wismeijer, D., and Laine, M. L. (2013). Influence of titanium on *in vitro* fibroblast-Porphyromonas gingivalis interaction in peri-implantitis. *J. Clin. Periodontol.* 40 (9), 841–849. doi:10.1111/jcpe.12136

Irwin, C. R., and Myrillas, T. T. (1998). The role of IL-6 in the pathogenesis of periodontal disease. *Oral Dis.* 4 (1), 43–47. doi:10.1111/j.1601-0825.1998.tb00255.x

Irwin, C. R., Myrillas, T. T., Traynor, P., Leadbetter, N., and Cawston, T. E. (2002). The role of soluble interleukin (IL)-6 receptor in mediating the effects of IL-6 on matrix metalloproteinase-1 and tissue inhibitor of metalloproteinase-1 expression by gingival fibroblasts. *J. Periodontol.* 73 (7), 741–747. doi:10.1902/jop.2002.73.7.741

Karatas, O., Balci Yuce, H., Taskan, M. M., Gevrek, F., Lafci, E., and Kasap, H. (2020). Histological evaluation of peri-implant mucosal and gingival tissues in peri-implantitis, peri-implant mucositis and periodontitis patients: a cross-sectional clinical study. *Acta Odontol. Scand.* 78 (4), 241–249. doi:10.1080/00016357.2019.1691256

Koldsland, O. C., Scheie, A. A., and Aass, A. M. (2010). Prevalence of peri-implantitis related to severity of the disease with different degrees of bone loss. *J. Periodontol.* 81 (2), 231–238. doi:10.1902/jop.2009.090269

Koutouzis, T., Eastman, C., Chukkapalli, S., Larjava, H., and Kesavalu, L. (2017). A novel rat model of polymicrobial peri-implantitis: a preliminary study. *J. Periodontol.* 88 (2), e32–e41. doi:10.1902/jop.2016.160273

Kumar, P. S., Mason, M. R., Brooker, M. R., and O'Brien, K. (2012). Pyrosequencing reveals unique microbial signatures associated with healthy and failing dental implants. *J. Clin. Periodontol.* 39 (5), 425–433. doi:10.1111/j.1600-051X.2012.01856.x

Lam, R. S., O'Brien-Simpson, N. M., Lenzo, J. C., Holden, J. A., Brammar, G. C., Walsh, K. A., et al. (2014). Macrophage depletion abates Porphyromonas gingivalis-induced alveolar bone resorption in mice. *J. Immunol.* 193 (5), 2349–2362. doi:10.4049/jimmunol.1400853

Lappin, D. F., MacLeod, C. P., Kerr, A., Mitchell, T., and Kinane, D. F. (2001). Anti-inflammatory cytokine IL-10 and T cell cytokine profile in periodontitis granulation tissue. *Clin. Exp. Immunol.* 123 (2), 294–300. doi:10.1046/j.1365-2249.2001.01448.x

Larsson, L., Kavanagh, N. M., Nguyen, T. V. N., Castilho, R. M., Berglundh, T., and Giannobile, W. V. (2022). Influence of epigenetics on periodontitis and peri-implantitis pathogenesis. *Periodontol* 90, 125–137. doi:10.1111/prd.12453

Li, J., Liu, Y., Lai, W., Song, L., Deng, J., Li, C., et al. (2023a). MicroRNA-126 regulates macrophage polarization to prevent the resorption of alveolar bone in diabetic periodontitis. *Arch. Oral Biol.* 150, 105686. doi:10.1016/j.archoralbio.2023.105686

Li, Y., Zhang, J., Wang, C., Jiang, Z., Lai, K., Wang, Y., et al. (2023b). Porous composite hydrogels with improved MSC survival for robust epithelial sealing around implants and M2 macrophage polarization. *Acta Biomater.* 157, 108–123. doi:10.1016/j.actbio.2022.11.029

Liang, B., Wang, H., Wu, D., and Wang, Z. (2021). Macrophage M1/M2 polarization dynamically adapts to changes in microenvironment and modulates alveolar bone remodeling after dental implantation. *J. Leukoc. Biol.* 110 (3), 433–447. doi:10.1002/jlb.1ma0121-001r

Lu, M., Sarruf, D. A., Talukdar, S., Sharma, S., Li, P., Bandyopadhyay, G., et al. (2011). Brain PPAR-γ promotes obesity and is required for the insulin-sensitizing effect of thiazolidinediones. *Nat. Med.* 17 (5), 618–622. doi:10.1038/nm.2332

Luo, H., Chen, D., Li, R., Li, R., Teng, Y., Cao, Y., et al. (2023). Genetically engineered CXCR4-modified exosomes for delivery of miR-126 mimics to macrophages alleviate periodontitis. *J. Nanobiotechnology* 21 (1), 116. doi:10.1186/s12951-023-01863-w

Martinez, F. O., Sica, A., Mantovani, A., and Locati, M. (2008). Macrophage activation and polarization. *Front. Biosci.* 13, 453–461. doi:10.2741/2692

Mayer, Y., Balbir-Gurman, A., and Machtei, E. E. (2009). Anti-tumor necrosis factor-alpha therapy and periodontal parameters in patients with rheumatoid arthritis. *J. Periodontol.* 80 (9), 1414–1420. doi:10.1902/jop.2009.090015

McInnes, I. B., and Schett, G. (2007). Cytokines in the pathogenesis of rheumatoid arthritis. *Nat. Rev. Immunol.* 7 (6), 429–442. doi:10.1038/nri2094

Metzger, Z. (2000). Macrophages in periapical lesions. *Endod. Dent. Traumatol.* 16 (1), 1–8. doi:10.1034/j.1600-9657.2000.016001001.x

Ming, P., Liu, Y., Yu, P., Jiang, X., Yuan, L., Cai, S., et al. (2023). A biomimetic Se-nHA/PC composite microsphere with synergistic immunomodulatory and osteogenic ability to activate bone regeneration in periodontitis. *Small*, e2305490. doi:10.1002/smll.202305490

Monje, A., Pons, R., Insua, A., Nart, J., Wang, H. L., and Schwarz, F. (2019). Morphology and severity of peri-implantitis bone defects. *Clin. Implant Dent. Relat. Res.* 21 (4), 635–643. doi:10.1111/cid.12791

Morris, D. L., Singer, K., and Lumeng, C. N. (2011). Adipose tissue macrophages: phenotypic plasticity and diversity in lean and obese states. *Curr. Opin. Clin. Nutr. Metab. Care* 14 (4), 341–346. doi:10.1097/MCO.0b013e328347970b

Mosser, D. M., and Edwards, J. P. (2008). Exploring the full spectrum of macrophage activation. *Nat. Rev. Immunol.* 8 (12), 958–969. doi:10.1038/nri2448

Nakao, Y., Fukuda, T., Zhang, Q., Sanui, T., Shinjo, T., Kou, X., et al. (2021). Exosomes from TNF-α-treated human gingiva-derived MSCs enhance M2 macrophage polarization and inhibit periodontal bone loss. *Acta Biomater.* 122, 306–324. doi:10.1016/j.actbio.2020.12.046

Ni, C., Zhou, J., Kong, N., Bian, T., Zhang, Y., Huang, X., et al. (2019). Gold nanoparticles modulate the crosstalk between macrophages and periodontal ligament cells for periodontitis treatment. *Biomaterials* 206, 115–132. doi:10.1016/j.biomaterials.2019.03.039

Obreja, K., Ramanauskaite, A., Begic, A., Galarraga-Vinueza, M. E., Parvini, P., Sader, R., et al. (2021). The prevalence of peri-implant diseases around subcrestally placed implants: a cross-sectional study. *Clin. Oral Implants Res.* 32 (6), 702–710. doi:10.1111/clr.13739

Oka, H., Miyauchi, M., Sakamoto, K., Moriwaki, S., Niida, S., Noguchi, K., et al. (2007). PGE2 activates cementoclastogenesis by cementoblasts via EP4. *J. Dent. Res.* 86 (10), 974–979. doi:10.1177/154405910708601011

Okuda-Shimazaki, J., Takaku, S., Kanehira, K., Sonezaki, S., and Taniguchi, A. (2010). Effects of titanium dioxide nanoparticle aggregate size on gene expression. *Int. J. Mol. Sci.* 11 (6), 2383–2392. doi:10.3390/ijms11062383

Olmedo, D. G., Paparella, M. L., Spielberg, M., Brandizzi, D., Guglielmotti, M. B., and Cabrini, R. L. (2012). Oral mucosa tissue response to titanium cover screws. *J. Periodontol.* 83 (8), 973–980. doi:10.1902/jop.2011.110392

Ortiz, P., Bissada, N. F., Palomo, L., Han, Y. W., Al-Zahrani, M. S., Panneerselvam, A., et al. (2009). Periodontal therapy reduces the severity of active rheumatoid arthritis in patients treated with or without tumor necrosis factor inhibitors. *J. Periodontol.* 80 (4), 535–540. doi:10.1902/jop.2009.080447

Palevski, D., Levin-Kotler, L. P., Kain, D., Naftali-Shani, N., Landa, N., Ben-Mordechai, T., et al. (2017). Loss of macrophage wnt secretion improves remodeling and function after myocardial infarction in mice. *J. Am. Heart Assoc.* 6 (1), e004387. doi:10.1161/jaha.116.004387

Park, M. D., Silvin, A., Ginhoux, F., and Merad, M. (2022). Macrophages in health and disease. *Cell* 185 (23), 4259–4279. doi:10.1016/j.cell.2022.10.007

Pers, J. O., Saraux, A., Pierre, R., and Youinou, P. (2008). Anti–TNF-α immunotherapy is associated with increased gingival inflammation without clinical attachment loss in subjects with rheumatoid arthritis. *J. Periodontol.* 79 (9), 1645–1651. doi:10.1902/jop.2008.070616

Pettersson, M., Kelk, P., Belibasakis, G. N., Bylund, D., Molin Thorén, M., and Johansson, A. (2017). Titanium ions form particles that activate and execute interleukin-1β release from lipopolysaccharide-primed macrophages. *J. Periodontal Res.* 52 (1), 21–32. doi:10.1111/jre.12364

Pirih, F. Q., Hiyari, S., Leung, H. Y., Barroso, A. D., Jorge, A. C., Perussolo, J., et al. (2015). A murine model of lipopolysaccharide-induced peri-implant mucositis and peri-implantitis. *J. Oral Implantol.* 41 (5), e158–e164. doi:10.1563/aaid-joi-D-14-00068

Pizarek, J. A., Fischer, N. G., and Aparicio, C. (2023). Immunomodulatory IL-23 receptor antagonist peptide nanocoatings for implant soft tissue healing. *Dent. Mater* 39, 204–216. doi:10.1016/j.dental.2023.01.001

Pongnarisorn, N. J., Gemmell, E., Tan, A. E., Henry, P. J., Marshall, R. I., and Seymour, G. J. (2007). Inflammation associated with implants with different surface types. *Clin. Oral Implants Res.* 18 (1), 114–125. doi:10.1111/j.1600-0501.2006.01304.x

Ramenzoni, L. L., Fluckiger, L. B., Attin, T., and Schmidlin, P. R. (2021). Effect of titanium and zirconium oxide microparticles on pro-inflammatory response in human macrophages under induced sterile inflammation: an *in vitro* study. *Mater. (Basel)* 14 (15), 4166. doi:10.3390/ma14154166

Renvert, S., Persson, G. R., Pirih, F. Q., and Camargo, P. M. (2018). Peri-implant health, peri-implant mucositis, and peri-implantitis: case definitions and diagnostic considerations. *J. Periodontol.* 89 (1), S304–S312. doi:10.1002/JPER.17-0588

Renvert, S., Roos-Jansåker, A. M., Lindahl, C., Renvert, H., and Rutger Persson, G. (2007). Infection at titanium implants with or without a clinical diagnosis of inflammation. *Clin. Oral Implants Res.* 18 (4), 509–516. doi:10.1111/j.1600-0501.2007.01378.x

Revell, P. A. (2008). The combined role of wear particles, macrophages and lymphocytes in the loosening of total joint prostheses. *J. R. Soc. Interface* 5 (28), 1263–1278. doi:10.1098/rsif.2008.0142

Rinke, S., Ohl, S., Ziebolz, D., Lange, K., and Eickholz, P. (2011). Prevalence of periimplant disease in partially edentulous patients: a practice-based cross-sectional study. *Clin. Oral Implants Res.* 22 (8), 826–833. doi:10.1111/j.1600-0501.2010.02061.x

Roos-Jansåker, A. M., Lindahl, C., Renvert, H., and Renvert, S. (2006). Nine-to fourteen-year follow-up of implant treatment. Part II: presence of peri-implant lesions. *J. Clin. Periodontol.* 33 (4), 290–295. doi:10.1111/j.1600-051X.2006.00906.x

Ruiz-Heiland, G., Yong, J. W., von Bremen, J., and Ruf, S. (2021). Leptin reduces *in vitro* cementoblast mineralization and survival as well as induces PGE2 release by ERK1/2 commitment. *Clin. Oral Investig.* 25 (4), 1933–1944. doi:10.1007/s00784-020-03501-3

Sasaki, H., Okamatsu, Y., Kawai, T., Kent, R., Taubman, M., and Stashenko, P. (2004). The interleukin-10 knockout mouse is highly susceptible to Porphyromonas gingivalis-induced alveolar bone loss. *J. Periodontal Res.* 39 (6), 432–441. doi:10.1111/j.1600-0765.2004.00760.x

Schlegel, K. A., Eppeneder, S., and Wiltfang, J. (2002). Soft tissue findings above submerged titanium implants--a histological and spectroscopic study. *Biomaterials* 23 (14), 2939–2944. doi:10.1016/s0142-9612(01)00423-9

Shaddox, L. M., Wiedey, J., Calderon, N. L., Magnusson, I., Bimstein, E., Bidwell, J. A., et al. (2011). Local inflammatory markers and systemic endotoxin in aggressive periodontitis. *J. Dent. Res.* 90 (9), 1140–1144. doi:10.1177/0022034511413928

Shafizadeh, M., Amid, R., Mahmoum, M., and Kadkhodazadeh, M. (2021). Histopathological characterization of peri-implant diseases: a systematic review and meta-analysis. *Arch. Oral Biol.* 132, 105288. doi:10.1016/j.archoralbio.2021.105288

Shen, Z., Kuang, S., Zhang, Y., Yang, M., Qin, W., Shi, X., et al. (2020). Chitosan hydrogel incorporated with dental pulp stem cell-derived exosomes alleviates periodontitis in mice via a macrophage-dependent mechanism. *Bioact. Mater* 5 (4), 1113–1126. doi:10.1016/j.bioactmat.2020.07.002

Sica, A., and Mantovani, A. (2012). Macrophage plasticity and polarization: *in vivo* veritas. *J. Clin. Invest.* 122 (3), 787–795. doi:10.1172/JCI59643

Sima, C., and Glogauer, M. (2013). Macrophage subsets and osteoimmunology: tuning of the immunological recognition and effector systems that maintain alveolar bone. *Periodontol* 63 (1), 80–101. doi:10.1111/prd.12032

Stashenko, P., Jandinski, J. J., Fujiyoshi, P., Rynar, J., and Socransky, S. S. (1991). Tissue levels of bone resorptive cytokines in periodontal disease. *J. Periodontol.* 62 (8), 504–509. doi:10.1902/jop.1991.62.8.504

Stienstra, R., Duval, C., Keshtkar, S., van der Laak, J., Kersten, S., and Müller, M. (2008). Peroxisome proliferator-activated receptor gamma activation promotes infiltration of alternatively activated macrophages into adipose tissue. *J. Biol. Chem.* 283 (33), 22620–22627. doi:10.1074/jbc.M710314200

Sun, X., Gao, J., Meng, X., Lu, X., Zhang, L., and Chen, R. (2021a). Polarized macrophages in periodontitis: characteristics, function, and molecular signaling. *Front. Immunol.* 12, 763334. doi:10.3389/fimmu.2021.763334

Sun, Y., Sun, X., Li, X., Li, W., Li, C., Zhou, Y., et al. (2021b). A versatile nanocomposite based on nanoceria for antibacterial enhancement and protection from aPDT-aggravated inflammation via modulation of macrophage polarization. *Biomaterials* 268, 120614. doi:10.1016/j.biomaterials.2020.120614

Tomasi, C., Tessarolo, F., Caola, I., Piccoli, F., Wennstrom, J. L., Nollo, G., et al. (2016). Early healing of peri-implant mucosa in man. *J. Clin. Periodontol.* 43 (10), 816–824. doi:10.1111/jcpe.12591

Tonetti, M. S., Greenwell, H., and Kornman, K. S. (2018). Staging and grading of periodontitis: framework and proposal of a new classification and case definition. *J. Clin. Periodontol.* 45, S149–s161. doi:10.1111/jcpe.12945

Tzach-Nahman, R., Mizraji, G., Shapira, L., Nussbaum, G., and Wilensky, A. (2017). Oral infection with Porphyromonas gingivalis induces peri-implantitis in a murine model: evaluation of bone loss and the local inflammatory response. *J. Clin. Periodontol.* 44 (7), 739–748. doi:10.1111/jcpe.12735

Viniegra, A., Goldberg, H., Çil, Ç., Fine, N., Sheikh, Z., Galli, M., et al. (2018). Resolving macrophages counter osteolysis by anabolic actions on bone cells. *J. Dent. Res.* 97 (10), 1160–1169. doi:10.1177/0022034518777973

Vodovotz, Y., Bogdan, C., Paik, J., Xie, Q. W., and Nathan, C. (1993). Mechanisms of suppression of macrophage nitric oxide release by transforming growth factor beta. *J. Exp. Med.* 178 (2), 605–613. doi:10.1084/jem.178.2.605

Wang, H., Wang, D., Huangfu, H., Chen, S., Qin, Q., Ren, S., et al. (2023a). Highly efficient photothermal branched Au-Ag nanoparticles containing procyanidins for synergistic antibacterial and anti-inflammatory immunotherapy. *Biomater. Sci.* 11 (4), 1335–1349. doi:10.1039/d2bm01212j

Wang, Y., Li, C., Wan, Y., Qi, M., Chen, Q., Sun, Y., et al. (2021). Quercetin-loaded ceria nanocomposite potentiate dual-directional immunoregulation via macrophage polarization against periodontal inflammation. *Small* 17 (41), e2101505. doi:10.1002/smll.202101505

Wang, Y., Lin, Q., Zhang, H., Wang, S., Cui, J., Hu, Y., et al. (2023b). M2 macrophage-derived exosomes promote diabetic fracture healing by acting as an immunomodulator. *Bioact. Mater* 28, 273–283. doi:10.1016/j.bioactmat.2023.05.018

Wang, Z., Maruyama, K., Sakisaka, Y., Suzuki, S., Tada, H., Suto, M., et al. (2019). Cyclic stretch force induces periodontal ligament cells to secrete exosomes that suppress IL-1β production through the inhibition of the NF-κB signaling pathway in macrophages. *Front. Immunol.* 10, 1310. doi:10.3389/fimmu.2019.01310

Whitaker, R., Hernaez-Estrada, B., Hernandez, R. M., Santos-Vizcaino, E., and Spiller, K. L. (2021). Immunomodulatory biomaterials for tissue repair. *Chem. Rev.* 121 (18), 11305–11335. doi:10.1021/acs.chemrev.0c00895

Wilson, T. G., Jr., Valderrama, P., Burbano, M., Blansett, J., Levine, R., Kessler, H., et al. (2015). Foreign bodies associated with peri-implantitis human biopsies. *J. Periodontol.* 86 (1), 9–15. doi:10.1902/jop.2014.140363

Wu, J., Yu, P., Lv, H., Yang, S., and Wu, Z. (2020a). Nanostructured zirconia surfaces regulate human gingival fibroblasts behavior through differential modulation of macrophage polarization. *Front. Bioeng. Biotechnol.* 8, 611684. doi:10.3389/fbioe.2020.611684

Wu, X., Chen, H., Wang, Y., and Gu, Y. (2020b). Akt2 affects periodontal inflammation via altering the M1/M2 ratio. *J. Dent. Res.* 99 (5), 577–587. doi:10.1177/0022034520910127

Wu, X., Wang, Y., Chen, H., Wang, Y., and Gu, Y. (2023). Phosphatase and tensin homologue determine inflammatory status by differentially regulating the expression of Akt1 and Akt2 in macrophage alternative polarization of periodontitis. *J. Clin. Periodontol.* 50 (2), 220–231. doi:10.1111/jcpe.13730

Wynn, T. A., Chawla, A., and Pollard, J. W. (2013). Macrophage biology in development, homeostasis and disease. *Nature* 496 (7446), 445–455. doi:10.1038/nature12034

Wynn, T. A., and Vannella, K. M. (2016). Macrophages in tissue repair, regeneration, and fibrosis. *Immunity* 44 (3), 450–462. doi:10.1016/j.immuni.2016.02.015

Xiao, L., Feng, M., Chen, C., Xiao, Q., Cui, Y., and Zhang, Y. (2023). Microenvironment-regulating drug delivery nanoparticles for treating and preventing typical biofilm-induced oral diseases. *Adv. Mater*, e2304982. doi:10.1002/adma.202304982

Yang, J., Zhu, Y., Duan, D., Wang, P., Xin, Y., Bai, L., et al. (2018). Enhanced activity of macrophage M1/M2 phenotypes in periodontitis. *Arch. Oral Biol.* 96, 234–242. doi:10.1016/j.archoralbio.2017.03.006

Yang, L., Tao, W., Xie, C., Chen, Q., Zhao, Y., Zhang, L., et al. (2023). Interleukin-37 ameliorates periodontitis development by inhibiting NLRP3 inflammasome activation and modulating M1/M2 macrophage polarization. *J. Periodontal Res*. doi:10.1111/jre.13196

Yang, Y., Lin, Y., Zhang, Z., Xu, R., Yu, X., and Deng, F. (2021). Micro/nano-net guides M2-pattern macrophage cytoskeleton distribution via Src-ROCK signalling for enhanced angiogenesis. *Biomater. Sci.* 9 (9), 3334–3347. doi:10.1039/d1bm00116g

Yu, T., Zhao, L., Huang, X., Ma, C., Wang, Y., Zhang, J., et al. (2016). Enhanced activity of the macrophage M1/M2 phenotypes and phenotypic switch to M1 in periodontal infection. *J. Periodontol.* 87 (9), 1092–1102. doi:10.1902/jop.2016.160081

Zhou, L. N., Bi, C. S., Gao, L. N., An, Y., Chen, F., and Chen, F. M. (2019). Macrophage polarization in human gingival tissue in response to periodontal disease. *Oral Dis.* 25 (1), 265–273. doi:10.1111/odi.12983

Zhuang, Z., Yoshizawa-Smith, S., Glowacki, A., Maltos, K., Pacheco, C., Shehabeldin, M., et al. (2019). Induction of M2 macrophages prevents bone loss in murine periodontitis models. *J. Dent. Res.* 98 (2), 200–208. doi:10.1177/0022034518805984

Zwerina, J., Redlich, K., Schett, G., and Smolen, J. S. (2005). Pathogenesis of rheumatoid arthritis: targeting cytokines. *Ann. N. Y. Acad. Sci.* 1051, 716–729. doi:10.1196/annals.1361.116

Frontiers in
Bioengineering and Biotechnology

Accelerates the development of therapies, devices, and technologies to improve our lives

A multidisciplinary journal that accelerates the development of biological therapies, devices, processes and technologies to improve our lives by bridging the gap between discoveries and their application.

Discover the latest Research Topics

See more →

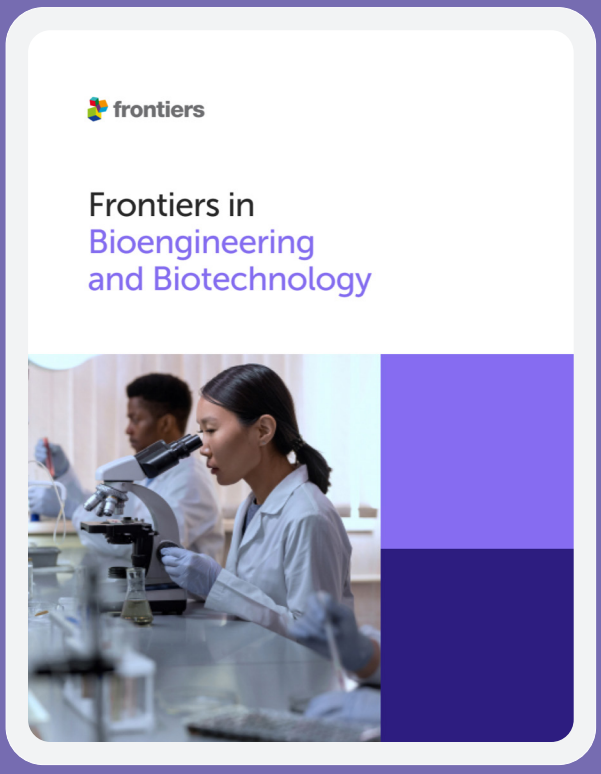

Frontiers

Avenue du Tribunal-Fédéral 34
1005 Lausanne, Switzerland
frontiersin.org

Contact us

+41 (0)21 510 17 00
frontiersin.org/about/contact